

# Hall D / GlueX Technical Design Report



March 20, 2014

## **Abstract**

Experiment GlueX is dedicated to the light meson spectroscopy. The main goal is to search and map out the spectrum of light hybrid mesons with exotic quantum numbers. The experiment is the main motivation for building of a new experimental hall at Jefferson Lab - Hall D, for physics with a linearly-polarized photon beam.

F. Barbosa, G. Biallas, E. Chudakov, C. Cuevas, H. Egiyan, M. Ito, D. Lawrence,  
L. Pentchev, Y. Qiang, E. Smith, A. Somov, S. Taylor, T. Whitlatch, E. Wolin, G. Young,  
B. Zihlmann, and C. Zorn  
*Jefferson Lab, Newport News, VA 23606*

D. Fassouliotis, P. Ioannou, and Ch. Kourkoumelis  
*University of Athens (Athens, Greece)*

G. B. Franklin, N. Jarvis, W. Levine, P. Mattione, M. McCracken, and C. A. Meyer (GlueX  
spokesperson)  
*Carnegie Mellon University (Pittsburgh, PA)*

F. J. Klein and D. Sober  
*Catholic University of America (Washington, D. C.)*

E. Brash and D. Doughty  
*Christopher Newport University (Newport News, VA)*

R. Jones and I. Senderovich  
*University of Connecticut (Storrs, CT)*

W. Boeglin, L. Guo, P. Khetarpal, and E. Pooser,  
*Florida International University (Miami, FL)*

V. Crede, P. Eugenio, A. Ostrovidov, and N. Sparks  
*Florida State University (Tallahassee, FL)*

D. Bennett, J. Bennett, M. Kornicer, R. Mitchell, K. Moriya, B. Schaefer, M. Shepherd,  
A. Szczepaniak, C. Tarbert, and G. Visser  
*Indiana University (Bloomington, IN)*

J. Dudek  
*Old Dominion University (Norfolk, VA)*

A. Gasparian  
*University of North Carolina A&T (A&T State, NC)*

L. Gan  
*University of North Carolina (Wilmington, NC)*

R. Miskimen  
*University of Massachusetts (Amherst, MA)*

G. Huber, S. Katsaganis, D. Kolybaba, G. Lolos, Z. Papandreou, E. Plummer, A. Semenov,  
I. Semenova, and M. Tahani  
*University of Regina (Regina, Saskatchewan, Canada)*

W. Brooks, S. Kuleshov and A. Toro  
*Santa Maria University (Valparaiso, Chile)*

T. Barnes  
*University of Tennessee (Knoxville, TN)*

# Contents

# Chapter 1

## Scientific Goals

### 1.1 Introduction

The primary goal of the GLUEX project is the definitive and detailed mapping of the spectrum of a new family of particles called *hybrid mesons*. Linearly polarized photons produced by electrons from an energy-upgraded CEBAF will be the probe used to uncover this spectrum. This experimental information is absolutely critical in finding the answer to an outstanding and fundamental questions in physics – a quantitative understanding of the confinement mechanism in quantum chromodynamics.

The spectrum of mesons and baryons uncovered during the 1960's led to the quark model within which mesons are bound states of a quark and antiquark,  $q\bar{q}$ , and baryons are bound states of three quarks,  $qqq$ . Further experimental work indicated that quarks are dynamical objects as well and this led to the development of quantum chromodynamics (QCD), the theory of quarks and gluons and their interactions modeled after the very successful theory of quantum electrodynamics (QED). Just as charged particles interact by the exchange of photons, quarks, with their color charge, interact by exchanging gluons. There are however important and fundamental differences between the two theories. There are three types of color charge as opposed to one kind of electrical charge. And the gluons of QCD also carry color charge and can interact with quarks and each other. In contrast, the photons of QED do not carry charge. Bound states involving quarks and gluons or quarks alone are thus possible and indeed should exist. QCD also incorporates the experimental fact that the quarks and gluons do not exist as free particles by requiring that only color singlet combinations exist as free particles in nature. In addition to the color singlet combinations  $q\bar{q}$  and  $qqq$  others are possible, such as  $q\bar{q}g$  (*hybrid mesons*) and  $gg$  or  $ggg$  (*glueballs*). These new states, collectively known as *gluonic excitations*, are fascinating since this is the only case of a theory in which the gauge particle is also a constituent. The analogous states in QED, like atoms of light, cannot exist. Although there is tantalizing evidence for these gluonic excitations, their spectra have not been mapped out.

The confinement of quarks and gluons within the particles of which they are the constituents is a unique feature of QCD. But a quantitative understanding of the confinement mechanism still eludes us. Theoretical progress is being made and lattice QCD, based on first-principle calculations, will ultimately be able to predict a detailed spectrum, including masses and decays, of hybrid mesons and glueballs. The experimental information about the spectrum of this new form of matter as predicted by QCD is an essential ingredient for the ultimate understanding of the confinement mechanism.

The low-lying glueball states will be searched for in the glue-rich  $J/\psi$  radiative decays as part of the planned CLEO-c project at Cornell's CESR. However the low-lying glueballs possess  $J^{PC}$  quantum numbers that are the same as  $q\bar{q}$  states and therefore mixing with conventional  $q\bar{q}$  mesons is possible and that can complicate glueball identification. In contrast, hybrid mesons can possess  $J^{PC}$  quantum numbers not possible for  $q\bar{q}$ . These *exotic hybrid mesons* thus have a *smoking gun signature*. Just as nonets of  $q\bar{q}$  mesons made of the three light quarks ( $u$ ,  $d$  and  $s$ ) exist, nature should also reveal nonets of hybrids with the same flavor quantum numbers but with now with the possibility of exotic  $J^{PC}$ . Hybrid mesons should also have widths comparable to conventional mesons. This is supported by theoretical considerations and by the possible sighting of an exotic hybrid in  $\pi^-$ -induced interactions.

Hybrid mesons can be thought of as  $q\bar{q}g$  bound states in which the gluon is a constituent. An attractive alternative picture is one in which a gluonic flux tube forms between the  $q$  and  $\bar{q}$  in a meson. This flux tube forms because of the self-interaction of the gluons and qualitatively accounts for confinement. It leads to a linear potential, or a force that is constant as the distance between the quark and anti-quark varies. Infinite energy is required to separate the quarks to infinity, thus qualitatively accounting for confinement. This notion of a relativistic string or flux tube between the quarks was introduced in the 1970's to account for the observed linear dependence of particle mass-squared ( $m^2$ ) on spin ( $J$ ). The flux tube concept is supported by lattice QCD studies. Within this picture conventional mesons result when the flux tube is in its ground state. Hybrid mesons arise when the flux tube is excited. The lack of information on this spectroscopy is due in part to the complicated decay modes favored by these states. Another is due to the apparent suppression of exotic hybrid mesons in production mechanisms with  $\pi$  or  $K$  probes. On the other hand production of exotic hybrid mesons is expected to be favored using beams of photons and essentially no data exist on the photoproduction of light mesons. The GLUEX project will remedy this situation.

In addition to providing for a linearly polarized photon beam of sufficient energy, the GLUEX project includes construction of a hermetic detector to allow for particle identification and momentum and energy determination sufficient to allow for complete kinematic reconstruction of events with a wide variety of final states. This is essential for the spin analysis – partial wave analysis (PWA) – needed to determine the  $J^{PC}$  quantum numbers, to map out the flavor quantum numbers of the hybrid nonets and to test assumptions about the details of confinement that would lead to predicting specific decay modes.

In this chapter we expand on the following:

1. *Spectroscopy of Light Mesons*. This will include a brief review of the conventional quark model and the status of the light quark meson spectrum.
2. *Gluonic excitations and the role in QCD*. This will include a discussion of how the gluons form flux tubes, and how their excitations lead to QCD mesons, in particular exotic hybrids. This general picture is not restricted to a particular model but follows from the first-principles QCD calculations.
3. *The current evidence for gluonic excitations*. The evidence comes from overpopulation of conventional nonets and from possible glueball and exotic hybrid sightings in  $\bar{p}p$  annihilations and  $\pi$ -induced interactions.
4. *Photons are expected to be particularly effective in producing exotic hybrids*. Its spin structure makes the photon a qualitatively different probe from  $\pi$  and  $K$  beams. The

first excited transverse modes of the flux tube can lead to exotic hybrids only when the quark spins are aligned. This argument is consistent with expectations from models based on phenomenological analysis of existing data that predict cross sections for photoproduction of exotic hybrids comparable to those of normal mesons. And there are essentially no data on photoproduction of light mesons so this is *terra incognita*. The existing photoproduction data will be discussed.

5. *The complementarity of this study with other planned projects that will study gluonic excitations.* We will compare this to searches in the charm quark or beauty quark sectors or  $e^+e^-$  annihilations, in particular the GSI Project and the CLEO-c Project at Cornell.
6. *The importance of the PWA technique in uncovering exotic mesons.* The PWA is a powerful analysis tool that has been successfully employed in experiments to uncover states which are not evident from a simple examination of mass spectra (bump-hunting). PWA is absolutely essential for this project as is the development of the formalism for incident photon beams and an understanding of the phenomenology. The importance of a hermetic detector with excellent resolution and rate capability and sensitivity to a wide variety of decay modes will be discussed.
7. *Linear polarization of the photon beam is essential for this study.* Linear polarization is important in the determination of the  $J^{PC}$  quantum numbers and it is essential in determining the production mechanism. Linear polarization can be used as a filter for exotics once the production mechanism is isolated.
8. *The ideal photon energy range.* In order to reach the desired mass range we need to be far enough above threshold so that the decay products of produced mesons can be detected and measured with sufficient precision. High enough energies are also important to avoid line-shape distortions of higher-mass mesons. We also want to be high enough in energy to kinematically separate production of baryon resonances from production of meson resonances. This need for higher energies, however is balanced by a need for sufficiently low energy to allow for a solenoid-only-based detector to momentum analyze the highest energy charged particles with sufficient accuracy. These considerations lead to an ideal photon energy in the range from 8 to 9  $GeV$ .
9. *The desired electron energy.* Having established the desired photon beam energy of 9  $GeV$  an electron energy must be sufficiently high compared to the desired photon beam energy to achieve a sufficient degree of linear polarization. With 12  $GeV$  electrons, the degree of linear polarization is 40%. If the electron energy drops to 10  $GeV$  the degree of polarization drops to 5%. The ratio of tagged hadronic rate to total hadronic rate in the detector drops as the electron energy approaches the desired photon energy. The conclusion is that an electron energy of 12  $GeV$  suffices but lower energies will severely compromise the physics goals.

## 1.2 Conventional light mesons

The early version of the quark model described the observed mesons as bound states of a quark and antiquark, where the quarks were assumed to be the  $u$ ,  $d$  and  $s$  quarks. Thus mesons were grouped in families with nine members – a nonet – characterized by a given  $J^{PC}$  determined

by the relative spin of the two quarks and their relative orbital angular momentum. Within the nonet three are members of an isotriplet with zero strangeness. Two are members of an isodoublet with positive strangeness and another two with negative strangeness. And the remaining two members have zero strangeness and isospin. This flavor pattern holds for all the nonets. Radial excitations are also allowed.

The rules for allowed values of  $J^{PC}$  follow from the requirements of a fermion–antifermion system: the quark spins can be parallel ( $S = 1$ ) or antiparallel ( $S = 0$ ) with relative orbital angular momentum ( $L$ ),  $\vec{J} = \vec{L} + \vec{S}$ ,  $P = (-1)^{L+1}$  and  $C = (-1)^{L+S}$ . Thus the low-lying nonet with  $\vec{L} = 0$  and  $\vec{S} = 0$  leads to  $J^{PC} = 0^{-+}$ , the pseudoscalar nonet, including the  $\pi$ ,  $K$ ,  $\eta$  and  $\eta'$  mesons. The nonet with  $\vec{L} = 0$  and  $\vec{S} = 1$  leads to  $J^{PC} = 1^{--}$ , the vector mesons, including the  $\rho$ ,  $K^*$ ,  $\omega$  and  $\phi$  mesons. The combination  $\vec{L} = 1$  and  $\vec{S} = 1$  leads to three nonets: scalar ( $J^{PC} = 0^{++}$ ), axial vector ( $J^{PC} = 1^{++}$ ) and tensor ( $J^{PC} = 2^{++}$ ).

Using the rules for determining  $J^{PC}$  for a fermion–antifermion system, certain  $J^{PC}$  combinations are not allowed for  $q\bar{q}$  systems and these include  $J^{PC} = 0^{--}, 0^{+-}, 1^{-+}, 2^{+-}, \dots$ . Such combinations are referred to as *exotic* quantum numbers. Indeed, that such combinations were not initially observed gave credence to the quark model.

Figure ?? shows our current knowledge of conventional  $q\bar{q}$  states. The exact association of an observed meson with a particular  $q\bar{q}$  state within a nonet depends on a good understanding of the various decay modes of the meson as well as its mass, width and production characteristics. Figure ?? also shows the expected range of masses for glueballs, hybrid mesons and meson-meson molecular states. These will be described in more detail below.

The range of masses of the known conventional meson nonets and their radial excitations extend from the  $\pi$  mass up to about  $2.5 \text{ GeV}/c^2$ . Figure ?? shows the spectrum of  $q\bar{q}$  states in more detail including radial excitations. There is also now clear evidence that the observed meson spectrum includes states which cannot be accommodated within the naive quark model. For example, there are at least five scalar states reported with masses below  $2 \text{ GeV}/c^2$ . These, along with indications of exotic  $J^{PC}$  sightings will be discussed below.

### 1.3 Gluonic excitations and confinement

The Standard Model of elementary particles includes electroweak theory and QCD, the latter describing the strong interactions among the quarks and gluons. At short distances – the regime of asymptotic freedom – perturbative techniques are applicable and QCD describes high energy experimental phenomena and data both qualitatively and quantitatively. At large distance scales – the confinement regime – the situation is far different. Here the successful calculational techniques of the perturbative regime cannot be used. We must rely on first-principles lattice QCD calculations or QCD-inspired models. There has been significant theoretical effort in this area recently and more progress can be expected in the near future, especially as multi-teraflop lattice QCD centers come into operation.

Understanding confinement in QCD requires a detailed understanding of the role of gluons. QCD is distinct from QED in that the force carriers of the former (gluons) carry color charge whereas for the latter the photons are electrically neutral. As illustrated in Figure ??, the force between two electrically charged particles falls off like the inverse square of the distance between the charges. The number of field lines intersecting a unit area midway between the charges and perpendicular to the line connecting them would decrease as the inverse square of the distance between the charges. In contrast, the color field lines between a quark and

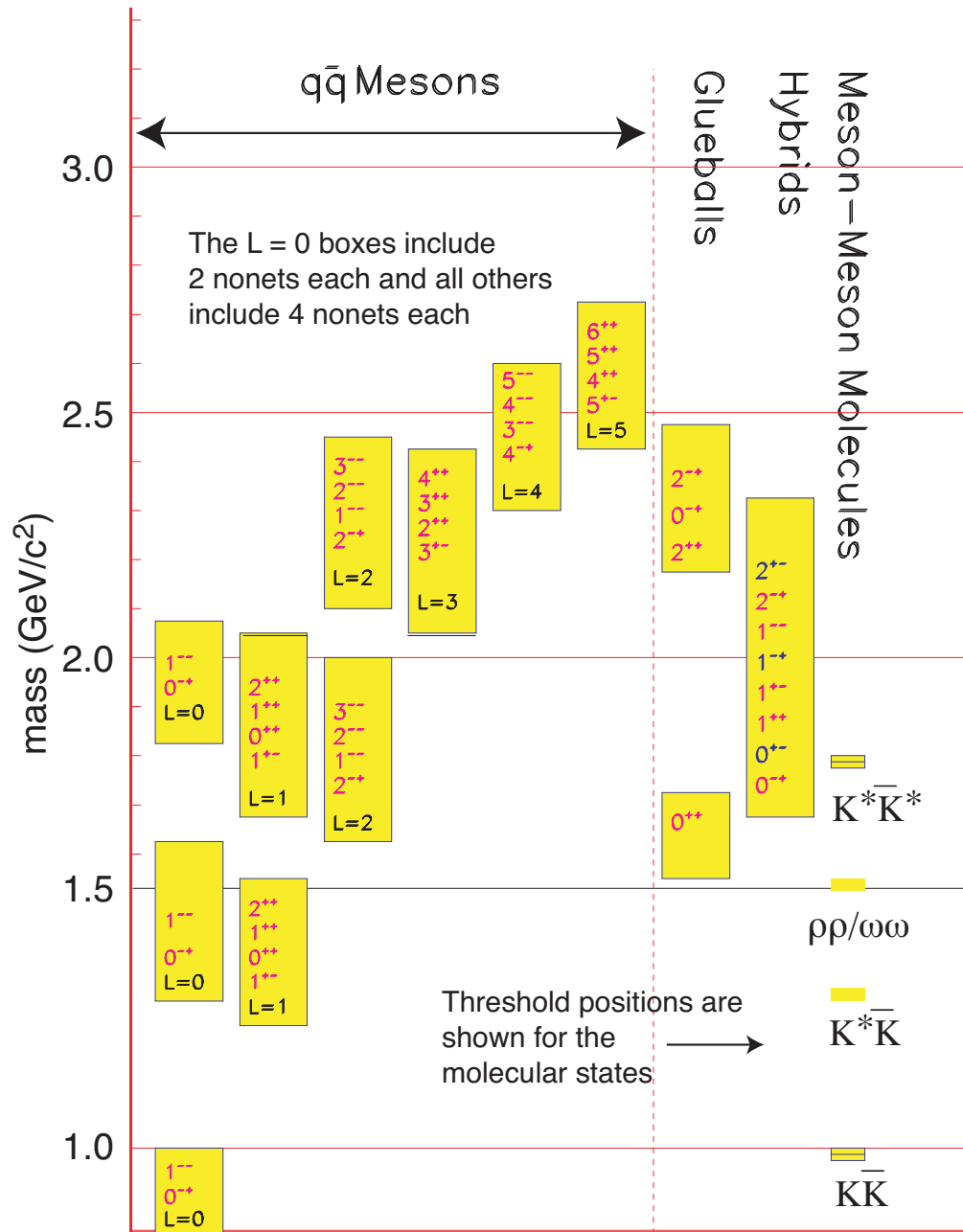


Figure 1.1: A level diagram showing conventional nonets and expected masses of glueballs, hybrids and molecular thresholds. The vertical axis is in units of  $\text{GeV}/c^2$ . For the  $q\bar{q}$  boxes the  $L$  refers to the angular momentum between the quarks and each  $J^{PC}$  refers to a nonet of mesons. Note also that exotic  $J^{PC}$ ,  $-0^{+-}$ ,  $1^{-+}$ ,  $2^{+-}$  – occur only among the hybrids for the range of masses shown.

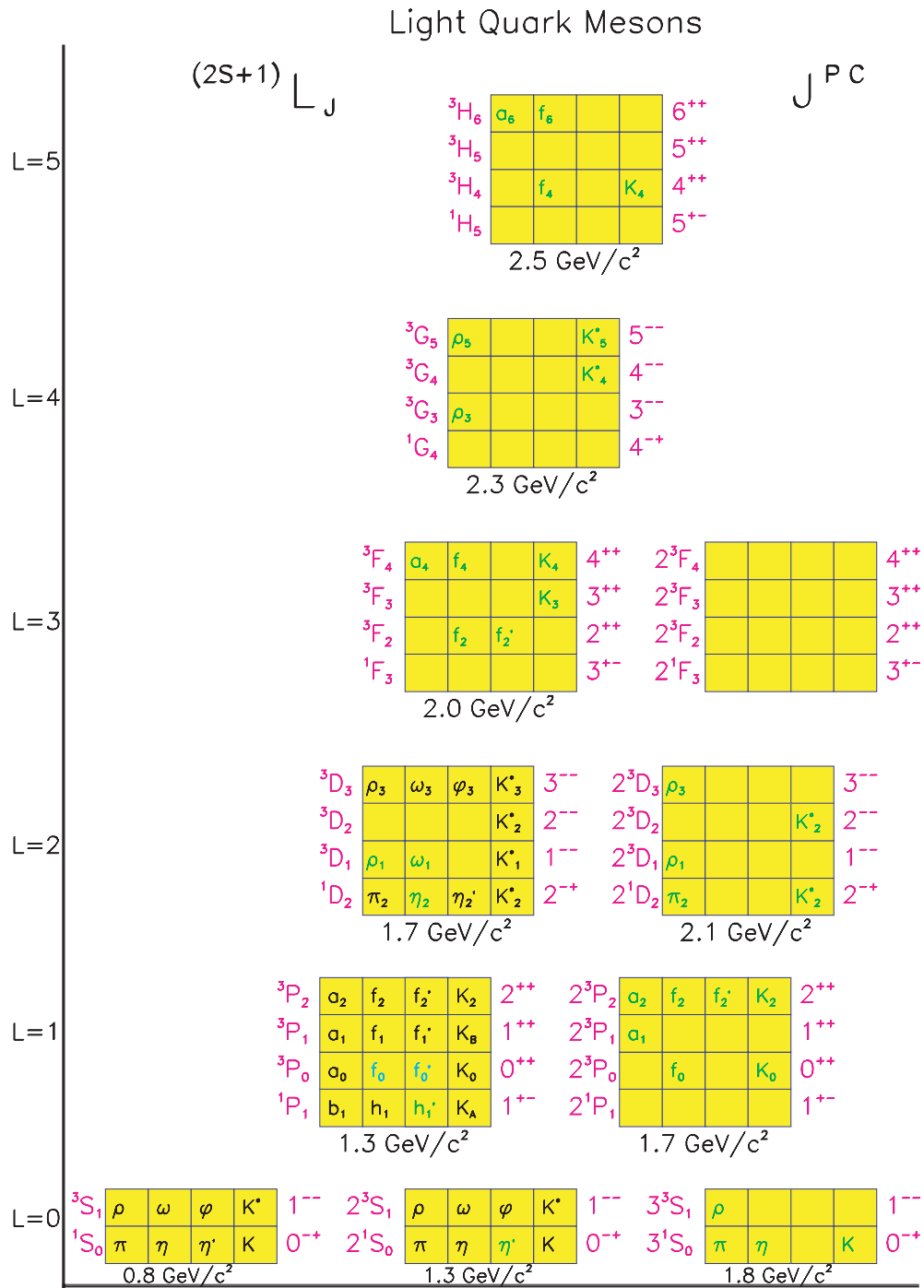


Figure 1.2: The  $q\bar{q}$  spectrum of states. The assignments of the light colored states are speculative, while the empty boxes are missing states. The orbital angular momentum of the nonet is plotted on the vertical axis, while the towers of radial excitations are shown along the horizontal axis.

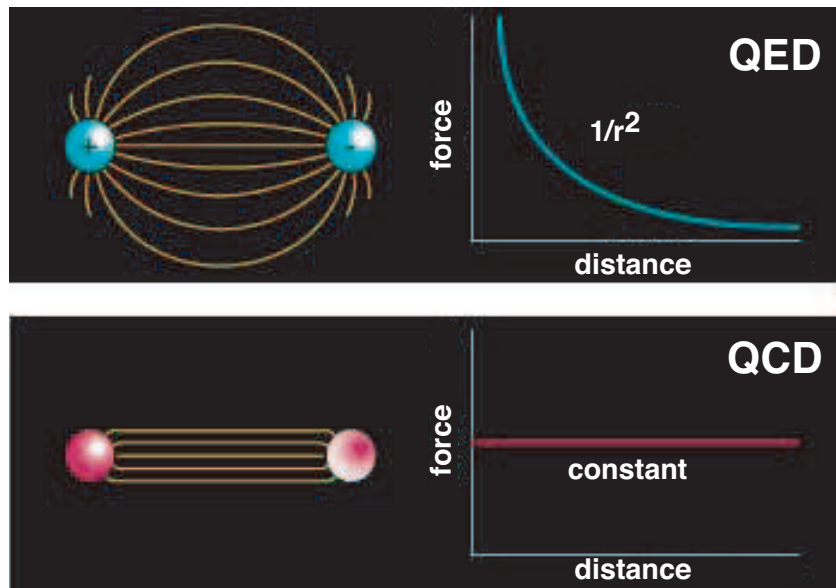


Figure 1.3: Field lines associated with the electrical force between two electrically charged particles (top) and the corresponding dependence of force on the distance between the charges and the field lines associated with the color force (bottom) between two quarks and the corresponding dependence of force on distance.

an anti-quark do not fill all of space as in the case with electrical charges. Rather the field lines form flux tubes. A unit area placed midway between the quarks and perpendicular to the line connecting them intercepts a constant number of field lines, independent of the distance between the quarks. This leads to a constant force between the quarks – and a large force at that, equal to about 16 metric tons. The potential associated with this constant force is linear and grows with increasing distance. It takes infinite energy to separate the quarks to infinity and thus, qualitatively at least, this accounts for confinement.

Lattice QCD calculations support this notion of the formation of a flux tube between the quark and anti-quark. Figure ?? shows the energy density in the color field between a quark and an anti-quark in a meson with a separation of  $1.2 \text{ fermi}$ . The density peaks at the positions of the quarks and is confined to a tube between the quarks. This calculation is for heavy quarks in the quenched approximation. Figure ?? also shows the corresponding potential between the quarks. The ground state potential has a  $1/r$  dependence at small distances and is linear for large distances.

This notion of the formation of flux tubes was first introduced in the 1970's by Yoichiro Nambu [?] to explain the observed linear Regge trajectories – the linear dependence of mass squared,  $m^2$ , of hadrons on their spin,  $J$ . This linear dependence results if one assumes that massless quarks are tied to the ends of a relativistic string with constant mass (energy) per length with the system rotating about its center. The linear  $m^2$  versus  $J$  dependence only arises when the mass density per length is constant, which is equivalent to a linear potential.

Within this picture, conventional mesons arise when the flux tube is in its ground state. Excitations of the flux tube lead to hybrid mesons that exhibit both the quark and gluonic

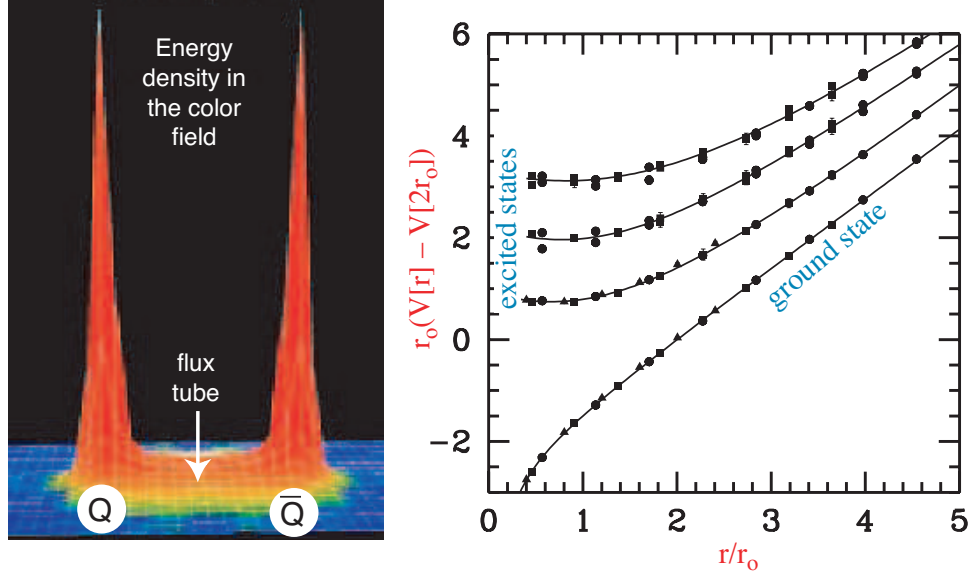


Figure 1.4: (left) A lattice QCD calculation of the energy density in the color field between a quark and an anti-quark. The density peaks at the positions of the quarks and is confined to a tube between the quarks. This calculation is for heavy quarks in the quenched approximation. (right) The corresponding potential between the quarks. The ground state potential has a  $1/r$  dependence at small distances and is linear for large distances.

degrees of freedom. The first excited state of the flux tube is a transverse excitation. The flux tube, or string, spins clockwise or counter-clockwise around the  $q\bar{q}$  line leading to two degenerate states – degenerate since the energy should not depend on which way the flux tube is spinning. Lattice QCD and flux tube models both indicate that the lowest excited flux tube has  $J = 1$  [?, ?, ?]. The linear combinations of the clockwise or counter-clockwise rotations are eigenstates of parity and charge conjugation leading to two possibilities for the excited flux tube:  $J^{PC} = 1^{-+}$  or  $J^{PC} = 1^{+-}$ . Suppose we start with the  $q\bar{q}$  in the  $S = 0$  and  $L = 0$  (or  $J^{PC} = 0^{-+}$  – the  $\pi$  or  $K$ ) configuration. Combining this with  $J^{PC} = 1^{-+}$  or  $J^{PC} = 1^{+-}$  of the excited flux tube results in hybrid mesons with  $J^{PC} = 1^{++}$  or  $J^{PC} = 1^{--}$ . These are non-exotic quantum numbers. If, however, we start with  $q\bar{q}$  in the  $S = 1$  and  $L = 0$  (or  $J^{PC} = 1^{--}$  – the vector photon) configuration, the resulting hybrid meson can have  $J^{PC} = [0, 1, 2]^{+-}$  for the flux tube with  $J^{PC} = 1^{-+}$  and  $J^{PC} = [0, 1, 2]^{-+}$  for the flux tube with  $J^{PC} = 1^{+-}$ . We note that of these six possible  $J^{PC}$  combinations, three are exotic:  $J^{PC} = 0^{+-}$ ,  $J^{PC} = 1^{-+}$  and  $J^{PC} = 2^{+-}$ . These states will not mix with  $q\bar{q}$  and thus have unique signatures.

Meson production proceeds with an incoming probe interacting with the target particle and one result of the scattering can be the excitation of the flux tube. If the probe is a  $q\bar{q}$  in  $L = 0$  and  $S = 0$  ( $\pi$  or  $K$ ), production of exotic hybrids will not be favored. But if the  $q\bar{q}$  probe has  $L = 0$  and  $S = 1$ , for example a photon, one expects exotic hybrids to be produced readily.

Finally we consider the expected masses for hybrid mesons. We would expect the mass difference between the ground state (conventional) mesons and hybrid mesons to be given by the level spacing between the ground state of the flux tube and the first excited transverse mode and that is simply given by  $\pi/r$  where  $r$  is the quark separation. When translated to

appropriate units this corresponds to about  $1 \text{ GeV}/c^2$ .

In this discussion the motion of the quarks was ignored, but we know from general principles [?] that an approximation that ignores the impact of the flux tube excitation and quark motion on each other seems to work quite well.

## 1.4 Observation of gluonic excitations

### 1.4.1 Glueballs

Lattice QCD calculations indicate that lightest glueball is a scalar with a mass in the range from  $1.5$  to  $1.7 \text{ GeV}/c^2$  [?, ?, ?, ?]. Indeed there is evidence from the Crystal Barrel experiment, which studied  $\bar{p}p$  annihilations at CERN, that the  $f_0(1500)$  is a leading candidate for a glueball [?, ?]. There are, however, indications that this state is not a pure glueball but is mixed with conventional  $q\bar{q}$  [?]. There are also strong indications that the scalar meson sector contains one or more glueballs since there are several more observed states than can be accommodated in the simple  $q\bar{q}$  model. However, the unique identification of a glueball is exacerbated by the possibility of mixing with  $q\bar{q}$ . Lattice QCD indicates a rich spectrum of glueballs, all with non-exotic quantum numbers, from  $1.5$  to  $2.5 \text{ GeV}/c^2$ . The lightest glueball with exotic quantum numbers is predicted to have  $J^{PC} = 2^{+-}$  and to have a mass of  $4 \text{ GeV}/c^2$  [?].

### 1.4.2 Exotic hybrid mesons

After about two decades of experimental searches there have been reports of experimental observations of states with exotic  $J^{PC} = 1^{-+}$  by the Brookhaven E852 collaboration in  $\pi^-p$  interactions at  $18 \text{ GeV}/c$ . One of these has a mass of  $(1593 \pm 8_{-47}^{+29}) \text{ MeV}/c^2$  and width of  $(168 \pm 20_{-12}^{+150}) \text{ MeV}/c^2$  and decays into  $\rho^0\pi^-$  [?].

This state was observed in the reaction  $\pi^-p \rightarrow \pi^+\pi^-\pi^-p$  at a beam momentum of  $18 \text{ GeV}/c$ . In Figure ??, the acceptance-corrected (average acceptance was 25%) distributions of the  $\pi^+\pi^-\pi^-$  and  $\pi^+\pi^-$  effective masses are shown. The positions of well-established meson states are shown, including the  $a_1(1260)$ , which does not show up as a prominent peak in the overall mass distribution. The partial wave analysis (PWA) performed on these data assumes an *isobar model* – a parent decaying into a  $\pi\pi$  state and an unpaired  $\pi$  followed by the decay of the  $\pi\pi$  state. The resulting decomposition into various waves is shown in Figure ?. The decomposition clearly shows the  $\pi(1800)$  in the  $0^{-+}$  wave, the  $a_1(1260)$  in the  $1^{++}$  wave, the  $\pi_2(1670)$  in the  $2^{-+}$  wave, and the  $a_2(1320)$  in the  $2^{++}$  wave. Evidence for the exotic  $1^{-+} \rho\pi$  is shown in Figure ?. If an isovector  $\rho\pi$  resonates in an  $L = 1$  wave, it has  $J^{PC} = 1^{-+}$ . Also shown in this figure is the effect of leakage of non-exotic waves. Finally in Figure ?? a coupled fit to the wave intensities and phase difference between the  $1^{-+}$  and  $2^{-+}$  waves is shown.

Another state reported by E852 has a similar mass,  $(1597 \pm 10_{-10}^{+45}) \text{ MeV}/c^2$ , but with a significantly larger width,  $(340 \pm 40_{-50}^{+50}) \text{ MeV}/c^2$ , and decays into  $\eta'\pi^-$  [?]. It has not been determined whether these represent two decay modes of the same state or whether they are due to two different mechanisms.

The E852 collaboration also reported observation of another  $J^{PC} = 1^{-+}$  state with mass  $(1370 \pm 16_{-30}^{+50}) \text{ MeV}/c^2$  and a width of  $(385 \pm 40_{-105}^{+65}) \text{ MeV}/c^2$  decaying into  $\eta\pi^-$  [?]. If an  $\eta\pi$  system is in a  $P$  wave, the resulting  $J^{PC}$  quantum number combination is exotic ( $1^{-+}$ ). In these studies the dominant state observed in the  $\eta\pi$  channel is the  $J^{PC} = 2^{++} a_2(1320)$

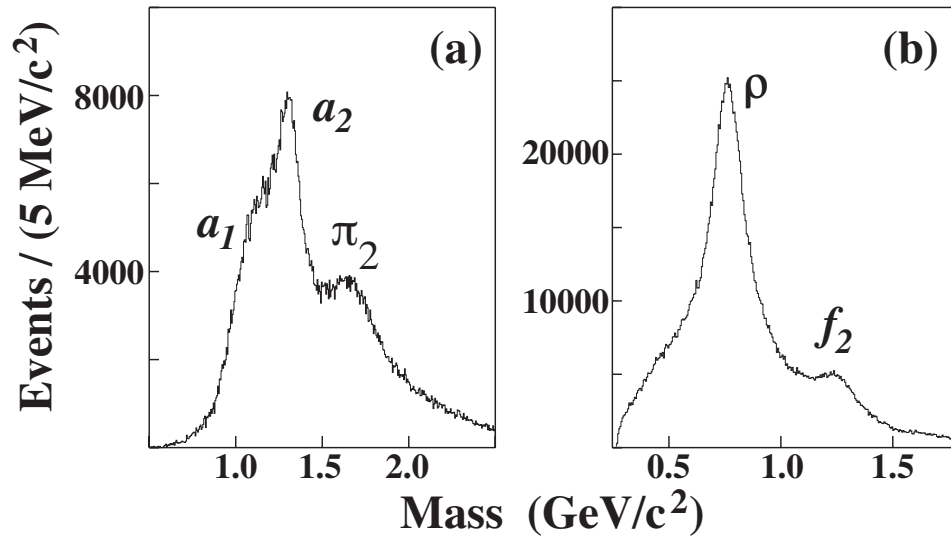


Figure 1.5: Acceptance corrected effective mass distributions for the (a)  $\pi^+\pi^-\pi^-$  combination and (b)  $\pi^+\pi^-$  combination (two entries per event) from E852 [?].

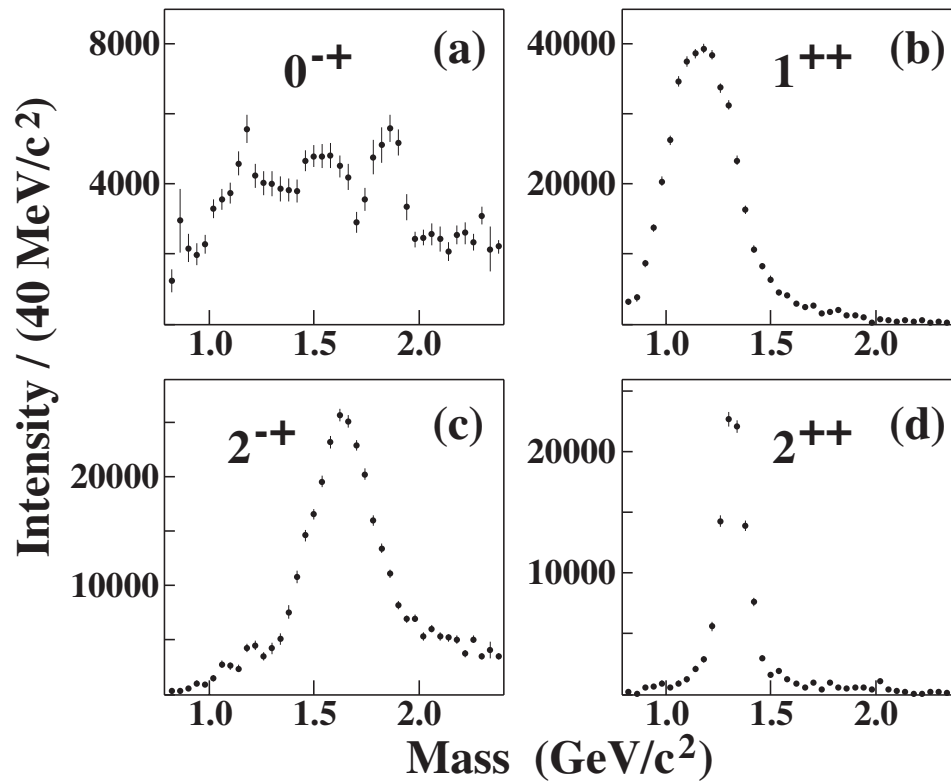


Figure 1.6: Combined intensities for all (a)  $0^{-+}$  waves; (b)  $1^{++}$  waves; (c)  $2^{-+}$  waves; and (d)  $2^{++}$  waves from E852 [?].

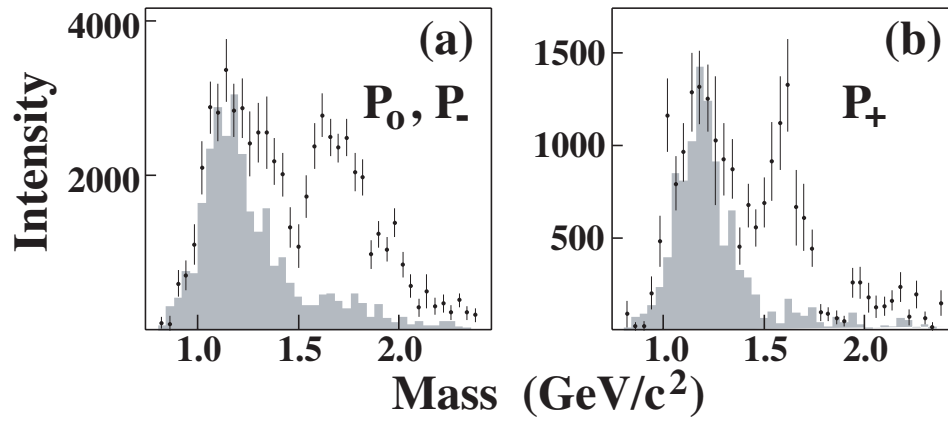


Figure 1.7: The intensities for the waves corresponding to  $1^{-+}$  into  $\rho\pi$ . The shaded distributions are an estimate of leakage due to non-exotic waves – from E852 [?].

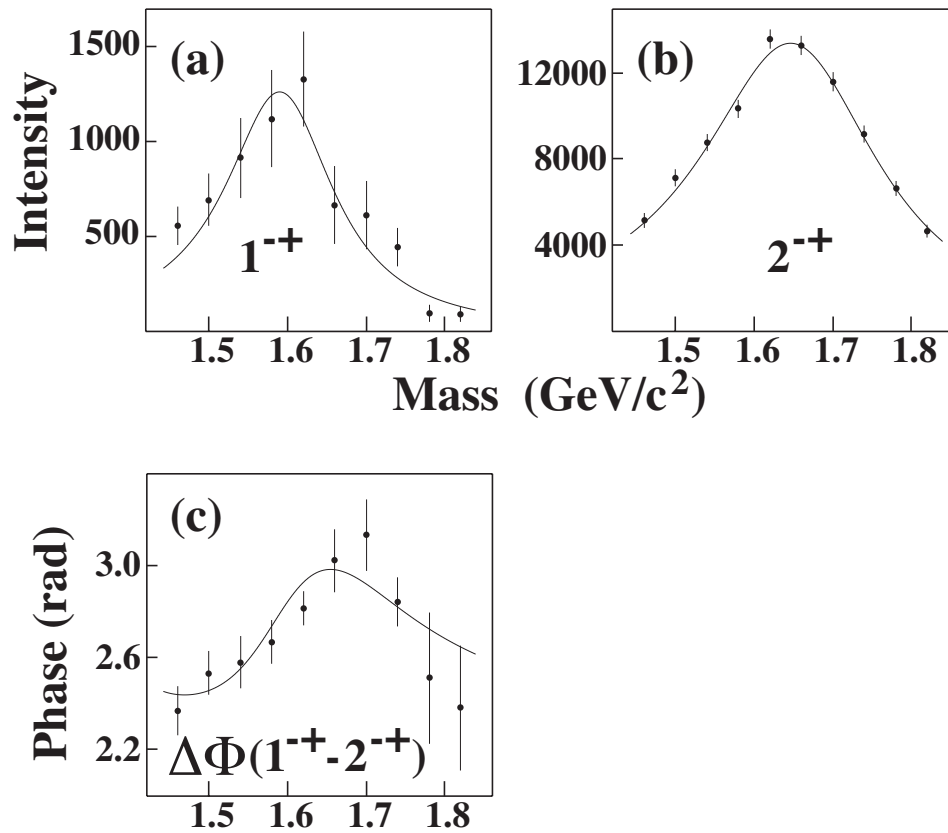


Figure 1.8: Results of a coupled mass-dependent Breit-Wigner fit of the  $1^{-+}$  and  $2^{-+}$  waves showing the phase difference as well – from E852 [?].

seen in the  $D$ -wave. Critical to the identification of this state is not only showing the presence of a  $P$ -wave, but also that the resulting line shape is consistent with a Breit-Wigner and that the phase motion of the  $P$ , as determined by its interference with the dominant  $D$ -wave, cannot be due solely to the  $a_2^-(1320)$  resonance. Soon after the E852 report, the Crystal Barrel Collaboration reported an exotic  $J^{PC} = 1^{-+}$  state produced in  $\bar{p}n \rightarrow \pi^-\pi^0\eta$  obtained by stopping antiprotons in liquid deuterium [?]. They reported a mass of  $(1400 \pm 20_{-20}^{+20}) \text{ MeV}/c^2$  and a width of  $(310 \pm 50_{-30}^{+50}) \text{ MeV}/c^2$ .

The first claim of an exotic meson decaying into  $\eta\pi^0$  with a mass of  $1400 \text{ MeV}/c^2$  was made by the GAMS collaboration in the reaction  $\pi^-p \rightarrow \eta\pi^0n$  [?] but a later analysis by the group [?] led to ambiguous results. The VES collaboration also presented evidence for a  $P$ -wave contribution in  $\eta\pi$  [?] and at KEK a claim was made for an exotic  $\eta\pi$  state [?] as well, but with a mass and width close to that of the  $a_2(1320)$ ; leakage from the dominant  $D$  wave could not be excluded.

In all the observations in  $\pi$ -induced reactions, the  $\eta\pi$   $P$ -wave enhancements have cross sections that are substantially smaller than the dominant  $a_2(1320)$  so this leakage, usually due to an imperfect understanding of experimental acceptance, is a source of concern. In contrast, the observed yield of the  $\pi_1(1400)$  yield in  $\bar{p}p$  annihilations is of the same magnitude as the  $a_2(1320)$ . Apart from these experimental issues, the interpretation of the nature of low-mass  $\eta\pi$   $P$ -wave amplitude and phase motion should be guided by the principle of parsimony – less exotic interpretations must also be considered. In a recent analysis of the  $\eta\pi^0$  system in the reaction  $\pi^-p \rightarrow \eta\pi^0n$  from data using the E852 apparatus, a  $P$ -wave is observed but it is not consistent with a Breit-Wigner resonance. The observed  $P$ -wave phase motion is consistent with  $\eta\pi^0$  final state interactions. This could explain the relatively wide width of the observed  $\eta\pi^-$  state and could also explain the broad  $\eta'\pi^-$  enhancement. The  $\pi^-p \rightarrow \eta\pi^0n$  and  $\pi^-p \rightarrow \eta\pi^-p$  have some notable differences. For the former charge conjugation ( $C$ ) is a good quantum number but not for the latter and for the former both the  $a_0(980)$  and  $a_2(1320)$  are prominently present but for the latter only the  $a_2(1320)$  is strongly produced. This is an important factor in selecting the physical solutions among mathematically ambiguous solutions.

The conclusion from these studies is that there indeed are tantalizing hints of gluonic excitations in both the glueball and hybrid sectors but the results are not conclusive. The large statistics samples of high quality data to be collected with the GLUEX detector will provide the definite resolution of the murky situation. Furthermore there is good reason to believe that whereas exotic hybrids may be suppressed in  $\pi$  production, they are enhanced in photoproduction where essentially no data exist. In the glueball sector, the large samples of glue-rich radiative  $J/\psi$  decays should shed light on the spectrum of these gluonic excitations.

## 1.5 Photoproduction of exotic hybrids

### 1.5.1 Why photoproduction?

Based on the arguments presented above, the photon is expected to be particularly effective in producing the *smoking gun* signature for gluonic excitations: hybrids with exotic  $J^{PC}$ . In this regard, we will compare the effectiveness of the  $\pi$  or  $K$  as a probe with that of the photon. In the former case, the meson is a  $q\bar{q}$  with spins anti-aligned ( $S = 0$ ) and in the latter, the photon is a virtual  $q\bar{q}$  with spins aligned ( $S = 1$ ). In both cases, the relative orbital angular momentum is zero ( $L = 0$ ) and the flux tube connecting the quarks is in its ground state.

Figure ?? illustrates the differences between a  $\pi$  probe and a  $\gamma$  probe. If the scattering results in excitation of the flux tube, one expects exotic hybrid mesons to be suppressed in  $\pi$ -induced interactions and enhanced in photoproduction.

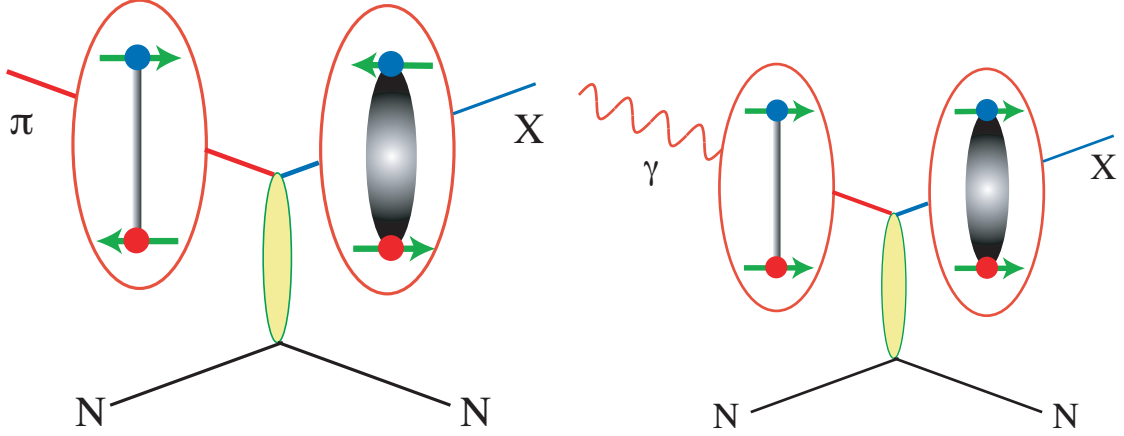


Figure 1.9: (left) With a  $\pi$  probe the incoming quarks have  $L = 0$  and  $S = 0$ . The excited flux tube from the scattering results in hybrid mesons with non-exotic quantum numbers. (right) With a photon probe the incoming quarks have  $L = 0$  and  $S = 1$ . When the flux tube is excited, hybrid mesons with exotic quantum numbers are possible.

Current phenomenology also supports the notion that photons should be more effective at producing exotic hybrids [?, ?]. Figure ?? shows an estimate of the photoproduction cross sections at 8  $GeV$  for the  $a_2(1320)$  and the exotic  $\pi_1(1600)$  [?]. The model uses as input the ratio of  $\pi_1(1600)$  to  $a_2(1320)$  as observed in E852. The model is compared with photoproduction of the  $a_2(1320)$  at 5  $GeV$ . Whereas in E852, with a  $\pi$  beam, the  $\pi_1(1600)$  is produced at about 5% of the rate for  $a_2(1320)$ , in photoproduction the rates for  $\pi_1(1600)$  are expected to be comparable for that of the  $a_2(1320)$ . In the case of the incident  $\pi$ , the  $\pi_1(1600)$  is produced by  $\rho$  exchange and the suppression at very low- $|t|$  due to angular momentum – spin 0 in and spin 1 out – decreases the cross section. This is to be compared to photoproduction of the  $\pi_1(1600)$  with  $\pi$  exchange where there is no suppression at very low- $|t|$  since now we have spin 1 in and spin 1 out. Furthermore the  $N\rho N$  coupling at the baryon vertex in the incident  $\pi$  case is lower by a factor of 4 compared to the  $N\pi N$  in the photoproduction case.

To underscore the differences between existing photoproduction and  $\pi$  production, the corresponding largest data sets on  $3\pi$  production are compared in the plots of Figure ?. The  $3\pi$  mass spectrum from the reaction  $\pi^- p \rightarrow \pi^+ \pi^- \pi^- p$  at 18  $GeV/c$  from E852 at Brookhaven is shown. Also shown is the  $3\pi$  mass spectrum from the reaction  $\gamma p \rightarrow \pi^+ \pi^+ \pi^- n$  at 19  $GeV$  from SLAC. We note the large difference in statistics between the two and we also note the differences in the structure of the spectra.

### 1.5.2 Current photoproduction data

Table ?? is a partial compilation of known photoproduction cross sections and the numbers of events from the existing experiments. The typical cross sections range from of order 0.1  $\mu b$  up to of order 10  $\mu b$ , with most measurements involving rather small numbers of events, typically

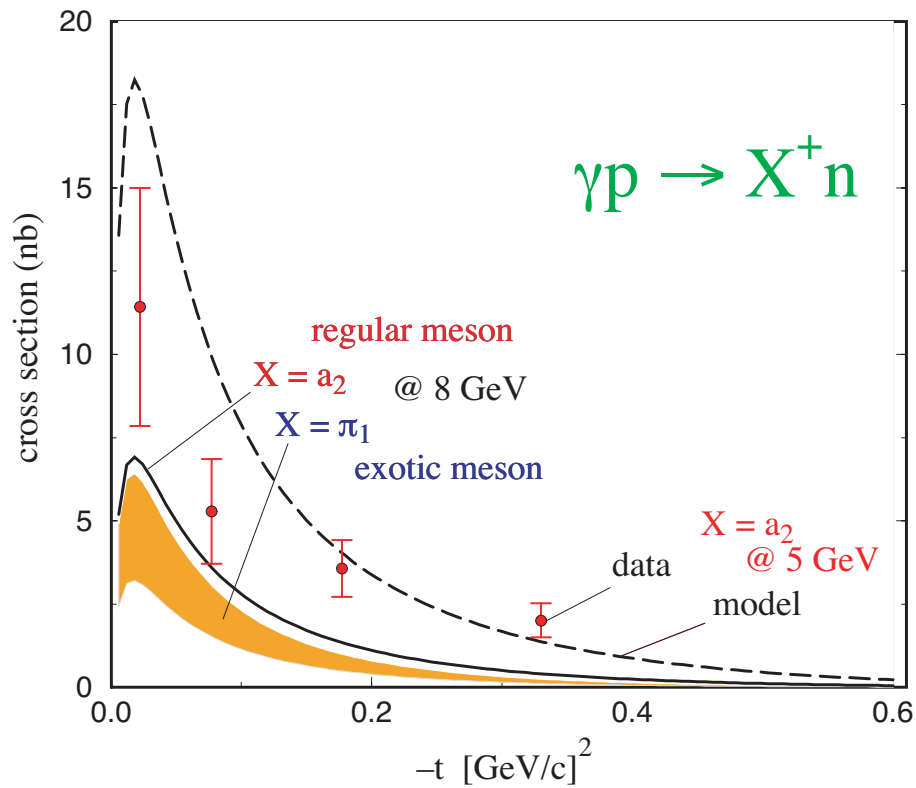


Figure 1.10: Estimates of the photoproduction cross sections for  $a_2(1320)$  and the exotic  $\pi_1(1600)$  at 8 *GeV* based on a phenomenological analysis described in [?]. The model uses as input the ratio of  $\pi_1(1600)$  to  $a_2(1320)$  as observed in E852. The model is compared with photoproduction of the  $a_2(1320)$  at 5 *GeV*.

Reaction	$E_\gamma$ GeV	$\sigma$ ( $\mu\text{b}$ )	Events	Ref.
$\gamma p \rightarrow p\pi^+\pi^-$	9.3		3500	[?]
$\gamma p \rightarrow p\pi^+\pi^-$	19.3		20908	[?]
$\gamma p \rightarrow p\pi^+\pi^-\pi^0$	2.8		2159	[?]
$\gamma p \rightarrow p\pi^+\pi^-\pi^0$	4.7		1606	[?]
$\gamma p \rightarrow p\pi^+\pi^-\pi^0$	9.3		1195	[?]
$\gamma p \rightarrow p\pi^+\pi^-\pi^0$	4.7–5.8	$13.5 \pm 1.5 \mu\text{b}$	3001	[?]
$\gamma p \rightarrow p\pi^+\pi^-\pi^0$	6.8–8.2	$11.8 \pm 1.2 \mu\text{b}$	7297	[?]
$\gamma p \rightarrow n\pi^+\pi^+\pi^-$	4.7–5.8	$4.6 \pm 1.4 \mu\text{b}$	1723	[?]
$\gamma p \rightarrow n\pi^+\pi^+\pi^-$	6.8–8.2	$4.0 \pm 1.2 \mu\text{b}$	4401	[?]
$\gamma p \rightarrow n\pi^+\pi^+\pi^-$	16.5–20		3781	[?]
$\gamma p \rightarrow p\pi^+\pi^-\pi^0$	20–70		14236	[?]
$\gamma p \rightarrow p\pi^+\pi^-\pi^+\pi^-$	4–6	$4.0 \pm 0.5 \mu\text{b}$	$\sim 330$	[?]
$\gamma p \rightarrow p\pi^+\pi^-\pi^+\pi^-$	6–8	$4.8 \pm 0.5 \mu\text{b}$	$\sim 470$	[?]
$\gamma p \rightarrow p\pi^+\pi^-\pi^+\pi^-$	8–12	$4.5 \pm 0.6 \mu\text{b}$	$\sim 470$	[?]
$\gamma p \rightarrow p\pi^+\pi^-\pi^+\pi^-$	12–18	$4.4 \pm 0.6 \mu\text{b}$	$\sim 380$	[?]
$\gamma p \rightarrow p\pi^+\pi^-\pi^+\pi^-$	15–20		6468	[?]
$\gamma p \rightarrow p\pi^+\pi^-\pi^0\pi^0$	20–70		8100	[?]
$\gamma p \rightarrow p\pi^+\pi^+\pi^-\pi^-\pi^0$	19.5		2553	[?]
$\gamma p \rightarrow \Delta^{++}\pi^-\pi^+\pi^-$	4–6	$1.65 \pm 0.2 \mu\text{b}$	$\sim 200$	[?]
$\gamma p \rightarrow \Delta^{++}\pi^-\pi^+\pi^-$	6–8	$1.8 \pm 0.2 \mu\text{b}$	$\sim 200$	[?]
$\gamma p \rightarrow \Delta^{++}\pi^-\pi^+\pi^-$	8–12	$1.1 \pm 0.2 \mu\text{b}$	$\sim 200$	[?]
$\gamma p \rightarrow \Delta^{++}\pi^-\pi^+\pi^-$	12–18	$1.15 \pm 0.2 \mu\text{b}$	$\sim 200$	[?]
$\gamma p \rightarrow p\omega$	4.7–5.8	$2.3 \pm 0.4 \mu\text{b}$	$< 1600$	[?]
$\gamma p \rightarrow p\omega$	6.8–8.2	$2.0 \pm 0.3 \mu\text{b}$	$< 1200$	[?]
$\gamma p \rightarrow p\omega$	4.7	$3.0 \pm 0.3 \mu\text{b}$	1354	[?]
$\gamma p \rightarrow p\omega$	9.3	$1.9 \pm 0.3 \mu\text{b}$	1377	[?]
$\gamma p \rightarrow p\phi$	4.7	$0.41 \pm 0.09 \mu\text{b}$	136	[?]
$\gamma p \rightarrow p\phi$	9.3	$0.55 \pm 0.07 \mu\text{b}$	224	[?]
$\gamma p \rightarrow na_2^+$	4.7–5.8	$1.7 \pm 0.9 \mu\text{b}$		[?]
$\gamma p \rightarrow na_2^+$	6.8–8.2	$0.9 \pm 0.9 \mu\text{b}$		[?]
$\gamma p \rightarrow na_2^+$	19.5	$0.29 \pm 0.06 \mu\text{b}$	$\sim 100$	[?]

Table 1.1: A sample of measured photoproduction cross sections from several references. Note the small numbers of events in any given channel.

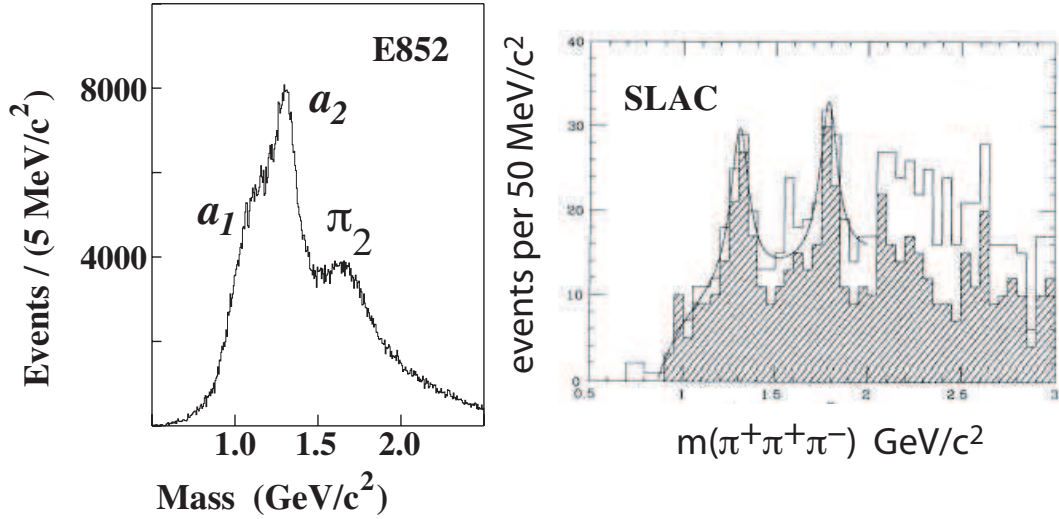


Figure 1.11: (left) The  $3\pi$  mass spectrum from the reaction  $\pi^- p \rightarrow \pi^+ \pi^- \pi^- p$  at 18 GeV/c from E852 at Brookhaven. (right) The  $3\pi$  mass spectrum from the reaction  $\gamma p \rightarrow \pi^+ \pi^+ \pi^- n$  at 19 GeV from SLAC.

on the order of a few thousand. The extant data from photoproduction are far too meager to perform the analysis necessary to unambiguously identify gluonic excitations. For example, after one year of low intensity running at  $10^7$  photons/sec, the yield of  $a_2(1320)$  in GLUEX will be five orders of magnitude greater than the same collected in the SLAC photoproduction experiment. The yield of the exotic  $\pi_1(1600)$  in the published E852 results will be increased by four orders of magnitude by GLUEX after one year of running.

There are reasonable sized data sets in  $2\pi$  and  $2\pi$  photoproduction from the CLAS detector at JLab that are currently under analysis. However, these arise from unpolarized photon beams and are produced from an incoherent Bremsstrahlung spectrum that peaks at around 5 GeV.

## 1.6 Complementarity with other searches

Gluonic excitations include both exotic and non-exotic hybrid mesons and glueballs. Hybrid mesons exist in both the light quark ( $u$ ,  $d$  and  $s$ ) and heavy quark ( $c$  and  $b$ ) sectors. Clearly, existing data collected with incident  $\pi$  beams, central collisions,  $\bar{p}p$  annihilations and  $e^+e^-$  collisions have not uncovered a wealth of information about these states. As discussed earlier, the focus of the GLUEX project is in the light-quark hybrid sector. The initial benchmark states will be the exotic hybrids, which cannot mix with  $q\bar{q}$  and therefore have a *smoking gun* signature. There are good reasons to expect that photoproduction will be particularly effective at uncovering the exotic hybrid mesons. And the existing photoproduction data are meager indeed.

The glueball and heavy hybrid sectors are not accessible to GLUEX. Glueballs are not preferentially produced in photoproduction because they do not couple to photons. Moreover, according to lattice QCD, the lightest exotic glueball has a mass of 4 GeV/c². One fruitful area of investigation are  $J/\psi$  radiative decays since the system recoiling from the photon should

be rich in two-gluon states. The planned CLEO-c project at CESR will collect a billion  $J/\psi$  radiative decays.

The direct production of exotic hybrids in  $e^+e^-$  collisions is complicated by the fact that the angular momentum barrier (the excited flux-tube carries  $J = 1$ ) suppresses this production mode.

Lattice QCD predictions about heavy-quark exotic hybrids are as reliable as for the light-quark hybrids but the experimental situation is far more problematic. The photoproduction cross-sections are a few orders of magnitude lower. At the higher energies needed to produce these more massive states many other uninteresting processes can contribute to background. Finally, to unambiguously tag a charm or beauty hybrid one must identify detached vertices, further complicating the experimental challenge.

## 1.7 Production and analysis of hybrid mesons

### 1.7.1 Kinematics

Consider a specific exclusive photoproduction reaction:

$$\gamma p \rightarrow X p \quad (1.1)$$

The center-of-mass energy squared,  $s$ , and the momentum-transfer-squared,  $t$ , between the incoming beam and outgoing  $X$  are defined in terms of the four-vectors of the particles:

$$s = (p_\gamma + p_p)^2 \quad (1.2)$$

$$t = (p_\gamma - p_X)^2 \quad (1.3)$$

The dependence of the cross section on  $s$  and  $t$  depend on the production mechanism, which is usually described in terms of the particle or particles which can be exchanged as shown in Figure ???. For example, if the exchange particle is the pomeron (diffractive process) the cross section is nearly constant in  $s$ . For meson-exchange processes, cross sections typically fall off with increasing  $s$ . The dependence on  $t$  is typically exponential:

$$\frac{dN}{dt} \propto e^{-\alpha|t|} \quad (1.4)$$

For the process (??) at high enough photon beam energy,  $E_\gamma$ , we can make the approximation  $s \approx 2 \cdot E_\gamma$  where  $E_\gamma$  is in  $GeV$  and  $s$  is in  $GeV^2$ . For fixed  $s$  and mass of  $X$ ,  $m_X$ , there is a minimum value of  $|t|$ , or  $|t|_{min}$ , needed to produce  $X$ . This  $|t|_{min}$  increases with increasing  $m_X$  for fixed  $E_\gamma$  and decreases with increasing  $E_\gamma$  for fixed  $m_X$ . Coupled with the steep dependence implied in equation (??), the dependence of  $|t|_{min}$  on  $m_X$  will affect event yields. In addition, the line shape of a resonance can be distorted if there is too rapid a variation of  $|t|_{min}$  across the width of a resonance.

Figure ?? shows an example of how the dependence in  $t$  is correlated with particle exchange. The distribution is in  $|t'|$  where  $t' = t - t_{min}$  for the  $D$ -waves after a PWA of the  $\eta\pi^0$  system from the reaction  $\pi^- p \rightarrow \eta\pi^0 n$  at  $18 GeV/c$ . The curves are fits to expected Regge exchanges for the various  $D$ -waves.

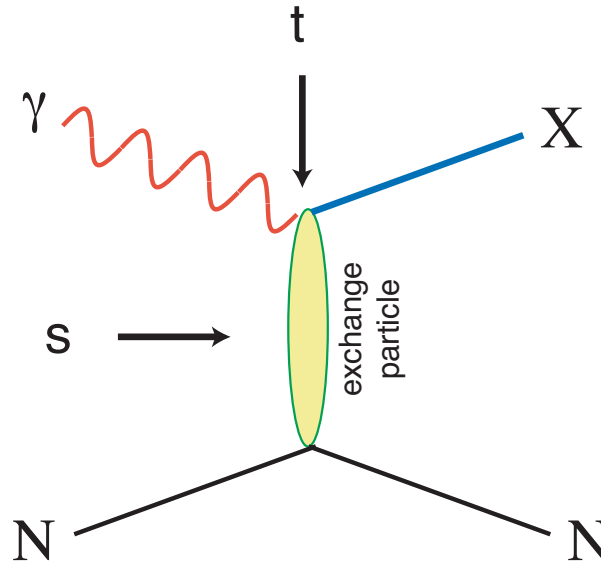


Figure 1.12: Diagram for the photoproduction of particle  $X$ . The variables  $s$  and  $t$  are the center-of-mass energy squared and the momentum-transfer-squared from incoming photon to outgoing particle  $X$ . The process shown here proceeds through the exchange of a particle in the  $t$ -channel.

### 1.7.2 PWA requirements

The PWA technique is described in a later chapter. It is important to stress here that the detector design focuses on hermeticity and resolution to insure nearly uniform coverage with well-understood acceptance functions for various decay angles for particle  $X$ . Kinematic fitting will also be used to identify exclusive processes. The design focuses on the requirements of the PWA. The existence of well established resonances will be used as benchmarks for the PWA. They also provide benchmarks for the phase variation of candidate exotic states. Furthermore, candidate exotics can appear with multiple decay modes which should give consistent results. As an example, a meson which decays into  $\eta\pi$  should be observed in channels where  $\eta \rightarrow \pi^+\pi^-\pi^0$ ,  $\eta \rightarrow 3\pi^0$ , and  $\eta \rightarrow 2\gamma$ . Each of these modes leads to different acceptances and systematics. This provides a powerful check on PWA results.

### 1.7.3 Linear polarization of the beam

#### Linear and circular polarization

We start with a review of the relationship between linear and circular polarization. A right-handed-circularly ( $|R\rangle$ ) polarized photon has  $m = 1$  while for a  $|L\rangle$  photon  $m = -1$ . These are related to the linear polarization states,  $|x\rangle$  (in production plane) and  $|y\rangle$  (perpendicular to production plane) by:

$$|x\rangle = \frac{1}{\sqrt{2}} (|L\rangle - |R\rangle) \quad (1.5)$$

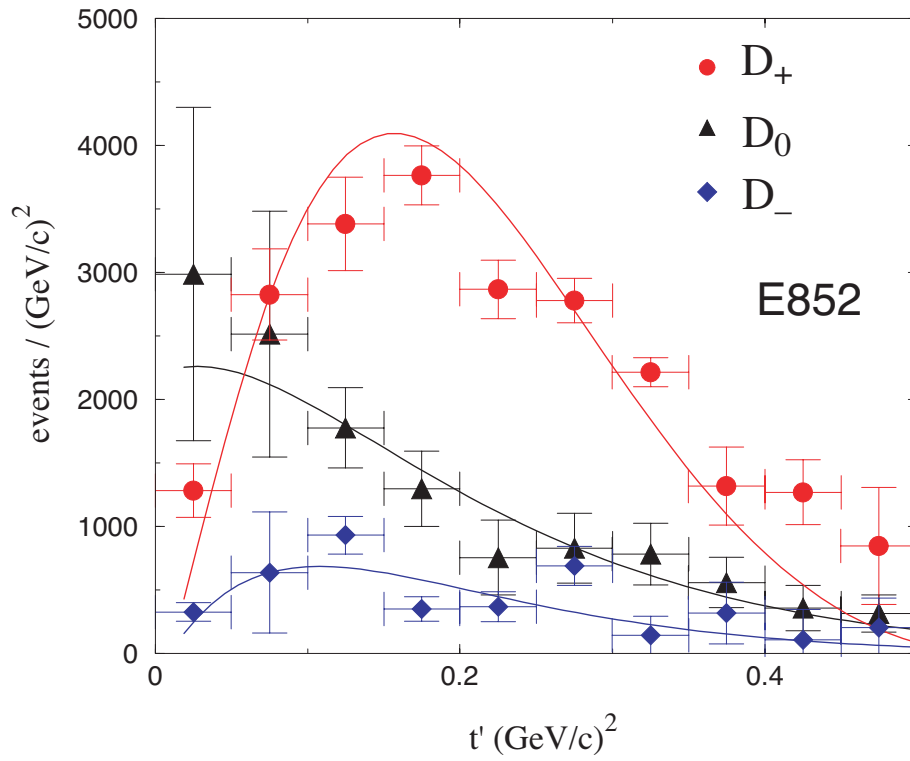


Figure 1.13: The distribution in  $|t'|$  where  $t' = t - t_{min}$  for the  $D$ -waves after a PWA of the  $\eta\pi^0$  system from the reaction  $\pi^-p \rightarrow \eta\pi^0n$  at  $18 \text{ GeV}/c$ . The curves are fits to expected Regge exchanges for the various  $D$ -waves.

$$|y\rangle = \frac{i}{\sqrt{2}} (|L\rangle + |R\rangle) \quad (1.6)$$

States of linear polarization are eigenstates of parity. We will use these relations in several straightforward cases to show how linear polarization:

1. can provide information on decays in lieu of statistics,
2. is essential in isolating production mechanisms, and
3. can be used as an exotics filter if the production mechanism is known.

### Linear polarization and statistics

To illustrate how linear polarization provides useful information in the PWA, consider the case of the photoproduction of a vector meson which subsequently decays into two pseudoscalar mesons. Possible examples are  $\rho \rightarrow \pi\pi$  or  $\phi \rightarrow K\bar{K}$ . Suppose the production mechanism produces the vector with the same helicity as the incident photon (or *s-channel helicity conservation*). In the rest frame of the vector the two-pseudoscalar wave function is described by

$$Y_1^m(\theta, \phi) \propto \sin\theta \cdot e^{im\phi} \quad (1.7)$$

For circularly polarized photons (either  $m = 1$  or  $m = -1$ ) the square of this amplitude carries no  $\phi$  information while for in-plane photons there is a  $\cos^2\phi$  dependence and out-of-plane a  $\sin^2\phi$  dependence in the decay angular distribution, since in these cases we have the sum or difference of  $Y_1^{+1}$  and  $Y_1^{-1}$  according to equations ( ??) and ( ??). Although not essential in determining spin, a gain of statistics is needed to recover a drop in the degree of linear polarization. For example, our Monte Carlo simulation studies indicate that when the degree of linear polarization decreases from 0.40 to 0.2 a factor of two increase in statistics is needed to achieve the same relative error in determination of spin amplitudes.

### Linear polarization and production mechanism

This is best illustrated by considering a specific example. Suppose we produce a vector particle ( $J^P = 1^-$ ) by the exchange of a scalar particle ( $J^P = 0^+$  – natural parity exchange) or a pseudoscalar particle ( $J^P = 0^-$  – unnatural parity exchange). We wish to determine whether the vector is produced by natural (amplitude  $A_N$ ) or unnatural (amplitude  $A_U$ ) parity exchange. In the center-of-mass of the vector particle, the momentum vectors of the beam photon and exchange particle are collinear. For circularly polarized photons, the  $m$  of the vector is the same as that of the photon. From parity conservation, the orbital angular momentum between the photon and exchange particle is  $L = 0$  or  $L = 2$  for natural parity exchange and  $L = 1$  for unnatural parity exchange. So for circularly polarized photons, with  $m = +1$ , the total amplitude is  $A_N + A_U$  whereas for  $m = -1$ , the total amplitude is  $A_N - A_U$ . This follows simply from the addition of angular momenta. Circularly polarized photons allow us to measure only the sum or difference of the two exchange amplitudes. If however, we have linearly polarized photons along the  $x$ -direction, we extract  $A_N$  using equation ( ??) and for polarization along the  $y$ -direction, we extract  $A_U$  using equation ( ??).

**Linear polarization as an exotics filter**

Using arguments similar to those above, it has been shown [?] that linear polarization can be used as a tool to filter exotics. For example, a  $\rho\pi$  system with  $I = 1$  has  $C = +$ . Suppose that one can determine the naturality of the exchange particle by selecting data within a range of  $|t|$ . For a produced  $C = +$  particle with spin one we can have natural parity ( $J^{PC} = 1^{-+}$  – exotic) or unnatural parity ( $J^{PC} = 1^{++}$  – non-exotic). In the case of natural parity exchange the in-plane polarization selects the  $J^{PC} = 1^{-+}$  wave while out-of-plane polarization selects  $J^{PC} = 1^{++}$ . For unnatural parity exchange the reverse is true. Note that in this case, we are specifying the naturality of the exchange and using linear polarization to select the naturality of the produced particle. In the previous section, we specified the naturality of the produced particle and used linear polarization to select the naturality of the exchanged particle.

## Chapter 2

# Photon Beam

### 2.1 Introduction

One of the unique opportunities presented by a CEBAF upgrade to energies of 12 *GeV* and beyond is the possibility of generating high-intensity continuous photon beams for high-energy photoproduction experiments. In this regime, photon beams represent an interesting extension to the meson spectroscopy program that has been actively pursued using beams of pseudoscalar mesons at hadron accelerator laboratories: with high energy photons one has essentially a beam of *vector* mesons. It is difficult, in fact, to conceive of any other way to obtain such a vector beam.

The requirements for photon beam energy and polarization were described in Chapter ????. This chapter describes a design for a real photon source that meets these requirements. Starting with a beam of monochromatic electrons, it provides an intense beam of high-energy photons with an energy spectrum that is dominated by a single peak. A significant fraction of the total power in the beam is concentrated inside this peak, which has a width of less than 10% f.w.h.m. At a fixed electron beam energy  $E_0$ , the peak energy of the photon beam can be varied anywhere up to 90%  $E_0$  simply by rotating a crystal. The photon spectrum inside the intensity peak has a large degree of linear polarization. The precise energy of an individual photon inside the peak is determined (“tagged”) from the momentum of the recoil electron measured in a dedicated “tagging” spectrometer. The design is formed around the expected parameters for the CEBAF beam following the energy upgrade to 12 *GeV*, although nothing prevents its operation at lower energies before the time that 12 *GeV* beams are available.

This chapter begins with a survey of the techniques for producing high-energy photons that were considered in the development of this design, and the reasons for the choice of coherent bremsstrahlung. The coherent bremsstrahlung source is then described in greater detail, followed by a discussion of the requirements that the design places on the electron beam that feeds the source. The tagging spectrometer design is described next, and the chapter concludes with a discussion of the considerations that govern the choice of beam intensity for particular measurements.

## 2.2 Choice of technique

Two basic methods have been considered for producing photons of the highest possible energy, flux and polarization from electrons of  $E_0 = 12 \text{ GeV}$ . The methods are bremsstrahlung and Compton scattering of light. Both are well-established methods of producing photon beams. Both techniques are actually described by the same Feynman diagrams, shown in Fig. ???. In the case of Compton scattering the incoming photon is real, whereas it is virtual for the case of bremsstrahlung.

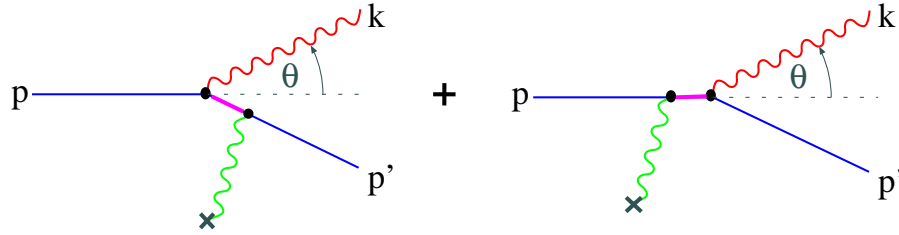


Figure 2.1: Generic diagrams for hard photon production from a high energy electron beam. The symbol  $\times$  represents either a static charge distribution, in the case of virtual photons in the initial state (i.e. bremsstrahlung), or an optical cavity, in the case of real photons in the initial state (i.e. Compton scattering).

Each of these techniques has its own limitations and advantages. In order to be suitable for GLUEX, the photon source must be capable of producing photons of energy at least 80%  $E_0$ , (9 GeV). The photon beam should have linear polarization. The energy resolution for individual photons in the beam should be as high as possible, *i.e.* on the order of the energy spread of the electron beam itself. It should be capable of producing intensities up to  $10^8/\text{s}$ . The contamination of the beam with photons outside the desired energy band should be as low as possible. It is also important that the source be reliable and require a minimum of down-time for maintenance. The suitability of each approach is discussed below in the light of these criteria.

### 2.2.1 Compton back-scatter

A Compton source begins with a beam of visible or ultraviolet light, typically from a laser that is aligned to intersect the incident electron beam at close to  $180^\circ$ . Some of the photons undergo Compton scattering with the beam electrons. In the lab frame, the scattered photons come out in a narrow cone about the incident electron direction and carry a significant fraction of the electron energy.

The basic design of the Compton back-scatter source for this study was put forward by C. Keppel and R. Ent [?]. The design entails the use of a four-mirror high-gain cavity pumped by a 10 kW argon-ion laser putting out 2 ps pulses at a frequency of 100 MHz. The pulses in the cavity are synchronized so that the light pulses intercept an electron bucket each time they pass through the beam. The total length of the cavity is 2 m with a crossing angle of  $1^\circ$ . Both cavity and electron beam are focused to a tiny spot of 10  $\mu\text{m}$  r.m.s. radius at the crossing point. A small spot size is necessary in order to get as high a scattering rate as possible. The gain of the cavity is  $10^4$ , which is conservative in view of recent advances in mirror technology.

The wavelength of the light is  $514 \text{ nm}$ . The rate spectrum of the back-scattered beam from this source is shown in Fig ??a for a  $1 \mu\text{A}$  electron beam at  $12 \text{ GeV}$ .

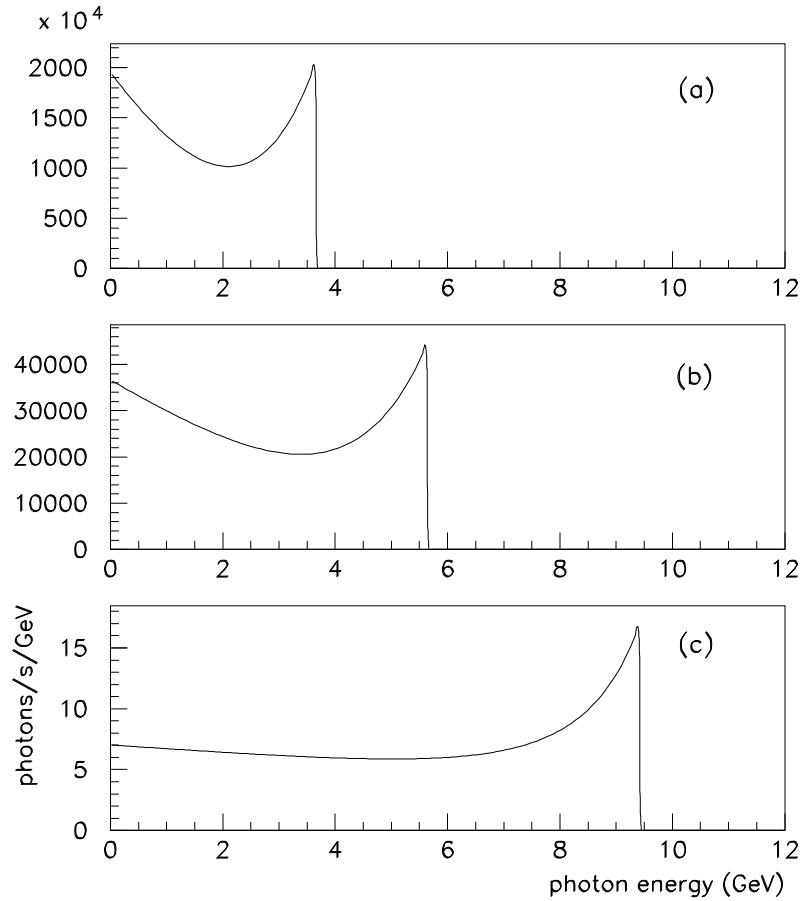


Figure 2.2: Photon energy spectrum from the Compton back-scatter source described in the text and a  $12 \text{ GeV}$  electron beam at  $1 \mu\text{A}$ . (a) cavity of gain 10000 driven by a  $10 \text{ kW}$  Argon-ion laser ( $514 \text{ nm}$ ) at  $100 \text{ MHz}$ . (b) cavity of gain 250 driven by  $3 \text{ kW}$  frequency-doubler ( $257 \text{ nm}$ ) pulsed at  $100 \text{ MHz}$ . (c) cavity of gain 1 driven by a hypothetical FEL source operating at  $20 \text{ eV}$  with the same time structure as CEBAF beam, peak power  $1 \text{ kW}$ .

From the point of view of flux, this source is marginal. With a few  $\mu\text{A}$  of beam and mirror improvements, it might produce  $10^8$  photons/s in the upper third of its energy spectrum. However, its maximum photon energy of  $3.7 \text{ GeV}$  is far short of the  $80\% E_0$  needed for GLUEX. To remedy this one must decrease the wavelength of the laser beam. This can be done by the use of a frequency-doubling crystal that absorbs the green light from the laser and produces

ultraviolet light at  $257 \text{ nm}$ . Storing this light in a cavity of similar design to that described above yields the back-scatter rate spectrum shown in Fig. ??b. The major reason for the drop in rate is the decrease in the cavity gain from 10000 to 250. This is imposed by the diminished reflectivities of mirrors in the UV. Other factors are the inefficiency of the doubling crystal, a factor of two in rate from the doubling itself, and the decreasing Compton cross section with energy. The maximum photon energy is still under 50%  $E_0$  and the flux is three orders of magnitude below the desired rate.

In order to reach photon energies of 80%  $E_0$ , initial photons of  $20 \text{ eV}$  are needed. The brightest source of these would be a synchrotron light source or a free electron laser (FEL). Mirrors that operate at these wavelengths typically have reflectivities around 70%. With these one could conceive of a scheme that uses a wiggler to extract energy from the  $12 \text{ GeV}$  beam before it enters the dump. This light would have the same time structure as incident beam, and so it could be reflected back and made to cross the incident beam at a small angle for a Compton back-scatter source. An indication of the level of flux that could be achieved with such a source can be obtained by using the laser cavity model described above, setting the gain to 1, the wavelength to  $62 \text{ nm}$ , and assuming  $1 \text{ kW}$  peak ( $1 \text{ W}$  average) of synchrotron light. The back-scatter rate is shown in Fig ??c. This plot shows that even if the full power of a  $1 \mu\text{A}$  on a  $12 \text{ GeV}$  beam were converted into  $20 \text{ eV}$  photons and back-scattered from the incoming beam, the rate would still fall far short of the requirements for GLUEX.

From the point of view of polarization, the Compton back-scatter source would be ideal. The polarization of the back-scattered beam is controlled by that of the laser, and can be essentially 100%. This source is also virtually background-free because the spectrum below any desired cutoff can be eliminated by collimation. The energy of the remaining beam can be measured to within the resolution of the electron beam by tagging. However the the combination of sufficient energy and sufficient flux for the purposes of the GLUEX experiment in HALL D cannot be achieved using this source.

### 2.2.2 Tagged bremsstrahlung

A bremsstrahlung source consists of a thin piece of material (the radiator) that is placed in the electron beam and converts part of the energy of the beam into bremsstrahlung radiation. Bremsstrahlung offers the only practical way, starting with an electron beam at CEBAF energies, to produce a photon beam with a significant flux in the vicinity of the end point. It produces a naturally collimated photon beam with a characteristic angular spread of  $m/E_0$ . This allows the low emittance of the CEBAF beam to be effectively transferred into the secondary photon beam.

Bremsstrahlung does not suffer from the kind of flux limitations that were encountered in the examination of Compton back-scatter sources. The radiator thickness must be kept below 1% of a radiation length in order to maintain good energy resolution in the tagger. Keeping the thickness below  $10^{-3}$  radiation lengths ensures that multiple scattering in the radiator does not significantly broaden the divergence angle of the photon beam. A  $10^{-3}$  radiator and  $1 \mu\text{A}$  of electrons would produce much more than sufficient flux for GLUEX.

A bremsstrahlung source is, however, deficient in some other respects. Averaged over the bremsstrahlung cone, the photon beam has zero linear polarization. Circular polarization can be achieved by polarization transfer from a polarized electron beam, but for the purposes of GLUEX it is linear polarization that is desired. A bremsstrahlung source also suffers from a large

low-energy flux in the beam. The power spectrum of a bremsstrahlung beam is approximately uniform from zero up to the energy of the incident electrons. This means that an experiment that uses the high-energy part of the beam must operate in a background of low-energy photons that are many times more frequent. The tagger is helpful in eliminating many of the false starts in the detector that arise from the background, but this technique becomes ineffective at rates above a few  $10^7$  tagged photons/s. For the typical experiment using tagged bremsstrahlung and open detector geometry, background from low-energy beam particles limits the rate at which the experiment can run to less than  $5 \cdot 10^7$  tagged photons/s. The goal for GLUEX pushes that limit to  $10^8$ /s by employing tagged *coherent* bremsstrahlung.

### 2.2.3 Coherent bremsstrahlung

The source described in the previous section meets most of the requirements for GLUEX, but is deficient in the areas of polarization and backgrounds. Both of these deficiencies can be remedied by replacing the conventional amorphous or polycrystalline radiator with a thin monocrystalline wafer. At special settings for the orientation of the crystal, the atoms in the radiator can be made to recoil together from the radiating electron. When they do this they produce a coherent enhancement at particular energies in the radiation spectrum, which correspond to the reciprocal lattice vectors of the crystal. The kinematics are such that a randomly oriented lattice vector would make a tiny peak located up at the end point of the energy spectrum, where the coherent gain factor is negligible. By careful orientation of the crystal, however, one of the lattice vectors can be aligned with the favored kinematics for bremsstrahlung, at which point its coherent peak appears well below the end point, and its coherent gain can be large enough that it contributes a large fraction of the total radiated power.

This is illustrated in Fig. ???. This plot shows the intensity ( $dP/dE$ ) or power spectrum of the coherent bremsstrahlung beam after collimation. The sequence of secondary peaks above the primary correspond to integral multiples of the fundamental reciprocal lattice vector and so they are always present. By careful choice of orientation angles it is possible to suppress all other vectors and isolate just one primary peak in the energy band of interest, as shown in the figure. By a small rotation of the crystal, the position of the peak can be moved from one end of the spectrum to the other. Note that the coherent peaks appear as enhancements on top of the incoherent bremsstrahlung continuum.

Unlike those from the incoherent process, coherent bremsstrahlung photons have significant net linear polarization in the plane given by the beam direction and the crystal lattice vector. This polarization is enhanced by collimating the photon beam below its intrinsic angular spread, as discussed in the next section. The loss in flux from collimation can be recovered by increasing the electron beam current. As will be shown in the following section, even in the case of very thin crystals and severe collimation, quite modest electron beam currents are needed to produce the required photon flux.

The use of coherent bremsstrahlung improves the background conditions of the beam by enhancing the spectral intensity in the desired energy band relative to the incoherent continuum. For measurements that do not require polarization, a crystal radiator can be used without collimation to reduce the low-energy beam background for a given rate of tagged photons. Where polarization is required, coherent bremsstrahlung is indispensable.

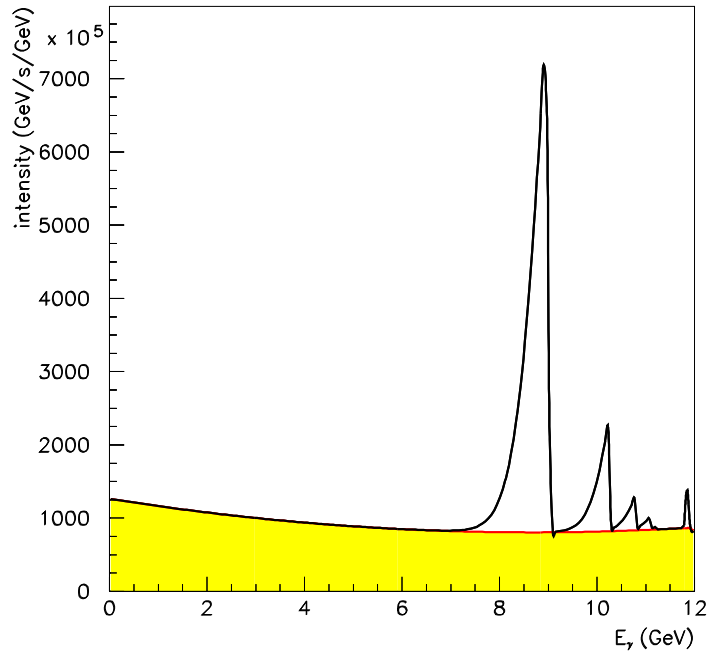


Figure 2.3: Photon power spectrum from an oriented diamond radiator. The  $y$  axis is  $dP/dE$  with power  $P$  expressed in  $GeV/s$  and  $E$  in  $GeV$ . The radiator thickness is  $10^{-4}$  radiation lengths and the electron beam current is  $1 \mu A$ . Shown is what emerges after the photon beam passes through a collimator  $3.4 \text{ mm}$  in diameter located  $80 \text{ m}$  downstream from the radiator.

### 2.3 Photon source

A horizontal plan view of the photon beam line is shown in Fig. ?? with the major components labeled. The electron beam enters the figure from below ground at the left and is bent into the horizontal plane to enter the tagger building. There it passes through two small dipoles to impinge upon the bremsstrahlung radiator. After its exit from the radiator, the electron beam passes into the tagging spectrometer where the primary beam is bent in the direction of the electron beam dump. The radiator crystal is thin enough that the average energy loss by the electrons in traversing the radiator is less than the intrinsic energy spread of the incident beam. Those electrons which lose a significant fraction of their initial energy inside the radiator do so by emitting a single bremsstrahlung photon. These degraded electrons are bent out of the primary beam inside the tagger magnet and exit the vacuum through a thin window, passing through air for a short distance to strike the focal plane of the spectrometer. The primary electron beam is contained inside vacuum all the way to the dump.

The photons that are produced in the radiator pass through a small hole bored in the return yoke of the tagger magnet in the forward direction. They then pass into an evacuated photon beam pipe and travel to the experimental hall. Just before entering the hall the photon beam passes through a system of collimators and sweeping magnets. They are housed in a

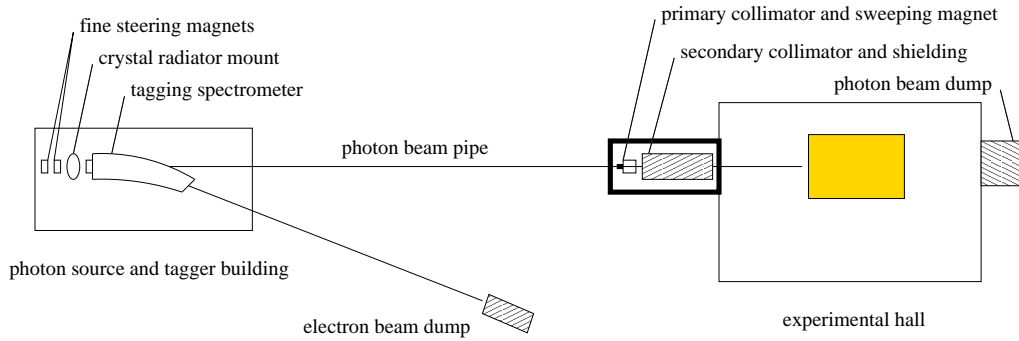


Figure 2.4: Schematic plan view of the photon beam line, shown in the horizontal plane as viewed from above. The objects in this figure are not drawn to scale.

separate enclosure for shielding purposes. The primary collimator is first. It defines the part of the photon beam that is allowed to reach the target. Debris from interactions along the inside surface of the collimator bore forms a halo around the photon beam that exits the primary collimator. The charged component of the halo is deflected away from the beam axis by a dipole “sweeping” magnet just downstream of the collimator. A secondary collimator follows the sweeping magnet to stop the deflected shower particles and block the halo of secondary photons generated by the first collimator. The secondary collimator is of a larger diameter than the primary and so sees a reduced rate of secondary interactions on the inner surface of the hole. What new showers are generated there are cleaned up by a second sweeping magnet. The beam then passes through a block of shielding material into the experimental hall. This triple-collimation system is similar to the setup at the SLAC coherent bremsstrahlung beam line [?].

The collimated photon beam, now only a few  $mm$  in diameter, is delivered to the experimental target. After passing through of order 3% radiation lengths of target, the photon beam passes through the detector and into the photon beam dump at the back of the hall. Based upon a design upper limit of 60  $kW$  (5  $\mu A$  at 12  $GeV$ ) being delivered to the electron beam dump, the total power in the photon beam is not more than 1.5  $W$  in the experimental hall and not more than 15  $W$  in the collimator enclosure.

### 2.3.1 Essential features

The adjective ‘coherent’ in coherent bremsstrahlung does not indicate that the photons in the beam are in a coherent state, as is light from a laser. Rather it refers to the coherent effect of multiple atoms in a crystal lattice in absorbing the recoil momentum from a high energy electron when it radiates a bremsstrahlung photon. In X-ray spectroscopy one encounters the same thing in the Mössbauer effect, except in that case the chief physical consequence is the disappearance of the recoil Doppler shift from the photoabsorption/emission spectrum. Here the chief consequence is the enhancement of bremsstrahlung at those particular kinematics for which the recoil momentum matches one of the reciprocal lattice vectors of the crystal.

Another useful way to view the process of coherent bremsstrahlung is as virtual Compton scattering. To the high energy electron, the atoms in the radiator appear as clouds of virtual photons. For a disordered radiator material, the virtual photon spectrum is given simply by the atomic form factor squared, averaged over the different species in the material. If the radiator is

a single crystal, however, the atomic form factor gets multiplied by the form factor of the crystal, which in the ideal case looks like a series of delta-functions located at the sites of the reciprocal lattice. In effect, the crystal provides a set of virtual laser beams, each one a standing wave tuned to a specific reciprocal lattice vector. In this view the process of hard bremsstrahlung is seen to be the same as Compton back-scattering of laser light. For a more detailed discussion of the physics of coherent bremsstrahlung there are a number of good references [?, ?, ?, ?].

The use of Compton back-scattering of laser light as a photon source was earlier noted as ruled out by the limitation of high-power lasers and cavities to wavelengths above 100  $\mu m$ . The characteristic wavelength of the crystal photons is a few Angstroms, three orders of magnitude shorter. In this case, 180° scattering would result in essentially 100% of the electron beam momentum being transferred to the photon in the lab frame. However, the Compton cross section contains a factor of  $1/(\vec{q} \cdot \vec{p})^2$  where  $\vec{q}$  is the virtual photon momentum and  $\vec{p}$  is that of the electron, which strongly favors incident photons with  $\vec{q}$  nearly orthogonal to  $\vec{p}$ . With reciprocal lattice vectors pointing in almost every direction, only those nearly perpendicular to the beam contribute appreciably to the scattering rate. This fact applies equally to ordinary bremsstrahlung; in fact, to a first approximation the bremsstrahlung spectrum from a single crystal is the same as from a disordered radiator. The reason is that, if the sum over crystal momenta were replaced with a continuous integral, one would recover the ordinary bremsstrahlung result for isolated atoms. Beyond a few unit cells from the origin in reciprocal lattice space, the atomic form factor and kinematic factors become slowly varying on the scale of the lattice spacing, and the sum becomes indistinguishable from the integral. Besides that, the uncertainty principle requires that atoms localized at the sites in a crystal undergo fluctuations about their mean position. This has the effect of attenuating the discrete peaks in the crystal form factor at progressively higher-order crystal momenta, eventually washing them out and filling in the gaps between them, so that the sum deforms smoothly into the integral at high momentum transfer. Hence, the sum over crystal indices that yields the final photon spectrum can be separated into two parts: a discrete sum over a limited set of small crystal indices and an integral over the continuum of momentum transfer values beyond. The latter appears in the coherent bremsstrahlung beam as an ordinary  $1/k$  bremsstrahlung spectrum, while the former appears as a set of peak structures superimposed upon it. The  $1/k$  continuum, referred to as the incoherent component, is invariant as the crystal is rotated, whereas the coherent peaks change in position and intensity, depending on crystal orientation.

A typical coherent bremsstrahlung spectrum is shown in Fig. ???. The distinction between incoherent and coherent components in the figure is artificial; it is there to show the part of the spectrum that shifts as the crystal is rotated. The vertical scale in the figure gives the photon rate for the given beam current and crystal thickness. Note that the intensity of the incoherent background is less than what would be obtained with an amorphous carbon radiator of the same thickness, because a part of the momentum transfer integral in the Bethe-Heitler formula has been moved into the discrete sum and contributes to the coherent part. The radiation length of diamond is actually an average over all orientations of the crystal. In the calculation for Fig. ??? the leading 400 lattice sites were included in the discrete part of the calculation, although it can be seen that, at the chosen crystal orientation, only two or three of them contribute with sufficient intensity to be individually visible in the spectrum.

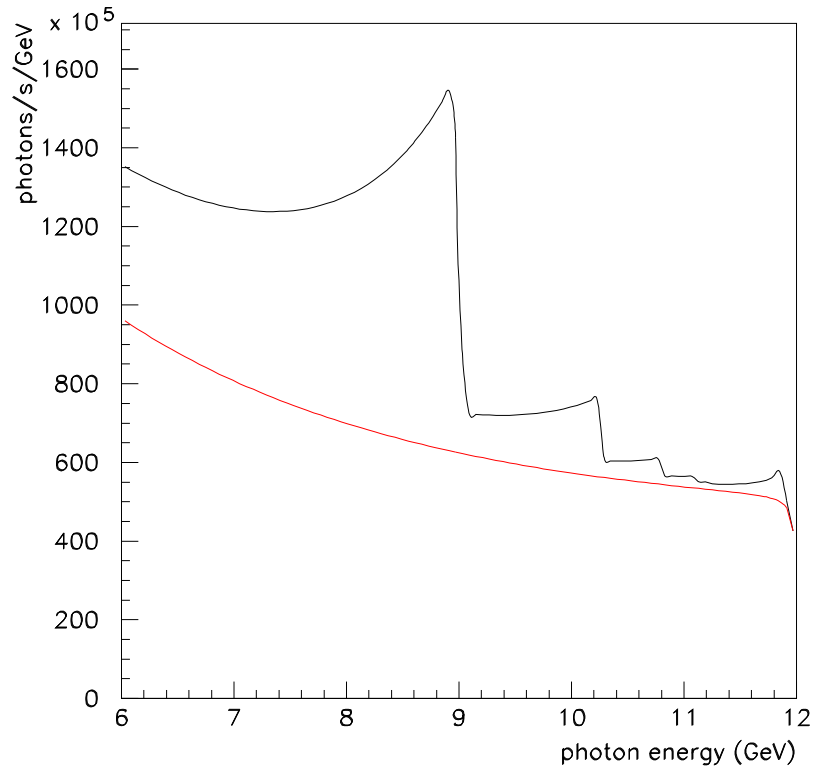


Figure 2.5: Uncollimated coherent bremsstrahlung spectrum, calculated for a diamond crystal radiator  $15 \mu\text{m}$  thick and a  $1 \mu\text{A}$  electron beam of  $12 \text{ GeV}$  energy. Typical values are used for beam emittance and crystal mosaic spread.

### 2.3.2 Use of collimation

The presence of the large incoherent continuum in Fig. ?? presents a significant handicap to a photoproduction experiment. Not only do the continuum photons produce background in the detector, but they diminish the polarization of the beam. The entire beam polarization appears in the coherent component; the underlying incoherent flux only serves to dilute the polarization. There is another difference between the two components that allows them to be separated to some extent. The kinematics of bremsstrahlung confines most of the intensity of the photon beam to forward angles within  $m/E$  radians of the incident electron direction. This is true both for the incoherent and coherent components. In the lab this is a small angle, but in the rest frame of the electron-photon system it subtends all angles in the forward hemisphere. The difference lies in the fact that a peak in the coherent component corresponding to a single reciprocal lattice vector has two-body kinematics, so there is a well-defined relation between the emission angle and the energy of the emitted photon in the lab: emission at  $0^\circ$  yields a maximum energy photon, with energy decreasing with increasing angle. This accounts for the shape of the coherent peaks in Fig. ??, with the sharp right-hand edge corresponding to  $0^\circ$

emission and the tail to lower energies corresponding to emission at higher angles.

The incoherent component, because it comes from a sum over momentum transfers at all angles, has essentially no correlation between photon energy and emission angle. This means that collimating away all photons beyond some angle  $\theta_{max} < m/E$  uniformly attenuates the incoherent spectrum at all energies, whereas it preserves all of the coherent photons from the maximum energy for the given peak down to some cutoff. The kinematic relations for coherent bremsstrahlung are as follows,

$$\theta^2 + 1 = \left( \frac{1-x}{x} \right) \left( \frac{x_{max}}{1-x_{max}} \right) \quad (2.1)$$

$$x_{max} = \frac{2\vec{p} \cdot \vec{q}}{2\vec{p} \cdot \vec{q} - m_e^2} \quad (2.2)$$

where  $x$  is the photon energy in units of the incident electron energy and  $\theta$  is the lab emission angle of the photon relative to the incident electron momentum axis, in units of  $m/E$ .

The effects of collimation are demonstrated in the calculated spectra shown in Fig. ?? . First, note that the collimation angles are very small, which requires a long flight path of order 100  $m$  in order that the collimator can be larger than the intrinsic beam spot size, otherwise the collimator is cutting in transverse coordinate instead of in angle. This distance is, in fact, a sensitive function of the electron beam emittance from the machine, and must be increased in inverse proportion to the beam emittance if the effectiveness of collimation is held constant. This issue, along with the associated demands placed on beam alignment and position stability, are taken up in more detail in the following section on the electron beam line.

Second, note that the cut imposed on the coherent peak by collimation does not produce a perfectly sharp edge as would be expected from two-body kinematics. This is because the collimator cuts on radius at some fixed distance which translates into a cut on emission angle only in an approximate way. Thus the curves in Fig. ?? are labeled by their collimator size and distance individually, rather than their ratio, which is the nominal collimation angle. Multiple scattering by the electron in the radiator prior to emission, and beam spot size and divergence are the major contributors to the error involved in translating a collimator radius into a cut on emission angle. All of these effects have been incorporated into the analytical calculation of the yields from a collimated coherent bremsstrahlung source that has been used in preparing this report. Crystal imperfections, which amount to an intrinsic spread in the direction of the incoming virtual photon, are also taken into account in the calculation.

Third, note that the relatively weak collimation at 5  $mm$  reduces the incoherent background without significantly affecting the coherent flux near the maximum, and thereby almost doubling the polarization of the beam at the peak relative to the uncollimated case. Further reducing the collimator diameter continues to narrow the peak and reduce the incoherent flux relative to the peak, albeit at some cost in peak intensity.

The 3.4  $mm$  collimator diameter has been chosen for this design because it provides for a maximum reduction in the incoherent flux while transmitting 95% of the coherent flux at the peak. Most of the total photon beam energy coming from the crystal is absorbed by the collimator. For this reason the collimator is located in a separate enclosure outside the experimental hall, and must be surrounded by a considerable amount of shielding. The peak in Fig. ?? for a 3.4  $mm$  collimator contains 33M photons/s for an electron beam current of 1  $\mu A$ , which will be increased by a factor of 3 for full-intensity running of the GLUEX experiment in HALL D.

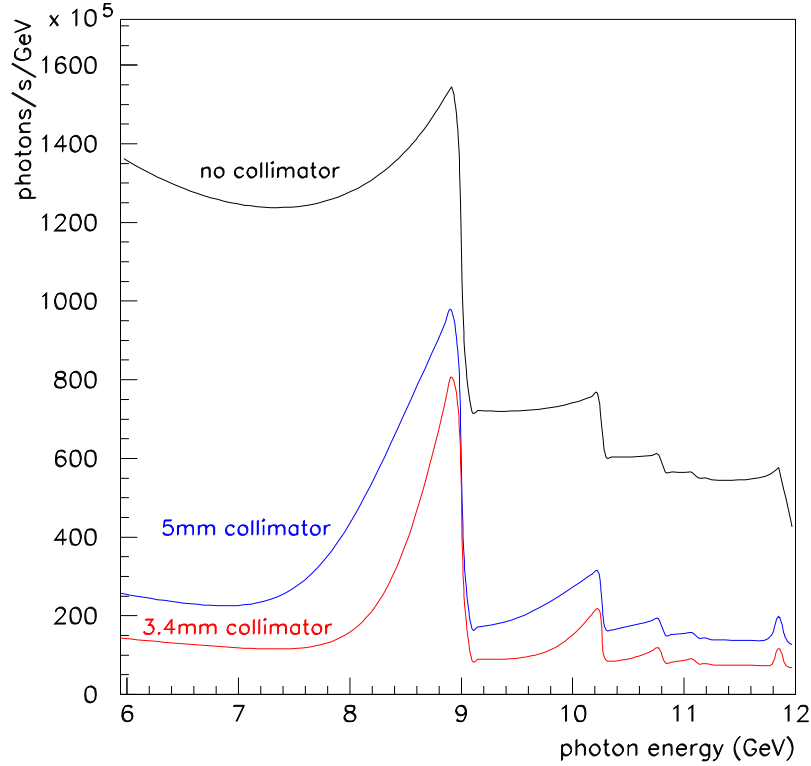


Figure 2.6: Coherent bremsstrahlung spectrum, calculated under the same conditions as in Fig. ?? , after collimation. The upper curve is the uncollimated spectrum from Fig. ?? . The middle curve corresponds to a 5 mm diameter collimator placed 80 m downstream of the radiator, or approximately  $0.75 m/E$  in collimator half-angle. The lower curve corresponds to a 3.4 mm collimator in the same position, approximately  $0.50 m/E$ . For the 3.4 mm collimator there are approximately  $3.3 \times 10^7 \gamma/s$  in the primary peak for a nominal electron beam current of  $1 \mu A$  and crystal thickness of  $15 \mu m$ .

Fourth, note that the rate seen in the focal plane of the tagging spectrometer corresponds to the upper curve in Fig. ?? , regardless of the collimation. This means that collimating the bremsstrahlung beam increases the rate in the tagger focal plane relative to what is seen at the detector. For full-intensity running at  $10^8$  photons/s on target in the coherent peak, Fig. ?? implies a rate of 240 MHz in the focal plane within a 600 MeV window around the peak. Combining this rate with the beam pulse spacing of 2 ns leads to an accidental tagging rate of about 50% and to a fraction of ambiguous tags of 40%. Even with ideal electronics the per-second yield of single-tag events is close to saturation at this intensity. The detector and tagging spectrometer design are based upon a maximum rate of  $10^8$  photons/s on target and 400 MHz per GeV in the tagger. A novel focal plane design is currently under study, to be discussed below in section ?? , which may enable the focal plane rate to be reduced by about a factor of two without any decrease in the collimated flux.

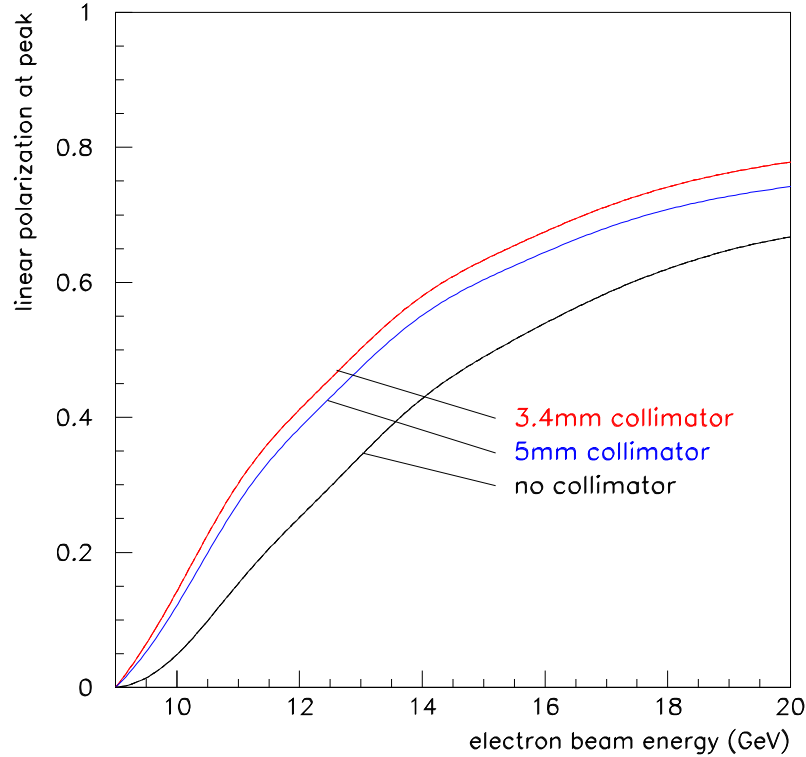


Figure 2.7: Linear polarization in the coherent bremsstrahlung peak as a function of electron beam energy keeping the energy of the coherent peak fixed at 9 *GeV*. The calculation is performed under the same conditions as in Fig. ??.

The linear polarization of the photons in the coherent peak is shown in Fig. ?? as a function of the energy of the electron beam. This figure demonstrates why it is essential to have electrons of as high energy as possible, even though photon energies of no more than 9 *GeV* are required. The intensity of the coherent peak, not shown in the figure, has a similar dependence on the electron beam energy in this region.

Shown in Fig. ?? is the linear polarization of the photon beam *vs* photon energy for fixed electron beam energy. The dashed curves show how the maximum polarization in the primary peak varies as the peak energy is changed by rotating the crystal. The polarization in all cases is zero at the end-point. Without collimation it rises as  $(E_0 - k)^2$ , one power coming from the intensity of the coherent peak relative to the incoherent component, and the other from the intrinsic polarization of the coherent photons. Collimation allows one to essentially isolate the coherent component, so that the polarization available to the experiment rises from zero at the end-point in a linear fashion. The dashed curves in Fig. ?? demonstrate this point.

In order to obtain the full polarization enhancement from collimation, it is necessary to have a distance between the radiator and collimator on the order of 100 *m*. This distance scale is set by the requirement that the collimator aperture must be large compared to the virtual

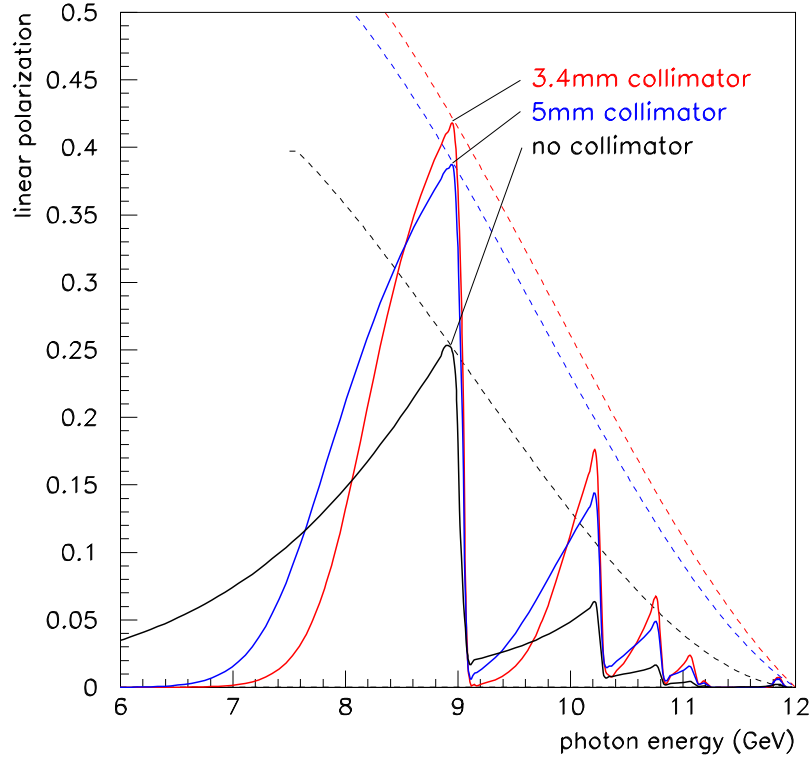


Figure 2.8: Linear polarization of the coherent bremsstrahlung beam for a fixed electron beam energy of  $12 \text{ GeV}$ , calculated under the same conditions as in Fig. ???. The dashed lines indicate the trajectory of the peak polarization as the peak energy is swept across the focal plane by rotating the crystal.

electron beam spot on the collimator but small compared to the actual photon spot size. The virtual electron beam spot is defined as the profile that the electron beam would have at the entrance to the collimator if it were allowed to propagate freely instead of being bent into the beam dump.

The size of the virtual spot at the collimator is determined by the beam emittance combined with an upper limit of  $20 \mu r$  on the angular spread of the electron beam at the radiator. The latter value was chosen to match the spread in the beam incidence angle to the mosaic spread of the crystal because it is the combination of the two that limits the definition of the coherent peak. Taking this value together with an emittance of  $10^{-8} m \cdot r$ , which has been projected for the CEBAF beam at  $12 \text{ GeV}$  leads to a virtual spot size of  $0.5 \text{ mm}$  r.m.s. ( $1.2 \text{ mm}$  f.w.h.m.). Note that this scale does not depend on the radiator-collimator distance. The size of the real photon spot is given by one characteristic angle  $m/E$  which defines a circle on the collimator containing approximately 50% of the total photon intensity. The real spot size is proportional to the radiator-collimator distance. At a distance of  $80 \text{ m}$  the ratio of spot sizes is 6, sufficient to allow collimator apertures that satisfy both of the above inequalities.

Fig. ?? shows the peak polarization of the beam as a function of radiator-collimator distance for a coherent peak at  $9 \text{ GeV}$ . In this calculation the collimator diameter is held constant at  $3.4 \text{ mm}$  to make sure that the virtual beam spot of  $1.2 \text{ mm}$  f.w.h.m. is well-contained within the aperture, which is the main condition for effective collimation. At zero distance the collimator has no effect except to attenuate the beam, and so the uncollimated polarization from coherent bremsstrahlung is obtained. At  $100 \text{ m}$  separation distance the polarization enhancement from collimation has saturated. The design for GLUEX calls for a radiator-collimator distance of approximately  $80 \text{ m}$ . However from the figure one can see that the performance of the photon source is not a very sensitive function of this variable.

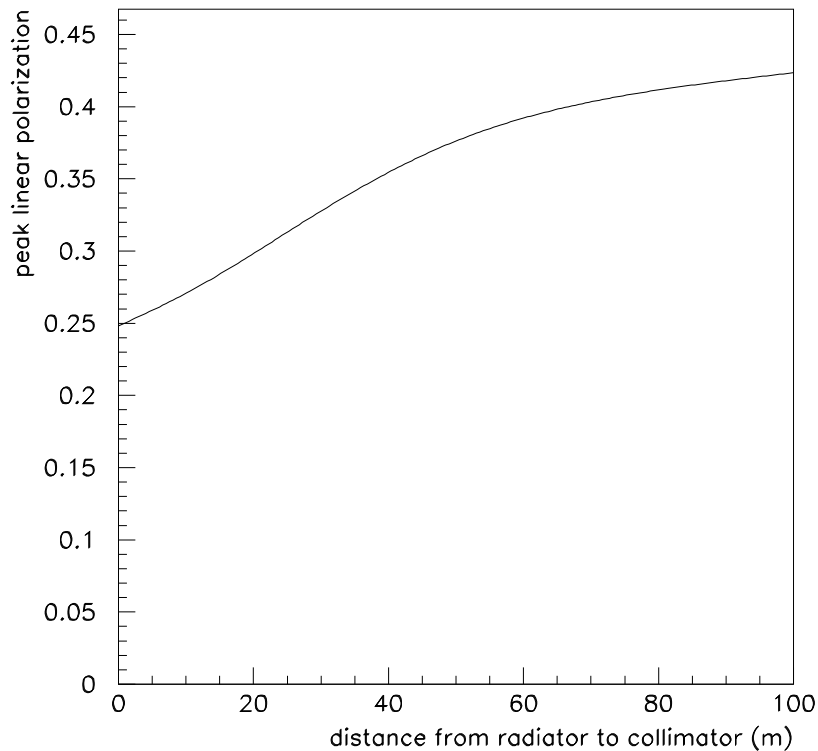


Figure 2.9: Maximum polarization *vs* radiator-collimator distance for a coherent peak at  $9 \text{ GeV}$ . The collimator diameter is held fixed in this calculation to keep a constant ratio between the sizes of the virtual electron spot and the collimator.

### 2.3.3 Choice of radiator

The ideal radiator would be a layered structure with strong transverse fields that alternate between layers spaced about  $50 \text{ nm}$  apart, thus simulating the standing wave in a cavity driven by a  $15 \text{ eV}$  laser. While it is possible to construct ordered materials with unit cells as large as this, the self-shielding of atoms means that beyond the atomic length scale the

crystal	best reciprocal vector	$P/P_{\text{diamond}}$
diamond	2,-2,0	1.00
beryllium	0,0,2	0.86
boron	2,0,8	0.38
silicon	2,-2,0	0.19
Be <sub>2</sub> C	2,2,0	1.10

Table 2.1: Figure of merit for various materials that might be used as a coherent bremsstrahlung radiator. This table is reproduced from Table 2 in Ref. [?].

residual fields are comparatively weak. Hence heterogeneous structures are not viable for use as a coherent radiator. Since the strong fields inside a solid are revealed at the atomic scale, the first requirement for a good radiator is that the unit cell be compact and closely packed. The best radiators are those with the smallest unit cells because these provide the best match between the atomic and the crystal form factors. This match is best for the light elements, and essentially prohibits the effectiveness of any materials heavier than carbon. An extensive survey of possible radiator materials is presented in Ref. [?]. In Table ?? is shown the figure of merit that those authors report for favored crystalline materials. The figure of merit is the product of the atomic times the crystal form factor evaluated at the leading peak, normalized to the value for diamond.

Table ?? shows that the list of viable materials for a crystal radiator is relatively short. Silicon would be an excellent choice from the point of view of price and fabrication, but unfortunately it is far inferior in terms of performance. Beryllium carbide is not a material that is familiar to the crystal growth industry, and nothing is known at present concerning its suitability for the growth of single crystals of large area. In general compound materials are more susceptible to radiation damage than are pure elements, which would argue in favor of diamond and beryllium metal. These two materials are comparable in terms of their performance.

Most of the experience to date with coherent bremsstrahlung has been with diamond radiators. Extensive expertise with large diamond crystals, such as would be required for the production of coherent bremsstrahlung radiators, already exists within the gem industry. However such capabilities are typically treated in that highly competitive business as sensitive corporate information, particularly as they pertain to the creation of large gem-quality synthetics. Researchers at the University of Glasgow have established contacts within the gem industry for procuring single-crystal diamonds of high quality and large surface area [?]. The techniques used for selecting and assessing the quality of the diamonds are discussed in the next section.

In general terms, diamonds are classified as type I or type II, where type II have been subjected to greater stresses during their formation than type I. Commonly, type II exhibit substantial plastic deformation. Diamonds are also classified according to the form in which nitrogen atoms are present in the crystal lattice. In type *a* the nitrogen is aggregated into clusters of atoms, whereas in type *b* the nitrogen is almost uniformly distributed throughout the crystal. For coherent bremsstrahlung radiators, type Ib diamonds are the most suitable. Unfortunately, type Ib natural diamonds are very rare and probably the most reliable source of Ib diamonds will be synthetics. At present synthetic diamond mono-crystals typically have

nitrogen concentrations around 100 ppm.

Synthetic diamonds are made using either vapor deposition (CVD) or high pressure high temperature (HPHT) techniques. CVD diamonds have an extensive mosaic and are unsuitable for coherent bremsstrahlung. However HPHT synthetics look very promising, and the Glasgow group have recently acquired a  $5 \times 5 \text{ mm}^2$  synthetic diamond less than  $18 \text{ }\mu\text{m}$  thick which has a [100] orientation. It produces a very good coherent bremsstrahlung spectrum and X-ray measurements show it has rocking curve widths of less than  $10 \text{ }\mu\text{r}$ , quite close to the ideal value for diamond.

Beryllium is another material that might be used as a crystal radiator. Beryllium metal is widely used in industry, being preferred for its high strength-to-weight ratio and robustness, in addition to its transparency to X-rays. Thin films of high-purity beryllium are routinely produced for vacuum window applications, which use some of the same vacuum deposition techniques that would be used for the growth of single crystals. As a radiator material, beryllium is distinguished as the metal with the highest Debye temperature, around  $1400^\circ\text{K}$ . The Debye temperature measures the temperature at which the thermal motion of the atoms in the lattice reaches the level of the zero-point motion due to their confinement in the lattice. A high Debye temperature indicates a stiff crystal lattice, in which the atoms have little liberty to move and so have large momentum fluctuations, as dictated by the uncertainty principle.

A high Debye temperature is important for a bremsstrahlung radiator material for three reasons. First, the cross section for coherent bremsstrahlung from a discrete crystal momentum vector  $\vec{q}$  contains a factor  $e^{-q^2/4M\theta_D}$  which reflects the fact that position fluctuations of atoms in the lattice diminish the coherent effect. This factor is near unity for the low-order crystal momenta provided that the Debye temperature  $\theta_D$  is sufficiently large. Second, the Debye temperature is, roughly speaking, a measure of the stability of the crystal structure and hence its capacity to survive significant doses of radiation. Third, the radiator material will inevitably be heated by the beam, and will normally operate in vacuum well above the ambient temperature. A high Debye temperature means that there is a large range of temperatures over which the material may operate without degraded performance as a crystal radiator. The Debye temperature of diamond is about  $2200^\circ\text{K}$ .

Past experience has shown that diamond meets all of the requirements for a good crystal radiator. Beryllium remains a second choice, to be investigated further in the case that affordable sources of large-area diamond crystals at some point are no longer available.

### 2.3.4 Crystal quality

In the calculation of the coherent bremsstrahlung spectrum it is necessary to take into account the fact that even the very best crystals have some dislocations and other defects. Besides locally disrupting the regularity of the crystal, these defects impose stresses which produce small ripples in the crystal planes. If these ripples were amplified, the surface of a crystal would appear like a mosaic of planar regions with approximately parallel surfaces. The scale of deviations from planarity across the face of a single crystal is termed the *mosaic spread* of the crystal. The mosaic spread contributes in the same way as electron beam divergence to the blurring of the exact energy-angle relation for coherent photons.

Besides dislocations, there are other kinds of crystal defects. The presence of foreign atomic species during the crystal growth process can result in the substitution of impurities at some lattice sites, or the formation of voids where impurities tend to collect in clusters of several

atoms. In the growth of diamond crystals under conditions of high pressure and temperature, the growth rate is greatly enhanced by the presence of a small amount of nitrogen. Thus it is normal that small amounts of nitrogen impurities should exist even in the best natural stones, as well as in the synthetics created by the HPHT process.

The ideal conditions for growth of a perfect synthetic crystal require pre-existing monocrystalline diamond with clean planar facets cleaved along the major crystal planes, upon which new layers of carbon are deposited in succession. If conditions are right, the registry of the atoms with the original crystal is preserved over millions of deposited layers, starting from the original seed. In principle, the expansion of the regular lattice should continue to match up perfectly at the boundaries between the different growth surfaces that originated on the facets of the seed, but in practice the strains from small imperfections that occur during the growth process tend to accumulate there, forming recognizable patterns of concentrated defects known as *growth boundaries*. If the stresses grow too large then new strain regions may develop, leading to a more pronounced mosaic pattern in the subsequent layers.

Unfortunately the growth process has proved difficult to control in a reproducible fashion. As a result, out of several dozen stones examined, only one or two may be of sufficient quality for use as a coherent bremsstrahlung radiator for HALL D. The selection process described below was formerly developed by the Glasgow group to supply crystals for the coherent bremsstrahlung source at Mainz, Germany and subsequently for the Hall B source at Jefferson Lab. The requirements for HALL D are very similar to those of Mainz and Hall B, except that the electron beam current will be higher by about an order of magnitude and the crystals will be cut much thinner.

The diamond ingots from the synthetic process are sliced into sections at the laboratory where they are produced. From these, thin wafers of about  $100 \mu\text{m}$  thickness are cleaved along the (1,0,0) axis and provided to the Glasgow group for assessment. The samples are first examined under a microscope with polarized light. Many of the stresses in the crystal lattice can be revealed in this way, particularly those which exhibit plastic deformation. If the diamond appears clear and featureless under polarized light then it is examined with X-rays. Two types of X-ray measurements are performed.

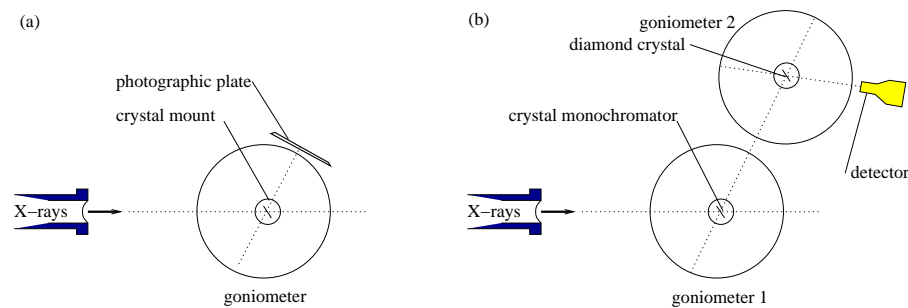


Figure 2.10: Experimental setup for assessment of diamond crystals at the Synchrotron Light Source beam line, configured for topograph measurements (a), and rocking curves (b).

### 1. Topographs

A topograph is a real-space image of a diamond formed from X-rays that Bragg-scatter from a particular set of planes in the crystal, as shown in Fig. ??a. Using the highly-parallel X-ray beam from the Synchrotron Light Source (SRS) and setting the detector

at twice the Bragg angle for a known set of planes for diamond, X-rays of the appropriate wavelength to satisfy the Bragg condition are scattered at a precise angle  $\theta$  into the detector. The X-ray image formed on the plane of the detector is a simple real-space projection of the crystal, called a *projection topograph*. If the vertical slits defining the X-ray beam are narrowed forming the incident beam into a thin ribbon a few  $\mu\text{m}$  wide, then the image at the detector reveals a slice through the crystal, called a *section topograph*. Projection topographs reveal any large-scale imperfections in the crystal. Section topographs can be used to examine the depth profile of imperfections. Topographs sample the whole volume of the crystal. Hence, by measuring projection and section topographs, a 3-dimensional picture of the diamond can be obtained. It is also possible to differentiate between screw and edge dislocations. The topograph image reveals dislocations, growth boundaries and any feature which suppresses or enhances Bragg scattering at the selected angle. In principle, topographs taken at different angles provide independent views of the crystal structure. In practice, however, the imperfections that are revealed with one set of planes appear in a similar fashion when viewed from other orientations.

## 2. Rocking curves

A rocking curve is a plot of Bragg-scattering intensity *vs* angle between the incident X-ray beam and the normal to the crystal planes. A diagram of the setup is shown in Fig. ??b. First the broad-band X-ray beam from the SRS is monochromated by scattering at a known fixed angle from a reference crystal, in this case silicon. This beam is then directed at the diamond crystal under study, from which it scatters a second time and is detected. The scattering is appreciable only when the diamond is at just the right angle with respect to the incident beam such that the Bragg condition is satisfied at both crystals. The variation in the scattering intensity with angle as the diamond wafer is rotated through the resonance is called the *rocking curve* for that diamond. A perfect crystal exhibits a rocking curve consisting of a single peak whose width is called the *natural width* and depends on the material. The natural width for diamond is about  $5 \mu\text{r}$ . Instead of a single peak, for actual crystals one typically sees a number of peaks spread out over a region in angle over known as the rocking curve width. Rocking curves widths, for a selected set of crystal planes, measure quantitatively how any defects or dislocations distort the crystal lattice. By adjusting the slits it is possible to examine the rocking curve of a region of the crystal or to examine the entire crystal at once. Using rocking curves it is possible to measure how close to ideal is the lattice structure of the diamond being investigated.

Figs. ??-?? show some of the results that were obtained at the SRS laboratory in Daresbury, England in January, 2002. At the left of the figures is shown a projection topograph taken using the (0,4,0) planes, the second harmonic of the (0,2,0) planes used for coherent bremsstrahlung. At the right is shown the corresponding rocking curve taken in combination with a silicon crystal set to reflect from the (3,3,3) planes at a wavelength of  $1 \text{ \AA}$ . The two diamond wafers had been cut from the same original type Ib stone, with Fig. ?? coming from the end close to the seed, and Fig. ?? coming from near the middle of the ingot. The topographs are negatives, meaning that the image is dark in regions where the X-ray intensity was largest.

The first thing to notice from the topographs is that both wafers are mono-crystalline; there are no regions where X-rays do not scatter. Even so, there are important differences between the two samples. The growth boundaries (the picture-frame pattern) which are visible

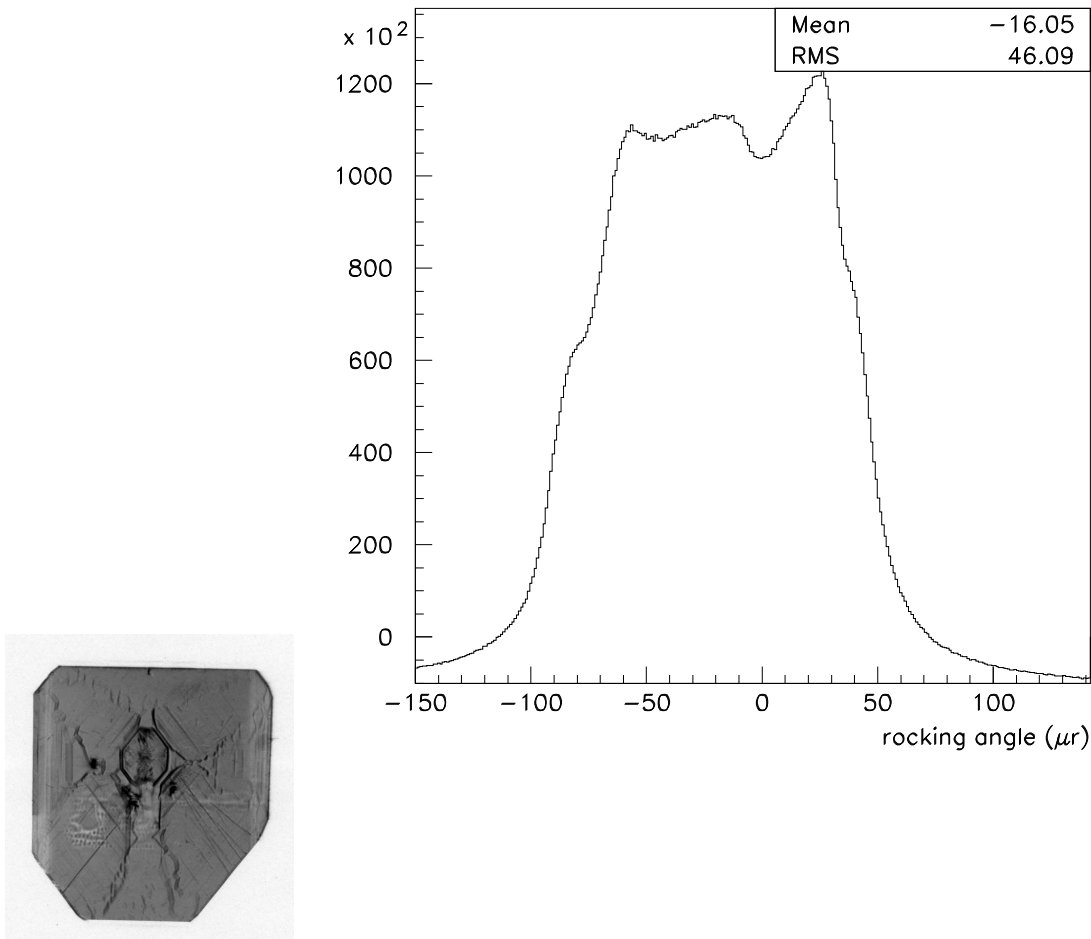


Figure 2.11: Experimental data collected using highly-parallel X-rays from the SRS light source for stone 1482A slice 3 (close to the seed). At the top is shown a projection topograph of the wafer taken using the broad-band X-ray beam and a Polaroid film placed at the angle for reflection from the (0,4,0) planes. The image is a magnified by a factor of 5. The graph shows the rocking curve for the same set of planes, taken using a NaI counter and 1 Å X-rays monochromated by a silicon crystal.

in Fig. ?? spread out and become less pronounced in slice 2 which was taken further from the seed. It is interesting that the strain pattern appears mostly as dark regions rather than light, which indicates stronger scattering in the defects than in the ordered regions, the opposite from what one might naively expect. It should be recalled that both crystals appeared clear and featureless under polarized light at visible wavelengths. The requirement for a diamond radiator useful for HALL D is that the rocking curve width be of the same order of magnitude as the divergence of the electron beam at the radiator, which when folded with multiple-scattering is about 25  $\mu r$  r.m.s. The conclusion is that slice 2 is a good candidate for use in the GLUEX experiment, and that slice 3 is not. Having confirmed the quality of slice 2, it should now be

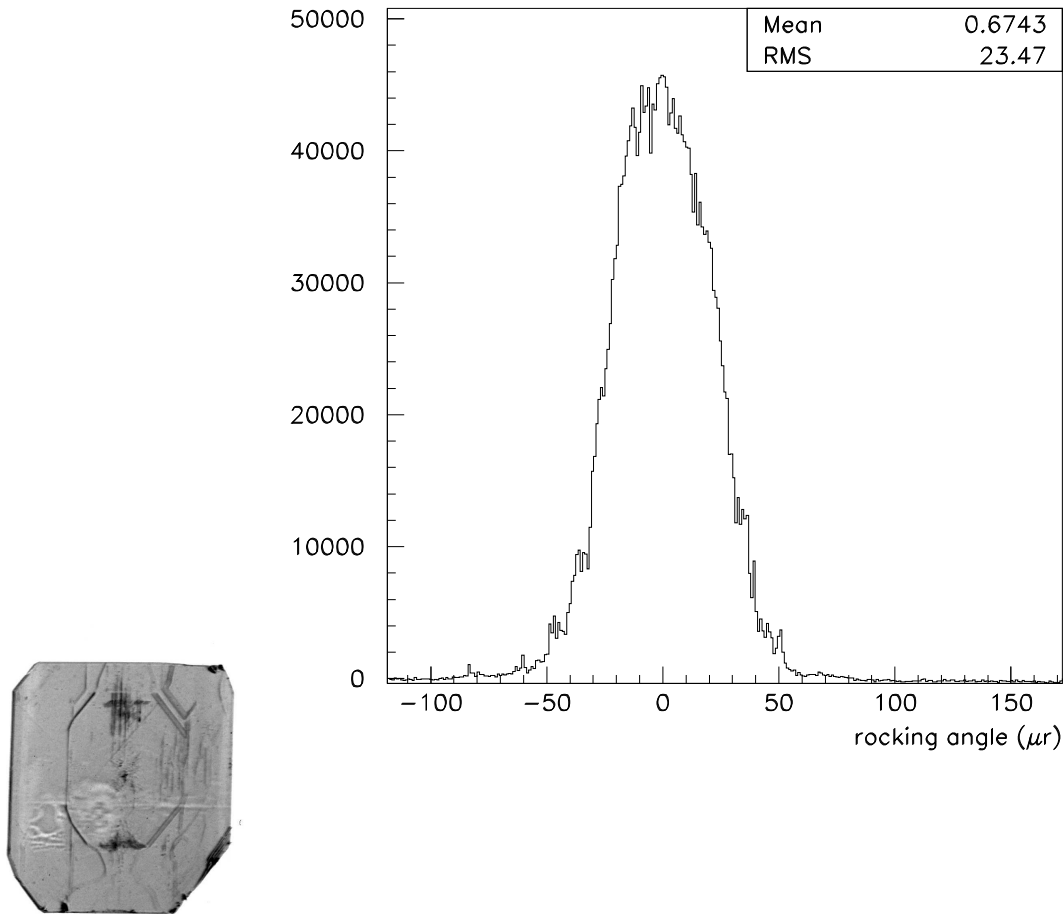


Figure 2.12: Experimental data collected using highly-parallel X-rays from the SRS light source for stone 1482A slice 2 (further from the seed). At the top is shown a projection topograph of the wafer taken using the broad-band X-ray beam and a Polaroid film placed at the angle for reflection from the (0,4,0) planes. The image is magnified by a factor of 5. The graph shows the the rocking curve for the same set of planes, taken using a NaI counter and 1 Å X-rays monochromated by a silicon crystal.

possible for the manufacturer to cut a dozen or more wafers of similar quality from that region of the original stone.

### 2.3.5 Crystal thickness

The range of permissible thicknesses for a crystal radiator is bounded both from above and below. It is bounded from above by multiple scattering of the electron beam as it passes through the radiator, which causes the divergence of the incident beam to grow, thereby enlarging the photon beam spot on the collimator face and degrading the degree to which collimation

discriminates against the incoherent component in favor of the coherent part. It is bounded from below by the fact that the crystal must have some minimum thickness in order to achieve the full coherent gain. In the calculation of the coherent bremsstrahlung process one begins by assuming an infinite crystal, although practically it is presumed to mean only that the crystal is large compared to some characteristic scale. It is important to identify what the characteristic scale is in this problem in order to know how thin one can make the crystal without hurting performance. In the analogous case of the Mössbauer effect, one can estimate the number of atoms participating in the collective absorption by looking at the emission time of the photon (lifetime of the radiating transition) and asking how many nuclei lie within the envelope of the photon wave packet. In the coherent bremsstrahlung process, the lifetime of the radiating system is given in the lab system by the uncertainty principle and by how far the electron energy deviates from its on-shell value between absorbing the virtual photon and emitting the real one. The latter quantity is almost exactly given by  $q_z$ , the virtual photon momentum component along the incident electron axis, which means that the electron travels a distance  $\lambda = \hbar c/q_z$  during the interaction. For a given coherent peak at normalized energy  $x$  in the photon spectrum, the coherence length is given by

$$\lambda = \frac{2E(1-x)}{xm^2} \quad (2.3)$$

in units of  $\hbar c$ . From this simple argument one sees that the coherent gain goes linearly to zero at the end-point, a result that is borne out by the full QED calculation. One also sees that the lower limit on crystal thickness imposed by the coherence length depends upon both the electron beam energy and the photon energy. For a 12 GeV beam energy and a 6 GeV coherent photon the coherence length is 18 nm, or about 50 unit cells for diamond. This shows that the coherence length does not impose a practical limit on how thin the radiator should be.

The effects of multiple scattering are best presented by showing the calculated spectra for various radiator thicknesses. In Fig. ?? is shown the photon spectrum for a  $10^{-4}$  and a  $10^{-3}$  radiation-lengths radiator to demonstrate the effect. The  $10^{-3}$  radiator spectrum is scaled down by a factor of 10 to facilitate the comparison. The calculation assumes a 3.4 mm collimator located 80 m downstream of the radiator. The loss in normalized intensity with the thicker radiator, as well as the broadening of the left edge of the peak, is due to the enlarging of the photon beam spot on the collimator face from multiple scattering of the electron beam in the crystal prior to radiation. A  $10^{-4}$  diamond radiator is 15  $\mu\text{m}$  thick. The goal for GLUEX is to run with crystals of thickness in the range 10  $\mu\text{m}$  to 20  $\mu\text{m}$ .

### 2.3.6 Crystal mount

It has already been shown that in order to achieve appreciable coherent gain the crystal must be oriented so that the coherent peaks appear well below the end point. Equation ?? then implies that the orientation must be such that the crystal momentum dotted with the beam momentum be of order  $m^2$ . Given a  $p$  of 12 GeV and  $q$  of 10 keV, this requires that the two vectors must be within 100  $\mu\text{r}$  of perpendicular to each other and that, within a range of angles of that order, the coherent peak sweeps out nearly the full range in  $x$  from 0 to 1.

Hence, to have a stable photon beam with the coherent peak positioned at the right energy, the angle between the incident electron beam and the crystal radiator must be adjustable in steps of a few  $\mu\text{r}$  and remain stable at this level. Since the angle of the incident beam is fixed by the beamline optics and the position of the photon collimator, all adjustments must be made

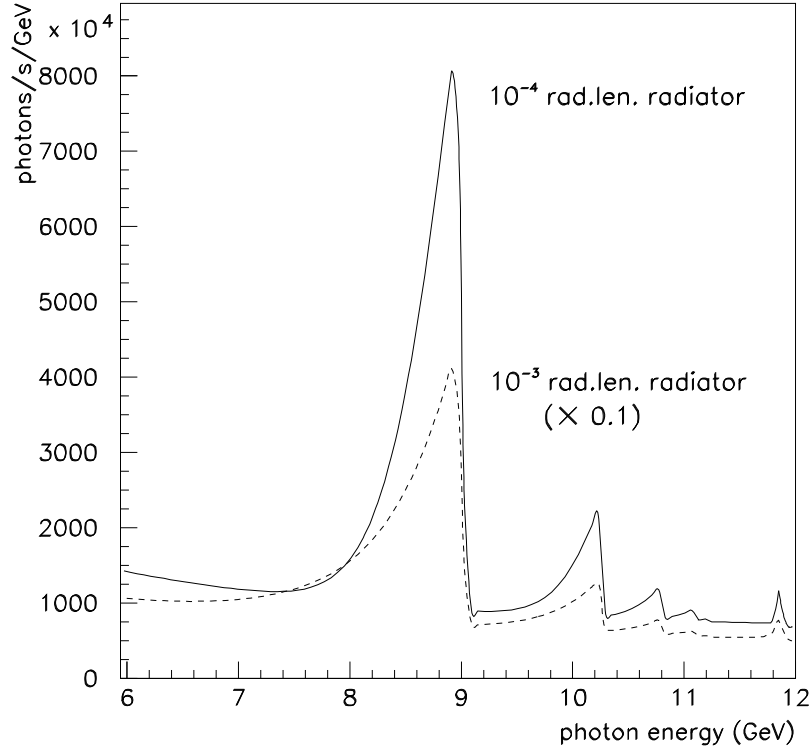


Figure 2.13: Collimated coherent bremsstrahlung spectrum from a  $1\mu\text{A}$  electron beam at  $12\text{ GeV}$  using diamond radiators of two different thicknesses. The calculation assumes a  $3.4\text{ mm}$  collimator located  $80\text{ m}$  from the radiator, and typical values for beam emittance and crystal quality.

by changing the orientation of the crystal. This is achieved with a precision goniometer (shown schematically in Fig. ??) which should provide motion on at least 5 axes. Rotation about the azimuthal axis  $\phi$  sets the orientation of the polarization plane, rotations about the  $\theta_v, \theta_h$  axes set the angle of the crystal relative to the beam, and  $x, y$  translations select the position of the beam spot on the crystal. Estimates of the approximate range and step size for each of the axes are given in Table ??.

In practice several targets need to be mounted in the goniometer. The minimum requirement is a diamond crystal, an amorphous radiator, and a blank. It is also desirable to have a screen to show the position of the beam spot and a spare diamond. This means either mounting some targets off-axis on the azimuthal plate (as in the Mainz setup), or having a sixth axis to allow a target ladder to sit inside the azimuthal plate (as in the Jlab Hall B setup). A goniometer with the required precision can be obtained commercially, and would be controlled with the slow controls system.

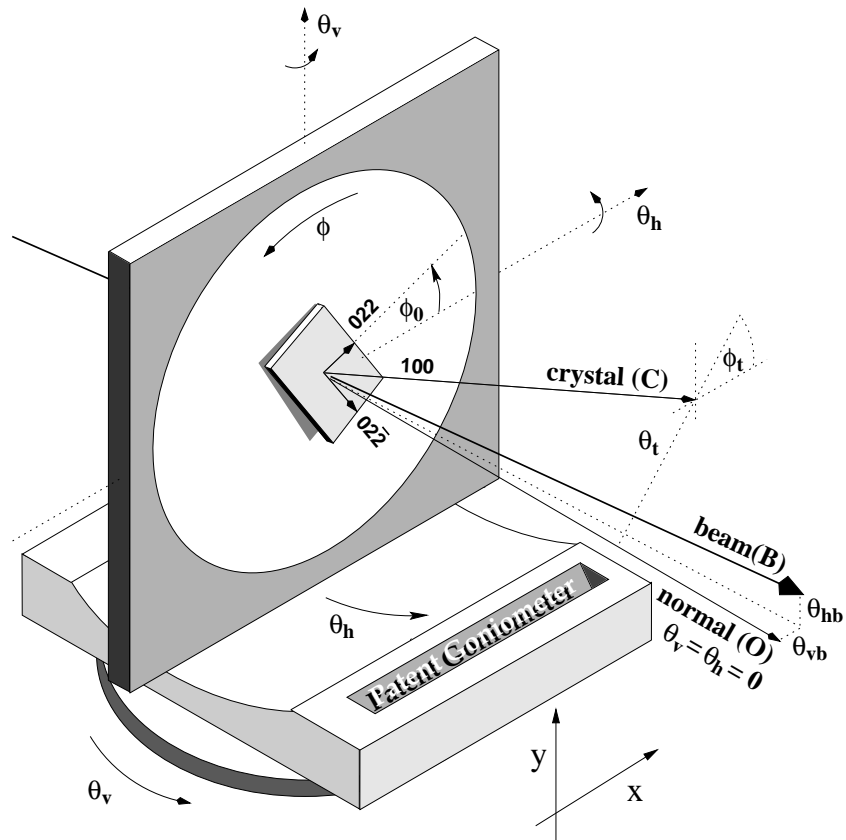


Figure 2.14: Schematic illustration of crystal mounted in goniometer

### 2.3.7 Crystal alignment and monitoring

As can be seen in Fig. ?? the goniometer setting  $\theta_v, \theta_h$  defines the direction of the normal to its inner plate (O). Ideally at its zero setting  $\theta_v = \theta_h = 0$  this would coincide with the electron beam direction (B), but in practice there are small offsets  $\theta_{vb}, \theta_{hb}$  which may vary according to the stability of the electron beam. There will also be a misalignment of the crystal lattice with respect to the inner plate due to imperfections in the mounting and in the cutting from the original stone. The 100 axis (C) will be tilted with respect to the inner plate at an angle  $\theta_t$  with

Axis	Motion	Range	Step size
x	horizontal translation	-50 mm – +50 mm	0.01 mm
y	vertical translation	-20 mm – +20 mm	0.01 mm
$\theta_v$	vertical rotation	-100 mr – +100 mr	10 $\mu$ r
$\theta_h$	horizontal rotation	-100 mr – +100 mr	10 $\mu$ r
$\phi$	azimuthal rotation	-100° – +100°	0.01°

Table 2.2: Requirements for goniometer axes

this maximum tilt occurring at an azimuthal angle  $\phi_t$ . In addition, the 022 vector will be offset by  $\phi_0$  with respect to the horizontal. Any motion about the azimuthal axis  $\phi$  changes the angle of the 100 axis (C) relative to the beam. The angle of the polarization plane is set by adjusting the azimuthal angle of the crystal  $\phi$ . Hence when a new crystal is installed, the default value  $\phi_0$  needs to be measured. Furthermore, to position the coherent peak at the required photon energy, the angle (or *offsets*) between the beam and 100 crystal axis (C) at the chosen value of  $\phi$  must also be established.

Feedback on the relative angle between the crystal and the beam is obtained from a photon energy spectrum derived from the tagger focal plane counters, either via scalers or a TDC hit pattern. The scaler spectrum does not show the effect of collimation (unless the scalers are gated with a downstream photon detector), but can be obtained very quickly since it does not require a triggered data acquisition system. The scaler readout is essential for the alignment process, where the offsets are measured by carrying out a series of scans in which 2d histograms of photon energy vs. crystal angle are built up by moving the goniometer in a sequence of small angular steps and reading the tagger scalers. In addition to providing the feedback required for alignment, the focal plane counters provide essential online diagnostics to monitor drifts in angles caused by the beam tuning, or thermal effects in the crystal mount. If necessary a feedback system could be implemented via the slow control system, where any drift in the position of the coherent peak could be corrected by periodically adjusting the goniometer within predefined limits.

The spectrum obtained from the tagger focal plane can also provide online monitoring of the photon polarization to within 5% by fitting with an analytic bremsstrahlung code. A more detailed discussion of polarimetry appears in the following sections.

### 2.3.8 Crystal lifetime

The best information regarding crystal degradation comes from X-ray studies performed by the Glasgow group of a diamond which had been used in the MAMI coherent bremsstrahlung source at Mainz for several years. The electron beam on the Mainz crystal had a diameter of about 100  $\mu m$  and it was estimated that around  $10^{20}$  electrons had passed through the diamond during its use in the source. There was a small greenish black spot where the beam had hit the diamond.

The X-ray rocking curve measurements showed that considerable damage had occurred to the integrity of the crystal structure in the center of the beam spot. However 2  $mm$  away from the damage center the width of the diffraction peak was the same as it had been for the pristine crystal, which indicates that the lifetime of the crystal could be extended by occasionally moving the beam spot on the face of the crystal.

The area of the MAMI beam spot on the radiator is two orders of magnitude smaller than what is being planned for GLUEX in HALL D. A larger spot means a longer crystal lifetime before radiation damage substantially degrades its crystal properties. Appropriately scaled, the exposure of the Mainz crystal would correspond to 15 years of running in HALL D at the full intensity of 3  $\mu A$  without a spot move. Plans for the HALL D source are to keep the exposure about three orders of magnitude less than this. At the SLAC coherent bremsstrahlung beam line it was found that the performance of their diamond radiators had degraded noticeably after a total charge of 3 Coulombs had been accumulated over a spot of size roughly 2  $mm$  r.m.s., leading to a limit of about 0.25 Coulomb/ $mm^2$  [?]. Taking this as a conservative estimate for the

allowed exposure, the source can run at a full intensity of  $3 \mu A$  for 60 hours before it is necessary to move the spot on the crystal. If it had no bad zones, a square crystal of  $5 \times 5 \text{ mm}^2$  would accommodate 5 spot moves before the crystal would need to be replaced. SLAC researchers were able to recover a good performance for the damaged crystals by putting them through an annealing process. Further research and development will be required to determine whether crystal recovery through annealing is an effective way to reduce the operating costs of the HALL D source.

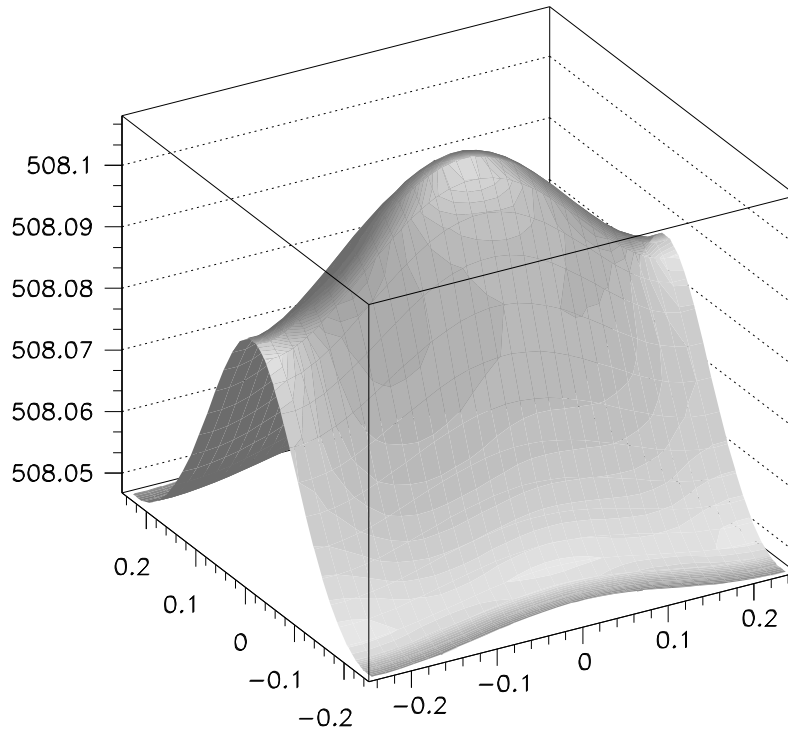


Figure 2.15: Calculated temperature profile of diamond crystal with a  $12 \text{ GeV}$  beam at  $3 \mu A$ . The crystal dimensions are  $5 \text{ mm} \times 5 \text{ mm} \times 15 \mu m$ . The ambient room temperature was taken to be  $27^\circ \text{ C}$  (300 K). The x-y asymmetry is caused by the elliptical shape of the electron beam spot on the radiator.

Another issue related to crystal degradation is that of heat dissipation for very thin crystals. The heat comes from the ionization energy loss of the beam as it passes through the crystal. Although this is small compared to the bremsstrahlung energy loss, it is not entirely negligible at these beam currents. It can be calculated using the restricted energy loss formula, which yields  $21 \text{ mW}$  for a  $15 \mu m$  ( $10^{-4}$  radiation lengths) crystal at a current of  $3 \mu A$ . This is not much power, but the crystal is very thin. Heat dissipation is through radiation and conduction. Diamond has a very high melting point; at low pressures it sublimates at about  $4027^\circ \text{ C}$ . However at normal pressures it begins to transform into graphite above  $707^\circ \text{ C}$ , at a rate that

depends on temperature. It is therefore important that the crystal at the center of the beam spot stay well below this limit.

The diffusion equation including a heating term and one for radiative cooling can be written as

$$\rho C_P a \frac{dT}{dt} = h(x, y) - 2\sigma\epsilon (T^4 - T_0^4) + \kappa a \nabla^2 T$$

where the heating term  $h(x, y)$  has units of power/area,  $\sigma$  is the Stefan-Boltzmann constant,  $\epsilon$  is the emissivity of diamond,  $\rho$  is the density,  $C_P$  is the heat capacity,  $\kappa$  is the coefficient of thermal conduction, and  $a$  is the thickness of the crystal.  $T_0$  is the ambient temperature of the environment and  $T$  is the local crystal temperature, a function of space and time coordinates. After a certain time,  $T$  converges to the steady-state solution shown in Fig. ???. The calculation used a crystal of dimensions  $5 \times 5 \text{ mm}^2$  and a beam current of  $3 \mu\text{A}$ . The conductivity of diamond is sufficient to prevent significant temperature gradients across the crystal even for very thin wafers, and radiative cooling alone is sufficient to dissipate the heat being generated by the beam passing through the crystal so that the crystal mount does not need to act as a heat sink. The time constant for warm-up and cool-down is approximately 10 s.

## 2.4 Electron beam

The performance of the photon source is dependent upon the parameters of the electron beam in several important areas. These parameters are listed in Table ??. The first column of numbers gives the set of parameters that have been adopted as the design goals for the source. These are the values that have been taken as input in calculating the characteristics of the coherent bremsstrahlung source. The second column of numbers was obtained from a concrete design of the HALL D beam line [?] that was carried out by members of the Jefferson Lab Accelerator Division. The exact choice of the final parameters has not yet been made, but the preliminary design shows that all of the design goals can be met within the available real estate. The reduction of the radiator-collimator distance from 80 to 75  $m$  does not significantly affect the performance of the source.

The following sections highlight the particular properties of the electron beam which have a special impact on the performance of the source.

### 2.4.1 Beam polarization

It has already been stated that to generate bremsstrahlung photons with linear polarization it is necessary to use an oriented crystal radiator. However photons with circular polarization are produced by ordinary incoherent bremsstrahlung any time the incident electrons are longitudinally polarized. In fact for 9  $GeV$  photons produced by 12  $GeV$  electrons, the transfer from electron beam longitudinal polarization to photon beam circular polarization is greater than 80%. This raises the question of what happens when one has longitudinally-polarized electrons incident on an oriented crystal radiator. What happens in this case is that the photon beam is elliptically polarized; it carries both circular and linear polarization. There is a sum rule that limits the sum of the squares of the linear plus circular polarizations to be no greater than 1. Hence one sees the linear polarization in coherent bremsstrahlung going to zero as one approaches the end-point energy (see Fig. ??) while at the same time the circular polarization goes to 1 at the end-point (assuming electrons of 100% longitudinal polarization).

parameter	design goals	design results
energy	12 $GeV$	12 $GeV$
electron polarization	not required	available
minimum useful current	100 pA	100 pA
maximum useful current	3 $\mu A$	5 $\mu A$
r.m.s. energy spread	< 10 $MeV$	7 $MeV$
transverse $x$ emittance	10 $mm \cdot \mu r$	10 $mm \cdot \mu r$
transverse $y$ emittance	2.5 $mm \cdot \mu r$	2.3 $mm \cdot \mu r$
$x$ -dispersion at radiator	none	negligible
$y$ -dispersion at radiator	none	< 1 cm
$x$ spot size at radiator	1.7 $mm$ r.m.s.	1.55 $mm$ r.m.s.
$y$ spot size at radiator	0.7 $mm$ r.m.s.	0.55 $mm$ r.m.s.
$x$ image size at collimator	0.5 $mm$ r.m.s.	0.54 $mm$ r.m.s.
$y$ image size at collimator	0.5 $mm$ r.m.s.	0.52 $mm$ r.m.s.
distance radiator to collimator	80 m	75 m
position stability	$\pm 200 \mu m$	

Table 2.3: Electron beam properties that were asked for (column 2) and obtained (column 3) in a preliminary optics design for the transport line connecting the accelerator to the HALL D photon source.

The statement in Table ?? that electron beam polarization is not required for the GLUEX experiment in HALL D is correct, but it is not correct to assume that the photon source is independent of the state of polarization of the electron beam. The presence of a non-zero circular polarization in the HALL D photon beam will, in principle, produce observable effects in the angular distributions measured in photoproduction reactions. This means that there will be an important coupling between the GLUEX program and the other experimental halls whose programs sometimes require them to have control over the beam polarization. This coupling can be eliminated by setting up the tune of the electron beam line to HALL D such that the longitudinal component of the electron beam polarization is rotated to zero at the crystal radiator. Whether the decision is made to rotate it away or simply to measure its value periodically, this consideration underlines the importance of having a means to measure photon beam polarization in a way that does not rely on *a priori* knowledge of the properties of the electron beam.

Although the ability of the source to produce photon beams with both circular and linear polarization complicates operation when one of them is desired without the other, it does increase the versatility of the source. The two kinds of polarization are controlled independently of one other, and together they give access to a more complete set of polarization observables than would be possible with only one or the other.

### 2.4.2 Beam emittance

The values for the electron beam emittances shown in Table ?? are estimates based upon the parameters of the current machine projected to 12  $GeV$  [?]. The definition of emittance used here is the product of the r.m.s. widths of the beam in transverse position and divergence angle.

Because synchrotron radiation inside the accelerator occurs mainly in the horizontal plane, the emittance values in  $x$  are generally larger than those for  $y$ . The two vertical bends required for bringing the 12  $GeV$  beam from the level of the accelerator up to beam height in HALL D do increase the vertical emittance a small amount over its value inside the machine; this effect has been included in computing the vertical emittance shown in Table ??.

The longitudinal emittance of the beam is important as it is the limiting factor in determining the ultimate energy resolution of the tagger. The design goal of 0.1% photon energy resolution is well matched to the energy spread expected for the CEBAF beam at 12  $GeV$ .

The place where transverse emittance plays a critical role is at the photon collimator. For optimum effectiveness in collimation it is important that the virtual electron beam spot at the collimator position be as small as possible. The electron beam does not actually reach the photon collimator, being bent into the dump by the tagger magnet shortly after the radiator. But considering the optics of the electron beam as if the tagger dipole were switched off, the electron beam at the radiator can be projected forward to form a virtual image on the collimator entrance plane. The position and size of this virtual spot determines the definition of  $0^\circ$  emission angle for the photons. If this spot is small compared to the collimator aperture and is correctly centered then the bremsstrahlung photons of a given emission angle  $\alpha$  intersect the entrance plane of the collimator in a well-defined ring of radius  $D\alpha$  concentric with the collimator aperture, where  $D$  is the distance between the radiator and the collimator entrance plane. In this way a collimator of diameter  $d$  passes only those photons of emission angle  $\alpha \leq d/2D$ . If however the size of the virtual spot is comparable to or larger than the collimator aperture then the ring image of photons of a given emission angle  $\alpha$  is smeared out, so that the effect of collimation is simply to reduce the intensity of the beam but not to enhance the coherent component.

Note that this analysis does not place any specific limits on the size of the beam at the radiator. The beam spot can and should be larger there to increase the lifetime of the crystal between spot moves. For the SLAC coherent bremsstrahlung source the beam spot at the radiator was about 2  $mm$  r.m.s., focused down to a 1  $mm$  r.m.s. virtual spot at the primary collimator positioned 91  $m$  downstream of the radiator.

The superior emittance characteristics of the CEBAF beam allow the transverse dimensions to be somewhat smaller than this for the HALL D source, more so in the vertical than the horizontal dimension. The difference between the horizontal and vertical emittance of the CEBAF beam implies that making the spot round at the radiator implies an elliptical virtual spot at the collimator, and *vice versa*. It is difficult to construct a collimator with an elliptical aperture, so the choice was made to make the virtual spot round. This is why the beam spot on the radiator is asymmetric.

Figure ?? shows how the collimated photon spectrum depends upon the transverse emittance of the electron beam. To generate this plot the increases in emittance were simply translated into an increased virtual spot size on the collimator. This was done because it was assumed that the spot size of the electron beam on the radiator, already close to 2  $mm$  r.m.s., cannot be further inflated and stay contained within the limits of the crystal. When the virtual spot size becomes comparable with the collimator aperture then the collimation is rendered ineffective, and the photon spectrum and polarization revert to their uncollimated values. There is another connection between focal spot size and beam emittance that is connected with the requirement that all electrons enter the radiator at the same incidence angle with respect to the planes of the crystal. Practically, the divergence does not broaden the coherent peak provided

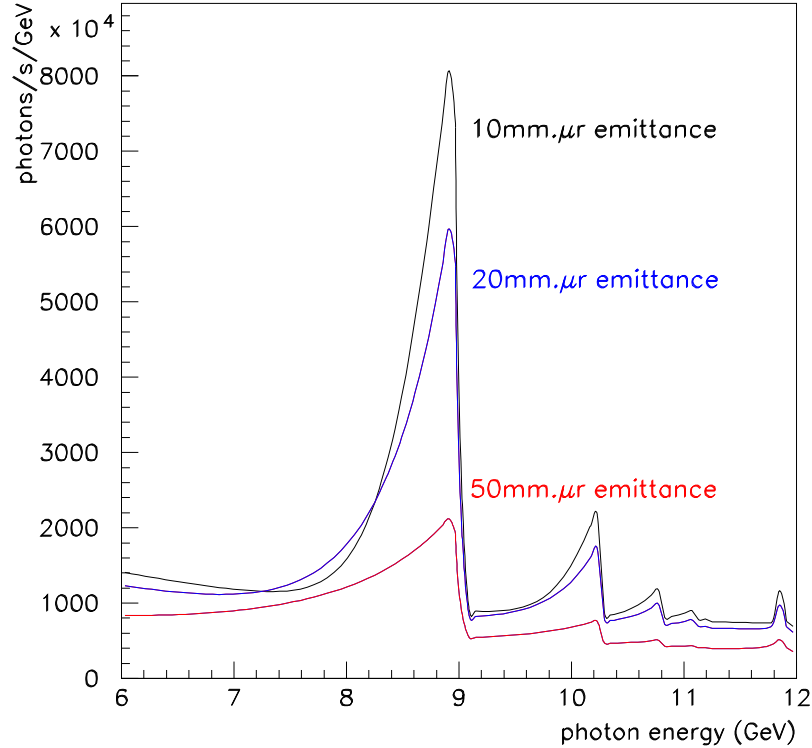


Figure 2.16: Coherent photon spectrum for three different values of the electron beam transverse emittance. The horizontal (shown on the plot) and vertical emittances are assumed to scale together. A 3.4 mm collimator located 80 m from the radiator was used for this calculation.

that it is kept below the mosaic spread of the crystal. A conservative value for the allowable angular divergence  $\delta$  in the electron beam at the radiator would then be  $20 \mu r$ . Taken together with a  $500 \mu m$  r.m.s. spot size at the focus, this leads to an emittance of  $10 mm \cdot \mu r$  at 12 GeV. This corresponds to the upper curve in Fig. ??.

### 2.4.3 Electron beam line optics

Translating the beam emittance into r.m.s. values for the beam radius and divergence requires the knowledge of the  $\beta$  function of the transport line between the accelerator and the radiator, defined as the ratio of the beam size to its angular divergence.

The preliminary optics design [?] of the HALL D beam line (see Table ??) is shown in Fig. ?. The horizontal and vertical beta functions are shown in the upper and lower panels, respectively. Between the two panels is shown a schematic of the transport lattice. The design begins at the exit of the beam from the end of the linac and ends at HALL D. The  $z$  coordinate is measured along the axis of the linac, with its origin at the mid-point of the accelerator. Fig. ??

shows the beta functions translated into r.m.s. beam size and shifted to place the radiator at the origin. The design allows the ratio of the spot sizes at the radiator and collimator to be adjusted over about an order of magnitude simply by changing the current in the beam line elements. In this way it will be possible to optimize the optics for a given size of crystal and collimator after beams are delivered to the hall, and more precise values for the emittances are in hand.

Not only must the virtual electron spot be small enough to fit within the collimator aperture, but it must also be centered on the aperture and stable. In order to maintain a stable beam position on the collimator, the SLAC experiment [?] instrumented the collimator with a secondary-emission detector. The detector was of the “pin-cushion” design and was installed between segments of the collimator near the position of the shower maximum. The readout was divided into four quadrants, which read equal currents when the beam was properly aligned on the collimator. The readout was connected via a feedback loop to the last steering elements on the electron beam line prior to the radiator. Over that distance a bend of only  $10 \mu r$  results in a shift of  $1 \text{ mm}$  at the collimator position. The small deflections that are necessary to keep the beam centered on the collimator do not produce appreciable walk in the beam-crystal angle. This means that an active feedback system can be set up between the instrumented collimator and deflection coils just upstream of the radiator, that can operate independent of the crystal alignment system to keep the electron beam aimed at the center of the collimator.

The experimental program in parity violation at Jefferson Lab has already demonstrated a position stabilization circuit that is able to keep the beam position steady to within  $20 \mu m$  over a  $20 \text{ m}$  lever arm. A less sophisticated version of this circuit will meet the position stability requirements for the HALL D photon source.

#### 2.4.4 Electron beam dump

The electron beam is dumped in the horizontal plane, as shown in figure ???. The horizontal bend offers several advantages over dumping the beam into the ground. The tagger magnet is easier to support if it sits in the horizontal position. It is also easier to mount and service the focal plane instrumentation in this position. The dump itself is also more accessible in case it needs to be serviced. An above-ground dump also affords the possibility of running parasitic beam dump experiments that do not interfere with the operation of the experimental hall.

The primary design requirement for the electron beam dump is that it has a sufficiently high capacity to handle beams of the highest intensities foreseen for the GLUEX experiment in HALL D. A  $60 \text{ kW}$  design would provide a healthy margin for operation of a  $12 \text{ GeV}$  beam at  $3 \mu A$  and sufficient capacity to handle  $3 \mu A$  at  $20 \text{ GeV}$  in the case of a further upgrade.

#### 2.4.5 Beam containment and shielding

There are three factors that must be taken into account in the design of the shielding for the HALL D beam line. The first is the constraint on the background radiation level that is allowed outside the beam enclosure. The second factor is the level of radiation in the experimental hall which can generate background in the detector during normal running. The third factor is the control of hazards which may occur in the event of a failure of one or more of the beam delivery systems. The first issue has been studied by the Jefferson Laboratory Radiation Controls Group, and will be discussed further in the chapter on Civil Construction. The latter two

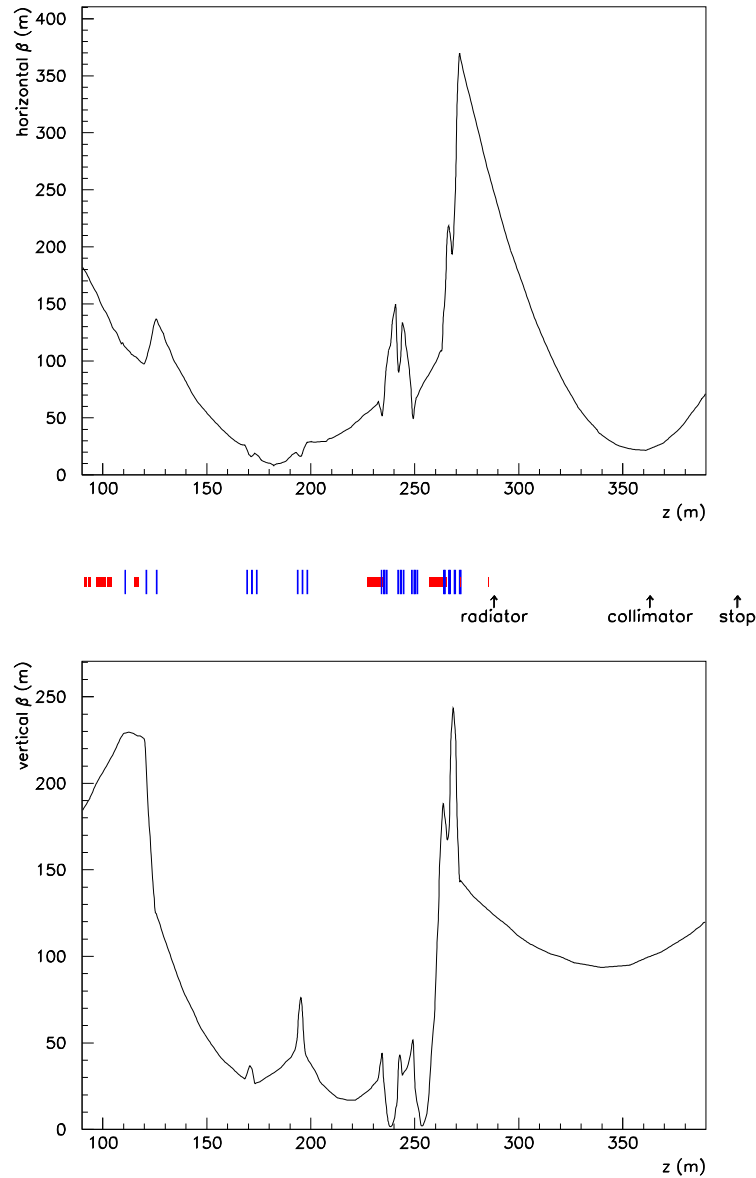


Figure 2.17: Horizontal (upper panel) and vertical (lower panel) beta functions from the preliminary optics design for the transport line from the accelerator to the HALL D photon source. The beam line lattice is shown schematically between the two panels, with dipole magnets represented by the short boxes and quadrupoles by the taller lines. The  $z$  coordinate is equal to the flight path length of the electrons starting at the center of the linac, up to an error of a few cm from the vertical motion of the beam.

considerations have been studied by a working group headed by L. Keller (SLAC). A summary of their recommendations [?] follows.

Assuming that the electron beam dump is shielded to the requirements of radiation safety, the next source of background radiation in the experimental hall is the photon collimator. The

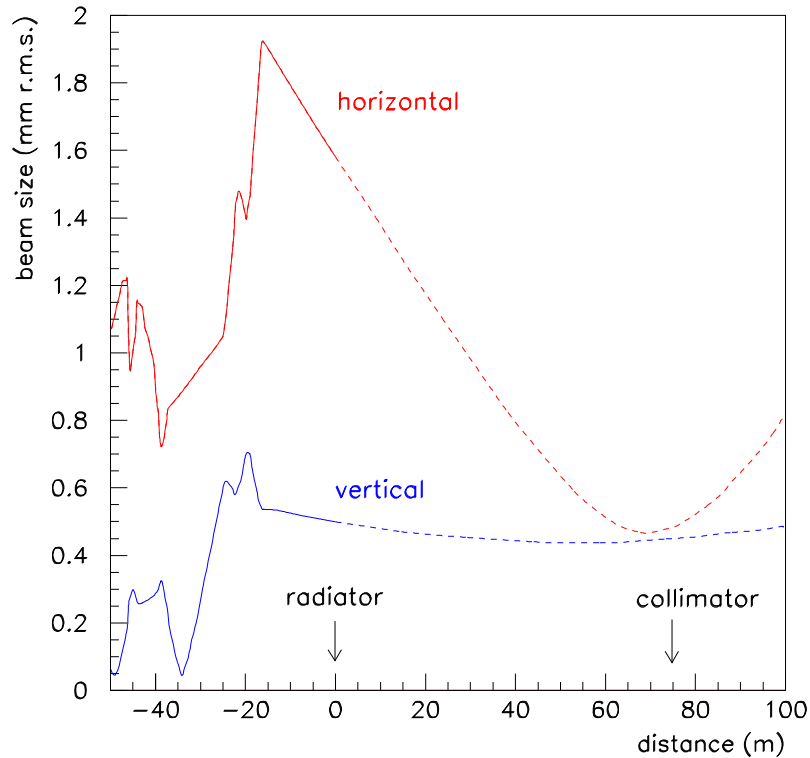


Figure 2.18: Horizontal and vertical r.m.s. envelopes for the electron beam in the region of the photon source, as derived from the beam emittance and beta functions of Fig. ???. The origin of the  $z$  coordinate has been placed at the radiator. In the region between the radiator and the collimator the envelope refers to the projected image of the electron beam, and does not describe the size of a physical beam that exists in that region.

most penetrating forms of radiation from the collimator are muons and neutrons. A Monte Carlo simulation, assuming a 13 radiation lengths tungsten collimator followed by a sweeping magnet and 5  $m$  of iron shielding, predicted a flux of  $1.4 \times 10^3 \mu^\pm/s$  incident on the detector at full operating beam intensity. This is a negligible rate compared with the trigger rate from photon interactions in the target. The flux of neutrons from the collimator is more difficult to calculate, but some fraction of 1  $m$  of concrete shielding will be needed surrounding the collimator enclosure to shield the hall from energetic neutrons.

With regard to hazards associated with the accidental failure of beam line elements or controls, the following measures were recommended in the Keller study [?] and have been incorporated into the HALL D design. The dipole string that bends the electron beam up towards the surface from the below ground and then bends it back horizontal will be connected in series so that failure of a magnet supply or current control electronics cannot result in the beam being steered into the ceiling of the tagger building. The power supply feeding this string of magnets will be protected by a meter relay that shuts off if the current varies from

its desired value outside a predefined tolerance. A similar meter relay will also be used on the power supply of the tagger magnet. An electron beam collimator with a burn-through monitor will be located just upstream of the radiator to prevent a mis-steered beam from using radiator support structures as a bremsstrahlung target. Permanent magnets will be located in the upstream region of the photon beam line to bend an errant electron beam into the ground in the case that beam is present while the tagger magnet is off. An emergency beam stop will be installed in the bottom of the photon beam line to catch the errant beam deflected by the permanent magnets. It will be equipped with a current monitor to shut down the primary beam any time electrons are sensed in the photon beam line. Ion chambers located upstream of the photon collimator, and also at the entrance to the photon beam dump behind the experiment, will monitor the total flux in the photon beam and shut off the beam if the flux exceeds a safe value.

## 2.5 Tagging spectrometer

### 2.5.1 Specifications

To satisfy the needs of the GLUEX physics program, the tagged photon spectrometer should meet the following specifications:

1. Photon energy detection from 70% to 75% of  $E_0$  with energy resolution of about 0.1% r.m.s. Percentages refer to the primary beam energy  $E_0$ , i.e. “0.1%” means 12 MeV energy resolution for a 12 GeV beam.
2. A detector system which allows a counting rate of at least  $5 \times 10^6$  electrons per second per 0.1% over this range of photon energies.
3. An additional capability for photon energy detection from 25% to 90% of  $E_0$ , with less stringent resolution and count rate requirements .
4. A quadrupole magnet between the radiator and dipole spectrometer which images the beam spot on the radiator onto a line on the focal plane. This feature makes it possible to envision the use of focal plane counters with two-dimensional readout, with which one could enhance the tagging efficiency of the source. Focal plane detectors with two-dimensional readout are considered as a possible upgrade beyond the baseline design presented in this chapter. Any improvements obtained using this technique would be over and above the performance figures presented in this report.

The system described below, based on a room-temperature design, meets all of these criteria. The option of a superconducting design was also studied. With a superconducting magnet, the spectrometer could operate at much higher fields, offering the possibility of some space savings in the size of the tagger focal plane array and larger head-room for future possible energy upgrades beyond 12 GeV. An iron yoke design was found which would clamp the 5 T field sufficiently to make it possible to operate normal phototubes on the nearby tagger focal plane. However, as shown below, rate considerations require a degree of segmentation in the tagging counters such that it is impractical to increase the dispersion along the focal plane above what is provided by a 1.5 T room temperature magnet. That being the case, it was decided that considerations of upgrade margin and electrical power alone do not justify the additional cost and complexity of a superconducting magnet.

### 2.5.2 Magnet

The original design of the tagger spectrometer, which incorporated a single, long dipole magnet  $\sim 6.1$  m in length weighing about 100 tons, has been changed to replace the single dipole with a configuration consisting of two identical dipoles in series with each other.

The main reasons for this change are:

1. It will be difficult to find a supplier of  $\sim 6.5$  m lengths of high quality magnetic iron at a reasonable cost.
2. Since the weight of the top and bottom yoke pieces for a single dipole tagger will weigh more than 20 tons, either a crane with a capacity of more than 20 tons or heavy duty lifting equipment will be necessary to install the magnet or undertake any future repairs or modifications.
3. The long structure of a single dipole tagger will be difficult to install.
4. Since the energy degraded bremsstrahlung electrons exit a tagger along the whole of its length, it is necessary to have the exit completely open. Due to the attractive magnetic force between the poles, the aperture along the exit will distort when the field is present. The effect of this distortion will probably be less for two smaller dipoles than for a single long dipole.
5. The smaller magnets can be made by more manufacturers and will probably be cheaper.
6. Building costs will be less for the two dipole option - cheaper crane, smaller access doors etc.

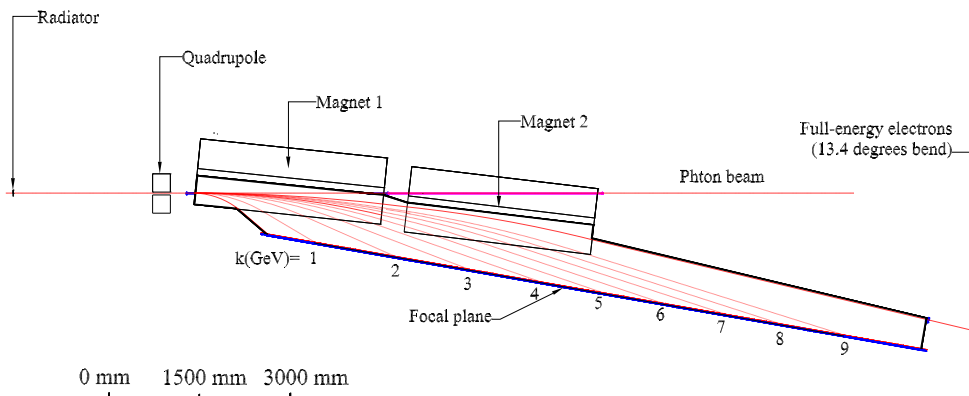


Figure 2.19: A plan view of the tagging spectrometer from above, showing the path of the primary beam and the trajectory of post-bremsstrahlung electrons of various recoil momenta.

The parameters of the two dipole tagger are shown in Table ???. The object distance is listed explicitly since it has been increased from 1.5 m to 3.0 m. This improves the resolution

by around 30% and gives more room for the goniometer vacuum chamber, the quadrupole and monitoring devices. A plan view of the layout of the spectrometer is shown in Figure ??.

Radius of curvature	26.7 m
Full-energy deflection	13.4 <sup>o</sup>
Object distance	3 m
Field at 12 GeV	1.5 Tesla
Gap width	3.0 cm
Length of each pole	3.1 m
Weight of each dipole	38 tons
Length of focal plane (25% to 90% of $E_0$ )	~ 9.0 m
Coil power	30 kW

Table 2.4: Design parameters for the two dipole tagging spectrometer.

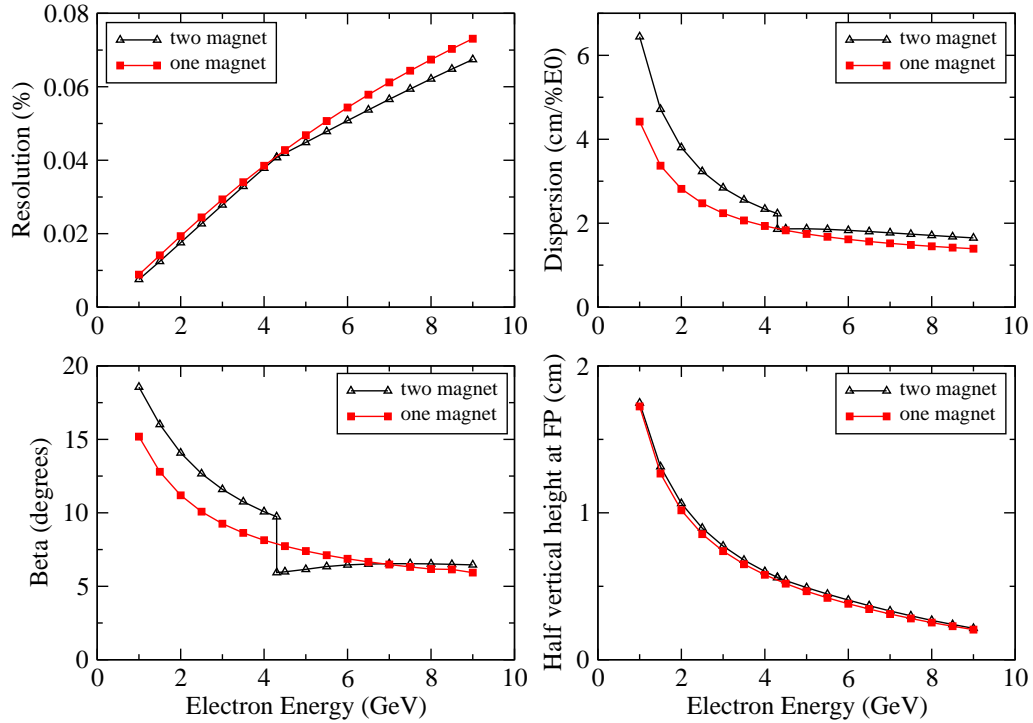


Figure 2.20: Comparison of optics properties between the one dipole and the two dipole tagger.

The coils for the two dipole tagger will be run in series from a single power supply.

The first dipole magnet analyzes electrons from 1 to 4.3 GeV corresponding to photon energies of 7.7 to 11 GeV, and the second magnet analysis electrons from 4.3 to 9 GeV, corresponding to photon energies of 3 to 7.7 GeV. This is ideally matched to GlueX which requires photons in the energy range covered by the first dipole. It is also clear that a two dipole magnet system is optimum, since with more magnets, the energy range required by GlueX would probably have to be shared between different dipoles.

The pole gap has been increased from 2.0 to 3.0 cm. The larger gap is more accessible, and

is less susceptible to any changes to the pole gap caused by the magnetic field. Furthermore since only  $\sim 30 kW$  are required for the  $3.0\text{ cm}$  gap -compared to  $\sim 17.6 kW$  for the  $2.0\text{ cm}$  gap - the coil power consumption remains modest.

The two dipole magnet configuration was only adopted after extensive investigations into the magnetic optics confirmed it is possible to design such a system with a continuous focal plane. First order TRANSPORT calculations of the dispersion, resolution and vertical height along the focal plane, as well as beta, the angle at which the analyzed electrons cross the focal plane, are compared for the single and two dipole magnet systems in Figure ??

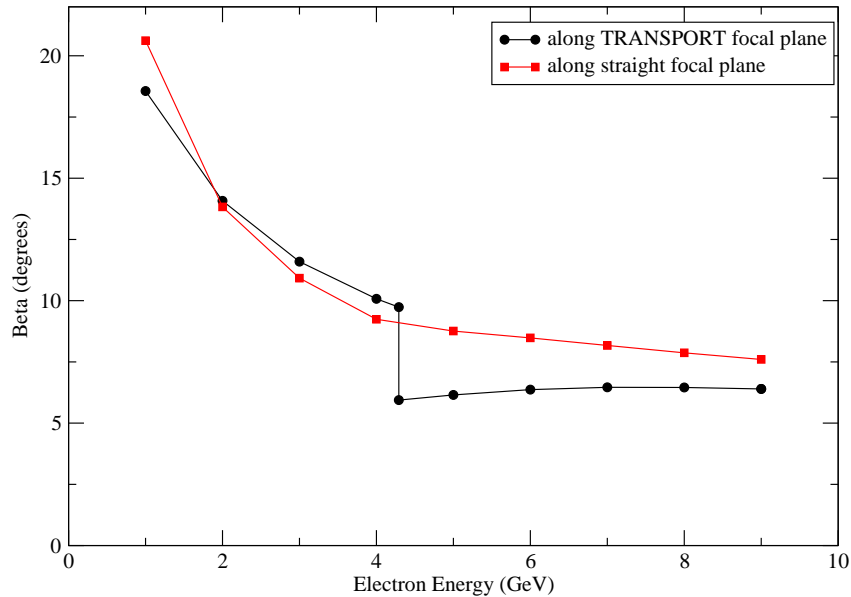


Figure 2.21: Comparison between the beta for the focal plane calculated using TRANSPORT and the beta for the straight focal plane determined according to the TOSCA results.

The resolution and vertical height are essentially unaltered. Although the dispersion shows a small discontinuity at an electron energy  $\sim 4.3\text{ GeV}$ , which is where the focal planes from the dipoles join, along the whole extent of the focal plane the dispersion from the two dipole tagger is slightly larger. However, beta shows a significant discontinuity at the join of the focal planes. This apparent effect was examined in more detail by ray tracing electron trajectories through a 3-D magnetic field obtained from TOSCA. The ray tracing calculations were also used to find an acceptable location for a straight focal plane which is displaced slightly from the curved TRANSPORT focal plane. Figure ?? compares the variation of beta along the straight focal plane obtained using TOSCA, and along the first order TRANSPORT focal plane. It shows that the realistic field computed by TOSCA leads to a smooth variation for beta and also shows that beta is larger for the higher energy section of the focal plane. The magnetic optics parameters, calculated by TRANSPORT along the straight focal plane, are shown in section ??.

Several designs have been considered for the vacuum system. The most promising approach is to use the magnet poles as part of the vacuum chamber. Either the poles could be welded to a stainless steel vacuum chamber, or the seals between the vacuum chamber and the poles could be made by compressing a viton O-ring between the top and bottom lids of the vacuum

k (GeV)	Bend (deg)	Drift (m)	Angle (deg)	cm/% $E_0$ perp.to ray	cm/% $E_0$ along FP
6	17.270	3.7790	6.035	1.467	13.956
7	17.664	3.2039	6.428	1.568	14.008
8	18.28	2.6276	6.992	1.716	14.096
9	19.108	2.0485	7.872	1.954	14.264
10	20.695	1.4626	9.459	2.407	14.644
11	24.608	0.8560	13.372	3.668	15.860

Table 2.5: Geometrical parameters of the tagging spectrometer for  $E_0 = 12$  GeV: Bend = deflection angle; Drift = distance from exit edge to focal plane; Angle = angle between electron path and focal plane;  $cm/\%E_0$  = dispersion in units of cm per percent of the incident energy

chamber and a lip machined round the pole shoes.

A reasonably detailed design for a two dipole magnet tagger, which incorporates a vacuum chamber using O-ring seals, has been completed. The design has been sent to Russian groups within the GlueX collaboration who will examine the technical feasibility of the design and investigate if ISTC funding can be obtained to construct the tagging spectrometer. It should be possible to assemble and test the complete spectrometer in Russia since a feature of the design which uses O-ring seals is that the spectrometer can be fully assembled and tested in the factory where it is built, and then be taken apart and subsequently re-assembled in Jefferson Lab.

The detector package is divided into two parts: a set of 141 fixed scintillation counters spanning the full energy range from 25% to 95%, and a movable “microscope” of more finely-segmented counters designed to span the region of the coherent peak.

The fixed array provides access to the full tagged photon spectrum, albeit at a modest energy resolution of 0.5% and reduced photon spectral intensity. These detectors are well suited for running with a broadband incoherent bremsstrahlung source. They enable experiments to be performed with the highest photon energies possible with the source. When running with a coherent source they play an essential role in the crystal alignment procedure, and provide a continuous monitor of the performance of the source. The microscope is needed in order to run the source in coherent mode at the highest polarization and intensities, and whenever energy resolution better than 0.5% is required. Using the microscope, the source is capable of producing photon spectral intensities in excess of  $2 \times 10^8$  photons/GeV, although accidental tagging rates will limit normal operation to somewhat less than this.

### 2.5.3 Spectrometer Optics

Table ?? and Table ?? give some of the tagger optics parameters as functions of the photon energy. They were calculated for the one-magnet spectrometer option, but the differences between the optics of the two-magnet and one-magnet designs are not very significant, as shown in Figs. ??-??. The energy resolution and transverse position resolution were calculated assuming the beam properties listed in Table ?. The intrinsic energy resolution (i.e. the energy resolution independent of detector size) is limited in most cases by the 0.08% energy spread of the primary electron beam.

k	(x x)	(y y)	(y y')	$\Delta k_{beam}$	$\Delta k_{spot}$	$\Delta k_{tot}$	$\Delta y_{tot}$	$y_{char}$
(GeV)	(mm/mm)	(mm/mm)	(mm/mr)	(% $E_0$ )	(% $E_0$ )	(% $E_0$ )	(mm)	(mm)
Without quadrupole:								
6	-0.701	2.737	18.882	0.080	0.081	0.114	1.372	0.804
7	-0.667	2.708	16.538	0.080	0.072	0.108	1.357	0.986
8	-0.625	2.670	14.178	0.080	0.062	0.101	1.337	1.207
9	-0.569	2.617	11.788	0.080	0.050	0.094	1.310	1.506
10	-0.494	2.539	9.341	0.080	0.035	0.087	1.270	1.989
11	-0.389	2.402	6.745	0.080	0.018	0.082	1.201	3.159
With quadrupole: (length = 50 cm, gradient = -0.4 kGauss/cm)								
6	-0.628	0.451	17.622	0.080	0.073	0.108	0.242	0.750
7	-0.583	0.348	15.121	0.080	0.063	0.102	0.190	0.901
8	-0.526	0.202	12.535	0.080	0.052	0.095	0.119	1.068
9	-0.449	-0.024	9.792	0.080	0.039	0.089	0.050	1.251
10	-0.338	-0.427	6.699	0.080	0.024	0.083	0.216	1.426
11	-0.162	-0.416	2.474	0.080	0.008	0.080	0.708	1.159

Table 2.6: Optical properties and resolutions of the tagging spectrometer at the focal plane, for  $E_0 = 12$  GeV: (x x),(y y),(y y') = first-order transport matrix elements where x and y are radial and transverse coordinates respectively; the focal plane is defined by (x x')=0.;  $\Delta k_{beam}$  = r.m.s. energy resolution due to beam energy uncertainty;  $\Delta k_{spot}$  = r.m.s. energy resolution due to spot size on radiator;  $\Delta k_{tot}$  = total r.m.s. energy resolution excluding detector size;  $\Delta y_{tot}$  = transverse r.m.s. position resolution due to spot size on radiator;  $y_{char}$  = transverse size corresponding to one characteristic electron angle  $\theta_{Ce} = (m/E_0)(k/(E_0 - k))$ .

At the focal plane, the characteristic bremsstrahlung angle corresponds to a few millimeters of transverse displacement. The vertical beam spot size at the radiator (0.5 mm r.m.s.) contributes a comparable amount because of the large transverse magnification in the dipole transport matrix. However, placing a quadrupole magnet between the radiator and the tagger dipole magnet reduces this magnification nearly to zero over a substantial range of photon energies without substantially changing the other optical properties. Including the quadrupole in the design makes possible a future upgrade of the photon source to employ tagging detectors with two-dimensional readout.

## 2.5.4 Tagger detectors

### Fixed focal plane array

Tagging of photons over the full range from 25% to 95% of  $E_0$  is not required as part of the physics program here proposed for GLUEX, but is desirable for two separate reasons. First, it will increase the flexibility of the source by providing a broad-band incoherent bremsstrahlung tagging mode, enabling access to photons of the highest energy possible at Jefferson Lab. Second, the process of aligning the crystal radiator for coherent bremsstrahlung requires rotation about several axes and rapid observation of the resulting energy spectra, as described in section ???. The low-energy portion of the spectrum, between about 25% and 50% of  $E_0$ , is most sensitive to these rotations, and experience with the coherent bremsstrahlung beam at Mainz [?, ?] indicates that the alignment process would be severely compromised if photon

energies below  $0.5 E_0$  were not measurable.

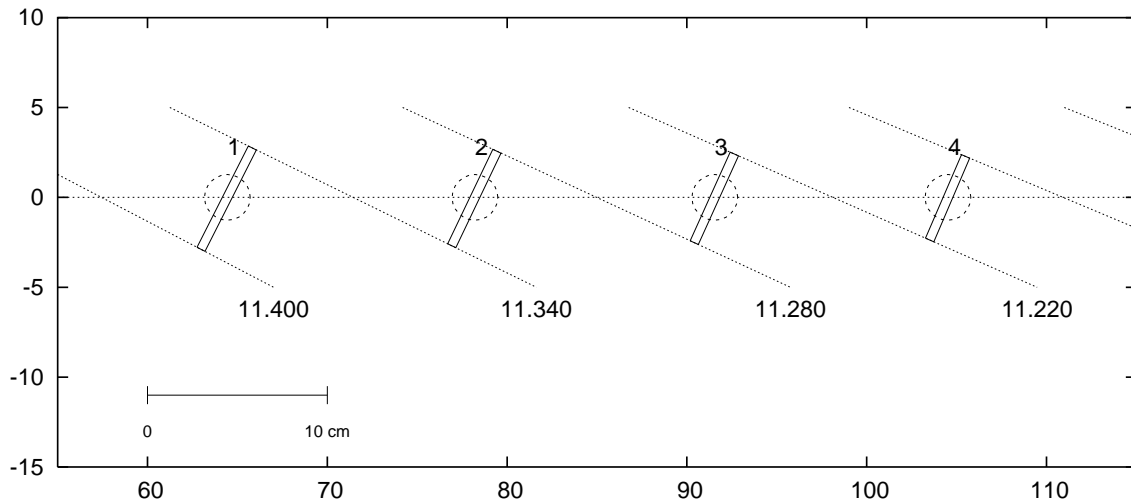


Figure 2.22: Layout of the tagging counters on the high-energy end of the tagger focal plane, corresponding to the lowest-energy electrons from the spectrometer. The view is from above.

The design for the fixed tagger focal plane array consists of 141 non-overlapping scintillation counters. The scintillators are  $0.5\text{ cm}$  thick and  $4\text{ cm}$  high and are read out by 1-inch phototubes located below the mid-plane of the spectrometer. The scintillator paddles are oriented perpendicular to the scattered electron rays and are distributed along the focal plane to give essentially 100% coverage of the range from 25% to 95% of  $E_0$ . The size and spacing of the counters varies along the focal plane, according to the dispersion and crossing angle listed in Table ???. The high-energy end of the array is shown in Fig. ??, which corresponds to the lowest-energy electrons from the spectrometer.

### Focal plane microscope detectors

The design energy resolution of 0.1% r.m.s. (see Table ??) is met by non-overlapping detectors which span an energy range of 0.1% each. The principal limitation on detector size is imposed by the design goal of tagging collimated photons at rates up to 100 MHz over the coherent peak. The nominal collimated coherent peak has its highest intensity between about 8.5 and 9 GeV (see Fig. ??). However, the the tagger sees both collimated and uncollimated photons, and the total tagging rate in this region is more than twice the collimated rate (see Fig. ??), about 250 MHz. The nominal position of the microscope on the focal plane is spanning the

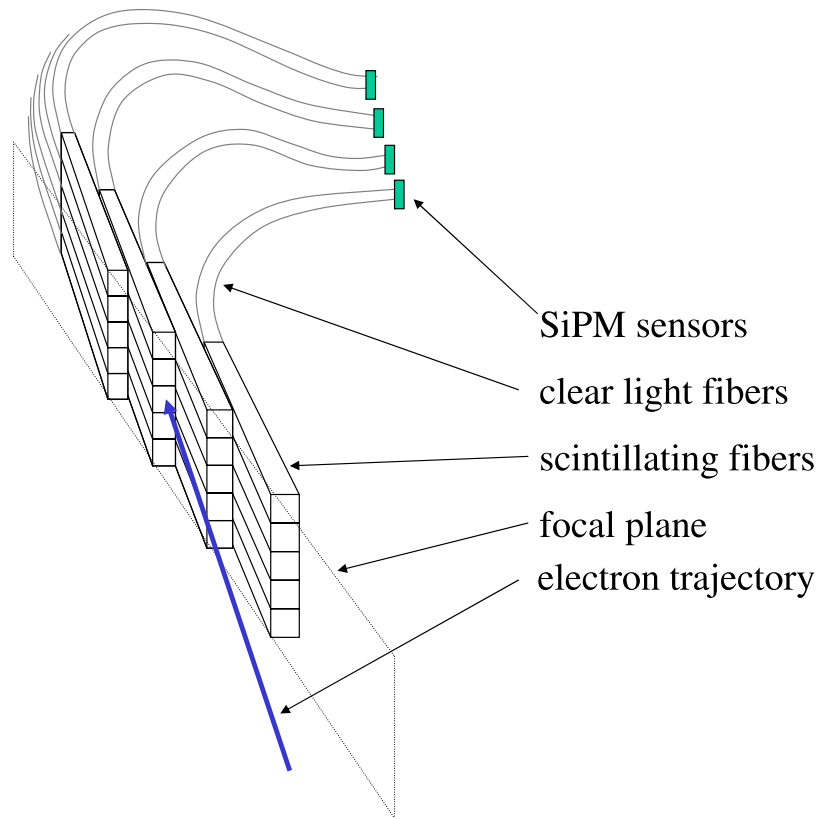


Figure 2.23: Conceptual design of a segment of the tagger microscope, showing the two-dimensional array of scintillating fibers and the clear fiber light guides that couple the light to the silicon photomultipliers.

region 70% - 75% of  $E_0$ . Dividing this range into 80 bins of equal size limits all channels to less than 5  $MHz$ , which is well within the operating range of the silicon photomultiplier (SiPM) devices foreseen to be used for this detector.

The detector is composed of a two-dimensional array of square scintillating fibers of cross section  $1 \text{ mm}^2$ , as shown in Fig. ?? . Electrons from the spectrometer follow a path approximately parallel to the axis of the fibers, creating a large light yield which effectively suppresses omnidirectional background in the hall and permits the operation of the SiPM detectors with a high discriminator threshold where their dark rate is low. Multiple scattering of electrons in the fiber material effectively produces some degree of overlap between the channels, but does not appreciably degrade the energy resolution of the device. Clear fibers attached to the back end of the scintillating fibers transport the light out of the spectrometer mid-plane to a region with low radiation where the SiPM detectors are located, each with an active area of  $1 \text{ mm}^2$ . The microscope will be located immediately in front of the fixed array.

In the baseline operating mode, all five fibers in a column shown in Fig. ?? will be summed into one electronics channel. The vertical segmentation of the device also permits its operation

in an enhanced mode, where only one fiber in each column is active. In the enhanced mode with the tagger quadrupole switched on, the detector counts only a narrow band of scattered electrons that lies close to the spectrometer mid-plane. This has the advantage that the tagger is blind to those electrons which scatter at large vertical angles in the radiator, whose corresponding photon will be lost on the photon collimator. This can be accomplished efficiently by delivering the power to the SiPM devices independently by row. Simply by selectively powering the individual rows of the array, the readout can be switched from tagging the full vertical range of the beam to counting only a central stripe which corresponds to the size of the photon collimator.

### 2.5.5 Beam dump optics

Although the full-energy beam leaving the tagger magnet is diverging in both directions, the range of angles is small enough that the beam does not blow up rapidly. For a dump distance of 30 *m* the r.m.s. beam size is 6.3 *mm* horizontal (dominated by the 0.08% beam energy spread) and 0.7 *mm* vertical (combination of vertical spot size and multiple scattering in a  $10^{-4}$  radiation length radiator.)

These values scale approximately linearly with distance from the magnet to the dump, and are not very sensitive either to the quadrupole or to small rotations of the exit edge of the tagger magnet. Thus the beam dump design is quite insensitive to the beam optics, and depends only on the lateral and longitudinal spread of the shower in the absorber.

## 2.6 Polarimetry instrumentation

labelsec:beam:polar

The majority of bremsstrahlung photons produced in the radiator are absorbed in the collimator system. If the radiator and collimator system are well aligned, the photon spectrum behind the collimators is dominated by the coherent peak. The beam parameters can be determined by using the intensity spectra from the tagger.

Nevertheless, in order to monitor the polarization parameters – degree ( $P_\gamma$ ) and direction ( $\epsilon_\gamma$ ) – of the collimated photon beam it is crucial to have an independent method, either a photon polarimeter detecting the asymmetry of a process that is well understood within theory (QED) or a well known hadronic process so that the measured beam asymmetry can be compared with theoretical (or experimental) expectations. At photon energies above 5 *GeV*, the forward production of vector mesons is described by vector meson dominance (VMD), resulting in a  $\sin^2\theta_{hel}\cos(2\psi)$  dependence of the vector meson’s decay distribution where  $\theta_{hel}, \phi_{hel}$  are the polar and azimuthal decay angles in the helicity frame and  $\psi = \phi_{hel} - \epsilon_\gamma$ . With  $\rho^0$  production accounting for about 10% of all hadronic triggers in the detector, this method suffers no lack of statistics. It is limited only by the accuracy of the VMD approximation, roughly 5 – 10% at these energies.

The other method, measuring the photon polarization by means of a polarimeter, can be realized by a pair polarimeter or a triplet polarimeter. It involves additional hardware components on the beamline between the collimator system and the spectrometer magnet. Both types of polarimeter require a thin radiator and a detector in a field free area followed by a dipole magnet and counters for the trigger. Space is available upstream of the spectrometer in HALL D for the insertion of a polarimeter.

QED based calculations for the latter process show that the angle and energy of the soft (triplet) electron is almost independent of the energy of the incident photon ( $\bar{E}_{triplet} \approx 0.7 - 0.9 MeV$ ). The low rate of this process and the technical challenge for a counter device measuring accurately the angular distribution of low energy electrons do not favor this type of polarimeter.

For pair production, on the other hand, the opening angle between the produced electron and positron decreases with increasing energy making the measurement more complicated at higher energies. A magnetic separation is not desirable because the deflection cannot be determined very accurately. The proposed polarimeter consists of a thin scintillator ( $d = 50 \mu m$ ) as an active target, 1.5 m in front of a silicon microstrip detector arrangement, followed by a dipole magnet and two scintillators 10 cm apart from the beamline for triggering on symmetric  $e^+e^-$  pairs. The microstrip detector consists of four layers having 512 channels each of silicon wafers with a spatial width for a single channel of  $25 \mu m$ . The second and third layer are oriented at  $\pm 60^\circ$  with respect to the first layer, the fourth perpendicular to one of the previous layers, thus allowing to measure the full angular range of produced  $e^+e^-$ -pairs without any gap in the acceptance. A Monte Carlo simulation of this device including multiple scattering in the target, the microstrip detector, and foils in the vacuum system (using GEANT) shows that an analyzing power of 25% is achievable (cf. fig ??). QED calculations predict an angular distribution for pair production proportional to  $(1 + P_\gamma \alpha \cos 2(\phi - \epsilon_\gamma))$  with an analyzing power of  $\alpha = 0.28$  for incident photons in the range of 6-10 GeV. Because of the thickness of the microstrip layers (300  $\mu m$ ) it is convenient to measure the beam polarization for fifteen minutes every time the orientation of the crystal radiator or the electron beam parameters have changed. The scintillator target as well as the detector device have to be mounted on motor driven stages so that they can be removed from the beamline.

A research and development program is underway at the Yerevan Physics Institute to test these ideas using the 2 GeV coherent bremsstrahlung beam line at YerPhi (Yerevan, Armenia). This 2-year program is funded by the U.S. Civilian Research and Development Fund, and supports a collaboration of Armenian and U.S. collaborators from the University of Connecticut. One of the primary goals of this project is to show the accuracy with which the polarization of a coherent bremsstrahlung beam can be calculated based upon QED and the measured shape of the intensity spectrum.

## 2.7 Operating beam intensity

Table ?? brings together the diverse set of parameters that must be considered in evaluating the optimum beam intensity at which an experiment using the coherent bremsstrahlung beam should operate. All four columns of numbers were obtained for the same beam conditions, except that the crystal orientation was adjusted to align the coherent intensity peak at the energy listed in row one. The second row, labeled  $N_\gamma$ , gives the integrated rate of beam photons in the coherent peak downstream of the collimator. Note the sharp decrease in the intensity of the coherent peak as the energy approaches the end point. By contrast, the incoherent bremsstrahlung flux is approximately constant over this range of energies. The third and fourth row show the height and width of the peak in the polarization spectrum of the beam. Rows five and six report the height and width of the peak in the tagging efficiency spectrum. The tagging efficiency is defined as the number of beam photons of a particular energy reaching the target divided by the corresponding rate in the tagging focal plane. Large tagging efficiencies are required in order to make effective use of tagging. The width of the peak in the tagging

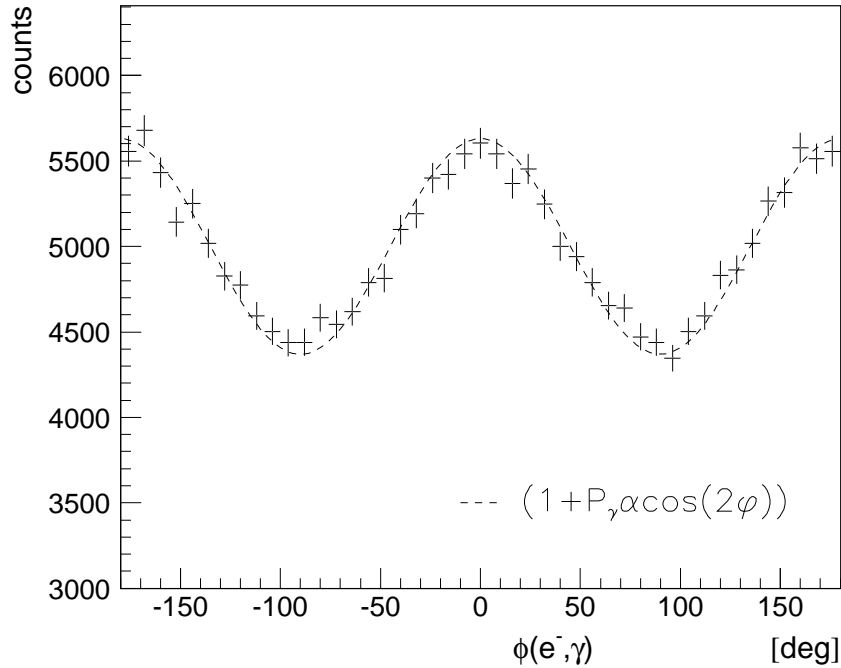


Figure 2.24: Angular distribution for pair production by linearly polarized photons as measured by a polarimeter in comparison with theoretical prediction (*dashed line*). The count rate corresponds to 15 minutes of data taking.

efficiency spectrum determines the width of the focal plane that would be active when running with collimation. The peak integral reported in row two is summed within the f.w.h.m. tagging efficiency window. Rows seven and eight give the photon beam power that is incident on the experimental target (and photon beam dump) and the photon collimator, respectively.

The last two rows in Table ?? give the inclusive and tagged rates for hadronic triggers from a 30 cm liquid hydrogen target placed in the beam following the collimator. Note that the total hadronic rate is dominated by background (*i.e.* non-tagged) events associated with the low-energy component of the beam. This is why the total trigger rate is essentially constant while the flux in the coherent peak varies with peak energy over an order of magnitude. This table illustrates the value of having an electron beam energy well above the photon energy needed for the experiment.

$E$ of peak	8 $GeV$	9 $GeV$	10 $GeV$	11 $GeV$
$N_\gamma$ in peak	185 M/s	100 M/s	45 M/s	15 M/s
peak polarization	0.54	0.41	0.27	0.11
(f.w.h.m.)	(1140 $MeV$ )	(900 $MeV$ )	(600 $MeV$ )	(240 $MeV$ )
peak tagging efficiency	0.55	0.50	0.45	0.29
(f.w.h.m.)	(720 $MeV$ )	(600 $MeV$ )	(420 $MeV$ )	(300 $MeV$ )
power on collimator	5.3 W	4.7 W	4.2 W	3.8 W
power on target	810 mW	690 mW	600 mW	540 mW
total hadronic rate	385 K/s	365 K/s	350 K/s	345 K/s
tagged hadronic rate	26 K/s	14 K/s	6.3 K/s	2.1 K/s

Table 2.7: Operating parameters for an experiment using the coherent bremsstrahlung beam. The calculation assumes a 12  $GeV$  electron beam energy and a 3.4  $mm$  collimator 80  $m$  downstream from a radiator of thickness  $10^{-4}$  radiation lengths. The electron beam current is taken to be 3  $\mu A$ . The rates in the detector (last two rows) are calculated for a 30  $cm$  liquid hydrogen target and an open hadronic trigger.

## Chapter 3

# The Superconducting Solenoid

### 3.1 Introduction

Momentum analysis in GLUEX will be provided by a 2.24 T superconducting solenoid magnet. This solenoid was built at SLAC ca. 1970 for the LASS spectrometer and was subsequently moved to LAMPF in 1985 for inclusion in the MEGA spectrometer. The MEGA experiment and the solenoid were decommissioned in place in 1995. The MEGA experimental equipment was dismantled and preparations for shipment started in the spring and summer of 2002. The solenoid was shipped from LANL to the Indiana University Cyclotron Facility (IUCF) for coil refurbishment and testing in October 2002. Currently all four coils have been extensively tested and coils one and two have been completely refurbished. Refurbishment efforts on coils three and four will start in the fall of 2004.

The magnet employs a cryostatically stable design and uses cryostats that were designed to be easily opened for service with hand tools. The inspection of the magnet performed at LANL in 2000 concluded that the solenoid was still in excellent condition and worthy the time and cost involved in relocation and refurbishment. Nevertheless, the magnet support systems are now 30 years old. Even though the magnet is in good condition, it still requires repairs, maintenance, updating, and modifications for use as part of the GLUEX experiment.

### 3.2 Brief Description

The magnet is described in a technical note [?] and some relevant portions of that description are quoted below. Table ?? summarizes important magnet parameters. The refrigeration units are not currently available and new ones are required.

The LASS solenoid magnet provides a 22.4 kG magnetic field parallel to the beam direction. The clear bore inside diameter of the magnet is 73 inches and its final - as modified overall length - is 195 inches. Within the clear bore region the field homogeneity is  $\pm 3\%$ . Along the beam axis the field homogeneity improves to  $\pm 1\%$ . The solenoid is constructed of four separate superconducting solenoidal coil-cryostat units [?] and uses a segmented 232 ton iron flux return path that surrounds and supports the coil assemblies. A common liquid helium reservoir is located on top of the solenoid providing the gravity feed of the liquid to the coils.

The liquid helium vessel is surrounded by a liquid nitrogen cooled radiation shield and this assembly is centered in the vacuum tank by a circumferential series of tie bolts designed for

Inside winding diameter of SC coils	80 <i>inches</i>
Clear bore diameter	73 <i>inches</i>
Overall length (iron)	195 <i>inches</i>
Inside iron diameter	116 <i>inches</i>
Outside iron diameter	148 <i>inches</i>
Coil-to-coil separation	11 <i>inches</i>
Total iron weight	232 <i>tons</i>
Central field	22 <i>kG</i>
Conductor current	1800 <i>A</i>
Total stored energy	36 <i>MJ</i>
Inductance	22 <i>H</i>
Total helium volume (including reservoir)	5000 <i>liters</i>
Operating heat load (liquid He)	30 <i>liters/hour</i>
Operating heat load (liquid nitrogen)	30 <i>liters/hour</i>
Cool-down time	2 <i>weeks</i>
Copper to superconductor ratio	20 : 1 (grade A) 28 : 1 (grade B)
Total conductor length	117,600 <i>feet</i>
Total conductor weight	29,000 <i>lbs</i>
Turn on time	20 <i>minutes</i>
Turn off time (normal)	20 <i>minutes</i>
Axial load per coil due to magnetic forces	280 <i>tons</i>

Table 3.1: Summary of characteristics of the solenoid as used in the LASS configuration.

minimum conductive heat flux to the helium bath. Radial centering and support are achieved by four low conductance hangers arranged in a spiral pattern. Various tie rods and hangers are instrumented with stress bolts to measure the tremendous forces on the assembly caused by the magnetic fields.

The inductance of the coil is 22 *Henries*, and the magnet is run at 1800 *Amperes*. The liquid helium volume is  $\approx 5000$  *liters* and the heat load is  $\approx 50$  *watts*. Refrigeration at Hall D will be supplied by a small local refrigerator of 200 watt capacity. This over-engineered nature of the design of the magnet, cryostat and the superconductor itself, has produced a stable, reliable and safe superconducting magnet.

### 3.3 Solenoid Refurbishment Activities

The LASS/MEGA solenoid was inspected in April 2000 by a team from the GLUEX collaboration, JLab staff and two of the original designers of the magnet. This team met at Los Alamos with the MEGA staff and inspected the MEGA magnet installation and the fourth coil. The fourth coil was found sealed in its original shipping crate. The fourth coil iron yoke ring, yoke stand and coil insertion tool were all found in storage. Magnet documentation and spare parts were also found. Jefferson Lab subsequently entered into negotiation with Los Alamos and the DOE to transfer ownership of the magnet to Jefferson Lab. The solenoid was next dismantled by a heavy rigging contract crew and shipped to IUCF in October 2002.

Currently, two coils have been refurbished and the other two are expected to be completed in early 2005. The first two are expected to be moved to JLab in early 2005. After the all coils are completely refurbished at IUCF, the remainder of the solenoid will be moved to JLab for addition of new support systems including the DC system, control system and cryogenic interface. Testing of individual coils at 4.5 Kelvin and a full solenoid recommissioning test are planned prior to installation in HALL D.

### 3.3.1 Detailed Tests of The Coils

Coil	N2 shield $10^{-5}$ torr-liter/s	He Vessel $10^{-5}$ torr-liter/s	External Vessel	Over Pressure
1	5	ok	12in bellows	ok
2	ok	0.2	12in bellows	ok
3	4	ok	12in bellows	ok
4	0.4	ok	12in bellows	ok

Table 3.2: Status of leak and pressure testing. To date, coils one and two have been tested and show no leaks. The status of “ok” indicates a leak rate of less than  $10^{-9}$  torr-liter/s

The detailed examination of the solenoid’s four coils began in May 2003. The goal of this detailed testing was to accurately determine the leak rates, verify pressure ratings and verify operation of all internal instrumentation. The solenoid has had a 30 year history of large internal leaks which complicated operations and raised the cryogenic heat load. The internal instrumentation was known to have deteriorated and accurate checks of coil electrical properties needed to be confirmed.

Coil	Resistance Across coil ( $\Omega$ )	Resistance LH Lead-Ground ( $\Omega$ )	Resistance RH Lead-Ground ( $\Omega$ )	Inductance (mH)
1	4.9	2.2	6.4	372
2	3.2	open	open	244
3	2.7	2.6	0.2	172
4	5.2	open	open	763

Table 3.3: Measured electrical properties of the four coils.

One of the goals of this effort was to carefully perform calibrated leak rate measurements of the four coils’ helium spaces, nitrogen spaces and vacuum spaces. This was necessary to quantify the leaks to guide the decision to repair. A decision was reached early on - when good leak detection sensitivity could not be achieved - to install 8 conflat on each of the four coils. This resulted in achieving leak detection sensitivity of  $1 \times 10^{-9}$  torr-liter per second. At this sensitivity the leaks were quickly identified and quantified. The complication due to 18 inch bellows failure was corrected by replacing the bellows. Coil four, which was not part of the MEGA experiment at LANL, had a non-standard vacuum pump-out flange that required replacing. The coil electrical properties and internal instrumentation were measured during

this time also. The instrumentation operability was confirmed and the wiring was verified and documented. The results of the testing are summarized in Tables ??, ?? and ??.

The work at IUCF to test the four coils in detail and to perform such repairs as to permit the testing was concluded in February 2004. At the conclusion of this work all four coils had been extensively tested, and the leak position had been determined in coils one and two.

Coil	Voltage Taps	Carbon Resistance Thermometer (4 to 300K)	Thermocouple (80 to 300K)	Platinum Resistance (40 to 300K)	Strain Gauge (new)
1	ok	7 of 8 ok	removed	30 new	6 new
2	ok	ok	removed	30 new	6 new
3	ok	ok	TBD	TBD	TBD
4	ok	4 of 7 ok	TBD	TBD	TBD

Table 3.4: Table of internal instrumentation and voltage taps. Each coil has voltage taps (VT) and Carbon Resistance Thermometers (CRT) in the Helium vessel and Thermocouples (TC) on the N2 shield and strain gauges (SG) on the support posts.

### 3.3.2 Refurbishment of Coils One and Two

Following the conclusion of the initial investigations, a contract was negotiated with IUCF to perform all repairs and proof testing on coils one and two. The scope of work of this effort included localizing and repairing all leaks. Replacement of all strain gauges as most had failed. To replace the thermal couples shield thermometers with Platinum resistance thermometers (PT100). The replacement of all wiring, and finally to replace the aluminized mylar multi layer insulation( MLI). A decision was made to retain the original Liquid Nitrogen shields due to their good state of repairs and functionality. The new PT100 thermometers were installed in small copper blocks soldered to the copper shield panels for good thermal contact and reliable mounting. The new strain gauges were installed on the outermost of the three nested cylinders of the cold to warm supports.

Coil one was previously determined to have a shield leak only. The most difficult part of completing coils one and two was reconnecting the shields and plumbing due to the out of sequence reassembly. This necessitated replacing the simple joints with more complex junctions that had only forward facing welds. This technique was used extensively on a magnet in JLABs Hall C namely the HMS Dipole. Both coils were cooled to approximately 120 Kelvin and no leaks were found. A side benefit of this testing was the confirmation of proper operation of the new shield PT100 thermometers and the wiring correctness. Both coils were pressure tested to 100 psi successfully. This concluded the testing and internal repair phase of coils one and two. The next step was to replace all the shield MLI insulation and perform a final evacuation as preparation for placing the coils in storage. Both coils one and two achieved vacuum in the range of  $1 \times 10^{-5}$ , passed a final leak check and were subsequently backfilled with N2 gas, sealed and moved to an inside storage location at IUCF.

### 3.3.3 Plans To Complete Coils Three and Four

As of September 2004, coils three and four have been moved into the working area at IUCF and contract negotiations for their refurbishment are underway. This work is expected to begin

in the fall of 2004 and be completed before summer 2005.

### 3.3.4 Plans To Complete The Solenoid at JLab

The remaining work to upgrade and re-assemble and test the solenoid is planned to occur at JLab. Activities during 2005 include securing a test and assembly space in the Test Lab at JLab, moving coils one and two to the space in the test lab and preparing the coils for cool-down to 4.5 Kelvin. This testing effort requires equipping and staffing the solenoid test area in the test lab and designing and fabricating a new single coil test interface. The original SLAC-designed test interface was never found so a replacement is required to support testing. The replacement will have connections matching JLab standards. A set of temporary cryogenic connection lines for use in the Test Lab will also need to be designed and fabricated. These two design and fabricate items will become the highest priority of the JLab HALL D design and engineering staff in FY 2005. This is to support the cool-down and test of one single coil by the end of FY 2005. This test would consist of cool down and fill at 4.5 Kelvin with helium, LN2 shield cool down and fill and only limited low current operation of the coil.

The solenoid also requires an entirely new control system. The original solenoid had only manual controls and instrument data were recorded in paper log books. The cryogenic control of the solenoid was completely absent and all cooling was achieved by manipulating a small Helium refrigerator. The replacement of the controls on the HMS SC magnets at JLAB at this time and the similarity of many systems and identical nature of others leads to common solutions. The prototype for the solenoid new controls is being tested as this is written. A full system of the prototype is planned for January and February 2005. Following debugging and commissioning of the HMS Dipole prototype system a clone will be prepared for the Hall D solenoid. The current plan calls for a more complete test of coil two using the new solenoid controls, new power supply (already on site) and would operate a single coil at full current. Test and re-assembly of the entire solenoid are pending and depend significantly on the year of availability of HALL D.

## 3.4 The Magnetic Field of The Solenoid

### 3.4.1 Magnetic Modifications Needed

The original SLAC configuration of the solenoid allowed for gaps in the return yoke so that wire chambers could be inserted from the outside. Further, in the LASS and MEGA installations the Cerenkov detector had to be located at large radius due to the presence of high magnetic fields near the downstream end of the solenoid. The source of these high fields has been investigated using a 3D TOSCA model of the yoke and coil and various methods to reduce these “stray” fields have been explored.

The following yoke modifications will reduce the saturation in the pole cap and lower the stray field in the region where the GLUEX Cerenkov will be located:

1. Replace the air gaps with iron rings. This lowers the required operating current to achieve the same central field. The lowering of the local fields especially around coil seventeen helps reduce pole cap saturation.
2. Increase the distance in “Z” between the seventeenth coil and the downstream pole cap. This lowers the local field near the pole cap and thus lowers the saturation.

3. Increase the thickness of the pole cap by adding an iron disk to dilute the pole cap field and reduce saturation.

These yoke modifications will reduce the stray field levels in the Cerenkov region from  $\sim 700$  gauss down to  $\sim 50$  gauss, low enough to be shielded by thin iron and Mu-metal shields.

### 3.4.2 TOSCA Simulations

The original solenoid magnet was designed without the benefit of modern 3D magnetic modeling, yet the magnet has worked long and well in two experiments. But there has been a persistent difficulty with downstream stray fields, as noted above. Thus we have created a 3D TOSCA model of the solenoids fields to study the problem in detail and design a remedy.

#### TOSCA Model

The yoke and coils have been modeled using the TOSCA 3D magnetic analysis software. This model was prepared with geometry that allowed simulating the effect of closing the yoke gaps or creating new gaps, or opening or closing the ends by simply changing materials definitions.

The solenoid magnetic field as currently modeled is based on the actual distribution of current within the four coil cryostats and the actual details of the yoke construction. The yoke modifications for the benefit of the GLUEX experiment have also been included. The current distribution of the solenoid can not be modified and therefore the details must be included to accurately model the magnetic fields for experiment simulation taken and to test the effect of various modifications. The TOSCA model also provides valuable design information about the magnetic environment as seen by each detector system. The modifications to the yoke are a mix of requirements from GLUEX physics, the need to lower external fields, and modifications to provide better access for the GLUEX detectors. The TOSCA model is designed to evaluate the yoke modifications needed to lower the external fields. The TOSCA modeled internal fields have already been valuable as the source of magnetic fields for the Geant simulations. Further magnetic simulation work will be performed to study more carefully the effect of all the above changes on the exact  $B$  vs  $I$  excitation curve, the inductance and stored energy and the forces on the coils. Generally filling in the yoke gaps will lower all of these quantities but the exact values remain to be confirmed.

#### Preliminary Results

Four GLUEX models were investigated. The original and last configurations are shown in Figure???. All four models use identical coil models and identical current densities. The integral field increases by 2.6 % as a result of filling the gaps. The other modifications have no significant effect on the total field. This effect can be easily understood since most of the flux must return through the original gaps. Thus filling them with iron must have a large effect on the field integral while only some of the flux is effected by the other changes, and thus a minimal effect on field integral is seen.

We briefly describe each configuration:

Hall D 107 has the iron yoke and coil configuration of the original LASS solenoid as it was used at SLAC. This model is to provide a baseline for comparison and to compare with historical calculations and measurements. The model has the original segmented yoke with

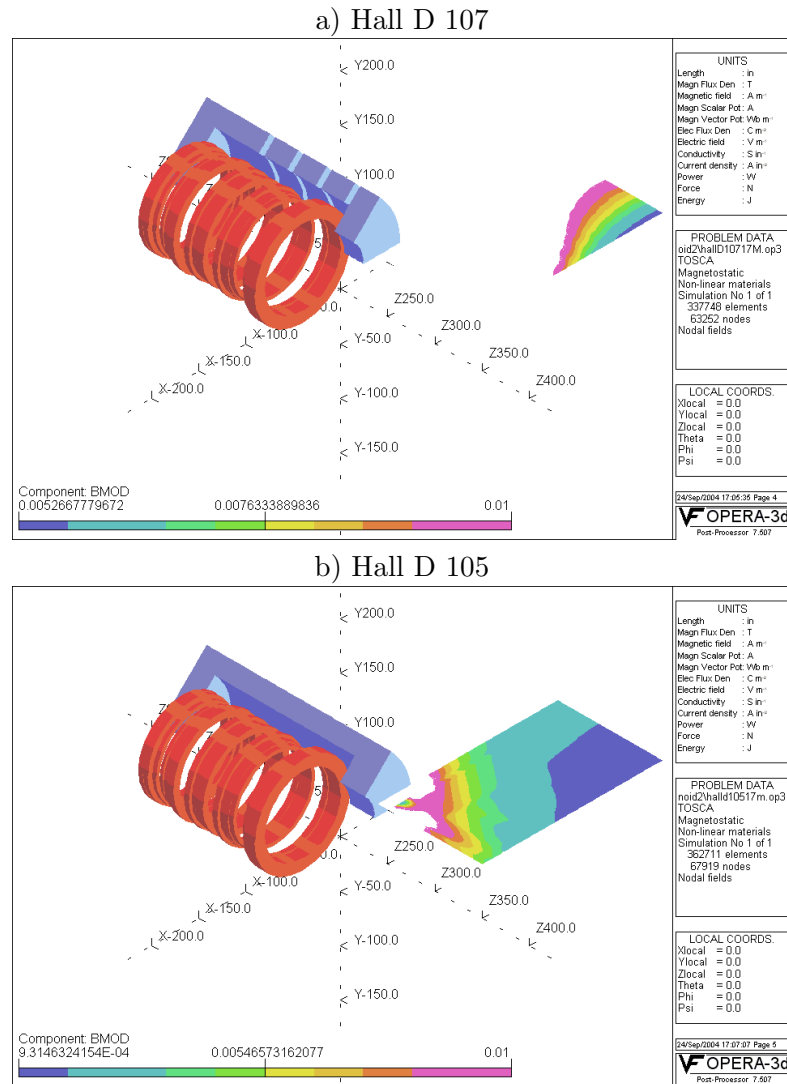


Figure 3.1: TOSCA models for a) the original magnet configuration and b) configuration that fills the gaps with iron, extends the fourth gap and thickens the pole. Both figures show the model for the coils (solenoid and 13th coil ring) and a 45 degree pie slice of the yoke iron. Also shown is a contour plot of fields which are less than 100 G in the region of 50 to 240 in radially and 190 to 300 in along the axis. This is a region that could be considered acceptable for placing photomultiplier tubes. Note that in the bottom configuration the region of low field begins at the iron, allowing detectors to be mounted near the solenoid. The magnetic field scale is in Tesla.

Model Number	Max Field (G)	Min Field (G)	Low-Field Area (%)	$\int B \cdot dl$ (T·Inches)
Hall D 107	1067	523.0	none	302.8
Hall D 106	351	82.5	none	311.0
Hall D 103	241	56.7	17	311.3
Hall D 105	158	45.7	50	310.8

Table 3.5: Field parameters for the region between 50 and 80 in radially, where Cerenkov photomultiplier tubes might be placed. The entries correspond to the maximum and minimum B fields, and fractional area with field below 75 Gauss. Also given is the on-axis field integral for each TOSCA model.

the four original 6 inch air gaps. *This model should be used to measure the effectiveness of the yoke changes which are the subject of the other three models.*

Hall D 106 has the SLAC yoke but with the four 6 inch gaps filled with the same iron as the rest of the yoke. This was a requested change and it has the effect of lowering the external fields. You can clearly see that the external fields are in general lower, especially in the regions where it would be desirable to locate photo tubes.

Hall D 103 has the four gaps filled with steel and gap four extended from 6 inches to 12 inches. This modification was selected because of the extreme saturation in the yoke that was observed around the 13th coil. Fields as high as 3 Tesla are observed near the 13th coil. Moving the yoke further away from the 13th coil will lower the yoke saturation and thus make the yoke more effective in collecting external flux and channeling it back within the yoke iron.

Hall D 105 has the down stream “pole cap” thickened from 20 inches to 26 inches. This is in addition to filling the gaps and extending the fourth gap. This modification was selected to further reduce saturation levels in the yoke and thus reduce further the external fields.

We studied the external fields in the region where Cerenkov photomultiplier tubes may be located. The region extends in z for 20 inches and in R from 50 to 80 inches. The model Hall D 105 has a substantial volume ( $\sim 50\%$ ) with fields between 46 and 74 gauss (see Table ??). These fields can be shielded by a combination of soft iron and Mu-Metal tubes. As this region extends from 65 to 80 inches in radius, the photomultiplier tubes for the Cerenkov could be located much closer to the detection volume. A maximum distance of about 2 meters ( $\sim 80$  inches) is certainly possible. Figure ?? plots the computed fields for the four models as a function of radial distance in the area where we expect to place sensitive detectors, and Table ?? summarizes the characteristics for each case. Clearly there are large regions close to the detection volume where tubes could be located. It is also obvious that simply moving further out can have the same effect. Indeed the original solution chosen at SLAC was to locate the tubes at 4 meters where the fields are  $\sim 75$  gauss for the original SLAC /LASS geometry. The modifications computed above can achieve these field levels in a much more efficient manner.

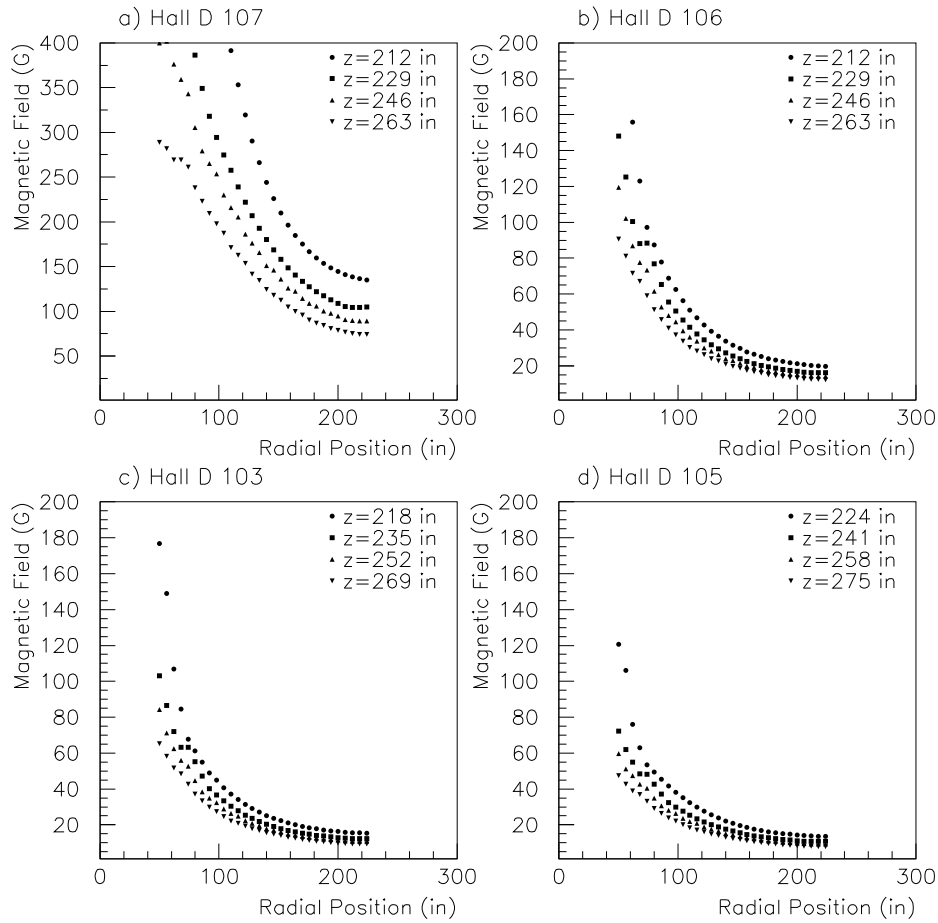


Figure 3.2: Magnetic field as a function of radial distance at constant distance along the  $z$  axis for the four different configurations of the solenoid. Note the scale change for plot a).

### 3.4.3 Compensation of the Upstream Plug

The collaboration desires a matching full aperture hole (73 inch diameter) in the upstream yoke to provide access to the detector volume for service, installation and support, and also to provide a route for cables to exit the upstream end of the magnetic volume. This upstream hole has the same effect on the internal field quality as the downstream hole and thus must be studied carefully. The downstream hole in the yoke is the same diameter as the cryostat inner diameter, 73 inches. This opening is equivalent in magnetic effect to boring a large hole in the center of the pole of a dipole magnet because the end yoke pieces for the solenoid are in fact the poles. The designers of the solenoid compensated for this large hole by increasing the current density in coil # 4, which has four times the average number of Amp-turns of the other 16 coils. This compensates for the missing iron and also contributes to the nearby yoke saturation and stray fields that we dealt with in the previous sections.

We examined four options to deal with the loss of field integral and flatness caused by

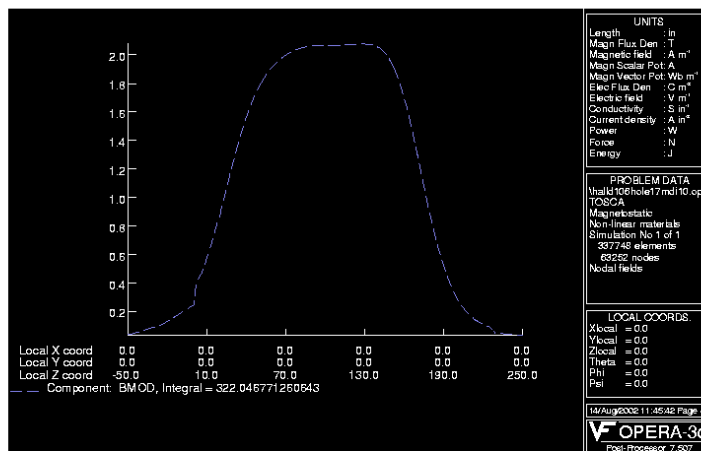
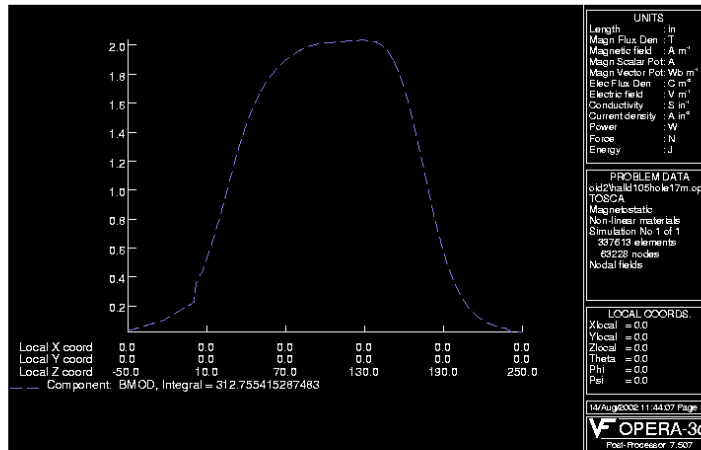
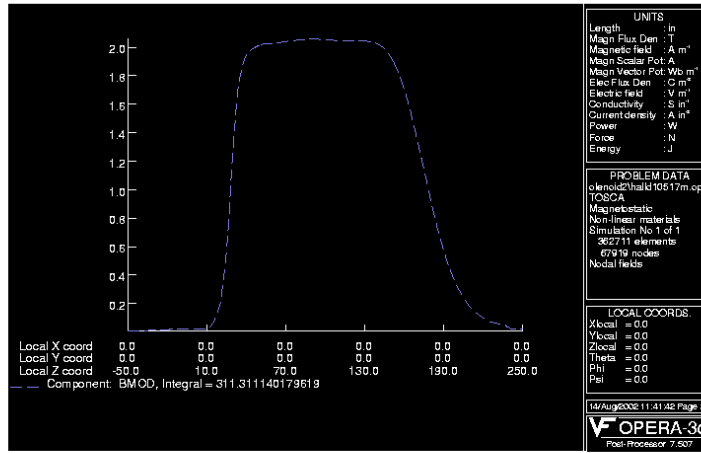
the new opening: a) no action, b) creating a gap in the upstream yoke and c) increasing the current by 15% in all the coils of cryostat # 1 Figure ?? and show the on-axis magnitude of the field through the solenoid for the various options discussed above. The first is the nominal configuration with the upstream plug in place and the second is with the new upstream hole. All other modifications mentioned earlier are included. The loss of field integral in the backward direction is not a significant problem, but the reduction of flatness has the effect of increasing the computation requirements for analysis. Clearly, an improvement in the upstream field flatness is desirable. We detail the three options considered.

#### New upstream yoke gap

Creating a new upstream yoke gap was examined in the first round of magnetic simulations and the conclusion was that this creates more of a problem than it solves. The new gaps make a lot of exterior field that can get into phototubes and it adds the complication to the assembly that cables, the yoke and detectors are now linked. The new gaps do not cause a loss of good field region but it does reduce the integral on axis.

#### Increase current in cryostat # 1

Increasing the current in the 7 coils inside cryostat # 1 by approximately 15% has the effect of increasing the local Amp-turns to boost the field back up and replace the flux lost by enlarging the upstream yoke hole. This can easily be accomplished by stacking a floating DC power supply across cryostat # 1 to enhance the current relative to the main current. The main current power supply provides 1800 A to all 4 cryostats in series. In this way all 17 internal coils are in series and have the same charging and discharging. The small biasing DC power supply that floats across cryostat # 1 permits a local current increase and is adjustable. This method if selected requires that a low amperage ( $\approx 300$  A) current lead be added to the new cryo-reservoir during the solenoid refurbishment. The new DC biasing supply is simply connected between one of the main current leads and the low current biasing current lead. This is an adjustable, low cost, and reliable method to boost the field back up and is identical in principal to the method used to boost the down stream field. Instead of adding turns, which is difficult, one just adds some extra current to the existing turns. The magnet control and quench protection stems are marginally more complex as a result of this solution. Precautions must be taken to guarantee that there can never be a current path through the biasing lead and power supply that conducts the main 1800 A solenoid current. Figure ?? is a graph of the central field with extra current in the 7 coils of cryostat #1.



## Chapter 4

# The GlueX Detector in Hall D

### 4.1 Overview

The goal of the GLUEX experiment is to search for gluonic excitations with masses up to  $2.5 \text{ GeV}/c^2$ . The identification of such states requires knowledge about their production mechanism, the identification of their quantum numbers  $J^{PC}$  and their decay modes. The production mechanism and  $J^{PC}$  determination require a partial wave analysis which in turn depends on the kinematic identification of exclusive reactions. The decay products of produced mesons must be identified and measured with good resolution and with full acceptance in decay angles. In many cases the decays of mesons involve a chain of particle decays. The GLUEX detector (see Figure ??) must therefore be hermetic with  $4\pi$  coverage and have the capability of measuring directions and energies of photons and momenta of charged particles with good resolution. Particle identification is also required.

The partial wave analysis technique depends on high statistics and in the case of incident photons, also requires linear polarization. The latter is needed to identify the production mechanism. The linear polarization is achieved by the coherent bremsstrahlung technique. The degree of linear polarization and flux of photons in the coherent peak fall dramatically as the photon energy approaches the endpoint energy. On the other hand, it is desirable to have photon energies high enough to produce the required masses with sufficient cross section and with sufficient forward boost for good acceptance. For a fixed incident momentum and a fixed resonance mass, it is also desirable to have a fairly constant  $|t|_{min}$  over the natural width of the resonance. This also requires sufficiently high incident photon energy.

An operating photon energy  $9.0 \text{ GeV}$  produced from a  $12.0 \text{ GeV}$  electron beam represents an optimization of beam flux, cross-section and degree of polarization. The GLUEX detector is therefore optimized for this energy range. Figure ?? is a schematic representation of the proposed GLUEX detector. The individual subsystems are discussed in more detail below.

### 4.2 The Target

The main physics program for the GlueX experiment will be conducted with a low-power liquid hydrogen or liquid deuterium target. We propose a design which is very similar to the cryogenic target presently in use in Hall B. This target should fit comfortably into the detector geometry. Solid targets, required for various calibrations, can easily be incorporated into this design. The

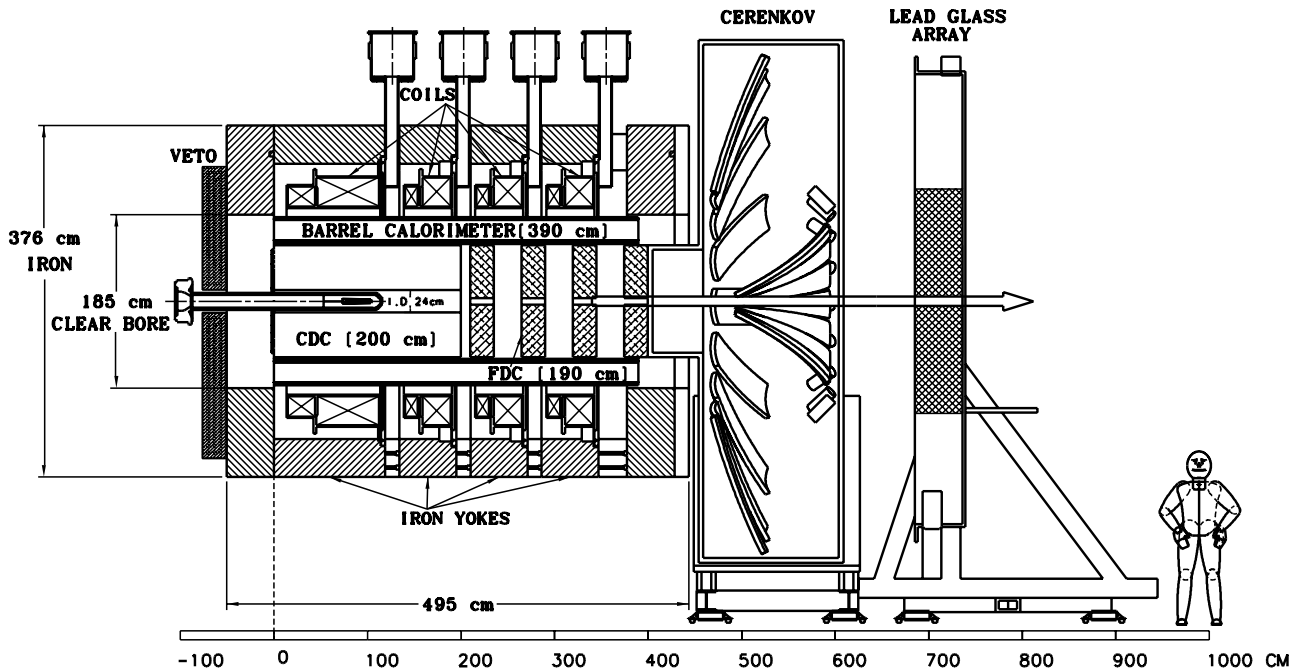


Figure 4.1: An overview of the GLUEX detector. The major subsystems are labeled and are discussed individually in the text.

maximum power deposited in the target by the beam is 100mW. In such low-power targets, natural convection is sufficient to remove heat from the target cell and a circulation pump is not required. These targets frequently employ mylar target cells. The mylar cell is often mounted on a metal base to provide for liquid entry ports and a reliable means of positioning the cell. The beam enters through a thin window mounted on a reentrant tube at the base of the cell. The diameter of this entrance window must be sufficiently large to allow the beam to enter the cell without scraping; taking into consideration the uncertainties that will be present in aligning the cell. The area between the reentrant window and the outer wall of the cell must be sufficiently large to allow for convection and to prevent bubbles from being trapped. A target cell diameter of three to six centimeters would seem reasonable. A smaller diameter cell would be possible with more stringent alignment requirements. A system such as this, containing a few hundred  $\text{cm}^3$  of liquid hydrogen, would be considered “small” by Jefferson laboratory standards and the safety requirements would not place any significant constraints on the target design or operation.

The target cell is connected to a condenser located upstream of the cell. In the Hall B target the condenser is formed by concentric cylindrical shells with the axis of the cylinders lying along the beam line. The heat exchanger should be sized to allow the target to be condensed in a reasonable period of time (a few hours). In some target systems the condenser is cooled by a separate refrigerator. In other systems liquid helium at 4.5K is used as the refrigerant. Because the magnet in Hall D will require liquid helium there seems little reason to operate a separate refrigerator for the target. The standard CEBAF delivery system supplies 5K 3 atmosphere fluid through a 1-3/8” diameter bayonet. This gas is expanded through a JT valve to produce liquid. This system is somewhat cumbersome for small loads. It would be much

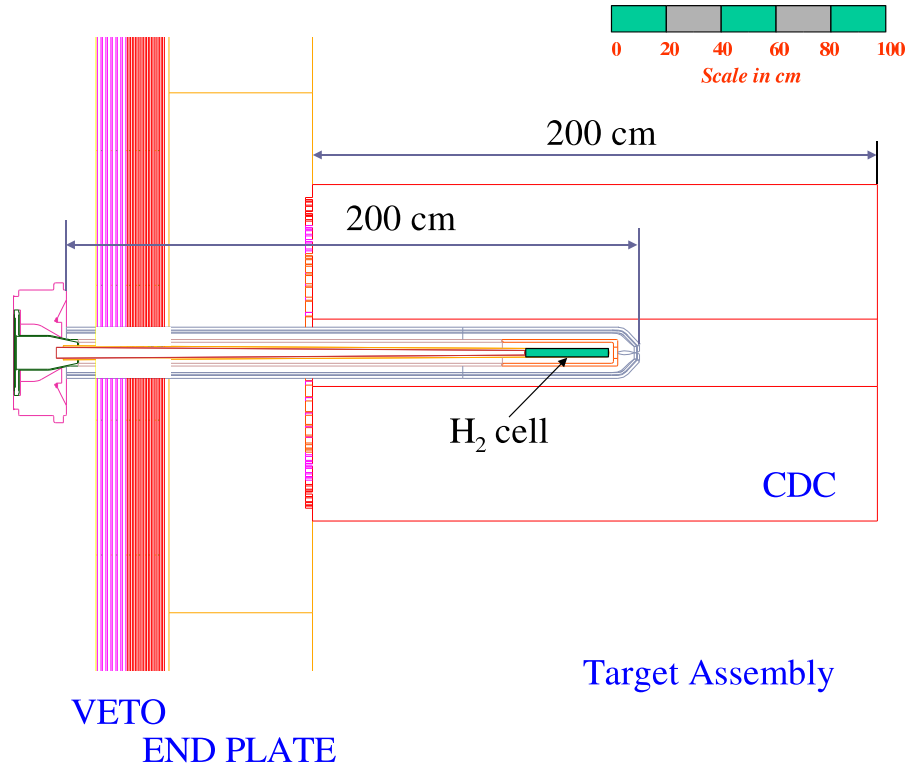


Figure 4.2: Target region including target cell, vacuum scattering chamber, start counter. Sufficient room exists for a vertex detector. Also shown for reference are the CDC and thickness of the magnet iron and upstream veto.

more convenient to supply the target with low-pressure 4.5K liquid through a small transfer line. It would be possible to draw liquid from the magnet if a port is available. In Hall B it was found convenient to draw liquid helium for the target from a buffer dewar which is filled by a JT valve. To allow for a similar arrangement in Hall D, a 4.5K supply bayonet and a 5K cold return bayonet should be provided.

The extent to which target components shadow the veto counter must be considered. Some shadowing of the veto counter will be unavoidable, since the cell must be supported. As we are relying on convection to remove heat from the target cell it would be favorable to locate the heat exchanger as close to the target cell as possible. This would result in increased shadowing of the veto counter. It is not clear that convection alone would be sufficient if the condenser were located outside the veto detector. This design could easily be tested using the Hall B test cryostat.

The hydrogen cell is located inside of a scattering chamber to provide an isolation vacuum. The walls of this chamber should be kept as thin as possible. In Hall B, plastic foam chambers have been used successfully. The target vacuum is likely to be shared with the upstream and downstream beam-lines. The target vacuum chamber would include a service port for the refrigerant, target gas and instrumentation connections.

Solid targets are required for purposes of calibration and studying detector response. It

may be desirable to replace the target cell with a multi-foil “optics target” from time to time. Installing the target and bringing it into operation will probably require two days. A mechanism to introduce solid targets either upstream or downstream of the hydrogen cell would be possible. Consideration should be given to the number of different targets required and to their placement.

Attaching the vertex detector and veto counter to the target vacuum chamber will locate those detectors accurately with respect to the vacuum chamber, but may complicate target assembly and disassembly. The cool-down and vacuum motion of the target cell relative to the vacuum chamber will remain major sources of uncertainty in the target cell position. The alignment requirements for this are not severe but should be considered early in the design stage. It is likely that a rail system would be used to position the target inside the magnet, as the insertion cart is used to position the cryogenic target in Hall B. Figure ?? illustrates a target cell similar to one which has been used in Hall B positioned inside the GlueX detector. In this design the cell incorporates an extended reentrant window to place all metallic components upstream of the veto detector.

## 4.3 Calorimetry

### 4.3.1 Global Design

The electromagnetic (EM) calorimetry for the GLUEX experiment is divided in three parts, each handled by a different detector sub-system.

The very forward angles ( $\theta < 14^\circ$ ) of the HALL D detector will be covered by an existing lead glass detector (LGD) used in the E852 experiment at BNL and re-stacked to meet the geometrical acceptance criteria for HALL D. The approximate polar angular range  $14^\circ < \theta < 138^\circ$  will be subtended by the barrel calorimeter. Finally, the upstream, large-polar angle region ( $\theta > 138^\circ$ ) will be the domain of the upstream photon veto.

Each of these three sub-systems is treated individually in a dedicated subsection within this chapter.

### 4.3.2 Forward Calorimeter

The most downstream subsystem of the GLUEX experiment is the lead glass detector (LGD), an electromagnetic calorimeter consisting of nearly 2500 lead glass blocks. The purpose of the LGD is to detect and measure forward-going photons from the decays of  $\pi^0$ ,  $\eta$  and other mesons. The LGD will also provide a fast energy sum to be used in the level-1 trigger.

Each block has dimensions of  $4 \times 4 \times 45 \text{ cm}^3$  and they are arranged in a nearly circular stack. The radius ( $\approx 1 \text{ m}$ ) is matched to the aperture of the GLUEX solenoid magnet. The type of glass used in E852 and RADPHI and proposed for use in GLUEX was produced in Russia and is called type F8-00. Its chemical composition is 45% PbO, 42.8% SiO<sub>2</sub>, 10.4% K<sub>2</sub>O and 1.8% Na<sub>2</sub>O. This glass has an index of refraction of 1.62, a density of 3.6 gm/cm<sup>3</sup>, a radiation length of 3.1 cm and a nuclear collision length of 22.5 cm. The blocks were machined to a precision of about 25 microns in transverse dimensions and flatness so stacking the array does not result in gaps. The Cerenkov light from each block is viewed by a FEU-84-3 Russian PMT. The PMT bases are of a Cockcroft-Walton (CW) design [?]. The PMT’s will be registered with respect to the glass using a cellular wall that includes soft-iron and  $\mu$ -metal shielding. The signal from each block will be digitized with an 8-bit 250 MHz FADC. A schematic of the calorimeter is shown in Figure ??.

Several of the GLUEX collaborating institutions have been involved in the design, construction and operation of calorimeters of a design similar to that presented here and in the analyses of data from those calorimeters. The first of these calorimeters was a 3000-block calorimeter used in the E852 experiment at Brookhaven Lab (BNL) which used an 18  $GeV/c$   $\pi^-$  beam and the multiparticle spectrometer (MPS). Details of the design and operation of prototype calorimeters and the one used in E852 have been published [?, ?]. Several physics results based on measurements with the E852 LGD will be discussed here.

An LGD was also used in the RADPHI experiment [?, ?] at JLab that was located downstream of the CLAS detector in HALL B and used in a bremsstrahlung photon beam produced with 5.4  $GeV$  electrons. The goal of RADPHI was a measurement of the radiative decay modes of the  $\phi$  meson resulting in five-photon final states. The experience gained with the RADPHI LGD is extremely valuable for GLUEX. As will be discussed below, the  $\pi^0$  and  $\eta$  mass resolutions based on measurements from the LGD improve as the distance from the production point of photons (the target) to the LGD increases. The resolutions also improve as the mean photon energy increases and thus as the beam energy increases. Photons produced in RADPHI resulted from interactions of beam photons of energies distributed almost uniformly in the range from 3 to 5.4  $GeV$  and the target to LGD distance was  $\approx 1$  m. For GLUEX the photon energy is 9  $GeV$  and the target to LGD distance is  $\approx 5$  m.

Based on the experience with the LGD's used in E852 and RADPHI we expect the GLUEX LGD to provide the granularity and resolution required to carry out the amplitude analysis needed to map the spectrum of gluonic excitations, the goal of this experiment.

In what follows we also address several technical issues regarding the GLUEX LGD including issues of the assessment of the E852 and RADPHI glass and PMT's that will be used in GLUEX, curing of radiation-damaged glass, electromagnetic backgrounds in the beam region, shielding PMT's from the fringe field of the solenoid, calibration and monitoring.

### The E852 Experience

The goal of E852 was a search for mesons with unusual quantum numbers using the MPS at BNL with a Lead-Glass Calorimeter. The E852 LGD was located 5.4 m from a liquid  $H_2$  target located mid-way inside a large dipole spectrometer magnet. E852 detected and measured both charged particles as well as photons from  $\pi^0$  and  $\eta$  mesons. The measured mass resolution for  $\pi^0$  and  $\eta$  mesons was 10 and 25  $MeV/c^2$  respectively.

Several physics results from amplitude analyses based solely on data from the LGD have been published. Events in which four photons were identified in the all-neutral final state  $4\gamma n$  led to analyses of the  $\pi^0\pi^0$  [?, ?] and  $\pi^0\eta$  systems [?, ?, ?]. Figure ?? shows a scatterplot of one  $\gamma\gamma$  effective mass combination versus the other  $\gamma\gamma$  effective mass from the reaction  $\pi^-p \rightarrow 4\gamma n$ . Clusters associated with the  $\pi^0\pi^0n$  and  $\pi^0\eta n$  final states are clearly observed.

The  $\pi^0\pi^0$  effective mass spectrum for the  $\pi^-p \rightarrow \pi^0\pi^0n$  reaction is shown in Figure ?? . The prominent feature in this spectrum is the  $f_2(1275)$  tensor meson. The spectrum also shows a sharp dip at  $\approx 1$   $GeV/c^2$  that is understood as evidence for the scalar meson  $f_0(980)$  interfering with the  $S$ -wave background. A partial wave analysis (PWA) of these data set was performed [?, ?] for events in various ranges in momentum transferred from the target proton to the recoil neutron and some of the results for the lowest momentum transfer range are shown in Figure ?? . Plots show open and filled circles corresponding to mathematically ambiguous solutions with the filled circles indicating the physical solutions based on other criteria. The  $S$ -

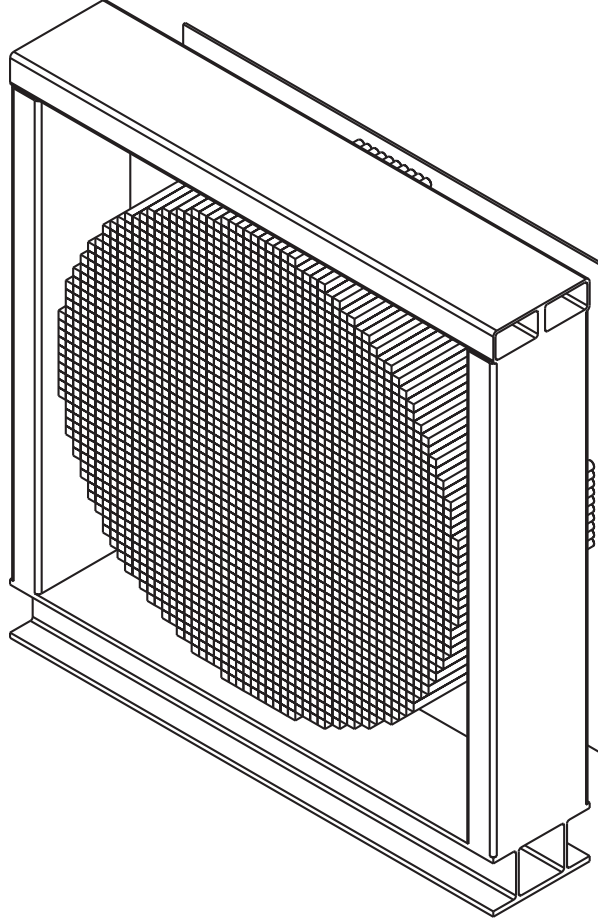


Figure 4.3: The lead glass detector as modified for GlueX . 2500 lead glass blocks will be arranged in a nearly circular stack of radius  $\approx 1$  m.

wave shows evidence for the  $f_0(980)$  scalar meson via its interference with a broad background, the  $D_0$ -wave shows the  $f_2(1275)$  and the phase difference between the  $S$ -wave and  $D_0$ -waves show the classic motion expected of a resonance.

Figure ?? also shows the  $\eta\pi^0$  effective mass spectrum for the  $\pi^-p \rightarrow \eta\pi^0n$  reaction. This spectrum features both the scalar  $a_0(980)$  and the tensor  $a_2(1320)$ . A partial wave analysis of this system has also been performed [?, ?, ?].

Figure ?? shows the  $\eta\pi^+\pi^-$  and  $\eta\pi^0\pi^0$  effective mass distributions where well known meson states are clearly observed. The  $\eta\pi^0\pi^0$  system requires the reconstruction of six-photons in the LGD. Other analyses involving photons and charged particles have also been published including a study of the  $a_0(980)$  in the  $\eta\pi^+\pi^-$  and  $\eta\pi^0$  spectra [?] and a partial wave analyses of the  $\eta\pi^+\pi^-$  [?],  $\omega\eta$  [?],  $\omega\pi^-$  [?] and  $\eta\pi^+\pi^-\pi^-$  [?] systems.

### The Radphi Experience

The RADPHI detector is shown schematically in Fig. ?. This detector was operated downstream of the CLAS detector in HALL B. The beam was incident on a 2.66-cm diameter, 2.54-cm long

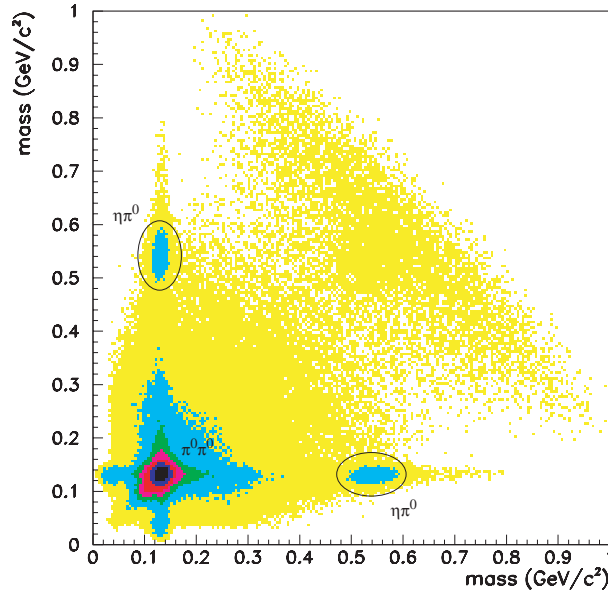


Figure 4.4: Scatterplot of one  $\gamma\gamma$  effective mass combination versus the other  $\gamma\gamma$  effective mass from the reaction  $\pi^- p \rightarrow 4\gamma n$ . These measurements were made using the E852 LGD.

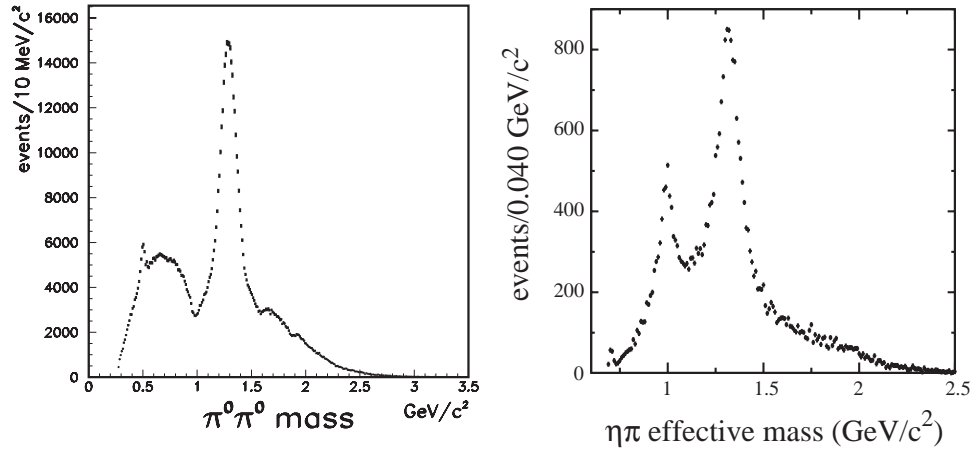


Figure 4.5: left: Distribution of the  $\pi^0\pi^0$  effective mass in the E852 reaction  $\pi^- p \rightarrow \pi^0\pi^0 n$ . right: Distribution of the  $\eta\pi^0$  effective mass in the E852 reaction  $\pi^- p \rightarrow \eta\pi^0 n$ .

beryllium target. Surrounding the target and extending forward to  $30^\circ$  from the beam axis was a cylindrical scintillator detector (BSD) which provided nearly full angular coverage for recoil protons. Surrounding the BSD was a cylindrical lead-scintillating fiber photon detector (BGD) which served to reject events (off-line) with large angle photons. The primary detector component was a 620-channel lead-glass wall (LGD) assembled to approximate a circle around the beam line with a  $8 \times 8\text{cm}^2$  central hole for the passage of the beam. The lead-glass detector was positioned 1.07 m downstream of the target and subtended an angle of approximately  $27^\circ$  from the beam line.

The RADPHI experiment provides an opportunity to understand the operation of a lead

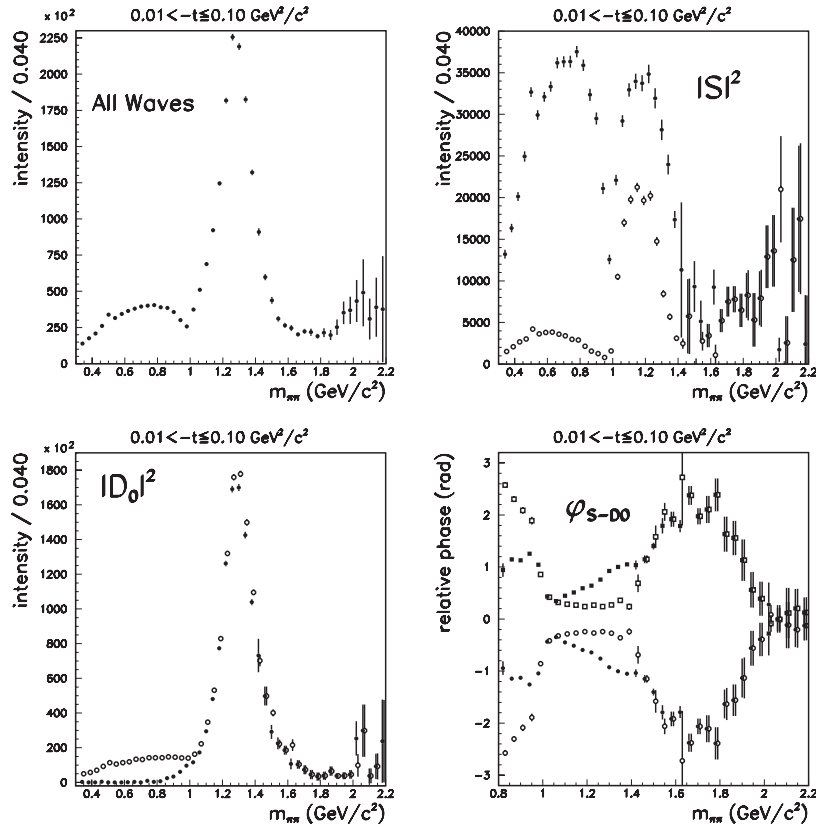


Figure 4.6: Results of a partial wave analysis of the  $\pi^0\pi^0$  system in the E852 reaction  $\pi^- p \rightarrow \pi^0\pi^0 n$  for low momentum transfer events. The sum of all waves (upper left), the  $S$ -wave (upper right), the  $D_0$ -wave (lower left) and the phase between the  $S$ -wave and  $D_0$ -wave (lower right) are shown. Plots show open and filled circles corresponding to mathematically ambiguous solutions with the filled circles indicating the physical solutions based on other criteria.

glass calorimeter in a bremsstrahlung photon beam. Two important issues are understanding the energy and spatial resolution of the detector (relevant for the reconstruction of  $\pi^0$  and  $\eta$  mesons) and electromagnetic backgrounds.

Lacking a source of electron or photon showers of a well-defined energy, the RADPHI experiment had to rely on the observed width of known mesons to deduce the energy resolution of the lead-glass calorimeter. The observed width of narrow mesons such as the  $\pi^0$  and  $\eta$  that undergo  $2\gamma$  decay is determined by the single-shower energy and position resolutions of the LGD. In cases where the spatial contribution can be neglected, the single shower energy resolution was extracted by selecting pairs with one of the two showers in a narrow energy window and examining the energy spectrum of the other, for a given cluster-separation angle. This energy spectrum shows peaks that correspond to the masses of the  $\pi^0$  and  $\eta$  and whose line-shapes are convolutions of the energy response functions for the two showers plus contributions from uncertainties on the shower centroid positions. The contribution from spatial resolution to the width of the peaks was minimized by focusing first on the  $\eta$ , which is associated with pairs of showers that are well separated on the face of the calorimeter. By analyzing the dependence of

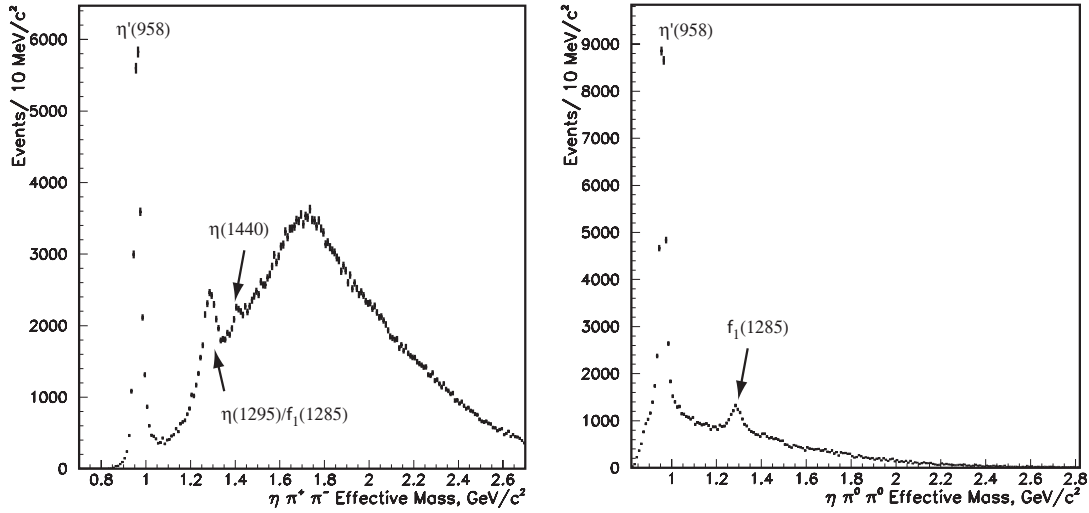


Figure 4.7: left: Distribution of the  $\eta\pi^+\pi^-$  and right:  $\eta\pi^0\pi^0$  mass distributions observed in E852.

the peak width on the energies of the individual showers, the convolution was inverted to obtain the r.m.s. resolution for single showers as a function of shower energy without introducing a model for the energy dependence. Once the energy resolution had been determined in this way, the spatial resolution was then examined by looking at the excess width of the  $\pi^0$  peak over what was expected based upon energy resolution alone. In the end, a unified analysis including both energy and spatial resolution effects was able to reproduce both the  $\pi^0$  and  $\eta$  profiles.

Assuming that the spatial resolution is not important for  $\eta \rightarrow 2\gamma$  decays, the r.m.s. shower energy resolution can be extracted without assuming any functional form for its dependence on shower energy. This model-independent solution was then compared with the standard parametrization [?] of the lead glass energy resolution given in Eq. ??.

$$\frac{\sigma_E}{E} = \frac{B}{\sqrt{E}} + A. \quad (4.1)$$

The first term on the right contains the effects of photoelectron statistics, while the second term wraps up all of the systematic block-to-block differences and calibration errors which prevent the width of the response function from collapsing to a delta function in the high-energy limit. In order to describe the  $\pi^0$  peak with the same parameters it is necessary to introduce a model for the shower spatial resolution, which itself depends upon shower energy. The energy dependence is proportional to  $1/\sqrt{E}$  with a proportionality constant that depends on the size of the LGD block [?]. Eq. ?? is adopted for showers at normal incidence, with the constant  $C$  expected to be around  $7 \text{ mm}\cdot\text{GeV}^{-\frac{1}{2}}$ .

$$\sigma_x = \frac{C}{\sqrt{E}}. \quad (4.2)$$

In the RADPHI geometry many of the showers are far from normal incidence and so the shower depth fluctuations of roughly one radiation length also contribute to the centroid position resolution along one of the spatial axes. This was taken into account in the analysis by projecting one radiation length from along the shower axis onto the transverse plane and adding it in

quadrature to the base term in Eq. ???. The final values for all parameters were determined by simultaneous analysis of the  $\eta$  and  $\pi^0$  data where all of the above effects are included for both.

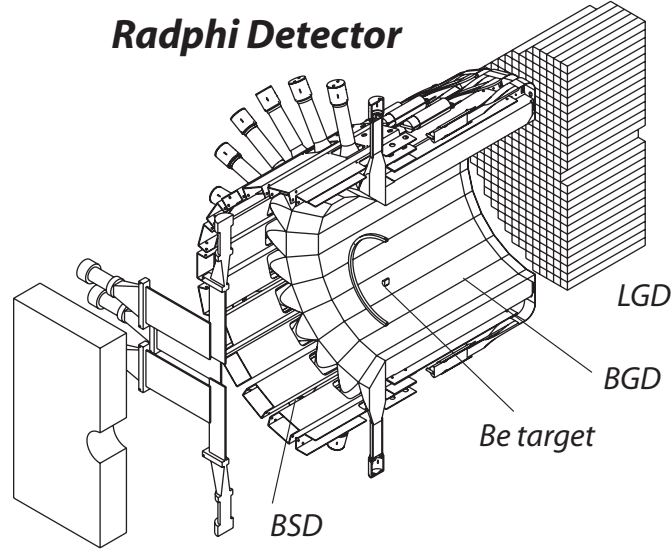


Figure 4.8: The RADPHI detector.

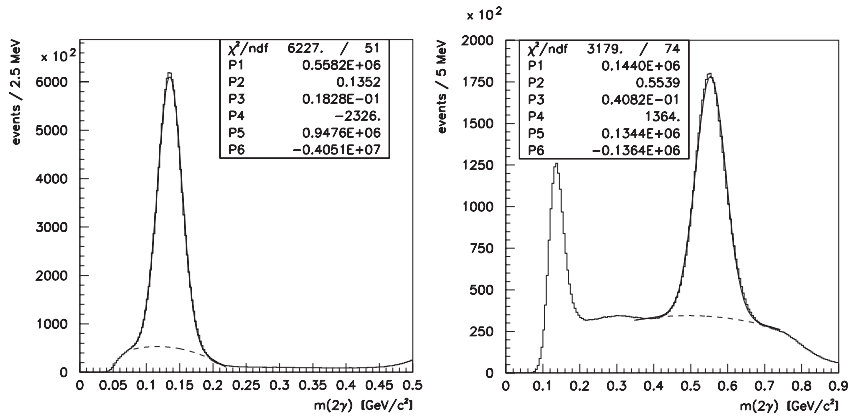


Figure 4.9: Invariant mass distribution of  $\pi^0 \rightarrow 2\gamma$  (left) and  $\eta \rightarrow 2\gamma$  (right). The parameters shown are the height (P1), mean (P2) and sigma (P3) of the Gaussian peak fitted to the data over a polynomial background described by parameters P4-P6.

### Estimating the GlueX $\pi^0$ and $\eta$ Mass Resolutions

The experience with the E852 and RADPHI detectors allows us to reasonably interpolate to expected GLUEX performance. Based on the discussion above and that of reference [?] we assume the energy resolution given by:

$$\frac{\sigma_E}{E} = 0.036 + \frac{0.073}{\sqrt{E}} \quad (4.3)$$

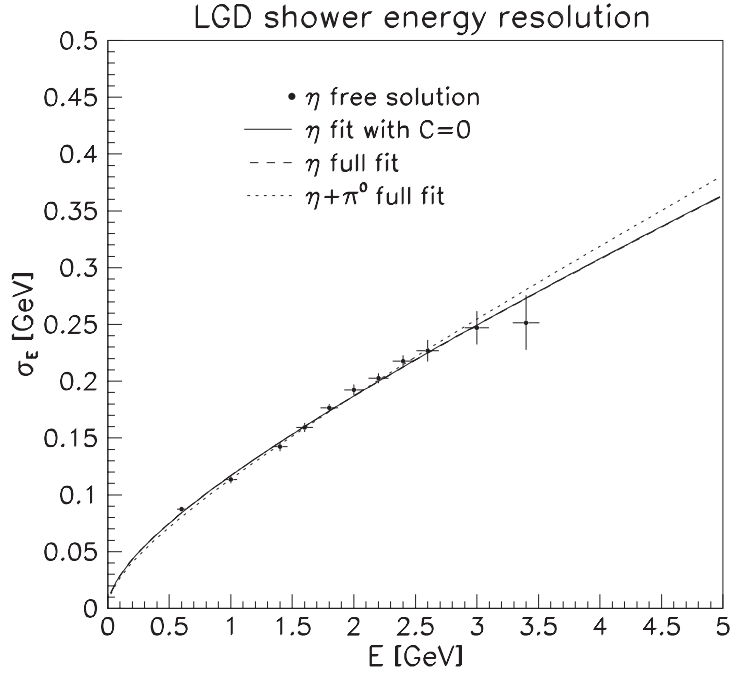


Figure 4.10: Energy resolution of showers in the LGD obtained from analysis of the  $2\gamma$  sample.

and the spatial resolution is given by:

$$\sigma_\rho = \sqrt{\left(\frac{7.1}{\sqrt{E}}\right)^2 + (X_0 \sin \theta)^2} \text{ mm} \quad (4.4)$$

where  $\rho$  locates the shower position in the plane of the LGD measured from the center of the LGD,  $\theta$  is measured from the normal to the LGD plane,  $X_0$  is the radiation length of glass (31 mm in this case) and  $E$  is the photon energy in GeV.

A Monte Carlo simulation of forward  $\pi^0$  and  $\eta$  production for RADPHI, E852 and GLUEX assumed:

1. A uniform photon beam between 3.0 and 5.4 GeV for RADPHI, 18.0 GeV for E852 and 9 GeV for GlueX;
2. A target to LGD distance of 1.0 m, 5.4 m and 5.0 m for the three experiments respectively.
3. Transverse LGD dimensions characterized by circular stacks of radii 0.5 m for RADPHI and 1.0 m for GLUEX and a 1.68 by 2.8 m rectangular stack for E852.
4. A minimum photon energy of 150 MeV and a minimum photon separation of 8 cm.

Simulation results are shown in the plots of Figure ???. We obtain  $\pi^0$  mass resolutions of 16 MeV for RADPHI and 8 MeV for E852 compared to measured resolutions of 18 and 10 MeV. For GLUEX we predict 9 MeV. For the  $\eta$  we obtain mass resolutions of 40 MeV for RADPHI and 27 MeV for E852 compared to measured resolutions of 40 and 25 MeV. For GLUEX we predict 30 MeV.

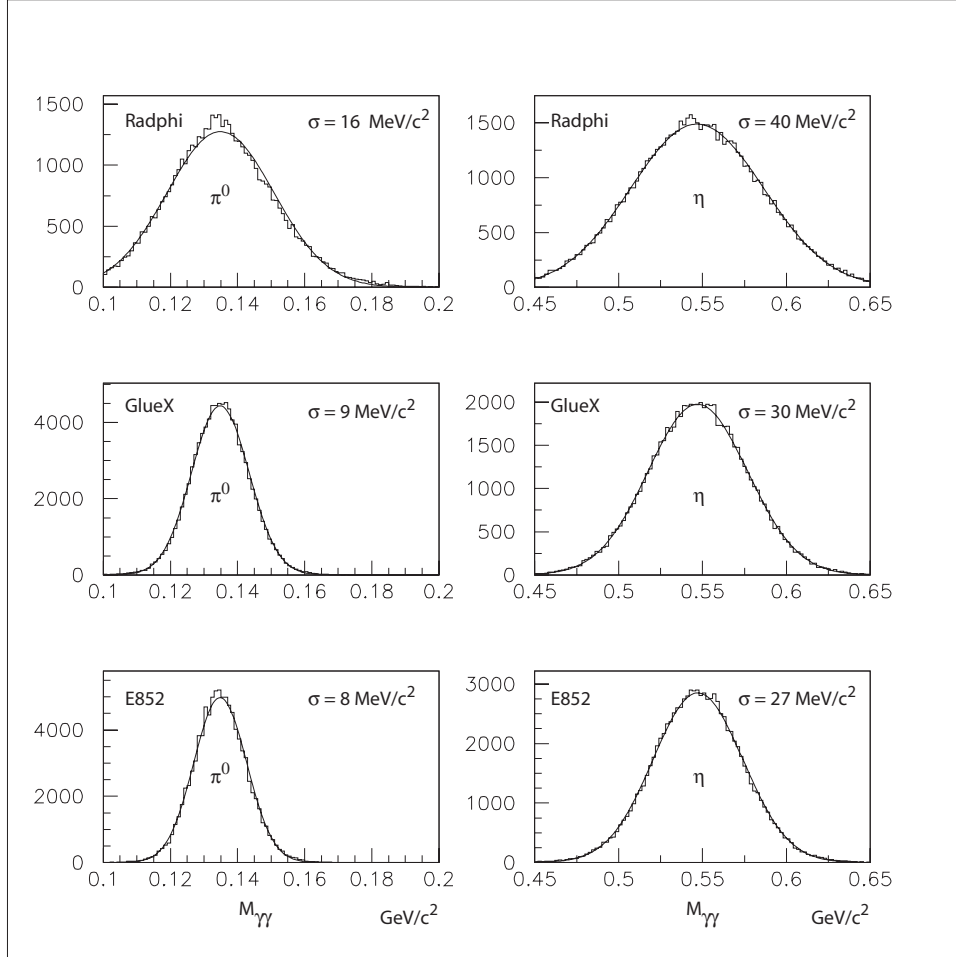


Figure 4.11: Simulated diphoton mass for the  $\pi^0$  and  $\eta$  using the Radphi, GlueX and E8652 geometry.

### Electromagnetic Backgrounds

The experience with the RADPHI LGD also allows us to compare estimates of electromagnetic backgrounds as calculated using GEANT with measured rates. Such a comparison is shown in Figure ???. The histogram in the figure is the Monte Carlo estimate for the LGD rates arising only from electromagnetic background. Note that for individual blocks, the expected hadronic rate is negligible on this scale. The simulation includes the principal components of the Hall B photon beam line starting at the radiator and including the (empty) CLAS target and downstream yoke aperture. Note that in Figure ??? a marked depression appears at small radius, relative to the observed rates. These blocks are in the vicinity of the beam hole and, in addition to suffering from the highest rates, these blocks also suffered from radiation damage. The eight blocks closest to the beam axis (first data point) are the most affected, but some effects can be seen at neighboring points.

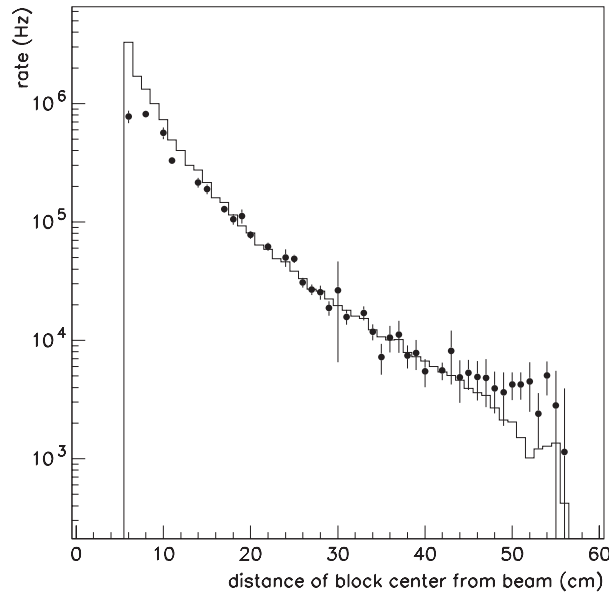


Figure 4.12: Characteristics of unbiased flux observed in individual blocks in the LGD as a function of distance from the beam. The points are derived from data and the histograms from a Monte Carlo simulation of the electromagnetic background coming from the beam and target. All hits over 15 MeV are recorded.

### Radiation Damage

Online monitoring of the LGD during the RADPHI experiment indicated that the 8 blocks immediately adjacent to the beam hole were becoming progressively reduced in gain as the run progressed. This observation was based upon the laser monitor system, the raw pulse-height distributions, and the channel gains which were periodically recalibrated during the run. A similar effect was seen, but to a lesser degree, for the next layer of blocks once removed from the beam hole. During a pause in the experiment, visual inspection of the blocks indicated that the glass was darkening, a well-known effect of radiation damage on lead glass. Figure ?? illustrates the gain reduction with beam time (roughly proportional to integrated radiation dose) for a typical block adjacent to the beam hole. It is apparent that the gain change is a gradual, cumulative effect rather than a sudden change which might be characteristic of a beam mis-steering event.

The magnitude of the gain loss (order 40%) was such that it could be compensated by adjustments of the PMT high voltages. This was done periodically during the experiment. The last datum in Figure ?? shows the result of one adjustment. However, this is only a partial solution, since the module suffers a loss of photoelectrons due to the radiation damage, and thus a degraded resolution. Thus it was desirable to ‘heal’ the radiation damage as much as possible.

Radiation damage in lead glass is known to be temporary, and to largely heal itself on the time scale of a few months. The healing can be accelerated by the use of ultraviolet (UV) light. This approach was adopted for the most affected blocks. During an extended down-time in the run, the PMT and base for selected modules were removed and a UV light guide attached to a quartz envelope Mercury vapor lamp was inserted. The output of the lamp was  $5 \text{ W/cm}^2$

in the range 300 to 480 nm, with a peak intensity at 365 nm. The affected blocks were each illuminated for periods of 6-8 hours. These blocks showed a gain increase of 30% following this treatment, nearly recovering their initial gains.

It should be noted that the change in the response of the modules due to radiation damage and the gain recovery following UV treatment was even more dramatic in the data from the laser monitoring system (typically a factor of two change). The difference between the shift in the pulser response and that seen in the gain constants from the calibration can be qualitatively understood by noting that the laser illuminates the front of the block and thus measures the transmission of the entire block, while the showers seen in the calibration data create Cerenkov light throughout the volume of the block, and are therefore less sensitive to attenuation effects in the upstream region of the block. The radiation damage is now known, from measurements, to be within 11 cm of the front surface of the detector, and this was confirmed by visual inspection, in qualitative agreement with the difference between the laser monitor data and the calibration data.

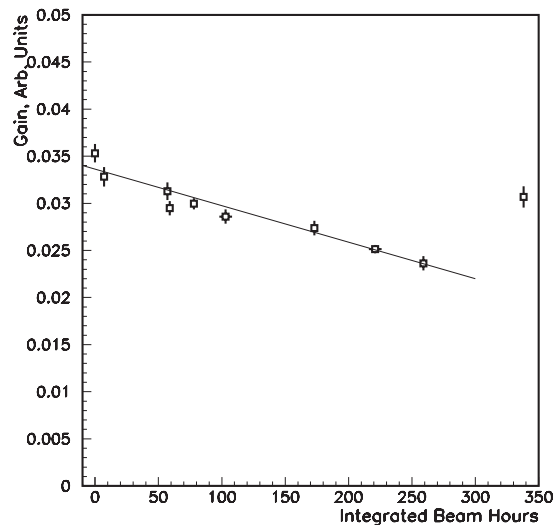


Figure 4.13: The effect of radiation damage on the central part of the detector. The last point shows the gain after an adjustment of the PMT high voltage.

**Heat Curing of Damaged Blocks** As part of the program to assess the glass used in E852 and RADPHI for use in GLUEX a spectrophotometer (Shimadzu UV-160) was modified to allow a lead glass bar to be automatically moved along its long axis to measure transmission through the 4 cm thickness. Based on the transmission dependence on wavelength, the transmission of the bar as a function of length was measured at 410 nm. Figure ?? shows the dependence of transmission as a function of length along the block for a block that visibly shows radiation damage. An alternative to UV curing, heating blocks in an oven has also been studied. The plot also shows the transmission curve for the same block after heating the block for several hours in an oven at 260 °C.

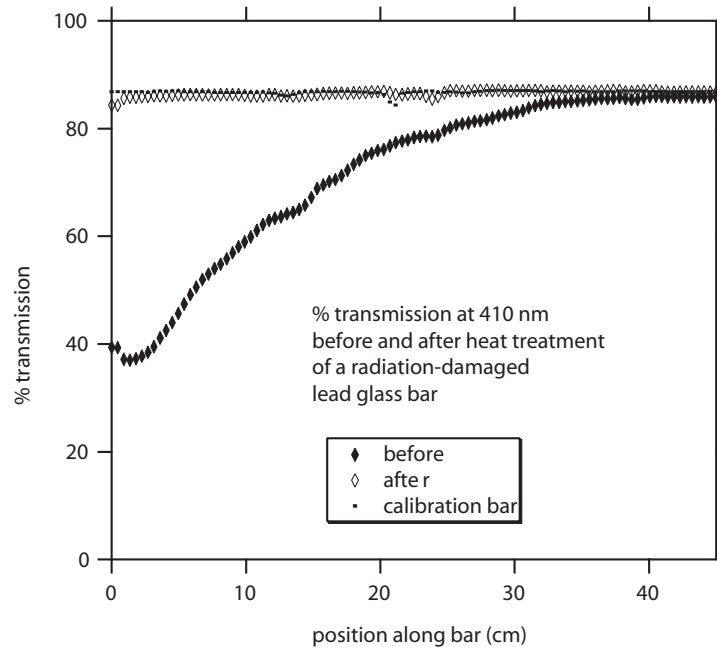


Figure 4.14: The effect of heat curing.

### Assessing Lead Glass Blocks and PMT's

**Lead glass block evaluation** Some of the lead glass blocks used in the E852 experiment were used in the RADPHI experiment. All of the blocks are being examined for mechanical and radiation damage – the latter being assessed using the spectrophotometer described above.

The transmission at a wavelength of 410 nm as a function of length along the block will be measured and recorded for each block. The reason for measuring the transmission at this wavelength can be understood from the data presented in Figure ?? where the transmission as a function of wavelength is measured for a block that suffered radiation damage and a block with no damage. The measurement was made approximately 2.5 cm from the upstream end of block where *upstream* refers to the orientation of the damaged block in the beam. At about 410 nm the undamaged glass reaches a transmission plateau.

**PMT Evaluation** The PMT's available for GLUEX were used in E852 starting in 1994. There is some concern about the aging of the PMT's so a program of testing the 3200 PMT's (including spares) has already started. A similar process was used prior to constructing the E852 LGD for rating PMT's and is described in reference [?]. For the current test a light-tight box will accommodate 25 PMT's at a time. The tubes will view a diffusing plate that is illuminated by two blue LEDs that will be pulsed. Under computer control the gain as a function of high-voltage will be recorded and random noise and correlated noise rate will be measured. The correlated noise rate will be measured within a fixed gate delayed by a few hundred nanoseconds after the LEDs are pulsed. Preliminary measurements with a random selection of PMT's indicate that the PMT's performance has not degraded.

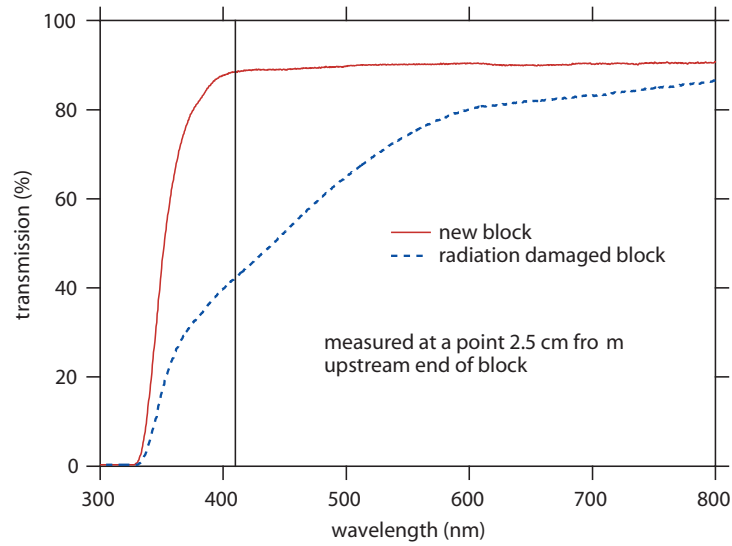


Figure 4.15: Transmission as a function of wavelength for radiation-damaged lead glass and undamaged glass. At about 410 nm the undamaged glass reaches a transmission plateau.

### Other Issues

**Electromagnetic Rates in the LGD** The RADPHI experience has forced us to deal with the issue of high rates in the central part of the detector and also how to use GEANT to estimate those rates. Those studies are currently underway for the GLUEX arrangement. We are also exploring the option of using another medium in the central region of the LGD, such a radiation hard lead glass, lead tungstate or another material. This will of course impact on shower reconstruction – especially for those showers that cross the boundary between media. Another option under investigation is to place a thin sheet of lead in front of the LGD blocks in danger of damage. The impact this has on resolution is also being studied.

**Magnetic Shielding** In E852 a cellular wall was used to register the PMT’s to the glass wall. That cellular wall consisted of two aluminum plates with holes into which cylindrical soft iron tubes were squeezed (the tubes were sandwiched between the plates). Epoxy was injected the space between the tubes and between the plates through small holes in the plates. Additional  $\mu$ -metal shields surrounded individual PMT’s before insertion into the soft iron tubes. The PMT’s were positioned against the glass blocks with an air gap in between. This entire cellular wall structure was surrounded by a thick iron frame to provide further shielding. The structure is described in reference [?]. A similar wall was used for RADPHI. In E852 the PMT’s were shielded from the fringe field of the BNL MPS dipole magnet.

Simulations of the fringe field of the GLUEX solenoid are currently underway for various assumptions about the structure and material in the vicinity of the LGD. More details about magnetic shielding are also discussed in the section on the TOF – the forward time-of-flight system.

For the LGD we plan to have the PMT photocathode recessed inside the iron shielding tube by about the diameter of the photocathode and we plan to study the use of short cylindrical glass segments to couple the lead glass to the PMT with proper index of refraction matching.

**Monitoring** The E852 and RADPHI LGD's were monitored [?, ?] by using light from a nitrogen laser illuminating a block of scintillator. The scintillator light was transported by several optical fibers coupled to the sides of a Plexiglass sheet large enough to cover the front face of the glass stack. This system was used for initial gain setting and to monitor gains throughout the run.

**Matt: Christina's paragraphs are immediately below**

The fcal relative-gain monitoring system is designed to track the stability of the Pb-glass output signals between calibrations with particles and at the same time check for any possible radiation damage. The system is composed of light emitting diodes (LED) light sources. Since the radiation damage - if present - is expected to be more pronounced in the blue region of the visible spectrum, we opted to calibrate using LEDs of different colours in order to continuously monitor the whole spectrum where the PMs are sensitive.

The monitoring system is mounted on Plexiglas panes which are mounted very close to the front faces of the 2800 Fcal Pb-glass blocks which are read by the xxx PMs . The layout of the fcal monitoring system is shown in Fig. ???. The space between the Plexiglas and the front faces of the Pb-glass arrays is about 3/8". The Plexiglas is divided into four different quadrants leaving a square hole in the middle for the beam passage. Each quadrant is flashed by a group of 10 LEDs , five on one side and five on the side perpendicular to the first one as shown in Fig. ???. Each group of four LEDs of different colour is assembled on the same board, called *fcal-LED4* board.

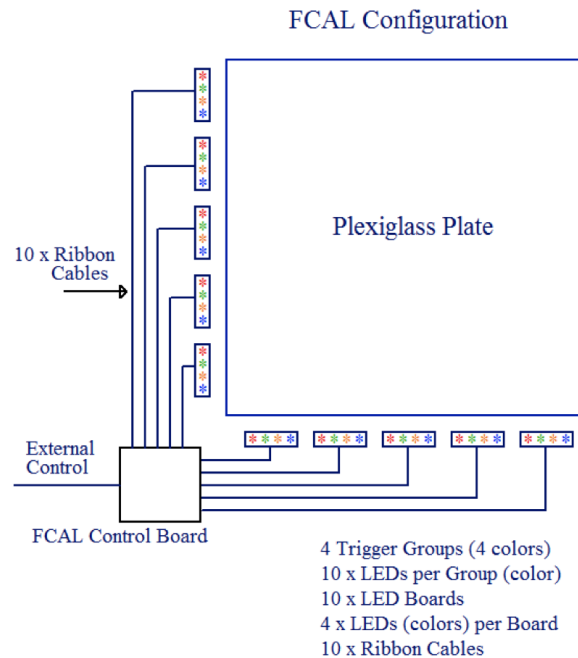


Figure 4.16: FCAL LED monitoring system configuration.

The LED boards shown in the top panel Fig. ??, have a height of 15mm – approximately equal to the thickness of the Plexiglas panes – and are driven by control boards (*fcal-CRTL*) shown in the bottom panel. Each LED of different colour is triggered independently of the other colours but is self triggered. So every *fcal-CRTL* of each quadrant, receives four triggers

from the outside world which are, in turn, fanned out, together with DC voltages for the LEDs, to the *fc*al-LED4 boards by ten ribbon cables. On the *fc*al-CRTL, a connector to the outside world where the triggers and the low voltage power will be connected is shown in Fig. ??.

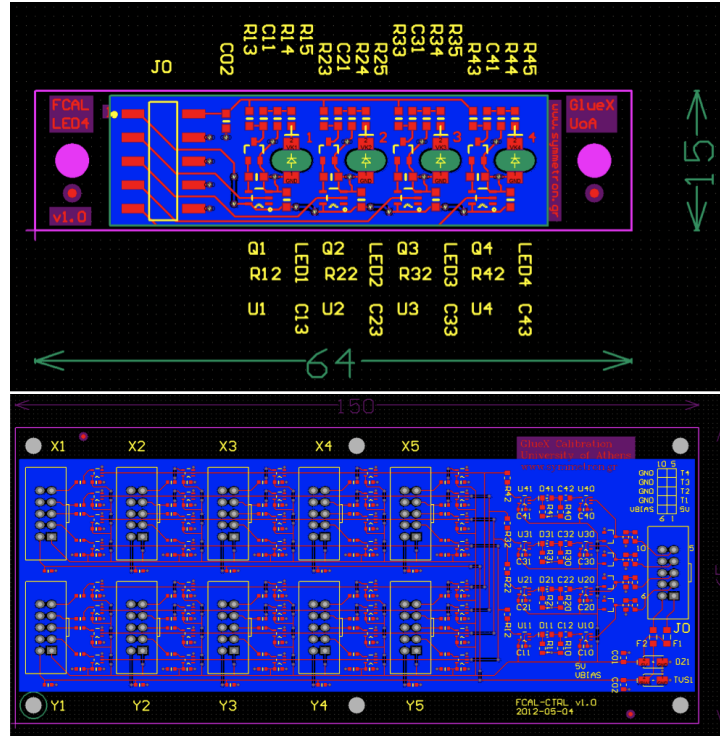


Figure 4.17: FCAL monitoring system LED and Controller boards.

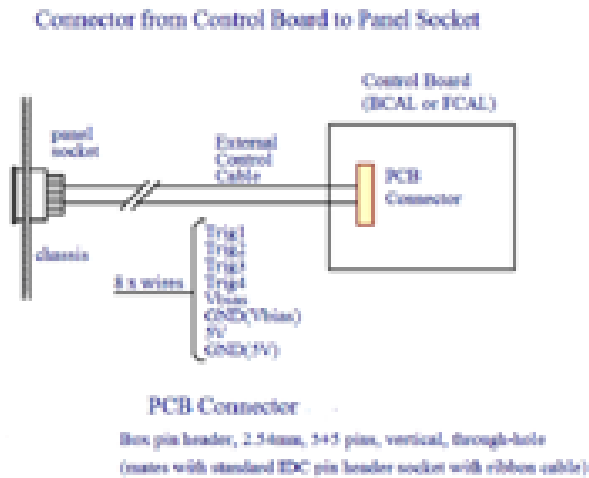


Figure 4.18: FCAL monitoring system PCB connection.

The ten *fc*al-LED4 boards are clamped on the side of the Plexiglas along its width- as shown in Fig. ???. The different colour LEDs come from the following companies: Satistronics

emitting at 390nm (UV) and Kingbright emitting at 470nm (blue), 525nm (green) and 574nm (green). The LEDs are attached to a single PCB board as explained above so that they emit light parallel to the long axis of the Plexiglas.

The FCAL monitoring system first article is now under construction and upon approval will proceed to the construction phase.

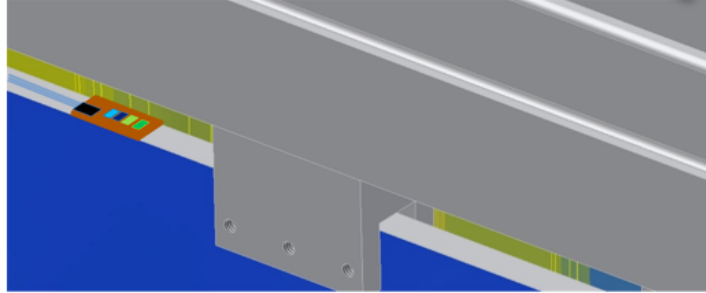


Figure 4.19: FCAL monitoring LED positioning on the Plexiglas edge.

**Calibration** GLUEX will base its LGD calibration system on the extensive experience gained with calibrating the E852 and RADPHI LGD's that is described in references [?] and [?].

**Triggering** An energy sum trigger was provided by the E852 and RADPHI LGD's [?, ?]. In addition the E852 LGD had a trigger processor that provided an estimate of the total effective mass of photons striking the LGD and this was used in the trigger.

### 4.3.3 Barrel Calorimeter

#### Introduction

The barrel electromagnetic calorimeter (BCAL) is a key component of the hermetic detector, built as a lead, scintillating fiber matrix at the University of Regina. It will be positioned immediately inside the solenoid, leaving a space of 2.7 cm radially between the two for supports and installation. This constrains the device's outer radius to be 90 cm, while its inner radius is fixed at 65 cm to allow adequate space for the CDC.

A principle goal of GLUEX calorimetry is to detect and to measure photons from the decays of  $\pi^0$ 's and  $\eta$ 's which, in turn, can come from the decays of produced mesons (normal or exotic) or possibly from excited baryons ( $N^*$  or  $\Delta$ ). The positions and energies of the photons must be determined to sufficient accuracy to allow for a complete kinematic reconstruction of the event. Adequate readout segmentation is required for an accurate determination of the azimuthal angle of tracks as well as for providing information on the energy deposition profile in depth, and for good cluster identification, while avoiding multiple occupancy. Detailed Monte Carlo studies [?] [?] indicate that the BCAL should be sensitive to photon energies in the range from 60 MeV to at least 2.5 GeV. Specifically, studies of the lowest energy photons in high-multiplicity reactions that are expected to yield exotic hybrids such as  $\gamma p \rightarrow b_1(1235)\pi n \rightarrow 2\pi^+\pi^-2\pi^0 n$  indicate that an energy threshold of 60 MeV suffices. The device will also provide timing information for charged particles and thus contribute to PID in the central region, in conjunction with the CDC. For events with only charged particles, it is essential to be able to

veto neutrons, therefore nearly hermetic coverage is critical. A further PID function for this device is to provide  $dE$  information.

The relevant parameters that determine the  $\pi^0$  and  $\eta$  mass resolutions are the photon energy ( $E$ ) and the polar and azimuthal position resolutions ( $\sigma_\theta$  and  $\sigma_\phi$ ). The energy resolution ( $\sigma_E$ ) depends on the number of photoelectrons ( $N_{pe}$ ) yielded by the photosensors, based on the collected light. The photoelectron statistics are strongly dependent on the stochastic fluctuations of the energy deposited by the electromagnetic shower in the scintillating fibres of the calorimeter. In addition,  $N_{pe}$  depends on the fraction of photon shower energy deposited in the fibres, the efficiency with which the resulting scintillation light is captured in and transmitted down the fibre to the photosensor, and the photon detection efficiency of the photosensor. The photon position is determined by the readout segmentation in the azimuthal direction and the difference in arrival time ( $\Delta T$ ) of the scintillation light between the two ends of the barrel. The time difference ( $\sigma_{\Delta T}$ ) resolution, and therefore the polar angle resolution, also depend on  $N_{pe}$ . The former is a critical input into the momentum resolution for photons and for charged particle PID [?,?].

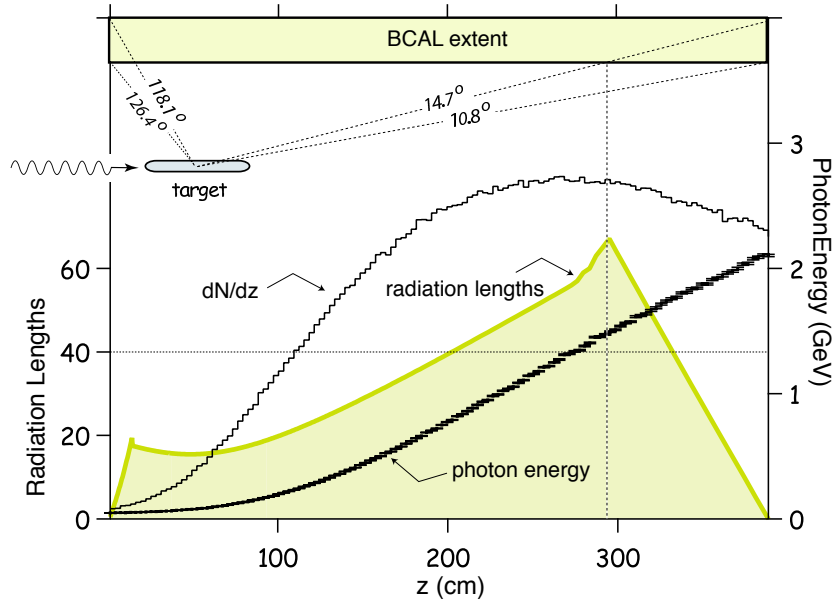


Figure 4.20: The distribution of photons, their energy and integrated path length through the Pb/SciFi matrix as a function of position along the length of the BCAL for one of the GLUEX signature reactions,  $\gamma p \rightarrow \eta\pi^0 p \rightarrow 4\gamma p$ , is shown. The target position and angular range subtended by the BCAL are also presented.

The performance metrics for these quantities were set by simulating hadronic photoproduction at GLUEX energies using Pythia [?] and also by simulating several of the signature reactions expected to yield exotic mesons. These studies included a GEANT-based simulation [?] of the entire GLUEX detector response, including detector material and cabling, photon reconstruction and kinematic fitting. The Pythia simulations indicate that 70% of the produced photons with energies up to about 2 GeV will be incident on the BCAL. The photon population in the BCAL for one of the signature reactions,  $\gamma p \rightarrow \eta\pi^0 p \rightarrow 4\gamma p$ , where the distribution in  $\eta\pi^0$  mass was uniform from 1.0 to 2.0 GeV/ $c^2$  and uniform in decay angles, is shown in Fig. ?? . The

distribution of photons ( $dN/dz$ ) is plotted as a function of position from the upstream end of the BCAL; the photons predominantly populate the downstream end of the BCAL. Also graphed is the average energy as a function of  $z$  with higher energy photons being more forward. The integrated thickness of the BCAL matrix, in number of radiation lengths, traversed by photons incident at various positions along the length of the BCAL is also displayed. The target occupies the region  $z = 33 - 63$  cm. Note that there is a narrow ( $\sim 1^\circ$ ) angular range near  $11^\circ$  where the photon trajectory intercepts a small number of radiation lengths of the Pb/SciFi matrix. Photons with angles less than  $10^\circ$ , with respect to the beam direction, will be detected in the FCAL.

### Spaghetti Calorimetry

The BCAL design is based on scintillating fibers embedded in a lead matrix, which results in a relatively high-resolution sampling calorimeter. Such materials have been used in calorimeter design and operation for nearly three decades. The ratio of the active scintillator to the passive high- $Z$  material, as well as the diameter of the fibers, can be tuned to enhance resolution, to determine the radiation length, and to achieve uniformity in the electromagnetic (EM) to hadronic response (the  $e/h$  ratio).

In general, the energy resolution of an electromagnetic calorimeter is expressed in the form:

$$\frac{\sigma_E}{E} = \frac{a}{\sqrt{E(\text{GeV})}} \oplus b \oplus \frac{c}{E(\text{GeV})}. \quad (4.5)$$

The  $a/\sqrt{E}$  term contains the combined effect of sampling fluctuations and photoelectron statistics, with the former dominating the resolution. This is commonly referred to as the stochastic term. The constant term,  $b$ , in Eq. ??, originates from all other energy-independent sources that contribute to uncertainties in the energy reconstruction and due to the intrinsic time spread due to the finite length in the  $z$  direction of the luminous point. These sources can be mechanical imperfections, material defects, segment-to-segment calibration variations, non-uniformity of response, instability with time and shower leakage. The noise term,  $c/E$ , results from noise electronics noise and pileup in high-rate environments. A similar equation governs the timing resolution:

$$\sigma_t = \frac{c}{\sqrt{E(\text{GeV})}} \oplus d. \quad (4.6)$$

In general, the constant term,  $d$ , is a result of residual calorimeter miscalibrations, but some fraction is also due to the finite width in  $z$  of the beam, which will contribute to the time difference resolution.

### BCAL Geometry and Parameters

The BCAL is modelled closely after the EmCal calorimeter built for the KLOE experiment at DAΦNE [?, ?, ?], which also operated in a solenoidal magnetic field for more than a decade. The KLOE collaboration developed tooling for the production of long-grooved lead sheets, pushed the technology for excellent fibers with long attenuation lengths ( $2.3 < \lambda < 3.2$  m) and built a device with inner radius of 2 m and 4.3 m length [?]. This device utilized 1 mm diameter scintillating fibers, with a fiber to lead to glue ratio of 48 : 42 : 10. The energy and timing

resolutions for KLOE [?] are

$$\frac{\sigma_E}{E} = \frac{5.4\%}{\sqrt{E(\text{GeV})}} \oplus 0.7\%, \quad \sigma_t = \frac{56 \text{ ps}}{\sqrt{E(\text{GeV})}} \oplus 133 \text{ ps}.$$

The latter yields a nearly constant  $\sigma_t \approx 180 \text{ ps}$  for photon energies above 150 MeV, and a diverging timing resolution for  $E_\gamma < 75 \text{ MeV}$ . The EmCal parameters and performance served as benchmarks for the BCAL.

A key instrumentation difference is that the EmCal employed conventional PMT readout at each end that was possible due to the lower field and more favorable field gradient of KLOE compared to GLUEX. The BCAL requires devices that are practically immune to magnetic fields; Silicon Photo-Multipliers (SiPM's) operate reliably in such conditions. Additionally, it is important to point out differences in the GLUEX and KLOE applications of barrel calorimetry. KLOE is a symmetric colliding beam experiment, with the intersection region at the center of its barrel calorimeter. As a result, that calorimeter is illuminated symmetrically and nearly uniformly by photons having 100-200 MeV energies, on average, and with very few photons greater than 400 MeV. On the other hand, GLUEX, is a fixed target experiment, resulting in a highly asymmetric photon distribution: 30% of the photons in the BCAL will have energies considerably higher than 500 MeV. Despite these differences, the KLOE experience provided valuable guidance in the design and construction of the BCAL. The KLOE resolutions are adequate for the GLUEX physics requirements, as indicated by our simulation studies. The extracted resolutions are a direct result of the internal PbSciFi matrix geometry such that similar resolutions should be expected for the BCAL [?].

For GLUEX, the tracking elements inside the magnet's bore require a radius of at least 65 cm in order to perform optimally, leaving about 25 cm of radial thickness for the BCAL. Together with the 4.5 m length of the solenoid these lead to a long, narrow, tube-like design. In this geometry, the readout is logically placed at the ends where space exists and where it can take advantage of the fact that all fibers run parallel to the axis of symmetry of the solenoid and therefore all light piped to the ends of the modules retains its azimuthal and radial information. With rise times of a few ns, good timing can be expected in collecting the light from a shower. Moreover, because the EM showers spread across the azimuthal boundaries, algorithms for finer positioning of the shower are required. A typical weighted position resolution is  $\delta x \approx 5 \text{ mm} / \sqrt{E}$ . For the BCAL design, this would lead to an azimuthal resolution of  $\approx 8.5 \text{ mrad}$ . Using the  $z$  position resolution of approximately 4 cm obtained from the time difference leads to a polar angular resolution at  $45^\circ$  of  $\approx 8 \text{ mrad}$ . The time difference from the two ends produces the  $z$  coordinate of the hit. Because we will use an array of readout devices on each end (segmented in azimuth and depth), redundant measurements are made of the  $z$  coordinate. These measurements of  $z$  correspond to different average radii and therefore help to establish the angle of the incoming photon. Finally, the fractional volume of scintillator in the detector naturally makes it efficient for detecting charged hadrons. The mean light collection time of the two readout ends can be used to determine the particle time-of-flight (TOF). TOF coupled with the track length and momentum then yields particle mass, thus contributing to PID information.

The BCAL design is depicted in Fig. ??, a zoomed-in view of the matrix is portrayed in Fig. ?? and the main parameters and properties of the BCAL are given in Tables ?? and ??, respectively. Forty eight modules were constructed, plus one spare.

The choice of readout device must bear in mind the considerable magnetic field (22.4 kG) inside the bore and the rapidly varying fringe field at the ends. The option chosen for the

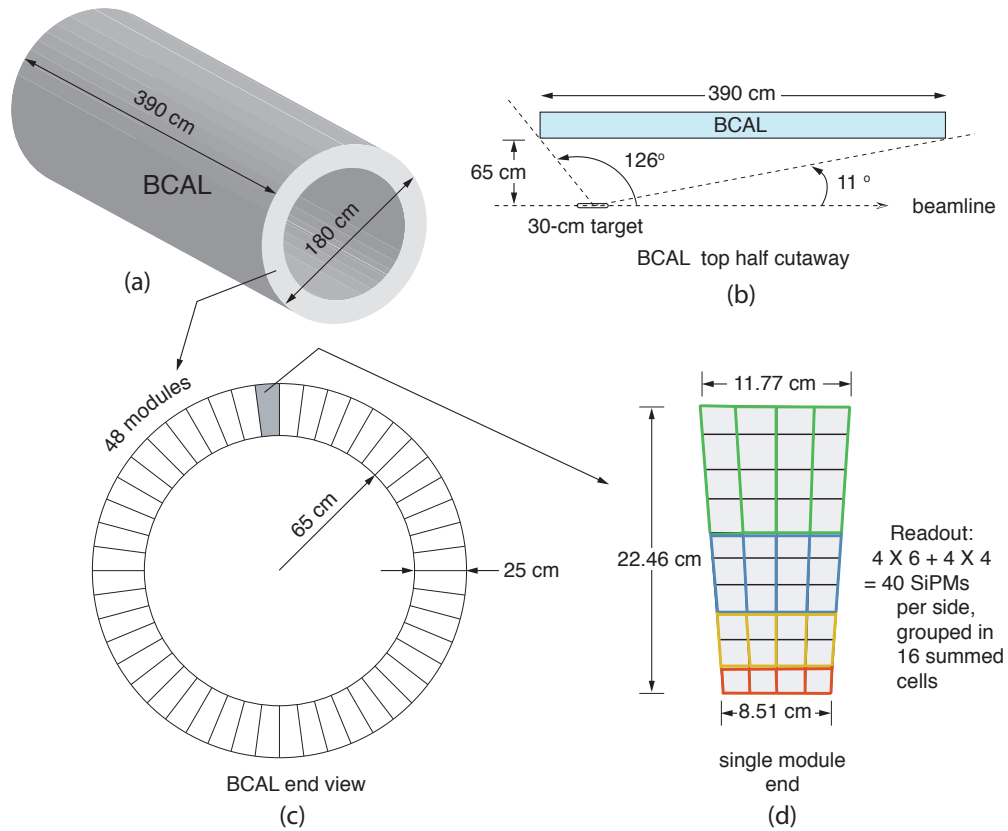


Figure 4.21: Sketch of Barrel Calorimeter readout. (a) A three-dimensional rendering of the BCAL; (b) top-half cutaway (partial side view) of a BCAL module showing its polar angle coverage and location with respect to the GlueX LH<sub>2</sub> target; (c) end view of the BCAL depicting all 48 azimuthal modules and (d) an end view of a single module showing the readout segmentation: four rings (inner to outer) comprised of sums of 1, 2, 3, and 4 readout rows, respectively, and four azimuthal slices (columns), resulting in a total of 16 summed readout zones. More details can be found in the text.

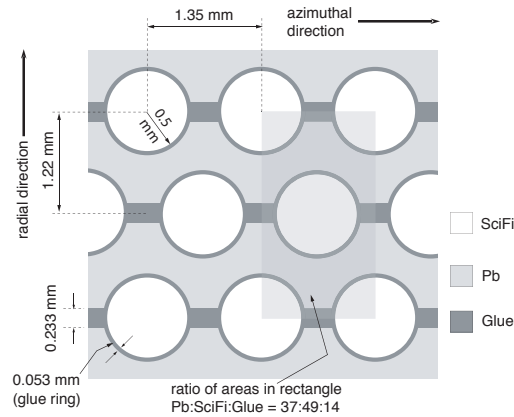


Figure 4.22: Close-up view of the BCAL matrix details.

Table 4.1: BCAL parameters. Superscript: *a* - design parameters of the BCAL specified for the final detector; *b* - quantities that have been measured; *c* - specifications from the manufacturer; *d* - from literature; *e* - parameter calculated from known quantities; *f* = parameter estimated from simulations. The number of radiation lengths and the resolutions are at  $\theta = 90^\circ$  incidence.

Property	Value	Ref.
Total weight <sup>a</sup>	25 metric tons	
Number of readout channels <sup>a</sup>	3840 SiPMs	
Number of modules <sup>a</sup>	48	
Module length <sup>a</sup>	390 <i>cm</i>	
Module inner cord <sup>a</sup>	8.51 <i>cm</i>	
Module outer cord <sup>a</sup>	11.77 <i>cm</i>	
Module thickness <sup>a</sup>	21.83 <i>cm</i>	
Module azimuthal bite <sup>a</sup>	7.5°	
Number of fibres <sup>b</sup>	736,800	
Radial fibre pitch <sup>b</sup>	1.22 <i>mm</i>	
Azimuthal fibre pitch <sup>b</sup>	1.35 <i>mm</i>	
Lead sheet thickness <sup>c</sup>	0.5 <i>mm</i>	
Fibre diameter <sup>c</sup>	1.0 <i>mm</i>	[?]
First cladding thickness <sup>c</sup>	0.03 <i>mm</i>	[?]
Second cladding thickness <sup>c</sup>	0.01 <i>mm</i>	[?]
Core fibre refractive index <sup>c</sup>	1.60	[?]
First cladding refractive index <sup>c</sup>	1.49	[?]
Second cladding refractive index <sup>c</sup>	1.42	[?]
Volume ratios <sup>b</sup>	37:49:14 (Pb:SF:Glue)	[?]
Effective mass number <sup>e</sup>	179.9	[?]
Effective atomic number <sup>e</sup>	71.4	[?]
Effective density <sup>e</sup>	4.88 g/cm <sup>3</sup>	[?]
Sampling fraction <sup>f</sup>	0.125	[?]
Radiation length <sup>e</sup>	7.06 g/cm <sup>2</sup> or 1.45 <i>cm</i>	[?]
Number of radiation lengths <sup>e</sup>	15.1X <sub>0</sub> (total thickness)	[?]

readout is based on a large-area application of SiPM's. These devices offer gain and timing resolution comparable to that of a PMT, superior energy resolution, are immune to magnetic fields, and require simple electronic amplification and summing circuits. Each channel will also include low-voltage bias and power for the preamplifiers, a flash ADC, discriminator, TDC and cabling. Multiple, independent light guides will be epoxied to the polished ends of the BCAL. A gain-stability, monitoring system is critical and will be based in part on small LED's glued directly to each of the 40 light guides at the ends of each module. An LED driver system has been designed and tested, and comprises small LED boards driven in four strings of 10 LEDs per

Table 4.2: BCAL properties. Superscripts are the same as in Table ??.

Property	Value	Ref.
Trapping efficiency <sup>c,d,e</sup>	5.3% (min) 10.6% (max)	[?, ?, ?]
Attenuation length <sup>b</sup>	(307±12) cm	[?]
Effective speed of light <sup>b</sup> , $c_{\text{eff}}$	(16.2±0.4) cm/ns	[?]
Critical energy <sup>e</sup>	11.02 MeV (8.36 MeV)	[?, ?]
Location of shower maximum <sup>e</sup>	5.0 $X_0$ (5.3 $X_0$ ) at 1 GeV	[?, ?]
Thickness for 95% containment <sup>e</sup>	20.3 $X_0$ (20.6 $X_0$ ) at 1 GeV	[?, ?]
Molière radius <sup>e</sup>	17.7 g/cm <sup>2</sup> or 3.63 cm	[?]
Energy resolution <sup>b</sup> , $\sigma_E/E$	5.4%/√ $E$ ⊕ 2.3%	
Time difference res. <sup>b</sup> , $\sigma_{\Delta T/2}$	70 ps/√ $E$	
$z$ -position resolution <sup>b</sup> , $\sigma_z$	1.1 cm/√ $E$ (weighted)	
Azimuthal angle resolution <sup>f</sup>	~ 8.5 mrad	
Polar angle resolution <sup>f</sup>	~ 8 mrad	

side, by a custom-designed controller board. All these are presented in more detail below.

### Module Construction

In order to build lead-SciFi modules, our collaboration studied and used the KLOE tooling techniques. Specifically, a “swager” (plastic deformation machine) was borrowed from KLOE and was used as a model to build our own. As a result, several prototypes were built, gradually increasing in dimensions and culminating in two full-sized (l: 400 cm x w: 13 cm x h:[21-24] cm) prototypes, termed Prototype 1 and 2. For the production, lead sheets were ordered from the manufacturer<sup>1</sup> at specified widths and Kuraray SCSF-78MJ, double-clad fibers<sup>2</sup> were used.

The modules were built by employing two custom-designed presses that pressed the matrix as it was being stacked with alternating layers of lead sheets and fibers, thereby expelling excess epoxy and allowing the bonded matrix to set. They consisted of a ~4.5 m steel bed, two tilting pistons that raised/lowered a group of 20 pistons to the top surface of the matrix, as well as associated electronics and pneumatics. The fibers were bonded in the lead channels with Bicon-600<sup>3</sup> optical epoxy: the internal matrix geometry is indicated in Fig. ??. Visual inspection revealed that only a handful of the approximately 15,350 fibres in each module were damaged during the construction.

A comprehensive report (how-to manual), training video, photos and movies were prepared to simplify the training of personnel and to document the methods employed [?, ?, ?, ?]. The final set of construction procedures were recorded in a step-by-step “Procedures Manual” – complete with photos – which details the entire production process [?].

Built modules were shipped for machining to an industrial firm<sup>4</sup>. The process included

<sup>1</sup>Vulcan Lead Inc (www.vulcanlead.com)

<sup>2</sup>Kuraray America Inc., Houston, TX, USA (www.kuraray-am.com)

<sup>3</sup>Saint-Gobain Crystals & Detectors, USA (www.bicon.com)

<sup>4</sup>Ross Machine Shop, Ltd. 40 Kress Street, Regina, SK, Canada

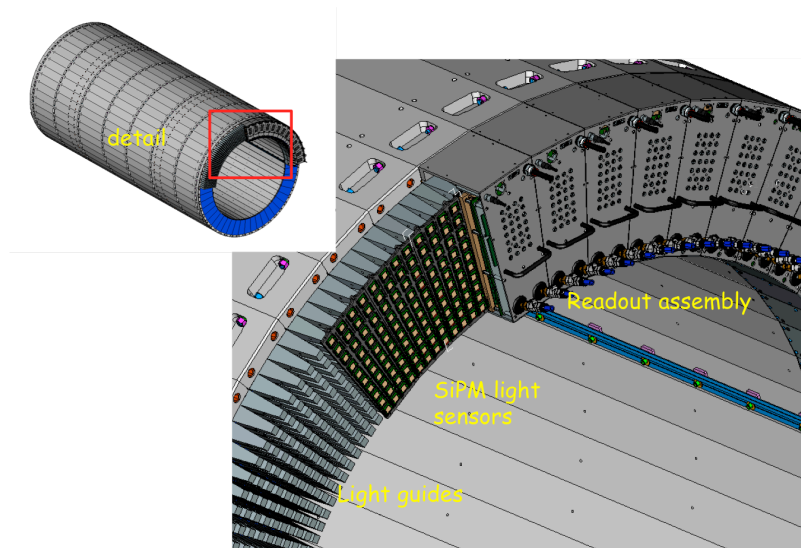


Figure 4.23: Three-dimensional rendition of the light guides mounted at the end of the BCAL as well as the readout assemblies mounted over them and containing the SiPMs and their electronics.

shaping the modules to their final dimensions within tight tolerances, polishing the two ends and machining features in the aluminum base and top plates.

### Light guides

The BCAL light guides connect the output face of the modules to the SiPM light sensors. The geometry of the light guides is azimuthally symmetric, consisting of four identical radial columns per BCAL wedge. Each column consists of ten light guides, which cover an azimuthal angle of  $1.875^\circ$  degrees. Both the input and output faces of the light guides are trapezoidal in shape. The bases of the guide are glued to the face of the BCAL and increase in width toward the outer edge of the wedge. The radial dimension of the bases is  $20.57\text{ cm}$  for the inner six guides and  $24.64\text{ cm}$  for the outer four. The base of the guide receives the light from the calorimeter and funnels it down to a smaller trapezoid covering the sensitive area of the SiPM sensors, which is  $1.27 \times 1.27\text{ cm}^2$ . The length of the light guides is  $8\text{ cm}$ . There is a  $0.5\text{ mm}$  air gap between the output of the light guide and the  $0.45\text{ mm}$  clear epoxy protective coating over the sensitive area of the SiPM. The light guide shapes is shown in Fig. ?? . The simulated acceptances for the ten guides ranged from 0.48-0.75%. [?]

The monitoring LEDs will be glued into a  $4\text{ mm}$ -diameter and  $2\text{ mm}$ -deep hole on the side of each light guide and located  $3.4\text{ cm}$  from the large-area end of the light guide, in order to

allow access for installation and service in the tight space between light guides. The simulation suggests that features of this size should affect the light collection by less than a couple of percent.

The light guides were fabricated from ultraviolet transmitting (UVT) acrylic at the Universidad Técnica Federico Santa María. Dimensional tolerances were kept under control to avoid interferences between wedges. Each light guide was covered with a Tedlar cover to avoid any optical cross talk between the firing cells. Measurements of different materials for the cover showed no significant differences in light collection [?], as might be expected if the collection efficiency is dominated by total internal reflection.

### Silicon Photomultiplier Arrays

The BCAL will reside inside a 2.2  $T$  superconducting solenoid with the magnetic field – in its readout region — calculated to be 1.5-2.2  $T$  upstream and  $\sim 0.5 T$  downstream. We have selected the new technology of silicon photomultiplier arrays (SIPM's), which can operate in fields well beyond this limit. This technology was developed through an extensive R&D effort between GLUEX and SensL<sup>5</sup>, a photonics firm from Ireland. This led to the “tiling” of 16  $3 \times 3 \text{ mm}^2$  SIPM's into a  $4 \times 4$  array of cells, having a  $1.26 \text{ cm}^2$  area. Such large area units have found broad appeal from subatomic physics to medical applications, with several manufacturers entering the field. Following a competitive bidding process, Hamamatsu<sup>6</sup> was selected to provide the readout devices for the BCAL.

The selected sensors are Hamamatsu S12045 MPPC arrays with a sensitive area of  $1.44 \text{ cm}^2$ . The basic SIPM unit is a  $3 \times 3 \text{ mm}^2$  cell with 3600  $50 \mu\text{m}$  micro-pixels, which are joined together on a common substrate and under a common load. The sensor is a  $4 \times 4$  array of cells with a dynamic range defined by the 57,600 micro-pixels in each array. The single micro-pixel gain is  $\sim 10^6$ , roughly the same order of magnitude as that of a traditional PMT. While each pixel operates digitally as a binary device, the output signal behaves as an analog detector that is proportional to the incident light intensity.

The SIPM's operate at an operational voltage  $V_{op}$  that is 0.9 V above the typical breakdown voltage ( $V_{br}$ ) of about 74 V. The gain is proportional to this overvoltage ( $V_{over} = V_{op} - V_{br}$ ). The relatively low voltage over voltage and the sensitivity of the breakdown voltage to temperature imposes considerable requirements on proper operation. The sensitivity of the breakdown voltage to temperature is  $56 \text{ mV}/^\circ\text{C}$  [?]. The gain, PDE and dark rates all depend on the breakdown voltage, which in turn is very sensitive to temperature. At  $V_{over}=0.9 \text{ V}$  and  $23^\circ\text{C}$ , these devices have a typical gain of  $0.75 \times 10^6$ , photon detection efficiency (PDE) of about 21% [?], but a relatively high dark rate of 16  $\text{MHz}$  per array.

A total of 3840 SIPM's are needed to instrument the BCAL and 90% have already been delivered. Quality control tests of the SIPM's has been carried out at JLab ( $\approx 1000$  units) and USM ( $\approx 3000$  units) and with selected tests at Regina mimicking the experimental conditions. The average geometrical mean from the Regina measurements of  $(24 \pm 2)\%$  is consistent with measurements at Jefferson Lab  $(21 \pm 1)\%$  [?] and USM  $(23 \pm 2)\%$  [?]. All measurements produced PDE values  $> 19\%$ , which was the contract specification and were also consistent to test data provided by Hamamatsu. The characteristics of the arrays measured are shown in Fig. ??.

<sup>5</sup>SensL, Blackrock, Cork, Ireland ([www.sensl.com](http://www.sensl.com))

<sup>6</sup>Hamamatsu Corporation, Bridgewater, NJ 08807, USA ([sales.hamamatsu.com/en/home.php](http://sales.hamamatsu.com/en/home.php))

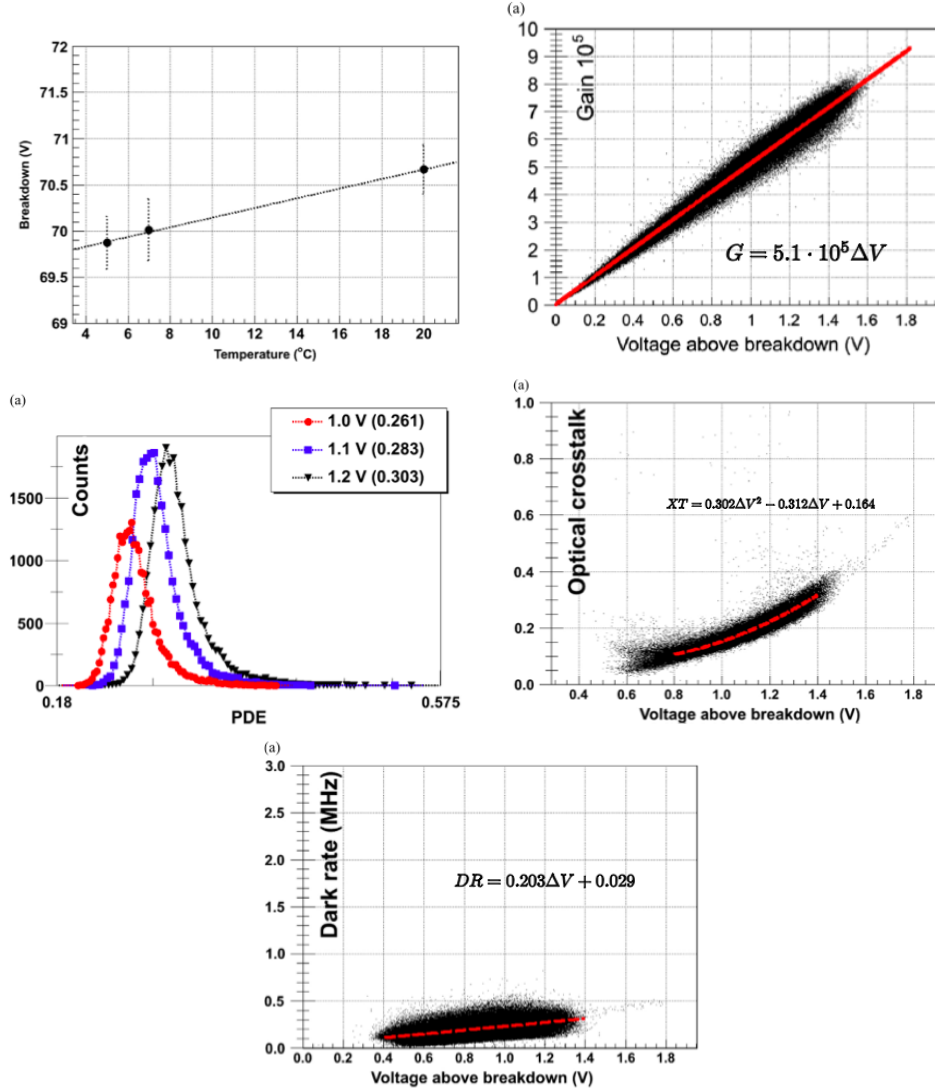


Figure 4.24: Measured characteristics of the production SIPM arrays (Hamamatsu S12045 MPPC's).

At a fixed over voltage, the gain and PDE are constant independent of temperature, but the dark rate is reduced at lower temperatures [?]. The dark rate also increases when exposed to neutrons at a rate of about  $16 \text{ MHz}$  per  $10^9 n_{eq}/\text{cm}^2$  [?]. We expect the dark rate to increase by a factor of 5 after eight years of high-intensity operation in Hall D. The dark rates of SIPM's that have not been irradiated meet our detector requirements at room temperature, but as the sensors accumulate dose during the operation of the experiment, the dark rate will increase outside our specifications and they will need to be operated below room temperature.

The readout assembly holds all forty SIPM's that collect light from one end of a module, the supporting infrastructure to operate them, and the electronics that produce output signals to feed the flash ADCs and pipeline TDCs. The temperature stabilization is an integral component of the assembly and is addressed using a two-fold approach. First, we have implemented a

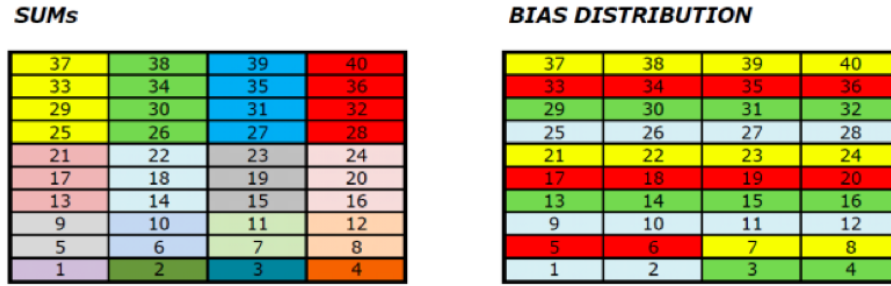


Figure 4.25: *Left panel:* Schematic layout of summed (1:2:3:4) SIPM outputs for upstream and downstream ends. *Right panel:* Assignment of bias voltages to groups of ten SIPM's: light blue is Bias line 1, green is line 2, red is line 3 and yellow is line 4. The summing is radially outward in the detector and the bias channels are assigned along rings of constant radii. The readout modules are viewed facing the SIPM sensors. The up- and downstream ends are mirror symmetric to facilitate cell number matching.

mechanical cooling system with the goal of maintaining the temperature of the sensors within  $\pm 2^\circ\text{C}$  of the operating point. The cooling system is composed of a chiller with water for initial operation at  $16^\circ\text{C}$  and water and 20% propylene glycol for operation at  $5^\circ\text{C}$ . The coolant flows through a copper pipe that is glued to the copper cooling plate, which is in thermal contact with the back of the SIPM sensors. Second, the bias to the sensor is adjusted using a thermistor to compensate for any temperature deviations from the nominal operating point and thereby maintain a stable output irrespective of changes to the environment. The relatively low overvoltage results in a relatively high sensitivity to the setting and stabilization of the bias voltage. The goal is to maintain the voltage set point to within 10 mV, which corresponds to a gain variation of less than 1%. The effect of any temperature changes must be kept to less than 1% also.

The granularity of the readout is shown in Fig. ???. The light guides are arranged in four rows of ten identical columns on the face of the BCAL modules. Each SIPM has its own pre-amplifier and summing (16 cells are read out as a one signal) boards. The BCAL is divided into four readout rows, within which individual SIPMs are summed column-wise in groups of 1, 2, 3 and 4, respectively. This scheme retains the complete azimuthal segmentation, but results in coarser longitudinal shower segmentation a decision taken based on electronics cost considerations (**GlueX-doc-1864**). Thus, forty SIPM's on each end of the BCAL are summed into sixteen groups, which are digitized by 250 MHz Flash ADC's, but only the first twelve sums are discriminated and fed into pipeline TDC's to measure their times. The bias lines deliver power to groups of ten sensors, but the grouping is orthogonal to the readout sums, as shown in the figure. This allows individual SIPM's to produce the sole output of a summed channel by appropriately enabling bias voltages during calibrations.

The temperature compensation circuit for BCAL is a voltage divider with one temperature dependent resistor element (thermistor). The values of the resistances coupled with the value for the  $V_{Supply}$  voltage allow the sharing of a single supply voltage among several SIPMs, while still providing a temperature compensated  $V_{op}$  value that stabilizes gain. The original calculations were performed based on Hamamatsu datasheet values for recommended  $V_{op}$  (given for  $25^\circ\text{C}$ ) and adjusted for a presumed operation temperature of  $5^\circ\text{C}$ . Operation at other temperatures

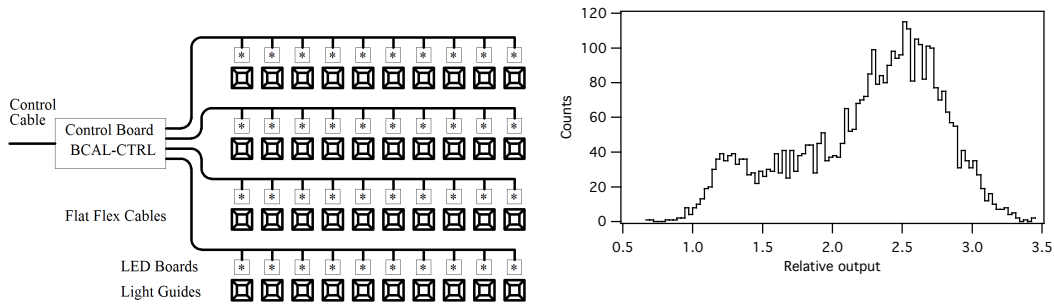


Figure 4.26: *Left panel:* Configuration of the BCAL monitoring system. *Right panel:* Relative output of all  $\sim 4,000$  BCAL LEDs driven by their respective boards.

besides  $5^\circ\text{C}$ , and with other offset voltages ( $V_{over}$ ) that differ from the adjusted  $V_{op} - V_{BR} = V_{over} = 1.2\text{V}$  necessitates a formula that takes into account the temperature dependent nature of the voltage divider circuit, and the errors from ideal operation induced by granularity of the trim values. Details are provided in reference **GlueX-doc-2394**.

#### 4.4 BCAL monitoring

The monitoring system is designed to track the stability of the SiPM output signals between calibrations with particles, about once per day. The system is composed of light emitting diode (LED) light sources, which are distributed one per light guide. They are placed in pockets drilled on the side of the light guide, which are  $4\text{ mm}$  in diameter and  $2\text{ mm}$  deep and located  $3.8\text{ cm}$  from the BCAL module. The light guides are  $8\text{ cm}$  long.

The LEDs<sup>7</sup> come in a standard surface mount package emitting blue light at  $471\text{ nm}$ , which is near the peak of the fiber emission spectrum [?]. Each LED is attached to a  $12 \times 13.5\text{ mm}^2$  PCB board so that it emits light parallel to the PCB, through the near light guide and toward the opposite side of the BCAL module. Light enters the fibers and is transmitted through the module to the sensor at the far end and also reflected from the near end of the module back into the near sensor. Due to attenuation through the module [?], the light intensity at the far end must be about  $\sim 3$  times greater than the near end in order to produce the same signal at both ends [?]. Tests were carried out on a  $58\text{-cm}$ -long prototype calorimeter using different LED's and pocket shapes. The near/far ratios measured for a blue LED ranged between  $2.8\text{-}3.2$ , thus proving the design requirement of approximately equalizing the LED signals on the near and far ends of each module.

As mentioned previously, the 40 LEDs at each module's end are grouped into four independent groups. The system configuration is shown in Fig. ???. Each group is attached to a flex ribbon cable and its 10 LEDs are pulsed simultaneously using a common trigger signal from a control board (BCAL Controller) located on the outer edge of each wedge. Each string is attached to a column of light guides, which is orthogonal to the cabling that provide the bias to the SiPMs. The technical specifications of the electronics are presented in more detail elsewhere [?]. The possibility of noise pickup in a SiPM induced by the BCAL monitoring system was investigated but no such pickup was detected as a result of proximity operation to both

<sup>7</sup>Model SMS1105BWC, Bivar, Inc., CA 92618, USA (www.bivar.com)

LED and controller boards.

3840 production LED mini boards plus 100 spares were tested and divided into groups of similar intensity. The relative light outputs of these LEDs are shown in Fig. ???. The variation between the LEDs in a single group is typically less than 1%. The fabrication and testing of the LED monitoring boards for the BCAL was completed in December 2012 and all units and electronics were delivered to Jefferson Lab.

## 4.5 BCAL Calibration

The absolute calibration of the BCAL will be accomplished using the energy deposition of particles. We can use the showers from photons from  $\pi^0$  and  $\eta$  decays and also charged particle ionization losses. No complete study has been conducted to date to demonstrate the detailed procedure that is needed to complete this task. But some preliminary studies have been made to estimate the coverage and anticipated statistics that could be expected.

Simulations have been used to interpret data from cosmic ray events in the Construction Prototype [?]. A calibrated Hamamtsu R329-02 PMT was used, coupled to a Winston Cone light guide [?]. Cuts were employed to define clean muon events. The muons deposit energy corresponding to about 60-65 photoelectrons in a standard  $2\text{ cm}^2$  calorimeter viewing area at  $195\text{ cm}$  from the PMT, which once corrected for attenuation length results in 300 photons/side/ $MeV$  [?]. Cosmic muons can be used for calibration as they provide  $2\text{ MeV}$  per readout cell energy deposition in the fibers. When the magnet is on, their trajectories will be curved but this can be simulated and understood.

Initial simulations have been carried out using charged pions and protons [?]. The detailed geometry of the matrix was simulated using FLUKA and GEANT 3.21 was used to simulate five modules next to each other, in order to ensure that energy escaping laterally from a module is recovered properly in an adjacent one. A realistic map of the GLUEX solenoidal field was implemented. Pions and protons were simulated having momentum of  $1\text{ GeV}/c$  and at  $20^\circ$ . The pions deposited  $\sim 7\text{ MeV}$  in cell (2,2) and  $1.4\text{ MeV}$  in cell (6,3). The proton numbers were  $8\text{ MeV}$  and  $0.8\text{ MeV}$ , respectively. This implies that the calibration of the inner layers of the calorimeter is less sensitive to the pion to proton ratio. There is an example of a successful weighting algorithm of H1 collaboration for pions of  $2\text{-}20\text{ GeV}/c$  with GEANT4, meaning that the simulation tools at present and when the experiment runs will be useful in the calibration process. Simulations were also carried out  $0.6\text{ GeV}/c$  and at  $40^\circ$  [?]. Experience with photon showers from the 2006 beam tests in Hall B as well as simulations are presented in section ??.

To estimate the statistics available for calibrations in the BCAL, we used BGGEN [?] to generate the equivalent of 10 s of data at a photon beam flux of  $10^7/s$  and selected events containing  $\pi^0$  and  $\eta$ s [?]. Photons were tagged as hitting the FCAL or BCAL, when their polar angle was between  $1\text{-}11^\circ$  or  $11\text{-}126^\circ$ , respectively. In order to have a robust sample of showers for the calibration, we required that both photons from each decay have at least  $0.5\text{ GeV}$  of energy. In ten hours of data at  $10^7\gamma/s$ , we expect approximately 17M  $\pi^0$  events and approximately 3M  $\eta$  events with both photons hitting the BCAL (see Fig. ???). Comparable number of events produce one photon in the BCAL and one photon in the FCAL. Although the data set with  $\pi^0$ s is larger, its angular distribution is such that the maximum angles sampled barely extend much past  $40^\circ$ . The range can be extended to  $60\text{-}70^\circ$  by lowering the photon energy selection to about  $0.2\text{ GeV}$ . The angular coverage for  $\eta$ s is wider and will be needed to provide showers at the upstream end of the bcal.

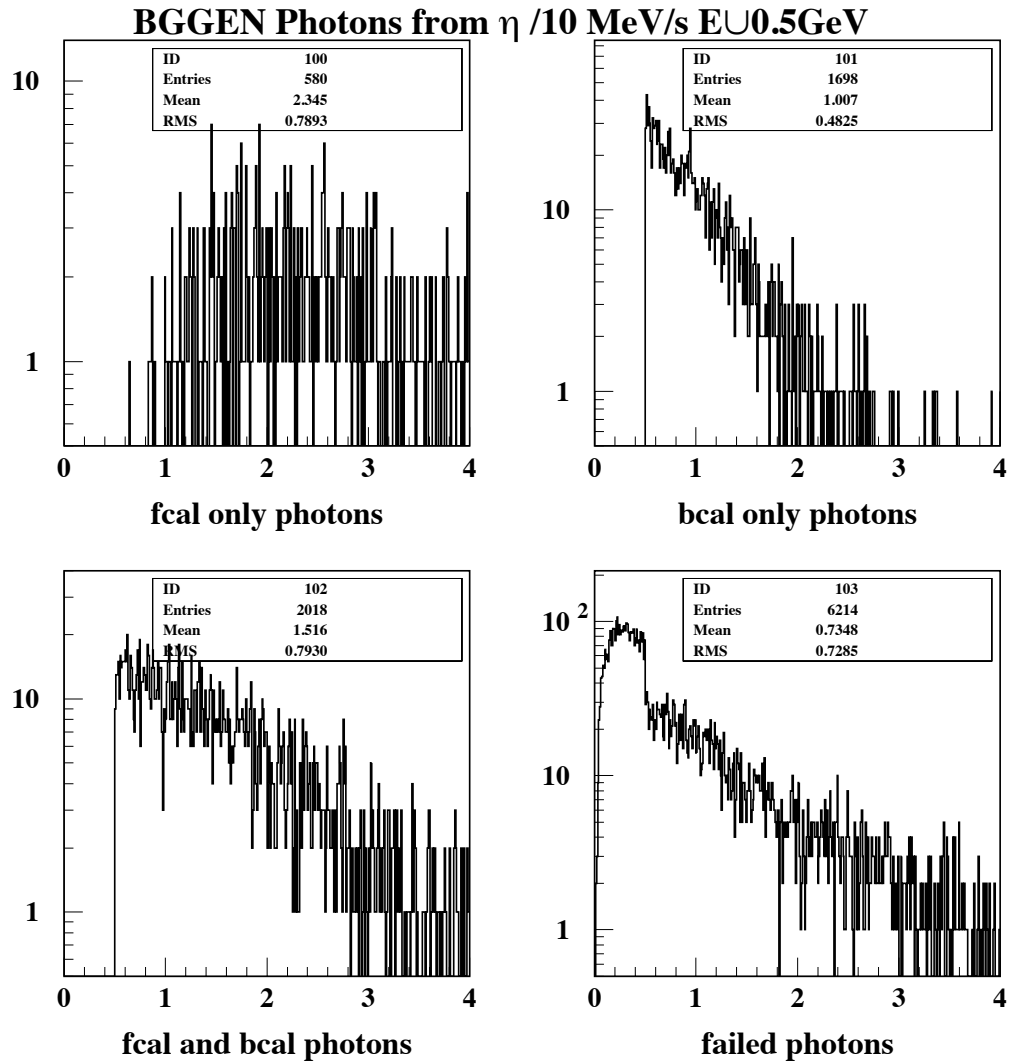


Figure 4.27: The energy distribution of photons greater than 0.5 GeV from  $\eta$  decays. Top left) Energy distribution when both photons hit the FCAL. Top right) Energy distribution when both photons hit the BCAL. Bottom left) Energy distribution when one photon is detected in the FCAL and one photon is detected in the BCAL. Bottom right) Energy distribution of photons from  $\eta$  decays when either photon misses both calorimeters or the energy of either photon is below 0.5 GeV.

For the BCAL calibration, we will likely begin with the sample of  $\pi^0$  events with one photon in each of the calorimeters and fix the FCAL response to that already determined. The calibration constants for each cell in the BCAL will then be adjusted to minimize the width of the  $\pi^0$  mass. There are 1536 adjustable channels in the BCAL; although for low-angle photons, only the inner layers contribute to the energy sums. The calibration constants can be confirmed or improved using the sample of  $\pi^0$  events that decay into two photons that hit the BCAL. Once a reasonable starting point is obtained, this later sample may be the only one needed for smaller updates. Finally, the sample of  $\eta$ s must be used to confirm the calibration over the full length of the BCAL, especially for any systematic effects near the upstream end.

## 4.6 Expected Performance

### Production Fibers

Due to the length of the BCAL superior quality fibers in terms of attenuation length and number of photo electrons were needed. Over three quarters of a million, 4-m-long Kuraray double-clad SCSF-78MJ (blue-green) scintillating fibers have been used in the construction of the BCAL. The response and quality of these fibers has been evaluated by employing a 373-nm UV LED to stimulate the fibers along their length and reading out the light using a spectrophotometer and a photodiode in order to extract the spectral response and the effective (bulk) attenuation length, respectively. In addition, diameter uniformity measurements were carried out. Nominally, 0.5-1% of the fibers were tested from each shipment, and the quality assurance results confirmed that the fibers were of high quality and complied with GlueX specifications. The key parameters tested were a) dimensional uniformity, b) spectral response, c) bulk attenuation length and d) number of photoelectrons. The measurements and conclusions from this extensive Quality Assurance (QA) exercise are summarized herein; detailed interim [?, ?, ?] and final reports [?] are available to the reader.

In order to assure a uniform matrix during the building, the fibers had to be uniform in diameter and free of defects such as protrusions. To this end, fibers were visually inspected and the fiber diameter was measured at three locations along the length of each sampled fiber (50 cm, 200 cm and 350 cm from one end) using a micrometer caliper, for 883 fibers from Shipments 1-29. The error on each measurement was 0.005 mm. A Gaussian fit to all the data yielded  $(0.997 \pm 0.006)$  mm. All measurements fell within the specifications: diameter of 1 mm with a  $RMS \leq 2\%$ .

### Spectral Response

Details on the experimental setup can be found in our past work [?, ?], and, therefore, are recounted only briefly herein. A USB4000 spectrophotometer<sup>8</sup> and the tested SciFi were coupled together in a robust manner. An RLS-UV380 ultra violet LED<sup>9</sup> – having a peak emission wavelength of 373 nm – stimulated the fiber. The LED translated across the length of the fiber and measurements were carried out in near darkness. As an additional precaution against UV damage, UV-absorbing film (TA-81-XSR<sup>10</sup>) was used to cover all overhead fluorescent lights and the desk lamps.

<sup>8</sup>Ocean Optics Inc., Dunedin, FL, USA ([www.oceanoptics.com](http://www.oceanoptics.com))

<sup>9</sup>Roithner Lasertechnik, Vienna, Austria ([www.roithner-laser.com](http://www.roithner-laser.com))

<sup>10</sup>Window Film Systems, London, ON, Canada ([www.windowfilmsystems.com](http://www.windowfilmsystems.com))

Measured wavelength spectra were fitted using double Moyal functions plus a flat background, with the LED positioned at 10 cm, 30 cm, 100 cm and 300 cm. The Moyal function is of the form:

$$f(x, a, \mu, \sigma) = a \cdot \exp\left(-\frac{1}{2}\left(\frac{(x-\mu)}{\sigma}\right)^2 + e^{-(x-\mu)/\sigma}\right) \quad (4.7)$$

These spectra are overlaid in Figure ?? together with the corresponding Kuraray spectra of a fiber from Lot JS072 [?]. The peak intensity and the integrated spectral strength scale as a function of distance from the light source in a similar manner for both sets of measurements. Minor differences in the spectral shapes owe perhaps to the measurement apparatus and/or specific choice of fibers tested.

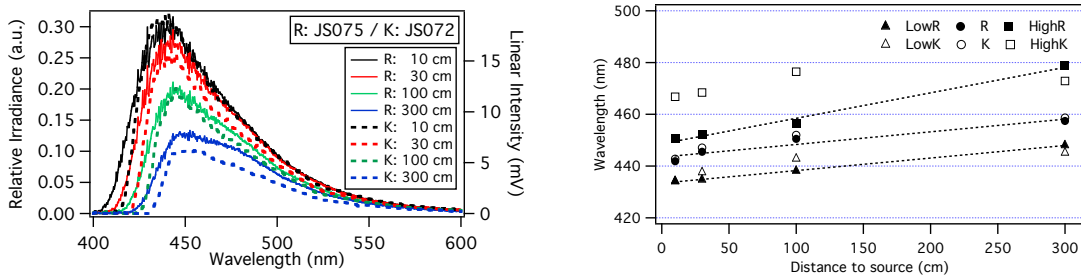


Figure 4.28: *Left panel:* Wavelength spectra, measured at Regina (‘R’ label) at source distances of 10 cm, 30 cm, 100 cm and 300 cm for a JS075-lot fiber are shown as solid lines, with the corresponding Kuraray spectra [?] (‘K’ label) for a JS072-lot fiber displayed as dotted curves. The former are relative irradiance measurements and the latter are in units of linear intensity. *Right panel:* The means of the single Moyal fits (‘R’ and ‘K’) as well as the double Moyal fits for the lower (‘LowR’ and ‘LowK’) and higher (‘HighR’ and ‘HighK’) peaks are plotted as a function of distance from the source. The standard errors on the means are at the few percent level and are encompassed within the size of the symbols. The dotted lines are fits to the Regina data.

### Attenuation length

Considering the large number of fibers to be tested, an expedient method was developed in order to extract the attenuation length, based on a Hamamatsu calibrated S2281 photodiode [?]. The end of each tested fiber was polished and connected to the photodiode using optical grease, and the device a picoammeter. The far end was blackened using black mat enamel paint (used for scale model painting). The results have been published elsewhere [?] and highlights are presented below.

The data from each fiber were fit using a single exponential fit of the form  $I = I_0 e^{-x/\lambda}$  in the 100-280 cm source distance range, as per the contractual agreement with Kuraray. The agreement is quite good in the shipment-to-shipment comparison. Moreover, similar features are present in both data sets. Since the measuring setups are different, the features are clearly a result of the fiber properties, which depend primarily on the secondary dye content. Finally, both Kuraray’s and Regina cumulative results had a standard deviation less than 10%, and therefore met the contractual specifications.

A single exponential fit to the fiber data is possible only over a limited range of source distance, as was carried out above. When the entire range is examined, and in particular source distances below 100 cm, a double exponential fit is required owing to the capture of short-wavelength light (blue region) which otherwise becomes absorbed leaving only the longer wavelengths. The following function was used:

$$I = I_0 \left( e^{-x/\lambda_L} + \alpha \cdot e^{-x/\lambda_S} \right) \quad (4.8)$$

where  $\lambda_L$  and  $\lambda_S$  are the long and short attenuation lengths, respectively,  $I_0$  is the readout current in units of  $\mu A$  and  $\alpha$  represents the relative strength between the two components. Most events were clustered in a peak centered around  $\alpha = 0.3$ .

The shipment results are shown in Figure ???. The error bars reflect the standard deviation of the error distribution from individual fiber measurements. Linear fits show the extracted averages. It is noted that a correction to the attenuation length due to the different treatment of fibers for Shipments 1-3 was not applied (a 3% increase), but this does not change any of the conclusions that all measured parameters were found to be comfortably within contract specifications, and overall this product was of high quality.

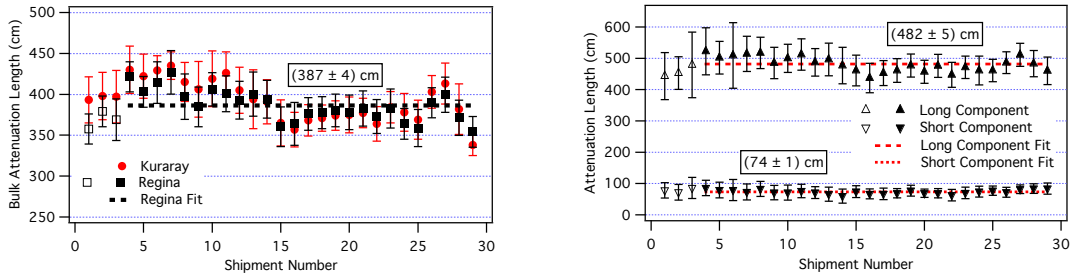


Figure 4.29: *Left panel:* The bulk attenuation length, from a single exponential fit between 100-280 cm is shown as a function of shipment number. *Right panel:* The short- and long-attenuation lengths of the fibers are plotted, resulting from a double-exponential fit of the data. All linear fits have the slope held at zero.

### Number of photoelectrons

Details on the  $N_{pe}$  measurements can be found in our final report [?], and, therefore, are only summarized herein.

One fiber end was coupled to a Hamamatsu R329-02 calibrated photomultiplier, with a standard progressive voltage divider, and the other to a SensL<sup>11</sup> silicon photomultiplier (SIPM) having a  $3 \times 3 \text{ mm}^2$  active area and based on their A20HD microcell. This particular SIPM had been calibrated with respect to its photon detection efficiency (PDE) versus a calibrated Hamamatsu S2281 photodiode when the scintillation light was provided by a Bicron<sup>12</sup> BCF-20 green fiber excited by a 375 nm laser [?]. Both fiber ends were coupled using optical grease. A  $^{90}\text{Sr}$  radioactive source, placed within a custom-designed Pb collimator, was located over the

<sup>11</sup>SensL, Blackrock, Cork, Ireland ([www.sensl.com](http://www.sensl.com))

<sup>12</sup>St. Gobain Crystals & Detectors, Hiram, OH 44234, USA ([www.bicron.com](http://www.bicron.com))

centre point of the fiber and approximately 200 cm from the SIPM end. A small  $\sim 9$  cm-long scintillator counter was coupled to a Burle 8575 PMT and was placed directly below the fiber, thus sandwiching the fiber between it and the source/collimator above. The counter provided the trigger for the data acquisition.

The results of the fit extractions for the  $N_{pe}$  are shown in Figure ???. The reader is reminded that only fibers from Lots 96–707 (Shipments 4–29) were analyzed; Lots 1–95 (Shipments 1–3) were excluded from this comparison due to different handling of the fiber ends, as mentioned previously. The top panel of this figure shows the results from every fiber fit, whereas, in the bottom panel, the results were averaged for each lot with the error bar being the RMS of those distributions. Clearly, there is lot-to-lot variation apparent in the number of photoelectrons, as was also manifest in the attenuation length measurements [?]. Kuraray observed a similar behaviour in measurements of their own, with the most likely candidate for the difference being small impurities in the secondary dye in the fiber’s chemistry, which cannot be controlled in the manufacturing process [?].

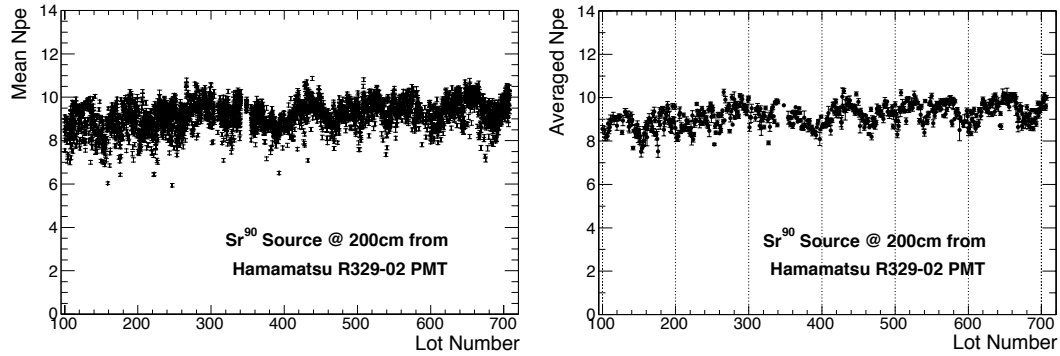


Figure 4.30: *Top panel:* The  $N_{pe}$  results are plotted for all fibers as a function of lot number (96–707), corresponding to Shipments 4–29. Multiple fibers were measured from each lot. *Bottom panel:* The  $N_{pe}$  results are averaged by lot number, and their average is graphed against the lot number.

### Photon Beam Test: Energy and Timing Resolution and Number of Photoelectrons

A photon beam test of Prototype-1 module was carried out in Hall B with the objective of measuring the energy and timing resolutions of the module as well as the number of photoelectrons generated [?]. Low current (1 nA) data were collected over the tagged photon energy range of 150 to 650 MeV at multiple positions and angles along the module. The results were  $\sigma_E/E = 5.4\%/\sqrt{E(\text{GeV})} \oplus 2.3\%$ ,  $\sigma_{\Delta T/2} = 70/\sqrt{E}$  ps, and 660 photoelectrons for 1 GeV at each end of the module, in line with the KLOE results. The photon beam was collimated with a 2.6 mm collimator, resulting in a beam spot of virtually uniform density with a diameter of 1.9 cm on the BCAL module. It should be stressed that this module was constructed out of Pl.Hi.Tech.0044 fibers, but, nonetheless, the measurements allow a lower limit at the expected performance of the matrix, as the Kuraray SCSF-78MJ fibers are superior. The module was divided into 18 readout segments, each with dimensions  $3.81 \times 3.81$  cm<sup>2</sup> and readout by PMTs.

The extracted energy resolution at  $\theta = 90^\circ$  and  $z=0$  cm was  $\sigma_E/E = 5.4\%/\sqrt{E(\text{GeV})} \oplus$

2.3% [?]; the fits were consistent with  $c = 0$ . Small variations in the fits produced relatively large variations in the floor term ( $2.3 \pm 1\%$ ) but little variation in the stochastic term ( $5.4 \pm 0.1\%$ ). The energy resolution plotted versus the mean tagger energy for the respective bin is shown in Figure ???. The extracted energy resolution shows degradation as the incident photon angle decreases. Specifically, the stochastic term increases from 5.4% at  $90^\circ$  to over 7% at  $15^\circ$ , at  $z = -100$  cm. This is consistent with Monte Carlo simulations [?]. Parameter  $a$  depends on the angle of incidence as shown in Figure ??, which is expected since fluctuations from intrinsic properties of the interaction mechanisms increase with the number of particles created as the shower develops. As the angle decreases, the particles transverse more of the radiator mass resulting in more interactions and of course increased fluctuations [?].

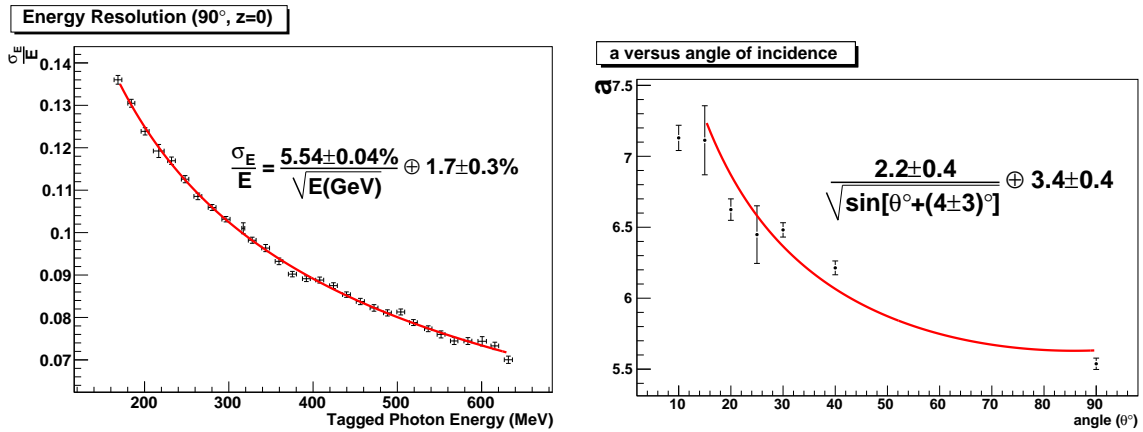


Figure 4.31: Energy resolution at  $90^\circ$  as a function of tagged photon energy. Resolution parameter  $a$  versus angle of incidence. As the angle decreases the energy term degrades. This is expected because the energy leakage from the sides and also from backscplash out of the front face of the module, increases.

The time difference of the BCAL will provide position information for neutral particles, which is needed to reconstruct their four-momentum. The position resolution is related to the time difference resolution by the effective speed of light within the calorimeter. Thus, by using measurements of the effective speed of light ( $c_{\text{eff}} = (17. \pm 0.4)$  cm/ns in Table ??) from a previous beam test at TRIUMF [?], the position resolution of the calorimeter can be easily extracted. The double-ended readout of the BCAL allowed for time difference measurements to be made. The time-walk-corrected spectra for each tagger timing counter were fitted by a Gaussian function. The timing for an event was found by summing the TDC values of all the segments in an event cluster, weighted by their energy.

The floor term from the fits was equal to the finite width of the beam, as expected. This implies that the intrinsic time resolution of the BCAL is consistent with zero for the constant term, and this why we quote the timing without a floor term below. The time difference resolution, after subtracting the beam width from the constant term, was found to be

$$\sigma_{\Delta T/2} = \frac{70 \text{ ps}}{\sqrt{E(\text{GeV})}}. \quad (4.9)$$

and should be compared to the KLOE result of  $56/\sqrt{E(\text{GeV})}$  ps [?]. Finally, the time difference resolution defines the position ( $z$ ) resolution along the length of the module, since  $\sigma_z = \sigma_{\Delta T/2} \cdot$

$c_{\text{eff}}$ . Therefore, the determined position resolution is calculated to be  $\sigma_z = 1.1$  cm for a 1 GeV photon.

The number of photoelectrons per end of the prototype BCAL module,  $N_{pe}$ , was estimated at  $z = 0$  cm and  $\theta = 90^\circ$ . The distribution in the ratio,  $R$ , of the North to the South readout sums, for each of ten bins in beam energy,  $E_j$ , from 150 MeV to 650 MeV, was expressed as

$$R(E_j) = \frac{\sum_{i=1}^{18} E_{N,i;j}}{\sum_{i=1}^{18} E_{S,i;j}}. \quad (4.10)$$

Using this ratio results in the suppression of shower fluctuations that dominate the statistical variance of the individual sums for each readout end. Under the assumption that each of the amplitude spectra has a Poisson-type shape, the ratio spectra were fitted to the function:

$$f(r) \sim \int P(x, N_{pe} \cdot \sqrt{R}) \cdot \frac{1}{r} P\left(\frac{x}{r}, \frac{N_{pe}}{\sqrt{R}}\right) \left[\frac{x}{r} dx\right] \quad (4.11)$$

where  $r$  is a North/South amplitude ratio,  $R$  is an average North/South amplitude ratio,  $N_{pe}$  is the average number of photoelectrons, and  $P$  is a Poisson-type probability. The resulting photoelectron yield per end was plotted as a function of beam energy and fit to a linear function, holding the y-intercept fixed at zero. This resulted in  $N_{pe} = 662 \pm 1$  photoelectrons per end at 1 GeV. In comparison, KLOE reported  $N_{pe} \sim 700$  per end at 1 GeV. The BCAL module used double-clad scintillating fibers, potentially giving rise to approximately 50% more photoelectrons than KLOE. However, the KLOE calorimeter had light guides combined with Winston Cone collectors that resulted in a much higher transport efficiency than the light guides used in the beam tests described in this work. This feature could easily compensate for the increased capture ratio of the fibers in the BCAL.

### Simulation Code: Shower Profile, Energy Resolution, Sampling Fraction, Leakage

A series of simulations [?] have been carried out using GEANT3, without the inclusion of the BCAL magnetic field. The micro geometry of the fiber matrix was encoded in two different ways. In the first, the glue boxes were approximated by trapezoids between the fibers and in the second, strips of glue were placed “inside” the lead with the fiber volumes on “top”. The first is termed *traps* and the second *strips*. Since these yielded consistent results only the latter were considered further.

If the depth in the material, expressed in radiation length units, is  $t = x/X_0$ <sup>13</sup> and the energy of the incident particle is  $E_0$  then

$$\frac{dE}{dt} = E_0 b \frac{(bt)^{a-1} e^{-bt}}{\Gamma(a)} \quad (4.12)$$

describes the evolution of the electromagnetic cascade in the material and, therefore, the shape of the longitudinal shower profile in the lead-fiber-glue matrix. The parameters  $a$  and  $b$  depend on the nature of the incident particle and the type of the absorbing material. The depth in the material, where the shower maximum occurs, depends on the incident particle’s energy  $E_0$  and the critical energy  $E_c$ . This parametrized longitudinal development of electromagnetic shower describes the shower reasonably well when the incident photon energy is larger than 1 GeV [?].

<sup>13</sup> $x$  is distance measured in cm.

The longitudinal shower profile for two different angles of the incident photon with respect to the beam direction, is shown in Figure ???. Simulations were run from normal incidence down to the minimum acceptance angle of the BCAL. Note that the abrupt termination of a curve corresponds to the end of the matrix due to the exhausted number of radiation lengths.

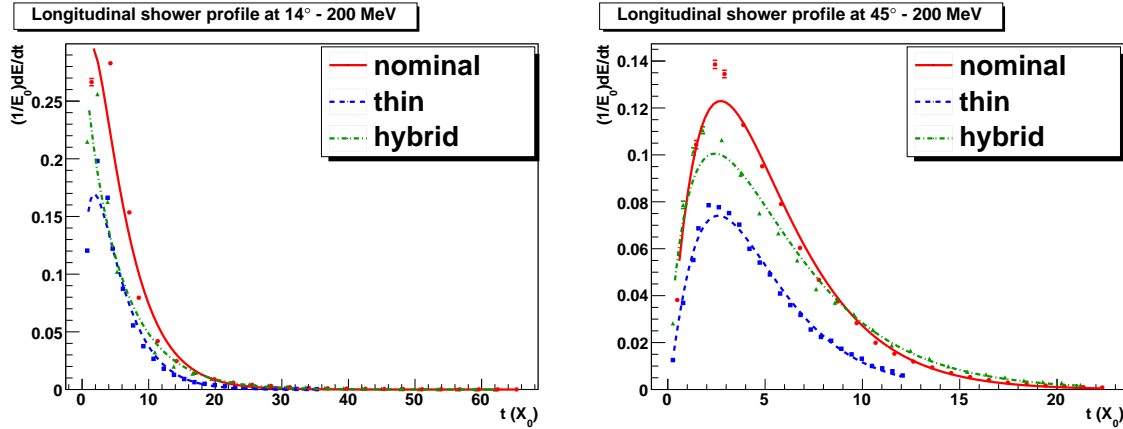


Figure 4.32: Longitudinal shower profile at various angles and energies. The data points correspond to the Monte Carlo results and are fitted with Equation ??? represented by the lines. The geometry used for the experiment is the one labeled ‘normal’.

The “data” points have been fitted with a function based on Equation ???. The simulated profiles exhibit the characteristic shower profile shape and expected evolution with increasing energy. At  $14^\circ$  the low energy particles deposit almost all of their energy in the first segment of the module. This explains why the fitted function does not describe the shower development as well as it does for  $45^\circ$  or  $90^\circ$ .

The simulated energy resolution is graphed in Figure ??? and is in agreement with past simulations [?]. The energy resolution is best at  $45^\circ$  as a result of the improved ability of the module to contain the electromagnetic shower at that angle. At  $14^\circ$  the situation changes dramatically. The resolution is worse, which is a manifestation of the increased shower leakage from the front of the module (albedo). The shower path at  $14^\circ$  is long enough to eliminate leakage from the back of the module and the relative improvement in the resolution, due to the increased sampling fraction of the thin and hybrid geometry, is apparent as is also expected. The floor term at  $14^\circ$  is significantly lower, reflecting the fact that less layers are intercepted and thus uncertainty due to structure irregularities is decreased.

The sampling fraction – the fraction of energy deposited in the SciFi’s – can be expressed as a ratio with respect to either the total energy deposited in the BCAL module ( $f$ ) or the incident photon energy ( $f_\gamma$ ), with  $f_\gamma < f$  since  $E_{mod} < E_\gamma$  owing to energy leakage outside the calorimeter volume. These quantities are difficult to measure in an experiment but fairly simple to simulate. A GEANT 3.21 simulation was developed to that end, based on modelling the BCAL as a standalone package. Individual fiber and epoxy volumes were programmed into the Monte Carlo with the appropriate Pb:SciFi:Glue ratios and material properties resulting in the geometry shown in Fig. ???.

Simulations indicate that  $f_\gamma$  decreases as a function of photon energy due to leakage, with the loss being constant above 200 MeV. Clearly,  $f$  depends only on the energy deposited in the matrix itself and is independent of the incident photon energy or overall geometry of the

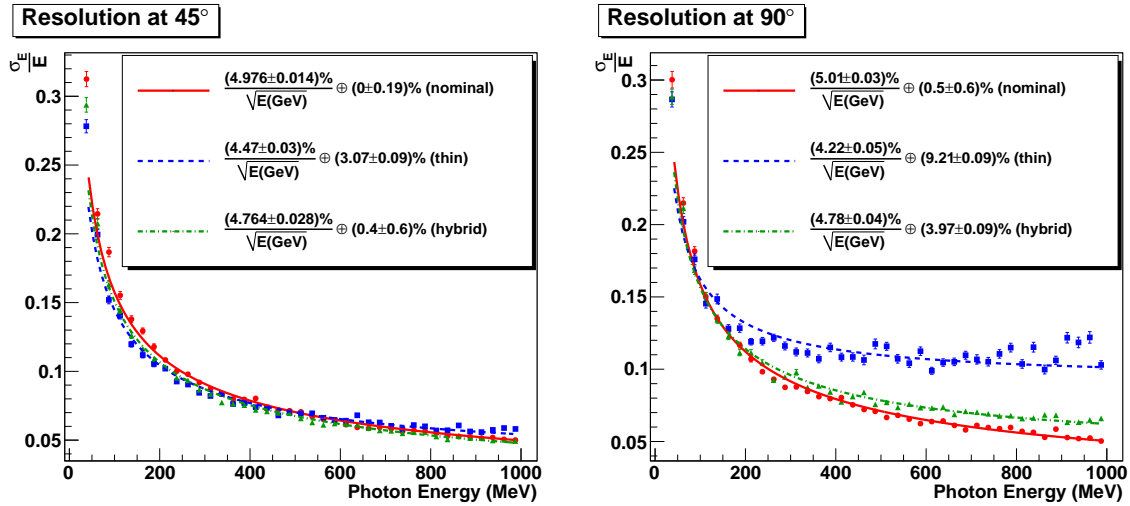


Figure 4.33: Energy resolution as a function of incident photon energy at  $14^\circ$ ,  $45^\circ$  and  $90^\circ$ . The points are simulated data whereas the lines represent fits.

module. Our most recent sampling fraction simulations are in general agreement with earlier ones, although the magnitude is less: 9.5% [?] instead of 11.5% in [?, ?]. This is expected due to the refining the SciFi volume to include the insensitive<sup>14</sup> two layers of cladding. The sampling fluctuations,  $\sigma_f/f$ , are the dominant contributor to the energy resolution, at about  $4.5\%/\sqrt{E(\text{GeV})}$ . Subtracting the simulated sampling fluctuation contributions from the measured energy resolution yields photoelectron statistics contribution to the energy resolution of about  $3.1\%/\sqrt{E(\text{GeV})}$  [?]. This is similar to the estimated value of  $\sim 2.7\%/\sqrt{E(\text{GeV})}$  from a KLOE beam test [?].

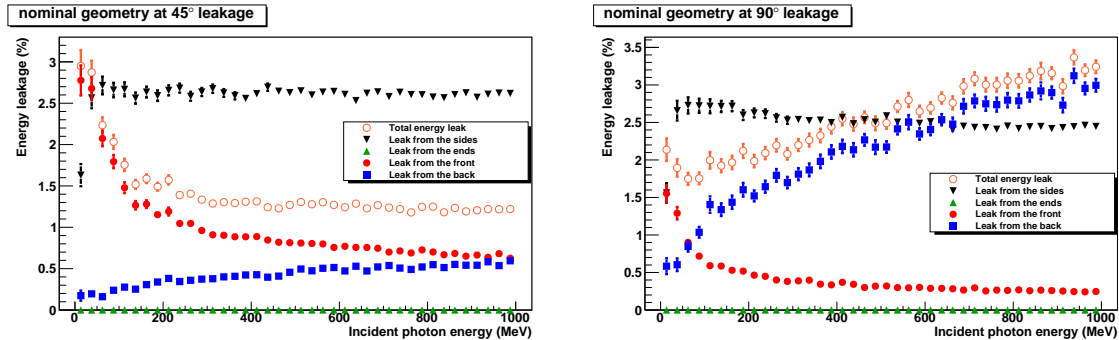


Figure 4.34: Simulated energy leakage (in percent) versus incident photon energy. Energy leakage from the sides is plotted but not added to the total energy leak curve. The leakage out the ends is consistent with zero in all cases except at  $12^\circ$ .

The percent energy leakage out the calorimeter volume is shown in Figure ???. The different symbols correspond to energy leaking out from different faces of the module. Front and back refers to the inner and outer faces of the module, respectively, with respect to the radial

<sup>14</sup>Insensitive in this context has the meaning of not contributing to the energy deposited in the fibers.

direction. Leakage from the ends refers to the energy leaking out from the faces of the module along the direction of the beam, where photo sensors will be placed. Leakage from the sides refers to the faces of the module that will be in contact with it's nearest neighbour modules. As the latter will be recovered in adjacent modules during the experiment, it was not included in the leakage sum. Indeed, total energy leakage refers to the sum of all energy leaking out the module from front, back and ends. For incident photon angles of  $90^\circ$ , irrecoverable energy leakage occurs mostly from the back of the module and it increases monotonically, following the evolution of  $t_{max}$ . It is interesting to note that the amount of energy leaking out from the sides is of the magnitude as the energy leaking from the back, although the former will be recoverable in the experiment. There is little energy leaking out the front face of the module (albedo) at  $90^\circ$ , but it increases with decreasing angle and dominates the leakage at small angles ( $12^\circ$ - $14^\circ$ ). It also tends to be larger at lower energies. Low energy particles have increased probability of interaction with only a few layers of lead before the secondary particles drop below the energy threshold for generation of secondaries. Furthermore, there is increased probability of low energy particles to back scatter and end up leaving the module out the front.

### Photon-Neutron Separation

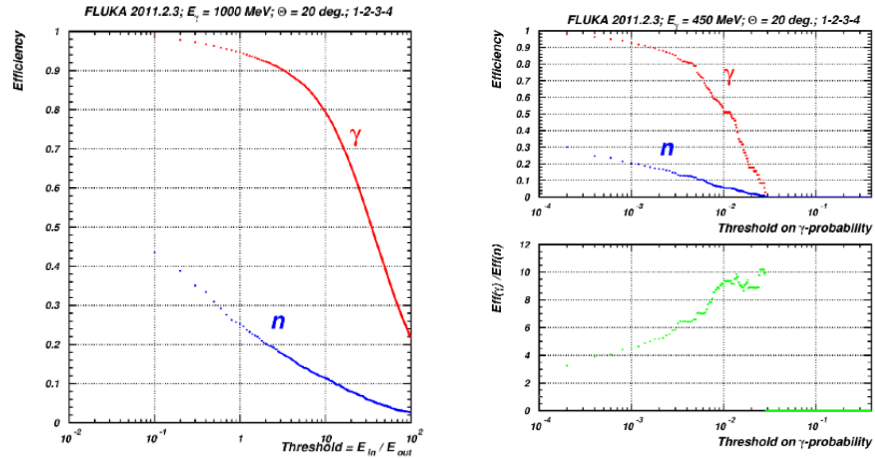


Figure 4.35: The efficiency of separation between photons and neutrons is plotted versus threshold and photon probability.

Dedicated simulations were carried out contrasting the energy deposition and patterns of photons to neutrons [?]. The aim was to separate photon-caused and neutron-caused showers of the same energy deposited in BCAL fibers. The kinetic energy of selected neutrons (of about  $1200MeV$ ) was significantly larger than the energy of correspondent photons. The differing deposition between photons and neutrons in the inner versus outer layers was an important factor in the decision to readout the cells in a 1:2:3:4 pattern [?]. A suppression of neutrons by a factor of about 2.5 is achievable without reducing the photon efficiency. The difference in the patterns between the two species is evident in Fig. ???. Finally, for each photon- or neutron-induced shower event, the probability was formed that this event came from the photon. The efficiencies in these probability for photon- and neutron-induced showers were simulated as a function of threshold on the photon probabilities and gave good photon ID with suppression of

neutrons up to a factor of 4. It should be noted that the higher neutron energy (viz., the more difficult the use of TOF), the better the suggested separation method works.

## 4.7 Tracking

The system of tracking chambers in the GLUEX detector must cover as close to a  $4\pi$  solid angle as possible over a wide range of particle momenta and must have sufficient momentum resolution to be able to identify missing particles. In order to achieve these goals, the LASS detector [?] design was used as our starting point. This device used several different tracking elements each optimized for a particular region in the detector. Figure ?? shows the GLUEX tracking regions. All tracking devices are located inside the barrel calorimeter which is in turn inside the  $2.24 T$  solenoid. Surrounding the target is a cylindrical straw-tube drift chamber (CDC) which provides very good  $r - \phi$  and good  $z$  resolution. In addition, this detector provides some  $dE/dx$  information to aid in the separation of  $\pi$ 's,  $K$ 's and  $p$ 's up to momenta of about  $0.45 GeV/c$  – a regime where  $dE/dx$  measurements work extremely well. In the forward region, round planar drift chambers (FDC) are arranged in four identical tracking packages. These packages allow tracking particles down to about one degree with respect to the beam line. A summary of the tracking chamber parameters are given in Table ??.

System	Radius		Length		Resolution	
	$r_{\min}$	$r_{\max}$	$z_{\min}$	$z_{\max}$	$\sigma_{r-\phi}$	$\sigma_z$
CDC	13.0 cm	59.0 cm	10 cm	210 cm	150 $\mu m$	1.5 mm
FDC	3.5 cm	59.0 cm	230 cm	400 cm	150 $\mu m$	fixed

Table 4.3: A summary of the tracking chamber parameters. The  $z$  values under *Length* indicate the smallest and largest  $z$  of the combined system. The  $z$  origin is at the upstream end of the magnet. The  $z$  resolution for the CDC comes from  $\pm 6^\circ$  stereo layers. The  $z$  resolution of the planar chambers is assumed to be given by their position in space.

The barrel calorimeter defines a maximum keep-out radius of about  $65 cm$ . The physical radius of all chambers has been limited to about  $60 cm$ . This provides  $5 cm$  of space for support and installation rails, and cables and gas feeds for the forward chamber packages.

### 4.7.1 Track Reconstruction

The  $22.4 kG$  solenoid field determines the physically measurable quantities, and hence, the momentum resolution. The transverse momentum,  $p_\perp$  and the dip-angle,  $\lambda$ , ( $\lambda = \frac{\pi}{2} - \theta$ ) are measured from the curvature of the tracks and their initial direction. The total momentum and the longitudinal momentum are then obtained from these as  $p_{total} = p_\perp \sec \lambda$  and  $p_\parallel = p_\perp \tan \lambda$ . The accuracy of the  $p_\perp$  measurement is completely dominated by the  $r - \phi$  resolution of the tracking chambers, while the  $\lambda$  measurement relies on an accurate measurement of both  $z$  and the distance traveled.

An example showing the typical charged particle momentum that needs to be measured comes from reaction ??. This final state consisting entirely of charged particles is fairly typical of the typical exotic-hybrid channel that will be studied.

$$\gamma p \rightarrow \eta_1(1800)p \rightarrow \pi^+ \pi^- \pi^+ \pi^- p \quad (4.13)$$

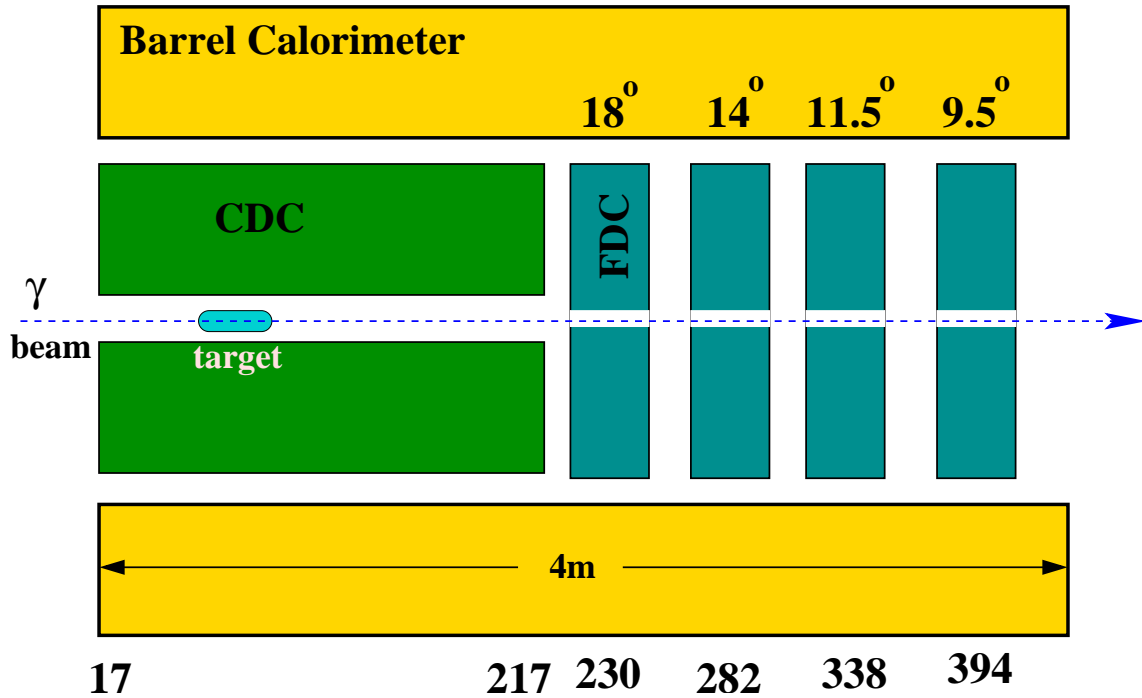


Figure 4.36: The GLUEX detector. The tracking is composed of two elements: a straw-tube chamber called the cylindrical drift chamber (CDC) and circularly-shaped planar chambers designated as the forward drift chambers (FDC). The small gap indicated in the middle of the FDCs is due to wires that will not be instrumented. If background studies merit, we could also consider a physical hole. The distances labeled along the bottom of the figure are the  $z$  coordinate of the upstream and downstream ends of the CDC, and the center of each FDC package. The angles labeled above the FDC packages are from the center of the target to the center of the outer edge of the chamber.

The exotic spin-one  $\eta_1(1800)$  is produced with a mass of  $1.8 \text{ GeV}/c^2$  and a typical  $t$  distribution. The incident photon energy is  $9 \text{ GeV}/c^2$ . Figure ?? shows the transverse and longitudinal components of momentum from the  $\pi$ 's in this reaction while Figure ?? shows the same distributions for the protons.

From the two sets of plots, several important features can be seen. The charged pions from the decay of the meson system are fairly forward peaked. Once  $\theta_\pi$  is larger than about  $40^\circ$ , there are almost no pions with a momentum larger than about  $1 \text{ GeV}/c$ . Additionally, there are almost no pions with  $\theta$  larger than  $100^\circ$ . The protons almost all fall within the angular range of  $20^\circ$  to  $60^\circ$  degrees. This is almost entirely covered by the CDC. Many of these protons will need to be identified by either time-of-flight for the BCAL or using  $dE/dx$  in the CDC. Good tracking resolution for high-momentum particles in the backward angle region is not required, so the rapid degradation of momentum resolution for these large angles as seen in Figure ?? is not a real issue for the detector's overall performance. In addition, most events have at least one particle moving in the forward direction at high momentum. The momentum versus angle for all particles in each event is displayed in Figure ?. Good tracking will be needed as close to the beam line as possible, hopefully extending down to  $2^\circ$ .

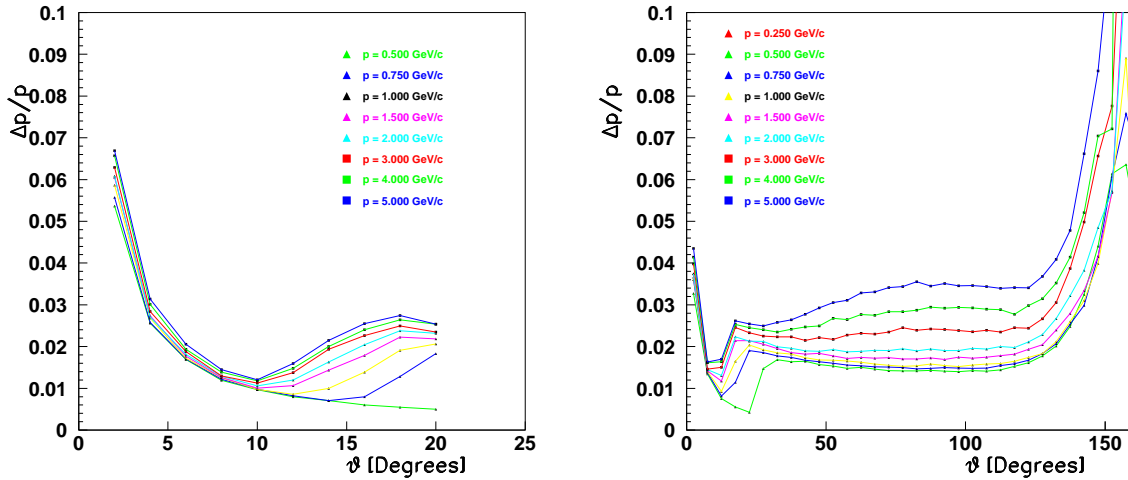


Figure 4.37: The resolution as a function of angle is plotted for several total momenta. The plots correspond to the detector design shown in Figure ???. For polar angles larger than  $70^\circ$ , the maximum detected momentum will be well under  $1\text{GeV}/c$  so even though the resolution for high-momentum tracks is poor in this large-angle region, it will not affect the overall tracking of physics events.

Another tracking issue is that many of the charged particles in GLUEX will produce spiraling tracks in the solenoid. Figure ??? shows the  $p$  versus  $\theta$  plane for tracks in the solenoid. Tracks which fall above the hyperbolic curve cannot spiral in the  $59\text{ cm}$  radius region containing the tracking chambers. Below the hyperbola are a series of approximately horizontal lines. Tracks below these lines spiral the number of times indicated. Based on the  $p$  versus  $\theta$  distributions in Figures ??? and ??, it is clear that most tracks at angles larger than  $50^\circ$  will always spiral at least once in the detector.

Pattern recognition is an important part of track reconstruction as well. This process requires finding local clusters of hits and associating them into small track segments that can be combined into larger tracks. In order for this procedure to work well, it is desirable to have sufficient hits in close proximity such that they will be easily associated. One useful comment on this issue is when the LASS experiment ran in similar conditions, they had severe pattern recognition issues due to the large magnetic field. They resolved it by building chambers with both anodes and cathodes which were read out, with the cathodes and anodes being arranged such that together they provided a 3-dimensional point. The GLUEX detector is trying to build on this experience by reading out both cathodes and anodes in the forward direction. We are also planning packages that consist of six closely spaced planes. Such packages will allow local identification of track segments with a reasonable measure of curvature. This has then been repeated four times to provide sufficient segments for high efficiency track-segment linking. In the CDC, the pattern recognition issue is dealt with by creating three sections containing several adjacent straight tube. These are then interleaved with two sets of crossed stereo layers.

The resolution necessary in the photon beam energy has been matched to the expected momentum resolution in the tracking elements of the GLUEX detector. This has been done by

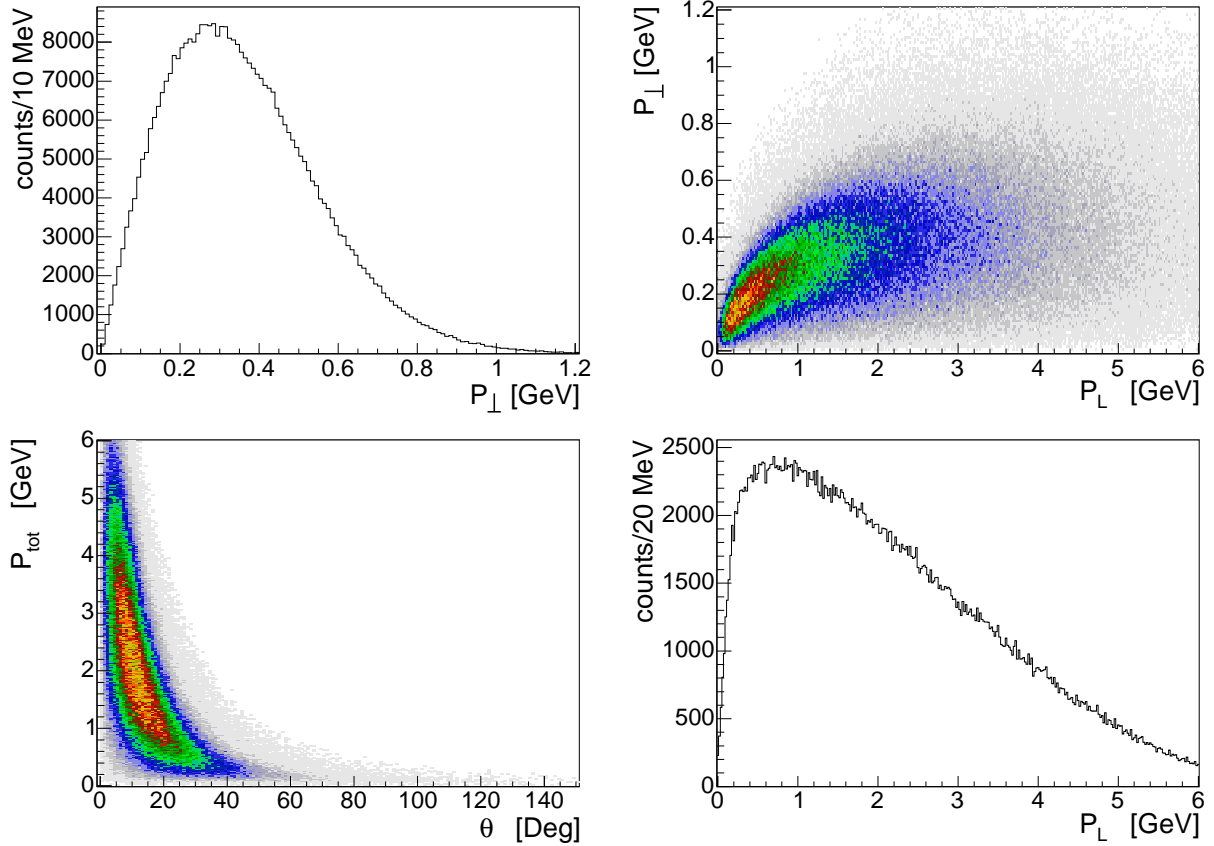


Figure 4.38: The momentum distribution of charged pions from the reaction  $\gamma p \rightarrow \eta_1(1800)p \rightarrow 2\pi^+2\pi^-p$ . The upper left-hand figure shows the momentum perpendicular to the beam direction. The upper right-hand figure shows the perpendicular versus the longitudinal momentum. The lower left-hand figure shows the total momentum versus the polar angle  $\theta$  and the lower right-hand figure shows the momentum along the beam direction.

looking at the missing mass resolution. As an example, consider reaction ??.



It is also assumed that the  $\pi^0$  in ?? is not detected. Using the reconstructed charged tracks, the known beam energy, and the assumption that the reaction took place on a proton target, the square of the missing mass is computed and shown in Figure ??(a) for a nominal 0.1% beam energy resolution. The distribution is centered at the square of the  $\pi$  mass, but it has a non-negligible width. In Figure ??(b) the width of the peak in (a) is plotted as a function of the beam energy resolution. For this particular reaction with a missing  $\pi^0$ , a beam energy resolution of 0.1 to 0.2% is well matched to the 200  $\mu m$  resolution of the tracking system.

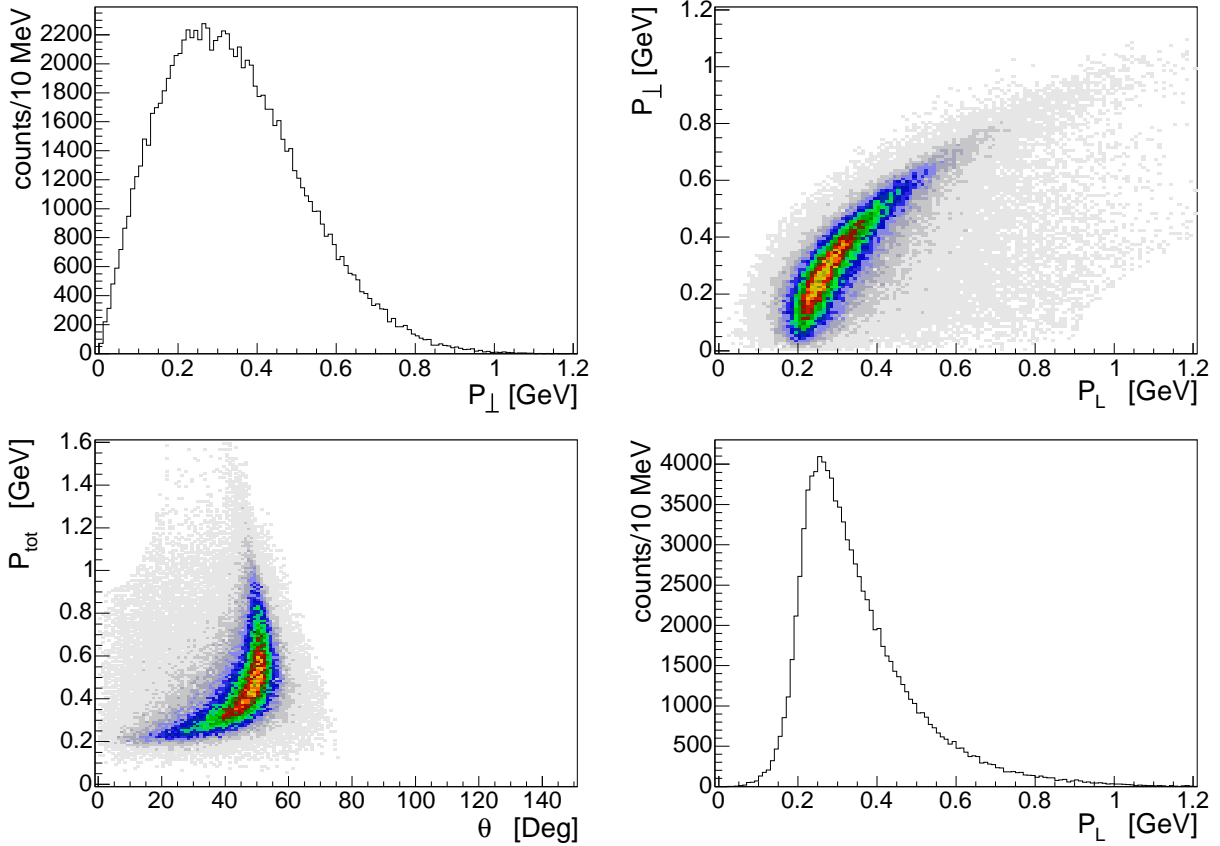


Figure 4.39: The momentum distribution of protons from the reaction  $\gamma p \rightarrow \eta_1(1800)p \rightarrow 2\pi^+2\pi^-p$ . The upper left-hand figure shows the momentum perpendicular to the beam direction. The upper right-hand figure shows the perpendicular versus the longitudinal momentum. The lower left-hand figure shows the total momentum versus the polar angle  $\theta$  and the lower right-hand figure shows the momentum along the beam direction.

### 4.7.2 Straw-tube Central Drift Chamber

#### Overview

The Central Drift Chamber (CDC) is used to track charged particles, providing timing and energy loss measurements. It is a cylindrical straw-tube drift chamber situated within the upstream end of the GlueX solenoid, surrounding the target and start counter, as shown schematically in Figure ??, with dimensions given in Table ?. Its active volume is traversed by particles coming from the target with polar angles between  $6^\circ$  and  $168^\circ$ , with optimum coverage for polar angles between  $29^\circ$  and  $132^\circ$ .

Prior to construction of the CDC, the proposed materials were evaluated and used to build two smaller prototype chambers. These prototypes were then used to study chamber characteristics and performance, including choice of gas mix and  $dE/dx$  simulations, reported elsewhere [?].

The CDC contains 28 layers of 1.6 cm diameter straw tubes, 3522 in total, located in the cylindrical volume from an inner radius of approximately 10 cm out to 56 cm from the beamline.

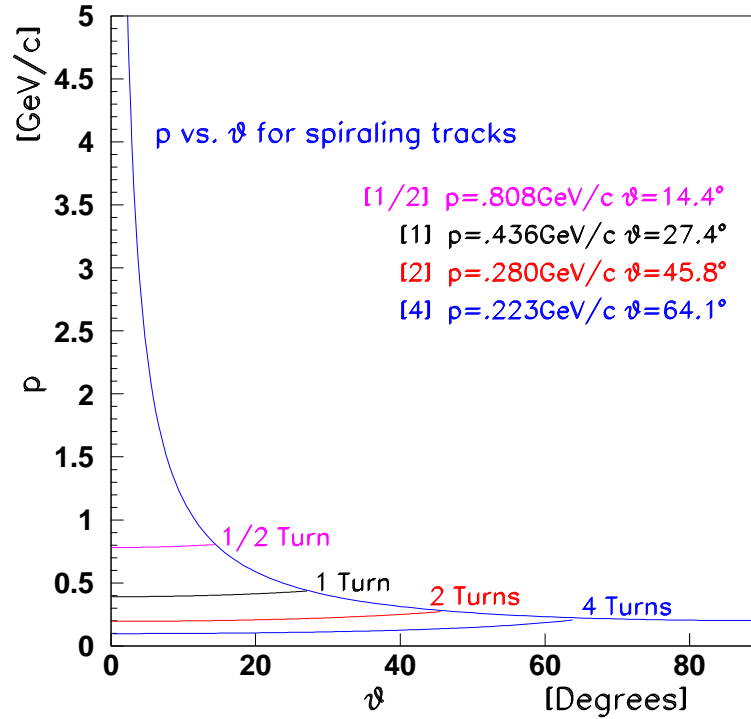


Figure 4.40: This figure shows the number of full circles made by charged particles in the magnetic field. The limit line corresponds to  $p_{\perp} = 0.2 \text{ GeV}/c$  tracks. The approximately horizontal lines indicate when the particle can make the indicated number of turns without leaving the magnet.

Active volume inner radius:	8.95 cm
Active volume outer radius:	57.62 cm
Active length:	150.0 cm
Chamber assembly inner radius:	8.75 cm
Chamber assembly outer radius:	59.74 cm
Thickness per layer:	$0.051 \text{ gcm}^{-2}$
Thickness per layer (rad. lengths):	0.0014
Thickness per 28 layers (rad. lengths):	0.0392
Upstream gas plenum length :	3.18 cm
Downstream gas plenum length :	2.69 cm

Table 4.4: Geometry of the CDC's active volume and gas plenums

Each straw tube contains an anode wire, of  $20 \mu\text{m}$  diameter gold-plated tungsten; the inner wall of the tube forms the cathode, ensuring uniformity of electric field around the wire. The straws contribute structural rigidity to the assembly, supporting the tension on the wires, and also prevent the wires from making contact with their neighbors and causing electrical problems in

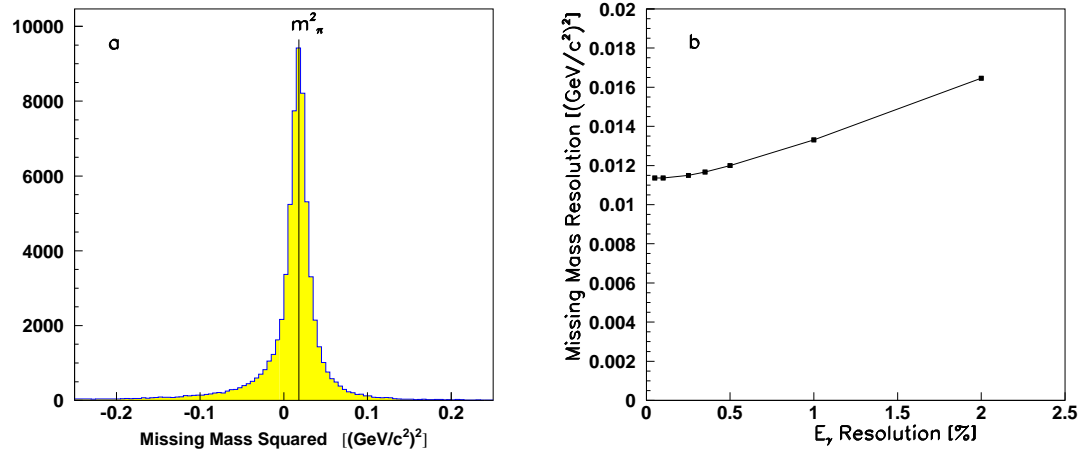


Figure 4.41: Missing mass squared from the reaction ?? where the  $\pi^0$  is assumed missing. (a) is for 0.1% beam energy resolution, while (b) is a plot of the missing mass resolution as a function of the beam energy resolution.

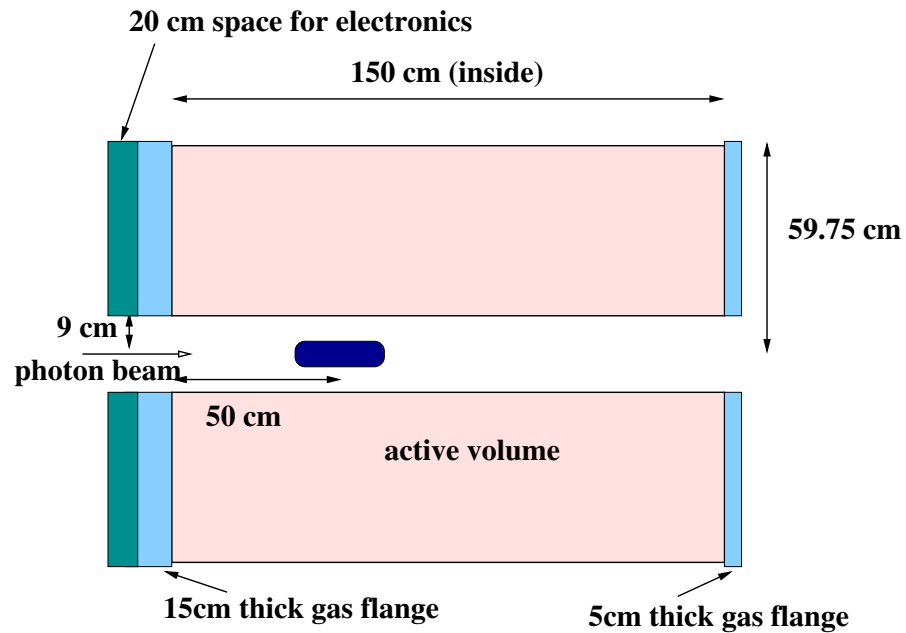


Figure 4.42: A side view of the CDC.

the event that one should eventually break. The number of straws in each layer is given in Table ??.

The tracking volume is enclosed by inner and outer cylindrical walls ('shells') of G-10 and aluminum, respectively, and endplates of carbon fiber, downstream, and aluminum, upstream. The endplates are linked by 12 aluminum support rods which were bolted into place to maintain

Layer	Straws	Radius (cm)	Layer	Straws	Radius (cm)
1	42	10.7219	15	135	34.4343
2	42	12.0797	16	135	35.8128
3	54	13.7802	17	146	37.4446
4	54	15.1447	18	146	38.8314
5	66	16.9321	19	158	40.5369
6	66	18.3084	20	158	41.9248
7	80	20.5213	21	170	43.6152
8	80	21.9009	22	170	45.0038
9	93	23.8544	23	182	46.6849
10	93	25.2362	24	182	48.0737
11	106	27.1877	25	197	50.3747
12	106	28.5712	26	197	51.7597
13	123	31.3799	27	209	53.3631
14	123	32.7577	28	209	54.7464

Table 4.5: This table shows the number of straws in each layer of the CDC, and the central radius of each layer, half-way between the endplates.

the relative location and orientation of the endplates after alignment. Fig. ?? shows the endplates, inner shell and support rods before the straws were installed. The holes in the endplates were milled precisely to support the ends of the straws in the correct location.

There is a cylindrical gas plenum next to each endplate - the upstream plenum has polycarbonate walls and a polycarbonate endplate, while the downstream plenum has Rohacell sidewalls and a ring-shaped endwall of mylar film, aluminized on both sides. The inner and outer shells are sealed along their seams and where they meet the endplates, forming an outer plenum around the straws. The materials used for construction were chosen to minimize the amount of material in the tracking volume, especially at the downstream end. They are listed in Table ??.

A further 20 cm of length is reserved for the electronics, which are mounted on standoffs on the polycarbonate endplate. Threaded holes in the polycarbonate endplate allow signal wires to pass through the gas plenum. These are sealed with an O-ring and a threaded bushing which is torqued into place.

### Straws

The straw tubes are 0.8 cm radius aluminized mylar tubes, manufactured by Lamina Dielectrics (UK) from 100  $\mu\text{m}$  thick mylar tape with approximately 30 nm of aluminum vapor-deposited onto one side, wound into a tube with the aluminum on the inside. The electrical resistance of each straw, from one end to the other, is between 75  $\Omega$  and 100  $\Omega$ . The straws are arranged in 28 radial layers surrounding the inner shell, as shown in Fig. ?. 12 of the layers are axial (parallel to the beam axis) and the remaining 16 are placed at stereo angles of  $\pm 6^\circ$ . These are ordered such that the innermost 4 layers are axial, followed by (at increasing radius) 4 layers at  $+6^\circ$ , 4 layers at  $-6^\circ$ , 4 axial layers, 4 layers at  $-6^\circ$ , 4 layers at  $+6^\circ$  and 4 axial layers. The layers are paired and located so that the first layer of each pair contains the largest number of straws possible for its radius, and the straws in the second layer are close-packed against those



Figure 4.43: CDC frame prior to the installation of the straw tubes.

in the first. This is illustrated in Fig. ??.

Each straw tube is glued to its neighbors in the same layer at three points evenly distributed along its length, using non-conductive epoxy. In the first layer of each pair, every sixth straw is also glued to the straw behind it. In the second layer of each pair, every straw is glued to the straw behind it. Fig. ?? shows straws in opposing stereo layers 8 and 9 and Fig. ?? shows the outermost row of straws, with the outer shell partly installed. The number of straws in each layer is listed in Table ??, together with the radius of each wire at the center of the chamber and at the inside face of the two endplates. Table ?? gives the  $(x, y)$  coordinates of the wires at each endplate and in the center of the chamber.

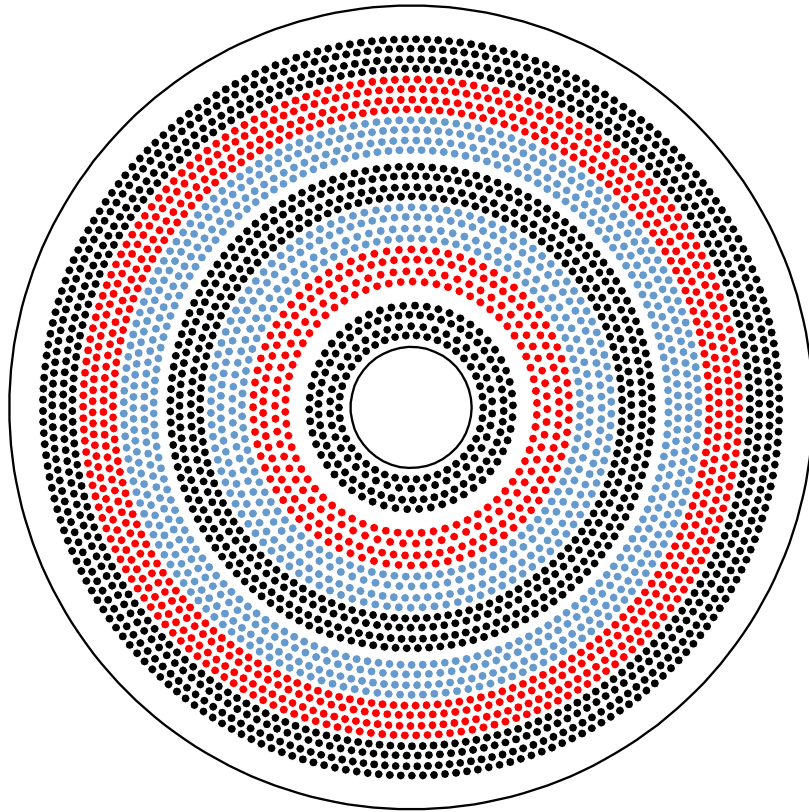


Figure 4.44: Diagram showing the position of the straws at the upstream endplate. The axial straws are shown in black, the  $+6^\circ$  stereo layers are shown in dark red and the  $-6^\circ$  stereo layers are shown in light blue.

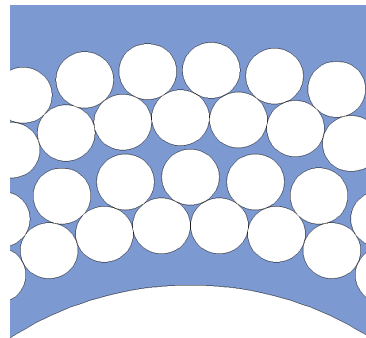


Figure 4.45: Diagram showing close-packing of the straws in a small section of rows 1 to 4.



Figure 4.46: Straw tubes in stereo layers 8 and 9.



Figure 4.47: Straw tubes in layer 28, with one half of the outer shell in place.

### Straw and wire assembly

The straw assembly components are shown in Fig. ?? . A ‘donut’ ring is glued inside each end of every straw, and a ‘feedthrough’ tube is glued through the endplate into the ring and so holds the straw in position. Noryl plastic donuts and feedthroughs are glued into the carbon fiber endplate with non-conductive epoxy, whilst aluminum donuts and feedthroughs are glued into the aluminum endplate with silver conductive epoxy. The conductive epoxy ensures that the electrical grounding of the aluminum endplate is shared with the aluminum feedthroughs, donuts and the aluminum layer on the inside of the straw. Sufficient epoxy is used to make each joint gas-tight.

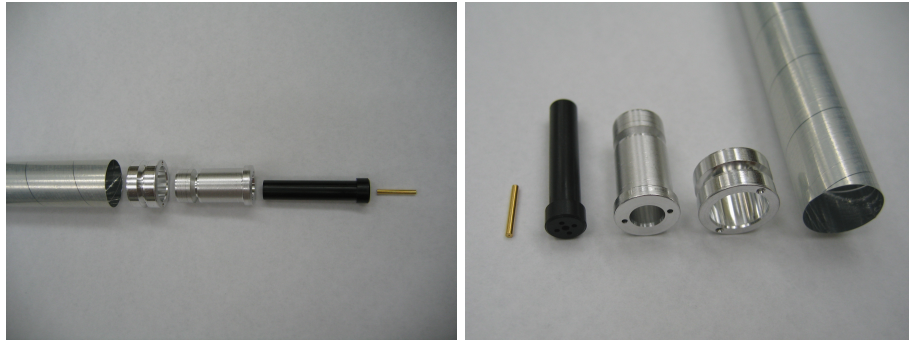


Figure 4.48: Straw, donut, feedthrough, pinholder and crimp pin.

The donuts and feedthroughs were manufactured to a CMU design which features a recess (‘glue trough’) partway down the outside of each component, accessed by 2 small holes (‘glueports’) bored into the component wall lengthwise. This permits epoxy to be injected through one glueport into the glue trough whilst air exits through the partner glueport, thus enabling a strong joint to form as the epoxy makes good contact with both surfaces. The dimensions of these components are given in Table ?? .

Component	Inner diameter	Outer diameter	Length
Donut	1.111 <i>cm</i>	1.562 <i>cm</i>	0.953 <i>cm</i>
Feedthrough	0.635 <i>cm</i>	1.111 <i>cm</i>	2.160 <i>cm</i>
Pinholder (top)	0.147 <i>cm</i>	0.792 <i>cm</i>	0.394 <i>cm</i>
Pinholder (rest)	0.508 <i>cm</i>	0.635 <i>cm</i>	3.155 <i>cm</i>
Crimp pin	0.0203 <i>cm</i>	0.147 <i>cm</i>	1.206 <i>cm</i>

Table 4.6: The dimensions of the straw assembly components

The anode wires are held in place by gold-plated copper crimp pins inside Noryl plastic tubes ‘pinholders’, which were inserted into the feedthroughs. The inner diameter of the pinholder top is at first 1.47 *mm*, a very close fit with the crimp pin, then after 6 *mm* of length it is stepped in slightly to 1.27 *mm* for a further 1.63 *mm* to hold the crimp pin in place, before opening out to 5.08 *mm* for the rest of its length.

The pins were crimped when the wire was under 30 *g* of tension, applied by suspending a weight from the wire, with the chamber orientated so that the wire was hanging vertically. The anode wire is 20  $\mu\text{m}$  diameter tungsten with a flash coating of gold, supplied by Luma-Metall

([www.luma-metall.se](http://www.luma-metall.se)). Each pinholder has 4 additional holes surrounding the crimp pin which permit gas to flow in and out of the straw.

### **Wire tension measurements**

The tension on each wire was measured a few weeks after stringing, and again some time later, using two Helmholtz coils and a control device which alternated between applying a sinusoidal voltage along to the wire and measuring the induced current on the wire. The wire tension was calculated from the frequency of the applied voltage when the system reached resonance. This technique is described elsewhere [?]. The tension measurements were interleaved with the stringing work and a few wires with very low tension were found and replaced during this time. When stringing was complete, all the wires had tension between 27 and 32 *g*. The chamber is shown with the Helmholtz coils in place in Fig. ??.



Figure 4.49: Wire tension measurement

### Gas flow

Six aluminum tubes of inner diameter  $6.35\text{ mm}$  run the length of the CDC, close to the inside wall of the outer cylindrical shell, taking the gas supply from outside the upstream end through the polycarbonate plate and both endplates into the downstream plenum, where the gas enters the straw tubes through the holes in the pinholders. The gas passes through the straw tubes into the upstream plenum and then through ten holes in the lower half of the aluminum endplate into the void between the straws and the outer shell of the CDC. Six holes near the top of the aluminum endplate permit the gas to leave the void through some exhaust tubes. Five thermocouples within each plenum allow the temperature of the gas to be monitored. The gas used is a mixture of 50%  $\text{CO}_2$  and 50% Ar at atmospheric pressure.

### Electrical shielding

Electrical shielding is crucial to minimize the amount of electromagnetic noise picked up by the signal wires. The aluminum endplate is the common ground for the straw tubes and also the outer shell, which provides electrical shielding around the tubes. Each half of the outer shell is glued to the aluminum endplate and G-10 outer hub with non-conductive epoxy. In order to ensure a good electrical connection, tabs of aluminum are glued over the join between the outer shell and the endplate with conductive epoxy at twenty points around the outer radius.

The long straight edges of the two halves of the outer shell were covered with non-conductive glass cloth electrical tape and then joined together with a layer of 2" wide military duct tape. A strip of 1" wide copper tape with a non-conductive backing was applied along the center of the duct tape. The copper tape is grounded to the endplate by a tab of copper and conductive epoxy, and then covered over with two more layers of the military duct tape. This arrangement ensures that the sidewalls of the cylindrical outer shell have a good connection to the grounded aluminum endplate, whilst the discontinuity between the two halves of the shell prevents eddy currents from spiraling around the CDC in the event of a magnet quench.

The upstream outer gas plenum sidewall is covered with 0.005" thick copper tape. A copper braid is soldered to the tape at intervals and glued to the aluminum endplate with conductive epoxy. The downstream plenum endwall material is mylar, aluminized on both sides. Rectangular tabs extend outwards from the endwall around its radius. These are glued to the sidewall and outer shell with conductive epoxy.

Grounded shielded extension cables are used for the downstream thermocouples along the length of the CDC and for all the thermocouples from the upstream end to the electronics racks in order to minimize any electrical pickup.

### Electronics

The hookup wires which pass through the polycarbonate endplate and onto the crimp pins inside the upstream gas plenum were made from RG-316 wire as follows: at one end of the wire, the inner conductor was exposed for approximately  $5\text{ mm}$  and the teflon dielectric was exposed for a further  $5\text{ mm}$ . The end of the shielding braid was sealed with epoxy to prevent gas from migrating along the cable inside the braid. A silver bead was soldered onto the end of the center conductor and then covered with a narrow tube of conductive rubber, approximately  $15\text{ mm}$  long, which fits tightly over the bead. Heat-shrink was then used to seal over the region from the end of the outer covering and braid to the end of the conductive rubber tube. An

O-ring and threaded bushing were fed onto the hookup wire before its other end was finished by stripping back the braid 10 mm and then soldering a ferrule to the braid, then stripping the dielectric 5 mm from the end of the wire. Two hookup wires, one complete and one partly assembled, are shown in Fig. ???. The length of wire used for each connection is between 9.3 cm and 12.5 cm, this is chosen to be as short as possible, without causing excessive strain on the solder joints.

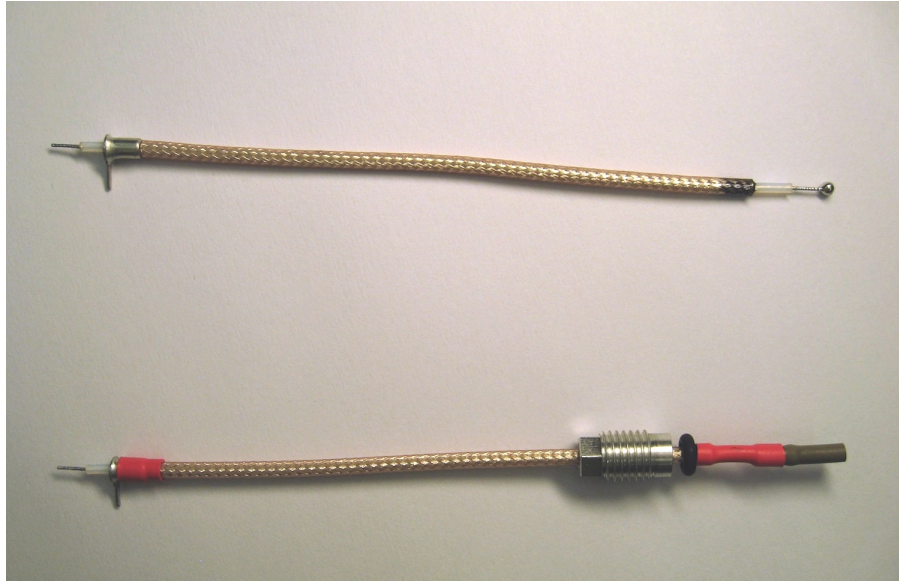


Figure 4.50: Two hookup wires, the upper wire is part-assembled and the silver bead is visible.

The polycarbonate endplate was polished to transparency so that the crimp pins would be clearly visible through it. Each hookup wire was installed by inserting it through a threaded hole in the polycarbonate endplate and sliding the conductive rubber over the corresponding crimp pin until it made a snug fit as the silver bead made contact with the end of the pin. The O-ring and threaded bushing were then fitted into the hole in the endplate and the ferrule and center conductor at the other end of the hookup wire were soldered onto pads on a transition board. The transition boards are mounted onto standoffs on the polycarbonate endplate - one standoff mounts directly to the polycarbonate endplate whilst the other (grounding) standoff threads onto another standoff which is mounted onto the Al endplate and protrudes through a hole in the polycarbonate endplate, sealed with an O-ring.

The hookup wires are soldered to the transition boards in groups of 20 to 24 wires from 3 to 4 neighboring rows of straws to each board, 149 transition boards in total. Some of the transition boards and standoffs are shown in Fig. ???. Each transition board houses a 30-pin connector for a high voltage board (HVB); this provides for high voltage (HV) of approximately 2 kV for up to 24 wires, 2 HV connections of approximately 1 kV for the shielding braids, 2 ground connections to the grounding standoffs and 2 unused connections which are located between the HV and ground connections. The HVBs also house the preamplifier cards.

The preamplifiers are charge-sensitive, with capacitive coupling to the CDC, and 24 channels per board. The preamplifiers are connected to 125 MHz 12-bit flash ADCs, three preamps to each fADC; the preamplifiers and fADCs are described in detail in the section on electronics.



Figure 4.51: Hookup wires and transition boards.

### Chamber operating parameters

The background noise present on the wires is important in determining the operating parameters for the CDC, and thus the range of  $dE/dx$  measurements possible. During calibration, measurements are made of the mean and standard deviation ( $\sigma$ ) of the pedestal height (the ADC value in the absence of an event). The pedestal height is adjusted by downloading a data file into the fADC, it is set at approximately  $3\sigma$  to  $4\sigma$  in order to maximize use of the fADC range.

The choice of the gas mixture is described elsewhere [?]. The anode voltage is chosen such that the minimum ionizing peak in the amplitude histogram from tracks at  $90^\circ$  to the straws lies above the background noise, this is done by setting the anode voltage to match the hit threshold, typically  $5\sigma$ , to a low percentile (99% to 95%) of the distribution within the 4095 channel range of the fADC. Table ?? shows estimates of the dynamic range for conditions typical of the small prototype chamber operating at voltages close to  $2\text{ kV}$  with a gas mixture of 50%  $\text{CO}_2$  and 50% Ar at atmospheric pressure giving a gas gain of approximately  $3 \times 10^5$ , and the  $5\sigma$  hit threshold matched to the lower 99<sup>th</sup> percentile. For  $\sigma$  of 15 channels this gives a dynamic range of approximately 20 times minimum ionizing at  $90^\circ$ . Table ?? shows similar estimates for the hit threshold matched to the lower 95<sup>th</sup> percentile, which gives greater dynamic range at the expense of detection efficiency for the minimum ionizing particles.

### Timing method and position resolution

The fADCs are programmed to output data in two alternative modes - a ‘raw’ mode, intended for development and diagnostics, where a full sample window of 512 samples is read out for each channel, and a ‘run’ mode, where the output consists of just two quantities, representing drift

Pedestal $\sigma$	Minimum ionizing peak	Dynamic range
10	140 (170 to 120)	30 (24 to 34)
15	210 (250 to 180)	20 (16 to 22)
20	280 (340 to 240)	15 (12 to 17)
25	350 (420 to 300)	12 (10 to 13)
30	420 (500 to 360)	10 (8 to 11)

Table 4.7: Table of estimates of the dynamic range of the CDC. There is some variation due to the shape of the Landau distribution, the data are given for ratios of the Landau parameters 4MPV/FWHM of 3.3 (3.0 to 3.6) and the  $5\sigma$  hit threshold is matched to the lower 99<sup>th</sup> percentile of the distribution within the range of the fADC.

Pedestal $\sigma$	Minimum ionizing peak	Dynamic range
10	90 (100 to 90)	44 (41 to 47)
15	140 (150 to 130)	29 (27 to 32)
20	180 (200 to 170)	22 (20 to 24)
25	230 (350 to 210)	18 (16 to 19)
30	280 (300 to 260)	15 (13 to 16)

Table 4.8: Table of estimates of the dynamic range of the CDC. There is some variation due to the shape of the Landau distribution, the data are given for ratios of the Landau parameters 4MPV/FWHM of 3.3 (3.0 to 3.6) and the  $5\sigma$  hit threshold is matched to the lower 95<sup>th</sup> percentile of the distribution within the range of the fADC.

time and energy loss, for only those channels where a hit occurs, and a word representing the hit pattern. The algorithms used to determine the drift time and energy loss were developed using the small 24-channel prototype chamber and are programmed directly into the FPGAs. The drift time is converted into a drift distance in offline software.

The timing algorithm is activated by the trigger signal and performs a search through the raw sample data buffered in the fADC to identify a hit signal, if there is one, and return the time corresponding to its leading edge. It uses several thresholds which can be related to the pedestal standard deviation,  $\sigma$ . These are determined during calibration and uploaded into the FPGA algorithm as constants. Values optimized using the small prototype are available as a starting point - hit identification threshold  $T_{hit} \sim 5\sigma$ , high timing threshold  $T_h \sim 4\sigma$ , low timing threshold  $T_l \sim \sigma$  and pedestal lead time  $N_p \sim 13$  for  $\sigma$  of 10 to 15 (for higher  $\sigma$  this can be determined from the slope of the hit signal's rising edge, which is shaped by the fADC and preamplifier).

1. The event pedestal,  $P_{evt}$ , is found, as the mean of 100 samples ending 10 samples before the trigger time.
2. The ADC data are upsampled from 50 samples before the trigger to 150 samples after the trigger, using the 8 ns sampling function to provide a new set of upsampled data at 1.6 ns intervals.
3. The upsampled data are searched for a hit, which is found if the data exceed a high threshold  $P_{evt} + T_{hit}$  at point  $x$ . If no hit is found, no further action is taken.

4. The local pedestal,  $P_{loc}$ , is obtained as the ADC value at  $N_p$  upsampled points before  $x$ .
5. The algorithm searches forward (to samples later in time) from point  $x - N_p$  to find point  $x_1$  where the data pass above a slightly less high threshold  $P_{loc} + T_h$ .
6. It then searches backward (to earlier samples) from  $x_1$  to find the point  $x_2$  where the data fall below a low threshold  $P_{loc} + T_l$ .
7. The algorithm then extrapolates a straight line from  $(x_1, T_h)$  through  $(x_2, T_l)$ ; the drift time is the time corresponding to the sample point where the line reaches the local pedestal,  $P_{loc}$ .

The drift time returned by the algorithm includes a constant offset,  $t_0$ , corresponding to the earliest possible drift time (when a track passes through a wire). This offset is determined during offline analysis and subtracted from the drift time returned by the algorithm to give the net drift time, which is then converted to a drift distance using look-up tables calculated beforehand using a Garfield model.

The CDC was designed to achieve a position resolution of  $150\ \mu m$ . Data obtained with the small prototype and cosmic rays and analyzed with a simple straight-line track-fitting code give a position resolution which averages around  $110\ \mu m$ ; the resolution improves with track distance from the wire, and also signal amplitude, as shown in Fig. ??.

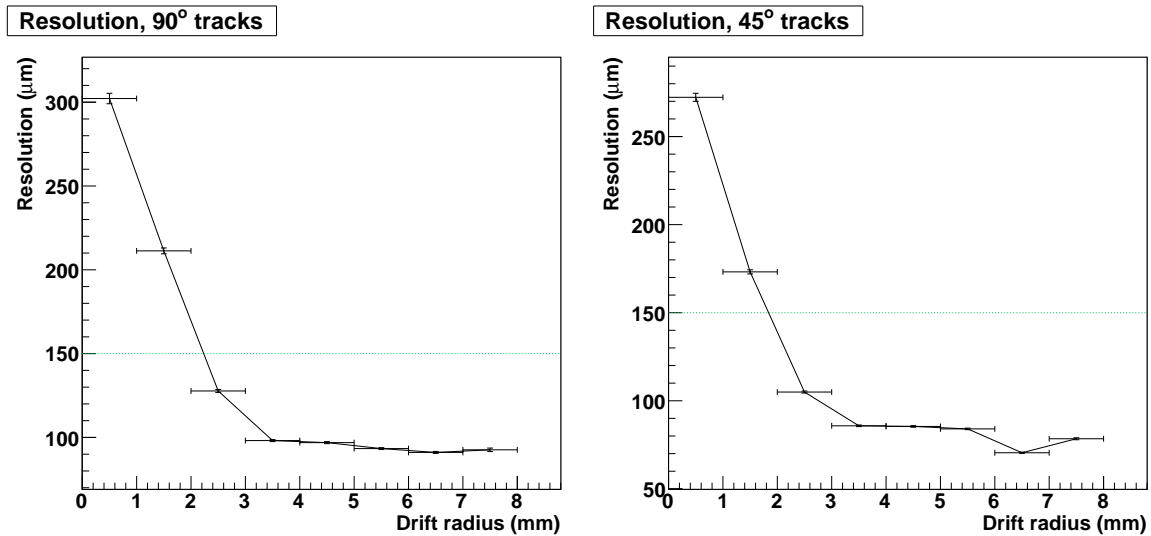


Figure 4.52: Position resolution for cosmic rays with 50/50 mix of Ar and  $CO_2$  at 2090V, with tracks at  $90^\circ$  (left) and  $45^\circ$  (right) to the wires.

### 4.7.3 Forward Drift Chambers

#### Overview

The Forward Drift Chamber system (FDC) is used to track charged particles coming from the target with polar angles up to  $20^\circ$ . Tracks at angles greater than  $10^\circ$  also pass through the CDC detector and its associated downstream end-plate. Due to the spiraling trajectories of

Upstream endplate:	0.9525 cm Al (3/8" plate)
Downstream endplate:	0.6 cm Carbon Fiber
Support rods (12):	Al
Upstream inner hub	Al
Downstream inner hub	G-10
Thickness of inner shell (mm):	0.5 mm G-10
Upstream outer hub	G-10
Downstream outer hub	G-10
Thickness of outer shell (mm):	1.6 mm Aluminum 6061
Outer shell joints:	Scotch 27 glass cloth electrical tape 5.04 cm wide strip of military duct tape 2.54 cm wide 1.27 mm thick Cu tape
Outer shell connections to endplate (21) :	approx. 3 cm x 2.54 cm x 0.05 mm Al tabs
Outer shell connections to endplate (2) :	approx. 3 cm x 2.54 cm x 0.05 mm Cu tabs
Strawtube (diameter):	1.552 cm OD
Strawtube (material):	Aluminized Mylar
Strawtube (thickness):	114(0.1) $\mu$ m Mylar(Al)
Upstream donuts and feedthroughs (3522):	Al
Downstream donuts and feedthroughs (3522):	Noryl plastic
Pinholders (7044):	Noryl plastic
Crimp pins (7044):	Au plated Cu
Anode wires (3522):	20 $\mu$ m gold-plated W
Upstream plenum sidewall:	3 mm Polycarbonate and 1.27 mm Cu tape
Upstream plenum endwall:	15.8 mm Polycarbonate
Downstream plenum sidewall:	2.54 cm Rohacell
Downstream plenum endwall:	50 $\mu$ m Aluminized Mylar
Gas pipes (6):	Al, inner diameter 6.35 mm
Gas line widgets (6):	plastic
Gas line widgets (6):	Al
Hose barbs (6):	stainless steel
Thermocouples (10)	Constantan Cu-Ni, Kapton coating
Conductive epoxy:	920-H
Non-conductive epoxy:	DP-190 (straw assembly)
Non-conductive epoxy:	DP-460NS (outer shell and hubs)

Table 4.9: Construction materials

the charged particles and the high multiplicity of charged tracks passing through the FDC, this system must be able to provide a sufficient number of measurements with appropriate redundancy to enable linking of the hits from the different tracks with high accuracy, while providing good spatial resolution with reasonable direction information. The chosen technology is a Cathode Strip Chamber in which the two cathode planes facing each wire plane are divided into strips at an angle with respect to the wires. In addition to the charge induced on the strips, the timing information from the wires is read out, enabling reconstruction of both a coordinate along the wire as well as a coordinate transverse to the wire (using the drift time). This allows to reconstruct "space points" and facilitates association of adjacent hits with each

Layer	Straws	Radius (cm) (center)	Radius (cm) (end plate)	Stereo (radians)
1	42	10.7219	10.7219	0.00000
2	42	12.0797	12.0797	0.00000
3	54	13.7802	13.7802	0.00000
4	54	15.1447	15.1447	0.00000
5	66	16.9321	18.6765	0.10470
6	66	18.3084	20.1945	0.11314
7	80	20.5213	21.9827	0.10470
8	80	21.9009	23.4606	0.11168
9	93	23.8544	25.1226	-0.10470
10	93	25.2362	26.5780	-0.11072
11	106	27.1877	28.3070	-0.10470
12	106	28.5712	29.7475	-0.10999
13	123	31.3799	31.3799	0.00000
14	123	32.7577	32.7577	0.00000
15	135	34.4343	34.4343	0.00000
16	135	35.8128	35.8128	0.00000
17	146	37.4446	38.2650	-0.10470
18	146	38.8314	39.6822	-0.10855
19	158	40.5369	41.2959	-0.10470
20	158	41.9248	42.7099	-0.10826
21	170	43.6152	44.3216	0.10470
22	170	45.0038	45.7326	0.10801
23	182	46.6849	47.3455	0.10470
24	182	48.0737	48.7539	0.10779
25	197	50.3747	50.3747	0.00000
26	197	51.7597	51.7597	0.00000
27	209	53.3631	53.3631	0.00000
28	209	54.7464	54.7464	0.00000

Table 4.10: This table shows the number of straws in each layer of the CDC. The radius at the center is the wire location half-way between the two endplates. The radius at the endplates is where the wire passes through the end plate. For axial layers, both radii are the same. For the stereo layers, the radius at the endplate is larger than it is at the center.

other, thereby enhancing pattern recognition.

The most critical requirement in the FDC design is to minimize the amount of the material not only in the active area of the chamber but also at the periphery: the frames, supporting systems and cables. The thickness of the detector in the active area limits the momentum resolution at low momenta. Photons from meson decays may convert in the detector frames or other material there and may not be properly reconstructed by the BCAL due to the strong magnetic field. Therefore the amount of the material at the periphery affects directly the efficiency of photon reconstruction. At the same time the mechanical structure must be robust enough to minimize the frame deformations and to allow for good gas tightness.

The central areas of the chambers close to the beam line require special configuration to

Layer	Straws	$\Delta\phi$	$x_u$	$y_u$	$x_c$	$y_c$	$x_d$	$y_d$
1	42	0.14960	10.7219	0.0000	10.7219	0.0000	10.7219	0.0000
2	42	0.14960	12.0460	0.9027	12.0460	0.9027	12.0460	0.9027
3	54	0.11636	13.7703	0.5246	13.7703	0.5246	13.7703	0.5246
4	54	0.11636	15.0746	1.4555	15.0746	1.4555	15.0746	1.4555
5	66	0.09520	16.9321	7.8813			16.9321	-7.8813
6	66	0.09520	17.8821	9.3834			18.6931	-7.6411
7	80	0.07854	20.6456	7.5497			20.3917	-8.2109
8	80	0.07854	21.7003	8.9161			22.0898	-7.9018
9	93	0.06756	23.8544	-7.8813			23.8544	7.8813
10	93	0.06756	25.5034	-7.4808			24.9402	9.1854
11	106	0.05928	27.1173	-8.1203			27.2560	7.6418
12	106	0.05928	28.7376	-7.6853			28.3924	8.8759
13	123	0.05108	31.3782	-0.3259	31.3782	-0.3259	31.3782	-0.3259
14	123	0.05108	32.7540	0.4965	32.7540	0.4965	32.7540	0.4965
15	135	0.04654	34.4335	0.2324	34.4335	0.2324	34.4335	0.2324
16	135	0.04654	35.7966	1.0749	35.7966	1.0749	35.7966	1.0749
17	146	0.04304	37.5553	-7.3360			37.3260	8.4250
18	146	0.04304	39.1008	-6.7679			38.5115	9.5679
19	158	0.03977	40.4909	-8.1144			40.5816	7.6479
20	158	0.03977	42.0358	-7.5580			41.8055	8.7427
21	170	0.03696	43.5551	8.2073			43.6730	-7.5549
22	170	0.03696	44.7775	9.2977			45.1997	-6.9613
23	182	0.03452	46.7735	7.3376			46.5901	-8.4239
24	182	0.03452	48.0273	8.3862			48.1186	-7.8451
25	197	0.03189	50.3719	-0.5328	50.3719	-0.5328	50.3719	-0.5328
26	197	0.03189	51.7589	0.2780	51.7589	0.278	51.7589	0.2780
27	209	0.03006	53.3622	0.3193	53.3622	0.3193	53.3622	0.3193
28	209	0.03006	54.7343	1.1504	54.7343	1.1504	54.7343	1.1504

Table 4.11: The location of the wires in the CDC. For each layer, the number of tubes, the angular rotation  $\Delta\phi$  between tubes, and the  $(x, y)$  coordinates of the wire at three  $z$  positions are given. The up-stream pair  $(x_u, y_u)$  are on the inside face of the up-stream endplate ( $z = 0$ ). The center pair are at the center of the chamber ( $z = 0$ ), and the down-stream pair  $(x_d, y_d)$  are on the inside face of the down-stream endplate ( $z = 150$ ). All distances are given in *cm* and angles in radians.

handle the otherwise unmanageable rates on the strips in this area.

The chambers will be positioned inside the bore of the solenoid where the strength of the magnetic field will be the largest. The direction of the magnetic field is roughly perpendicular to the wires. Not only does this affect the drift time of the electrons toward the wires but the Lorentz force causes a deflection of the avalanche position along the wire relative to the no magnetic field case. The latter effect can be minimized with an appropriate choice of gas mixture. Further details are provided in Section ??.

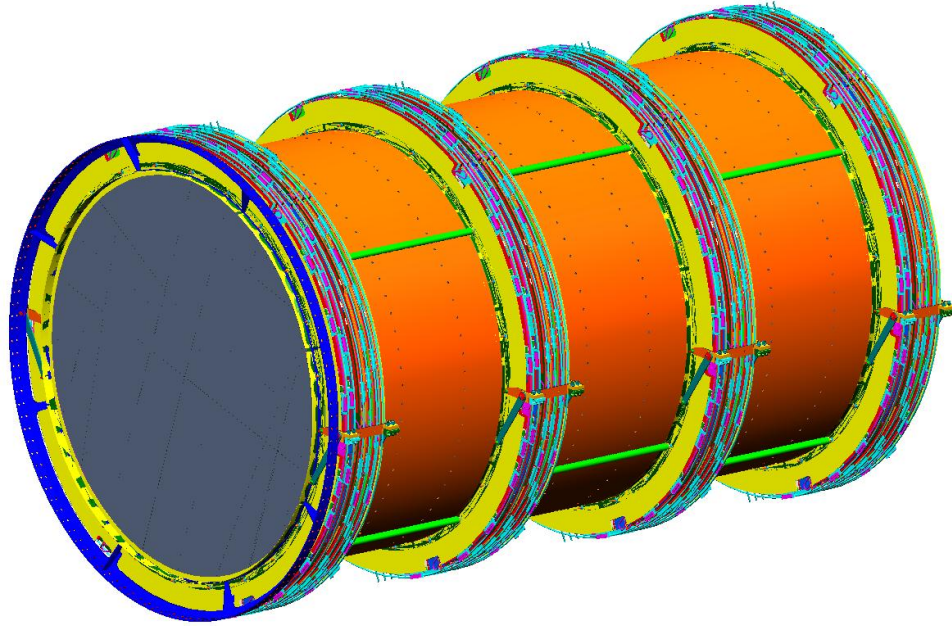


Figure 4.53: FDC detector: four tracking packages, each having six separate drift chambers (cells). Active area diameter is 97 cm, detector diameter 120 cm and total length of 174 cm.

The FDC detector includes four separate but identical <sup>15</sup> disk-shaped packages as shown in Fig. ???. Each package includes six independent planar drift chambers, or cells, with separate gas volumes. Each cell consists (Fig. ??) of a wire frame with alternating anode and field-shaping wires sandwiched between two cathode strip planes. Aluminized Mylar planes (ground planes) in between the cells shield the strips electrically and also separate the gas volumes of the different cells. Additional layers of thicker Mylar are added at the two ends of the package (end windows) to close the package gas volume, giving also some mechanical protection.

### Wire planes

The basic chamber element is a circular frame on which alternating sense and field wires are strung as cords across the chamber in one plane. Each plane contains 96 sense and 97 field wires, with the two side wires being field ones. The length of the sense wires varies from 20 cm on the sides to 97 cm in the middle of the chamber. The sense wires are 20  $\mu\text{m}$  diameter gold-plated tungsten, while the field wires are 80  $\mu\text{m}$  copper-beryllium also gold-plated wires. With a field-to-sense wire spacing of 5 mm and distance to both cathodes also of 5 mm, an electric field cell is formed around the sense wires of  $10 \times 10 \text{ mm}^2$  in a plane perpendicular to the wires. Positive HV is applied on the sense wires to achieve a gas gain of  $\sim 5 \cdot 10^4$ . Negative HV is applied on the field wires to improve the circular symmetry of the electric field in the cell (Fig. ?? right panel).

The frame itself is a 5 mm thick lamination (Fig. ??) consisting of three rings: a fiberglass (G10) ring, a Rohacell ring, and a printed circuit board (PCB) ring; all three elements are glued

<sup>15</sup>Except for the size of the deadened area on the wires discussed later

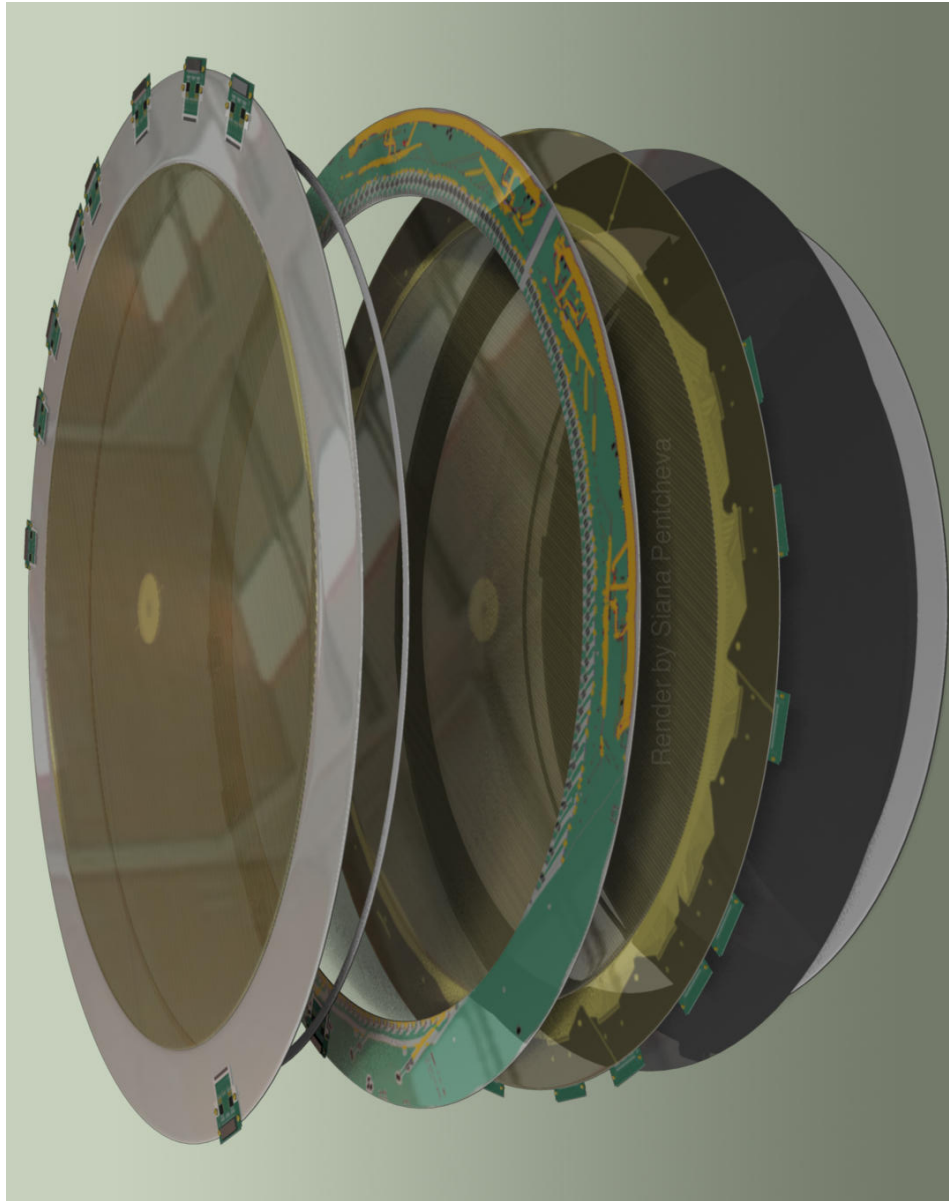


Figure 4.54: One detector cell (artistic view) from left to right: upstream cathode, spacer ring, wire plane, downstream cathode with ground plane on the back, end window (only at the end of the package).

together <sup>16</sup>. The inner and outer diameter of the frame are 100 and 120 cm correspondingly. To reduce the amount of the frame material, 80% of the G10 ring area was milled from 4.14 mm down to 0.8 mm thickness. This area was filled with sectors made out of Rohacell glued together <sup>17</sup> as a ring. The remaining 20% form a solid G10 ring that covers the holes for the mounting rods and supports mechanically the package assembly.

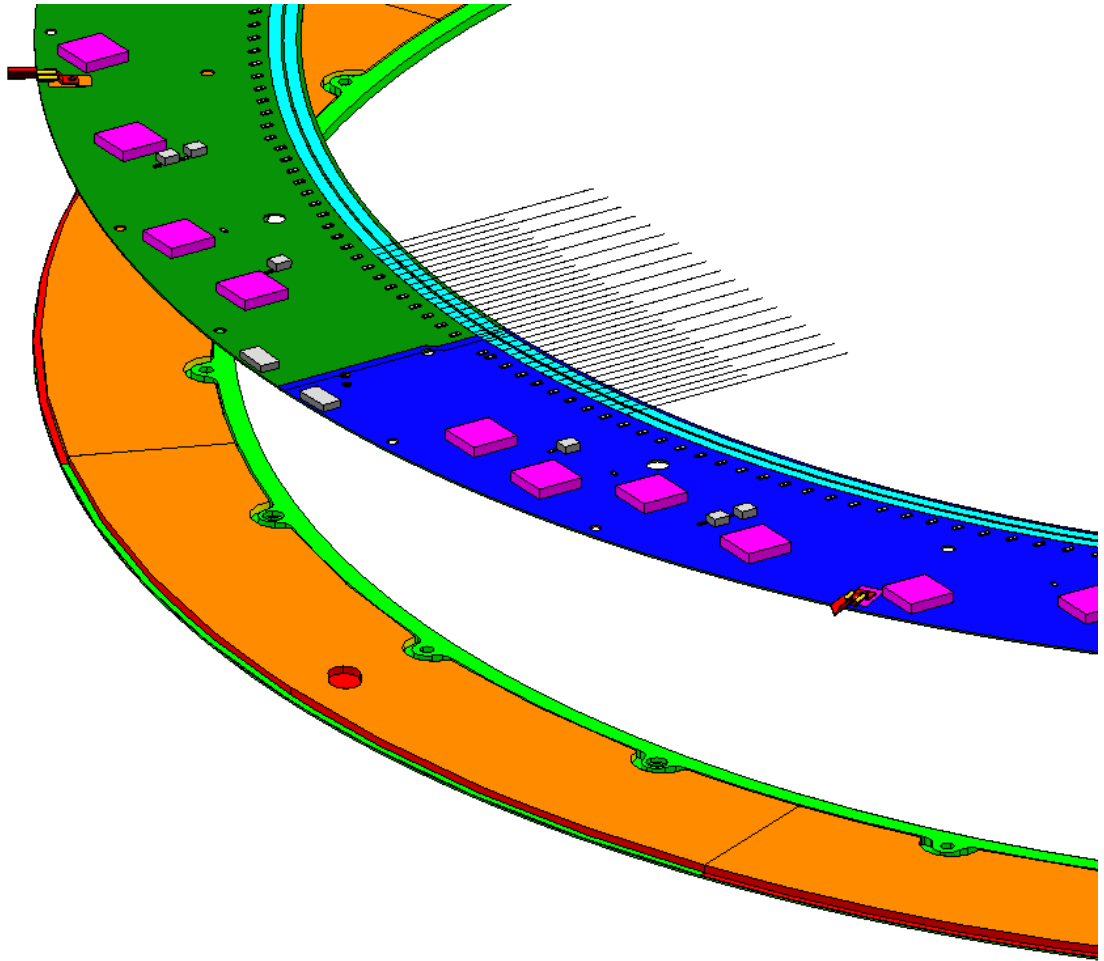


Figure 4.55: Wire frame lamination: PCB ring (top green and blue) with sense and field wires soldered on it (not all wires shown), Rohacell sectors (bottom orange with red sides), G10 frame (bottom green)

The PCB ring is formed by gluing <sup>18</sup> together six separate circuit boards. Two of the boards (4-layer PCB) are at the signal side of the wires, another two boards (2-layer PCB) are at the high voltage side of the wires, and the last two boards form the sides of the ring. As a first step, the G10 and Rohacell rings are glued together, after which the PCB ring is laminated to them.

<sup>16</sup>Using Hysol epoxy RE2039 resin and HD3561 hardener

<sup>17</sup>Using Scotchweld 1838 epoxy

<sup>18</sup>Scotchweld 1838 epoxy

The sense and field wires are strung between the high voltage and signal PCBs. First, the wire frame is mounted on a strong-back placed on a granite stringing table. Then the wires are strung above the frame between high precision pins attached with rails to the ends of the table. Next, the position of the strong-back (and the wire frame) is adjusted with respect the wires and the frame is raised so that the wires are just touching the wire pads on the boards. At this position the wires are fixed to the boards by applying small adhesive Kapton dots. Then the wires are glued<sup>19</sup> and soldered<sup>20</sup> to the boards.

The wire positions are measured (and corrected if needed) using a stepper motor<sup>21</sup> attached to a worm gear with a sensor running across the wires. The positions are kept within 50  $\mu\text{m}$  from the nominal value with a R.M.S. less than 25  $\mu\text{m}$ . Tensions of 20 g and 130 g are applied on the sense and field wires respectively. They are checked using a permanent magnet placed close to the wire and applying variable current from a function generator, thus finding the main resonance frequency that is related to the tension. The measured tensions did not vary by more than 2 g for the sense and by 10 g for the field wires.

Each high voltage PCB is divided into two independent sectors supplying positive HV for 20 (inner) and 28 (outer) sense wires respectively. Similarly the negative HV supply is split in two on each board. In total, on one wire plane we have 4 positive and 4 negative independent HV sectors connected to different channels on the HV supply.

The signal PCBs have HV capacitors separating the sense wires from the signal part of the board. The capacitors are positioned at the inner side of the PCBs, which is inside the gas volume. Due to improper soldering by the manufacturer that resulted in solder balls and enhanced leakage currents, all the HV capacitors had to be replaced<sup>22</sup>. Each signal PCB has two connectors for the pre-amplifiers, each serving 24 sense wires; in total there are four connectors or 96 channels per wire plane. Protective resistors of 1 M $\Omega$  are installed on both HV and signal PCBs. These resistors limit the current on each sense and field wire in case of sparks.

### Cathode strip planes

The cathode planes are copper coated Kapton foils stretched on G10 frames. The cathode G10 frame is similar in shape to the wire G10 frame. It has a thick ring covering the mounting holes and thin periphery on which the Kapton foil is glued<sup>23</sup>. Unlike the wire frames, there is no Rohacell material in the cathode frames. The Kapton foil thickness is 25  $\mu\text{m}$  while the copper layer is only 2  $\mu\text{m}$  to minimize the amount of the material in the active area.

Due to the big size of the cathode, one cathode foil is made out of three separate foils. The three pieces are first cut, aligned together, and then attached by gluing<sup>24</sup> thin (25  $\mu$ ) Kapton tape over the non-copper side of the foils. Thus, the cathode foil is made as a circle with the copper layer forming the strips, grounds, traces and connectors. The foils, and therefore strips, are aligned with a precision better than 100  $\mu\text{m}$ . The cathode foil is first glued to a transfer

<sup>19</sup>Epon Resin 828 and Versamid 140 hardener

<sup>20</sup>Almit Solder PN-KR19SHRMA Sn60-P2-0.3mm

<sup>21</sup>Parker S/SX 83-93 with ACR 9000 controller

<sup>22</sup>Using 220 nF AVX 1825JC102 rated for 4 kV except a few of the boards where AVX 1825HC102 rated for 3kV were used

<sup>23</sup>Using Hysol epoxy RE2039 resin and HD3561 hardener

<sup>24</sup>Using Hysol epoxy RE2039 resin and HD3561 hardener

ring so that it can be tensioned (500 N/m) and then glued <sup>25</sup> to the cathode frame.

The optimum cathode readout pitch is determined by the width of the induced charge distribution. It has been shown by several groups that minimal differential non-linearity is achieved when the cathode pitch is equal to the wire-cathode distance of 5 mm (e.g. [?]). This value is employed in the FDC design. Due to the higher rates, the central 24 strips are split in two halves. Thus, on one cathode there are 216 strips with lengths varying from 29 to 100 cm.

The strips end up with traces on one side leading to 24-channel connectors with the pads imprinted on the cathode. They are connected to the pre-amp cards with so called rigid-flex assemblies, each consisting of a flexible PCB (flex) and a daughter board on which the pre-amp is plugged. The flex part is needed to accommodate connection to the opposite side of the cathode frame (through an opening there) where there is space for the daughter boards to be installed. The soldering of the flex to the cathode turned out to be a delicate operation with some possibility of destroying the thin (2  $\mu\text{m}$ ) copper pads and thus the whole cathode. Therefore, the flexible sections are glued to the cathode pads using anisotropic conductive tape <sup>26</sup> that conducts only in the direction perpendicular to the surface. The tape is a head-bondable film with small (50  $\mu\text{m}$ ) silver-covered glass balls distributed randomly. After the tape is placed between the two contact areas, pressure and heat is applied with a specially designed tool to make the bond between the contacts.

To make sure this new technology works, samples were made and tested at significant temperature changes and also irradiated up to 1 kRad, the dose that is expected to be accumulated at this place of the detector in the hall for 10 years. Even all these tests didn't show problems, during the cathode production it turned out that some of the channels may have a resistance on the contacts that varies from few Ohms to several tens of Ohms, depending on the pressure applied and deformation at the contact area. The tests show that this is not aging but just mechanical problem related to frame deformations when handling of the cathodes. To mitigate the problem, special tools were designed to keep the cathodes flat in all the operations after the cards are glued.

The cathode described above is called type-1 cathode. There are two other types of cathodes with some modifications to the above description as explained in the next subsection.

### Package design

The chamber elements described above are installed in the package forming six separate cells. In addition at the two sides of the package there are end windows: 2 mil aluminized Mylar stretched on G10 frames similar to those for the cathodes. The ground planes (0.5 mil aluminized Mylar) that separate the cells are part of so called type-2 cathodes, a modification of the described above type-1 cathode, on the back side of which, 5 mm apart from the cathode foil, a 0.5 mil aluminized Mylar foil is stretched and glued to the frame. All the cells have the same structure except the outer cathodes of the two outer cells. These are type-3 cathodes, a modification of the type-2 cathode with holes punched through the ground plane. In this way the end windows take the atmospheric-chamber pressure difference.

Thus, starting from the upstream side, the package consists of:

- Upstream end window,

---

<sup>25</sup>Using Hysol epoxy RE2039 resin and HD3561 hardener

<sup>26</sup>3M Anisotropic Conductive Film Adhesive 7303 (5 mm width)

- cell #1 with type-3 cathode, spacer ring, wire frame, type-2 cathode
- cell #2 with type-1 cathode, spacer ring, wire frame, type-2 cathode
- ... same for cells #3, #4, and #5
- cell #6 with type-1 cathode, spacer ring, wire frame, type-3 cathode
- Downstream end window

In each cell the strips of the top and bottom cathode are oriented with respect to the wires at  $75^\circ$  and  $105^\circ$  respectively. Neighboring cells are rotated by  $60^\circ$  with respect to each other in order to improve track reconstruction decisions on the corresponding anode wire left/right ambiguities, hence improving the overall resolution.

Each cell forms a gas volume (Fig. ??) separated from the neighboring cells by the ground planes. There are gas holes at the periphery of all cathode planes to equalize the pressure on both sides and keep the cathode foil flat. The gas tightness of the package is achieved by Viton O-rings<sup>27</sup> installed in between all the chamber elements. There are O-ring grooves on one side of the the wire frames, type-1 cathodes and end-windows, and on both sides of the spacer rings. While testing the first production package it was found that there is significant oxygen contamination, up to few percent, inside the gas volume. It turned out that the oxygen penetrates between the O-rings and grooves especially on the G10 frames due to the fiber structure of the machined grooves. Therefore, the wire and cathode grooves are coated with epoxy<sup>28</sup>. In addition vacuum grease<sup>29</sup> is applied on all the O-rings. Thanks to this, the oxygen contamination in a package is reduced down to a negligible level of less than 100 ppm.

At the same time it turned out that the combination of Viton O-ring and vacuum grease prevents the appearance of corrosion on the copper layer of the cathodes that faces the O-rings. Significant damages of the thin copper layer especially at the traces leading to the connectors, were found on the first packages where EPDM O-rings were used, which required their refurbishment.

Two aluminum gusset rings (L-shape profile) at both sides of the package connected with 24 aluminum threaded rods through holes in all the package planes are used to compress the O-rings and hold the package elements together. Cuts are made in the gusset rings and then connected with carbon fibers to avoid closed loops inside the magnet.

The total thickness in the active area of each package is estimated to be  $\sim 0.43\%X_0$  (Table ??). Most of it comes from the cathode materials, dominated by the  $2\mu\text{m}$  copper layer and then from the Kapton itself.

### Central chamber area

The area of the chambers close to the beam line requires special treatment. First, the material along the beam should be minimized to reduce the additional background production there. There is no copper on all the cathodes in the area around the beam line within  $3.4\text{ cm}$  diameter, same for all the packages. This reduces the material along the beam line to  $0.26\%X_0$  per package (from Table ??), or  $1.04\%X_0$  in total, to be compared to  $3.5\%X_0$  thickness of the LH target.

<sup>27</sup>Viton 55 durometer

<sup>28</sup>Hysol epoxy RE2039 resin and HD3561 hardener

<sup>29</sup>Apiezon-L

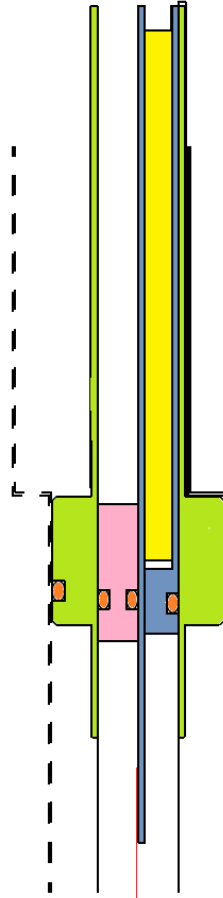


Figure 4.56: Cross-section showing separation of the different frames within one chamber cell. Top corresponds to the outer side of the detector, the gas volume is at the bottom side. From right to left: cathode type-2 (green frame) with ground and cathode foils on it (black lines), wire plane (gray frame with yellow Rohacell) with wires (red line), spacer ring (pink), cathode type-1 with cathode foil (black line), cathode type-2 from the next cell which ground foil and frame are shown with dashed line. The orange circles indicate the O-rings.

Material (description)	Thickness $\mu\text{m}$	Quantity	Total cm	$X_0$ cm	Fraction of $X_0$ %
Kapton (on all cathodes)	25	12	0.030	28.60	0.105
Copper (on Kapton)	2	12	0.0024	1.43	0.168
Mylar (on type-2,3 cathodes)	13	7	0.009	28.7	0.031
Aluminum (on type-2,3 cathodes)	< 0.1	7	< 0.00007	8.9	< 0.0008
Mylar (on end-windows)	50	2	0.010	28.7	0.035
Aluminum (on end-windows)	< 0.1	2	< 0.00002	8.9	< 0.0002
Argon (gas mixture)	13cm $\times$ 40%	1	5.2	10944	0.047
$CO_2$ (gas mixture)	13cm $\times$ 60%	1	7.8	18310	0.043
Total					0.430

Table 4.12: FDC material in the active area for one package

Second, the detector itself should be insensitive in a certain region around the beam line so that the rates on the electronic channels are reduced to a manageable level. The rates on the FDC have been studied by Monte Carlo simulations of the electromagnetic background [?]. A safe limit of  $\sim 130$  kHz was assumed for all the electronics channels. This requires insensitive areas with diameters 5.8 cm, 6 cm, 6.1 cm, and 7.8 cm respectively for the first, second, third, and fourth package. To have two pairs of interchangeable packages it was decided the insensitive area of the first two packages to be 6 cm and for the last two packages 7.8 cm diameter.

An electroplating technique with copper sulfate solution was used to thicken the sense wires (Fig. ??) from 20  $\mu\text{m}$  to  $\sim 80$   $\mu\text{m}$  and thus making the chamber insensitive in that area. The procedure consists of several plating cycles intervene with polishing cycles in which the polarity is reversed. The current on the electrodes and the timing of the cycles were optimized to obtain a smooth surface. A micro-controller system was developed [?] to control the electroplating procedure. After the procedure the wires are cleaned with water and alcohol.

### Package subsystems

- Gas system.

The six cells of the package are supplied with gas in parallel with manifolds at the supply and exhaust side. The gas enters the cell volume through nine 1 mm holes in the spacer ring of the cell and exits the volume in the same way at the opposite side of the ring. In addition there is a hole in the spacer ring connected to an individual gas line that is used to monitor the internal pressure of each cell separately. We assume a nominal gas flow through one package of 250 sccpm (standard cubic centimeters per minute) and a pressure in each cell of  $\sim 100$  Pa above the atmospheric..

- Grounding.

To minimize the noise the grounds of the wire and cathode planes are connected at many places at the periphery of the package. There are 16 connections per cell that bridge the grounds of the downstream cathode, wire frame, upstream cathode, and the downstream cathode of the next cell. The connections are done with 4 mil copper strips 1 cm wide



Figure 4.57: Wire deadening: a container filled with  $CuSO_4$  is raised against the wires; voltage is applied between the sense wires and a copper electrode inside the container.

pressed against the ground areas with clips. There are 16 additional connections per cell that bridge the elements of one cell on both sides (where possible) of the cathode readout cards. This is needed to ground the cards as close as possible to them. At the same time this provides mechanical strength of the cathode frame at the places where the cards are installed thus avoiding deformation of the conductive tape contacts. In total there are about 200 such ground connections per package.

- Cooling system.

The power dissipated by the pre-amplifier cards of one package is expected to be  $\sim 200$  W and therefore cooling is needed. Fluorinert<sup>30</sup> will be used as coolant which compared to water, will avoid fatal damages of the detector and the electronics in case of leakage. Six copper tubes (one per cell) of 4 mm outer diameter and 0.6 mm wall thickness, are shaped as circles and installed around the package using brackets attached to the pre-amplifier cards. There are two plastic manifolds at the input (each serving three cells) and two at the output of the tubes connected to the Fluorinert supply. Care has been taken to avoid closed conductive loops. A nominal pressure of 37 psig at the input and 4 psig at the output will allow to have temperature variations over the cooling loops of less than  $3^{\circ}$  C.

- HV connections.

All the positive high voltage (HV) sectors of one package are connected to a Radial 52-pin connector mounted at one of the package holding brackets with wires running at the upstream side of the package. Each individual channel has connectors at the upstream

---

<sup>30</sup>FC-770 by 3M

side of the package which simplifies the package assembly and allows for additional testing of each HV sector. The wiring of the negative HV sectors is analogous. The wires are running at the downstream side and a 52-pin connector is attached to the other holding bracket. Two HV cables coming from CAEN A1550P/N HV units are connected to one package serving the 24 positive/negative HV channels of the package.

- LV connections.

The low voltage (LV) of 3 V needed for the pre-amplifier cards (each drawing  $\sim 0.5$ A) is distributed with 18 m long cables, each supplying four cards in parallel. In addition, the same cables are used to distribute the threshold voltage to the wire discriminator cards. Due to the space limitation for the LV connectors the thickness of the wires is limited that results in a voltage drop along the cables of about  $\sim 3$  V. This increases the power dissipated inside the magnet by about 20%. Three types of cables are used that differ by the number of connectors (2 for the wire planes and 4 for the cathodes), and the distances between the connectors.

- Signal cabling.

132 signal cables are connected to the pre-amps of one package. To reduce the stress on the connectors, the cables are tightened to the gusset rings and the package spacers. The cables are shielded with copper braid and thin aluminum tape, but the braid is removed for the part of the cables that is inside the magnet. The cables are subdivided into four quadrants and bundled together outside of the magnet.

- Fiducialization.

Four targets are attached to the gusset rings of each package. They can be surveyed even when the detector is installed and cabled but only in one direction, along the beam axis, both from upstream and downstream sides. Additional optical targets are attached at the most upstream and downstream side of the FDC system.

## Readout Electronics

Two types of pre-amplifier cards are mounted on the chambers. One is for the strip readout which is a charge-sensitive preamplifier with pulse-shaping. It has a gain of 2.6 mV/fC, 130 fC dynamic range and 14 ns peaking time. The other type used to read the sense wires has a 0.77 mV/fC pre-amplifier with 260 fC dynamic range and in addition - a built-in discriminator that outputs LVDS signals. Both cards use GAS-II ASIC and have resistors that define the different settings.

The FDC readout will employ 125 ps F1 TDCs for the anode wire drift time readout and 125 MHz FADCs for the cathode readout. This would enable commonality with the readout electronics planned for the other GLUEX detector subsystems. Note that with a clock rate of 125 MHz on the FADCs, time fitting algorithms matched to the chamber pulse shape can be employed to provide a time resolution of  $\sim 2$  ns (amounting to  $\sim 40\%$  of the time bin width). This timing information from the cathode signals would aid in pattern recognition of multiple tracks passing through the chamber volume.

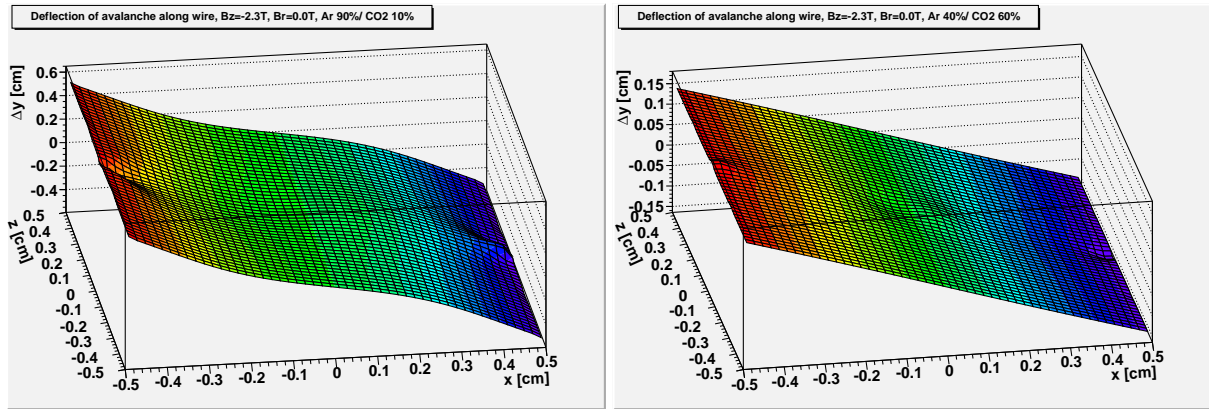


Figure 4.58: Results of GARFIELD calculations for the deflection of the avalanche position (relative to the  $B=0$  case) as a function of the position of the ionization within the cell for two different gas mixtures: 90% Ar / 10%  $\text{CO}_2$  (left) and 40%Ar / 60%  $\text{CO}_2$  (right). The high voltage settings were  $S=+1550$  V,  $F=-200$  V, and  $S=+2200$  V,  $F=-500$  V, respectively.

### Gas Considerations

There are several basic requirements that need to be met by the chamber gas that will be used for the FDC system. These include a high drift velocity (50-60  $\mu\text{m}/\text{ns}$ ), low Lorentz angle ( $< 10^\circ$ ), and for safety, we much prefer a non-flammable mixture. It is important to understand that the performance of a cathode chamber in terms of cathode position resolution is reasonably insensitive to the exact values of the gas parameters. Here variations of the drift velocity or non-uniform drift velocities as a function of  $E/p$  (i.e. electric field/pressure) are relatively unimportant. For the same reason, the cathode readout operation is immune to modest variations of temperature and pressure. Variations in gas gain on the order of 20% do not strongly affect the cathode resolution since a relative charge measurement in adjacent strips is involved.

However, the gas mixture and its control are essential to consider carefully for the operation of the MWDC. In order to enable accurate calibrations of the drift times, it is essential that the gas mixture is stable, which amounts to constructing a gas handling system that carefully controls the gas mixture, as well as hall controls to fix the temperature and relative humidity as much as possible.

For an Argon/ $\text{CO}_2$  mixture, the smaller the percentage of Argon, the smaller the amount of deflection of the avalanche position along the wire due to the Lorentz force under operating electric field configurations. Figure ?? compares the deflection along the wire as a function of the position of the ionization within a drift cell for a 90%/10% Ar/ $\text{CO}_2$  mixture and a 40%/60% mixture. We have opted for the 40% Ar/ 60%  $\text{CO}_2$  mixture, for which the maximum deflection is about a factor of four smaller than for the 90%/10% Ar/ $\text{CO}_2$  mixture for the highest magnetic field we expect to see in the region of the chambers. Figure ?? shows the field lines for two possible wire configurations (with and without field-shaping wires). The drift-to-time relationship for the 40%/60% mixture is shown in Figure ?. The presence of a non-zero magnetic field lengthens the minimum drift time for ionizations occurring near the field wires by a relatively small amount relative to the  $B=0$  case.

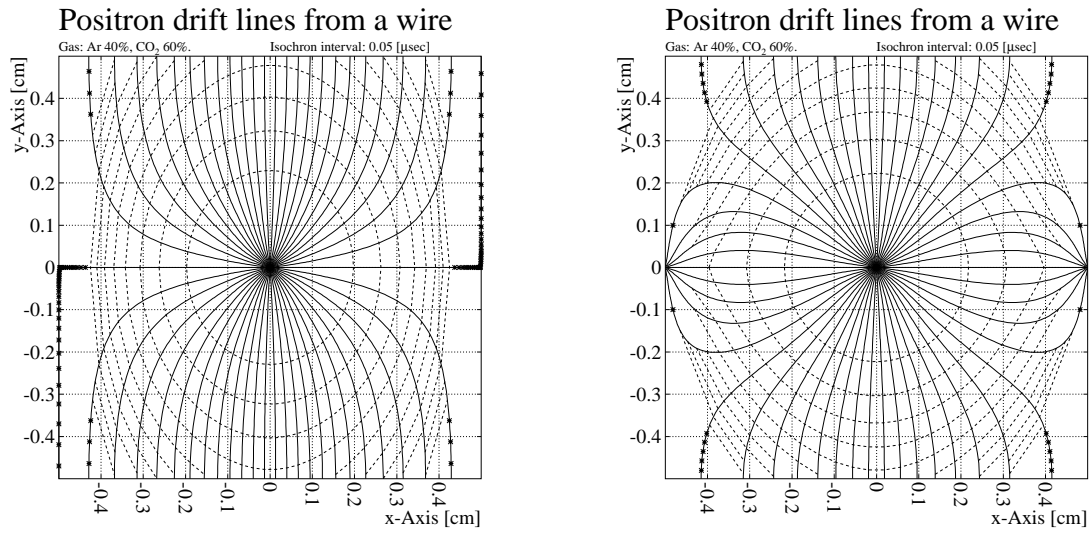


Figure 4.59: GARFIELD calculations of electric field lines (for a  $B = -2.3$  T field configuration) within a square drift cell for a 40% argon - 60% CO<sub>2</sub> gas mixture for electrode configurations without (left) and with (right) field-shaping wires.

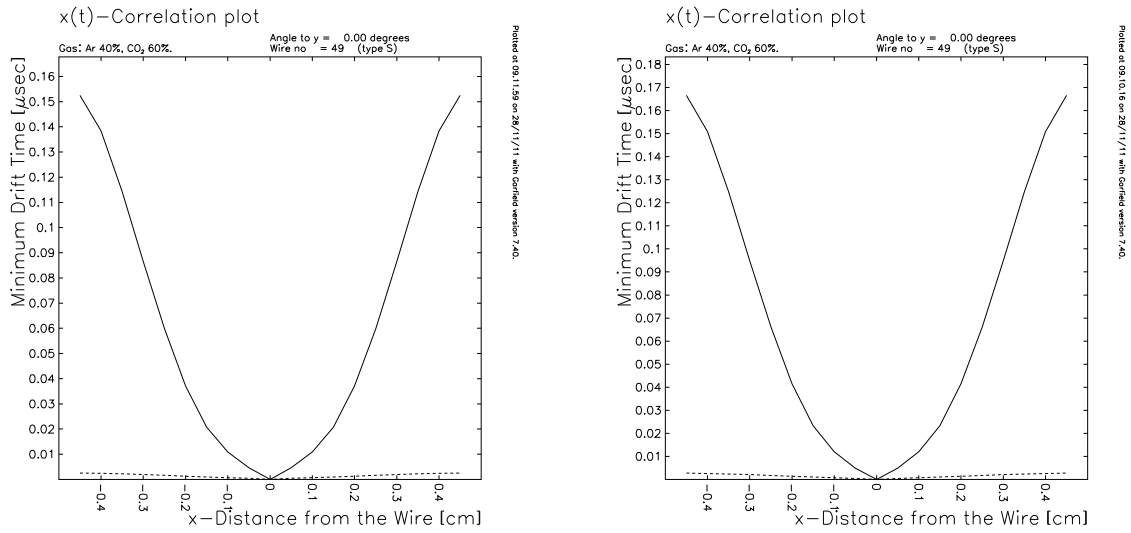


Figure 4.60: Relationship between drift time and distance for  $B=0$  (left) and  $B=-2.3$  T (right) from a GARFIELD calculation for an FDC cell.

## 4.8 Particle Identification

### 4.8.1 Overview

Particle identification in the GLUEX detector (i.e., the separation of pions, kaons, and protons) will incorporate information from at least four different subsystems – two subsystems in the central region and two in the forward region.

1. Low momentum central tracks will be identified using  $dE/dx$  measurements from the Central Drift Chamber (CDC).
2. A time of flight measurement from the barrel calorimeter (BCAL) will also provide identification information for central tracks. The CDC and the BCAL working in conjunction will provide an excellent means for identifying recoiling protons from the target.
3. Higher momentum forward-going kaons and pions will be distinguished using a Cerenkov detector. Two possibilities for this detector exist – a threshold gas option (CKOV) using  $C_4F_{10}$ , and a Quartz-based DIRC option; each will be discussed in detail in a later section.
4. Time of Flight (TOF) information for forward-going tracks with momenta less than around  $2.5 \text{ GeV}/c$  will be provided by a scintillator wall 500 cm downstream of the target.

Once information is gathered from each of these four elements, the information will be combined into likelihoods in order to provide a unified way of making a particle identification decision. The likelihood method will be discussed in section ??.

To illustrate the overall features of the particle identification, consider the reaction  $\gamma p \rightarrow K^* \bar{K}^* p$ . This reaction has kinematics that are typical of the reactions to be studied by the GlueX experiment. The  $K^* \bar{K}^*$  system is produced peripherally with a  $t$  dependence of  $e^{-10t}$ . The proton recoils predominantly in the central region with a momentum below  $2 \text{ GeV}/c$ . The central kaons from the  $K^*$  decays range in momentum up to  $5 \text{ GeV}/c$ ; central pions range up to  $3.5 \text{ GeV}/c$ . Forward kaons and pions have higher momenta, in general, than those in the central region, kaons ranging up to  $7 \text{ GeV}/c$ , and pions up to  $5 \text{ GeV}/c$ .

Each of the five tracks in the final state can be categorized according to the particle identification elements it encounters. Figure ?? shows the percentage of tracks from  $\gamma p \rightarrow K^* \bar{K}^* p$  encountering each of the eight possible combinations of PID detectors. Cases 1 (CDC) and 2 (CDC,BCAL) are purely central tracks; cases 6 (CKOV,TOF) and 7 (CDC,CKOV,TOF) are the dominantly forward tracks. Notice that the proton usually lands in the central region, and larger fractions of the pions and kaons go forward.

In the central region, the CDC and BCAL effectively work together to identify the recoiling proton. Figure ?? shows the momentum spectrum of the central protons from  $\gamma p \rightarrow K^* \bar{K}^* p$  overlaid with  $K/p$  and  $\pi/p$  separations from the CDC and BCAL. For the  $dE/dx$  measurements from the CDC, an Argon-based gas was assumed and the resolution was estimated to be 10%. A 250 ps time resolution was assumed for the BCAL, and a typical path length of 2 m was used for the figure. The entire range of the central proton momentum spectrum is well covered. Protons in the forward region also have low momenta and are easily identified by the TOF wall.

In addition to the recoiling proton, however, a fraction of the pions and kaons in the reaction  $\gamma p \rightarrow K^* \bar{K}^* p$  end up in the central region. Figure ?? shows estimated  $\pi/K$  separation curves (using the same detector parameters as above) overlaid on the pion and kaon momentum

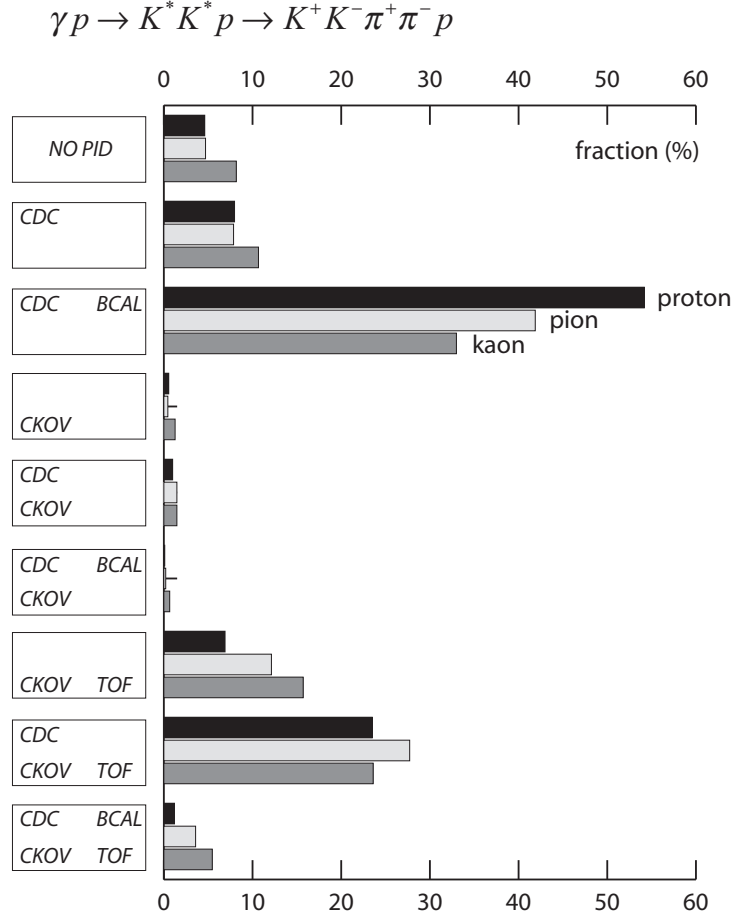


Figure 4.61: The fraction of tracks from the reaction  $\gamma p \rightarrow K^* \bar{K}^* p$  detected by different combinations of particle identification elements.

distributions. Some fraction of the higher momentum tracks cannot be identified, but the strong separations in the forward region compensate.

The momentum spectra of forward-going pions and kaons from the  $\gamma p \rightarrow K^* \bar{K}^* p$  reaction are shown in Figure ???. These will be identified by a time of flight measurement from the forward TOF wall in conjunction with either a gas Cerenkov system (CKOV) or a DIRC. The expected  $\pi/K$  separations from each option are overlaid on the momentum spectra. Typical TOF parameters were used in generating the time separation: a detector time resolution of 70 ps, a typical flight length of 5.0 m, and a conservative momentum resolution of 1% and length resolution of 1% added on when projecting different particle hypotheses to the wall.

The performance of the gas Cerenkov system is expressed in terms of the average number of photoelectrons,  $N_{pe}$ , for  $\pi$  mesons traversing 80 cm of  $C_4F_{10}$  gas with index of refraction  $n = 1.0015$ . The momentum threshold for  $\pi$  and  $K$  mesons are 2.5 and 9.0  $GeV/c$  respectively and the light yield per radiator length is given by:

$$\frac{dN_{pe}}{dx} = N_o \cdot \sin^2 \theta_c = N_o \cdot \left(1 - \frac{1}{\beta^2 n^2}\right) \quad (4.15)$$

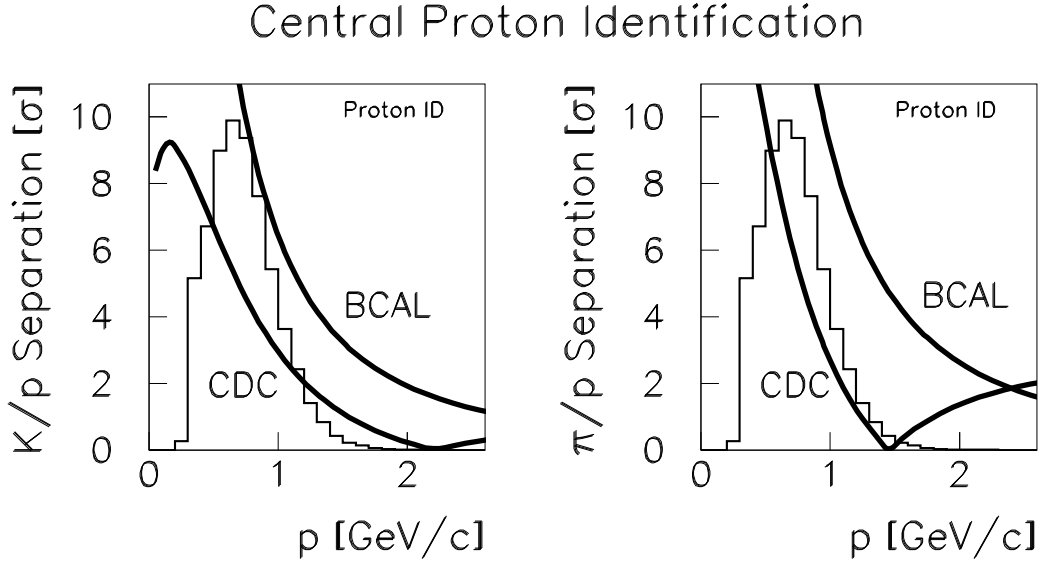


Figure 4.62: Identifying protons in the central region of the detector. The left plot shows  $K/p$  separation; the right shows  $\pi/p$ . The histogram in each is the momentum distribution for central protons from the reaction  $\gamma p \rightarrow K^* \bar{K}^* p$ . The curves are estimates of the separating power (in numbers of sigma) of the CDC  $dE/dx$  and the BCAL time of flight measurements.

and since  $n \approx 1$ , in the relativistic limit  $\beta \rightarrow 1$ :

$$\frac{dN_{pe}}{dx} \approx N_o \cdot 2(n-1) \quad (4.16)$$

$N_o$  is the figure of merit of a Čerenkov counter taking into account all efficiencies in the system and for a counter of reasonably good design  $N_o \approx 90 \text{ cm}^{-1}$ . Based on this, the average photoelectron yield for the Čerenkov counter will be about 21 in the relativistic limit.

The gas Čerenkov option leaves a significant gap in momentum where the  $\pi/K$  separation is restricted. The TOF separating power falls below  $3\sigma$  at a momentum near  $2 \text{ GeV}/c$ , while the pion threshold in the  $\text{C}_4\text{F}_{10}$  gas is  $2.5 \text{ GeV}/c$ .

The DIRC option, on the other hand, will use a higher index of refraction (Quartz) to make a measurement of the Čerenkov opening angle:

$$\cos \theta = \frac{1}{\beta n} \quad (4.17)$$

The estimated  $\pi/K$  separation of figure ?? assumed a resolution on the opening angle measurement of 2.1 mrad. More details on the DIRC will be given in a later section.

**Required Design Parameters** For the Čerenkov counter, assuming that the inefficiency for detection is given by  $e^{-N_{pe}}$ , then the efficiency for detecting pions exceeds 95% when the  $\pi$  momentum is above  $3 \text{ GeV}/c$ . At this momentum the TOF difference is about 210 ps. For 95% ( $3\sigma$ ) efficiency to separate pions and kaons with the TOF at this momentum, the time resolution,  $\sigma_t$  should be less than about 70 ps.

## Central Pion/Kaon Identification

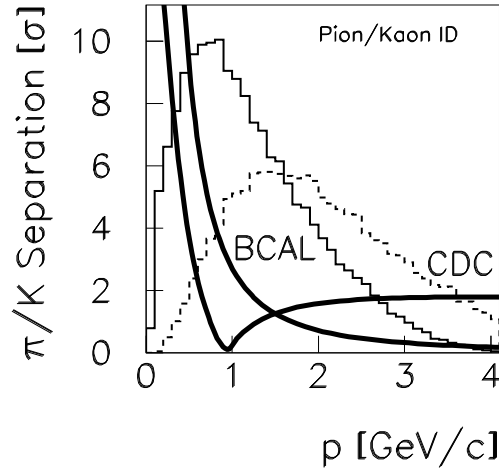


Figure 4.63: Identifying pions and kaons in the central region of the detector. The solid histogram is the central pion momentum spectrum; the dashed histogram is the momentum spectrum of central kaons. The curves are estimates of the separating power (in numbers of sigma) of the CDC  $dE/dx$  and the BCAL time of flight measurements.

#### $dE/dx$ in the chambers

As described above, there is a subset of the low momentum charged particles which will not reach a time of flight counter, or will reach them after spiraling so many times in the magnet that the TOF information will be very difficult to use. For these particles,  $dE/dx$  information from the CDC chamber will be the primary source of identification. Fortunately, these particles all have momenta smaller than about  $450 \text{ MeV}$ , which is exactly where  $dE/dx$  will work the best. This detector has been discussed in an earlier section.

### 4.8.2 The Time-of-flight System

#### Barrel Time-of-flight Measurement

The design of the barrel calorimeter is dictated primarily by the available space inside the magnet and the method chosen for photon conversion. Charged particles emitted at large angles to the beam often have low velocity so even moderate time resolution is sufficient to distinguish pions from kaons. The lead/fiber design of the barrel calorimeter provides a large number of scintillator samples as a particle traverses the individual fibers. The KLOE collaboration has demonstrated [?] an RMS time resolution of  $252 \text{ ps}$  for minimum ionizing particles traversing 19 layers of lead and fiber. This value will be used as an estimate of the performance that can be achieved in the TOF measurement from the calorimeter in HALL D. This detector has been discussed in an earlier section of this report.

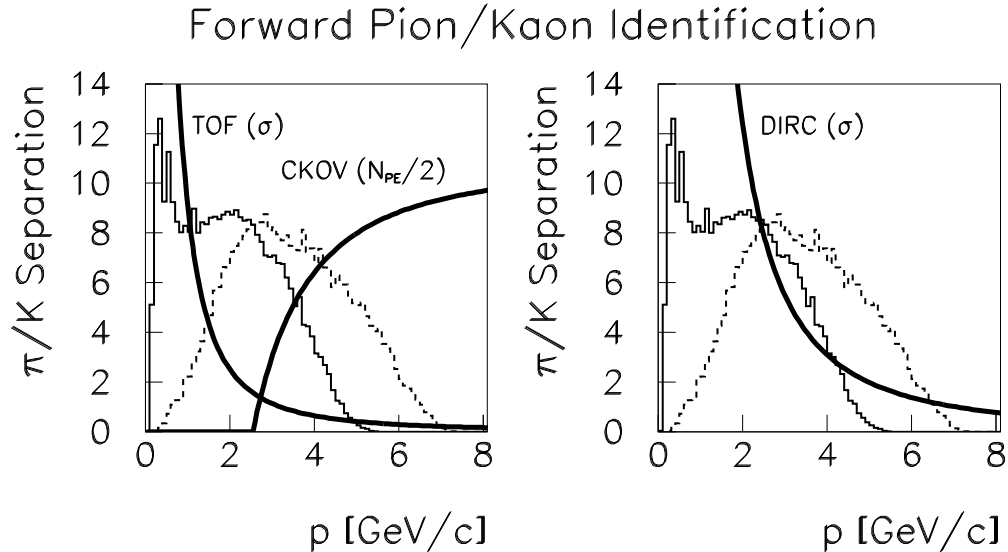


Figure 4.64: Identifying pions and kaons in the forward region of the detector. The left plot shows the gas Cerenkov option; the right plot is for the DIRC option. In each case, the solid histogram is the forward pion momentum distribution; the dashed is the forward kaon distribution. The curves of the left plot are the estimated  $\pi/K$  separations of the TOF and CKOV systems. The TOF  $\pi/K$  separation is expressed in numbers of sigma; the CKOV performance is plotted as the number of expected photoelectrons divided by two. The right plot shows the DIRC  $\pi/K$  separation in numbers of sigma. (Note the TOF will be used in conjunction with either option but is shown only in the left plot.)

### The Lead Glass Forward Calorimeter

Located just upstream of the forward electromagnetic calorimeter, the LGD, and downstream of the Čerenkov counter will be the forward time-of-flight system, the TOF. The goal of the forward TOF is to separate  $K^\pm$  from  $\pi^\pm$  among forward-going charged particles. The TOF will also provide a forward multiplicity count to be used in the level-one trigger.

Assuming a momentum resolution of about 1% and a particle path length resolution of 1% an overall TOF time resolution of 80 ps should allow for  $K/\pi$  separation at the  $3\sigma$  level up to a momentum of  $2.5 \text{ GeV}/c$ . The TOF will consist of two planes of scintillation counters, each 2.5 m long, 6 cm wide and 1.25 cm thick. Each counter will be read out at both ends. The counters in one wall will be oriented perpendicular to the other wall. The total module count is 84 modules and the total channel count is 168 for the number of FADC's, constant fraction discriminators and TDC's.

The scintillator bars need to be 2.5 m long to cover the active regions of the Čerenkov counter. The 6 cm width of the bars is set by the requirement that the overlap of charged particles from the same event at the TOF in any one bar be acceptably small ( $< 2\%$ ). From Monte Carlo simulations of  $\gamma p \rightarrow K^* \bar{K}^* p$  it was found that a 6 cm width satisfies the occupancy requirement. (We studied four reactions, but are most vulnerable to this one because of its low Q value.) Specifically we find a probability of 0.22% that two charged particles go through just

one bar in both the front and back planes. The thickness of the scintillation bars, the dimension along the beam direction, is set by the requirement that sufficient light be produced to meet the time resolution requirements, while at the same time minimizing the amount of material in front of the LGD.

### Prototype Studies

Extensive prototype studies have been carried out to optimize the TOF system design. Data using scintillation bars of various dimensions and manufacture and various phototubes were collected using a cosmic ray test facility at Indiana University. Data were collected in several data runs with hadron beams at the Institute for High Energy Physics (IHEP) in Protvino, Russia. During the data runs we also explored the possibility of using Čerenkov light in Plexiglas (non-scintillating) bars to exploit prompt Čerenkov light to build a TOF system. Results of the IHEP tests have been presented at various instrumentation conferences and publications [?, ?, ?, ?]. Further beam tests at IHEP are planned using 2.5 m scintillator bars with four elements in each of two walls in early 2005.

**Cosmic Ray Test Facility** Figure ?? shows part of the cosmic ray test facility. A large light-tight box was prepared to accommodate a 2-m long scintillator bar and a cosmic ray telescope consisting of two small scintillation counters that can be positioned along the bar. The scintillation bar under test is read out at both ends with Phillips XP2020 PMT's and their signals are read into separate channels of a TDC and ADC. Trigger electronics use signals from the telescope to define the passage of a cosmic ray particle and define the start signal for the TDC and gate for the ADC.



Figure 4.65: Part of the cosmic ray test facility showing a light-tight box inside of which is a 2-m long scintillator bar, read out at both ends, as well a trigger telescope with two small scintillation counters that can be positioned along the bar.

**Measurements Made in a Hadron Beam at IHEP** Several data runs testing TOF prototype modules were made at the IHEP accelerator. The setup for these runs is shown in Figure ???. The two bars under test were coupled to PMTs T1 through T4 at their ends. The bars could be moved transverse to the beam. We define  $x$  as the position of the center of the long scintillator relative to the beam with  $x=0$  at the center of the bar.

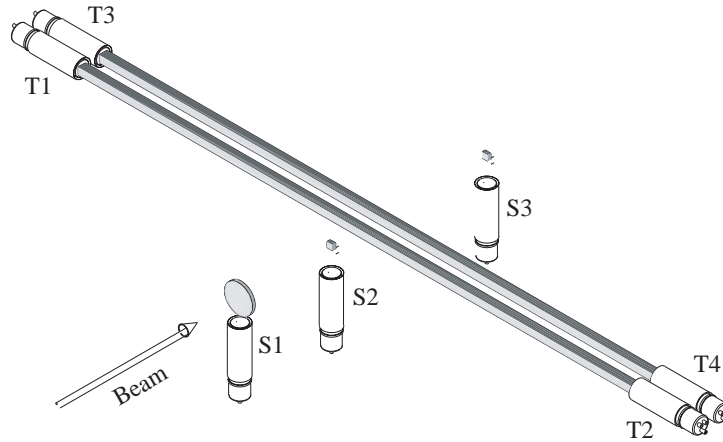


Figure 4.66: The setup for the beam tests at IHEP at Serpukhov.

The beam defining counters shown in Figure ?? are S1, S2, and S3. The cross sectional size of the beam was large compared to the 2 cm by 2 cm size of S2 and S3. S2 and S3 were each 1.25 cm thick and both coupled to an XP2020 phototube with a 5 cm air gap. S1 was not used for timing purposes, nor to define the effective size of the beam.

The first data run at IHEP was used to test 2-m long counters with square cross sections of  $2.5 \times 2.5 \text{ cm}^2$  and  $5.0 \times 5.0 \text{ cm}^2$ . The scintillator is type EJ-200, produced by the Eljen Corporation. This scintillator has a decay time of 2.1 ns, a bulk attenuation length of 4 m, an index of refraction of 1.58, a peak in the emission spectrum at 425 nm, and a light output equal to 64% of that of Anthracene. The surfaces of two of the four long sides of each bar were in contact with the casting form and had no other preparation. The other two long sides and the two ends of each bar were diamond fly-cut in order to minimize losses due to surface imperfections. A phototube was placed on each end of each bar. The two bars, with their phototubes, were placed in a light-tight box. The beam was a 3 to 40 GeV/c positive beam with variable energy.

Table ?? shows the results for average time resolution measured for various combinations of scintillation bars and PMTs. Figure ?? shows the variation of time resolution as a function of position of the beam along the bar ( $x=0$  at the center) for the two types of bars.

In a later data run 2 m-long bars of cross sections  $2.5 \times 6.0 \text{ cm}^2$  were tested using a 5 GeV/c beam. A typical PMT pulse observed after a 40 m cable is shown in Figure ???. These signals went to constant fraction discriminators (CFD) to eliminate time corrections associated with variations of signal amplitude. Measurements using leading edge discriminators (LED) and Analog to Digital Converters (ADC) were also made. In this case a time vs. amplitude correction

Table 4.13: Time resolution for various phototubes.

Phototube	$T_{av}$ Time Resolution (ps)
<b>2.5 cm Bar</b>	
XP2020	102
FEU 115	172
Hamamatsu R5506	167
Hamamatsu R5946	102
<b>5.0 cm Bar</b>	
XP2020	89
XP2020/UR	82

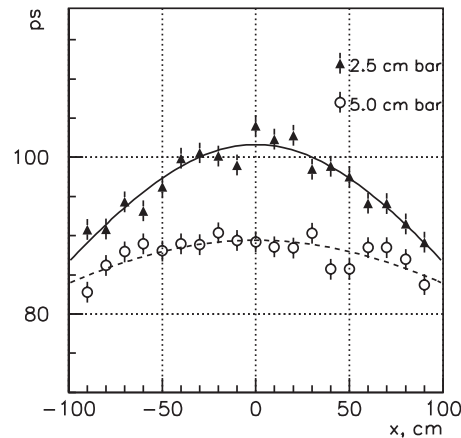


Figure 4.67: The average time resolution for a 2 m-long scintillation counter read out at both ends with Phillips XP2020 PMTs as a function of position of a charged particle beam along the bar ( $x=0$  at the center of the bar). Bars of square cross section  $2.5 \times 2.5 \text{ cm}^2$  and  $5.0 \times 5.0 \text{ cm}^2$  were tested.

was made using measured signal pulse heights. Custom made Time to Digital Converters (TDC) with 26.5 ps least count were used for time measurements. The S3 signal was used as the common start and signals from the other beam counters and the bars under test were used as stop signals. The intrinsic time resolution of the electronics was 18 ps (r.m.s.) as measured by using the S3 signal to both to start and to stop the TDC. The measured time resolution of S2 and S3 was 70 ps.

Figure ?? shows the average time resolution as a function of the position of the beam along the 2 m-long scintillator bar ( $x=0$  at the center of the bar). In Figure ??a and figure ??b the open circles show resolution using a single bar and the closed circles show resolution using information from both bars. In (a) the beam passed through 2.5 cm of scintillator and in (b) through 6.0 cm of scintillator. In (a) and (b) a constant fraction discriminator was used and in (c) pulse height information was used to do the time-walk correction for the case when the beam passed through 2.5 cm of scintillator.

Using constant fraction discriminators the time resolution for two bars was measured to

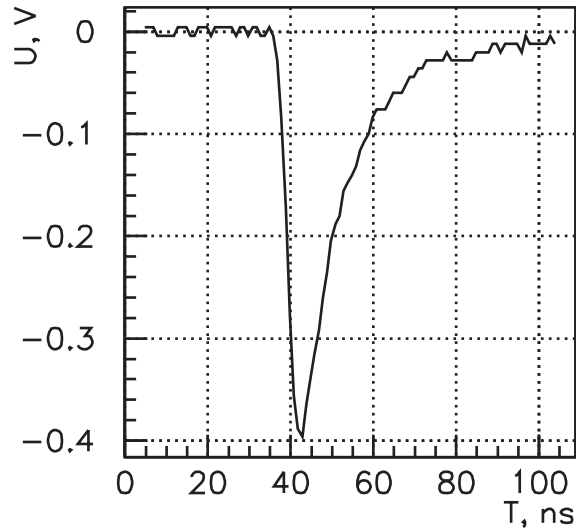


Figure 4.68: A typical pulse a Phillips XP2020 PMT attached to a 2 m long scintillation bar after the signal passed through a 40 m delay cable.

be less than 40 and 60 ps when particle cross 6.0 cm and 2.5 cm of scintillator respectively. The results obtained with leading edge discriminators and corrected for time walk effect were similar to those measured with CFDs.

The tests described above in the hadron beam are described in more detail in references [?, ?]. In order to minimize the amount of material in front of the LGD bars of 1.25 cm thickness were tested and compared and those measurements were reported in reference [?].

Comparison of timing properties for the  $1.25 \times 6.0 \text{ cm}^2$  and  $2.5 \times 6.0 \text{ cm}^2$  bars shows that the time resolutions at the center of the bar are better by factor of  $\approx 1.4$  for the  $2.5 \times 6.0 \text{ cm}^2$  bar. But the time resolutions at the bar edges are the same in both cases indicating that near the PMT's the time resolution does not depend on photoelectron statistics.

### Conclusions and remaining issues

Based on the results presented above, therefore, we have chosen the 1.25 cm thick, 6 cm wide bar for the TOF wall. As shown in Figure ??a, the time resolution for two bars of this size is 80 ps or less at all point on the bar – satisfying our design criterion.

In addition to optimizing the time resolution, a practical consideration in the choice of bar geometry is the ability to accommodate magnetic shielding for the approximately 200 G magnetic field in the vicinity of the XP2020s. For a 6 cm wide bar the phototubes can simply be attached to scintillator snouts and then surrounded by magnetic shielding; this cannot be done for bars less than 6 cm wide.

### 4.8.3 The Start Counter

#### Overview

The purpose of the GlueX Start Counter will be, in coincidence with the tagger, to identify the electron beam bucket associated with the detected particles resulting from 9 GeV linearly

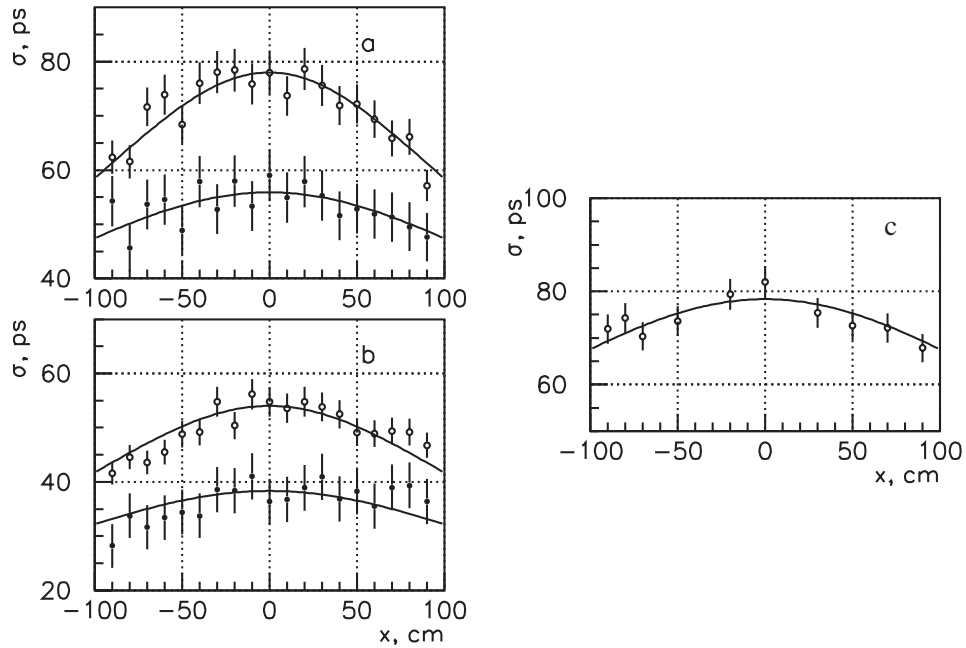


Figure 4.69: Average time resolution as a function of the position of the beam along the 2 m-long long scintillator bar ( $x=0$  at the center of the bar). In (a) and (b) the open circles show resolution using a single bar and the closed circles show resolution using information from both bars. In (a) the beam passed through 2.5 cm of scintillator and in (b) through 6.0 cm of scintillator. In (a) and (b) a constant fraction discriminator was used and in (c) pulse height information was used to do the time-walk correction for the case when the beam passed through 2.5 cm of scintillator.

polarized photons incident on a liquid  $H_2$  target. It is designed to operate at tagged photon intensities of up to  $10^8 \gamma/s$  and will provide a fast signal which is used in the level-1 trigger of the experiment. Furthermore the Start Counter detector will provide excellent solid angle coverage,  $\sim 90\%$  of  $4\pi$ hermicity, and a high degree of segmentation for background rejection. EJ-200 scintillator material manufactured by Eljen Technology, which provides a decay time on the order of 2 ns and a long attenuation length, will be used in order to properly identify the beam buckets which are about 2 ns apart. The detector consists of a cylindrical array of 30 scintillators with *pointed* ends that bend towards the beam at the downstream end. The support structure will be kept at an absolute minimum in the active region of the detector, and is to be made up of Rohacell and carbon fiber. Silicon PhotoMultiplier (SiPM) detectors have been selected as the readout system. These detectors are not affected by the high magnetic field produced by the GlueX superconducting solenoid magnet. Moreover, the SiPMs will be placed as close as possible ( $< 1$  mm) to the upstream end of each scintillator element, thereby minimizing the loss of scintillation light.

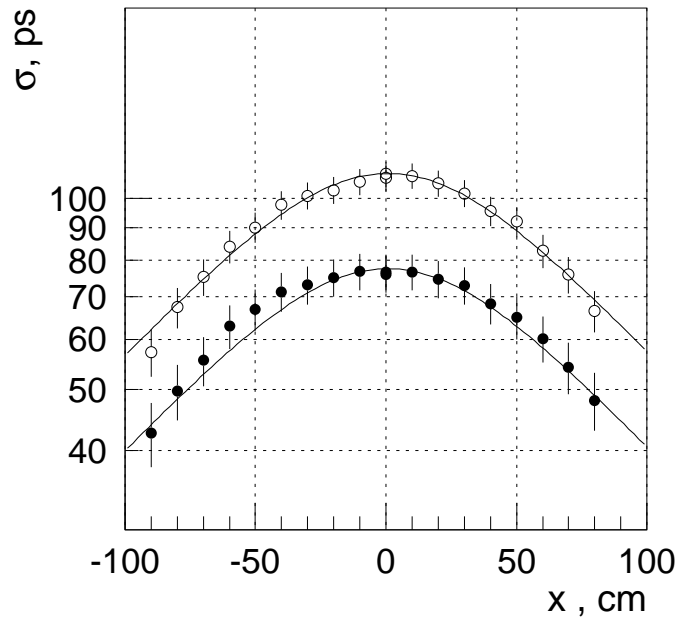


Figure 4.70: The time resolution for one (○) and two (●)  $1.25 \times 6.0 \text{ cm}^2$  bars viewed by XP2020 PMT's.

### Paddle Geometry

Each individual paddle of the Start Counter is machined from a long, thin, plastic (polyvinyl toluene) EJ-200 scintillator bar that is initially manufactured by Eljen Technology to be 600 mm in length, 3 mm thick, and  $20 \pm 2$  mm wide. Eljen Technology bends each scintillator around a highly polished aluminum drum by applying localized infrared heating to the bend region. The bent scintillator bars are then sent to McNeal Enterprises, a plastic fabrication company, where they are machined to the following desired geometry (see figure ??). The paddles are designed to consist of three sections, described from the upstream to the downstream end of the target. First is the straight section, that runs parallel to the target chamber, is 394.65 mm in length. Second is the bend region which consists of a  $18.5^\circ$  arc of radius 120 cm which is downstream of the straight section. Third is the tapered region, which is downstream of the target chamber, that bends towards the beam line and ends at a height of 20 mm above the beam line. After the straight bar is bent to the desired geometry, the two flat surfaces that are oriented orthogonal to the wide, top and bottom surfaces, are cut at a  $6^\circ$  angle. During this process the width of the top and bottom surfaces are machined to be 16.92 mm and 16.29 mm wide respectively. Each of the 30 paddles may be rotated  $12^\circ$  with respect to the paddle that preceded it so that they form a cylindrical shape with a conical end (See figure 2). The geometry of the Start Counter increases solid angle coverage while minimizing multiple scattering. The complete assembly is designed to have a diameter of  $\sim 155$  mm at the upstream end and a diameter of 40 mm at the downstream end of the target(see figure ??).



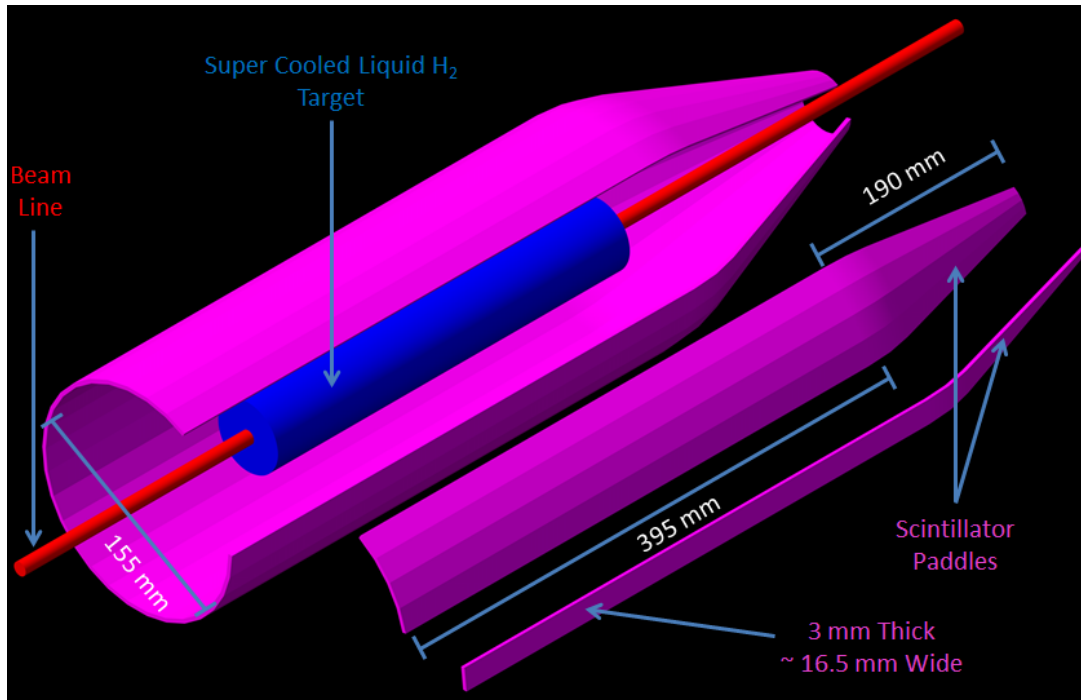


Figure 4.72: Start Counter with pieces removed revealing the target and beam line.

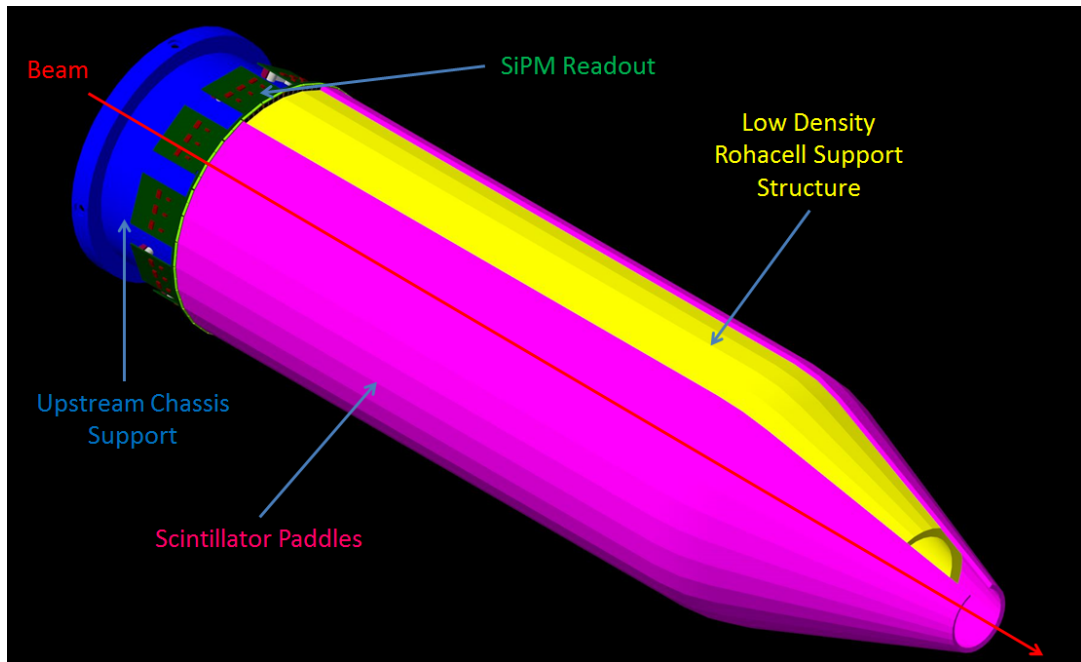


Figure 4.73: Partially assembled Start Counter.

Digital Converter (TDC) output. The ADC outputs will be readout *via* of two 16 channel flash ADCs (JLab 250 MHz Flash, fADC250), while the TDC outputs will be applied to two 16

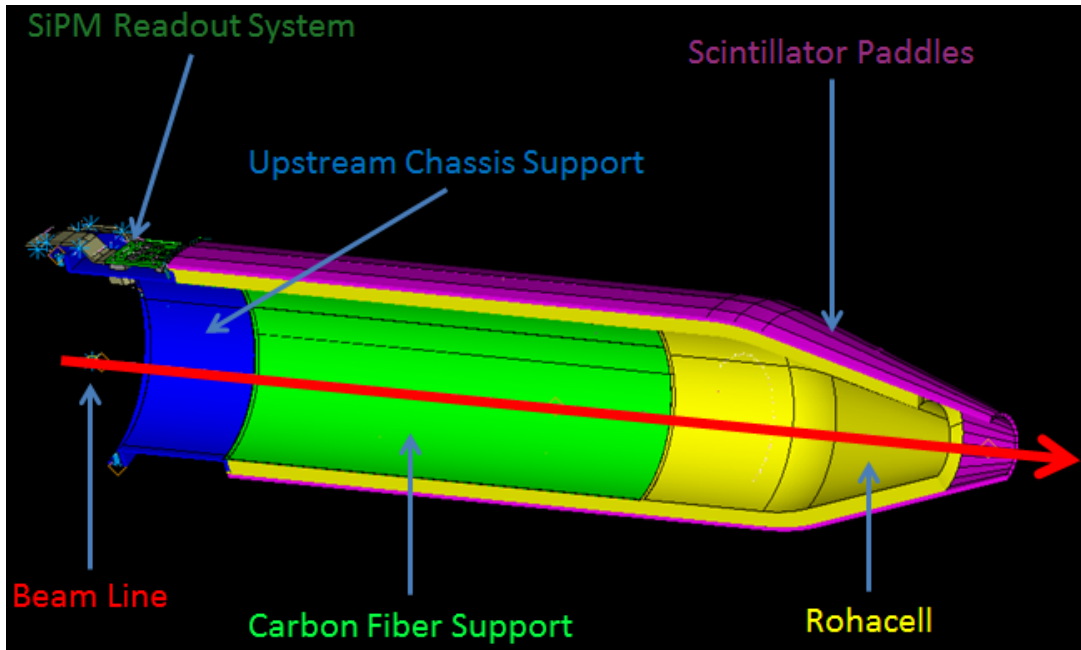


Figure 4.74: Cross sectional view of the fully constructed Start Counter.

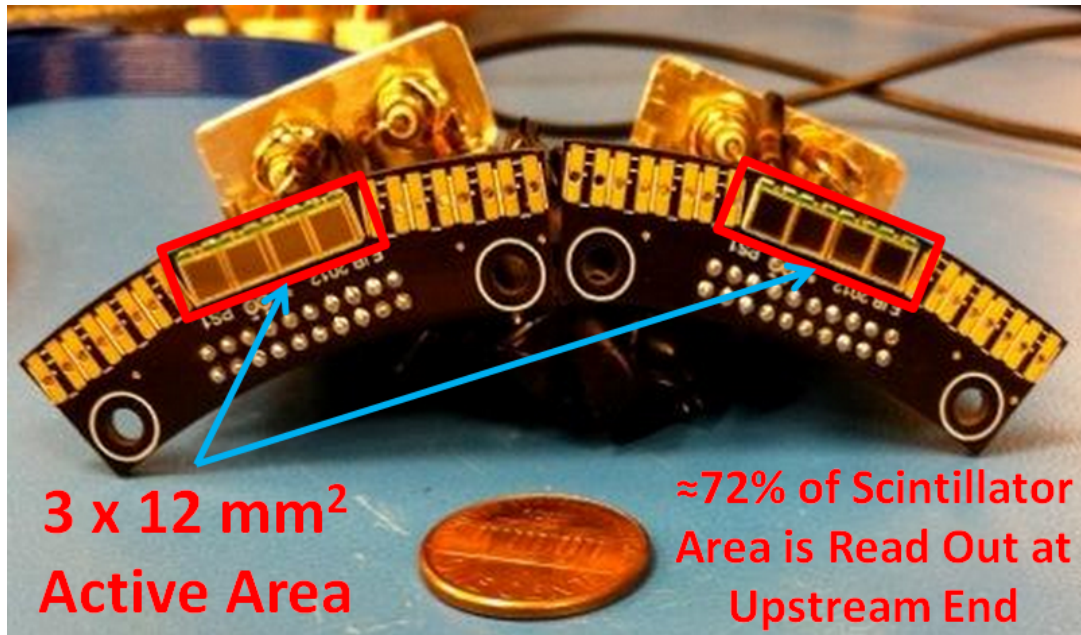


Figure 4.75: Two ST1s of the SiPM readout system placed side by side. The two holes at the bottom of ST1s PCB is the point of attachment for the SiPMs to the upstream chassis support. The SiPMs will be connected to the chassis *via* two pairs of nuts and bolts.

channel leading edge discriminators (JLab LE discriminators), followed by a 32 channel flash TDC (TDC JLab F1-TDC). Furthermore, each group of four SiPMs utilizes a thermocouple for



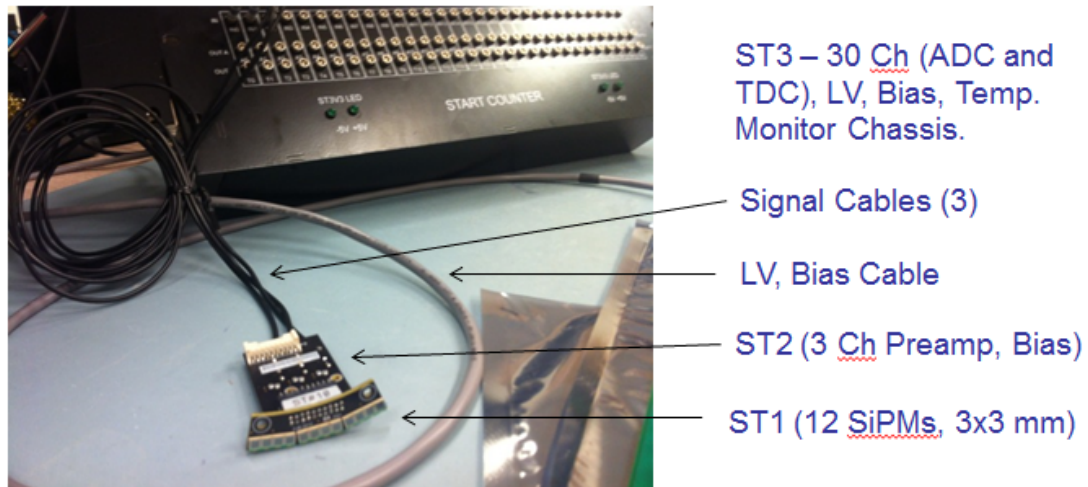


Figure 4.77: Complete Start Counter readout system.

## Measurements

Many data have been collected regarding long thin scintillator bars, of different dimensions, and varying scintillator materials. Data was also taken to study the different responses of various PMTs and SiPMs coupled to scintillator bars. These data consist of measurements for both straight bars as they were received from Eljen Technology, and bars that have been machined to the specific geometry of a GlueX Start Counter paddle. The data proved that the optimal dimensions of the pre-machined paddles were to be  $600 \times 3 \times (20 \pm 2) \text{ mm}^3$ . Moreover, it was determined that the aforementioned SiPM and readout system would be suitable for our needs. In addition, studies showed McNeal Enterprises provided better quality machined scintillators than the competing plastics companies, *e.g.* Plastic Craft. While many tests of machined scintillators utilized the EJ-212 scintillator material, manufacturing requirements from Eljen Technology stipulated a change to the EJ-200 scintillator material. Further tests showed that there is no substantial difference between the two types of scintillator material.

## Experimental Set-up for Testing Scintillators

In order to test individual paddles, a radioactive Strontium-90 ( $^{90}\text{Sr}$ ) source was placed at fixed distances along the path of the scintillator.  $^{90}\text{Sr}$  undergoes  $\beta^-$  decay to  $^{90}\text{Y}$  (yttrium). In turn,  $^{90}\text{Y}$  undergoes  $\beta^-$  decay to  $^{90}\text{Zr}$  (zirconium). The resulting decay of  $^{90}\text{Sr}$  provides a continuum of electron energies from  $\sim 0.5 \text{ MeV}$  to  $2.2 \text{ MeV}$  which closely mimics the energy of minimum ionizing particles. The scintillation light is produced in the scintillator by the electrons traversing through the scintillator material. The subsequent photons are then detected using a SiPM that is coupled to the upstream end of the scintillator. A trigger PMT coupled to a scintillator is employed to provide timing information. The signals from the two detectors are then processed through various Nuclear Instrumentation Modules (NIMs) and Computer Aided Measurement And Control (CAMAC) modules. These signals are processed through a Data Acquisition (DAQ) system and software where the ADC and TDC data are stored in ROOT files for analysis. The resulting spectra are fit with Gaussian distributions and the fit data are stored in data files. These data are then analyzed utilizing custom computer programs to

illustrate the scintillator properties, *e.g.*  $L_{attn}$ , and  $\sigma_{tr}$

## Results

Five scintillator bar prototypes machined to the finalized geometry were tested extensively upon arrival (06/2013) at FIU. The aforementioned testing procedure was implemented in an identical manner for all five of the scintillators. Figure ?? shows the typical behavior that is observed when measuring the various time resolutions as a function of source distance for scintillator paddles which are machined the unique Start Counter geometry. The red vertical line indicates the end of the straight section and the beginning of the bend/nose region. It is clear that the time resolution increases linearly in the straight section (0 - 39.5 cm), as one expects, while we observe the worst time resolution, *i.e.* least amount of light, in the bend region (39.5 - 43.3 cm), see figures ?? & ?. An interesting phenomenon occurs in the nose region (43.3 - 59.5 cm)

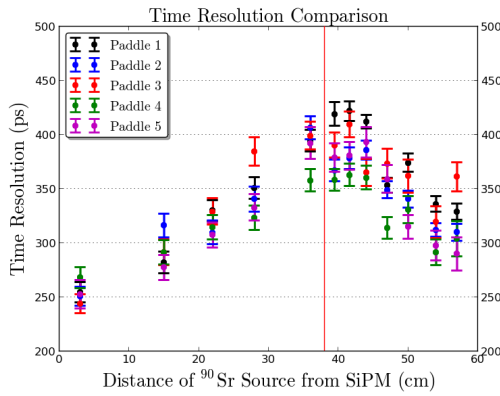


Figure 4.78: Time resolution.

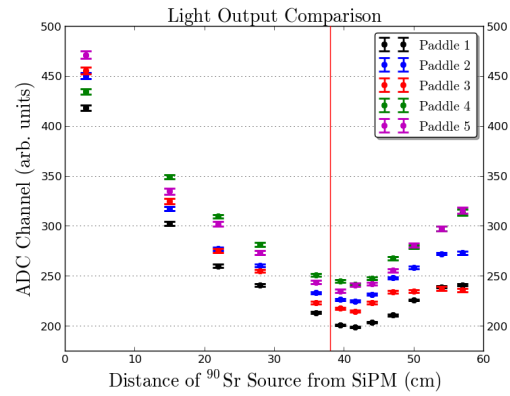


Figure 4.79: Light output.

downstream of the bend. The time resolution begins to decrease, *i.e.* improve, as the source moves downstream of the SiPM. This effect was studied extensively *via* GEANT4 simulations, and the same result was observed. Thus, it is clear that this effect is purely a consequence of the unique geometry of the nose section. Upon comparing figures ?? & ?? it is clear that time resolution is clearly dominated by light output. This effect is advantageous for our purposes as the majority of the charged particles produced in GlueX will be forward going, *i.e.* small  $\theta_{lab}$  values. Based on the data and simulations, the Start Counter will be able to provide a  $\sigma_{tr} < 350$  ps and be able to successfully identify the electron beam buckets to within 99 % accuracy.

## Wrapping of Scintillators

In order to increase the amount of light collected at the scintillator-detector interface, it is common practice to wrap plastic scintillators with reflective materials. Both 2  $\mu\text{m}$  thick aluminized Mylar and 16.5  $\mu\text{m}$  thick food grade aluminum foil were investigated extensively as potential wrapping materials for individual scintillator paddles (see figure ??). It should be noted that the bar that was tested in this study is a prototype manufactured prior to the batch of five paddles that was discussed previously. The time resolution achieved with this bar (labelled Bar 3) was worse than what was achieved with the batch of five prototypes. To ensure light tightness in the

event of microscopic holes in the reflective wrapping material, it is advantageous to wrap the scintillator, in addition to the reflective material, with black Tedlar film. Figure ?? illustrates the effect of wrapping a machined bar with  $2\mu\text{m}$  aluminized Mylar and food grade aluminum foil, as well as black Tedlar Film. As can be seen in figures ?? & ?? the data indicates that

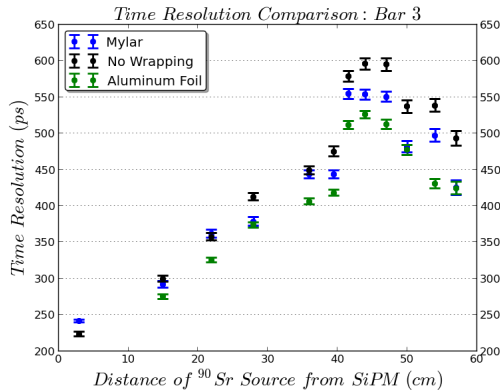


Figure 4.80: Reflective material.

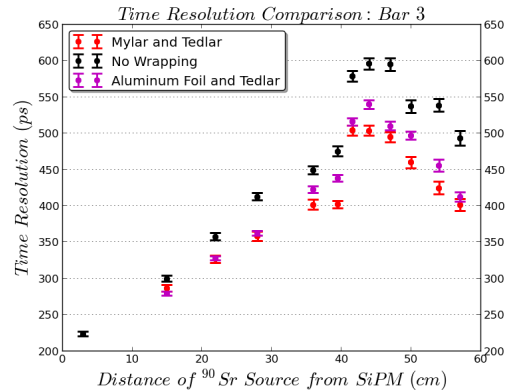


Figure 4.81: Reflective material &amp; Tedlar.

wrapping the scintillators with both reflective material and black Tedlar film has no effect on the quality of the time resolution and light output. While the time resolution only improved by about 10% when comparing wrapped and unwrapped scintillator paddle, the reflective materials did indeed improve the amount of light that was collected by the SiPM. These measurements prove the advantage of utilizing reflective materials in order to increase light output. Cross talk measurements were also conducted in order to determine the effect of the reflective materials ability to reducing the amount of cross talk between two adjacent scintillator paddles. These measurements verified the advantage of wrapping scintillators in reflective material in that the cross talk was reduced by a factor five when compared to scintillators that were tested with no reflective material between them. However, no difference was noticed between wrapping the scintillators with Mylar and food grade aluminum foil. This, coupled with previous wrapping tests indicating no substantial difference in time resolution between utilizing the Mylar and aluminum foil wrapping materials, it was decided that the individual scintillator paddles would be wrapped in aluminum foil since it is much easier to handle when wrapping scintillators.

## Deterioration

A common occurrence in scintillators is a phenomenon known as crazing. Crazing can occur in scintillators for a multitude of reasons. Some of the most common causes of crazing is that the scintillator comes into contact with chemicals other than isopropyl alcohol. Even the acids and oils from ones skin can diffuse into the medium of the scintillator and cause them to craze. Furthermore, machining of scintillators increases the possibility of crazing occurring. Due to the stresses and strains undergone during the machining process, it is possible for the scintillators to develop crazing over time, which may have not been visible during the initial visual inspection. In going through many prototypes of Start Counter paddles, it was found that some scintillators deteriorated in quality over time (see figure ??) and began to show visible signs of both surface and internal crazing. Many prototypes were made, and many of them deteriorated over time and were rendered useless. After extensive discussions with both

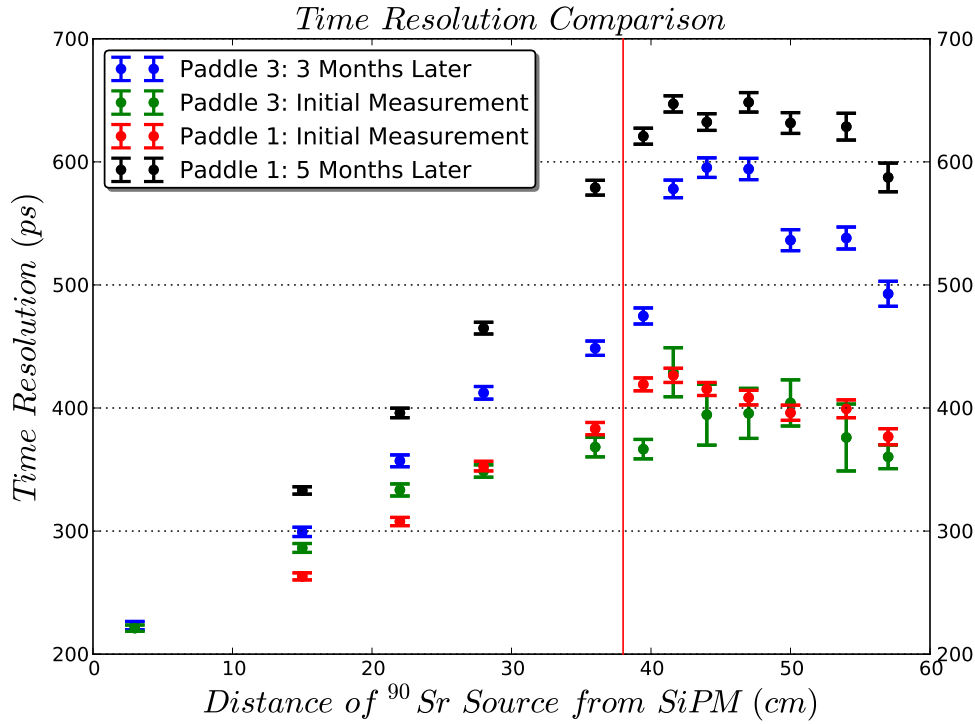


Figure 4.82: Deterioration Measurements. These data are an example of a batch of prototypes that deteriorated over time. It was discovered that after five months time, a ( $\sim 175$  ps), or 36% increase in time resolution had ensued resulting in an unacceptable quality of scintillator material.

Eljen Technology and McNeal Enterprises, the minimization of these deteriorating effects was accomplished. The most recent batch of five prototypes were monitored closely for a period of three and a half months in order to monitor for deterioration, which has proven to be a problem with previous prototypes. After close monitoring it was discovered that the scintillators were in fact not deteriorating (see figures ?? & ??) over time. The quality of the five scintillators received in the most recent batch of prototypes from McNeal Enterprises have proven to be of the necessary quality to fulfil the needs of the GlueX Start Counter.

### Test Stand

A new test stand was designed and built in order to improve the reproducibility of the measurements conducted on machined scintillator paddles (see figure ??). The scintillator is held in place by two scintillator support pieces that are rigidly attached to the frame of the test stand at fixed locations. The scintillator is held in place by spring loaded locking plungers that come into contact with a piece of protective foam which sits atop the surface of the scintillator. The frame has twelve grooves, machined at precise locations, cut out of the frame so that the trigger PMT may be held fixed at well defined locations along the path of the scintillators. The trigger PMT is held in place by a custom case designed to mount the  $^{90}\text{Sr}$  source above the scintillator and the PMT below the scintillator. This design allows for the source and PMT to

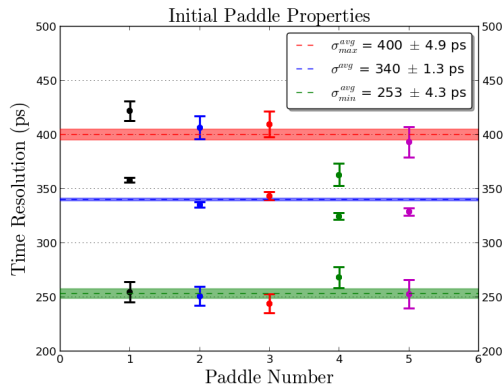


Figure 4.83: Initial Measurements.

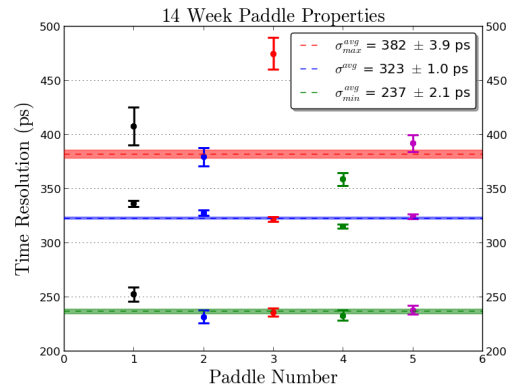


Figure 4.84: 14 Week Measurements.

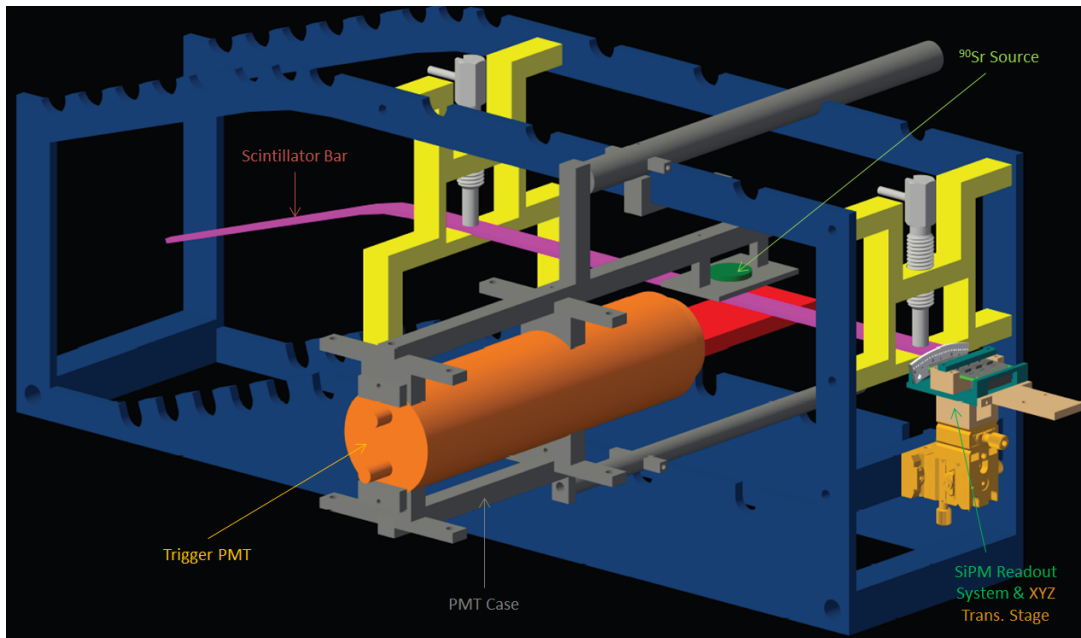


Figure 4.85: Start Counter test stand.

be moved as one unit, reducing the possibility of misalignment relative to one another, as well as their alignment relative to the scintillator. A SiPM and its readout system is placed at the upstream end of the scintillator while sitting atop a miniature dovetail XYZ translation stage. The translation stage allows for precise coupling of the SiPM relative to the upstream end of the scintillator. This design reduces any misalignment of the scintillator-SiPM interface which is crucial for maximizing the amount of light collected by the SiPM.

## Assembly of the GlueX Start Counter

### Description & Components

A preliminary design of an assembly jig is complete. The Rohacell support structure will be rigidly attached to a cylindrical chassis. A locking rotation device that is able to rotate in  $12^\circ$  intervals will be placed between two square bracket bearings that are centered on a square plate that is attached to the chassis. 10 ST1 and ST2 components will then be attached at fixed locations to the lip of the chassis. All of the devices will be supported by a stand. Two identical rings will each have 30 holes tapped through, separated by  $12^\circ$  of arc relative to the surface of the rings. Swivel screws with pads will then screw into the holes of the rings which will be placed around the Rohacell. The rings will be free-floating, only supported by swivel screws, and placed at two locations along the path of the straight section of the Rohacell support structure. Two pneumatic cylinders, with steel rods that extend to a predetermined stroke length, are to be controlled by a pressurized air system and solenoid valves. The cylinders will be oriented perpendicular to the plane of the table that the stand will rest on. They will be supported by a bar that is to be welded to a large existing metal frame. The retractable steel rod of the pneumatic cylinders are extendible so that the tip will come into contact with surface of a scintillator that is being installed.

### Installation

To install a scintillator paddle, the pneumatic cylinders will be retracted, as well as 2 of the 30 swivel screws that are oriented perpendicular to table. The scintillator will then slide down the surface of the Rohacell until it is placed as close as possible to the active area of the SiPM. The pneumatic cylinders will then be extended to hold the scintillator in place. Fine adjustments of the scintillator will be made so that the best possible alignment is achieved. The alignment of the scintillators with the SiPMs will be monitored closely with specialized camera optics. Once the scintillator is in a suitable position, the swivel screws will then be adjusted in order to come into contact with the scintillator, and the pneumatic cylinders will then be retracted. Upon completing the installation of one paddle, the whole device will be rotated by  $12^\circ$  and then another paddle will be installed in the exact same manner. This process will be repeated until all 30 paddles have been successfully installed. In order to keep all of the scintillators firmly in place in the absence of the rings and plungers, wrapping material (which has yet to be determined) will be installed. Once the assembly is successfully completed, the GlueX Start Counter will undergo extensive testing and calibration.

### 4.8.4 Cherenkov Counter

The Cherenkov detector for GLUEX is unfortunately not as well defined as the rest of the equipment. This is due to the fact that the first group to express interest in this detector pulled out of GLUEX because of the long time scales involved and detector became an *orphan* for several years. After the granting of CD0 to the JLab upgrade and GLUEX in the spring of 2004, a pair of groups from Tennessee approached the collaboration about joining GLUEX and taking on a large detector responsibility. The natural piece of hardware was the orphaned Cherenkov system.

Based on this interest, it was felt that a completely fresh look should be taken at the system. This should consider both the physics of GLUEX and technological developments that

have occurred over the last several years. The result of this effort is a proposal to build a DIRC detector rather than the gas Cherenkov system that had been proposed earlier. Because this proposal is so new, and the collaboration is still evaluating its implications, we have presented both the newer DIRC material and the older gas Cherenkov material here. A final decision on this clearly depends on many factors including physics, manpower, costs and timescales. The collaboration is currently evaluating these.

In the case of both Cherenkov designs, it is possible for the GLUEX experiment to start taking quality data without this system in place. There is a very solid physics program with pions that does not need the Cherenkov. However, as the collaboration begins to study final states with both hidden and open strangeness, the Cherenkov system will be crucial. What follows are first a discussion of the DIRC option followed by the earlier work on the gas Cherenkov detector.

### A DIRC Cherenkov Detector

The Cherenkov detector, DIRC, of the BABAR experiment at the PEP-II asymmetric  $B$ -factory of SLAC has proven to be a successful novel technique for pion and kaon identification [?, ?, ?]. The DIRC (acronym for **D**etection of **I**nternally **R**eflected **C**herenkov (light)) is a ring imaging Cherenkov detector. It provides the identification of pions, kaons, and protons for momenta up to 4.5 GeV/c with high efficiency. This is needed to reconstruct CP violating  $B$ -decays and to provide  $B$ -meson flavor tagging for time-dependent asymmetry measurements. The DIRC radiators consist of long rectangular bars made of synthetic fused silica and the photon detector is a water tank equipped with an array of 10,752 conventional photo-multiplier tubes (PMT). By the summer 2004, BABAR had recorded about 227 million  $\bar{B}B$  pairs, exceeding the design luminosity of  $3 \cdot 10^{33}/\text{cm}^2\text{s}$ . The observation of direct CP violation with more than 4 standard deviations in the decay  $B^0 \rightarrow K^+\pi^-$  [?], which has to be distinguished from  $B^0$  decays into  $\pi^+\pi^-$  and  $K^+K^-$ , is a successful demonstration of the DIRC's capabilities.

Similar to the physics program of BABAR, the spectroscopy program of GlueX depends on the capability to identify charged kaons. We discuss the possibility to adapt the DIRC concept for the GlueX detector to complement the particle identification information of the tracking chambers and the time-of-flight (TOF) detector for momenta above 1.5 GeV/c.

### The BABAR DIRC

The physics program of the BABAR [?] detector is to observe CP violation and to probe the Standard Model of Particle Physics by collecting enough  $B$ -meson decay channels to over-constrain predictions. The source of  $B$  mesons is the PEP-II asymmetric  $e^+e^-$  collider [?], where 9 GeV electrons strike 3.1 GeV positrons producing  $\Upsilon(4S)$  resonances with a boost of  $\gamma\beta \simeq 0.56$ . The  $\Upsilon(4S)$  resonance decays nearly exclusively in a pair of  $B$  and anti- $B$  mesons. This allows precise measurements of time-dependent asymmetries in  $B$  meson decays which can be related to the CP violation phase in the Cabbibo-Kobayashi-Maskawa (CKM) matrix.

BABAR is a typical collider detector but asymmetrically placed around the interaction point to ensure nearly full solid angle coverage in boost (forward) direction (see Fig. ??). The location of the particle identification system is radially between the drift chamber and a CsI(Tl) crystal calorimeter. Therefore, a small radiation length is preferred to avoid deterioration of the excellent energy resolution of the calorimeter. The DIRC minimizes the radial dimension and keeps the amount of required calorimeter material (cost) small. Up to a momentum of 700 MeV/c,

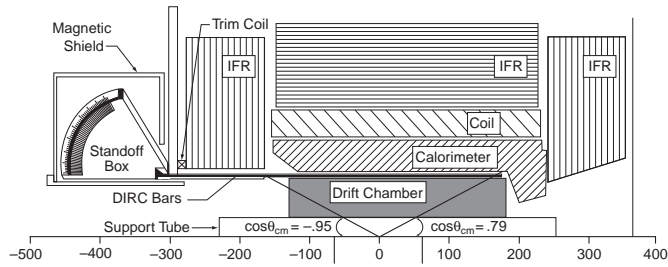


Figure 4.86: The side-view of the BABAR detector with the components of the DIRC indicated (units in cm).

the drift chamber can provide pion-kaon separation based on the  $dE/dX$  measurement. Only if pion-kaon separation up to  $4.5 \text{ GeV}/c$  particle momentum is available can one distinguish the channels  $B^0 \rightarrow \pi^+\pi^-$  from  $B^0 \rightarrow K^+\pi^-$  or  $B^\pm \rightarrow \phi\pi^\pm$  from  $B^\pm \rightarrow \phi K^\pm$ , interesting for the measurement of indirect or direct CP violation. Moreover, the flavor content of the recoil  $B(\bar{B})$  needs to be tagged by identifying kaons in its successive decays with momenta below  $4 \text{ GeV}/c$ . In addition,  $\tau$ , charm-, and light-quark meson spectroscopy profit from kaon identification.

The difference in the Cherenkov angle between a pion and a kaon at  $4.0 \text{ GeV}/c$  momentum is  $6.5 \text{ mrad}$ . Therefore, a 3 standard deviation  $\pi/K$  separation requires resolution of the Cherenkov angle for given a track of  $2.2 \text{ mrad}$  or better (see Fig. ??). Finally, to operate successfully in the high-luminosity environment of PEP-II, the Cherenkov detector has to be radiation hard, fast, and tolerant of background.

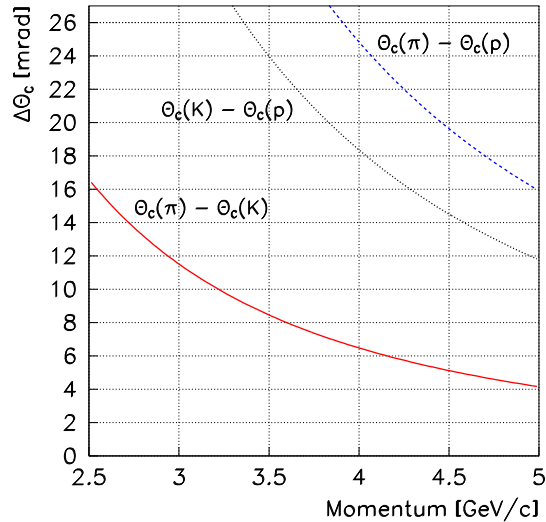


Figure 4.87: The difference in the Cherenkov angles between pions, kaons, and protons in synthetic quartz.

### Principle of the BABAR DIRC

The DIRC uses thin, long rectangular bars made of synthetic fused silica (quartz)<sup>31</sup> ( $H \times W \times L = 17 \text{ mm} \times 35 \text{ mm} \times 4900 \text{ mm}$ ) both as Cherenkov radiators and light guides (refractive index  $n_1 \approx 1.47$ ). Bars are glued together from four pieces, each 1225 mm long. All together, 144 bars are arranged in a 12-sided polygonal barrel with a radius of about 84 cm around the beam axis. The DIRC bars extend 178 cm forward from the interaction point of BABAR covering 87% of the polar solid angle in the center-of-mass frame. The azimuthal coverage is 93%, since there are gaps between the bars at the 12 sides of the radiator polygon. Every 12 bars are housed in a bar-box surrounded by nitrogen at STP (index  $n_2 \approx 1$ ). The box is built mostly of aluminum honeycomb material. The radiation length ( $X_0$ ) of the bars is 14%, and 19% for the full assembly at perpendicular incidence. A schematic view is presented in Fig. ??.

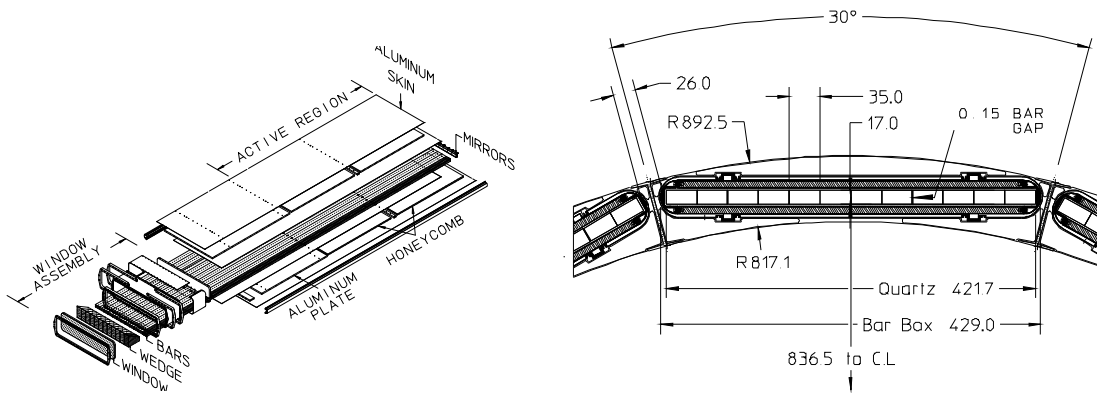


Figure 4.88: Left: View of a bar-box assembly. 12 bar-boxes surround the drift chamber. Right: Placement of the bar-box in the BABAR detector above the cylindrical drift chamber.

The principle of the DIRC is shown in Fig. ?. The DIRC imaging works like a pinhole focus camera with the bar cross section small compared to the imaging plane.

Since the refractive index of the radiator bar  $n_1$  is larger than  $\sqrt{2}$ , a certain fraction of the Cherenkov photons produced by a relativistic charged particle traversing the quartz bar will be totally internally reflected, regardless of the incidence angle of the track, and propagate along the length of the bar. Only one side is viewed by the PMT array and a mirror (reflectivity  $\approx 92\%$ ) is placed perpendicular to the bar axis on the other end, where positrons enter the BABAR detector. Due to the boost of the  $\Upsilon(4S)$  there is a higher density of charged tracks towards the mirror side and hence it is less preferable for the readout. Since the rectangular bar is of high optical precision (mean surface reflectivity  $\approx 99.96\%$  per bounce at 442 nm photon wavelength), the initial direction of the photon is preserved throughout its propagation, modulo left/right, up/down and forward/backward ambiguities. The latter is resolved by the measurement of the photon arrival time. The bars have very high light transmission (99.9% at 442 nm photon wavelength) required for the typical photons path-lengths of 6 to 20 m.

Photons exiting the bar in the downward direction, or with large exit angles with respect to the bar length axis, are partly recovered into the instrumented area by a prism (wedge). This

<sup>31</sup> The provider of fused silica: TSL Group PCL, P.O. Box 6, Wallsend, Tyne & Wear, NE28 6DG, England. Quartz Products Co., 1600 W. Lee St., Louisville, Kentucky 40201. Manufacturer of quartz bars: Boeing, Rockedyne Division, 2511 C Broadbent Parkway NE, Albuquerque, New Mexico 87107.

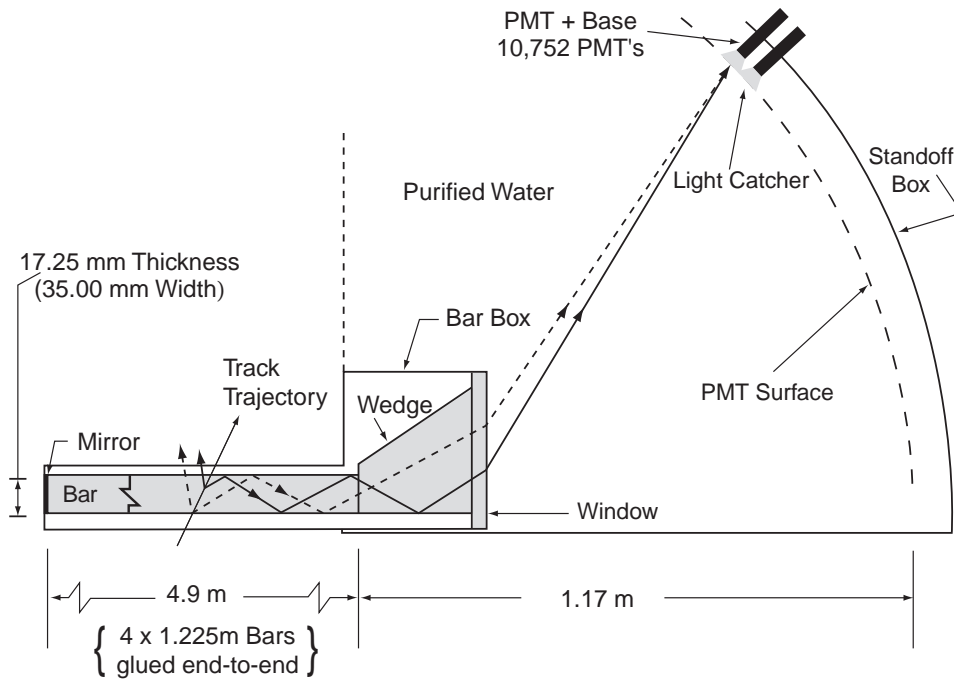


Figure 4.89: The principle of the BABAR DIRC.

optical element is 91 mm long and the top side has a  $30^\circ$  opening angle. The bottom side is slightly tilted upwards by 6 mrad. It reduces the required photon-sensitive area by more than a factor of two.

A thin (9 mm) quartz window separates the prism from the so called standoff box (SOB), a water tank filled with 6000 liters of purified water ( $n_3 \approx 1.33$ ) in a toroidal shape. The backplane of the SOB is divided into 12 sectors, each equipped with 896 conventional photo-multiplier tubes<sup>32</sup> ( $\approx 25\%$  quantum efficiency at 400 nm wavelength, 250 nm – 650 nm spectral range), facing the wedge of a corresponding bar box. Hexagonal reflectors (light catchers) with water-resistant rhodium surfaces surround the PMT cathodes improving the detection efficiency by about 20%. The ratio of refractive indices  $n_1/n_3$  is nearly wavelength independent. It reduces internal reflection at the bar-box wedge. Furthermore, the exit angle is magnified by this ratio, increasing the position resolution of the photons.

The detector provides a three dimensional measurement of the photon in the variables  $(\alpha_x, \alpha_y)$ , the photon exit angles with respect to the bar axis, and the arrival time of the photon  $t_a$ . The spatial position of the bar through which the track passed and the particular PMT hit within a certain readout time interval is used to reconstruct the photon vector pointing from the center of the bar end to the center of the tube. This vector is then extrapolated back into the quartz bar using Snell's law, where the photon exit angles  $(\phi_C, \theta_c)$  with respect to the track are calculated. Most of the photon phase space  $(\alpha_x, \alpha_y, t_a)$  is mapped onto the Cherenkov angles  $(\phi_C, \theta_c)$  with less than a three-fold average ambiguity.

<sup>32</sup> Manufacturer of photo-tubes: Electron Tubes Limited, (formerly: Thorn EMI Electron Tubes), Bury Street, Ruislip, Middlesex HA47TA, U.K.

The timing information apart from the resolution of the forward-backward propagating photons, is not competitive with the position information, but it is crucial for suppression of beam background. The expected arrival time of the Cherenkov photon is a sum of the time-of-flight of the charged particle from its origin to the quartz bar (typically 2-3 ns), the photon propagation time in the quartz bar and the wedge along its reconstructed path, and the traveling time through the water before reaching the surface of the PMT. Applying the reconstructed mean arrival time of the photons in an event as correction for the uncertainty in the bunch-crossing time yields a precision of about 1.5 ns in the time between photon creation and photon arrival, which is close to the intrinsic time resolution of the PMTs. This allows restriction of the event time interval to 8 ns.

Particle identification uses likelihood ratios for different particle hypotheses based on the number of photons above and below threshold and the Cherenkov angle. Another way to use the information is to compare the ring pattern in the PMT plane with expected patterns for the different particle hypotheses.

### Imaging with Synthetic Fused Silica

The Cherenkov angle separation between particle types is the Cherenkov angle difference in Fig. ?? divided by the Cherenkov angle resolution  $\sigma_C$ . This resolution, in turn, depends primarily on the precision of the track angle of incidence as provided by the tracking detectors,  $\sigma_t$ , and the single photon Cherenkov angle resolution in the DIRC,  $\sigma_{C,\gamma}$ , and the number of photo-electrons contributing to the measurement,  $N_\gamma$ , as follows:

$$\sigma_C = \sqrt{\sigma_t^2 + \sigma_{C,\gamma}^2 / N_\gamma}. \quad (4.18)$$

The dominant contributions to the error of the single photon measurement are

chromatic	5.4 mr
imaging (bar size) and detection (PMT size)	7.5 mr
transport (through the bar)	1.0 mr .

These add in quadrature to  $\sigma_{C,\gamma} = 9.3$  mr. The number of Cherenkov photons per track for di-muon events versus the track polar angle with respect to normal incidence is shown in Fig. ?? b). The number varies between 25 and 60 photons. Therefore, with negligible tracking resolution,  $\sigma_C$  decreases from 1.9 mr to 1.2 mr in the extreme forward direction where tracks have the highest momenta in BABAR due to the boost. The imaging and detection error can be improved by extending the distance between bar end and PMT plane. For instance, with a distance of 1.4 m we obtain a single photon angle resolution of about 8.3 mr. With a slightly increased bar thickness and shorter bars the minimum number of photons per track can be increased to 25 or higher.

### Features of the BABAR DIRC

Here we summarize the main advantages of the BABAR DIRC type Cherenkov detector:

- The BABAR DIRC separates kaons from pions to better than 3 standard deviations below 4 GeV/c. It is an imaging device in the required momentum range with high photo-electron yield (25 or more). It also works as a threshold detector for different particle types with momenta below 0.92 times the particle's mass.

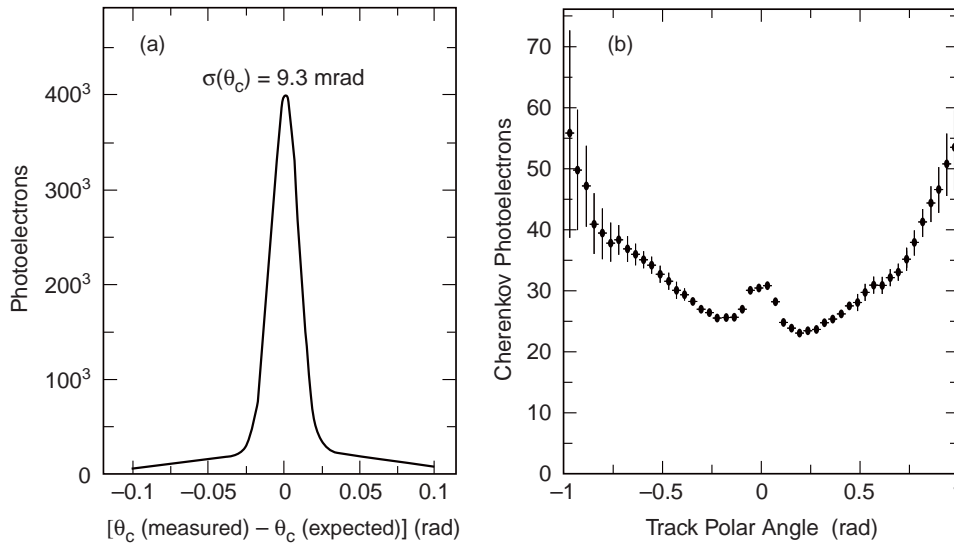


Figure 4.90: (a) The Cherenkov angle resolution for single photons associated with a particle track. (b) The number of Cherenkov photons per track versus the track polar angle with respect to normal incidence. The slightly lower efficiency in forward direction is due to the reflection in the mirror and the increased photon path-length in the bar.

- Compact: The total thickness between tracking and calorimeter is less than 5 cm. The total radiation length ( $X_0$ ) for a full assembly is 19%.
- Radiation robust: It has been demonstrated that there is no efficiency loss in the wavelength regime above 280 nm after irradiation with 250 krad [?].
- Fast device: The photon collection time is less than 100 ns.
- Insensitive to background: The BABAR DIRC is a 3-dimensional device; the photon arrival time and the location of the PMT are correlated, allowing reconstruction of the true arrival time of the Cherenkov photons originating from the same track with a precision of 1.5 ns. Therefore, the event time interval can be smaller than 10 ns.
- Robust device: The radiator is passive and needs only to be kept in a dry atmosphere. Conventional photo-multiplier tubes are used which can be easily accessed. The DIRC is the subsystem within BABAR that requires the least maintenance.

### Requirements for GlueX

In the previous design a gas-Cherenkov detector is placed behind 4 layers of FDCs and before the TOF system. It extends into the inner cylinder of the solenoid and has an effective length along the beam axis ( $z$ -axis) of 1.4 m. Instead of this detector a DIRC system can be positioned at some short distance behind the solenoid opening. To evaluate the situation with GEANT simulations [?] we place a virtual ( $xy$ ) plane perpendicular to the beam direction at  $z = 450$  cm, which is about 10 cm behind the solenoid opening. Without modification of the bar-imaging concept of the DIRC detector, the bars would line up along one axis in that plane and leave a gap for the beam to pass through.

**Particle Momenta and Angle of Incidence** In a typical reaction  $\gamma p \rightarrow (\text{mesons}) p$  with strangeness production, 50% of the pions and kaons (somewhat fewer protons) produced with momenta between 1  $GeV/c$  and 5  $GeV/c$  arrive at the Cherenkov detector plane. In many cases strangeness conservation can be used to recover the final state if the remaining particles are identified with high efficiency. Highly efficient and redundant kaon identification is required to access a large variety of final states and to reduce combinatorial background in the search for new signals. A particle identification coverage with constant efficiency and low mis-identification rate over the full momentum range is essential to perform angular analysis of their decays. Figure ?? shows the momentum spectra for the pions, kaons, and protons which arrive at the Cherenkov-detector plane for the two reactions:

$$\begin{aligned} \gamma p &\rightarrow K^{*0}(892)K^{*0}(892)p & (4.19) \\ &\rightarrow K^+\pi^-K^-\pi^+p \end{aligned}$$

$$\begin{aligned} \gamma p &\rightarrow K_1(1270)K^-p & (4.20) \\ &\rightarrow K^{*-}\pi^+K^-p \\ &\rightarrow K^-\pi^0\pi^+K^-p. \end{aligned}$$

These are typical reactions with more than two final state pions and kaons. In these final states kaon-pion separation is required up to a momentum of 5  $GeV/c$ . Based on  $dE/dX$  and TOF a 3 standard deviation separation is obtained up to 1.5  $GeV/c$  momentum, while with the kaon threshold in a DIRC at 0.45  $GeV/c$  enough photo-electrons are created for efficient Cherenkov imaging. The proton spectrum extends to 2  $GeV/c$  and below 1  $GeV/c$  a DIRC detector acts as a threshold Cherenkov detector for this particle type.

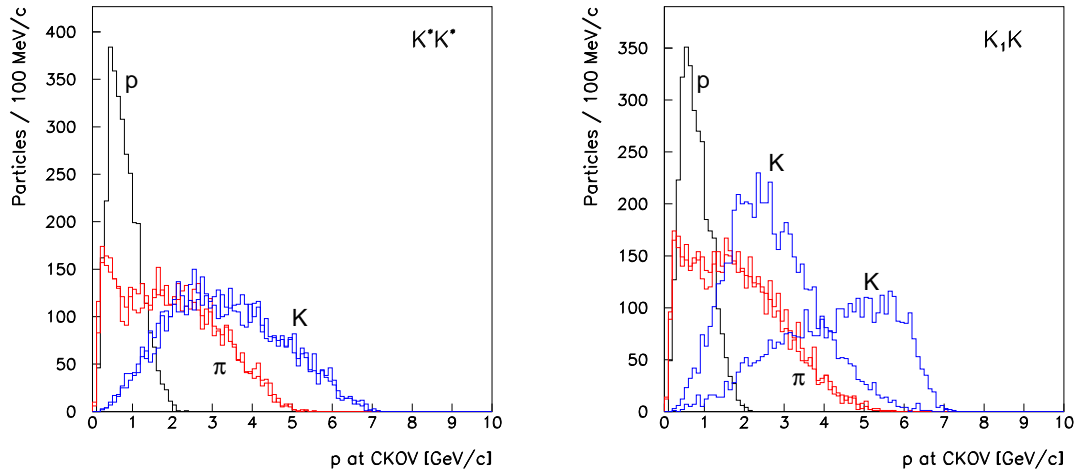


Figure 4.91: The particle momenta at the Cherenkov detector plane ( $z = 450$  cm) for the two reactions described in the text ( $\pi$ :pions,  $K$ :kaons,  $p$ :protons).

Figure ?? shows the polar angle with respect to the  $z$ -axis for the charged final state particles in the reactions Eq. ?. This angle typically does not exceed 15 degrees. Pions with polar angles greater than 15 degrees typically have momenta below 1  $GeV/c$ .

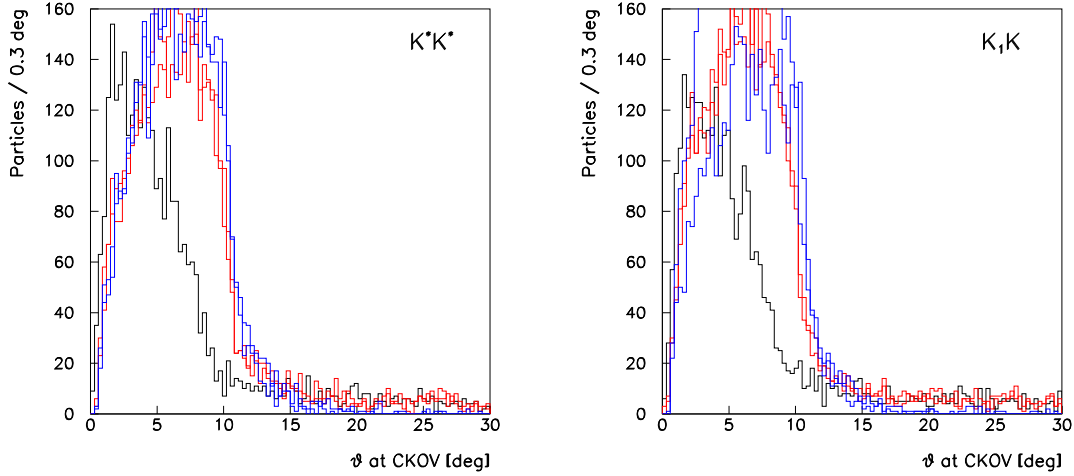


Figure 4.92: The polar angle with respect to the normal incidence at the Cherenkov detector plane ( $z = 450$  cm) for pions, kaons, and protons in the two reactions described in the text.

**Beam Background** We assume an electron beam current of  $3 \mu\text{A}$ . This is the high-luminosity scenario for the Hall-D project. We use a full GEANT simulation of the GlueX detector [?] to track primary and secondary particles. The charged particle background which can create Cherenkov light consists mostly of electrons and positrons coming from upstream or from photon conversions in the Cherenkov detector.

Figure ?? shows the combined electron-positron rate along the  $y$ -axis in our virtual detector plane at  $z = 450$  cm. We obtain rates below 100 kHz per cm (200 kHz per 2 cm) at distances of about 6 cm from the beam axis. The total rate integrated over all of  $x$  and from  $\pm 6$  cm to  $\pm 65$  cm (the hole radius) of  $y$  is at the most 900 kHz. The integration from  $\pm 10$  cm to  $\pm 65$  cm of  $y$  yields a total rate of 580 kHz.

Figure ?? shows the photon rate per cm along the  $y$ -axis integrated over all of  $x$  in the virtual detector plane at  $z = 450$  cm. We expect 600 kHz/cm photons at distances near  $y = 6$  cm. The total rate integrated over all of  $x$  and from  $\pm 6$  cm to  $\pm 65$  cm of  $y$  is 29.6 MHz; from  $\pm 10$  cm to  $\pm 65$  cm of  $y$  it is 24 MHz.

Each electron or positron potentially creates 30 detected photons in the struck bar. A beam photon converts with a probability of about 15% into a electron-positron pair somewhere inside the DIRC generating an average of 20 photons per lepton track. We estimate, that a DIRC placed at a distance of  $\pm 6$  cm away from the beam axis produces Cherenkov light into the readout tank at a rate of 210 MHz. If the DIRC has a central gap of  $\pm 10$  cm the total rate is 160 MHz. The time to collect photons out of the bars is less than the 100 ns for the long BABAR DIRC bars. We estimate the number of beam-background related Cherenkov-photons within 100 ns for a gap in the plane along the  $y$ -axis of  $\pm 6$  cm ( $\pm 10$  cm) to be 21 (16). After reconstruction we can reduce the time window for the photon arrival to less than 10 ns, which reduces the background photons to 2, while we expect 25 or more signal Cherenkov photons in a limited region of the readout plane.

The hit rate in a single PMT depends also on the optics at the bar end (opening angle of the wedge) and the profile of the background shown in Fig. ?? and Fig. ?. Assuming that

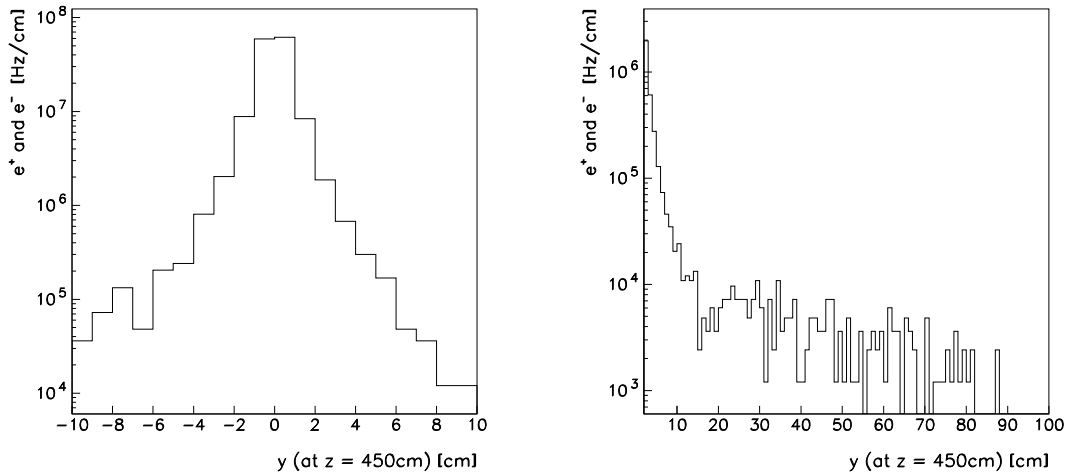


Figure 4.93: The rate of electrons and positrons per cm along the  $y$ -axis integrated over all of  $x$  at the location  $z = 450$  cm. Left: rate/cm below  $\pm 10$  cm in  $y$ . Right: rate/cm versus  $y$ . The innermost 3 cm are omitted.

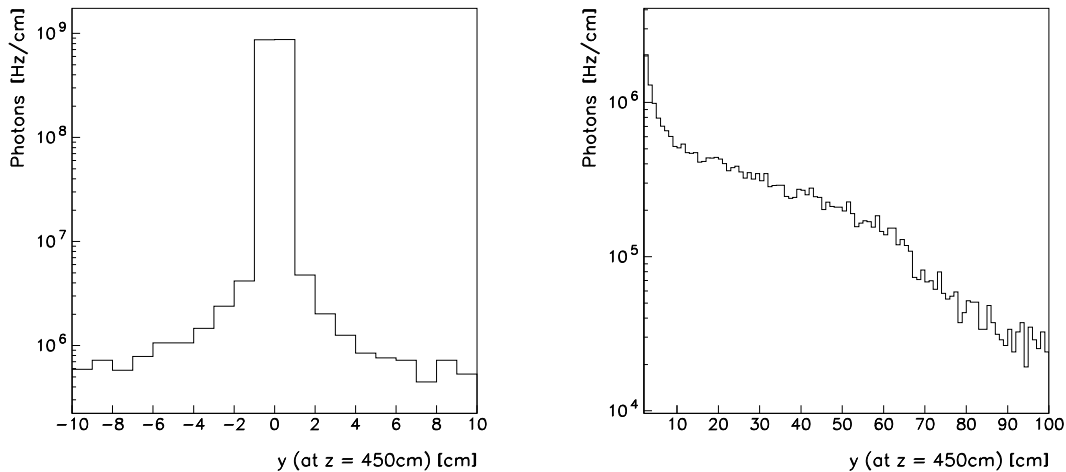


Figure 4.94: The rate of photons per cm along the  $y$  axis integrated over all of  $x$  at the location  $z = 450$  cm. Left: rate/cm below  $\pm 10$  cm; Right: rate/cm versus  $y$ . The innermost 3 cm are omitted.

typically 1000 PMTs are randomly hit, the rate per tube is 210 kHz. This is the average rate encountered by PMTs in the BABAR DIRC which tolerates up to 1 MHz.

**Magnetic Field** The solenoid has strong fringe fields. We simulate the situation with the TOSCA program [?]. At a distance of about 3 m left or right of the solenoid center the field strengths are below 100 Gauss. Efficient operation of conventional photo-multiplier tubes

requires shielding. In BABAR a magnetic field strength transverse to the PMTs of less than 0.2 Gauss is achieved with metal shielding and bucking coils.

**Irradiation** From the penetration rate with charged particles we estimate the radiation dose per year. We assume that the dominant component is secondary electrons and positrons created upstream or in the bars by photon conversions. The flux versus radius is shown in Fig. ???. It stays below  $100 \text{ kHz/cm}^2$  for radii greater than 3 cm. For a flux of  $100 \text{ kHz/cm}^2$  and a minimum ionizing  $dE/dx = 1.6 \text{ MeVcm}^2/\text{g}$  we estimate a yearly dose of 51 krad. This rate is well below the negligible dose of 250 krad tested with a  $^{60}\text{Co}$  source [?].

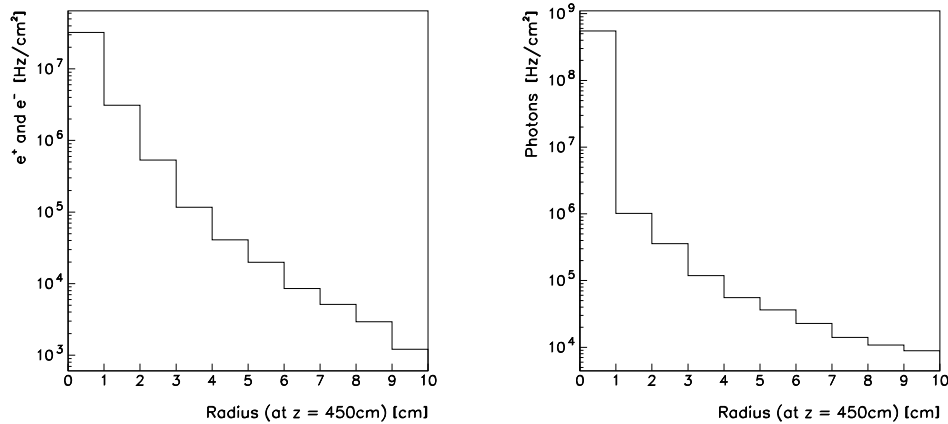


Figure 4.95: Left: The rate of electrons and positrons together per  $\text{cm}^2$  versus radial distance from the beam axis in the virtual plane at  $z = 450 \text{ cm}$ . Right: The same for photons.

### Conceptual Design

At this point we discuss a geometry and imaging concept similar to that in the BABAR DIRC. In fact, we can even envision the use of four of the DIRC bar-boxes which would only need the design of a new support and a new shielded readout tank.

However, for a new design the bar dimensions can be optimized. Because azimuthal and polar angles of incidence are comparable and we expect a higher background rate per bar closer to the beam compared to BABAR, a width of 2 cm is more appropriate than 3.5 cm. The thickness can be increased from 1.7 cm to 2 cm to increase the photon yield and the structural stability. The modularity should be kept, with say, 14 bars in a box. Altogether four boxes provide a geometrical match. In principle, the bars could follow the circular boundary of the magnet opening. Also, the gap can be partly covered from the readout side. This would result in bars with different lengths.

The water tank should be placed on the side of the magnet, shielded, and away from secondary tracks which are produced in the forward direction in the central calorimeter or in the magnet yoke. This may also require that the bars be somewhat farther downstream (greater  $z$ ). Hence, the length of the bars and their  $z$  position is a matter of further optimization. We explore the possibility that the purified water can be kept sealed in the tank for several years without maintenance.

In our first approach we allow the bars to extend into a region where there are no spatial restrictions and the transverse magnetic field [?] at the location of the PMTs is about 10 Gauss, while the longitudinal field drops below 45 Gauss. This corresponds to about 3 lengths of BABAR DIRC bars. Figure ?? shows the technical drawing of a first draft design of the bar arrangement with bars of 1.225 m length and a front area of  $2 \times 2 \text{ cm}^2$ . We have not optimized the bar length to follow the circular shape of the hole. Each 14 bars are housed in a separate bar-box. Two bar-boxes are placed below and two above the center leaving a gap for the beam to pass through. The readout side is shown in Figure ?. The maximum upward opening angle at the readout is 52 degrees. The sides open up with an angle of 30 degrees. Each tube covers an angle of 2 degrees. In this scenario the number of photo-tubes is 1512. A three-dimensional view of the half open bar-boxes and the readout tank is presented in Fig. ?.

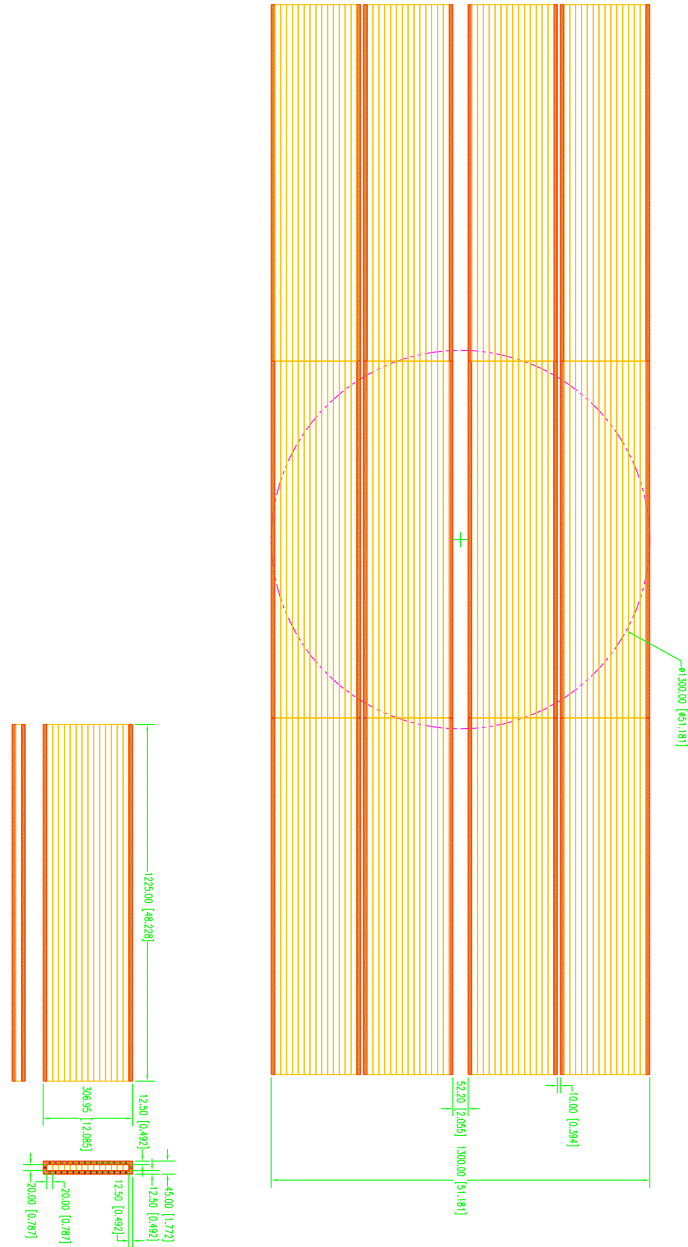


Figure 4.96: Arrangement of the bar-boxes in front of the solenoid. The circle indicates the size of the inner radius of the cylindrical calorimeter inside the solenoid. The bar-boxes will be placed asymmetrically with respect to that hole.

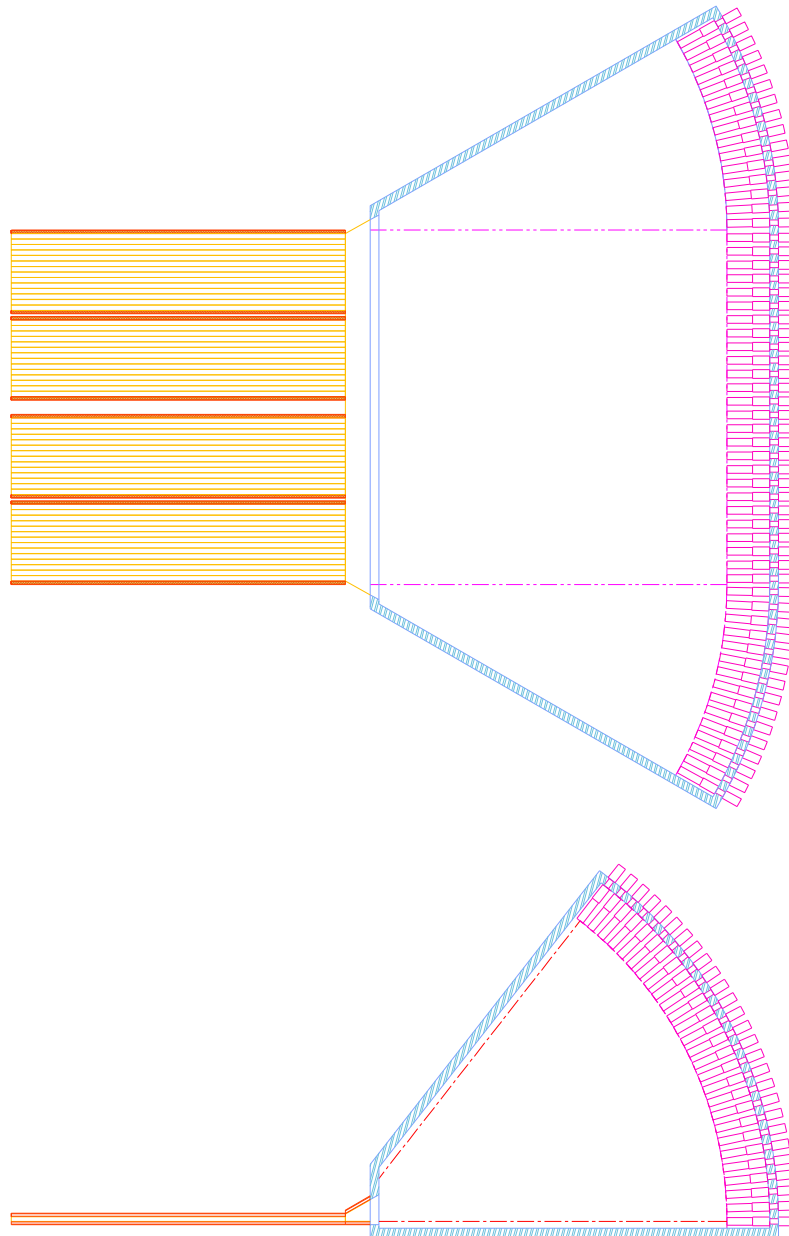


Figure 4.97: The readout side of the bars. The volume will be filled with water and the photo-multiplier tubes will be immersed in the water as in the BABAR DIRC.

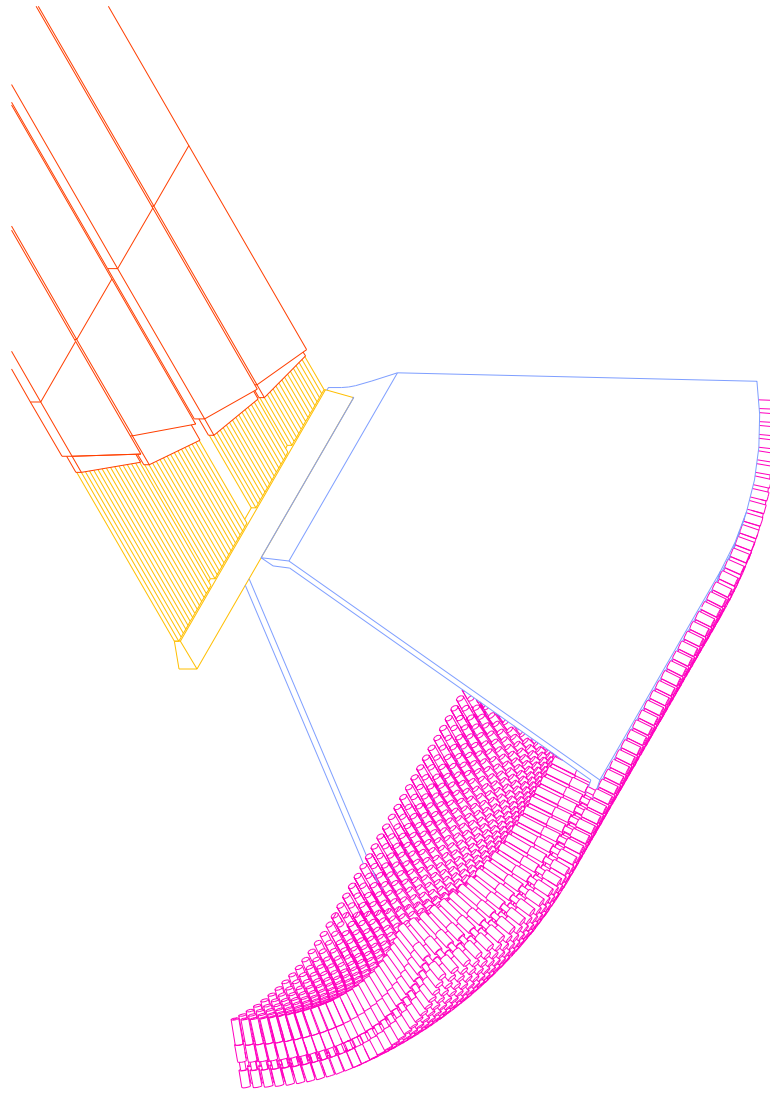


Figure 4.98: A 3-D view into the four half open bar-boxes and the readout tank.

### The Gas Čerenkov Counter System

TOF measurements alone will not provide particle identification above  $3 \text{ GeV}/c$ , and thus TOF does not suffice for typical reactions of interest. Therefore a threshold Čerenkov detector has been included in the HALL D design. The primary function of this detector is to signal the presence of pions over a large part of the expected momentum range (see Figure ??).

Several radiator materials have been considered for the design. A pressurized gas radiator has the advantage of allowing one to match the index of refraction to the desired momentum range. A prototype of such a detector was developed for CLEO-III [?]. However this method requires the use of thick gas containers in the downstream detector region. This results in unwanted photon conversions and hadronic interactions, as well as safety concerns. Two atmospheric-pressure radiators were found to produce high acceptance rates: aerogel ( $n = 1.008$ ), and  $C_4F_{10}$  gas ( $n = 1.00153$ ). The  $C_4F_{10}$  gas radiator has been chosen for HALL D because it has a threshold momentum of  $2 \text{ GeV}/c$  for pions, which complements the TOF system's useful range of  $3 \text{ GeV}/c$  and below. The kaon threshold of  $9 \text{ GeV}/c$  in this gas is nicely above the momenta that will be encountered in the experiment, overlapping less with the TOF system.

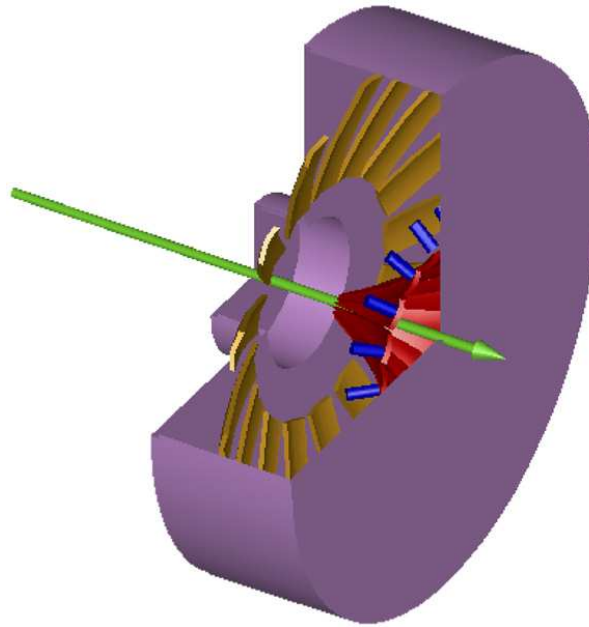


Figure 4.99: A schematic drawing of the HALL D Čerenkov detector system. The particles enter from the left into the gas volume in the center. The Čerenkov light is then reflected off the mirrors in the center (shown in dark) into the phototubes at the outer rim (shown as dark cylinders).

Gas-filled Čerenkov detectors have been used in many particle physics experiments. The original LASS spectrometer [?] used a freon radiator in a design similar to the one in HALL D. The primary changes we will make in the LASS design are the use of an environmentally friendly gas (freon is no longer available) and mirrors made of low-density carbon-fiber composite materials. The gas handling system will be patterned after a similar system now in use on the JLab CLAS spectrometer. The detector will be segmented into sixteen azimuthal regions, each

housing a single mirror that focuses light onto its own photomultiplier tube. Light emitted into the region within 10 *cm* of the beam axis will not be collected in order to suppress accidental coincidences in the detector. A sketch of the optical design is shown in Figure ???. The minimum radiator thickness encountered by a particle traversing the detector is approximately 90 *cm*. The measured performance of the JLab CLAS Čerenkov detector was used to estimate the photoelectron yield of the HALL D design, adjusting for radiator length and the number of mirror reflections. This results in an expected average yield of 5.0 (3.3) photoelectrons for 5.0 (2.9) *GeV/c* pions. Particles that traverse thicker regions of the detector will register proportionately larger signals.

The optical design of the detector (two ellipsoidal mirrors) was chosen to produce a strong focus at the photomultiplier tubes. This produces small linear magnification and allows good light collection from the wide range of particle trajectories exiting the solenoid. Prototype mirrors were constructed and tested for their focal properties. These were found to be mechanically and optically stable after cutting to shape. Having two mirrors in the design also offers flexibility as to the placement of the photomultipliers. This freedom was used to place the axis of the tubes perpendicular to the ambient magnetic field. This was done to optimize the effectiveness of the passive magnetic shields surrounding the photomultipliers.

A finite-element analysis of the shielding requirements was performed with the FLUX-3D computer code. A four-layer shield with axial symmetry was found to produce adequate reduction in the magnetic field. The predicted transverse field at the photocathode is less than 0.1 gauss. Burle 8854 photomultipliers were chosen for their high detection efficiency and low noise level.

A Monte Carlo simulation of the Čerenkov detector efficiency was made for the events in the following reaction:

$$\gamma p \rightarrow X p \rightarrow K^* \bar{K}^* p \rightarrow K^+ \pi^- K^- \pi^+ p \quad (4.21)$$

The geometry, mirror reflectivity, kinematics and photomultiplier response were modeled in the simulation, which yielded the detector efficiency as a function of pion momentum (see Figure ??).

#### 4.8.5 Acceptance of The Particle Identification System

Since each of the particle identification subsystems works most effectively in different regions of momentum and different regions of particle production, and since no subsystem alone can provide particle identification for all the events necessary for GLUEX analyses, it is crucial to integrate the information from the different subsystems in the most effective way possible. An algorithm based on assigning likelihoods to different particle hypotheses using information from all the relevant subsystems is one natural and straightforward way to proceed.

Given a track with a measured momentum, the basic idea is to use information from the different particle identification elements ( $dE/dx$  from the CDC, times from the BCAL and forward TOF, and Čerenkov photoelectrons or Čerenkov opening angle) to assign this track a set of likelihoods, each likelihood corresponding to a different particle hypothesis. For example,  $L(\pi)$  and  $L(K)$  are the likelihoods a given track is a pion or a kaon, respectively. Once these likelihoods are known, a statistical test can be performed to discriminate between hypotheses. One of the most convenient tests, the likelihood ratio test, works by forming the  $\chi^2$  statistic

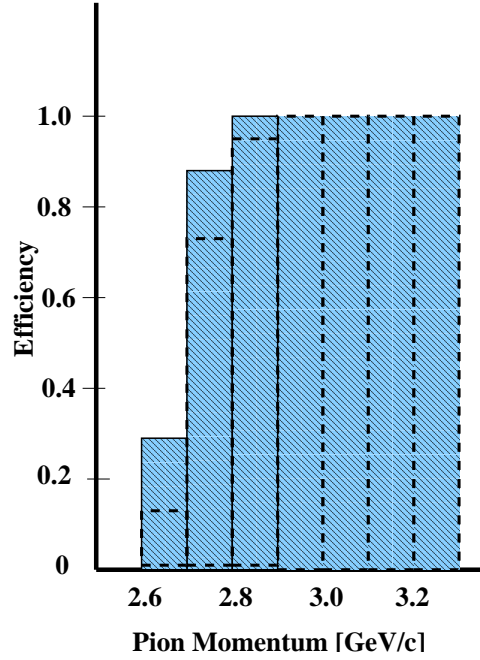


Figure 4.100: Predicted pion detection efficiency as a function of average pion momentum. The solid histogram is for a one-photoelectron detection threshold and the dashed line is for a two-photoelectron threshold.

$R(i)$  for each particle hypothesis  $i$  ( $i = \pi, K, p$ ):

$$R(i) = -2 \ln \frac{L(i)}{L(\pi) + L(K) + L(p)}. \quad (4.22)$$

Making the requirement

$$R(i) > 2.7 \quad (4.23)$$

rejects hypothesis  $i$  at the 90% confidence level.

This method lends itself well to the GlueX environment since separate likelihoods can be calculated for each subdetector individually and then combined into overall likelihoods. For example, the likelihood a given track is a kaon is computed from individual detector likelihoods as:

$$L(K) = L^{CDC}(K)L^{BCAL}(K)L^{CKOV}(K)L^{TOF}(K). \quad (4.24)$$

To illustrate how likelihoods are calculated for specific detector elements, consider the forward TOF system. Start with a track with measured momentum  $p$ . The expected time required for this particle to traverse a distance  $L$  from the target to the TOF wall can be calculated under different assumptions for the particle mass:

$$t_i = \frac{L}{c} \left( \frac{m_i^2}{p^2} + 1 \right)^{\frac{1}{2}}, \quad (4.25)$$

where  $i = \pi, K, p$ . This time will have an associated error  $\sigma_i$ , which can be obtained by combining the inherent resolution of the scintillator and electronics ( $\approx 70$  ps) with the effects of

momentum resolution and the uncertainty in the path length. Assuming the time measurement follows a gaussian distribution, the likelihood for hypothesis  $i$  is then:

$$L^{TOF}(i) = \frac{1}{\sigma_i \sqrt{2\pi}} \exp \frac{-(t - t_i)^2}{2\sigma_i^2}, \quad (4.26)$$

where  $t$  is the measured time the particle spent between the target and the TOF wall. The closer the measured time  $t$  is to a calculated expected value  $t_i$  the more likely the particle being considered is of type  $i$ . Likelihoods for the other detectors are calculated in a similar way, using predicted and measured  $dE/dx$  for the CDC, predicted and measured time at the BCAL, and the expected and observed numbers of photoelectrons in the gas Cerenkov (or the predicted and measured Cerenkov angle in a DIRC detector).

A simulation of the integrated GlueX particle identification system using the likelihood methodology was carried out for  $\gamma p \rightarrow K^* \bar{K}^* p$  events. The properties of these events have already been described at the beginning of this chapter (see figures ?? to ??). The generated events were sent through a full GEANT simulation and hits were recorded at each of the subdetectors associated with particle identification.

Relevant track measurements were smeared at each subdetector according to their expected resolutions. The  $dE/dx$  measurement of the CDC was smeared by 10%; the time of flight at the BCAL by 250 ps; and the time of flight at the forward TOF wall by 70 ps. In addition, the momentum and path length of each track was perturbed randomly by 1% to simulate uncertainties in the tracking. For the simulation using the Gas Cerenkov option (CKOV), the generated number of photoelectrons were distributed according to a Poisson distribution with an 80 cm  $C_4F_{10}$  radiator length with index of refraction  $n = 1.0015$  and efficiency  $N_0 = 90\text{cm}^{-1}$  (see equation ??). The Cerenkov opening angle of the DIRC option was smeared by its estimated resolution, 2.1 mrad. The particle separations in numbers of sigma versus momentum using these parameters were shown previously (figures ?? to ??).

Likelihoods were then calculated for each track at each detector and combined into total likelihoods according to the method described above. Particles were identified by rejecting hypotheses at the 90% confidence level, as prescribed in equation ?. A particle is called a pion if the kaon hypothesis is rejected and the pion hypothesis is not rejected:

$$R(K) > 2.7, R(\pi) < 2.7.$$

Similarly, a particle is identified as a kaon if:

$$R(\pi) > 2.7, R(K) < 2.7.$$

Finally, to find protons, both the pion and kaon hypotheses must be rejected, but the proton hypothesis is not rejected:

$$R(\pi) > 2.7, R(K) > 2.7, R(p) < 2.7.$$

This is perhaps the most basic algorithm possible for this situation. Certainly improvements could be made, such as incorporating strangeness conservation.

The results of this exercise can now be studied in several different pieces. Case 1(CDC) and case 2(CDC,BCAL) tracks are referred to as “central” (see figure ??); case 6(CKOV,TOF) and case 7(CDC,CKOV,TOF) tracks are “forward.”

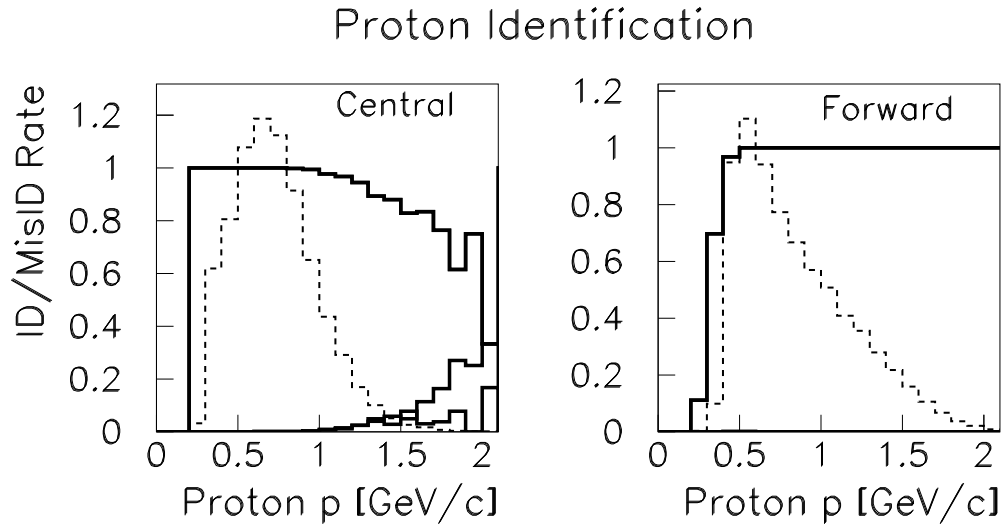


Figure 4.101: The acceptance of proton tracks in the reaction  $\gamma p \rightarrow K^* \bar{K}^* p$ . The left plot shows central tracks and the right plot shows forward tracks. The top curve is the correct identification rate; the bottom is the misID rate. The starting momentum spectra for proton tracks in the central or forward regions are shown in the background.

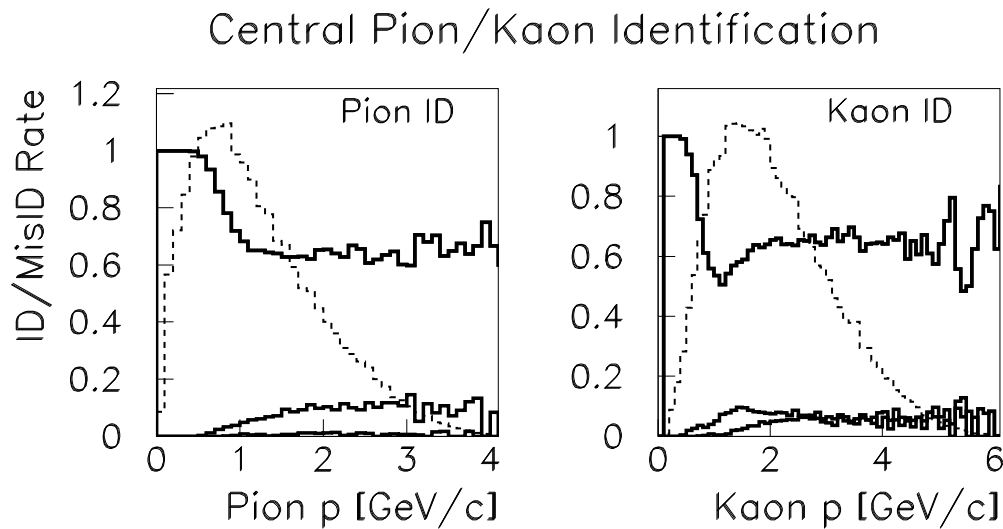


Figure 4.102: The acceptance of pions and kaons in the central region of the detector. The left plot is for pions; the right for kaons. The histograms in the background are the starting momentum spectra for pions and kaons in the central region. Each plot shows the identification and misidentification rates.

First consider proton identification. Figure ?? shows a nearly perfect proton identification rate for both the central region and the forward region; there is a drop in efficiency for central tracks above 1  $GeV/c$ , but it has little effect on the overall identification rate. In addition, only a small fraction of tracks are misidentified.

Next, pion and kaon identification rates in the central region of the deceptor are shown in figure ?. Tracks less than 1  $GeV/c$  are identified reliably; above that the efficiency drops to around 60%. Higher momentum central tracks are relying entirely on  $dE/dx$  information from the CDC in the relativistic rise region. With a  $dE/dx$  resolution of 10% this should be achievable at the 2  $\sigma$  level (also see figure ?). Table ?? tabulates all the particle id results for central tracks.

	$\pi$	$K$	p
Starting Number	50368	43665	62581
ID Rate	76.4%	64.0%	99.2%
MisID Rate	5.6%	10.1%	0.6%

Table 4.14: Particle identification in the central region for  $\gamma p \rightarrow K^* \bar{K}^* p$  events. The statistics are for case 1(CDC) and case 2(CDC,BCAL) tracks. The starting number is the number of  $\pi$ ,  $K$ , or  $p$  in the central region out of 100,000 total events generated.

Results for tracks in the forward region of the detector are shown in figure ?. The top two plots use the gas Cerenkov option. Notice the drop in efficiency between 2 and 3  $GeV/c$  where the momentum is too high for the TOF wall to be effective, but still not high enough to reliably measure photoelectrons from pions in the Cerenkov detector. The DIRC option solves this problem; its results are shown in the bottom two plots. Table ?? summarizes the efficiency numbers of forward tracks under the two different Cerenkov options. Finally, the central and forward cases are combined into overall pion and kaon identification rates in figure ?. The overall rates are tabulated in table ?.

	Gas Option			DIRC Option		
	$\pi$	$K$	p	$\pi$	$K$	p
Starting Number	38793	38789	30267	38793	38789	30267
ID Rate	94.4%	91.4%	99.1%	98.6%	90.3%	99.2%
MisID Rate	1.5%	4.8%	0.02%	0.3%	2.0%	0.8%

Table 4.15: Particle identification in the forward region for  $\gamma p \rightarrow K^* \bar{K}^* p$  events. The statistics are for case 6(CKOV,TOF) and case 7(CDC,CKOV,TOF) tracks. The starting number is the number of  $\pi$ ,  $K$ , or  $p$  in the forward region out of 100,000 total events generated.

It should be remembered that one of the crucial design parameters of the GLUEX experiment – in addition to, and perhaps more important than, the total efficiency numbers – is the uniformity of acceptances in the angles that will be used in Partial Wave Analyses. Efficiencies based on identification rates for the Gottfried-Jackson  $\cos \theta$  angle of the  $K^* \bar{K}^*$  system are shown in figure ?. This acceptance rises at  $\cos \theta \approx \pm 1$  and falls at  $\cos \theta \approx 0$  for the gas Cerenkov option for the following reason. When  $\cos \theta$  is near its extremes, the final state particles are typically divided into high momentum (along the decaying resonance direction) and low momentum (against the decaying resonance direction) cases. The high momentum tracks are

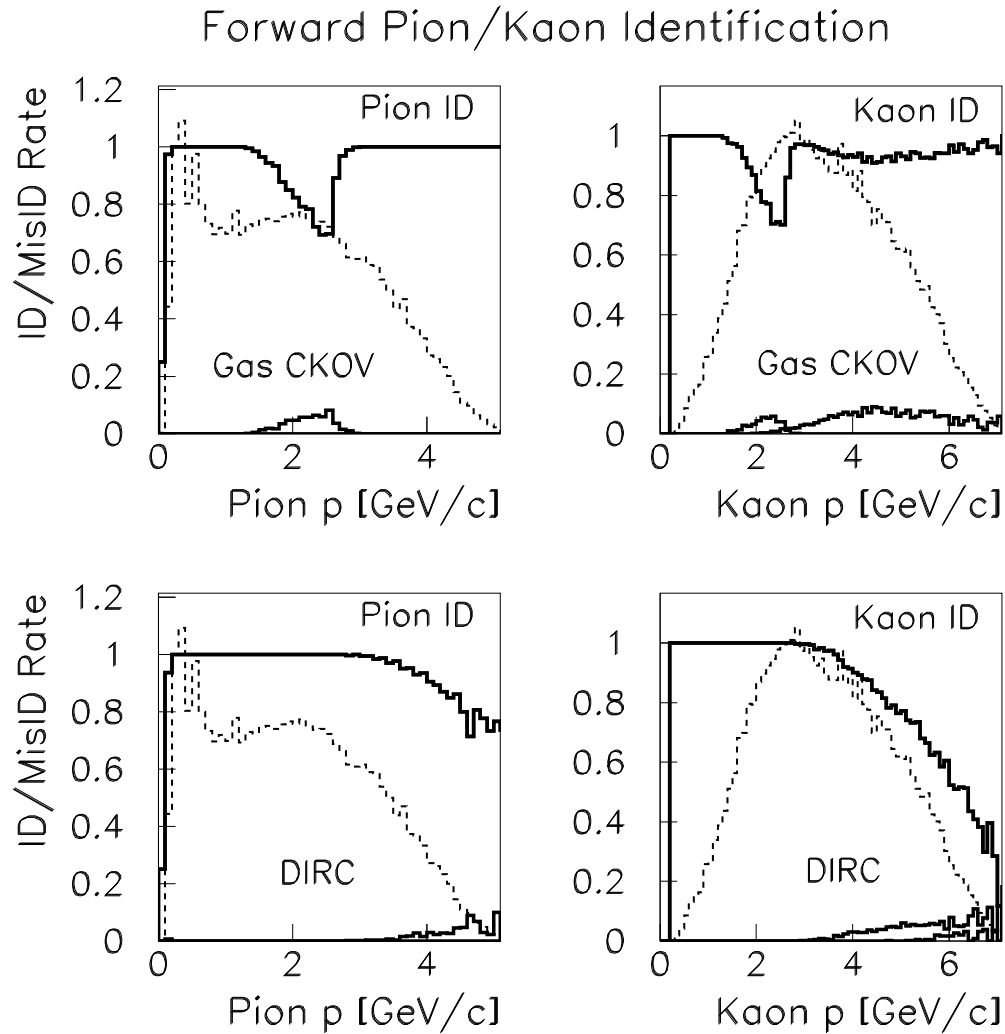


Figure 4.103: The acceptance of pions and kaons in the forward region of the detector. The top two plots are for the gas Cerenkov option; the bottom two are for the DIRC option. The left plots show pions; the right kaons. The histograms in the background are the starting momentum spectra for pions and kaons in the forward region. The curves in each plot represent the identification and misidentification rates.

above pion threshold and are identified by the gas Cerenkov system; the low momentum tracks are effectively identified by the TOF wall. On the other hand, when  $\cos\theta$  is near zero, final state tracks tend to fall in the momentum region where neither the TOF nor the gas Cerenkov is effective.

The DIRC option avoids this problem. Consequently, the  $\cos\theta$  acceptance of the second plot of figure ?? is significantly more uniform.

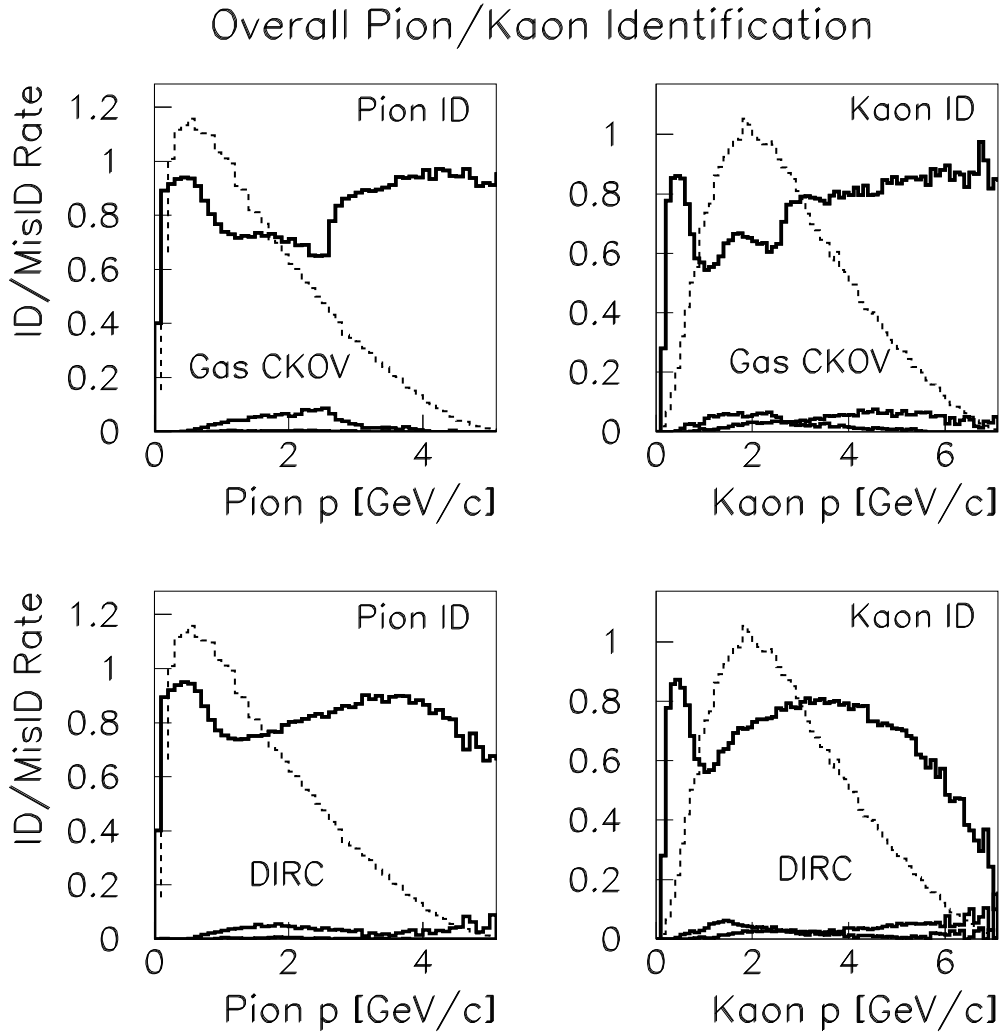


Figure 4.104: The overall acceptance of pions and kaons in all regions of the detector in the reaction  $\gamma p \rightarrow K^* \bar{K}^* p$ . The top two plots are for the gas Cerenkov option; the bottom two are for the DIRC option. The left plots show pions; the right kaons. The histograms in the background are the overall starting momentum spectra for pions and kaons. Each plot shows the identification and misidentification rates.

## 4.9 Detector Integration

The assembly and integration of each of the detector subsystems into the GLUEX detector requires careful coordination and attention to many diverse issues. The magnetic field configuration outside the magnet dictates the location and orientation of standard PMTs and/or use of high field devices such as HPMTs and SiPMs. The field distribution can be affected by magnetic materials used for support structures such as iron and, therefore, care must be

	Gas Option			DIRC Option		
	$\pi$	$K$	p	$\pi$	$K$	p
Starting Number	100000	100000	100000	100000	100000	100000
ID Rate	80.4%	71.2%	94.3%	82.9%	71.9%	94.7%
MisID Rate	3.5%	6.8%	0.4%	2.9%	5.3%	0.8%

Table 4.16: Overall particle identification for the reaction  $\gamma p \rightarrow K^* \bar{K}^* p$ . The statistics are for all track cases.

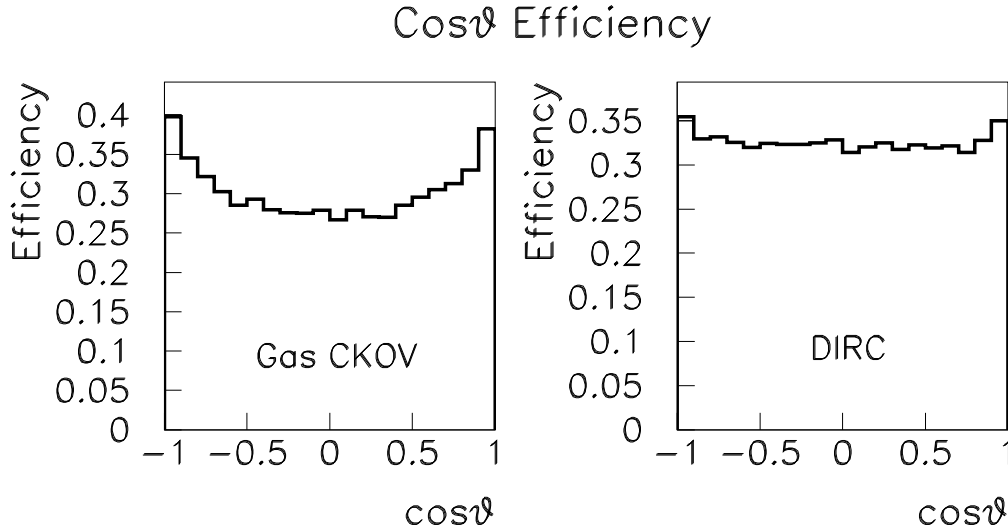


Figure 4.105: Angular efficiencies for  $\cos\theta$  in the Gottfried-Jackson coordinate system for  $\gamma p \rightarrow K^* \bar{K}^* p$  events. The left plot is for the Cerenkov option, the right for the DIRC option.

taken in choosing common materials for the various support systems. The magnetic field in the vicinity of the Čerenkov counter is estimated to be approximately over 1  $kG$  at the location of the readout devices and between 0.300  $kG$  and 0.160  $kG$  at the position of the PMTs for the forward LGD. The mounting and assembly of detectors must allow for the delivery of services required for their operation, including cryogenics, cooling, electrical power, ventilation, gas connections, high voltage and signal and monitoring cables for all detectors. Moreover, access to each sub-system must be facilitated for purposes of maintenance or repair.

The detector sub-systems are shown in Figure ?? while the general layout of HALL D with all detectors extracted is shown in Figure ?. As the detector will need to be in its extracted position for both installation and servicing, it is important that its layout in the HALL D building accommodate access to the detector. Figure ?? shows a sketch of the detector in HALL D. The cryogenic connections to the solenoidal magnet are brought in from the north-west corner of the building, opposite the ramp used for truck access. This permits a large staging area in front of the door and minimal blocking of crane movement by the cryogenic lines. These lines can also be used to feed other cryogenic systems such as the liquid hydrogen target and potentially VLPCs used in the start counter. Gas lines from external mixing systems can also

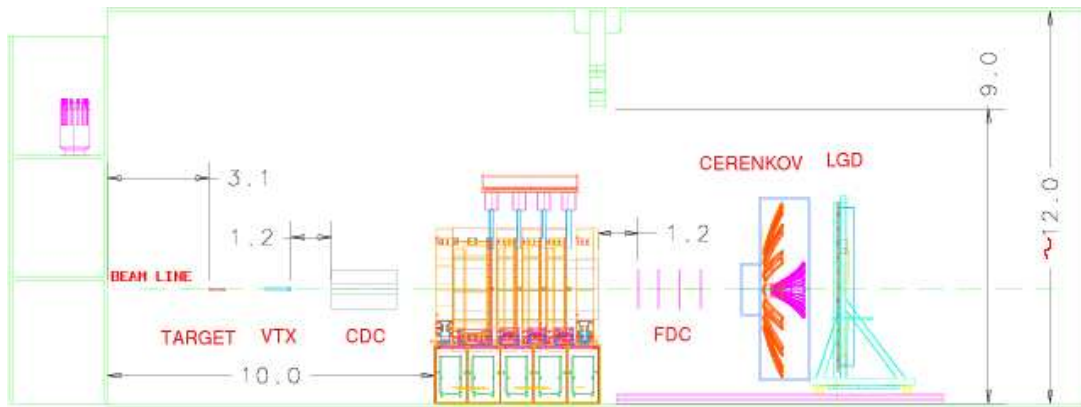


Figure 4.106: Exploded view of detector showing the detector subsystems in their extracted positions. The magnet does not move and detectors are inserted both from upstream and downstream into their nominal positions for normal operation.

be run along this common path to minimize obstructions for crane and assembly operations.

Electrical power will be most likely delivered in trenches in the floor from breaker panels located on the north wall of the building. Clean power will be provided to detector electronics using isolation transformers as close to the detector as possible. As an example, the estimated power consumption of the forward calorimeter is 30 KW. All detector frames will be connected to the building ground network both for safety and to minimize electrical noise.

In terms of installation, most of the detector is fairly open and can be quickly accessed with minimal disruption of operations. However, the limited space inside the solenoidal magnet deserves special attention. This space contains the BCAL and its support structure, the Straw-tube Chamber, CDC, the Forward Drift Chambers, FDC, and the structures which both align and support these chambers as well as the mechanisms for extracting them. Finally, inside the CDC is space for the liquid hydrogen target, the beam pipe and the Start counter. Space allocation also needs to be made to assure that signals cables can be brought out from the detectors, while voltage and monitoring cables as well as gas, cryogenics and cooling lines can be brought to the appropriate detectors. Table ?? shows the radial space allocation inside the solenoid. The spaces labeled *keep out* are reserved for support, installation structures, signal and power cables, and other necessary services to the detectors such as gas and cooling.

Detector Name	$r_{min}$	$r_{max}$
Solenoid	92.7 cm	
Keep Out	90 cm	92.7 cm
Barrel Calorimeter	65 cm	90 cm
Keep Out	59 cm	65 cm
Straw Tube Chamber	13 cm	59 cm
Forward Drift Chambers		59 cm
Keep Out		12 cm

Table 4.17: A radial space allocation map for the space inside the GLUEX solenoid.

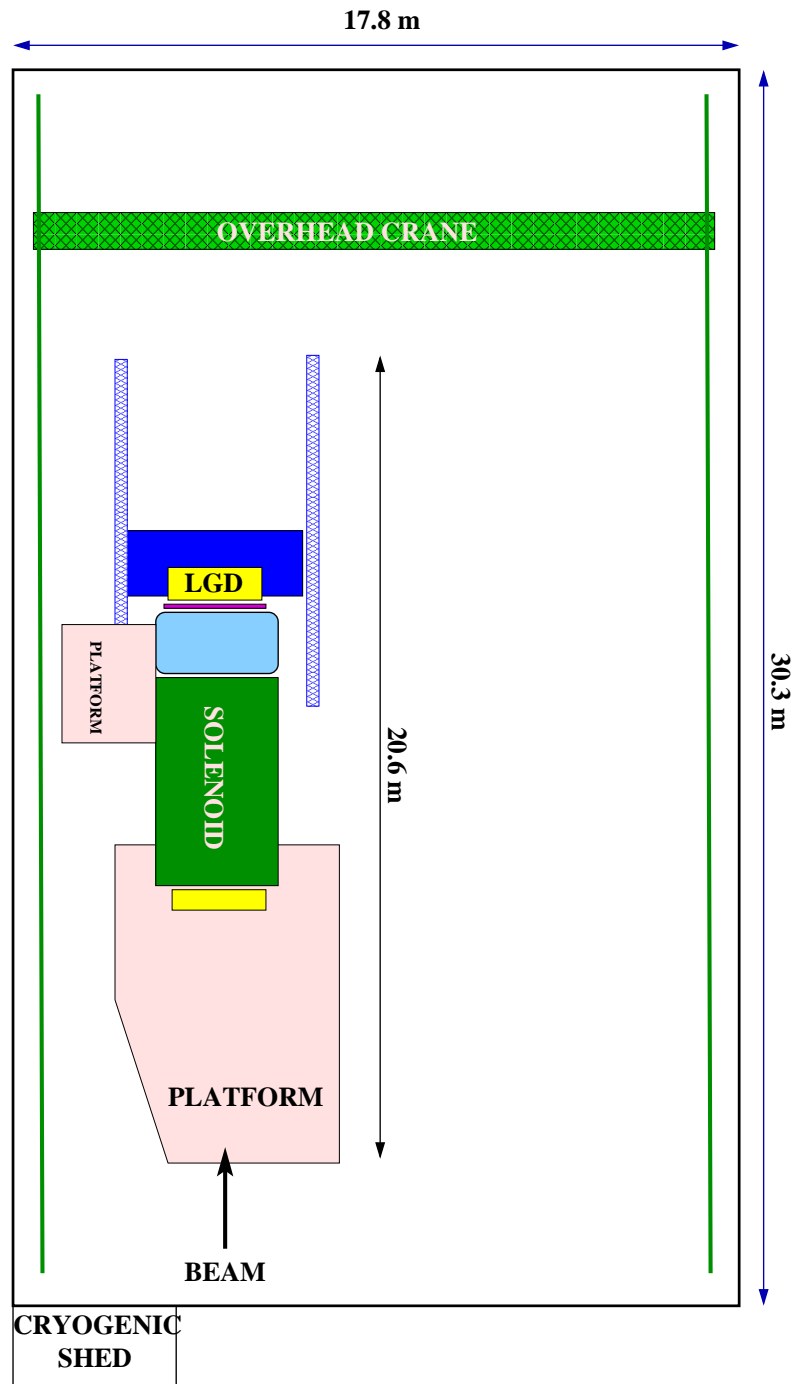


Figure 4.107: Plan view of the GLUEX experiment in HALL D.

### 4.9.1 Assembly and Mounting

As much of the GLUEX detector will need to be assembled in HALL D, the construction of the building is critical to any time line of the experiment. It is absolutely necessary that JLab do everything possible to guarantee early construction of this building. Once the building can be occupied, the assembly of the detector can begin. The first item will be the solenoidal magnet. It is transported in sections and will need to be re-assembled inside HALL D. It is also expected that both the BCAL and the LGD calorimeters will be assembled in HALL D. The assembled LGD will not fit through the door. It is also possible that parts of other detectors would be assembled in the HALL D building as well.

Of all the in-hall assemblies, the BCAL is likely to be another time line bottle neck. The time from start of construction until delivery at JLab is estimated at three years, but it is likely that the detector would arrive in several shipments spread out over the 3-year time frame. There are currently two possible assembly scenarios. The first follows what was done with the KLOE detector. This would have the BCAL being assembled inside the solenoid. The draw back to this plan is that the assembly of th BCAL cannot begin until the solenoid is fully installed. A second scenario would be to assemble the BCAL in a vertical orientation outside the solenoid, and then rotate it to horizontal and roll it into the solenoid as a single unit. This latter scenario both allows assembly to proceed in parallel with the solenoid and requires less service space between the outside of the BCAL and the inside of the solenoid. In both scenarios, the BCAL would be held in place with bolts that come through ring girders in the gaps between the magnet coils. These would connect to the 2.5 cm thick Aluminum backing plates on the BCAL modules as shown in Figure ???. In both installation scenarios, an assembly and installation jig will need to be designed and built. These options are currently under study by the engineering staff at JLab.

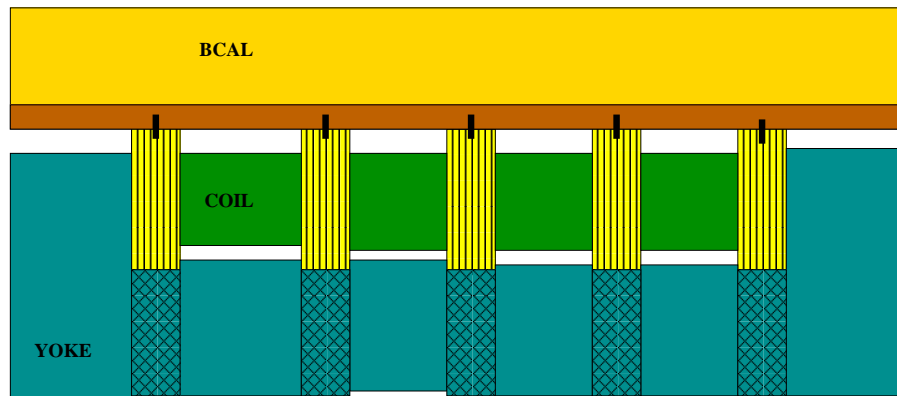


Figure 4.108: The Barrel Calorimeter bolted to the inside of the solenoid.

Once the BCAL has been mounted on the inside of the magnet, only the readout electronics

will be accessible. Because of its design, it is anticipated that once it has been installed, it will not be removed. If for some reason it became crucial to replace a modules, a fairly extensive down time would need to be scheduled. However, given that there is nothing that can be serviced except for the readout electronics, such an event is considered highly unlikely over the lifetime of the experiment. Finally, to facilitate the installation of the tracking devices inside the solenoid, we anticipate placing a protective cover over the inner face of the BCAL. This will both protect the calorimeter and provide a surface to which the chamber supports can be mounted.

After the BCAL has been mounted in the solenoid, it will be necessary to install a pair of rails along the length of the detector. These rails will be used to support the CDC and FDC packages. Extensions can be added to allow for installation and extraction of the chambers. There is some possibility of the lead in the barrel calorimeter settling slightly over time. While we are currently investigating this, we also recognize that the rails will need to be fitted with bearings that have some play to prevent things from locking up due to small shifts in the *bed rock*. Both because of the difficulty of maintaining precision alignment between two rails over the 4 m length of the magnet and the possibility of settling in the BCAL, we anticipate no more than one precision rail, with the 2'nd rail being used for load bearing.

The CDC will be inserted from the up-stream end of the magnet, while FDC will be inserted from down-stream end. On the down-stream end, the Čerenkov, TOF and LGD detectors will be rolled back to make room for the FDC packages. On the up-stream end, the UPV will need to be put in place after the CDC has been installed. Then the START counter and target will be inserted into the CDC from the upstream end. They will be mounted on an independent cantilever system.

The Čerenkov counter and forward calorimeter will be mounted on independently movable support frames which can be moved in and out of their nominal location for access to the FDC. The TOF detectors will be mounted on the frame for the forward calorimeter. Each support structure will be self-contained, including electrical power and the appropriate readout electronics. Access platforms will be provided to allow easy access to the PMTs and readout electronics.

#### 4.9.2 Survey and Alignment

In order to achieve the physics goals of the experiment, a system must be devised that can measure and maintain at least  $100\ \mu\text{m}$  relative alignment of all of the tracking packages inserted into the magnet. The locations of the drift chamber wires relative to each other and the magnetic field are the most critical alignment tasks for the experiment. In addition, for ease of maintenance, the positions of the chambers should be either reproducible at that level, or a system needs to be established that can easily survey them into position at this accuracy. It will also be important to have an on-line monitoring system in place to dynamically correct for time dependent shifts in alignment. Such shifts might arise due to settling of the BCAL, thermal expansion and contracting of the chambers themselves, or accidental moving of the chambers when other detectors are being serviced. The collaboration is currently exploring the use of a system used by ATLAS for maintaining alignment.

As the CDC and FDC are inserted from opposite ends of the magnet, the mating and initial alignment are blind. The  $z$  positions of these chambers can be accurately registered at a single point by surveying in stops along the guide rail. We will also need a remote adjustment system

that allows for correction of possible *pitch*, *roll* and *yaw* of the chamber packages.

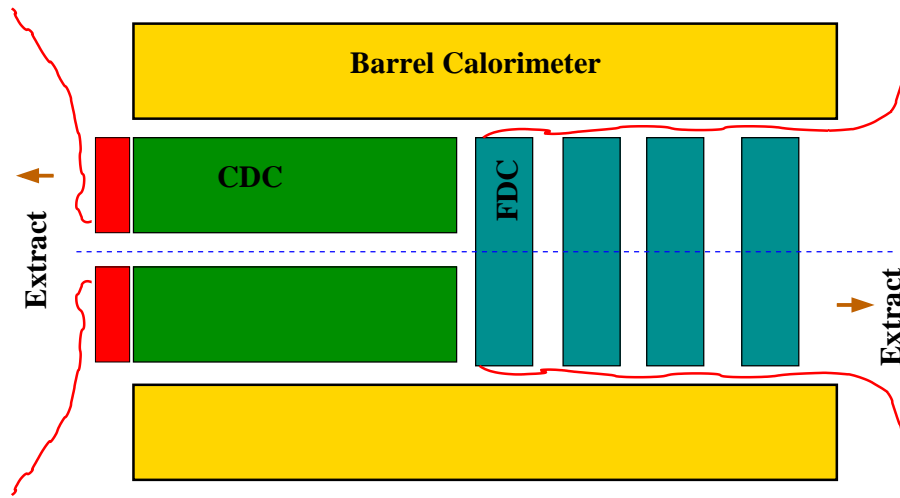


Figure 4.109: The insertion of the Central and Forward Tracking chambers inside the Barrel Calorimeter.

### 4.9.3 Access

Ease of access to the detector for maintenance ensures short commissioning and debugging times. Our goal is to allow maintenance of all detector components in less than one day. In order to maintain or check the upstream BCAL readout, the UPV will have to be removed and the service platform must be designed in a way to allow access to readout both above and below the horizontal scattering plane of the detector. To service the CDC, the UPV, the target and START detectors must be moved out of the way. All serviceable elements are located on the upstream end of the CDC. To access the FDC and/or the downstream BCAL readout, the Čerenkov and forward calorimeter must be moved on their rail systems, as shown in the exploded view in Figure ???. Service to the FDC is likely to be the most involved operation. Once the downstream detector packages are moved out of the way, a support structure will need to be craned in, and the chambers extracted from the solenoid.

The readout electronics for all the systems will be accessible without having to move any detector component. The PMTs for the Čerenkov, TOF and LGD will be accessible by at most moving the forward calorimeter carriage. Access to the LGD enclosure will in principle be easy, but radiation levels must be measured and deemed to be at a safe level prior to any access.

### 4.9.4 Interaction Between Subsystems

The detectors in the forward direction (Čerenkov, TOF and LGD) are relatively isolated mechanically and operate independently of other systems. The detectors inside the magnet, however, are in close proximity and mounted on the same mechanical frames that are anchored on the BCAL and/or the solenoid. Therefore, cabling, power consumption, and access for maintenance must be coordinated carefully.

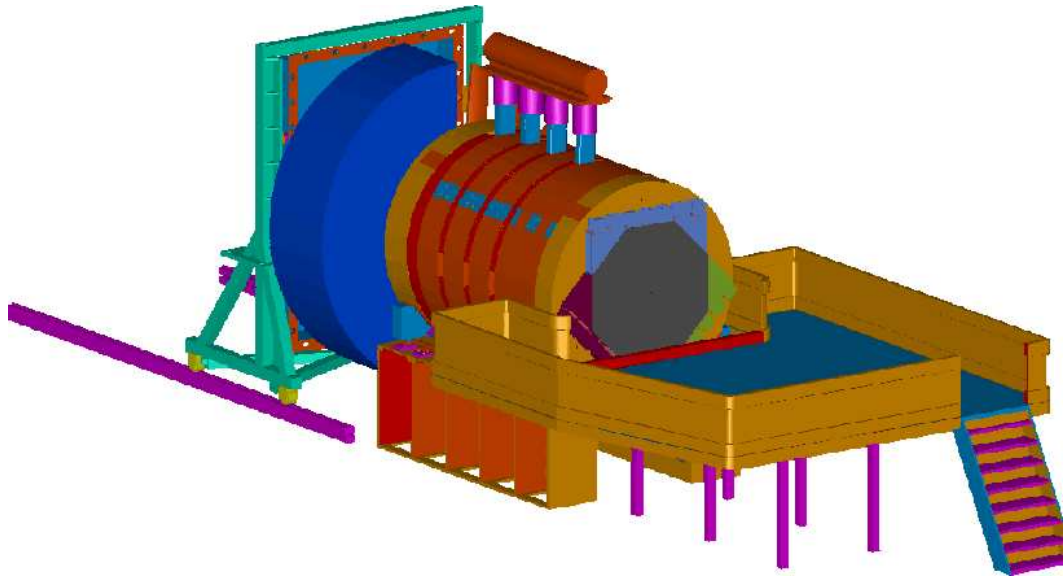


Figure 4.110: Detector and upstream platform for service of the inner detector packages.

#### 4.9.5 Cabling

All detector electronics will be located near the detector itself. This will minimize cable lengths and eliminate the need for large cable runs from the detector to electronic racks far from the detector. The racks of electronics servicing the inner detectors will be located on a platform upstream of the magnet with ample space for access. A possible *Access Platform* is shown in Fig.?? with the primary aim being that detectors can be operated both inside and outside the solenoid without making any disconnections. This implies that either the cabling for START detector, CDC and FDC will have enough slack so that they can be moved in or out of the magnet without any disconnections, or that the electronics will themselves move along with the detector elements. It is crucial that the detectors can be operated in the extracted position for testing and the installed position during normal operation without wiring changes.

# Chapter 5

## Readout Electronics

### 5.1 Overview

The goal of the GLUEX readout electronics system is to digitize and read out the detector signals for level 1 trigger rates of up to 200  $kHz$  without incurring deadtime. A pipelined approach is required. The digitized information will be stored for several  $\mu s$  while the level 1 trigger is formed. Multiple events must be buffered within the digitizer modules and read out while the front ends continue to acquire new events.

A summary of the GLUEX detector subsystems from an electronics viewpoint is shown in figure ??.

Two basic types of readout electronics will be used in GLUEX, FADCs and TDCs. Detectors which measure energy will be continuously sampled with flash ADCs while detectors which require precise time measurements will use a multi-hit TDC. No currently available commercial solutions exist. These boards will be designed by our collaboration. Prototypes have been constructed, and are being tested.

The number of channels in the GLUEX detector is not large enough to justify the financially risky development of custom integrated circuits. ICs developed for other experiments will be used as well as commercially available chips. Programmable logic devices will be extensively used for data path, memory, and control functions.

Technology is constantly evolving, and the optimum solution for the GLUEX detector depends on when funding becomes available and the construction schedule. Presented here is a preliminary design which could be implemented with currently available components.

### 5.2 FADCs for Calorimetry

The calorimeters will be read out with 8-bit, 250  $MHz$  FADCs. The 250  $MHz$  sampling clock will be derived from the 1499  $MHz$  accelerator clock. This sampling rate and bit depth is well matched to the FEU84-3 PMTs used in the Forward Calorimeter, and is adequate for the silicon PMTs used in the Barrel Calorimeter. Additional FADC channels will read out the Photon Tagger, Backwards Veto, Start Counter, Čerenkov Detector, and time-of-flight PMTs.

Figure ?? shows an FEU84-3 PMT pulse digitized by the prototype FADC described in section ??. Note that the sum of the samples from 120 to 180  $ns$  is 1429; for this PMT the 8-bit FADC is equivalent to a 10 or 11-bit conventional charge-integrating ADC. To address

**Summary of GlueX Detector Subsystems**

Detector	Photon tagger	Upstream Photon veto	Start counter	Central drift	Forward drifts	Cerenkov	Time-of-flight	Barrel calorimeter	Forward calorimeter
<b>Type</b>	Scintillator	Scintillator	Scintillator	Straw tube	Planar chamber	Gas	Scintillator	Sci fibers	Lead glass
<b>Energy resolution</b>	0.1% (segmentation)	10%/√E	N/A	20%	N/A	N/A.	N/A	10% @ 1 GeV	3.6% + 7.1%/√E
<b>Channel count</b>	192	20	40	3240	2900 anode 11,400 cathode	40	168	960	2500
<b>Signal source</b>	PMT	PMT	PMT	Straw tube	anode wires cathode strips	PMT	PMT	SIPMT	PMT
<b>Physics signal</b>	100 pe	100 pe	100 pe	25 e	25 e	5 pe	500 pe	100 pe/GeV	250 pe/GeV.
<b>Gain in detector</b>	10 <sup>6</sup>	10 <sup>6</sup>	10 <sup>3</sup>	10 <sup>4</sup>	10 <sup>4</sup>	10 <sup>6</sup>	10 <sup>6</sup>	10 <sup>6</sup>	10 <sup>6</sup>
<b>Typical charge</b>	16 pC	16 pC	16 pC	40 fC	40 fC anodes 4 fC cathodes	1 pC	80 pC	16 pC/GeV	40 pC/GeV
<b>Preamp gain</b>	no	no	no	10 <sup>3</sup>	10 <sup>3</sup> anodes 10 <sup>4</sup> cathodes	10 <sup>2</sup>	no	no	no
<b>Discrimination</b>	constant fraction	no	constant fraction	no	yes (anode) no (cathode)	no	constant fraction	constant fraction	no
<b>Time resolution</b>	100 ps	1 ns	350 ps	1 ns	1 ns	3 ns	80 ps	200 ps	400 ps
<b>Dynamic range</b>	5	100	100	1000	100 anodes 1000 cathodes	10	10	1000	1000
<b>FADC</b>	8 bits 250 Msps	8 bits 250 Msps	8 bits 250 Msps	10 - 12 bits 125 Msps	Cathodes: 10 - 12 bits 62.5 Msps	8 bits 250 Msps	8 bits 250 MSPS	8 bits 250 Msps	8 bits 250 Msps
<b>TDC</b>	62 ps yes (low rate runs)	no	62 ps track count	no	Anodes: 125 ps	no	31 ps	62 ps track count	no
<b>Level 1 trigger</b>		no	count	no	no	no	track count	track count energy sum	energy sum

Figure 5.1: Detector subsystems

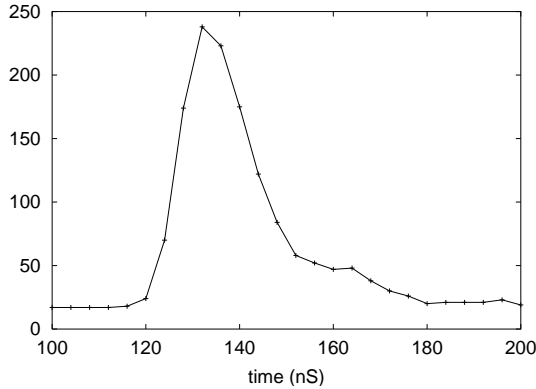


Figure 5.2: Digitized FEU84-3 pulse.

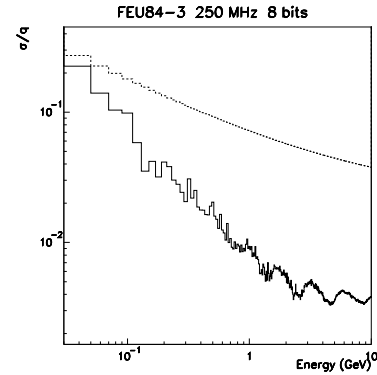


Figure 5.3: Dashed - calorimeter resolution, Solid - FADC resolution.

resolution concerns, simulations were performed to show that the proposed FADC provides an adequate measurement. Pulses measured with a digital oscilloscope were fitted to determine their functional form. The response of the FADC was simulated using this functional form and the time integral of the function was compared to the summed output of the simulated FADC for many pulses. Since the relationship between deposited energy and pulse height in this type of calorimeter is known, direct comparison of the resolution due to the FADC and the resolution of the calorimeter is possible. Figure ?? shows the result of this comparison. Clearly, above 0.15  $GeV$  the resolution of the FADC is small compared to the intrinsic resolution of the calorimeter.

The FADCs will also give a measurement of the time a photon arrived at the calorimeter. Previous work [?, ?] indicates that a time resolution better than the FADC sampling interval can be achieved by fitting the FADC waveform. To study how well this time could be determined a “library” of pulses from phototubes of the type to be used was created using a digital oscilloscope with a 2.5  $GHz$  sampling frequency. The leading edge of these sampled pulses were fitted to a 9th order polynomial to determine the location of various “features” of the pulses. The features considered were the time the pulse achieved 10, 25, 50, 75, 90 and 100% of its maximum value. These features carry the arrival time information of the pulses and were used as reference times.

To determine how well the FADC could determine the pulse arrival time, the samples from the digital oscilloscope (2.5  $GHz$ ) were averaged over 10 samples (to 250  $MHz$ ) and quantized to 8 bits. These transformed samples are what would be expected from the FADC system proposed here. Using only the bin containing the pulse maximum and the two samples preceding it and a simple algorithm, it was found that the 50% crossing time could be determined with a resolution of 160  $ps$  compared to the time determined by the detailed fitting described above. This resolution is sufficient to determine if a pulse is in time with an event (rejecting background) or to determine the time of the event sufficiently well to select the beam “bucket” that initiated the event.

### 5.2.1 Prototype

A single channel prototype of the calorimeter FADC has been designed and built at Indiana University. A block diagram is shown in Fig. ?? and a photo in Fig. ??.

A differential amplifier inverts the negative PMT signal and shifts the voltage levels to

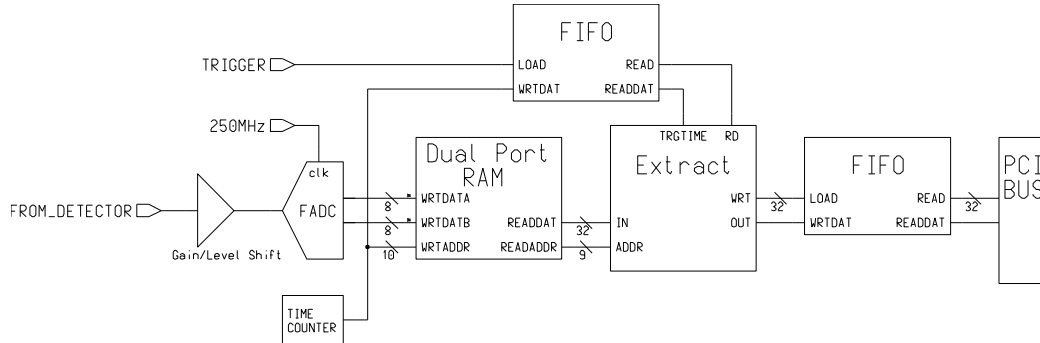


Figure 5.4: Block diagram of prototype FADC board.

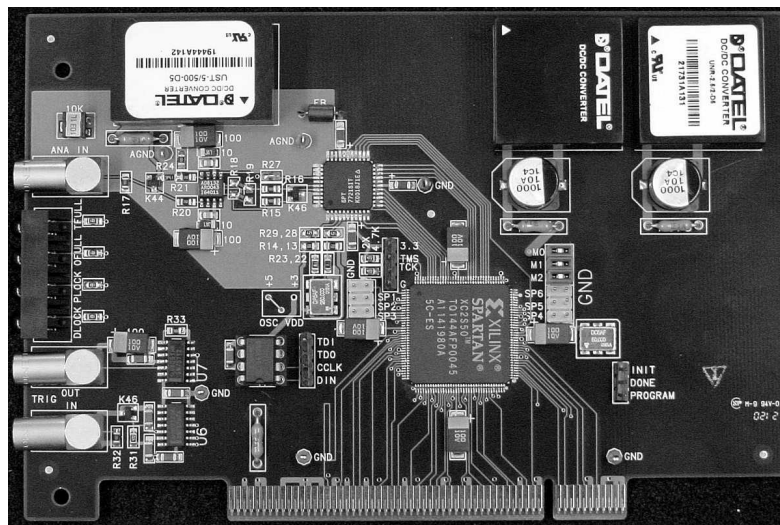


Figure 5.5: Photograph of prototype FADC board.

match the input range of the digitizer integrated circuit. The digitization is performed by an SPT7721 integrated circuit manufactured by Fairchild Semiconductor<sup>1</sup>. This IC costs about US\$20. An 8-bit value is produced internally every 4 ns; two samples are output every 8 ns (125 MHz).

All digital functions are performed in a Xilinx<sup>2</sup> XC2S50 programmable gate array. This IC costs about US\$10. A dual port RAM configured as a circular buffer stores the data for 8 microseconds. Upon receipt of a trigger signal the data from the time window of interest is copied to an output FIFO which can buffer the data from multiple events. This FIFO is interfaced to a 32 bit, 33 MHz PCI bus<sup>3</sup>.

<sup>1</sup> Signal Processing Technologies: <http://www.spt.com>

<sup>2</sup> Xilinx: <http://www.xilinx.com>

<sup>3</sup> More information on this prototype is available <http://dustbunny.physics.indiana.edu/~paul/hallDrd>

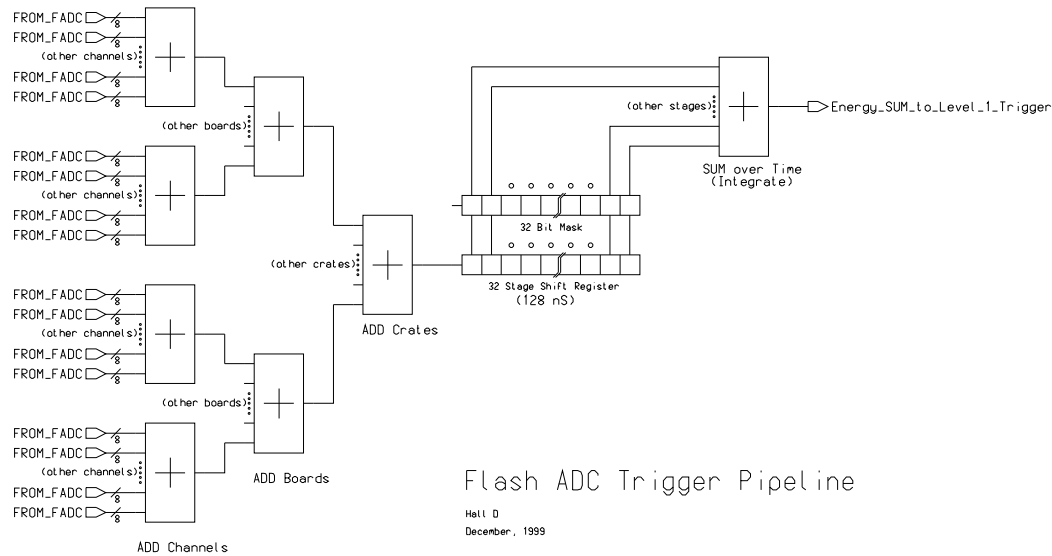


Figure 5.6: Block diagram of energy sum.

### 5.2.2 Additional requirements for final version

The final version of the calorimeter FADC board will include pipelined adders operating at the 125 MHz digitizer output clock which continuously sum the digitized information from all channels on a board. Additional pipelined adders will sum the information from all boards in a crate, and then sum the information from all the crates associated with a detector. The sum of all channels will be passed through a shift register giving a time history. Successive samples within a programmable time window will be summed, analogous to the gate in a conventional charge sensitive ADC. Energy sums from the Forward and Barrel Calorimeters will be used in the level 1 trigger. A block diagram is shown in Fig. ??.

Assuming a 100 ns time window, each FADC channel will produce 25 bytes of data per level 1 trigger. In the final version of the FADC we will want to suppress the readout of channels with no data. The FADC data will be processed in real time to provide an energy and time measurement. We believe that the raw FADC data can be reduced to about 10 bytes per channel. This zero suppression and pulse shape processing may be done at the channel level in the gate array, at the board level, the crate level, the detector system level, or in some combination of these levels.

## 5.3 FADCs for Tracking

The Central Tracking Drift Chamber anodes will be read out with 10 or 12-bit, 125 MHz FADCs. The additional dynamic range is required for the  $dE/dx$  measurement. The Forward Tracking Drift Chamber cathodes will be read out with 10 or 12-bit 62.5 MHz FADCs. The exact read out electronics requirements for these detectors is the subject of ongoing R&D efforts.

## 5.4 TDCs

The Photon Tagger, Start Counter, Forward Drift Chamber anodes, Čerenkov Detector, Barrel Calorimeter, and Time of Flight detectors will be read out by multi-hit TDCs.

### 5.4.1 Jefferson Lab TDC

A high resolution pipeline TDC module has been developed for use at Jefferson Lab. The design is targeted to meet the requirements of current experiments, as well as to serve as a prototype for future experiments at Jefferson Lab, including Hall D. The design is implemented as a VME-64x module. This bus standard was chosen because it is already in use at Jefferson Lab, has good (and evolving) data transfer capabilities, and reasonable channel densities are possible.

The module is built around the TDC-F1 integrated circuit from acam- messelectronic gmbh<sup>4</sup>. The TDC-F1 chip was designed for the COMPASS experiment [?] at CERN, and costs about \$130 each in small quantities. The chip utilizes purely digital delay techniques to measure time. In normal mode the TDC-F1 chip provides 8 input channels with resolution of 120 ps (LSB). In high resolution mode channels are combined in pairs to yield a resolution of 60 ps for 4 input channels. The dynamic range for measurement is 16 bits. The resolution of the chip is tunable about its nominal value. A PLL circuit adjusts the core voltage of the chip to compensate for temperature and supply voltage variation, assuring stability of the resolution value. On-chip buffering for input channels, triggers, and output data allows for multihit operation with nearly zero deadtime. The chip also has a complex trigger matching unit that can filter out hits unrelated to the input trigger. When enabled, only hits that are within a programmed timing window and latency from the trigger time are kept. The trigger matching feature is used in common start and synchronous measurement modes. In common start mode, an external start signal resets the internal measurement counter and a delayed trigger signal sets the measurement window. In synchronous mode, an external 'sync reset' signal is used to reset the internal measurement counter and clear internal buffers. Internal start signals are then automatically generated at a programmable rate.

Figure ?? shows a block diagram of the TDC module. The 8 TDC-F1 chips on the module provide 64 channels in normal mode, or 32 channels in high resolution mode. Front panel input signal levels are differential ECL to be compatible with existing systems at Jefferson Lab. Timing control signals are also available through backplane connections for ease of system integration. A 128K word deep FIFO is attached to each TDC-F1 chip to buffer its output data. In addition, a global 1K word FIFO buffer is implemented within the single FPGA that controls the module. The external RAM shown in the figure is not present on this version. The module can be set up to interrupt the crate controller after a programmable number of triggers have been received. During read out the module will provide a block of data associated with a programmed number of triggers, and then terminate the transaction. To enhance system performance a set of TDC modules may be read out as a single logical read using a multiblock read protocol. This involves passing a token between modules along a private daisy-chain line. In this setup, only the first module in the chain will generate the interrupt, and only the last module in the chain will terminate the transaction. Configuration parameters for the 8 TDC-F1 chips are stored in non-volatile memory on the module and may be updated by the user. The

---

<sup>4</sup> Details of the "F1" chip can be found at <http://www.acam.de>

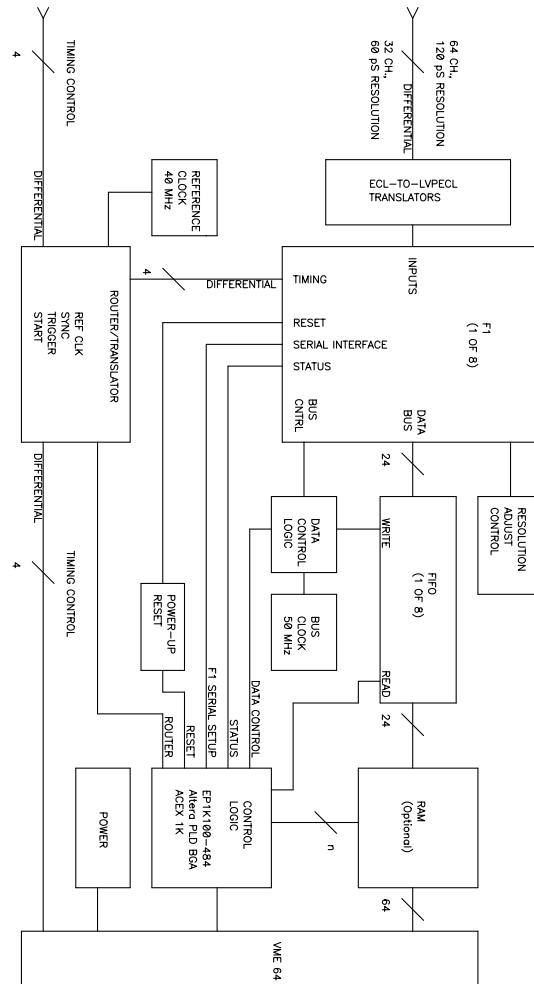


Figure 5.7: Block diagram of TDC board.

configuration process is automatic at power up.

A photograph of the module is shown in Figure ???. Fifty TDC modules have been produced and are currently being installed into Jefferson Lab experiments in Halls B and C.

### 5.4.2 TDC Performance

Figure ?? shows the timing distribution for an input signal that has a fixed time relationship to the start signal. The TDC was operated in high resolution mode. Unfolding the uncertainty of the input signal (33 ps) from the measured distribution yields a TDC resolution (RMS) of 61.2 ps. Figure ?? shows the equivalent distribution for a TDC operated in normal resolution mode. The resolution is 86.2 ps. These resolutions were confirmed across the entire dynamic range of the TDC, and for trigger rates up to 200 KHz. Full crate tests have been performed using the multiblock readout protocol. Sustained data transfer rates of 40 Mbytes/s over the

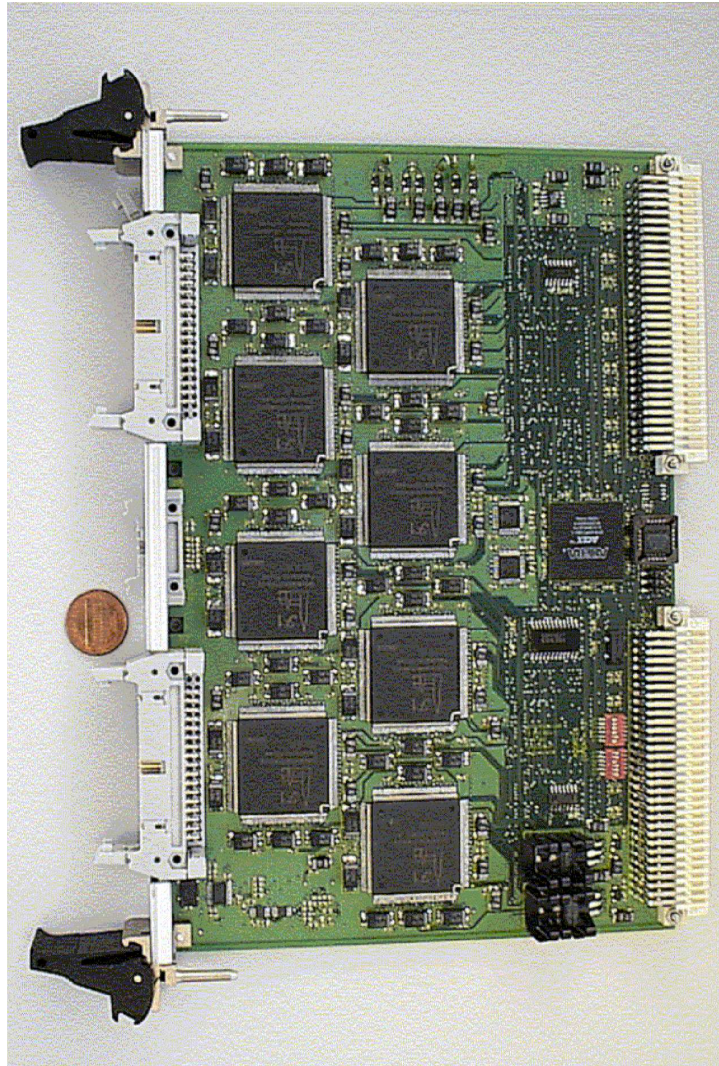


Figure 5.8: Photograph of TDC board.

VME bus have been achieved.

### 5.4.3 Additional requirements for final version

A 62.5 MHz clock phase-locked to the accelerator will be distributed to all TDC modules so that every channel has the same time calibration. With this clock frequency, LSB resolutions will be 125 ps for the standard version and 62.5 ps for the high resolution version.

A commercial TDC module, the CAEN<sup>5</sup> v1290, based on the HPTDC chip developed at CERN, is being evaluated by Jefferson Lab. It might be possible to use this type of TDC to provide 31 ps LSB resolution for the time-of-flight counters.

---

<sup>5</sup> CAEN: <http://www.caen.it>

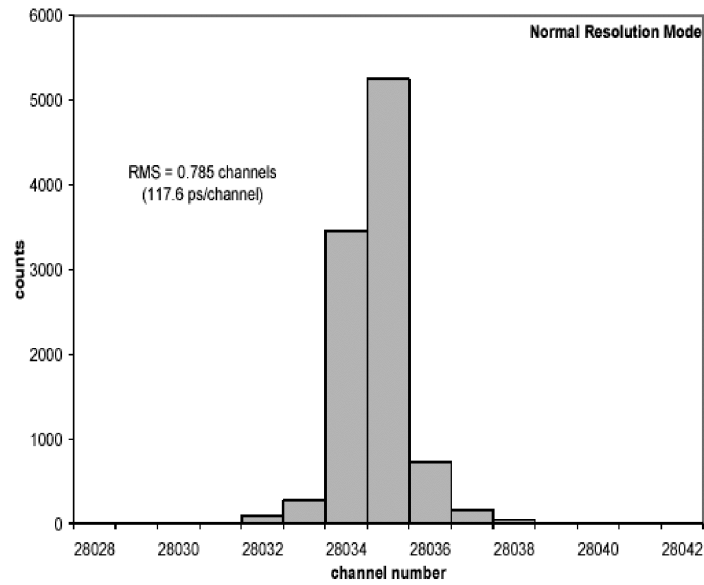


Figure 5.9: TDC performance in low resolution. (resolution=86.2ps)

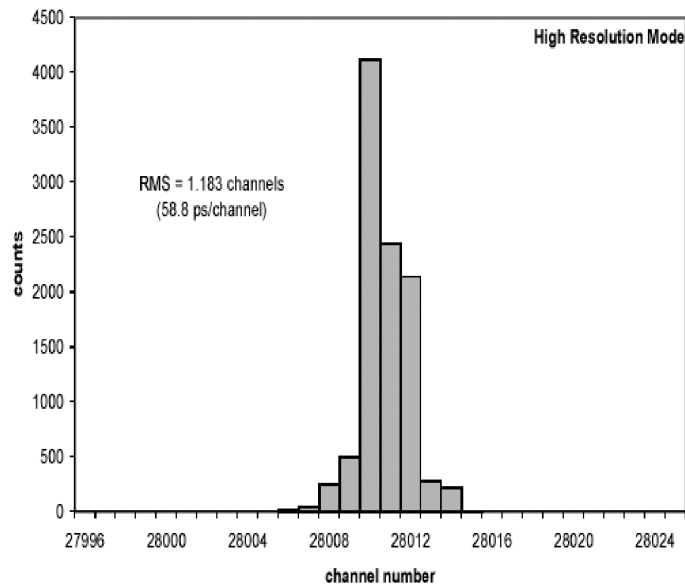


Figure 5.10: TDC performance in high resolution. (resolution=61.2ps)

## 5.5 Track Count

The Start Counter, Barrel Calorimeter, and Time of Flight detectors will require pipelined adders to implement a track count for use in the level 1 trigger.

## 5.6 Clock Distribution and Pipeline Synchronization

A 62.5 MHz global front end clock will be phase-locked to the 1499 MHz accelerator clock. This global clock will be distributed to all readout electronics crates and used directly by the TDCs and Forward Drift chamber cathode FADCs. The Calorimeter and Central Drift chamber FADCs will phase-lock their higher frequency clocks to the global front end 62.5 MHz clock. A global reset will be distributed to synchronize all pipelines. The level 1 trigger as well as calibration and other special triggers will also be distributed globally.

## 5.7 Discriminators and Amplifiers

Detectors which provide precise timing (Photon Tagger, Start Counter, Barrel Calorimeter, and Time of Flight counters) will require “constant fraction” discriminators. The Forward Drift Chamber anodes require leading-edge discriminators mounted on the chambers inside the solenoid. The Central Drift Chamber anodes and Forward Drift Chamber cathodes will need an amplifier to drive their FADC inputs. These amplifiers should be located on the chambers. ICs developed for the Atlas <sup>6</sup> detector are being considered for all chamber mounted electronics.

## 5.8 High Voltage

The Forward Calorimeter PMTs will be powered by Cockcroft-Walton voltage multipliers [?] which will be built at Indiana University. This type of base provides for the very low power consumption necessary for such a tightly packed array and is controlled over a CAN communication link. One hundred prototypes of these bases have been built at Indiana University and are being tested. The other GLUEX PMTs will likely use conventional resistive divider bases powered by commercial HV power supplies. The Tracking Chambers will use commercial HV power supplies with sensitive current monitoring.

## 5.9 Packaging

The calorimeter FADC circuit requires about 50 cm<sup>2</sup> of board space and adjacent channels will need to be about 2 - 3 cm apart. This implies a density of about 8 channels on a 6U board or possibly 16 channels on a 9U board.

The tracking FADCs will be designed at Jefferson Lab. Sixteen channels of 125 MHz FADC for the Central Drift chamber should fit on a 9U board. The exact requirements for the Forward Drift cathode FADCs have not been determined; it should be possible to put 64 channels of 62.5 MHz FADC on a 9U or possibly even a 6U board.

In the low resolution (125 ps) version of the TDC 64 channels fit on a 6U board. This version of the TDC is used for the Forward Drift Chamber anodes.

The Photon Tagger, Start Counter, Barrel Calorimeter, and Time of Flight counters require the high resolution (62.5 ps) version of the TDC; the density is 32 channels per 6U board.

Assuming a maximum of 18 boards in a crate, and 3 9U or 4 6U crates in a 7 foot tall rack, figure ?? summarizes the space required for the readout electronics. Estimated counts for high voltage, gas handling, level 1 trigger, and other necessary racks are also included.

<sup>6</sup> ATLAS ASD chip: [http://bmc.bu.edu/bmc/asd/asd\\_chip.html](http://bmc.bu.edu/bmc/asd/asd_chip.html)

**Summary of GlueX Rack Space**

Detector	Type	Channels	Modules	Crates	Racks
Photon Tagger	6U, 8 channel, 8 bit, 250 Msps FADC	192	24	2	
	6U, 32 channel, 62 ps TDC	192	6	1	
	High voltage	192		1	1
Upstream Photon Veto	6U, 8 channel, 8 bit, 250 Msps FADC	20	3		
Start Counter	6U, 8 channel, 8 bit, 250 Msps FADC	40	5		
	6U, 32 channel, 62 ps TDC	40	2	1	
	High voltage (includes UPV)	60		1	1
Central Drift	9U, 16 channel, 125 Msps FADC	3240	203	12	4
	High voltage			1	1
	Gas				2
Forward Drift anodes	6U, 64 channel, 125 ps TDC	2900	46	3	1
Forward Drift cathodes	9U, 64 channel, 10 bit, 62.5 Msps FADC	11,400	179	10	4
	High voltage			1	1
	Gas				2
Time of Flight	6U, 8 channel, 8 bit, 250 Msps FADC	168	21	2	
	6U, 16 channel, 31 ps TDC	168	11		
Cerenkov	6U, 8 channel, 8 bit, 250 Msps FADC	40	5	1	1
	High voltage (includes TOF)	208		1	1
	Gas				2
Barrel Calorimeter	6U, 8 channel, 8 bit, 250 Msps FADC	960	120	7	
	6U, 32 channel, 62 ps TDC	960	30	2	3
Forward Calorimeter	6U, 8 channel, 8 bit, 250 Msps FADC	2500	313	18	5
	Cockcroft Walton control, misc				1
Level 1 Trigger				4	1
Totals				68	31

Figure 5.11: Rack space

The readout electronics will be located as close to the detector as possible to minimize signal cable runs. Note that the Tagger electronics will be located in a separate building 80 *m* upstream of the main detector. The Time of Flight and Forward Calorimeter electronics will be downstream of these detectors. Cabling from detectors inside the solenoid will exit at the upstream and downstream ends of the magnet and connect to nearby electronics. Fiber optic cables will transport the data from the crate readout processors to the level 3 trigger processor farm in the GLUEX counting house.

## 5.10 Readout Bus

FASTBUS crates are no longer being manufactured, and FASTBUS is not being considered for GLUEX. CAMAC crates are fairly slow and have limited board space and power available. Some legacy devices like discriminators, trigger logic or HV supplies which are not part of the data readout may be packaged in CAMAC, but not the bulk of the readout electronics.

VME is popular at Jefferson Lab and the TDC prototype is constructed on a VME64x card. Compact PCI is used extensively in the telecommunications industry and can be driven directly by typical FPGA ICs without the need for bus interface ICs. Predefined PCI interface “cores” are available, minimizing design time. One disadvantage of cPCI is that bridges are required for a system with more than 8 slots, although commercial bridges which consume no slots are available. VXI and PXI are “instrumentation” extensions to VME and cPCI. Shielding, triggering, clock distribution, and additional power are added to the basic bus standard.

The FADCs require a low skew fanout of the 250 *MHz* clock, a synchronization signal, and the level 1 trigger. The need to form a digital global energy sum for the level 1 trigger will probably drive the choice of packaging for the calorimeter FADCs. Some sort of custom backplane will be required to support the trees of adders which form the energy sum and track counts.

The telecommunications industry is moving towards “Switched Serial Fabrics.” This adds a high speed serial connector to the backplane which can support Ethernet and other high speed serial technologies. For VME the applicable standard is VXS (VITA 41) and for cPCI the standard is cPSB (PICMG 2.16). For a 16 channel FADC module producing 25 bytes per channel per level 1 trigger; a level 1 trigger rate of 200 *kHz*; and a 2% occupancy the data readout bandwidth required for a module is 16 Megabits per second, well within the capability of a 100baseT Ethernet connection.

## 5.11 Construction

Indiana University has experience building large electronic systems for experiments at Fermilab, Brookhaven, and Jefferson Lab. The GLUEX experiment is larger and more complex than past experiments and will require the development of new techniques. High reliability is crucial to the success of the GLUEX experiment. We plan to begin long term tests of GLUEX electronics as soon as they are produced giving early identification of problems and failure modes.

A robotic electronic assembly machine<sup>7</sup> shown in figure ?? was purchased and used to construct 100 prototype Forward calorimeter Cockcroft-Walton PMTbases. This device dispenses

---

<sup>7</sup> Beamworks Spark 400: <http://www.beamworks.com>



Figure 5.12: Selective assembly robot.

solder paste, picks and places components, and uses infrared lasers to selectively solder components without disturbing nearby devices. This facilitates building a board in stages and testing partial assemblies, a technique especially useful in producing the Cockcroft-Walton PMT bases. The infrared lasers are particularly useful for removing and replacing defective components.

Producing electronics assemblies in house has several advantages over having a commercial firm doing the assembly. To achieve the lowest cost, a commercial service would assemble a large batch all at once. This risks learning about problems after it's too late to change anything. Assembling smaller batches in house allows immediate feedback to the assembly process.

The lifetime of the GLUEX experiment will be long enough that we must plan for maintenance and repair of the custom electronics. Sufficient spare parts must be purchased at construction time to avoid the risk of a component manufacturer discontinuing some crucial part. Spreading the purchase of components over too long a time also risks some components becoming unavailable.

Jefferson Lab used a commercial board assembly contractor to build the 50 TDC boards used in Hall C. No major problems were associated with this contract assembly, although it was necessary to quickly test the first few units before committing to assembling the remainder.

## 5.12 Review

The GLUEX electronics were reviewed by one internal and two outside reviewers in July of 2003. The report of this review is attached as an appendix. The review was scheduled at an early stage in the development of GLUEX so that their recommendations could be incorporated into final designs. The guidance of the committee has been extremely useful in the continued prototyping and design of the system.

The present design for the GLUEX electronics differs in a few ways from the reviewers recommendations:

At the time of the review it was believed that a single FADC module could be used for all detectors. The detector characteristics have been further defined since the review and it seems unlikely that one type of FADC is optimal for all detectors. The channel count for the Forward drift cathodes has grown substantially; the overall system cost will likely be lowered by designing a module specifically for this detector. The different types of FADC will be as similar as possible; it may be possible to use a common printed circuit board stuffed with different components.

The reviewers recommended locating the readout electronics in a radiation free area. The collaboration believes the advantages of shorter signal cables outweigh the access considerations and is planning to locate the electronics in crates adjacent to the detector. Access to the above ground GLUEX detector should be easier than access to the existing underground experiments at Jefferson lab.

## Chapter 6

# Rates, Trigger and Data Acquisition

### 6.1 Expected rates

#### 6.1.1 Overview

We estimate trigger and background rates in GLUEX using measurements of the hadronic cross section combined with the CLAS experience. The hadronic rate between any two photon energies  $E_1$  and  $E_2$  can be written as

$$R = \int_{E_1}^{E_2} n\sigma(E) \frac{dN}{dE} dE$$

where  $n$  is the number of target protons per unit area,  $\sigma(E)$  is the hadronic cross section as a function of energy, and  $dN/dE$  is the photon energy spectrum. The photon flux is composed of a coherent and incoherent sum as detailed in Chapter 4. Background rates are dominated by the broad-band incoherent flux. The signal rates result from the photon flux in the coherent peak, which will depend on the radiator crystal structure and its orientation. The coherent peak will be optimized to the specific physics program. For our rate estimates, we use the typical case for the flux computed on a diamond radiator with the coherent peak at  $E_\gamma = 9 \text{ GeV}$ .

Both coherent and incoherent fluxes are proportional to the electron beam current and radiator thickness. Multiplying the number of electrons per second by the radiator thickness in radiation lengths gives the product  $N_0$  which we will use in the following calculations. For conditions which we will refer to as “low intensity” (300 nA beam on a  $10^{-4}$  radiator),  $N_0 = 1.9 \times 10^8/\text{s}$ . For the coherent peak at 9 GeV the tagged photon flux between 8.4 and 9.0 GeV is  $R_{tag} = 0.14 N_0$ . The average tagging efficiency over this interval is 0.375, so the tagged photon flux on target is  $1.0 \times 10^7/\text{s}$ . “High intensity” running, where the tagger becomes ineffective as part of the level 1 trigger, nominally corresponds to  $N_0 = 1.9 \times 10^9/\text{s}$  and yields  $10^8/\text{sec}$  tagged photons on target.

The total hadronic  $\gamma p$  cross section<sup>1</sup> is plotted in Fig. ???. For the experimental conditions defined above and a 30 cm liquid hydrogen target, the total hadronic rate in the detector is

$$R_0 = 2 \times 10^{-4} N_0 \tag{6.1}$$

and a tagged hadronic rate

$$R_T = 7.4 \times 10^{-6} N_0 \tag{6.2}$$

---

<sup>1</sup>We use measured cross sections [?, ?] with actual data obtained from the Durham Data Base [?]

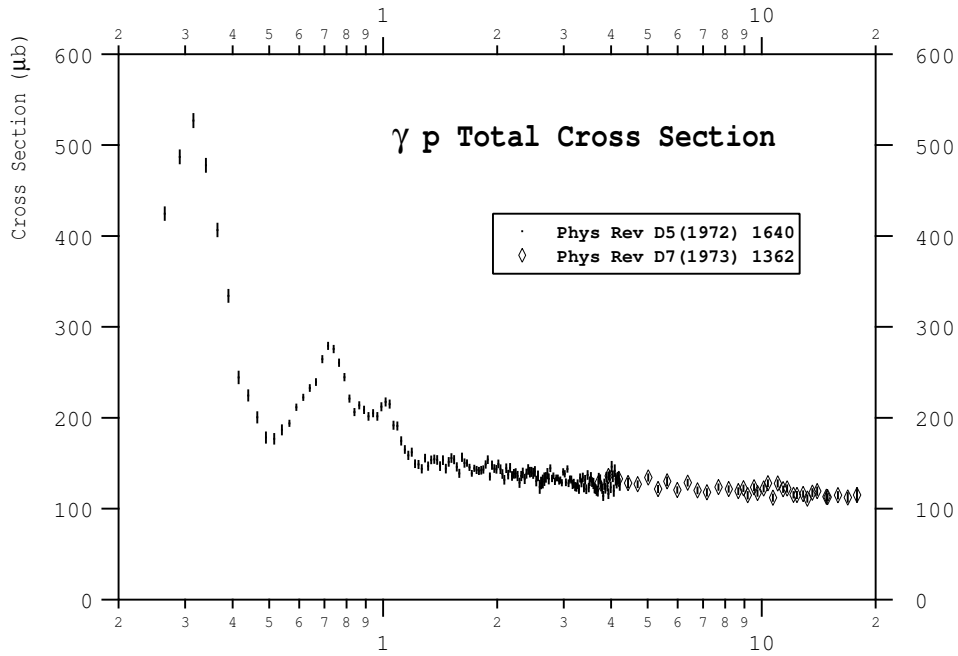


Figure 6.1: Total cross section for  $\gamma p \rightarrow \text{hadrons}$  as a function of photon energy.

For low intensity, the expected total hadronic rate is  $37 \text{ kHz}$  and the tagged hadronic rate is  $1.4 \text{ kHz}$ .

### 6.1.2 Trigger elements

We make some rudimentary assumptions about the trigger elements in order to estimate various rates. These assumptions are discussed further in the Trigger section of this document. Initial commissioning of the detector at low rates will use a level 1 trigger to select events of interest. At higher rates a sophisticated level 3 software trigger<sup>2</sup> is required. We concentrate here on discussion of rates at lower photon beam fluxes.

The trigger consists of coincidences between several counter elements of the detector. It must select the tagged hadronic rate in the presence of accidentally coincident backgrounds. The first trigger element is the photon tagger, essentially a segmented scintillation counter. The rate in this counter is determined by  $N_0$ , which is controllable (within limits) by the experiment.

The second trigger element is the start counter/vertex chamber. This detector package will provide position and timing information with sufficient resolution for track reconstruction. In comparing the demands of the GLUEX start counter to the CLAS experience, it is useful to note that the GLUEX target is inside a solenoidal magnetic field which will protect the start counter from the flux of low-energy Compton scattered electrons emerging from the target. The CLAS start counter does not enjoy this protection.

The tagger and start counters are small, and are therefore the best candidates for determining the precise event timing. For this discussion, we will assume that coincidences between them can be identified within a time window  $\Delta T_1 = 15 \text{ ns}$ .

<sup>2</sup>We are reserving level 2 for a possible intermediate level hardware trigger

Interesting events will have particles in the final state other than the one that satisfied the start counter requirement. These particles may be energetic, forward-going charged particles, forward or large angle photons, and/or charged particles with sufficient transverse momentum to reach the bore of the solenoid. Any particles of this type will be registered in other elements of the detector and these signals can be used as further requirements in the trigger. This refines the loose interaction definition given above. We refer to this collection of signals as the global level 1 trigger. As its elements are counters of extended size, we take a coincidence time window  $\Delta T_2 = 100 \text{ ns}$  when the global level 1 trigger is required.

### 6.1.3 Accidental rates

The rate of interesting events given by Eq. ?? is  $1.4 \text{ kHz}$  ( $N_0 = 1.9 \times 10^8/\text{s}$ ) and  $14 \text{ kHz}$  ( $N_0 = 1.9 \times 10^9/\text{s}$ ) for low and high intensity beams respectively. However, various other processes will form accidental coincidences at the different trigger stages, and we need to recognize these. It is most important that these do not form the bottleneck for the data acquisition system, regardless of our ability to reject them offline.

We consider two sources of accidental background. They are not entirely mutually exclusive, but we consider them separately for ease of explanation. The first ( $A_1$ ) of these comes from purely random time coincidences between the trigger elements, in which case we compute the time overlap based on the various counter singles rates. The second ( $A_2$ ) is more “physical”, considering hadronic photoproduction that is outside the tagging range, but in accidental coincidence with the tagging system.

First consider purely random coincidence events. A coincidence between the tagger and start counter loosely defines an interaction in the target. The rate  $A_0$  of this coincidence is given by

$$A_0 = SR_{tag}\Delta T_1 \quad (6.3)$$

where  $S$  is the total rate in the start counter. Based on the experience in CLAS, we take  $S = 0.03N_0$ , scaled using appropriate factors for collimation and beam intensity. This is most certainly an upper limit because of the solenoidal shielding effect. For  $R_{tag} = 2.7 \times 10^7/\text{s}$  we find  $A_0 = 2.3 \times 10^6/\text{s}$ , considerably larger than the tagged hadronic rate  $R_T = 1400/\text{s}$ . Further refinements are achieved by the global level 1 trigger.

The rate of the global level 1 trigger,  $f_{L1} \times R_0$ , is taken to be the total hadronic rate<sup>3</sup> reduced by the rate for single pion production for  $E_\gamma \leq 0.5 \text{ GeV}$  ( $f_{L1} = 0.5$ ). A loose trigger which uses a charged particle track count in the start counter and requires neutral energy in the barrel and/or forward calorimeter (see Section ?? below) should easily be able to eliminate these low energy events. The accidental rate using both the interaction and global level 1 triggers is

$$A_1 = A_0 f_{L1} R_0 \Delta T_2 = S f_{L1} (0.28 \times 10^{-4}) N_0^2 \Delta T_1 \Delta T_2 \quad (6.4)$$

where we have substituted from Eqs. ?? and ?? and used  $R_{tag} = 0.14 \times N_0$ . The second accidental background comes from true hadronic events, and therefore would pass the global level 1 trigger. They are out of time with the precise RF signal, but that is much smaller than the online resolving time  $\Delta T_1$  of the interaction coincidence. Ignoring the “true” events that

<sup>3</sup>The cosmic-ray rate is small and has been neglected.

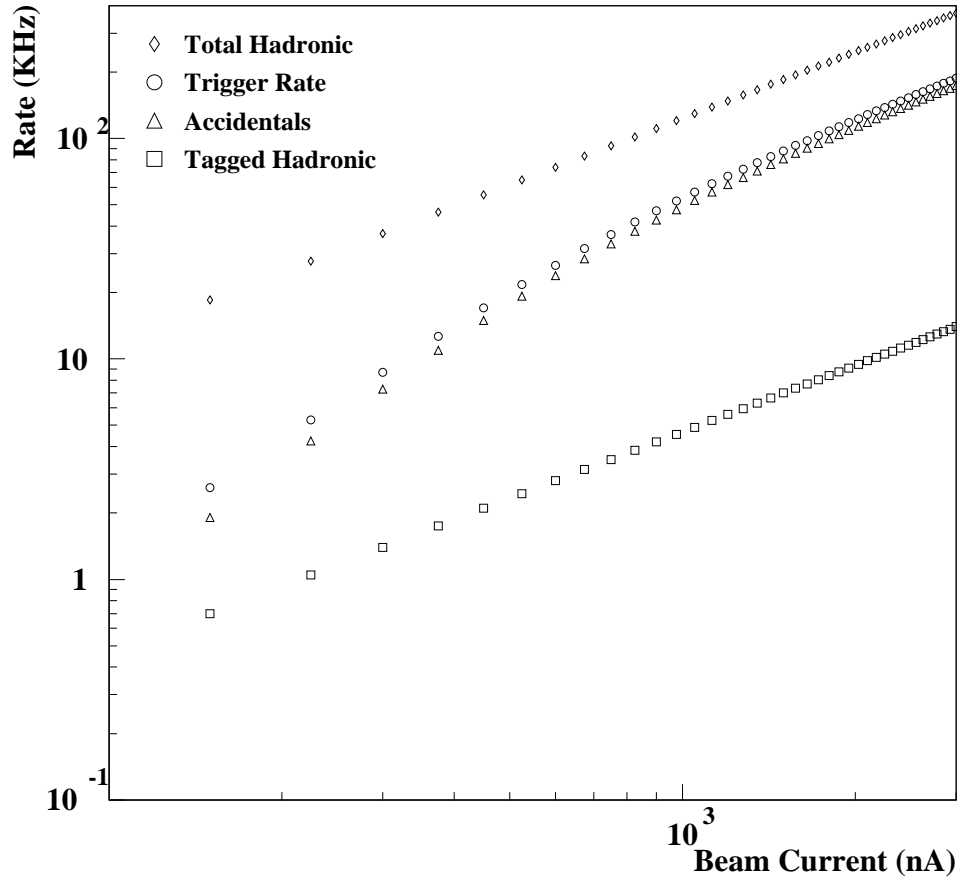


Figure 6.2: Estimated rates as a function of electron beam current. Plotted is the total hadronic rate and the estimated trigger rate, which is the sum of accidental coincidences and the tagged hadronic signal.

are part of this rate, one calculates

$$A_2 = f_{L1} R_0 R_{tag} \Delta T_1 = f_{L1} (0.28 \times 10^{-4}) N_0^2 \Delta T_1 \quad (6.5)$$

In order to evaluate the total accidental contribution numerically, correlations must be taken into account. This reduces the sum of the above estimates. For  $N_0 = 1.9 \times 10^8/\text{s}$ , the accidental contribution to the trigger is  $7.3 \text{ kHz}$ , and the tagged hadronic rate is  $R_T = 1.4 \text{ kHz}$ . We note that as the photon flux increases, the start counter and tagger lose their effectiveness in reducing trigger rates, so the trigger rate asymptotically becomes proportional to the hadronic rate. At higher currents, a DAQ system with a software level 3 trigger is required. A summary of the rates is shown in Fig. ?? as a function of electron beam current.

#### 6.1.4 Rates in tracking chambers

At the high photon flux anticipated for GLUEX, one concern is that the occupancy rates in the drift chambers may be too high to allow reconstruction. In order to estimate these occupancies,

a test of high intensity running with photons was performed in the CLAS detector.<sup>4</sup> Measurements were taken at 10, 80, 250 and 320 nA with a  $10^{-4}$  radiator, and rates were measured in the forward TOF scintillators (7.5-12.5 deg), the electromagnetic calorimeter (8-45 deg), and the drift chambers. The drift chamber occupancies at the highest current (320 nA) are given in Table ??.

Beam	Region 1 S1	Region 1 S2	Region 2 S3	Region 2 S4	Region 3 S5	Region 3 S6
Photon	2.3%	2.3%	0.3%	0.4%	0.7%	0.9%

Table 6.1: Drift chamber occupancies for each superlayer (in percent) for run 21998 at the maximum beam current of 320 nA (logbook entry #7031).

Although the conditions of the test did not duplicate precisely the conditions expected in GLUEX, reasonable estimates can be made by appropriate scaling. In Table ?? we compare the differences in target, collimation and beam energy. As the majority of background results from lower energy photons, we assume the energy dependence of the measured rates is small. The rates are scaled by a factor of 1.7 (ratio of target lengths) and the beam current is scaled up by a factor of 5.33, which is the expected collimation ratio. The drift chambers in region 1 are completely unshielded by any magnetic field in CLAS, whereas the drift chambers in region 2 are shielded by the field of the CLAS torus. The 2.2 T solenoidal field for GLUEX is expected to be at least as effective as a shield as the CLAS torus. Therefore, we expect the occupancies in the GLUEX drift chambers to be as low or lower than those in CLAS for comparable granularity.

	Hall B Test	Hall D
Beam Current	80 nA $\rightarrow$ 320 nA	300 nA $\rightarrow$ 3 $\mu$ A
Radiator	$10^{-4}$	$10^{-4}$
Collimation keeps	80%	15%
Target Length	18 cm	30 cm
Beam Energy	2.4 GeV	12 GeV
Trigger	Restricted	Open

Table 6.2: Comparison between conditions in Hall B during high rate test and anticipated running parameters for GLUEX. A current of 3  $\mu$  A in GLUEX corresponds to  $10^8$  photons/s in the coherent peak.

Extrapolating measured occupancies in region 2 to a current of 3  $\mu$ A (GLUEX with  $10^8$  photons/s in the coherent peak), we expect an occupancy of 0.6%. The rates are plotted versus electron current scaled to GLUEX in Figure ?. This is well below the typical operational limits of 2.3% imposed for the region 1 drift chambers in CLAS during electron beam running, a rate at which tracks can still be reconstructed with reasonable efficiency. We note that the extrapolated rates in region 1 for a beam current of 3  $\mu$ A is approximately 5%, exceeding usual operational limits by a factor of 2, but this figure is for a configuration which is completely

<sup>4</sup>This information is taken from CLAS-NOTE-2000-004 High-Rate-Test by Elton Smith.

unshielded by any magnetic field whatsoever and thereby represents an absolute maximum to the expected rates. We note that the operation of a polarized target in Hall B (which replaces the mini-toroid with a solenoidal field) allows running at twice the normal luminosity. Thus we expect that for comparable segmentation, raw rates in the GLUEX detector at the maximum design current will be similar to the current experience with CLAS. The conclusion is that the GLUEX detector should be able to handle rates up to  $10^8$  photons/s.

## 6.2 Trigger

### 6.2.1 Overview

In order to achieve the roughly 20-1 reduction in event rate, GLUEX will use a two-stage trigger, combining a hardware-based level 1 trigger with a software (reconstruction) based level 3 trigger. An essential feature of the GLUEX design is to build pipelining into the entire trigger, digitizer, and data acquisition systems at the outset. This has the twin virtues of allowing adequate time for the level 1 trigger to do its job, while eliminating signal degradation involved in delaying the signals while the trigger operates. Pipelining in this way also allows us to upgrade from initial photon fluxes of  $10^7$  photons/sec to eventual fluxes of  $10^8$  photons/sec without any significant changes to the trigger/DAQ architecture. Eliminating conversion deadtimes will allow us to acquire events which occur very close together in time.

Figure ?? shows a schematic of the implementation of the GLUEX level 1 trigger. The level 1 trigger makes a decision based on detector elements which measure hadronic multiplicities (track counts) and energies. In the schematic shown, the start counter and barrel calorimeter and forward TOF detectors provide the track count while the barrel and forward calorimeters determine the energy. A tight tagger OR/start counter coincidence is used as input to the level 1 trigger for low photon fluxes of  $\approx 10^7$  photons/sec.

For high photon fluxes ( $\approx 10^8$  photons/sec), the tagger OR/start counter coincidence is not a useful requirement, and the level 1 trigger will probably only be able to cut the rate down from 385 KHz to around 180 KHz. Most of this background comes from multi-pion events caused by untagged (low energy) photons. In order to reduce this rate by a factor of 10, a very accurate reconstruction of the photon energy is required. Because of the complexities involved in accurately determining track momenta and then linking information from the different detectors, we believe the best approach is to use a software level 3 trigger embedded in the DAQ architecture, rather than to build a series of specialized level 3 trigger processors. This level 3 trigger will do a simplified full reconstruction of the event, using all of the data, in order to throw out events from low energy photons.

### 6.2.2 Level 1 trigger

The level 1 trigger consists of five subsystems, and a global trigger processor (GTP) which combines these five outputs into the global level 1 trigger. Each of the subsystems continuously (via a digital pipeline) computes a parameter, then compares it against a number of programmed value/function pairs. The trigger pipeline would sample input data at the rate of the FADC clock (250 MHz) or possibly at half that rate (125 MHz). A value function pair might be an energy value and a  $<$ ,  $=$ , or  $>$  function. When any of the value/function requirements is satisfied, the subsystem sends a timestamped subsystem event report (SER) to the GTP. The GTP

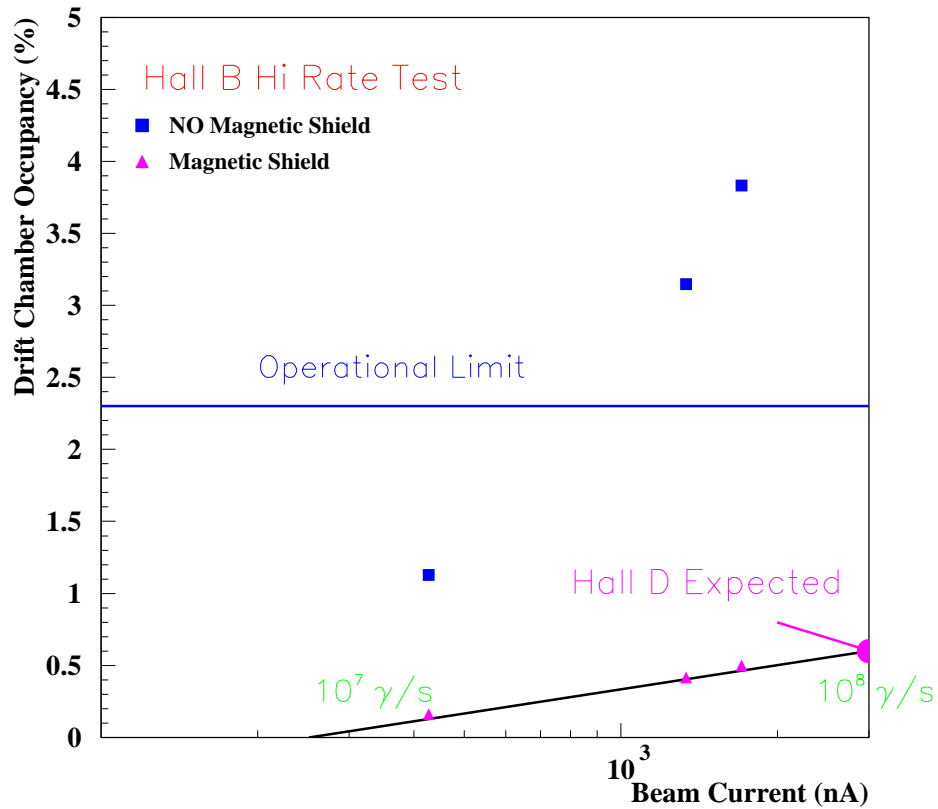


Figure 6.3: Drift chamber occupancies (scaled by target thickness = 1.7) plotted versus beam current (scaled by collimation factors = 5.33) expected for HALL D operation. The drift chambers in region 1 (squares) are completely unshielded by any magnetic field in CLAS, whereas the drift chambers in region 2 (triangles) are shielded from backgrounds by the main torus field. The nominal low current operation in GLUEX ( $10^7$  photons/s in the coherent peak) corresponds to 300 nA. The 2.2 T solenoidal field for GLUEX is expected to be at least as effective as a shield as the CLAS torus.

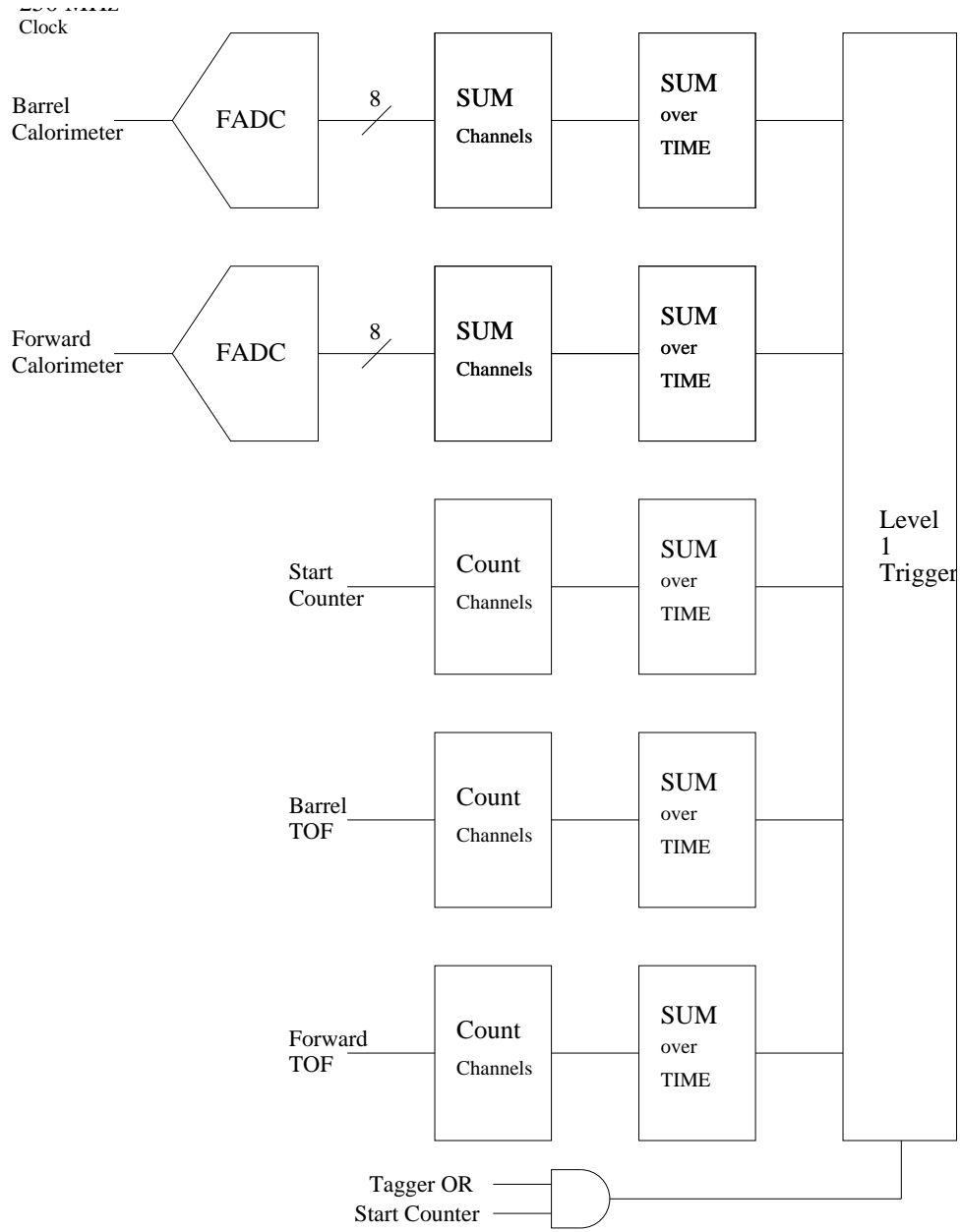


Figure 6.4: A schematic diagram of the GLUEX trigger.

is programmed with a number of different level 1 trigger configurations, each combining different value/function pairs from the subsystems, along with a trigger coincidence window (TCW) specifying the maximum time window for coincidence of the different trigger requirements.

The five level 1 trigger subsystems are:

1. **A track count** - obtained from the start counter. The start counter discriminator signals are used to create the prompt OR for coincidence with the tagger, but are also sent into a *track count pipeline* to determine the number of tracks. Two different track counts may be programmed, each with a  $<$ ,  $=$ , or  $>$  criterion attached.
2. **A track count** - obtained from the barrel calorimeter. The discriminator signals from the central calorimeter are sent into another *track count pipeline* which determines the number of tracks. This pipeline runs synchronously with the start counter track count pipeline. Two different track counts may be programmed, each with a  $<$ ,  $=$ , or  $>$  criterion attached.
3. **An energy sum** - obtained from the barrel calorimeter. The barrel calorimeter will be digitized by 8 bit, 250 MHz flash ADCs (FADC). All channels are then digitally added together (in a pipeline tree) to form the barrel calorimeter energy sum. The energy sum then passes through a shift register thus making available a time window. Successive samples within this time window are added together. This is analogous to the gate width in a conventional charge sensitive ADC. Two different energy values may be programmed, each with a  $<$ ,  $=$ , or  $>$  criterion attached.
4. **A track count** - obtained from the forward TOF. Discriminator signals from the forward TOF are sent into a *track count pipeline* which determines the number of tracks. This pipeline runs synchronously with all the other level 1 pipelines. Two different track counts may be programmed, each with a  $<$ ,  $=$ , or  $>$  criterion attached.
5. **An energy sum** - obtained from the forward calorimeter. This sum is constructed in the same manner as for the central calorimeter, except that the selection of which digitized analog sums are added together to form the forward energy sum, is programmable. Two different energy values may be programmed, each with a  $<$ ,  $=$ , or  $>$  criterion attached.

As mentioned above, the GTP may be programmed with several different triggers. Programming a single trigger means selection of

1. Either a minimum, maximum, or exact number of tracks in the start counter.
2. A minimum, maximum, or exact number of tracks in the barrel calorimeter.
3. A minimum, maximum, or exact number of tracks in the forward TOF.
4. A minimum or maximum for the global energy in the barrel calorimeter.
5. A minimum or maximum for the global energy in the forward calorimeter. Certain areas might be programmed out of this sum.
6. The appropriate boolean combination of elements 1-5.

The trigger will have the capability to have at least eight simultaneously defined triggers. This trigger is very flexible and can be programmed to be very loose (say one track in the start counter) or very tight and complex (specific track counts and energy thresholds in each detector). Examples of triggers which can be programmed in this model include:

1. At least two tracks in the start counter AND at least one track in the downstream TOF.
2. At least one track in the start counter AND a minimum energy in the downstream calorimeter.
3. At least two tracks in the start counter AND at least one track in the barrel calorimeter AND a minimum requirement of energy in the barrel calorimeter AND a minimum requirement in the forward calorimeter.

All subsystems will run synchronously and will be timed so that the time stamps from average momentum tracks ( $\sim E_{\text{beam}}/3$ ) will match at the GTP. Higher and lower momentum tracks will be slightly out of time, but this effect should be less than  $20 \text{ ns}$ , and this is compensated for by programming the TCW value. The synchronous output of the level 1 trigger will then be ANDed with the coincidence of the tagger OR and the start counter OR. This allows the timing to be determined by the tagger and start counter, and removes the synchronous nature of the trigger.

The rate of the global level 1 trigger,  $f_{L1} \times R_0$ , is taken to be the total hadronic rate<sup>5</sup> reduced by the rate for single pion production for  $E_\gamma \leq 0.5 \text{ GeV}$  ( $f_{L1} = 0.5$ ). A loose trigger which uses a charged particle track count in the start counter and requires neutral energy in the barrel and/or forward calorimeter should easily be able to eliminate these low energy events. The resultant level 1 trigger rate is about  $180 \text{ kHz}$ . We note, however, that 80% of the hadronic rate comes from photons with energies below  $2 \text{ GeV}$ . This energy cut, which would require a more sophisticated trigger, would reduce the level 1 rate to  $70 \text{ kHz}$ .

### 6.2.3 Trigger simulation

As mentioned above, background events are typically due to low energy photons, resulting in low energy events. Not only are these background events lower in energy, but they are also less forward, due to reduced Lorentz boost. Thus, good events typically deposit a larger fraction of their energy in the forward calorimeter, and have more tracks and hits in the forward time-of-flight. The goal of the Level 1 trigger is to use these differences to cut as large a fraction as possible of the background events, while minimizing the number of good events lost. The goal for the data reduction in the level 1 trigger is to remove at least 50% of the background events, without losing more than 0.5% of the good events.

In order to test the the trigger, the six reactions listed in Table ?? were simulated and studied. The simulated events include two low energy delta production channels, and four interesting physics channels at low (background) and high energies. Reaction events were generated using *Genr8* [?]. After generation the events were then run through *HDGeant* [?] for simulation. This provided the necessary data needed. For each reaction 10,000 events were generated giving 120,000 events.

---

<sup>5</sup>The cosmic-ray rate is small and has been neglected.

A function of the form given in Eq. ?? was used as the basis for deciding cuts. When the calculation is less than Z the event is cut. A genetic algorithm was used to optimize the coefficients and Z. The fitness function was weighted such that keeping good events was given a higher score than cutting background events. If good events were cut then it would be penalized and if it cut too many then the score received was zero. As shown in Table ?? the best set of coefficients cut nearly all of the delta's and most of the low energy background events. On average 72% of the background events are cut, while no single good event channel lost more than 0.5%.

$$\begin{aligned}
 Z \geq & A * [NumberTracksForwardTOF] \\
 & + B * [EnergyForwardCal] \\
 & + C * \frac{[EnergyForwardCal + 1]}{[EnergyBarrelCal + 1]}
 \end{aligned} \tag{6.6}$$

Reaction	Energy(GeV)	Percent Cut
$\gamma p \rightarrow \rho^0 \pi^+ n \rightarrow n \pi^+ \pi^- \pi^+$	1	67.99%
	2	41.68%
	9	0.05%
$\gamma p \rightarrow \rho p \rightarrow p \pi^+ \pi^-$	1	70.48%
	2	54.82%
	9	0.50%
$\gamma p \rightarrow X^*(1600)n \rightarrow (\eta^0 \pi^+)n \rightarrow n \pi^+ \gamma \gamma$	1	90.10%
	2	56.24%
	9	0.11%
$\gamma p \rightarrow X^+(1600)\Delta^0 \rightarrow (\pi^+ \pi^+ \pi^-)(n \pi^0) \rightarrow \pi^+ \pi^+ \pi^- n \gamma \gamma$	9	0.23%
$\gamma p \rightarrow \Delta \rightarrow n \pi^+$	0.337	99.99%
$\gamma p \rightarrow \Delta \rightarrow p \pi^0$	0.337	98.75%

Table 6.3: Trigger cut rates for reactions and their energies.

## 6.3 Data acquisition

### 6.3.1 Overview

The GLUEX data acquisition system is being designed to accept a 200 KHz Level 1 input rate, and will be pipelined so as to incur no deadtime. Front-end boards will continually digitize and store several microseconds worth of data to allow time for the Level 1 trigger decision. When a Level 1 accept arrives the boards will extract the appropriate time slice of data from the digitizing memory and move it into a large secondary memory store. Readout controllers will collect data from many boards over a backplane, then transmit the data to event building processors over a network. Note that the readout controllers likely will not need to run a hard real-time operating system (e.g. VxWorks) due to the large memories on the digitizing boards, an important simplification.

Complete events will be shipped from the event builders via a network to a large farm of Level 3 processors. The Level 3 farm will reduce the event rate by approximately a factor of 10 before shipping the remaining events to event recording processors, which will then write the events to a staging disk in preparation for transfer to tape. We are designing the system to handle a recording rate of 100 Mb/s. During initial running at low luminosity ( $10^7$ ) this system will be able to record all events to disk, and no Level 3 rejection will be needed.

Most of the hardware components needed to build the DAQ system described above are available now or will be available soon, so there should be no problem finding hardware a few years from now. The main challenge will be to develop the DAQ, online, monitoring, and controls software.

### 6.3.2 Data flow and rates

GLUEX will have approximately 12500 FADC channels. Assuming a typical occupancy of 2%, a 250 MHz, 8-bit FADC, a time window of 100 nanoseconds, and readout of the full time window, the total amount of FADC data would potentially be:  $12500 \text{ channels} * 0.02 \text{ (occupancy)} * 25 \text{ bytes/channel} = 6.25 \text{ Kbytes per event}$ .

The 25 bytes/FADC channel will be used to extract an energy and a time signal. Previous work [?, ?] indicates that a time resolution better than the FADC sampling interval can be achieved by fitting the FADC waveform (see also Chapter 7). Thus we plan to reduce the FADC data to an energy, time, and channel identifier in real-time using special on-board hardware. The amount of data per hit will drop from 25 bytes to 10 bytes per FADC channel, thereby lowering the total FADC data to a more manageable 2.5 Kbytes per event.

In GLUEX there will be approximately 8000 TDC channels so the data volume for the TDCs will be:  $8000 \text{ channels} * 0.02 \text{ (occupancy)} * 4 \text{ bytes/channel} = 640 \text{ bytes per event}$ .

There will be little data from devices other than TDCs and ADCs (scalars, latches, etc.) so the total event size will be about 4 Kbytes per event. Taking 5 Kbytes per event as the design goal gives  $5 \text{ Kbyte/event} * 200 \text{ KHz} = 1 \text{ Gbyte/sec}$  off the detector. Assuming 100 front-end VME crates (cPCI will need more) gives a backplane rate of 10 Mbytes per second, easily handled by current technologies.

Event building will be done in parallel on 8-16 event building processors. Event analysis will be performed in parallel on 50-200 Level 3 farm processors (see below). Event recording will be done in parallel on 2 to 8 event recording processors. In all cases existing network switches can easily route the volume of data between stages. Note that we are investigating use of advanced (e.g. layer 7 routing) network switches to further simplify transfer of data between stages.

### 6.3.3 Level 3 trigger

If the Level 1 trigger rate for low intensity running ( $10^7$  tagged photons/s) is less than 20 KHz, or 100 Mbytes/sec, the Level 3 trigger farm will not have to cut any events since the DAQ system is being designed to handle this rate to disk. In high intensity mode, where the Level 1 rate may be as high as 200 KHz, the Level 3 trigger must be able to reduce the event rate by a factor of ten.

Most of the unwanted events result from an untagged, mostly lower energy photon interacting in coincidence with a tagged photon. To reject these events Level 3 must be able to estimate the energy of the photon which produced the event. This involves reconstructing

	Low Rate	High Rate
Event Size	5 KB	5 KB
Event Rate to Farm	20 KHz	200 KHz
Data Rate to Farm	100 Mbytes/s	1000 Mbytes/s
Num Links to Farm	1	10
Data Rate per Link	100 Mbytes/s	100 Mbytes/s
Link Technology	Gigabit Ethernet	Gigabit Ethernet
Events/s per Link	20000	20000
SPECints/ev for L3	0.1	0.1
Num SPECints/link	2000 SPECints	2000 SPECints
Num SPECints/link x 2	4000 SPECints	4000 SPECints
Num 200 SPECint processors/link	20	20
Total Num 200 SPECint processors	20	200

Table 6.4: Rates, sizes, and processing requirements for the Level 3 trigger.

tracks, matching them with the calorimeters, and adding additional energy deposited by neutral particles in the calorimeters. This is most simply and easily done in a commodity processor Level 3 farm, rather than in specialized hardware.

We estimate the required processing power required as follows. The Hall B online hit-based event reconstruction system obtains 3% momentum resolution using about 5 milliseconds of cpu time on a 20 SPECint processor, or about 0.1 SPECint per event (full reconstruction with better than 1% resolution takes about 45 milliseconds). Assuming the same for GLUEX gives 20000 SPECints total for the full Level 3 farm at 200 KHz event rate. Assuming 50% processor utilization (due to I/O overhead, etc.), approximately 40000 SPECints or 200 processor boxes at 200 SPECint each are needed (150 SPECint boxes are currently running in the JLab farm system). Depending on the improvement in cpu performance over the next few years, far fewer boxes will likely be required, perhaps 1/4 as many.

Table ?? shows the rates, sizes, and processing requirements for the Level 3 trigger.

### 6.3.4 Monitoring and Control

Monitoring and control tasks include hardware configuration and control (“slow controls”), bookkeeping, online event monitoring, alarm systems, and messaging systems. These are less demanding tasks than data acquisition in GLUEX, and should not present unusual challenges. We plan to follow some examples from Hall B, but to also make use of lessons learned there. In particular, we plan to integrate offline data analysis tools with the online software at the outset to reduce the total cost of software development.

The framework for slow controls will be uniform for all subsystems in GLUEX, but the framework choice is not obvious. VME-based EPICS works in Hall B, but does not mesh well with the online requirements and has proven to be manpower intensive. In fact, a number of Hall B systems do not use EPICS or VME, but instead resort to CAMAC or other options. We believe that an open, message-based system that takes advantage of commodity hardware and

software, and that implements a uniform user interface to diverse underlying hardware is best. The JLab Data Acquisition group is currently developing an agent-based system meeting these requirements.

Bookkeeping tasks include all recordable activities of the experiment other than raw and calibration data. We expect this will be done using object/relational databases. Current commercial and public domain database technology should be adequate.

The alarm and messaging framework allows sub-systems to communicate their state to monitoring programs and operators. This system needs to be integrated across the entire online, DAQ, and database systems in a simple, uniform manner. The scale and performance requirements of this system are modest, and similar to other systems running or in development at Jefferson lab.

# Chapter 7

## Computing

### 7.1 Overview

GLUEX will be the first Jefferson Laboratory experiment to generate petabyte scale data sets on an annual basis (One petabyte, 1  $PB = 10^{15}$  Bytes). In addition, the need to generate physics results in a timely fashion has been identified as a primary goal of the GLUEX collaboration since its inception. For these reasons, a well-designed, modern, and efficient computing environment will clearly be crucial to the success of the experiment.

Currently, there are a number of particle physics projects world wide which also will produce very large data sets, and which will function with large dispersed collaborations. It seems quite reasonable, then, to expect that over the coming years, many new tools will be developed which will aid in effectively processing and managing these large volumes of data. As a collaboration, GLUEX will undoubtedly make effective use of these tools, which will include such things as grid middle ware, distributed file systems, database management tools, visualization software, and collaborative tools.

Nonetheless, it also is clear that the GLUEX collaboration will need to develop a suite of tools which are dedicated to this experiment. This will include data acquisition and trigger software, experiment monitoring and control software, data reduction tools, physics analysis software, and tools dedicated to the partial wave analysis (PWA) effort.

The rest of this chapter outlines in some detail the approach taken by the GLUEX collaboration. First, a review the approaches taken by current experiments with similar computing requirements, along with the GLUEX specific features and numerical constraints is given. Then an outline of the GLUEX strategy to meet these demands, and also the specific tasks that will be divided up among the collaboration members. Finally, a summary of computing milestone within the GLUEX collaboration will be presented. By keeping abreast of developments and new technologies that may be applicable to the GLUEX software environment, the collaboration will be able to carry the computing effort through from design to implementation and into the steady state running through a steady evolution of the system.

### 7.2 Background

In developing the GLUEX computing design, one can draw from two experiences, both of which are ongoing activities. These are the experiments using the CLAS detector in Hall B at JLab,

and the CERN LHC experiments.

CLAS is of course particularly relevant, as it is also a multi-particle spectrometer arrangement at JLab, and is a good measure of how one may best use the existing infrastructure at the laboratory. An important difference, however, between CLAS and GLUEX is the volume of data acquired and analyzed. Based on the most recent numbers achieved in CLAS, the trigger rates and data volume are still a factor of three less than those projected for GLUEX. (See Sec. ??). It is clear then that the JLab computing infrastructure will need to be significantly upgraded in support of GLUEX.

As the CERN/LHC experiments, CMS and ATLAS, began to take shape in the 1990's, it was realized that these large international collaborations would be acquiring previously unheard of amounts of data. It was further realized that all members of the worldwide collaborations would need ready access to this data, and that recent advances in computing could in fact make this possible. CERN commissioned the MONARC<sup>1</sup> (“Models of Networked Analysis at Regional Centres for LHC Experiments”) project in 1998, to study various configurations of distributed data analysis, based on “regional centers”. The results of this study were published in 2000, and it was concluded that a multi-tier system of regional centers was the best solution to the problem.

CMS and ATLAS are now, in fact, following this model in their own computing efforts. Indeed, several large scale collaborations, mainly connecting physicists and computer scientists, have appeared in the U.S. and elsewhere, to realize this computing model for nuclear and particle physics in general. These include the DoE/SciDAC funded Particle Physics Data Grid<sup>2</sup> (PPDG), and the NSF/ITR funded Grid Physics Network<sup>3</sup> (GriPhyN) and International Virtual Data Grid Laboratory<sup>4</sup> (iVDGL). These collaborations are devoted to developing the tools needed to realize the promise of large scale distributed computing and data handling, as it pertains to nuclear and particle physics.

The PPDG, GriPhyN, and iVDGL projects are based on the concept of a “virtual data grid”. This concept, which takes its name from the analogy with the public electrical utility network, aims to provide the user with an invisible layer of “middle ware” so that data sharing is carried out straightforwardly and quickly, regardless of the geographic separation of the actual physical data. Grid technology relies on the observation that the rate of increase of deployed network bandwidth is faster than the rate of increase in affordable computing power, and the assumption that these relative trends will continue for a number of years to come. This appears well founded based on historical trends [?], and are presumably driven by economics and the needs of society.

### 7.2.1 Special features of GlueX

There are important differences between GLUEX and the CERN LHC experiments ATLAS and CMS, which can be traced to the primary physics goals. Events in ATLAS or CMS will be very complicated, with very large amounts of data per event, and these will consequently consume a lot of CPU time to reduce. By comparison, GLUEX events will be simpler to disentangle. However, the subsequent analysis of GLUEX events will be both computationally and data

---

<sup>1</sup> MONARC: <http://monarc.web.cern.ch/MONARC>

<sup>2</sup> PPDG: <http://www.ppdg.net>

<sup>3</sup> Grid Physics Network: <http://www.griphyn.org>

<sup>4</sup> Virtual Data Grid Laboratory: <http://www.ivdgl.org>

intensive, requiring sophisticated visualization and data handling tools, as large amounts of both “real” and Monte Carlo data are brought together in order to carry through an amplitude decomposition analysis.

The primary goal of GLUEX is the systematic identification and categorization of short-lived meson states, unraveled from the raw, multi-particle reaction data using the techniques of “Partial Wave Analysis” (PWA). Achieving this goal requires simultaneous access to two large and independent data sets, namely the actual reduced experimental data and the simulated Monte Carlo data, each sorted for the particular multi-particle reaction(s) under consideration. It is quite probable that these data sets will be distributed physically over multiple locations, and that the access will be from other separated sites, associated with the group who has undertaken that particular analysis.

This not only impacts the structure of the data grid, but also implies that new analysis tools need to be developed. This especially includes visualization tools, as one searches for the appropriate combination of partial waves which best describe the reaction. That is, as one fits the parameters associated with a certain set of partial waves, some visual inspection mechanism is needed to evaluate how well the fit reproduces distributions in angles and invariant mass, for the many possible combinations. A universal set of tools is important in order to come to a more or less standard set of measures that would be applied by the analysis groups.

### 7.2.2 CPU, Storage, and Bandwidth Requirements

The GLUEX computing requirements are driven primarily by the projected data volume. GLUEX will use a multi-level triggering system, and it is projected that at the peak tagging rate, GLUEX will acquire 15,000 physics events per second which pass the Level 3 trigger requirement, or  $1.5 \times 10^{11}$  events in a live year, (assumed to be  $10^7$  seconds). The event size will be  $\approx 5$  kB. Consequently, the data acquisition system must handle 100 MB/sec, which corresponds to storing 1 PB of raw Level 3 data per year.

It is important that the Level 3 raw data be reconstructed somewhat faster than real time, for the purposes of monitoring the detector performance as well as the experiment setup. It takes on the order of 250 msec to process a multi-track event in a detector with complex geometry, on a standard workstation computer available in 2000. Using a conservative interpretation of Moore’s Law, i.e. CPU speed doubling every two years, this is reduced to 15 msec by 2008, so  $2.25 \times 10^9$  CPU-sec to process one year’s running. A reasonable goal is to process these data in one-third the time it took to acquire it, i.e.  $1.0 \times 10^7$  sec. Consequently, 225 circa 2008 CPU’s will be required to process the raw data.

An accurate and detailed simulation will be critical for successful partial wave analysis. For any given reaction channel, one needs a greater number of simulated events than actual events, so that the result is not limited by the statistical precision of the generated sample. The goal will be to generate a factor of three times more simulated events than actual actual events for the data sample representing the final states for which one carries out a more detailed analysis. At the same time, one will, at least initially, be interested in analyzing a specific set of reaction channels. Taking both of these factors into account, and assuming a similar event size for reconstructed data, we estimate that the simulations will produce an additional 1 PB/year of simulated data.

Significant CPU resources will be required to generate the Monte Carlo sample. Ideally, one would generate only those events which in fact are accepted by the apparatus, correcting for

Table 7.1: CPU, Storage, and Bandwidth Requirements for GLUEX

Raw Data Processing		Monte Carlo Data Processing	
Level 3 Data Rate	100 MB/sec	Simulated data	1 PB/year
Raw data storage	1 PB/year	Generation CPU's	700
Reconstruction CPU's	450		

the fraction of phase space assumed at the beginning. It is very difficult in practice, however, to achieve this optimal “importance sampling”. A reasonable assumption is that only 1/2 of the events generated events will actually be accepted by the simulated experimental trigger. Consequently, one must generate a number of events

$$N_{\text{gen}} = 2 \times (N_{\text{anal}})$$

where  $N_{\text{anal}} = 1.5 \times 11^{11}$  is the number of (fully) analyzed hadronic events per year from the data stream. Consequently,  $N_{\text{gen}} = 3 \times 10^{11}$  events. Generating Monte Carlo events requires detailed simulation of various detector components, and then these events must pass through the same analysis program as the raw data. Thus, more CPU time is required per simulated event than for real data. A starting assumption is to use a factor of two, namely 30 msec, or  $1.0 \times 10^{10}$  CPU·sec for a year's worth of simulated data. to generate this data in one-half of a calendar year, ( $\approx 1.5 \times 10^7$  sec), translates to approximately 700 circa 2008 CPU's necessary for generating and processing the Monte Carlo data set. Table ?? summarizes the CPU and storage requirements for computing in GLUEX.

Physics analysis for GLUEX will be carried out by a worldwide collaboration, which will require access to both the reconstructed data, as well as the processed Monte Carlo data. It is probable that the reconstructed data, simulated data, and as well the CPU's upon which the physics analysis is carried out, will physically reside at locations separate from one another, and also separate from the typical user. Sufficient bandwidth is necessary to connect the user to these resources in order to make appropriate use of the data grid.

## 7.3 Computing Strategy

In Fig. ??, we show a conceptual plan of the GLUEX data processing and computing environment. In the following sections, we will discuss the important features of this plan.

### 7.3.1 Jefferson Lab Computing Resources

Clearly, the nature of this experiment dictates that a significant computing infrastructure must exist at Jefferson Lab. As shown in Fig. ??, the computing facilities at JLab will coordinate the experiment monitoring and control, data acquisition, Level 3 raw data storage, slow controls monitoring, and data reduction.

#### Data Storage

Currently, at JLab, raw data from experiments are written to tapes housed in a tape silo in the JLab computer center, and this is one option that we have considered for the GLUEX Level

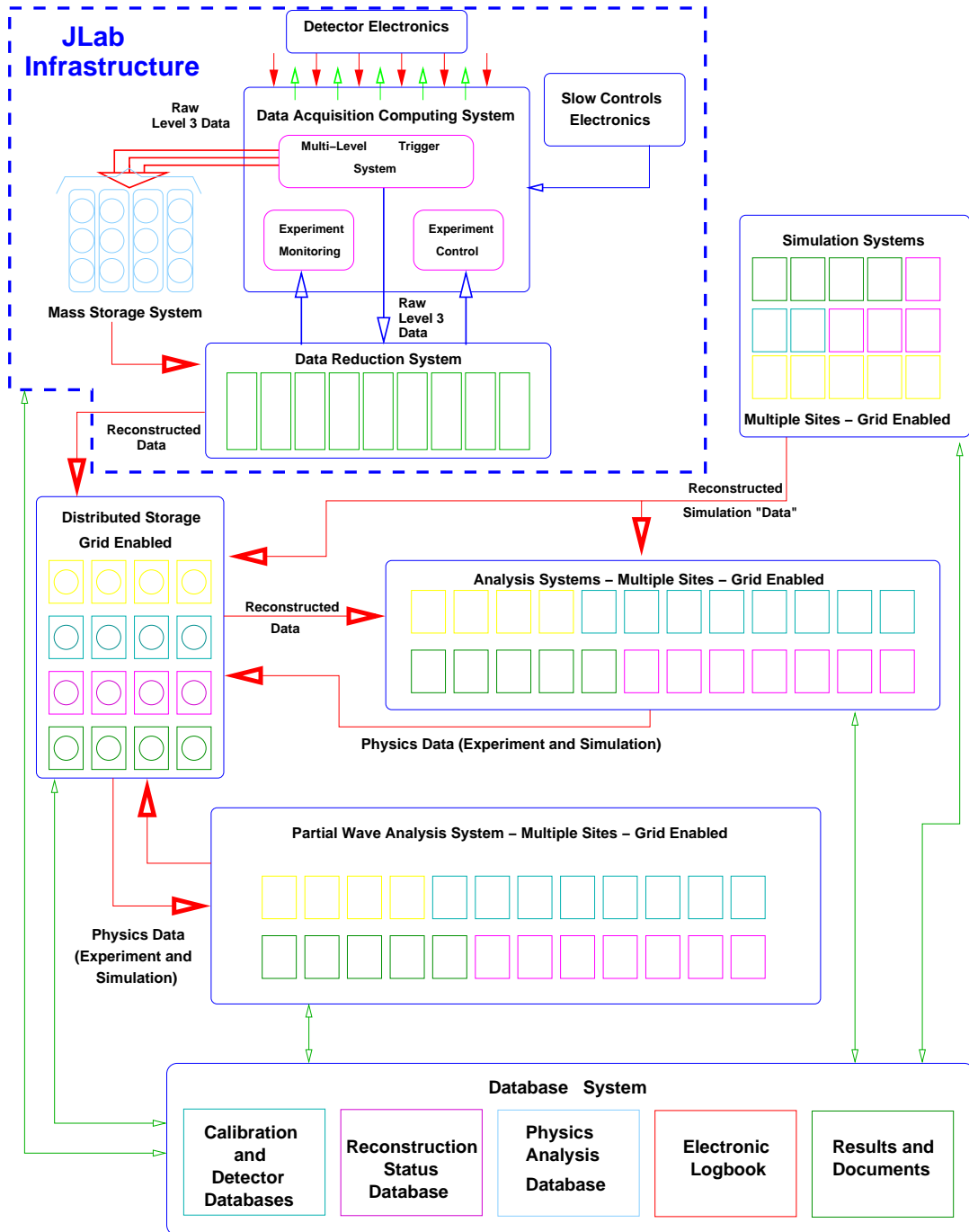


Figure 7.1: The GLUEX Computing Environment

3 raw data. Current tape speeds are 30 MB/sec onto 200GB cassettes, and should exceed 100 MB/s onto 1 TB cassettes when GLUEX data taking begins. At a data rate of 100 MB/s, and accounting for tape mount times and redundancy, GLUEX would need three to four tape drives dedicated to on-line data recording.

A tape silo typically holds 6000 tapes, or 6000 TB at 1 TB/tape. Thus, JLab would need to purchase one tape silo to store GLUEX raw and processed data, and would need adequate tape archive and storage facilities. Tape costs should be less than for CLAS, as much of CLAS data was written to low capacity tapes, and tape costs remain constant independent of capacity.

One should also note that at the present time, the relative prices of tape and disk storage are scaling in such a way that by the time GLUEX is in the data taking phase, it may be more practical to store the raw data directly on disk. Even with current RAID technology, high reliability disk storage may be achieved with mirroring or optical archiving techniques.

It is also important to note that while not explicitly shown in Fig. ??, the reconstructed data will almost certainly be stored primarily at JLab, and will therefore comprise a significant portion of the grid-enabled mass storage system.

### **Data Acquisition and Interface to Electronics**

The projected raw data rate into the Level 3 trigger system from the detector is 1 GB/sec (5 kB/Event  $\times$  200 kEvent/s). Our goal is a reduction factor of 10 in the Level 3 trigger, resulting in a Level 3 recorded raw data rate of up to 100 MB/sec. There can be no software, or otherwise computing related, impediments to this goal. The computer center staff, working closely with the data-acquisition group, will be responsible for assembling a system that allows direct transfer of the data from the acquisition electronics to the mass storage media, while providing for adequate experiment monitoring and control. It must also provide a natural interface to the data reduction software, which would be used on line for at least a subset of the monitoring activities.

Speed is a premium, and this software will be dedicated to on-site operation at JLab. Consequently, there are few constraints on the software model used to build it. However, we should also keep in mind that we must have the ability for detector and hardware experts located remotely to monitor detector performance and provide diagnostic information.

### **Experiment Calibration and Detector Monitoring**

The calibration database will be an important input to both the raw data reduction and to the event simulation. Good indexing will be necessary to track any changes in the detector or its performance over time, and correlate that to analysis and simulation. The database records themselves will be used to monitor detector performance over time, including both long term drifts as well as failure modes.

The calibration procedure will also involve the use of a set of raw data dedicated to detector calibration. It is important that these data have high availability, and thus the calibration data sets would be replicated at multiple sites to achieve this.

### **Data Reduction: Reconstruction from Raw Data**

Event reconstruction will be a CPU intensive task. It will include, for example, accurate particle tracking through the (approximately) solenoidal field to determine the momentum vectors of

the individual particles; the event vertex and any secondary vertexes; conversion of time-of-flight and Čerenkov information to particle identification confidences; identification of electrons and photons from the electromagnetic calorimeters; and determination of the corresponding tagging event, with confidences.

The computing hardware requirements for the data reduction facilities at JLab were discussed in detail in the previous section, with the principal motivation being that the Level 3 raw data be reconstructed in approximately real time. To reiterate, it is anticipated that we will require 450 Year 2008 CPU's for this task.

We require this code to be portable, as the same code used for reconstruction of the raw data will be used for reconstruction of the simulated data. These tasks will almost certainly be carried out at different sites with different computers.

### Other Tasks

Jefferson Lab needs to extend their high speed network to Hall D, and to establish specific computing resources to acquire and process the raw data from GLUEX. This includes storage capacity for the raw data, CPU power to reduce it, and the ability to store the resulting reduced data. A high speed network, capable of sustaining the necessary bandwidth to support the connections to off-site analysis and simulation centers, must be established at the laboratory.

### 7.3.2 Off-site Computing Infrastructure

Again referring to Fig. ??, the distributed computing facilities associated with GLUEX will comprise both distributed mass storage, as well as computational resources devoted to physics analysis and simulation. It is envisioned that the facilities located at these distributed centers will be matched to the specific data-intensive activities, such as detector calibrations, Monte Carlo simulation, and the various stages of physics analysis that are being pursued by the groups located at these institutions. The storage capacity that needs to exist at a center will depend on the specific activity it represents. For example, a typical analysis of 100 GB of reconstructed data may require 300 GB Monte Carlo of simulated data to be loaded and stored at the center simultaneously.

### Distributed Data Storage Considerations

The distributed mass storage system (data grid) which we envision is a powerful concept, but it relies on both high speed networks between the centers, as well as networks which are reliable and available. For the purposes of this discussion, we refer to the OC standard for network bandwidth; OC-1 = 51.85 Mbit/second and OC-N =  $N \times$  OC-1 rate. Of critical importance will be the connection to JLab, which will be dispensing the reconstructed data to possibly several analysis sites at any one time; and the Monte Carlo center, which would dispense simulated data at about four times the rate of reconstructed data. For example, it takes approximately two days to transfer a 400 GB simulation data set at 20Mbits/sec (13% of an OC-3 connection). With several analysis running at once, it seems clear that we would saturate the currently available OC-3 bandwidth. *It is likely that we would need an OC-24 (1244 Mbits/second) or better connection between the Monte Carlo simulation center, and the physics analysis sites.* Even with high speed networks coming into the universities, it can often be problematic to move the data through the universities' internal networks. However, the few examples that we

have within the GLUEX collaboration have found that the university computer centers have been very interested in resolving these problems. Nevertheless, this may not always be true, particularly for smaller universities, where the “last mile” problem may still be an issue.

### **Physics and Detector Simulations**

An accurate Monte Carlo simulation will be crucial to the success of the detailed partial wave analysis that are the goal of GLUEX. This will begin with some physical model for the final states to be studied, followed by “swimming” charged particles through the (nearly) solenoidal magnetic field and then simulating the signal on the various detector components. This will be a CPU intensive task, which will then be followed by the event reconstruction code. The collaboration needs to establish the Monte Carlo farm for generation, reduction, and storage of the simulated data sets. These are critical sites, and the connection bandwidth to JLab and to other users must be realized.

It is likely that event generation will take place at either one physical site, or perhaps a small number of sites, so the portability of the code will not be a large constraint. However, this activity may well benefit from distributed computing, and in that sense, portable code may prove to be a significant asset.

### **Partial Wave Analysis: Methodology and implementation**

The PWA code must be flexible enough to allow for a large number of different final states within the same framework. Further, it is a CPU intensive task, involving the minimization of a complicated, multi-parameter function, as part of the extended maximum likelihood fit. New visualization tools, which need to be interfaced to the raw and simulated data sets through the data grid, should be developed to help assess the degree to which the assumed wave set describes that data.

The code will run on many different computing systems, depending on which collaborator may be using it at any one time. Consequently, the portability of the running code will be important.

### **Record-keeping and Collaboration Interface**

One key to operating an experiment with an active worldwide collaboration is to keep records (including the experiment “logbook”) accessible to anyone in the collaboration at any one time. Such a portal can also be used as the basis for virtual meetings over the Internet, and a deposit for presentation materials, publications, internal notes, and other important avenues for information dissemination, both external and internal to the collaboration.

### **7.3.3 Software Model**

An object-oriented framework will be established for all software that becomes an integral part of the GLUEX computing environment. The use of design patterns and other best practices from object-oriented design will encourage maintainable code. Unit testing, static analysis, and similar light-weight additions to the process will encourage a scalable software development and testing cycle.

Grid-based computing environments are in large part described by protocols, interfaces, and schema’s. Software components built upon XML interfaces and metadata fit into the notion by

providing collaboration access to analysis, simulation, and visualization tools as "web services", a popular theme in current grid computing initiatives. Some work in this direction has already begun at Jefferson Lab [?,?].

So long as the collaboration adheres to the above framework, it is not critical to decide on any specific programming language. Indeed, a language-agnostic approach will encourage the development of interface compliant, loosely coupled software components. Dependence on legacy code will be limited to the extent that XML interfaces exist (or are written by proponents) which hide the details of the code underneath.

A software distribution and revision control system needs to be set up and maintained. The system should be designed from the outset to not only include code for various purposes, but also documentation, dissemination materials, log books, and other archival information.

## 7.4 Organization

Clearly the successful development and implementation the of the GLUEX computing environment will require extensive coordination between both the GLUEX collaboration and the JLab computing center and data-acquisition groups. Crucial to this is both the dynamic definition and the completion of various computing milestones. Figure ?? shows the currently identified milestones that need to be achieved to meet the computing requirements for GLUEX. Note that Monte Carlo simulations are already in progress and much progress has been made to date in developing the simulation code for detector, beam line, and trigger simulations. In addition, the collaboration is aggressively pursuing the development of the PWA codes and tools which will be crucial in extracting physics results from the data. While it is certainly true that the computing power per dollar invested continues to increase at a dramatic rate, it is not a viable option for the collaboration to wait until the last possible moment to purchase the necessary computing hardware infrastructure. The reason is that a large fraction of the software that will be needed to carry out the project must be developed by the collaboration. One cannot simply use a set of "canned" packages. In order to develop this software, as well as the associated physics analysis techniques, the computing infrastructure, both at JLab and at the university centers, must be at least partially in place well ahead of time. Thus, this infrastructure must be ramped up in the upcoming years. Indeed, a segment of the collaboration is in the process of securing funds to develop a dedicated center for PWA studies (Indiana University). As well, integration of several of the already existing and future computing clusters for initial grid computing studies (Carnegie Mellon, Connecticut, Indiana, JLab Regina) will be tested in the coming months.

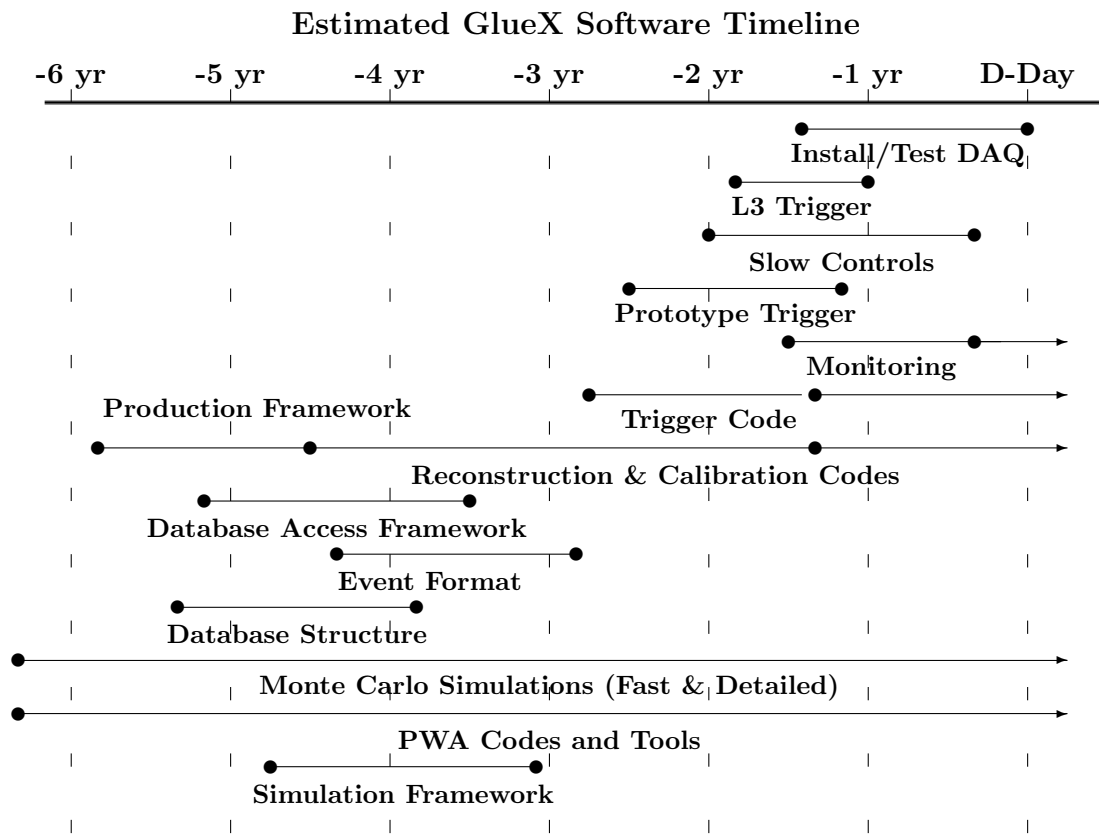


Figure 7.2: Milestones for GLUEX computing projects and tasks.

## Chapter 8

# Simulation

Monte Carlo simulations of photoproduction reactions and the detector response are an integral part of data analysis for GLUEX. Monte Carlo data sets an order of magnitude larger than the real data for specific channels must be produced and analyzed within a unified analysis framework. The computer resources needed for this task were discussed in the previous chapter. This chapter describes how the simulation is to be carried out, the specific software components that exist at present, and some preliminary results regarding detector acceptance and resolution.

During the conceptual design phase of GLUEX two parallel paths of Monte Carlo development have been followed. The first has been focused on simulating reconstructed events for acceptance and resolution studies, and for tests of partial-wave analysis. On this path the simulation of particle interactions in the detector followed by track/cluster reconstruction is replaced by a model which accounts for the smearing of the final particle momenta according to detector resolution. This so-called *fast* Monte Carlo approach is computationally very efficient and permits the exploration of large regions of detector parameter space during design. In fact, important parts of the design evaluation can only be accomplished by this approach, before a full event reconstruction package is available.

When the event reconstruction package arrives, a different sort of simulation code will be needed. This so-called *physics* simulation relies on a detailed geometrical description of the detector and a library of known particle-material interactions to estimate the detector response to a given event as accurately as possible. From this response it forms a simulated event record that is analyzed by the reconstruction package in a similar way as real events. The physics simulation package should come first in the order of software development because it provides useful test data for debugging the rest of the analysis chain. The physics simulation is also useful at the design stage for estimating background rates in detector and trigger elements. This is the second path of Monte Carlo development being pursued by GLUEX.

These Monte Carlo simulation programs are the first components in what will grow to be a large body of code for the GLUEX experiment. It is useful to consider at the outset what pieces of these codes might be of broader use than strictly for simulation. For example, the reconstruction code will need access to the same alignment data as is used by the simulator. Some of the requirements for simulation can be met by incorporating existing software packages from other sources; however their use must be coordinated to avoid conflicts and unwanted dependencies in the future. Software developed at this early stage of the experiment must undergo numerous stages of evolution if it is to be of lasting usefulness. The incorporation of industry standards into the code wherever possible lays the groundwork for a smooth evolution

in the foreseeable future. All of these things come together in the formulation of a software *framework* for the experiment.

In the sections which follow are discussed, first, the software framework, followed by a description of the individual components of the simulation package. The following three sections summarize the results from early design studies carried out with the fast Monte Carlo. The final section describes the general method how simulation results are incorporated into a partial-wave analysis.

## 8.1 Monte Carlo framework

In this context, a framework refers to a set of specified interfaces through which the different software components in a system interact and exchange information, together with a set of common tools that facilitate access to information through these interfaces by application programs. Use of a framework allows builders of individual components to have a relative degree of independence in their implementation choices, knowing what requirements they must satisfy in order to work successfully with the other pieces. Before proceeding to the specifics, it is worthwhile to note two general principles that have been adopted for HALL D code development.

1. All data within the framework must be viewable in a well-formed xml document format that expresses the structure and relationships within the data.
2. All major interfaces should be implemented as web services, in addition to the normal API.

Not specified in this list is any mandated set of languages, operating systems, or disk file formats. While prudence suggests a restricted set of choices for each of these for developing new code, it was decided that the benefits of the freedom to borrow existing programs from a variety of sources outweighs the cost in complexity. Where necessary, legacy code can be wrapped in such a way that it provides its functionality through a protected interface. In any case, software technology is changing too fast at present to allow a final decision on such questions at this point in the life-cycle of the experiment.

The overall data-flow scheme for GLUEX is shown in Fig. ?? . Data flows from the top to the bottom of the figure. On the right-hand side, digitized events come from the detector, are converted to hits by applying corrections derived from the calibration database, and are passed to the reconstruction programs for further processing. On the left-hand column, events start off as lists of particles and their momenta coming from a physics event generator and are converted to hits in the simulator, after which they follow the same path as the real events.

The remainder of this chapter is concerned mainly with what happens to the left of the vertical line in Fig. ?? . For clarity, we will distinguish between event *generation* (first step) and *simulation* (next step) in the Monte Carlo process. As far as the framework is concerned, the only thing of concern is how programs (or people) can access what is inside the boxes. The details of how data is stored inside the boxes, or what happens inside the processing steps is beyond the scope of the framework. The generator needs to be able to find out what kind and how many events to generate. The simulator needs to be able to get from the generator a sequence of event specifications, and it must be able to provide its event hits to the reconstruction code in a format that it understands. Not shown in the figure but also important are the detector

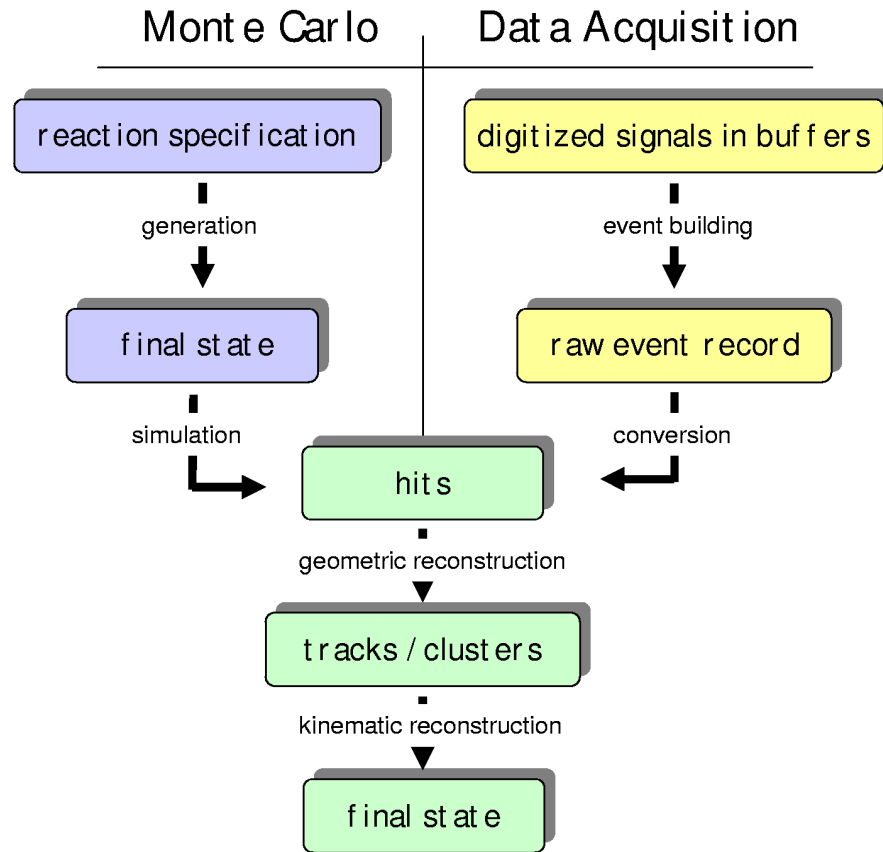


Figure 8.1: Data flow diagram showing the major software components responsible for data processing in HALL D.

geometry information and the simulation control data which the simulator also needs. Within the GLUEX framework, all of these data have the common property that they are viewable in xml. When the software components are fully incorporated into the framework then each of the processing steps will be available on the GLUEX grid as a web service.

The formal specification of all of these interfaces is incomplete at present. The most complete specification is that of the detector geometry information, which has been published [?] on the web. It is described in more detail in a later section. A draft specification for the event description has also been published. [?]. Depending on the location along the data-flow pipeline, different pieces of event information are available. However it is decided that access to all event data by application code within the GLUEX framework is through a single interface. That interface must provide a mechanism for determining what kinds of information are available in an event and for providing what is available in a standard way to the client program.

This is all quite easy to do by specifying the interface in terms of an xml schema. However doing event input/output through xml libraries is very expensive for large data sets, not only in terms of data volume but also cpu overhead. This is why the framework specifies that all data should be *viewable* in xml, not necessarily *stored* in xml. No restrictions are placed on what data formats are actually used internally by applications, or how events are stored in disk

files. In practice it proved convenient for the purposes of Monte Carlo to create a self-describing event data format that is very close to the underlying xml, called *hddm*. An *hddm* event stream (or file) begins with an event template in plain-text xml that describes the information that is available for each event, followed by the actual event data. The tags have been suppressed in the event data and the values written in binary format, so that the event record size is roughly equivalent to other binary formats. Framework tools exist which can automatically generate a miniature c or c++ library that contains the calls needed by an application program to access the event data, just by reading the first few lines in an *hddm* event file. Applications built with one of these libraries automatically verify that the data they require are present in the file before access is attempted. Finally, a single pair of translators called *hddm-xml* and *xml-hddm* exist which are capable of converting any *hddm* data stream to and from xml.

Thus the interface to the data in each of the boxes in Fig ?? is expressed in a xml specification that serves as an event template. The specification contains an inheritance mechanism that makes it easy to extend the event definition, so that producers and consumers of event data can decide to exchange additional information through the extended interface without interfering with the operation on the same data by older programs that rely on the base interface. All of this is verified automatically by the framework API library without any need for checks by application code. Writers of application code have the choice of accessing the data through the API (currently provided in c and c++ only) or by reading and parsing the xml. Use of the API is more efficient in that it eliminates the xml parsing step, but the choice of languages is restricted. On the other hand, standard tools are available in all major languages that make it easy to read and write xml. The advantage of this design is that anyone in any language that has the capability of reading ascii text has access to the event data in a standard way.

The *hddm* scheme is effectively an efficient mechanism for prototyping interfaces to event data. Eventually the information content of an event will stabilize to the point where the interface can be frozen, at least for the early stages of the pipeline. At that point the choice of the format for event data decouples from the interface. Different event formats at various stages along the data-flow path may be adopted based upon considerations of efficiency and prevailing technology. None of this has practical consequences for application code, provided that the interface remains everywhere the same.

## 8.2 Monte Carlo generators

There are two physics event generators available for use within the GLUEX Monte Carlo framework, known as *genr8* [?] and *cwrap* [?]. Both programs are capable of describing a complex decay chain of intermediate states, where decays into two or three bodies are supported at each step. The invariant masses of each particle produced is sampled from a Breit Wigner distribution, whose mass and width is taken from the PDG. A general *t*-channel process is assumed, with the distribution in *t* drawn at random from the standard form for a peripheral reaction

$$\frac{d\sigma}{dt} \propto e^{-b|t|}$$

where the *b* parameter is specified by the user. Both meson and baryon decay chains are allowed. In the case of *genr8* the user may specify the *t*-distribution in the form of a histogram in place of specifying a value for *b* in the above formula. *b* may be specified by an input histogram.

The angular distributions at each decay vertex are generated according to phase space. This may appear to be a severe restriction in an experiment whose goal is partial-wave analysis, but in fact that is not the case. To see how the physical model for particle spins and decay asymmetries are applied to phase-space Monte Carlo data, see section ??.

Both *genr8* and *cwrap* were imported from other experiments, and so write their output events in different and somewhat esoteric formats. To incorporate them into the GLUEX framework it was sufficient to provide translators from their private formats to a common hddm format that can be viewed as xml. The present draft specification for the standard xml interface to generated events is found in Ref. [?]. At present a second standard interface is also being supported known as *stdhep*. This somewhat archaic Fortran-based standard was in use by many HEP experiments over the last decade, and there are a number of useful Monte Carlo tools that rely on it, including *MCFast* (see section ??). Currently translators exist to supply generated events from either generator through either the xml or the *stdhep* interface.

Both generators use cryptic private formats for the input data that specify the reaction and desired number of events. At present there does not exist a single unified interface for specifying the reaction to be generated. The task of incorporating *genr8* and *cwrap* into the GLUEX framework will not be complete until that interface has been specified, and translators have been written to convert that information from xml to a form understandable to the generators.

### 8.3 Detector Geometry

One of the most basic requirements for the simulation is access to a detailed description of the geometry of the experiment. Included in geometry is the shape and location of all relevant components, their properties in terms of material composition, density, etc., and the map of the magnetic field. Any objects with which beam particles may interact on their way to a detector are a part of the geometry, starting with the primary collimator and ending with the photon beam dump. Any application within the GLUEX framework that needs access to detector geometry data obtains that information through one unified interface. This interface is specified in the form of a xml *document type definition* (DTD) which details what tags exist in the document, what are their arguments, and their structural relationships. The basic structure of the DTD was borrowed from the ATLAS experiment at CERN and adapted for the needs of GLUEX. It describes the detector as a tree of volumes, each with specified shape, size, position and material properties. It allows elements to be grouped together and positioned as a unit, so that a survey datum can be expressed by a single element. More details on the interface can be found in Ref. [?].

Application code has access to geometry data through the standard xml libraries. Programs can scan the entire tree or ask for specific pieces of information, such as the position of the center of the target. At present the only consumers of geometry information are the simulation codes. The Geant simulator (see section ??) is capable of modeling any geometry, provided that the xml conforms to the DTD. The MCFast simulator (see section ??) supports a more limited geometrical description. A special set of tags in the geometry DTD have been created to describe the detector elements in simplified terms for MCFast, in places where the translation from the hierarchical description require some imagination. As more applications are created that depend upon access to specific pieces of geometry information, it will be necessary to extend the interface beyond the DTD to specify the presence and location of specific tags. Investigation is underway to determine if these more complex constraints might be better expressed using

xml schema than the DTD.

At present the geometry description is implemented in a set of plain xml text files and organized under a sequential version system. In the future they will probably be stored in a database and indexed by date or run number.

## 8.4 Physics Simulation

The physics simulation for GLUEX is provided by a program called *HDGeant*. The simulator requires four data interfaces: an event source, detector geometry data, simulation control information, and event output. HDGeant is capable of simulating events from any one of three sources.

1. events from a Monte Carlo generator
2. coherent bremsstrahlung source generator
3. automatic single-track generator (for testing)

The first of the three is an external event source described in section ???. Events from the generator are distributed uniformly along the length of the beam-target interaction volume and final-state particles followed out into the detector from there. The other two sources are internal to the simulator, and are used for special purposes. The coherent bremsstrahlung source generates uncollimated photons with the energy, angle and polarization characteristics of bremsstrahlung from an oriented diamond radiator. These photons enter the setup upstream of the primary collimator and are followed through the collimator region into the experimental hall, where interactions in the detector are allowed to take place. This simulation mode is useful for estimating detector backgrounds, and for studying the systematics of the collimated photon beam. The single-track generator is used for development of various parts of the simulation, and will be useful later in debugging the event reconstruction package.

The choice of the source for input events is specified in an input file known as the *control* file. Also in the control file are a number of switches that control the simulation mode, such as the number of events to simulate, cutoffs for a variety of physics processes, and debug options. HDGeant obtains the detector geometry directly from the standard geometry interface. Input events from the Monte Carlo generator are accessed through the the standard event interface implemented in the hddm library. Output events are likewise written out using the hddm library.

The output from the simulation is a list of *hits*, which are time and energy data from each detector element that received a signal during the propagation of the event through the detector. The hit data are stored in physical units appropriate to the signal (eg. ns, MeV) which is what the simulation directly produces. No provision is made in the simulator to convert these data back into ADC or TDC data in the form produced by the data acquisition hardware; that would require couple the simulation to the the detector calibration database, and introduces an unnecessary complication to the simulation. If events in that form were desired at some point, a separate converter could be written to generate simulated raw events from the simulator output.

The major effort in the ongoing development of the simulation is to have a reasonably accurate model of the detector response in each of the detector elements. A basic model presently exists in the code for each of the detector components. These must be improved by

uncollimated beam	44 ms
1GeV $\pi^+$ at $15^\circ$	55 ms
3GeV $\gamma$ at $10^\circ$	200 ms
1GeV $\gamma$ at $45^\circ$	90 ms
$\gamma p \rightarrow \pi^+ \pi^- p$	210 ms
$\gamma p \rightarrow \pi^+ \pi^- \pi^0 p$	430 ms
$\gamma p \rightarrow \eta \pi^0 \pi^0 p$	670 ms

Table 8.1: Average time required by HDGeant to simulate a single event of various kinds. The tests were carried out on a single Pentium III 1GHz processor. The times are reduced by about a factor of 1.8 on the Athlon MP 1800+ cpu.

the incorporation of intrinsic resolutions for each of the detectors. For example, the impact parameter of tracks in a straw tube of the central drift chamber is converted to a hit time value using a simple linear model for the time *vs* radius. For another, for the response of the lead-glass calorimeter, the total energy loss of charged particles is reported as the hit energy, without taking into account the difference in the Čerenkov response between different kinds of particles. Nevertheless, in its present form the simulator is useful for estimating many aspects of detector performance.

In addition to the detector hits, the simulation is also capable of writing out certain kinds of auxiliary information about the simulated event, for example the actual 3-d points of track impacts on the planes of the forward tracker or the true energy of a photon creating a cluster in the barrel calorimeter. Such information is called *cheat* data because it is not available for real events. However it is invaluable for Monte Carlo studies prior to the development of event reconstruction code, and will be useful in that development for checking the fidelity of the reconstruction.

In Table ?? is shown the average time required to simulate a single event on a cpu that is available today, for a few sample reactions. The beam simulation uses the simulator's internal coherent bremsstrahlung generator, and exercises mainly the electromagnetic shower simulation in the collimator region upstream of the detector. The single-track case is included to show the cost of tracking charged particles through the the magnetic field. The gammas show the corresponding cost for photons. The two are put together in the reactions which follow.

In order to obtain a reliable simulation of backgrounds from the collimator region, two enhancements to the standard Geant simulation library were incorporated into HDGeant. The first of these is the addition of hadronic interactions by photons in materials, and the second was Bethe-Heitler muon pair production. The standard Geant electromagnetic shower simulation does not include hadronic photoproduction processes or muon pair production because their cross sections are several orders of magnitude less than the dominant electromagnetic processes and their presence is generally not important to simulating calorimeter response. For the purposes of HALL D however, the high intensities of showers in the collimator enclosure and the heavy shielding against electromagnetic backgrounds makes them important. In particular there are two kinds of penetrating radiation that must be considered: neutrons and high-energy muons.

The incorporation of muon Bethe-Heitler production into Geant was straight-forward to do, simply by replicating the code for electron pair production with a changed mass, and the

cross section reduced by the factor  $m_e^2/m_\mu^2$ . The inclusion of photonuclear processes is more daunting. Rather than launch a development of our own, it was decided to incorporate a package that was developed earlier for use by the BaBar experiment known as *Gelhad* [?]. This package breaks provides four models of hadronic photoproduction that are applicable at different scales: single nucleon knockout, two-nucleon knockout via the quasi-deuteron process, single pion photoproduction in the delta-resonance region, and diffractive vector production in the diffractive region. From the point of view of photonuclear physics, this model is far from complete. It will not be used by GLUEX to generate photoproduction events in the target. What it does provide is a starting point for estimating neutron fluxes in the hall from the collimator region.

The present HDGeant package is based on the widely-used version 3 of the CERN Geant library. Discussion has started regarding moving the development for GLUEXover to the C++ simulation package known as Geant4 that is being used by some of the LHC experiments. Given that the Geant-3 library is written almost entirely in Fortran and is no longer being actively supported by the CERN computer division, its long-term viability depends upon support by the user community. The LHC Alice experiment has taken the major components of Geant-3 and wrapped them for use in a C++ environment known as *AliRoot*. The choice of a long-term solution for a physics simulation for GLUEX has not yet been finalized.

## 8.5 Fast simulation

A fast Monte Carlo package has been developed to understand the performance of key aspects of the GLUEX detector systems. This package consists of a collection of modules, each serving some particular function. The modules consist of individual programs and library routines which use common event input/output formats. Figure ?? illustrates this modular structure.

First, a Monte Carlo four-vector generator is used to create phase-space distributed events. Next is the detector simulation, *HDFast*, which is a fast and flexible simulation program based upon the MCFast package developed by the simulation group at Fermilab. The Monte Carlo output includes (but is not limited to) the following data objects:

- generated event
- detector hits
- resolution modified (smeared) event
- time-of-flight information
- dE/dx information
- threshold Čerenkov information
- particle trajectory information

*HDFast* is a fast and flexible simulation program based upon the MCFast package developed by the simulation group at Fermilab<sup>1</sup>. MCFast consists of a set of modularized Monte

---

<sup>1</sup> Information on MCFast may be obtained via the WWW at <http://fnpspa.fnal.gov>

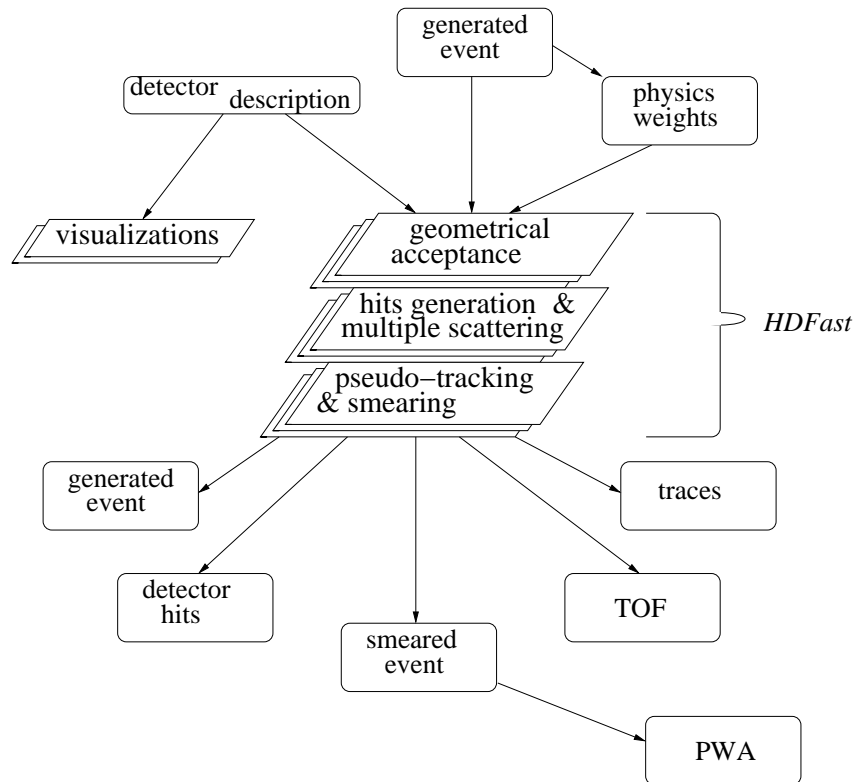


Figure 8.2: An illustration giving an overview of the GLUEX Monte Carlo software which emphasizes its modular nature.

Carlo library routines. It is designed to perform parameterized tracking by assembling a covariance matrix for each track that takes into account materials, efficiencies, and resolutions for all measurement planes, and use this matrix to smear the track parameters randomly. The covariance matrix is first diagonalized so as to properly account for effects due to correlations when parameters are smeared. In principle, the distribution of smeared tracks produced by this method would be similar to the distribution of real tracks that were measured by a real detector (with the same parameters) and analyzed with an idealized track fitting procedure.

*HDFast* is controlled via a set of user routines which act as an interface to the MCFast package. They control the tracking and smearing of the four-vectors, in addition to the booking and filling of monitoring ntuples and histograms. The detector geometry is controlled by an ascii file which is read in during program execution. This allows the user to quickly create or modify the detector geometry without the need to recompile the executable. In addition, ROOT [?] was used to develop an event display which reads in the ascii geometry file and displays a two-dimensional visualization (see Figure ??) of the detector configuration and event track projections.

## 8.6 Acceptance studies

In order to better understand the effects of finite acceptance of a proposed detector configuration, a simple study of the acceptance as a function of total meson effective mass for various final states has been performed. In doing the Monte Carlo acceptance studies we considered the following reactions: schematically shown in Figure ???. This configuration is composed of the following:

- 2.24 Tesla solenoid magnet –LASS magnet,
- 5-layer Vertex Chamber (VTX),
- 22-layer Central Drift Chamber (CDC),
- 5 6-layer Forward Drift Chambers (FDC),
- Barrel Calorimeter which also acts as central TOF(BCAL),
- Cerenkov Detector,
- Forward time-of-flight (FTOF),
- Forward Lead Glass Detector (LGD) 172x172 cm with 8x8 cm beam hole,
- target-beam vertex distribution at  $r = 0.0$  cm,  $z = 50$  cm with  $\sigma_r = 0.3$  cm,  $\sigma_z = 15.0$  cm ( $\hat{z}$  is along the magnet axis; the origin is located at the upstream face of the solenoid).

### 8.6.1 Acceptance performance

In the simulation, an event was accepted if the following minimum conditions were met:

- all charged tracks were found with a minimum of four hits per track, and
- all gammas were detected in either the BCAL and/or LGD.

The acceptance as a function of total effective meson mass is shown in Figure ???. It is important to note that at higher beam energies the forward boost results in more forward-going high-momentum tracks. And even though the mass acceptance seems good, the resolution of the forward-going higher-momentum tracks degrades. This issue has been studied in detail and is discussed in HALL D Note #7 [?].

In Figure ?? through Figure ??, we show the acceptance for the Gottfried-Jackson decay angles (the particle decay angles often used in the partial wave analysis). It is clear that the Gottfried-Jackson angular acceptance is quite good. The acceptance for gammas is also rather high, but it suffers more from holes in the forward and backward regions. The hole in the backward region results from backward-going gammas, which is the dominant factor at lower beam energies. The forward hole, due to gammas passing through the beam hole in the LGD, becomes important for higher beam energies. Figure ??a displays an event for reaction  $\gamma p \rightarrow p\eta\pi^0\pi^0$  at  $Mass(X) = 2.0$  GeV/c<sup>2</sup> and beam of 5 GeV that was lost due to the upstream hole. For this channel 75% of the lost events were of this type. On the other hand, for a 12 GeV beam and the same final state about 50% of the lost events are due to the beam hole(See Figure ??b). While the beam hole is unavoidable, the hole in the backward region suggests the need

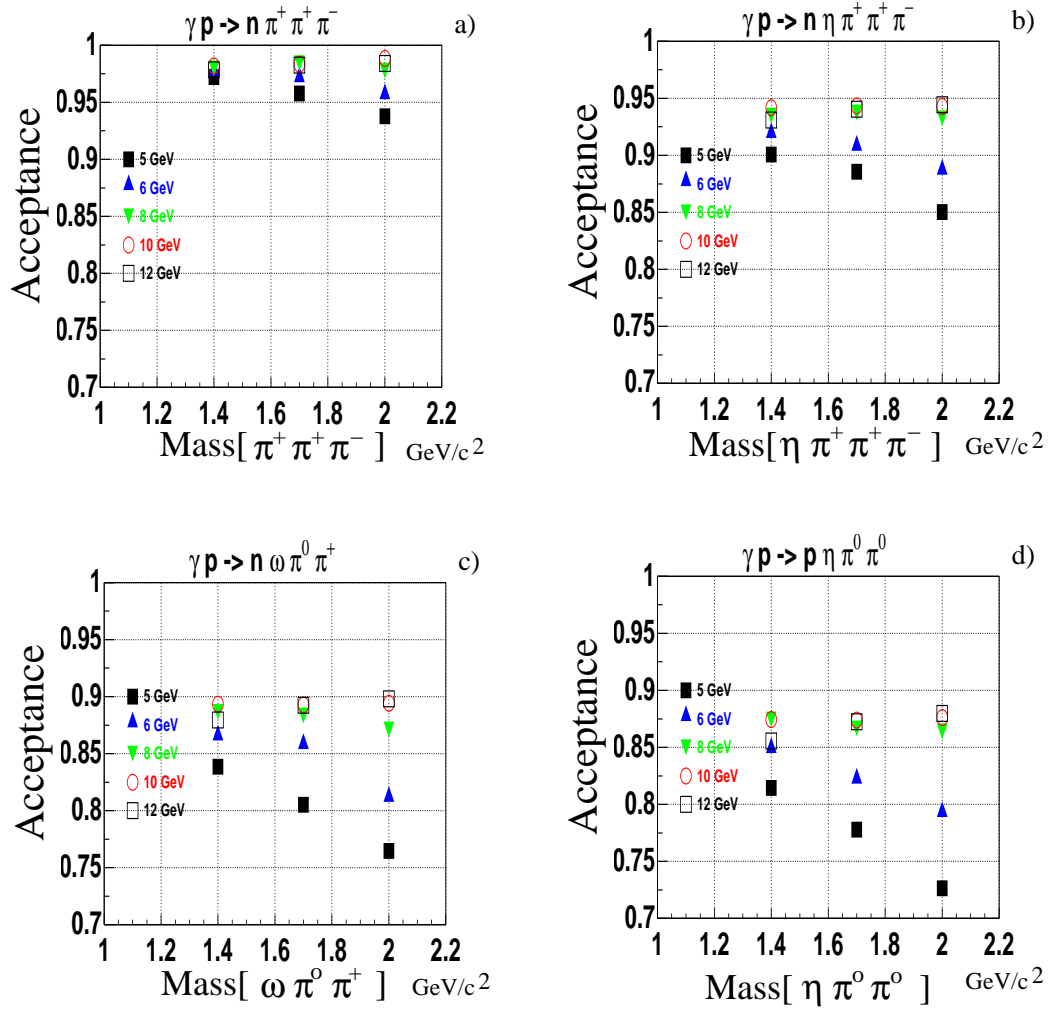


Figure 8.3: The acceptance as a function of total effective meson mass: a)  $X^+ \rightarrow \pi^+ \pi^+ \pi^-$ , b)  $X^+ \rightarrow \eta \pi^+ \pi^- \pi^+$ , c)  $X^+ \rightarrow \omega \pi^0 \pi^+$ , d)  $X^0 \rightarrow \eta \pi^0 \pi^0$ . The acceptance studies were performed for effective meson masses of 1.4, 1.7, and 2.0  $GeV/c^2$ , and at each mass point the photon beam energy was varied from 5 to 12  $GeV$ .

at the lower beam energies for a backward gamma veto. Regardless of this, the acceptance for the Gottfried-Jackson decay angles is flat and not strongly dependent on  $Mass(X)$  or the beam energy. This is important for partial wave analysis because, although the effects of acceptance distortions are accounted for in the method, large acceptance corrections can lead to large systematic errors in the results.

## 8.7 Monte Carlo Study of Photon Energy Resolution

In this study the GENR8 program was used to generate the events. Four different exclusive reactions were studied, two with photons produced at the baryon vertex:

$$\gamma p \rightarrow N^*(1500)\pi^+ \rightarrow (n\eta)\pi^+ \rightarrow n\pi^+\gamma\gamma \quad (8.1)$$

$$\gamma p \rightarrow X^+(1600)\Delta^0 \rightarrow (\pi^+\pi^+\pi^-)(n\pi^0) \rightarrow \pi^+\pi^+\pi^-n\gamma\gamma \quad (8.2)$$

The  $\Delta^0$  reaction (reaction ??) has a  $3\pi$ -meson mass of  $1.600\text{GeV}/c^2$ , and a width of  $300\text{MeV}/c^2$ . The two meson vertex reactions are:

$$\gamma p \rightarrow X^+(1600)n \rightarrow (\eta\pi^+)n \rightarrow n\pi^+\gamma\gamma \quad (8.3)$$

$$\gamma p \rightarrow X(1600)p \rightarrow (\pi^+\pi^-\pi^0)p \rightarrow p\pi^+\pi^-\gamma\gamma \quad (8.4)$$

In both reactions ?? and ??, the meson systems were generated with a Breit–Wigner distribution of mass  $1.6\text{GeV}/c^2$  and a width of  $0.3\text{GeV}/c^2$ .

Each of the above reactions were simulated using a beam energy of  $8\text{GeV}$ , and a  $t$ -channel slope of  $5\text{GeV}/c^2$ . The production and decay vertex was assumed to be at the center of the target. For each system, 10,000 events were generated. The direction and energy of the photons were recorded and analyzed.

### 8.7.1 Photon Detector Energy Resolution

The photons produced in the above decays were traced into the Barrel Calorimeter and the Lead Glass Detector. Figure ?? and ?? show the percentage of photons that would enter, but not be detected by the Barrel Calorimeter due to the minimum energy thresholds.

Currently, the design calls for the energy sensitivity of 20 MeV for the Barrel Calorimeter. One can see that this results in around a 1% loss of photons which is quite acceptable. However, if this energy can not be met, the percentage of photons lost rises rapidly with the increased energy threshold, especially for the  $\Delta^0$  (reaction ??) decay. For example, if the threshold is 50 MeV, then 5% of the  $3\pi$  reaction is lost, and 10% of the  $\Delta^0$  reaction is lost. The situation for the  $\eta$  reactions is not so severe, as would be expected from the higher energy photons in the  $\eta$  decay (figure ??).

The results for the Lead Glass Detector are similar, but the percentage rise is not so significant at higher energy thresholds. The only system with significant loss in the lead glass array is the  $3\pi$  (reaction ??) decay. At the sensitivity threshold of 100 MeV, the lead glass detector will not see 0.718% of the photons. The design calls for a 150 MeV detection minimum in the LGD. At this energy, the detector will miss 1.86% of the photons (figure ??).

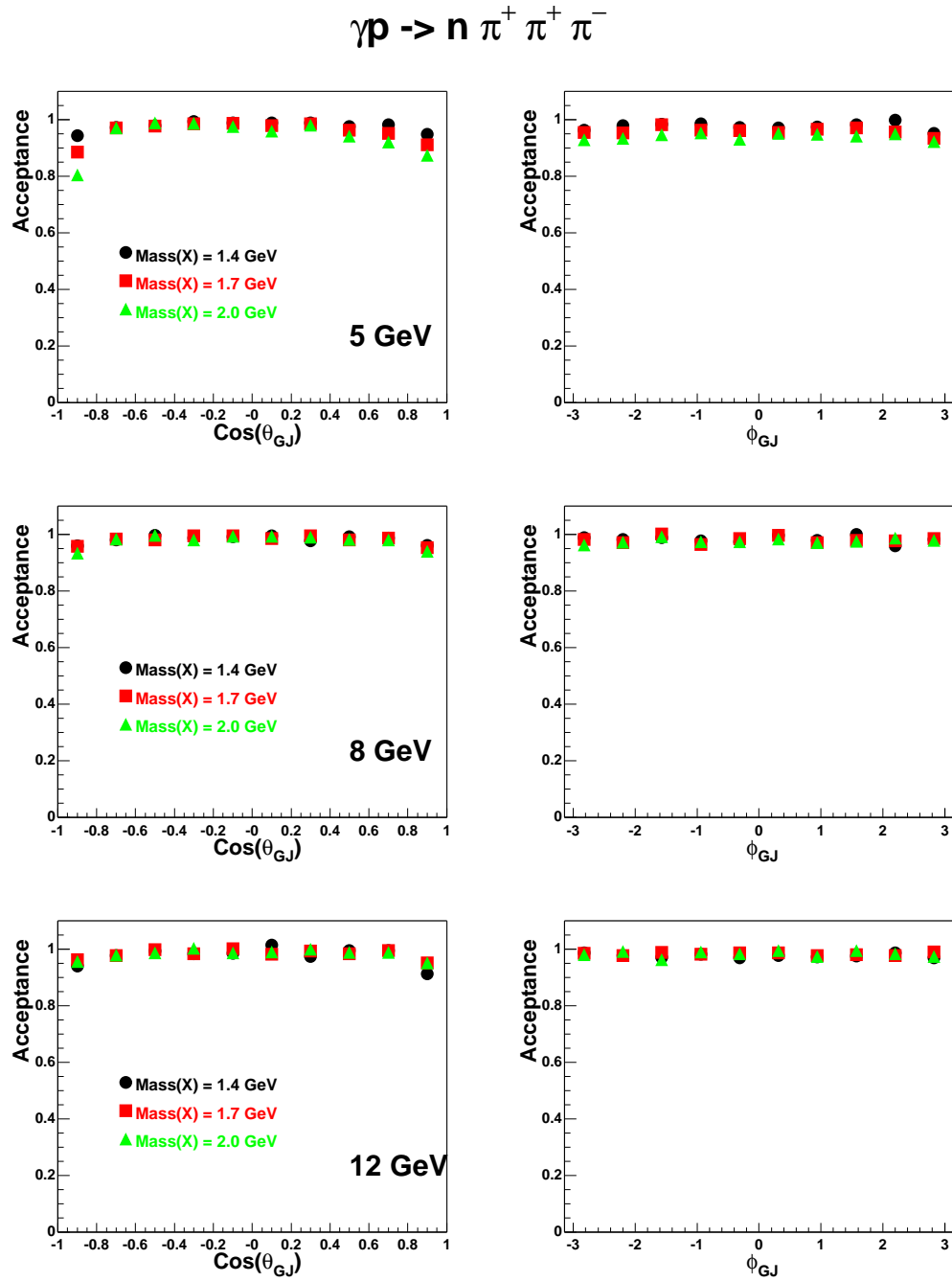


Figure 8.4: The acceptance in  $\text{cos}(\theta_{GJ})$  and  $\phi_{GJ}$  for  $X^+ \rightarrow \pi^+ \pi^+ \pi^-$ . The acceptance was studied for  $X^+$  effective masses of 1.4, 1.7, and 2.0  $\text{GeV}/c^2$ , and for different photon beam energies of 5 $\text{GeV}$  (top), 8 $\text{GeV}$  (middle), and 12 $\text{GeV}$  (bottom).

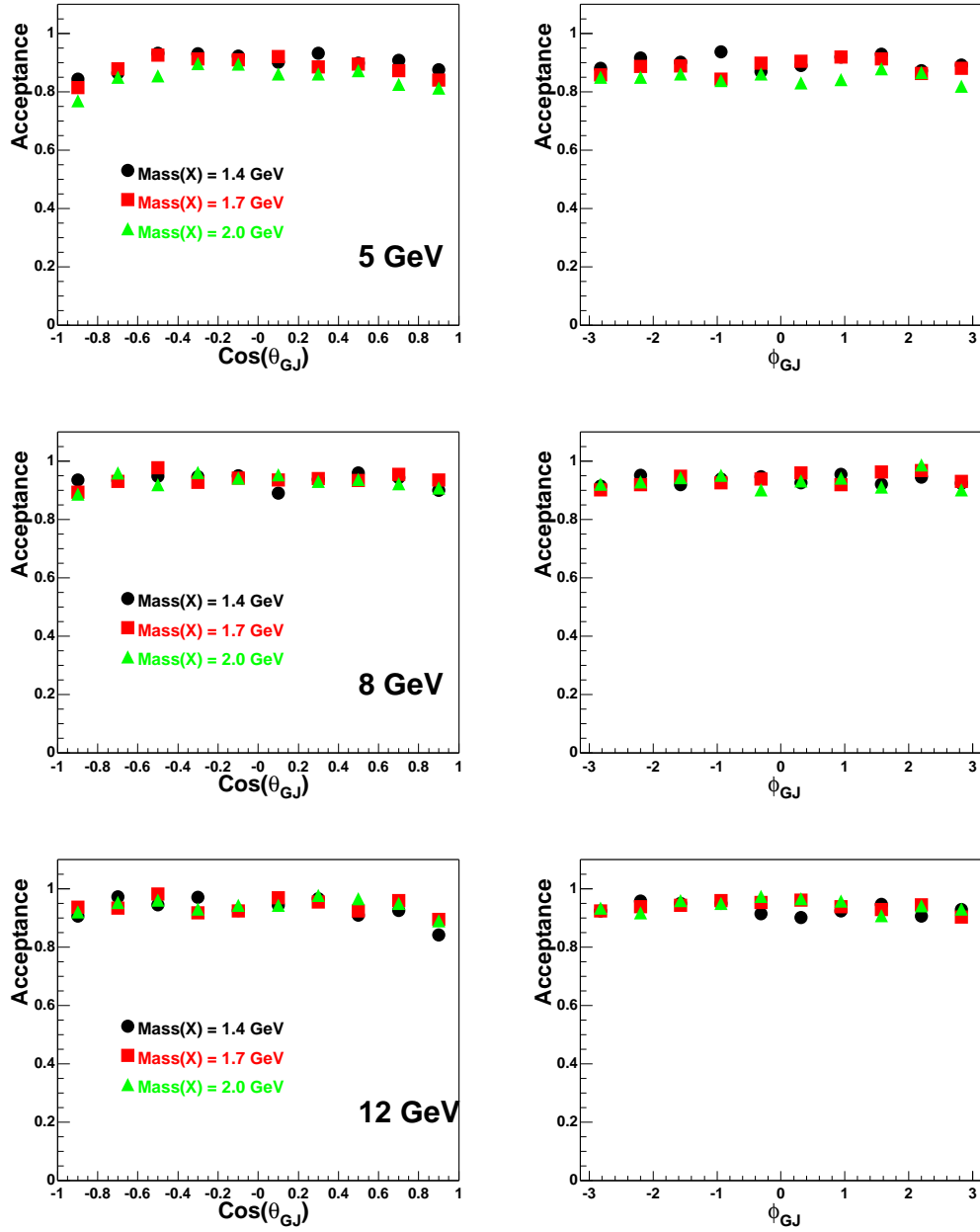


Figure 8.5: The acceptance in  $\text{cos}(\theta_{GJ})$  and  $\phi_{GJ}$  for  $X^+ \rightarrow \eta \pi^+ \pi^+ \pi^-$ . The acceptance was studied for  $X^+$  effective masses of 1.4, 1.7, and 2.0  $\text{GeV}/c^2$ , and for different photon beam energies of 5 $\text{GeV}$  (top), 8 $\text{GeV}$  (middle), and 12 $\text{GeV}$  (bottom).

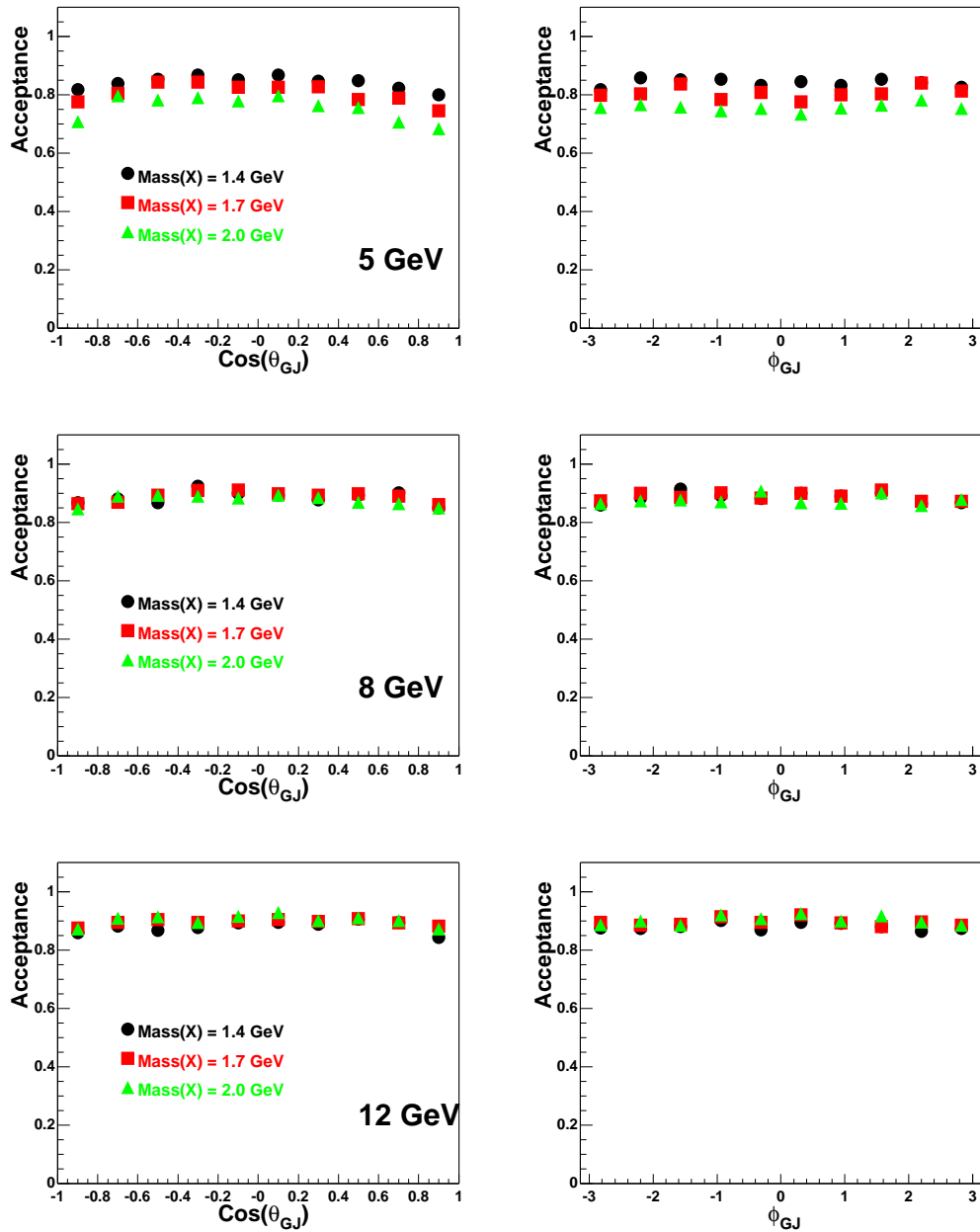
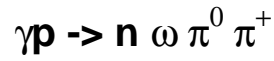


Figure 8.6: The acceptance in  $\text{cos}(\theta_{GJ})$  and  $\phi_{GJ}$  for  $X^0 \rightarrow \omega \pi^0 \pi^+$ . The acceptance was studied for  $X^+$  effective masses of 1.4, 1.7, and 2.0  $\text{GeV}/c^2$ , and for different photon beam energies of 5 $\text{GeV}$  (top), 8 $\text{GeV}$  (middle), and 12 $\text{GeV}$  (bottom).

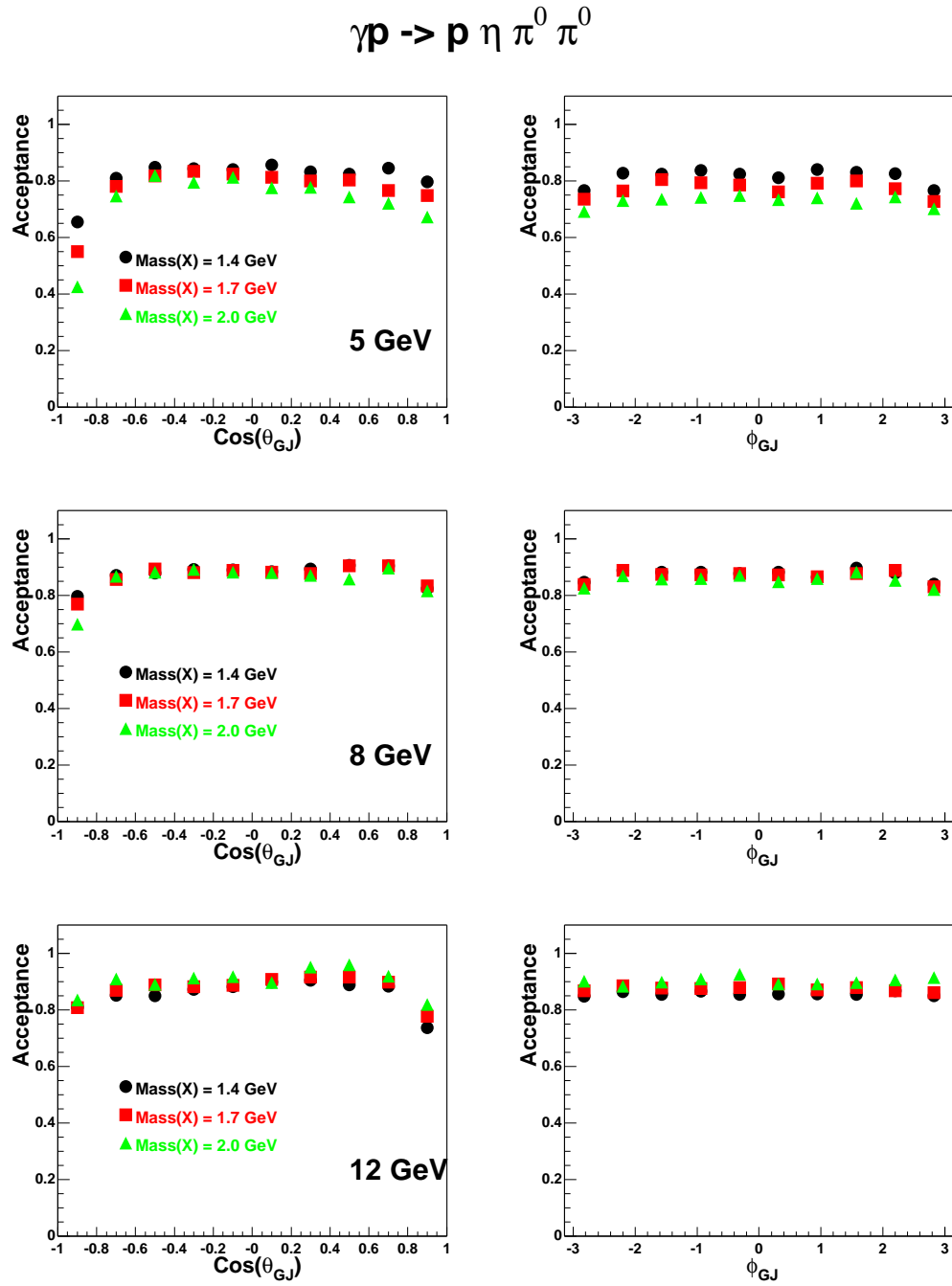


Figure 8.7: The acceptance in  $\text{cos}(\theta_{GJ})$  and  $\phi_{GJ}$  for  $X^0 \rightarrow \eta\pi^0\pi^0$ . The acceptance was studied for  $X^+$  effective masses of 1.4, 1.7, and 2.0  $\text{GeV}/c^2$ , and for different photon beam energies of 5 $\text{GeV}$  (top), 8 $\text{GeV}$  (middle), and 12 $\text{GeV}$  (bottom).

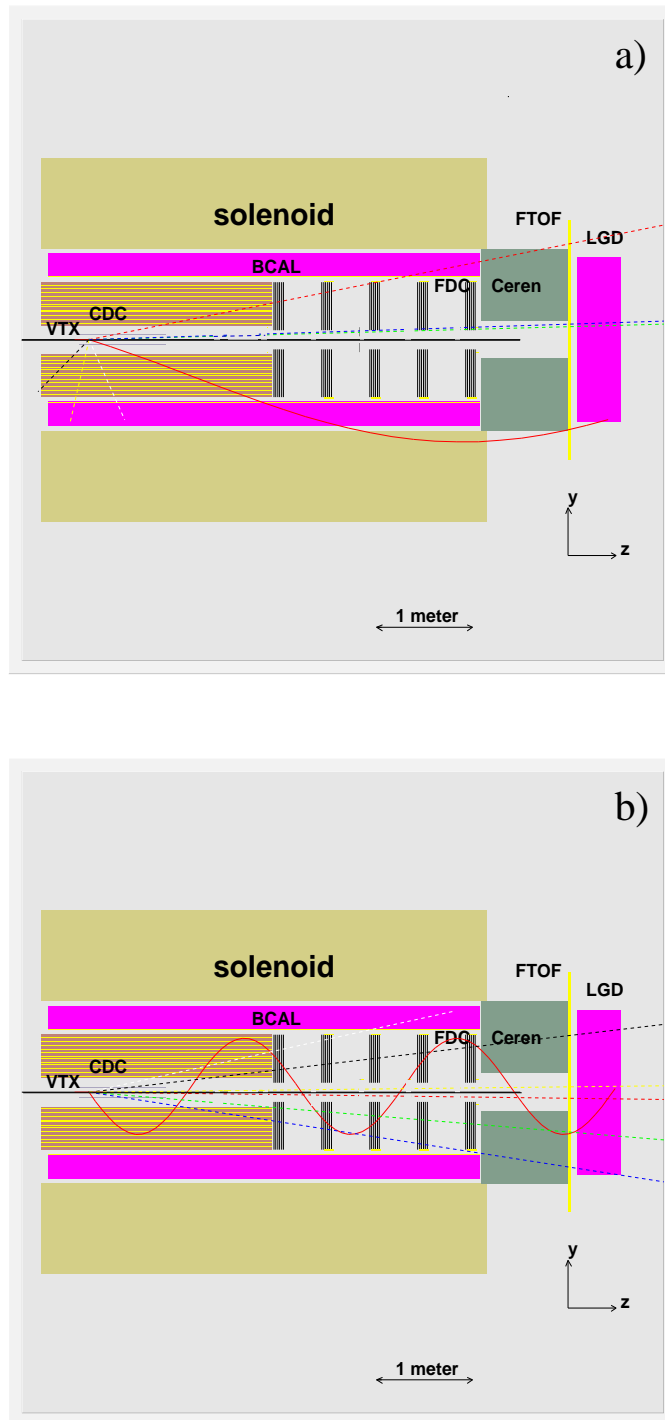


Figure 8.8: Event displays of lost events for  $\gamma p \rightarrow p\eta\pi^0\pi^0$  for  $Mass(X) = 2.0 \text{ GeV}/c^2$ : (a) backward missed gamma at a beam energy of 5 GeV, and (b) forward missed beam hole gamma at a beam energy of 12 GeV. The events shown contain both charged particles (solid lines) and photons (dashed lines).

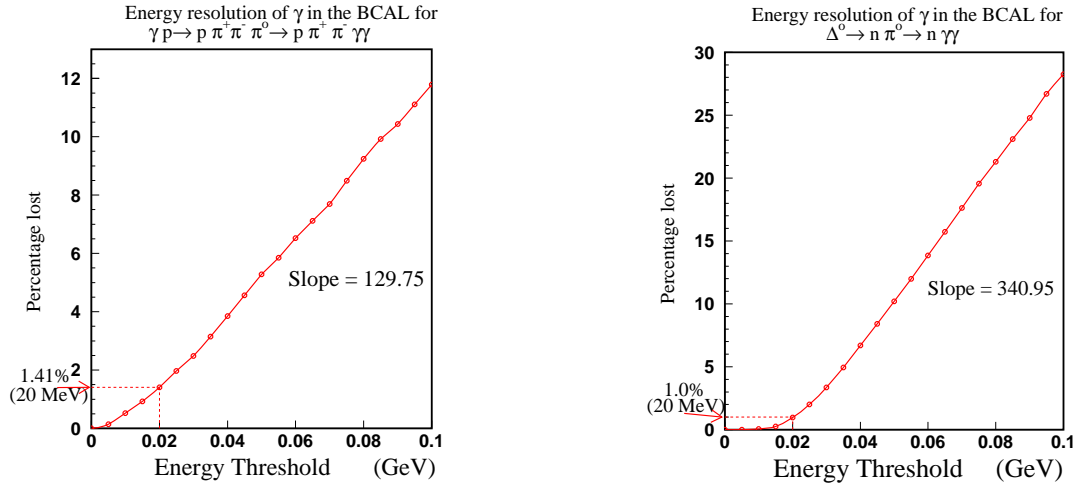


Figure 8.9: The percentage loss due to the energy threshold of the BCAL. Left is for reaction  $\gamma p \rightarrow p \pi^+ \pi^-$ , while the right figure is for the  $\Delta^0$  decay from reaction  $\Delta^0 \rightarrow n \pi^0 \rightarrow n \gamma \gamma$ . The percent of the total photons entering the Barrel Calorimeter for reaction  $\gamma p \rightarrow p \pi^+ \pi^-$  is 57% and reaction  $\Delta^0 \rightarrow n \pi^0 \rightarrow n \gamma \gamma$  is 87%.

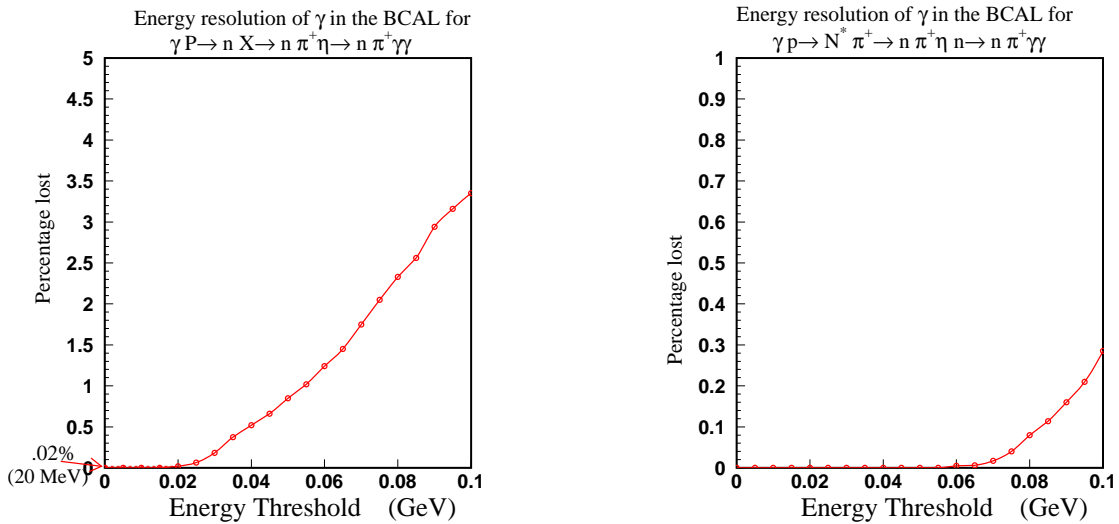


Figure 8.10: The percentage loss due to the energy threshold of the BCAL. The left plot is for reaction  $\gamma p \rightarrow n X \rightarrow n \pi^+ \eta \rightarrow n \pi^+ \gamma \gamma$ , and right is for reaction  $\gamma p \rightarrow N^* \pi^+ \rightarrow n \pi^+ \eta \rightarrow n \pi^+ \gamma \gamma$ . The percent of all the photons entering the Barrel Calorimeter for the  $\eta X$  (reaction  $\gamma p \rightarrow n X \rightarrow n \pi^+ \eta \rightarrow n \pi^+ \gamma \gamma$ ) and the  $\eta N^*$  (reaction  $\gamma p \rightarrow N^* \pi^+ \rightarrow n \pi^+ \eta \rightarrow n \pi^+ \gamma \gamma$ ) are 55% and 88% respectively.

Figure 8.11: The percentage of undetected photons for a given energy threshold of the lead glass detector. From reaction  $\gamma p \rightarrow n X \rightarrow n \pi^+ \eta \rightarrow n \pi^+ \gamma \gamma$ .

## 8.8 Physics Event Weighters

Conceptually, what one would like to do in the analysis of any given reaction is to write down as complete as possible a set of diagrams leading to the final state and sum their amplitudes as a function of a minimal set of unknown parameters. This model would then be fed to the event generator to produce a Monte Carlo sample which could be reconstructed and compared to the data. By repeating this procedure for different values of the parameters through a fitting procedure, the best values of the parameters and an overall evaluation of the model could be derived.

Practically, this is not what is done because it is too expensive to recompute the entire Monte Carlo sample at every step in the fit. Instead a single Monte Carlo sample is produced using an initial crude approximation to the physics model distribution, and then corrections are applied using a weighting procedure after the sample has been simulated and reconstructed. The initial approximation is defined by the following three simple assumptions; (a) particles from high-energy photoproduction are produced independently from meson and baryon vertices; (b) the momentum separation between the two vertices is described by an exponential distribution in the Mandelstam variable  $t$ ; (c) within each vertex the particles are produced through a cascade of two- and three-particle decays which are each distributed according to a phase-space density function. If this approximation were an adequate model of the physics then there would be no need for the GLUEX experiment. Nevertheless it is a useful starting point because it can be used to produce a Monte Carlo sample of events with adequate coverage over the full kinematic range of interest.

Assuming the independence property of the Monte Carlo sampling technique, every event in the Monte Carlo sample is independent of the others. Each reconstructed Monte Carlo event carries with it the information about the original generated kinematics, from which the physics amplitudes can be calculated. For a given set of model parameters these amplitudes can be summed to form a probability for each event, which is called a *weight*. If all sums over the Monte Carlo sample during partial wave analysis are carried out including these weight factors then the foregoing conceptual procedure is recovered. Although the statistical errors in the weighted Monte Carlo sample are no longer simple Poisson factors, they are straightforward to calculate. In general these errors are larger for the weighted technique than for an unweighted procedure, but that is readily offset by generating a somewhat larger sample. Exactly how much larger depends on how different the weighted distribution is from the initial, but usually this factor is not larger than two. Ultimately it is not known until the final stages of the analysis how large a Monte Carlo sample is adequate for any given channel, but for the purposes of the design a conservative factor of 10 more Monte Carlo than real events has been adopted as a benchmark.

The above method is well-established for partial wave analyses in high-energy physics. To gain experience within the context of GLUEX it was decided to apply the procedure to a photoproduction reaction. To this end, an event generator for the  $3\pi$  final state has been written using the one-pion charge-exchange mechanism as discussed in reference [?] for reaction ??.

$$\vec{\gamma}p \rightarrow X^+n \left( X^+ \rightarrow \left[ \rho^0 \rightarrow \pi^+\pi^- \right] \pi^+ \right) \quad (8.5)$$

A schematic of this process is shown in Figure ??. One- $\pi$  charge exchange requires both a spin-flip at the nucleon vertex, and that the  $X^+$  particle carry the helicity of the incoming  $\gamma$ , ( $M_X = 1$ ). Any number of resonances  $X^+$  with different masses, widths and production strengths can be included in the generator. In addition, the photon beam can have any polarization desired. An

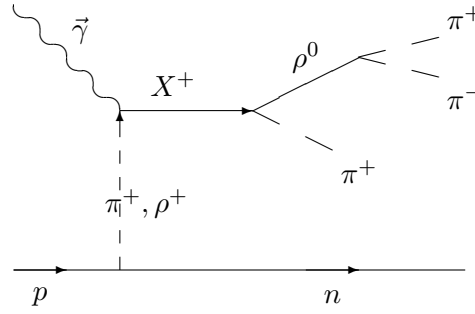


Figure 8.12: A schematic diagram of the photoproduction amplitude via one- $\pi$  or  $\rho$  exchange. The state  $X^+$  then decays via  $\rho^0\pi^+$ , and the  $\rho$  subsequently decays into  $\pi^+\pi^-$ .

extension to this program allows for  $\rho$ -exchange under the same conditions as the  $\pi$  exchange. These two amplitudes represent *unnatural* and *natural* parity exchanges respectively. Events produced using one of the phase space generators can then be weighted according to the physics weighter, and then passed through the GLUEX Monte Carlo program. These can then be used as input to the partial wave analysis as described in the next chapter.

A sample of the output of this generator is shown in Figure ???. These events have been generated with four resonances:  $a_1(1260)$ ,  $a_2(1320)$ ,  $\pi_2(1670)$  and an exotic  $\pi_1(1600)$ . The masses and widths are all consistent with current accepted values. In addition, one can see the  $\rho^\circ$  in the  $\pi^+\pi^-$  invariant mass spectra. A full list of known resonances [?] that could be put in this generator is given in table ???.

Resonance	Mass	Width	$L_{\rho\pi}$
$a_1^+(1260)$	$1.230\text{GeV}/c^2$	$.250 \text{ to } .600\text{GeV}/c^2$	$L = 0, 2$
$a_2^+(1320)$	$1.318\text{GeV}/c^2$	$.105\text{GeV}/c^2$	$L = 2$
$\pi_1^+(1600)$	$1.593\text{GeV}/c^2$	$.168\text{GeV}/c^2$	$L = 1$
$a_1^+(1640)$	$1.640\text{GeV}/c^2$	$.300\text{GeV}/c^2$	$L = 0, 2$
$a_2^+(1660)$	$1.660\text{GeV}/c^2$	$.280\text{GeV}/c^2$	$L = 2$
$\pi_2^+(1670)$	$1.670\text{GeV}/c^2$	$.259\text{GeV}/c^2$	$L = 1, 3$
$a_2^+(1750)$	$1.752\text{GeV}/c^2$	$.150\text{GeV}/c^2$	$L = 2$
$a_4^+(2040)$	$2.014\text{GeV}/c^2$	$.361\text{GeV}/c^2$	$L = 4$
$\pi_2^+(2100)$	$2.090\text{GeV}/c^2$	$.625\text{GeV}/c^2$	$L = 1, 3$
$a_6^+(2450)$	$2.450\text{GeV}/c^2$	$.400\text{GeV}/c^2$	$L = 6$

Table 8.2: A list of known charged  $3\pi$  resonances that could be produced in photoproduction and decay via  $\rho\pi$ . The column  $L_{\rho\pi}$  are the allowed orbital angular momentum between the  $\rho$  and the  $\pi$  when the resonance decays. Because we require non-zero isospin, many states can not be produced.

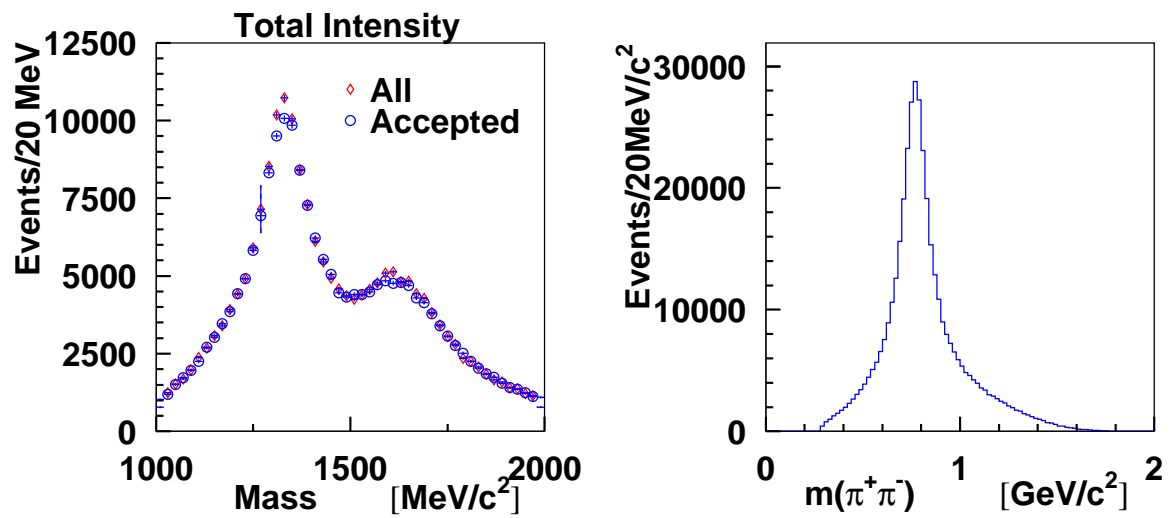


Figure 8.13: (Left) The generated  $3\pi$  mass spectrum using four intermediate resonances,  $X^+$ . The diamonds correspond to all generated events, while the circles correspond to events which have been run through the GLUEX Monte Carlo program. (Right) The  $\pi^+\pi^-$  invariant mass from the  $3\pi$  events. The peak corresponds to the  $\rho^0(770)$ .

## Chapter 9

# Partial Wave Analysis

### 9.1 Introduction

To identify the  $J^{PC}$  quantum numbers of a meson it is necessary to perform a *partial wave analysis* (PWA). In the simplest terms, a partial wave analysis determines production amplitudes by fitting decay angular distributions. The fit includes information on the polarization of the beam and target, the spin and parity of the resonance, the spin and parity of any daughter resonances and any relative orbital angular momenta. The analysis seeks to establish the production strengths, production mechanisms and the relative phase motion of various production amplitudes. Phase motion is critical in determining if resonance production is present.

While the implementation of a partial wave analysis is in principle straightforward, there are both empirical and intrinsic difficulties. Empirically, instrumentation effects, such as detector acceptance and resolution, can conspire to make one distribution look like another. These similar distributions lead to *leakage* in the partial wave analysis. Here, cropping, smearing, or incorrect acceptance corrections of two physically different distributions may lead to distributions which are apparently indistinguishable. These difficulties can be minimized by properly designing the experiment, (see section ??). Full angular coverage in the distributions can be achieved by using a nearly  $4\pi$  detector with excellent resolution. In addition, high statistics are critical to be able to separate these partial waves with accuracy. Thus, thorough partial wave analysis requires nearly  $4\pi$  coverage, excellent resolution, high statistics and a very good understanding of the detector.

The PWA method is subject to intrinsic mathematical ambiguities for certain final states. Two or more different choices of amplitudes lead to identical observables, *e.g.* moments. Here there are at least two approaches. The first assumes some *a priori* physics knowledge that allows one to choose one solution over another, *e.g.* at threshold low angular momentum waves should dominate high angular momentum waves. The second is to examine simultaneously several final states to which the resonance can decay. While the distributions may be confused in one final state, such as  $\eta\pi$ , they are likely to be different in a second such as  $\rho\pi$ . This latter approach assumes that the detector has been optimized for many different final states and that relative normalizations between these are understood.

This latter approach of looking at multiple final states not only allows one to separate different waves, but in itself yields key information about the relative decay rates of mesons. It is this latter information that is critical to understanding the underlying wave functions of the mesons — their content and mixing with other states. This ability to measure accurately

many final states and to perform a simultaneous partial wave analysis is a key feature of the GLUEX spectrometer.

The use of photon polarization will also allow one to simplify the analysis and to access additional information on the production of mesons. This will provide key checks on the stability of the analysis itself. While a circularly polarized beam may yield some information in a few special cases, the true gain comes from linear polarization. Linear polarization defines a *new spatial direction* beyond the photon direction, which is not the case for circular polarization. Linearly polarized light can be expressed as a coherent sum of helicity (circular polarization) states which leads to interference terms not present for unpolarized light. This yields additional angular dependence which simplifies the PWA analysis. Furthermore, linear polarization is necessary to discriminate between different production mechanisms.

Backgrounds are always a problem in a partial wave analysis. These limit one's ability to measure phase motion, and can be particularly severe in a region of dense overlapping resonances. Backgrounds involve a different final state accidentally reconstructing as the channel under study. Either a particle is missed by the detector or, when putting the final state back together, multiple interpretations are possible. This can be minimized with a good  $4\pi$  detector with high efficiency for detecting all final state particles with good resolution. One needs all particles to be reconstructed well enough to allow for a complete kinematic identification of a specific final state.

Finally, while the PWA is in principle straight forward, the machinery itself can become rather cumbersome. There are several different equivalent bases in which the analysis can be done. In addition, small coding errors can lead to errors which may not be easily detected in the results. As such, the GLUEX collaboration is developing independent PWA packages. Currently two such packages have been implemented. These use two different formalisms (one uses the so called reflectivity basis and the other helicity basis), which can be used to cross check results of fits.

## 9.2 Beam and final state normalizations

It will be necessary to show, in the first results from GLUEX, that our experiment produces results that are consistent with previous investigations, albeit with much greater statistical precision. These will include total cross sections (at various photon energies) for various inclusive multi-particle photoproduction reactions [?], invariant mass distributions and differential cross sections for exclusive reactions [?, ?] and density matrix element determinations in processes for which polarized beams have been available [?].

Each of the measurements cited above has been carried out with relatively low flux photon beams (for which the beam normalization is rather straightforward) and using bubble chambers for particle detection (which therefore provide excellent, flat acceptance functions). Moving to high intensity beams and sophisticated electronic detectors, while leading to enormous gains in statistical precision, makes it more difficult to determine normalizations. Since one of our main goals is to determine such things as relative branching ratios and production cross sections of new states, it is important to establish consistent connections with these previous measurements. Furthermore, it is likely that our experiment will run with different triggers for different running periods, and these data sets need to be merged as seamlessly as possible. All of these goals will need accurate controls of beam normalization and detector acceptance, as well as a clear determination of their inherent systematic uncertainty.

Beyond demonstrating that earlier measurements can be reproduced, an accurate normalization plays a critical role in the physics of GLUEX. To measure relative decay rates of mesons it is critical to have accurate normalizations between different final states. This requires the ability to count incident photons and also the ability to understand systematics due to the trigger hardware and software on the event rates.

### 9.3 A partial wave analysis study

To study the design of the GLUEX detector, and to help in understanding the limits of the Partial Wave Analysis, a study was undertaken to perform a PWA on simulated data. The goals of the study are twofold: to both qualitatively and quantitatively understand the role of the photon polarization in the partial wave analysis and, to determine what limits are placed on the PWA due to the finite acceptance and resolution of the detector. The aim is to ultimately perform such a study over many different final states but, to develop the tools to perform this, the initial studies have concentrated on the reaction ?? for  $E_\gamma = 8.5 \text{ GeV}$ .

$$\gamma p \rightarrow \pi^+ \pi^+ \pi^- n \quad (9.1)$$

This is a good candidate reaction for exotic  $\pi_1$  searches. If a  $\pi^+ \pi^-$  pair comes from the decay of a  $\rho^0$  meson then the  $3\pi$  final state has  $G\text{-Parity} = (-1)$  and is an isovector. Thus, a resonant  $\rho^0 \pi^+$   $P$ -wave would correspond to a charged member of the  $J^{PC} = 1^{-+}$  exotic multiplet.

#### 9.3.1 The Role of Linear Polarization

Monte Carlo studies have been made with unpolarized, 100% linearly polarized and fractionally polarized photons. The data can best be examined by looking at the  $3\pi$  system in the Gottfried–Jackson (GJ) frame, (see Figure ??). The GJ frame is the rest frame of the  $3\pi$  system with the  $z$  axis chosen to be along the photon beam direction. The  $y$  axis is defined as the normal to *neutron– $3\pi$*  production plane (which is invariant under boost to the rest frame of the  $3\pi$  system). The photon polarization is fixed in the lab frame. However, in the GJ frame it is at some angle  $\alpha$  with respect to the  $y$  axis (where  $\alpha$  varies on the event–by–event basis). The  $3\pi$  system decays into a  $2\pi$  system, and a spectator  $\pi$ . In the GJ frame, the orientation of this decay is given by  $\theta_{\text{GJ}}$  and  $\phi_{\text{GJ}}$  as shown in Figure ?. In the case of linearly polarized photons, one expects there to be a dependence on both the angle  $\alpha$  and the azimuthal angle  $\phi$ . This would not be true for unpolarized photons.

The  $3\pi$  data have been generated using a phase–space Monte Carlo, and the events have been weighted using a one–pion exchange (OPE) production mechanism that includes  $3\pi$  resonances decaying via  $\rho\pi$  [?]. All known  $\rho\pi$  resonances in the with mass less than  $2\text{GeV}/c^2$  that can be produced in OPE have been included. (These are listed in Table ??). At low momentum transfer, OPE is expected to be the dominant production mechanism [?, ?].

The effect of polarization can be directly seen in Figure ?. In the absence of polarization, there is nothing to define a  $\phi$  direction in the GJ frame. As such, a plot of  $\phi$  versus  $\alpha$  is flat, (in the unpolarized case,  $\alpha$  is taken as the angle between the  $y$  axis in the GJ frame and the  $y$  axis in the Lab frame). However, if photon polarization is non-zero, there is clear structure in the  $\phi$  versus  $\alpha$  plots. Near  $\alpha = 0^\circ$ , the  $\phi$  distribution is  $\sin^2 \phi$ , whereas near  $\alpha = 90^\circ$ , the distribution is  $\cos^2 \phi$ , consistent with the expected  $(1 - \cos [2(\alpha - \phi)])$  dependence.

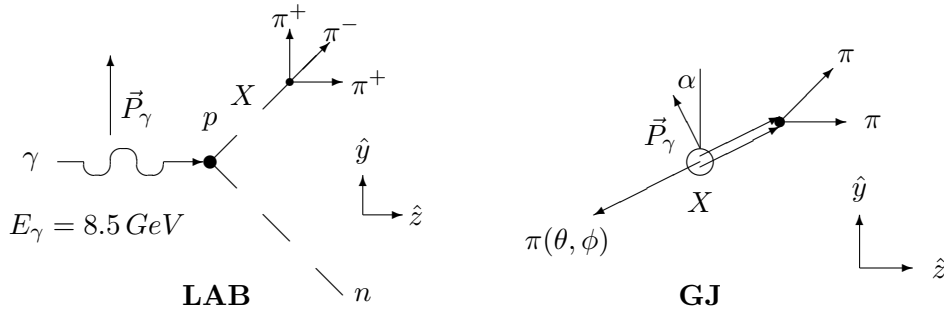


Figure 9.1: The reaction  $\gamma p \rightarrow \pi^+ \pi^+ \pi^- n$  as seen in the lab frame and in the Gottfried–Jackson, (GJ), frames. The  $y$  direction in the GJ frame is defined as the normal to the reaction plane. The angle  $\alpha$  locates the photon polarization direction with respect to the  $y$  axis in the GJ frame.

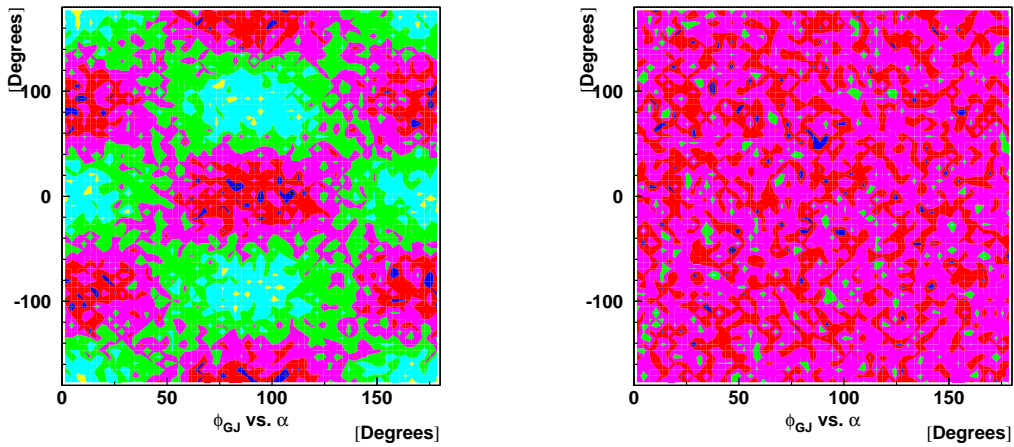


Figure 9.2: Plots of  $\phi_{GJ}$  versus  $\alpha$  in the Gottfried–Jackson frame for a band of  $3\pi$  masses near the peak of the  $a_2(1320)$ . The left hand figure is for 100% polarized photons, while the right hand figure is for unpolarized photons.

Because the only production mechanism used is OPE, all particles are produced, it is also possible to get additional information about the naturality of the produced resonances. Pion exchange corresponds to unnatural parity exchange, so depending on the naturality of the produced  $3\pi$  system, the  $\sin^2 \phi$  and  $\cos^2 \phi$  will flip (the dependence on  $\phi$  changes to that of  $90^\circ - \phi$ ). For natural parity,  $(0^+, 1^-, 2^+, \dots)$ , it will be like the  $a_2$ , while for unnatural,  $(0^-, 1^+, 2^-, \dots)$ , it will be opposite to that. This behavior can be seen in Figure ?? which shows  $\phi$  versus the  $3\pi$  mass for  $\alpha$  near  $90^\circ$ , (left) and  $\alpha$  near  $0^\circ$  (right). These figures show a clear band at the  $a_2$  mass, which is  $\cos^2 \phi$  in the left, and  $\sin^2 \phi$  on the right. There is also a second band visible near a mass of  $1.7 \text{ GeV}/c^2$ , which if one looks carefully, has the opposite angular distributions as the  $a_2$ . Since in this test, the exchange mechanism is known, the opposite structure means that the naturality of the particle at  $1.7 \text{ GeV}/c^2$  is opposite that of the  $a_2$ . In the real experiment the exchange mechanism will not be known. However, the PWA can

		Resonance				$J^{PC}$	$L$	Wave
		Mass [GeV]	Width ( $\Gamma$ [GeV])	$\Gamma_{3\pi}/\Gamma$	$\sigma_\gamma$ [nb]			
1	$a_1$	1260	400	99%	30	$1^{++}$	0	S
2				1%			2	D
3	$a_2$	1320	110	70%	500	$2^{++}$	2	D
4	$\pi_2$	1670	110	30%	20	$2^{-+}$	1	P
5				1%			3	F
6	$\pi_1$	1600	170	50%	20	$1^{-+}$	1	P

Table 9.1: The resonance contributions to the weighting function. The column labeled  $L$  corresponds to the relative angular momentum between the  $\rho$  and the  $\pi$  in the decay of the  $3\pi$  resonance.

determine the naturality of the produced particle, and this can then be used to determine the naturality of the exchange.

There is still additional information in these plots. For masses below that of the  $a_2$ , there is a diffuse band that has the opposite angular distribution as the  $a_2$ . This corresponds to the  $a_1(1260)$  in the data. Finally, for masses just below the  $\pi_2$ , there is an even more diffuse structure whose angular distribution is opposite that of the  $\pi_2$ . This most likely corresponds to the  $\pi_1$ . The fact that the photon beam is linearly polarized allows us to read significant information about the resonances and their production directly from such a plot.

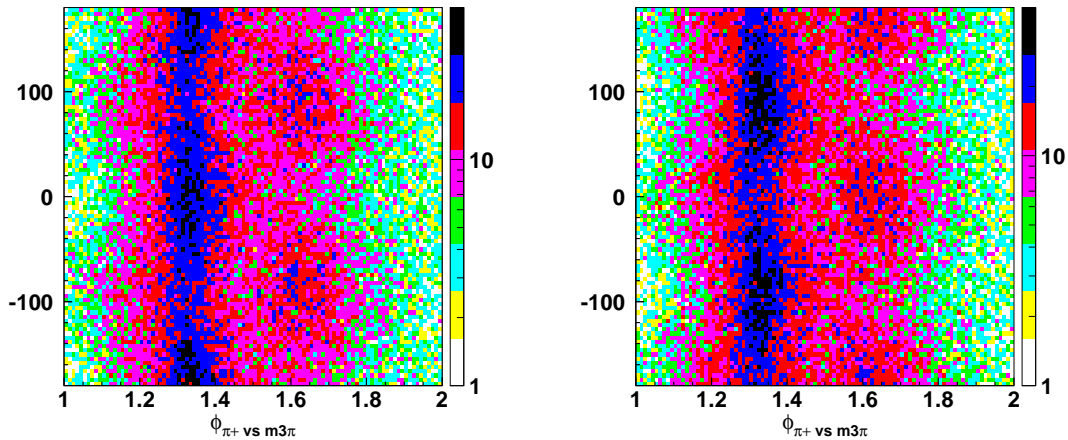


Figure 9.3: Plots of  $\phi_{GJ}$  versus  $3\pi$ -mass for 100% polarized photons. The figure on the left is for  $\alpha$  near  $90^\circ$ , while that on the right is for  $\alpha$  near  $0^\circ$ .

### 9.3.2 The PWA Formalism and Results

There are several equivalent formalisms in which the PWA can be performed. All of these initially look at the decay of the meson state in the GJ frame, and require that the polarization

be expressed in that frame. The spin density matrix of a linearly polarized photon in the helicity basis can be written in terms of the angle  $\alpha$  in the GJ frame as in equation ??.

$$\rho_{\lambda_\gamma \lambda'_\gamma} = \begin{pmatrix} \frac{1}{2}(1 + P \sin 2\alpha) & \frac{P}{2} \cos 2\alpha \\ \frac{P}{2} \cos 2\alpha & \frac{1}{2}(1 - P \sin 2\alpha) \end{pmatrix} \quad (9.2)$$

$$\rho_{\epsilon_\gamma \epsilon'_\gamma} = \begin{pmatrix} (\frac{1}{2} - \rho_{1-1}) & (\frac{1}{2} - \rho_{-1-1}) \\ (\frac{1}{2} - \rho_{-1-1}) & (\frac{1}{2} + \rho_{1-1}) \end{pmatrix} \quad (9.3)$$

One particular choice for the analysis is the reflectivity basis. The eigenstates of reflectivity are eigenstates of reflection in the production plane. The density matrix of a linearly polarized photon in the reflectivity basis expressed in terms of the helicity basis elements is given in equation ?. In the reflectivity basis, photons polarized along either the  $x$  axis or the  $y$  axis in the GJ frame are eigenstates of reflectivity. However, photons that are polarized in some other direction are coherent mixtures of the two eigenstates. The eigenvalues of reflectivity depend on the naturality of particles involved in the reaction. For a given produced resonance, linear polarization enables one to distinguish between naturalities of the exchanged particles. This is the main handle on the production mechanism. Second, if the production mechanism is known (*e.g.* from momentum transfer or energy dependence), linear polarization enables one to filter resonances of different naturalities, as shown in the study of  $\phi$  dependence discussed above. In the case of a known production mechanism, the same quality PWA can be done with about 50% as much polarized data as with unpolarized data.

To date, independent fits have been carried out using two different codes. Ones using the reflectivity representation, and the other using a moments fit. Both return the same results, and have provided a very good cross check of our understanding of the procedure. In fact, the development of two parallel versions of the PWA code, and cross checking results against each other will be an important handle on systematic errors in the GLUEX experiment. The results in Figure ?? are from the latter fit using the same formalism as in the weighting function. (These fits do not use input modified by the acceptance or resolution). What is of particular interest is the sensitivity limit in these data. The two extremely weak waves (at well less than 1% of the total intensity) are just at the limit of being resolved in this data set. This is seen in the  $a_1$ D wave in Figure ?. The data set used in these fits represents about 1% of the reconstructed statistics from one year of running at  $10^7 \gamma/s$ . The statistics of the experiment will clearly be large enough to resolve such small signals. They will also be large enough to provide statistically meaningful sample on much rarer final states. (The  $3\pi$  mode chosen for this study is one of the largest contributors to the total  $\gamma p$  total cross section.)

Figure ?? below shows the results of a double-blind Monte Carlo exercise that was performed to assess the ability to extract a small exotic signal from mix of various non-exotic waves. Specifically events corresponding to  $\gamma p \rightarrow \pi^+ \pi^+ \pi^- n$  were generated assuming a mix of seven waves including the  $a_1$ ,  $a_2$ ,  $\pi_2$  and the  $J^{PC} = 1^{-+} \pi_1$ . The latter was about 2.5 % of the total sample. The generated four-vectors were smeared and the sample was then put through the acceptance requirements. The acceptance assumptions were included in the PWA fitter. The statistics shown correspond to several days of running.

The second fitting procedure is done in the reflectivity basis. In the reflectivity basis, the total amplitude for some final state can be written as in equation ?. The subscript  $\beta$  refers to a given partial wave, ( $J^{PC} M^\epsilon$ ). The indices  $\epsilon_x$  and  $\epsilon_\gamma$  refer to the reflectivities of the state  $X$

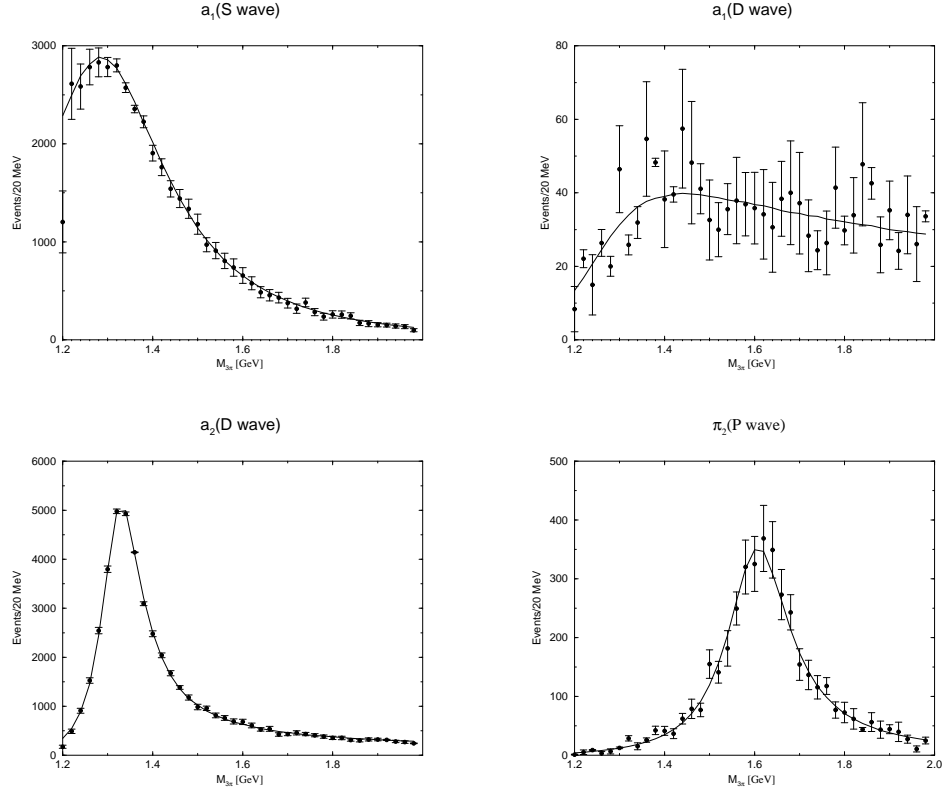


Figure 9.4: Fits to a  $4\pi$  acceptance data set showing the four of the six partial waves from table ???. The error bars arise purely from the statistics of the data set which is about 1% of one year's running.

and the  $\gamma$  respectively. The indices  $\lambda$  and  $\lambda'$  refer to the initial and final state nucleon spin-states. Parity reduces the total number of helicity amplitudes by a factor of two and connects the reflectivity of the beam and exchange particles to the reflectivity of the produced state ( $\epsilon_\gamma * \epsilon_e = \epsilon_X$ ).

Additionally, in the case of OPE only the nucleon helicity-flip amplitude contributes and the  $\lambda$  and  $\lambda'$  indices are suppressed as in ???.

$$R_{\beta}^{\epsilon_x, \epsilon_\gamma} = V_{\beta, \lambda, \lambda'}^{\epsilon_x, \epsilon_\gamma} \times A_{\beta}^{\epsilon_x, \epsilon_\gamma} \quad (9.4)$$

The set of complex parameters,  $V$ 's, are known as the production strengths. These are usually determined by fitting to the data. The  $A$ 's are decay angular distributions which are functions of the angles in the various frames as well as resonance parameters of any daughter resonances into which the state  $X$  decays. The amplitude,  $A$ , for the decay of a particle with spin  $J$  and  $|J_z| = M$  into two particles with helicities  $\lambda_1$  and  $\lambda_2$  ( $\lambda = \lambda_1 - \lambda_2$ ) in the resonance rest frame is given by [?]:

$$A = \langle \vec{p}\lambda_1; -\vec{p}\lambda_2 | \mathcal{M} | JM \rangle = F_{\lambda_1 \lambda_2}^J \mathcal{D}_{M \lambda}^{*J}(\phi, \theta, 0) \quad (9.5)$$

Calculation of the decay amplitudes for a resonance is done recursively within the isobar model, regarding the  $n$ -body final state as a result of a series of sequential, generally 2-body, decays

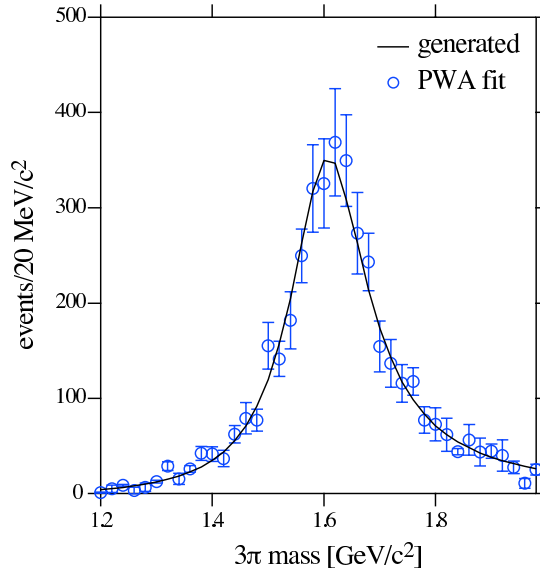


Figure 9.5: The results of a double-blind Monte Carlo exercise showing the  $J^{PC} = 1^{-+}$  exotic wave after fitting (open circles) and the exotic wave input (curve) into the mix of  $\gamma p \rightarrow \pi^+\pi^+\pi^-n$  events that were generated in this study. Details are given in the text.

through intermediate isobar states. The total decay amplitude is the amplitude for the resonance to decay into its intermediate daughters times the amplitude for each of its daughters to decay.

This total amplitude,  $R$  can then be used to predict the intensity distributions of the final state particles. For a particular point in phase space,  $\tau$ , the intensity is given as in equation ?? . Finally, for amplitudes that do not interfere, (denoted by  $\alpha$ ) *e.g.* from production via different initial and final spin configurations, a sum over these

$$I(\tau) = \sum_{\alpha} \text{Trace} \left[ \sum_{\epsilon_{\gamma}, \epsilon_{\gamma'}} \left[ \left( \sum_{\beta'} R_{\beta'}^{\epsilon_{\gamma'}, \epsilon_{\gamma'}} \right)^{\dagger} \rho_{\epsilon_{\gamma}, \epsilon_{\gamma'}} \left( \sum_{\beta} R_{\beta}^{\epsilon_{\gamma}, \epsilon_{\gamma}} \right) \right] \right] \quad (9.6)$$

gives the intensity.

The data are binned in mass of  $X$  and the momentum transfer  $t$  and a fit is performed for the full set of  $V$ 's in each bin. The results for such a fit for 100% linearly polarized photons are shown in Figure ?? . In this fit, a comparison is made between the generated data and the Monte Carlo corrected data. In the  $3\pi$  channel, the acceptance corrections are fairly small. The data shown are only for the positive reflectivity solutions, but a more or less identical set for the negative reflectivity are also produced. While visible, the acceptance effects are small, and do not hinder the extraction of the partial waves. It is also possible to extract the two rather small waves that are in the generated data set. These correspond to a second decay for each of  $1^{++}$  and  $2^{-+}$  waves. The main decays proceed with orbital angular momentum between the  $\rho$  and the  $\pi$ ,  $L_{\rho\pi}$  of 0, (S-wave), and 1, (P-wave) respectively. In addition, decays could occur via  $L = 2$ , (D-wave) and  $L = 3$ , (F-wave), respectively. The relative rates between the two decays of a given resonance is an important quantity which can be compared to several models. Its extraction will be an important GLUEX measurement. Figures ?? and ?? show the fits to these

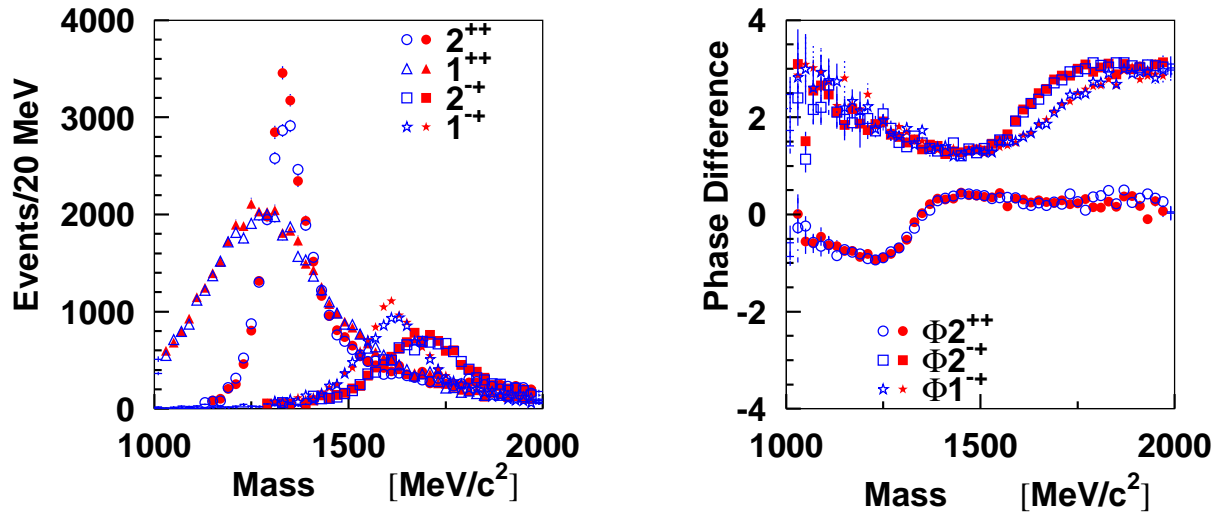


Figure 9.6: Fits to the weighted data using wave 1,3,4 and 6 from table ???. These fits compare generated data (solid shapes) to data that has been run through the GLUOX Monte Carlo, (open figures). The left figure compares the fits to the intensities of four waves, while the right figure shows the phase differences between the listed waves and the  $1^{++}$  wave.

two waves. In each case, the left plot is the intensity of the positive reflectivity wave, while the right hand figure is the phase difference between the two decays of a given resonance. In the absence of final state interactions, the phase difference should be either  $0^\circ$  or  $180^\circ$ , which both fits show in the region where the intensity is non-zero.

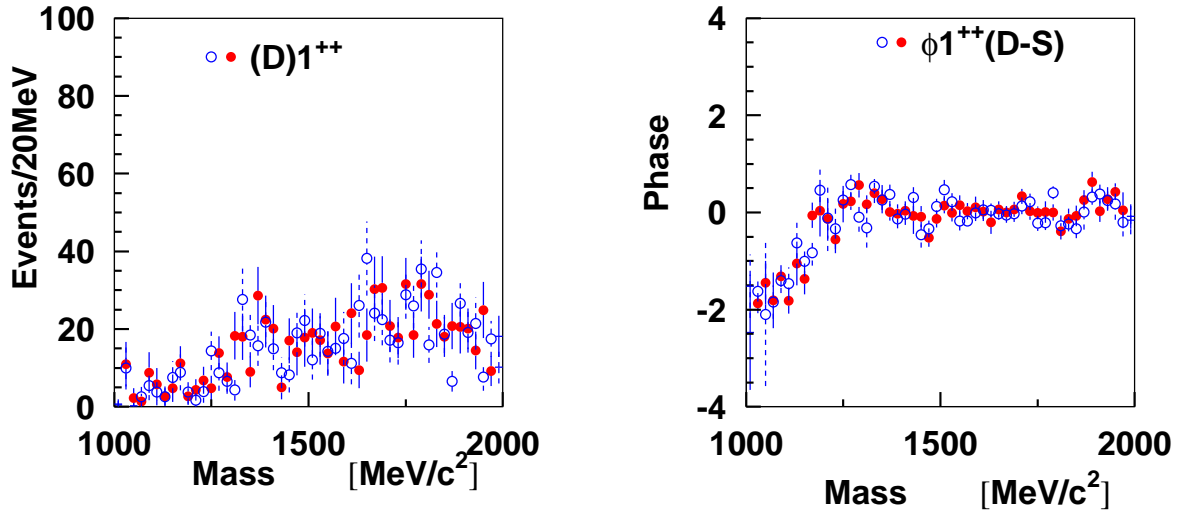


Figure 9.7: Fits to the D–wave decay of the  $1^{++}$  wave from table ???. The figure on the left shows the intensity for the positive reflectivity wave. The right hand figure shows the phase difference between the S and D–wave decays. The open markers correspond to data that has been run through the GLUEX Monte Carlo, while the solid markers are the generated events.

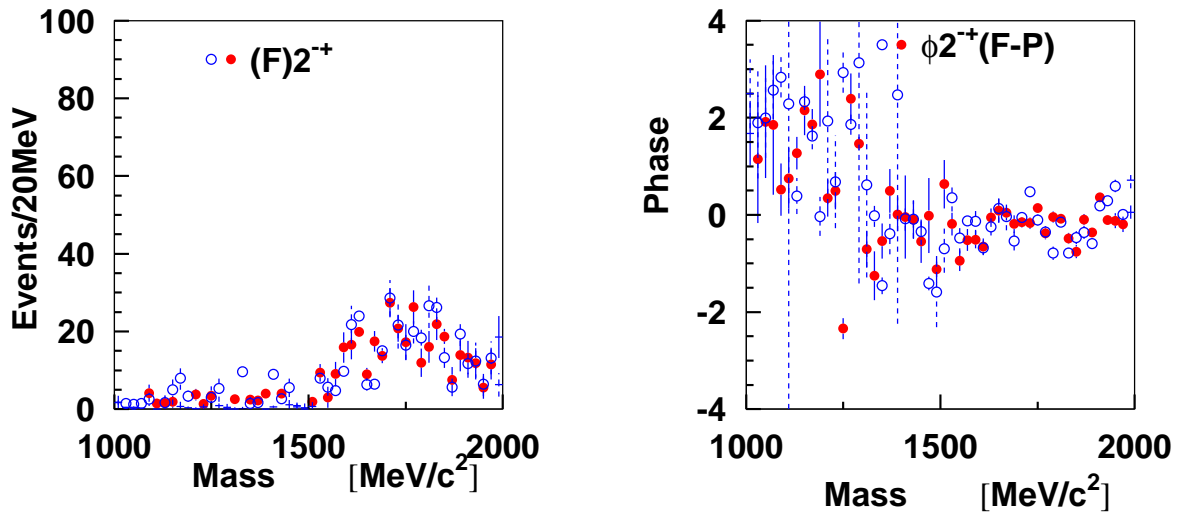


Figure 9.8: Fits to the F–wave decay of the  $2^{-+}$  wave from table ???. The figure on the left shows the intensity for the positive reflectivity. The right hand figure shows the phase difference between the P and F–wave decays. The open markers correspond to data that has been run through the GLUEX Monte Carlo, while the solid markers are the generated events.

In addition to the small waves, another common problem in PWA is leakage from one wave into another wave. A small distortion in the acceptance that is not fully understood can cause one wave to look like a different wave. This has been examined by adding six additional waves which were not in the generated data set, and repeating the fits with these waves in them. These waves correspond to  $J^{PC}(M^\epsilon)$  of  $3^{++}(1^+)$ ,  $3^{++}(1^-)$ ,  $2^{++}(2^+)$ ,  $2^{++}(2^-)$ ,  $2^{-+}(2^+)$  and  $2^{-+}(2^-)$ . Figure ?? shows the results for two of these. The main point is that there is virtually no intensity in any of these waves, and certainly no structure leaking in from one of the strong waves in the events. At least in this study, the leakage appears to be an insignificant issue.

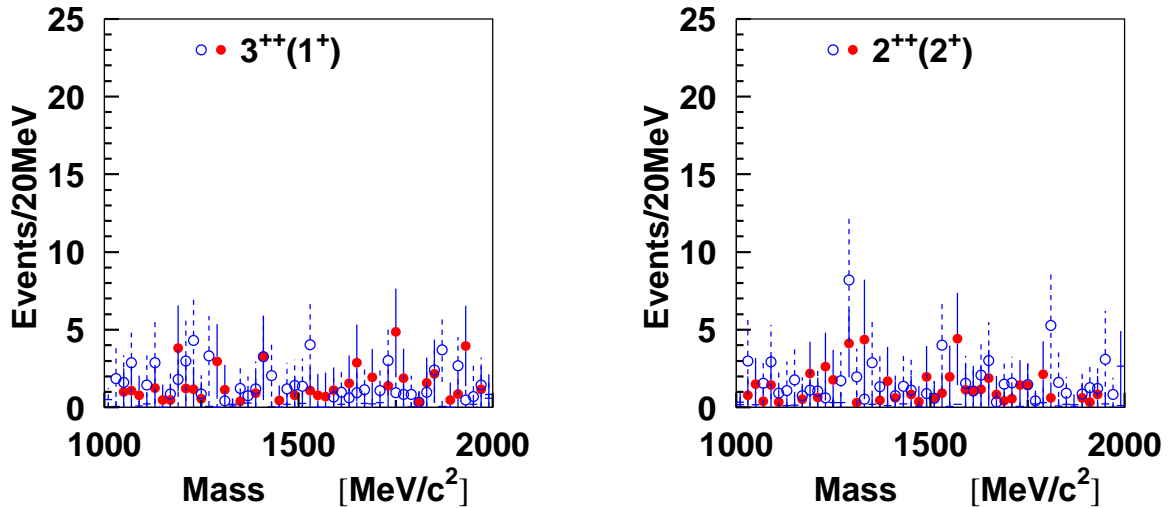


Figure 9.9: Fits to two partial waves which are not in the generated set. The figure on the left is a  $J^{PC}(M^\epsilon) = 3^{++}(1^+)$  wave, while that on the right is a  $J^{PC}(M^\epsilon) = 2^{++}(2^+)$  wave. There is virtually no leakage into these waves from resolution effects in the detector simulation. The open markers correspond to data that has been run through the GLUEX Monte Carlo, while the solid markers are the generated events.

A comparison can also be made between an unpolarized data set and a 100% polarized data set. Because the positive and negative reflectivity distributions do differ in their  $\cos\theta_{G,J}$  distributions, it is possible to separate them with unpolarized data. The separation is just not as clean as it is for polarized data and in the absence of information on the production mechanism, this separation becomes more difficult, especially if multiple production mechanisms are present. The best way to view these results is to look at the errors in the wave intensities for both the polarized and the unpolarized data sets. These are shown in Figure ?. If one averages over all of the partial waves, the unpolarized errors are about  $\sqrt{2}$  times larger than those for the polarized data set with the same number of events. Roughly speaking, in this test, the polarization reduces by a factor of 2 the statistics needed to achieve a given level of sensitivity. It should be pointed out that this is not the entire story as discussed below.

Finally we have examined the case of simultaneous production via unnatural ( $\pi$ ) and natural (*e.g.*  $\rho$ ) exchange. The point is to illustrate the need for linear polarization. As discussed earlier at the nucleon vertex OPE flips helicity and is proportional to  $\delta_{\lambda',-\lambda}$ . At the

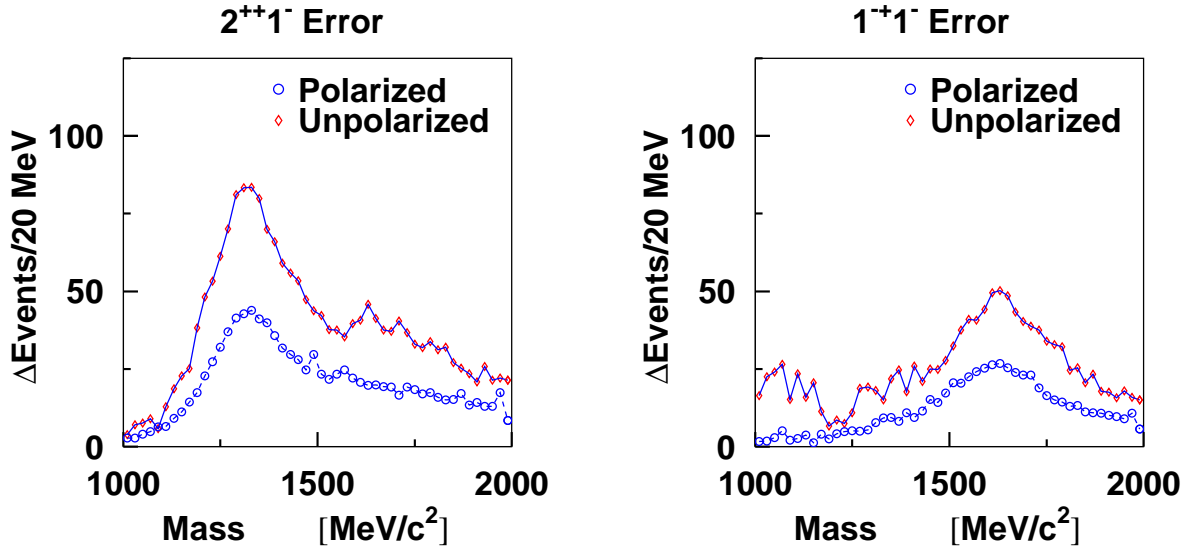


Figure 9.10: The errors in the fit results for two of the partial waves from the fit. The polarized and unpolarized data sets are the same size, and both sets are for generated data, (no acceptance corrections). The errors for the unpolarized data are on average about a factor of the  $\sqrt{2}$  larger than those for the 100% polarized case.

meson production vertex the helicity structure is given by  $\delta_{\lambda\gamma,\lambda_X}$  for unnatural, and by  $\tau_{\lambda\gamma,\lambda_X}^3$  for natural resonances respectively. For the spin-1  $\rho$  exchange, the number of different helicity couplings is quite large, however, if the nucleon helicity is flipped then coupling is proportional to  $\tau_{\lambda\gamma,-\lambda}^3$  and if the helicity in the photon-resonance vertex is conserved, natural exchange leads to the  $\delta_{\lambda\gamma,\lambda_X}$  and  $\tau_{\lambda\gamma,\lambda_X}^3$  dependencies for the natural and unnatural exchanges respectively, *i.e.* opposite to the case of unnatural exchange.

In an additional study a  $\rho$  exchange intensity that is about 50% of the  $\pi$  exchange has been added to all six partial waves given in Table ?? using Monte Carlo generated with 100%, 50%, 25% and 0% linear polarization. These two exchanges are incoherent, so the fit to the intensity is actually a fit to the sum of the two exchange mechanisms. As seen in Figure ??, this sum is well fit independent of the degree of linear polarization. One way in which the two can be separated is to fit the difference of the two exchanges (dashed curves in Figure ??). Here it is seen that the degree of linear polarization place a crucial role in a fit to this difference. With 100% polarization the difference is well fit, while for 0% polarization the difference is ambiguous. Any two values with the correct sum will work. Similar to this would be to examine the  $\phi_{GJ}$  and  $\alpha$  dependence of a given partial wave as in Figure ??.

To study on the effect of linear polarization in determining the production mechanism, data have been selected near  $\alpha = 0^\circ$  and near  $\alpha = 90^\circ$  in the Gottfried-Jackson frame of the resonance. These two states correspond to eigenstates of reflectivity. In the case of single pion exchange, (the naturality of the  $\pi$  is negative), the produced reflectivity state of the resonance is opposite to that of the photon. In the case of natural parity exchange, (such as  $\rho$  exchange), the two reflectivities will be the same. Partial wave analysis has been performed independently on the two data sets. Figure ?? shows the results for the  $1^{-+}$  wave. The figure on the left shows

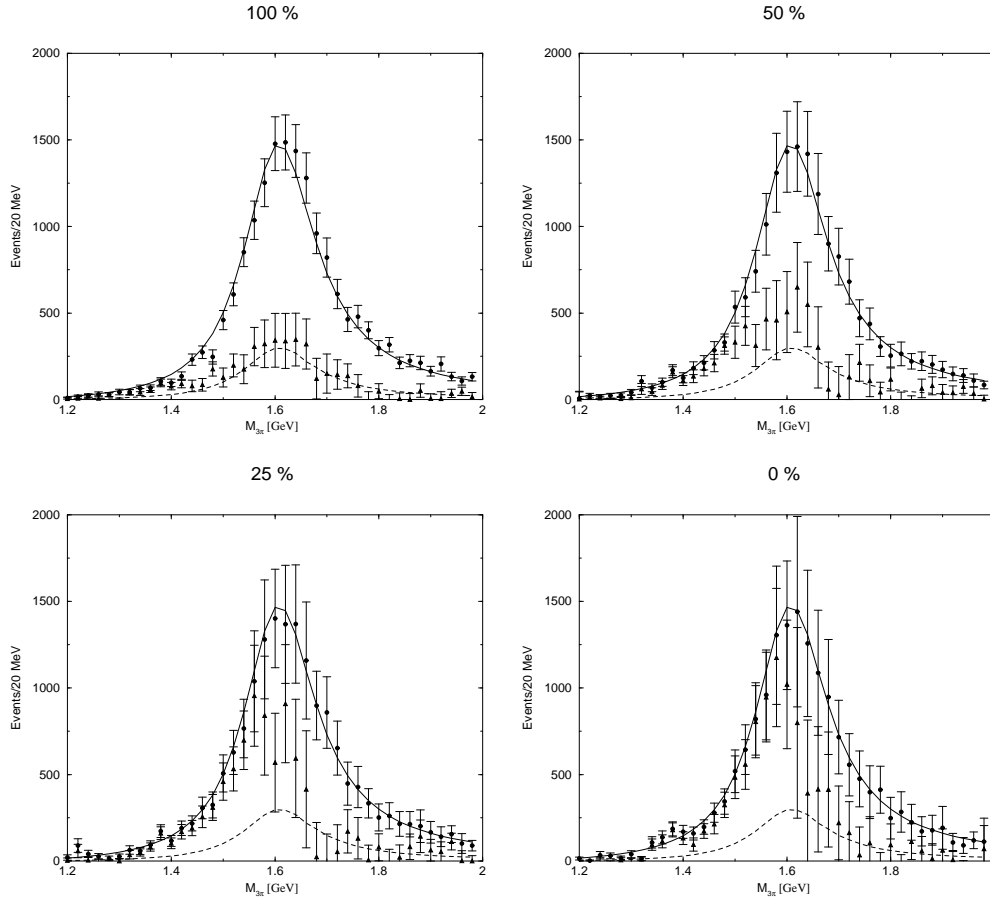


Figure 9.11: Fits to  $\pi_1(1600)$ ,  $4\pi$  acceptance data sets generated with a combination of  $\pi$  and  $\rho$  exchange mechanisms. The solid line is the sum of the two, while the dashed line is the difference. The four plots correspond to 100%, 50%, 25% and 0% photon linear polarization. The sum of the two is well fit for all values of polarization, while the difference becomes unclear as the polarization is decreased.

the positive reflectivity  $1^{-+}$  wave,  $M^e = 1^+$ . Only the events near  $\alpha = 0^\circ$  contribute, while the  $\alpha = 90^\circ$  gives nearly no contribution. The exact opposite happens in the  $M^e = 1^-$  wave on the right. Had the production mechanism been of opposite naturality to the pion, these figures would have been reversed. If both mechanisms had been present, then the exact mixture could have been read directly off these plots as long as the degree of linear polarization is known. In the case of unpolarized photons, no such separation is possible. Of course the real data will involve a more general fit to this, but with linear polarization, the naturality of the exchange particle is trivially known, while for no linear polarization, there is no handle on this.

### 9.3.3 Joint production of excited baryons and mesons

In the kinematic region of GLUEX it is probable that baryon resonances will be produced in addition to the meson states we have been discussing. Processes such as the two shown in Figure ?? will interfere with each other and they must be taken into account in the analysis. In general

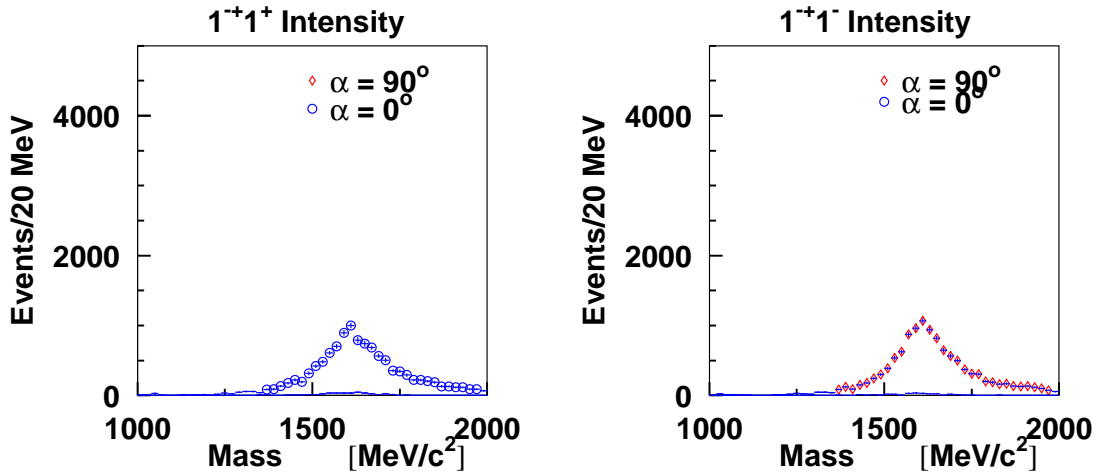


Figure 9.12: (Left) shows the fit to the positive reflectivity part of the  $1^{-+}$  intensity for events near  $\alpha = 0^\circ$  and  $90^\circ$  degrees. (Right) shows the same for the negative reflectivity waves. The key point is that for  $\pi$  exchange, (negative naturality), only the positive reflectivity wave is produced near  $\alpha = 0^\circ$  while only the negative reflectivity is produced near  $\alpha = 90^\circ$ . If the exchange mechanism had opposite naturality, then exactly the opposite would have occurred. These fits can lead to an exact decomposition of the exchange mechanism as long as one knows the degree of linear polarization.

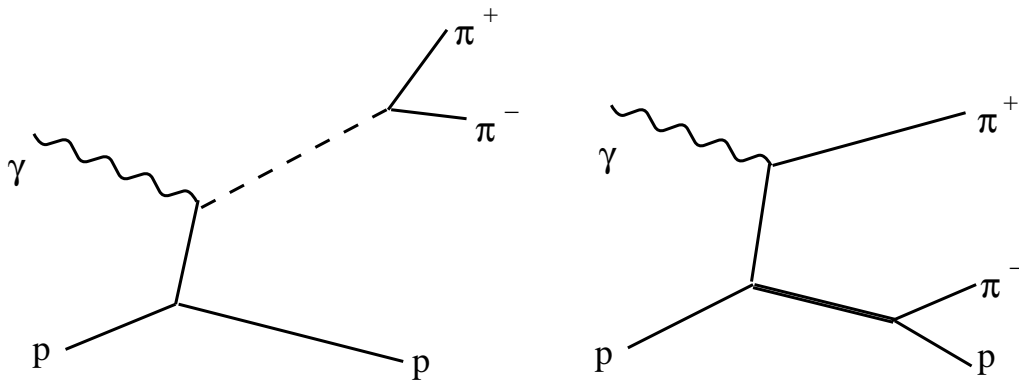


Figure 9.13: Example of interfering baryon and meson processes.

this could lead to ambiguities, since the baryon states can be described as an infinite sum over meson states. In practice, however, the sum over meson states is truncated to a finite number of resonances, and will not well describe the distribution due to the baryon resonance. Hence, in order to get a good description of the intensity distribution, the baryon resonances must be included explicitly. Effects of ambiguities are mitigated at the cost of requiring a physically motivated *ansatz* of states *i.e.*, truncating the set of waves to the minimal set required by the fit. The impact of any ambiguities created will vary with the reaction being studied, but can be well determined using Monte-Carlo methods.

## 9.4 Leakage studies

Of crucial importance in Partial Wave Analysis is the leakage or feed through from one partial wave to another. This leakage is usually caused by an imperfect understanding of the detector acceptance, and being able to minimize this is crucial in carrying out an excellent PWA. In order to study this in the GLUEX detector, a detailed study has been carried out using Monte Carlo simulations and the PWA code [?]. In this study, two  $3\pi$  physics data sets were generated according to the reactions:

$$\gamma p \rightarrow \pi^+ \pi^+ \pi^- n$$

and the isospin related reaction

$$\gamma p \rightarrow \pi^+ \pi^0 \pi^0 n$$

. Included in the physics were the production of  $a_1(1260)$ ,  $a_2(1320)$  and  $\pi_2(1670)$ , but no exotic wave from the  $\pi_1(1600)$ . These events were then tracked through the GLUEX Monte Carlo program, and the output was then fed into a partial wave analysis. Additional sets of phase-space generated events were then produced for the normalization integrals in the PWA. These were tracked through a version of the GLUEX Monte Carlo in which the geometry description of the detector had been changed with respect to the physics samples. Examples of the types of changes made were distortions in the magnetic field, changing the location of the forward tracking chambers, changing the resolution of the tracking detectors, changing the low energy photon cut-off in both the forward and the barrel calorimeters, and changing the resolution of the two calorimeters. The most striking result was that it was extremely difficult to produce leakage in the exotic  $\pi_1$  channel with any of these changes. Figure ?? shows typical examples of the leakage from the study. While it is possible to induce 10% size leakages from the S-wave decay into the D-wave decay of some resonances, this is not the norm. In order to do this, resolutions need to be off by a factor of 2, or magnetic fields need 20% distortions.

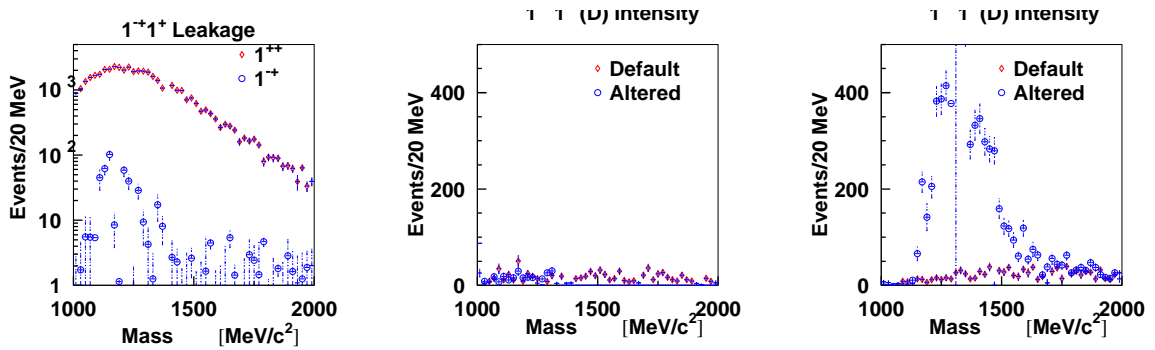


Figure 9.14: **Left:** Typical leakage induced in the exotic  $\pi_1$  channel from the most extreme changes in the detector. It is difficult to get leakage larger than a few percent. **Center:** shows the typical leakage from the  $a_1$  S-wave into the  $a_1$  D-wave. **Right:** shows the most extreme leakage from the  $a_1$  S-wave into the  $a_1$  D-wave.

The most important conclusions of the study is that it is difficult to produce feed through into the exotic channel from other meson channels. For almost all changes made here, the amount of feed through was less than 1% of a strong channel, with the feed through for the nominal design values being something like 0.1%. However, it is possible to get significant

leakage from the  $a_1$  S-wave decay into the  $a_1$  D-wave decay, with even small changes in the nominal detector design. This sort of feed through is fairly straight forward to understand. An S-wave decay is nominally flat, however, if we have losses near  $\cos\theta = \pm 1$ , the easiest description of this is with a D-wave component. In order to produce a P-wave component, it is necessary to produce a forward-backward asymmetry in the Jackson frame – something that appears fairly difficult to do with the GLUEX detector.

## 9.5 Summary

The GLUEX collaboration is currently performing partial wave analysis on data that have been run through the GLUEX detector simulation package. The initial studies have concentrated on the reaction  $\gamma p \rightarrow \pi^+ \pi^+ \pi^- n$ . The collaboration has two different software packages under development. These use different formalisms and fitting procedures to perform the PWA. The comparison of the results from the two efforts will allow us to better understand the systematic problems associated with the procedures.

Fits have been performed with varying degrees of linear polarization to understand the balance between polarization and raw statistics when the production mechanism is known and to demonstrate the need for linear polarization in disentangling the natural and unnatural exchange mechanisms in resonance production. These initial studies give us confidence that we are designing the appropriate detector with the capabilities needed to find and understand exotic mesons.

In order to continue to develop the partial wave analysis, both in terms of formalism, and its connection to phenomenology and to lattice QCD, some members of the GLUEX collaboration organized the first of what is hoped to be several workshops focused on this topic. This first workshop was held in June of 2002 at Carnegie Mellon University and was attended by approximately 35 experts in the field. The proceedings will be published in early 2003 [?]. The second workshop is expected to take place at Jefferson lab in the late spring of 2003.

# Appendix A

## Civil Construction

The GLUEX experiment will reside in a new experimental hall (HALL D) located at the end of a new beamline off the stub at the east end of the North Linac. Figure ?? gives a schematic view of the accelerator site and the proposed location for HALL D. The elevation of the beamline is 1.24 *m* below the nominal grade level. This height balances considerations of the beamline optics, radiation shielding issues, and civil construction cost. The figure in the foldout shows the plan and elevation views for the HALL D beamline and associated buildings.

Civil construction includes breaking through the accelerator stub, tunnel construction, beam transport system and instrumentation. The above ground facilities include the tagger building, HALL D, service buildings, beam dumps, control room, roads, and parking area. Basic infrastructure for all utilities is provided for all buildings.

We have had numerous meetings with JLab civil construction, accelerator, and RadCon staff, and conclude that there are no serious civil construction issues. The main problem is to minimize cost while satisfying GLUEX requirements. In particular, the beamline and buildings will fit on DOE/SURA land, building construction should be straightforward, and RadCon problems can be handled by standard techniques. A formal agreement to use a portion of land owned by SURA for the GLUEX project is under consideration.

### A.1 General requirements

Requirements and specifications assuming a maximum electron beam energy of 12 *GeV* are given in Table ?? and below:

- Single electron energy available for the D line
- HALL D is designed for a photon beam only (i.e. no primary electrons into HALL D)
- Civil construction compatible with 24 *GeV* beam (e.g. 80 *m* bend radius)
- Accelerator tangency point to radiator = 87 *m*
- Radiator to collimator distance = 75 *m*
- Tagger building = 7 *m* x 15 *m* x 3.5 *m* (height). Nominal beam height above tagger floor = 1.5 *m*. The beam is nominally 4.5 *m* from the south wall and 2.5 *m* from the north tagger wall.

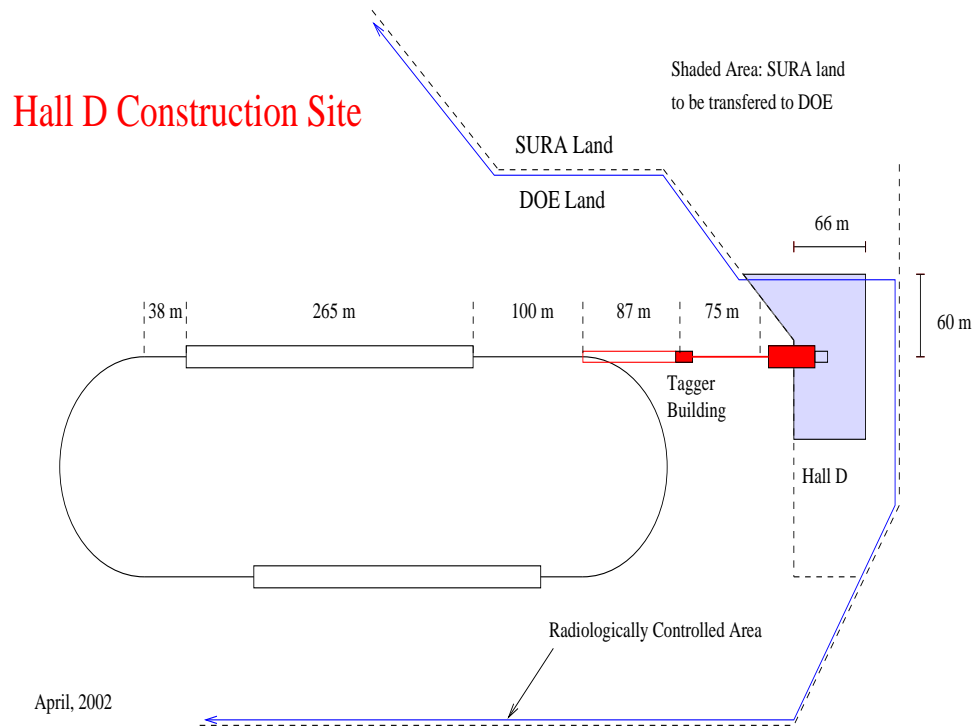


Figure A.1: An overall view of the accelerator site and HALL D.

- Housing for sideways electron beam dump =  $3\text{ m} \times 5\text{ m} \times 3\text{ m}$  (height)
- Detector building =  $17\text{ m} \times 30\text{ m} \times 9\text{ m}$  (clear hook height). The nominal beam height above the HALL D floor =  $3.5 \pm 0.3\text{ m}$ ,  $10\text{ m}$  from the south wall, and  $7\text{ m}$  from the north wall in HALL D.
- The collimator alcove is  $4.5\text{ m} \times 12\text{ m} \times 3\text{ m}$  (height). The beam is nominally  $1.5\text{ m}$  above the floor and  $2\text{ m}$  from the north wall.
- Permissible building settlements:  $1\text{ inch}$  initial;  $2\text{ inches}$  max over lifetime

### A.1.1 Compatibility with future upgrades

The allocation of space for the beamline instrumentation and layout of the site is designed such that an accelerator upgrade to 24 GeV would be possible using proposed buildings and tunnels. We assume that during 12 GeV operation HALL D would only receive 5.5-pass beam. For 24 GeV operation HALL D would receive 4.5, 3.5 or 2.5-pass beam; the number of passes will be switched at most annually. This implies that conditioning for the HALL D beam cannot start before the tangency point and no recombiner area is required. For 24 GeV operation, an east two-way RF separator would be used to extract the beam; the configuration could be changed during long shutdowns by relocating extraction and transport elements.

Parameter	Operating Value	Design Goal
Max Electron Current	3 $\mu\text{A}$	5 $\mu\text{A}$
Min Electron Current	$\sim 0.0001 \mu\text{A}$	0.0001 $\mu\text{A}$
Electron Energy	12 $\text{GeV}$	12 $\text{GeV}$
Power	36 KW	60 KW
Photon Power (Collimator)	7 W	10 W
Photon Power (Detector)	1 W	1.5 W

Table A.1: Beam parameters for a 12  $\text{GeV}$  electron beam.

## A.2 Personnel protection

The Jlab Beam Containment Policy requires that personnel be protected from accidental beam loss by at least three independent devices built using at least two different technologies.

### A.2.1 Failure scenarios

The following failure scenarios were identified:

- Failure of vertical beam transport, shooting electron beam into the sky.
- Poor tuning or steering of electron beam.
- Excessive current in electron beamline.
- Tagger magnet failure, directing electrons down the photon line.
- Excessive photon flux (resulting from obstructions in the electron beamline, poor vacuum, etc).

### A.2.2 Beam containment proposal

In the following we list the active and passive safety devices that assure the primary electron beam reaches the diamond radiator and the electron dump. We believe these devices satisfy the Laboratory beam containment rules as well as the SLAC beam containment rules, where there are currently two “above ground” primary electron beams in operation. See Ref. [?].

#### Electron beam on diamond radiator

1. There should be a beam current monitor near the exit from the linac which will turn off the beam if the current exceeds the Hall D requirement.
2. The bend string, which brings the beam up from the accelerator and back to horizontal, must be in series on the same power supply.
3. The bend string power supply should be equipped with a “meter relay” which shuts off the primary beam if the supply current varies by  $\pm 10\%$  from its desired value.

4. Preceding the diamond radiator there should be a small aperture protection collimator with a burn-through monitor and a beam-loss detector, such as an ion chamber, which will shut off the beam if it hits the protection collimator.

### Electron beam on the dump

1. There should be a meter relay on the tagger magnet power supply to turn off the beam if the supply current varies by more than  $\pm 10\%$  from its desired value.
2. There should be a beam current monitor set to a low threshold in the photon beam line just downstream from the tagger magnet which will shut off the primary beam if it detects a charged beam in the photon line.
3. Following the current monitor there should be a permanent magnet to bend a charged beam downward.
4. There should be small aperture protection collimators with burn-through-monitors on either side of the permanent magnet with ion chambers or other type of beam loss detectors near the protection collimators.
5. There should be a beam current monitor just upstream of the 60 KW electron dump. This current reading can be compared to the current reading at the exit of the accelerator and shut off the beam if the readings differ by more than a few percent.

## A.3 Environmental and radiation concerns

The civil construction includes shielding for all buildings which is sized based on preliminary, but conservative, estimates of expected radiation doses. Guidance was provided by the original calculations by Lewis Keller, who has served as a consultant on this project. The Jlab RadCon group has refined his estimates using GEANT based simulations and a realistic geometry for the buildings.

### A.3.1 Site dose limits

**On-Site** The design goal at Jefferson Lab for a controlled area is 100 mrem/yr which may include occupancy as a factor and is based on guidelines from the Jefferson Lab RadCon Manual. Based on exposures of less than 2000 hours/yr, this sets an average dose limit of less than 50  $\mu$ rem/hour. There is also an instantaneous accident dose rate limit which is identified in the Jefferson Lab Beam Containment Policy as 15 rem/hour based on maximum credible beam loss conditions.

**Site boundary** The integrated dose limit at any point on the site boundary is 10 mrem/yr, or 2  $\mu$ rem/hour using an occupancy period of 5000 hours/yr.

### A.3.2 Beam on radiator

For the purpose of estimating dose rates, RadCon assumes that losses along the transport line are of order 0.1%. Following the vertical bends, two burn-through monitors with small apertures

preceding the radiator are needed. In addition there should be a 1-2 *m* steel wall downstream from the last vertical bend, as in the beam lines to existing halls. The surface is shielded from the tunnel by 4 *m* of earth. For comparison, we note that a similar vertical string configuration for the Hall B beamline is shielded by 2.3 *m* of earth.

### A.3.3 Tagger building

Jlab rules require that the instantaneous dose rate in occupied areas (outside the building) during a beam accident be less than 15 R/hr, assuming the beam will be turned off in less than 1 second. Using a safety factor of 10-15, it was determined that 4 *m* of earth was required for the shielding against photons and neutrons.

### A.3.4 Tagger hodoscope

Assuming the dump is 60 *m* from the hodoscope elements and that there is a 5 *cm* vacuum pipe leading to the dump, the neutron rate coming backward from the dump is  $3 \times 10^6$ /s, and the photon rate is  $0.9 \times 10^8$ /s for a 60 KW beam on the dump.

### A.3.5 Electron beam dump

The electron beam dump proper will be based on a design similar to the existing BSY 120 kW dump<sup>1</sup> at Jlab. Beam dumps with similar characteristics are in use at SLAC [?]. We have extensive operational experience with the BSY dump and detailed calculations [?] of neutron production and ground water activation for this geometry. This dump is designed so that all the primary beam energy is dumped in solid metal. The closed water circuit for cooling sees only thermal energy, not beam energy, and there is no hydrogen generation. The dump will require regular service, which can generally be performed from outside the building itself. The absorption of longitudinal showers, including muons, will be accomplished with the beam dump proper, aided by an additional 10 *m* of Fe downstream to insure containment. JLab requires that the dose rate must be less than 50  $\mu$ rem/hour in controlled areas. Therefore, the lateral containment of photons and neutrons resulting from the 60 KW beam, also requires 1 *m* of steel and 5 to 6 *m* of earth on the top and sides of the building.

### A.3.6 Collimator enclosure

Assuming a dose limit of 50  $\mu$ rem/hour outside the building, a 10 W photon beam, and a safety factor of 10, 1.0 *m* of steel is needed on the top and sides of the collimators for high-energy neutrons, and 1.7 *m* of earth or concrete is needed in the backward direction for the giant-resonance neutrons. The design and specifications of the photon beam are given in Chapter 4.

### A.3.7 Detector building

The calculations of radiation dose for the HALL D building and site boundary were modeled with a GEANT code used by the JLab RadCon group. The program has been tested favorably

---

<sup>1</sup>An identical dump is available, which is located in the north linac "stub" and was used in commissioning days, but must be removed during the construction of the HALL D transport tunnel. It has a closed circuit water system attached, along with steel shielding for neutrons.

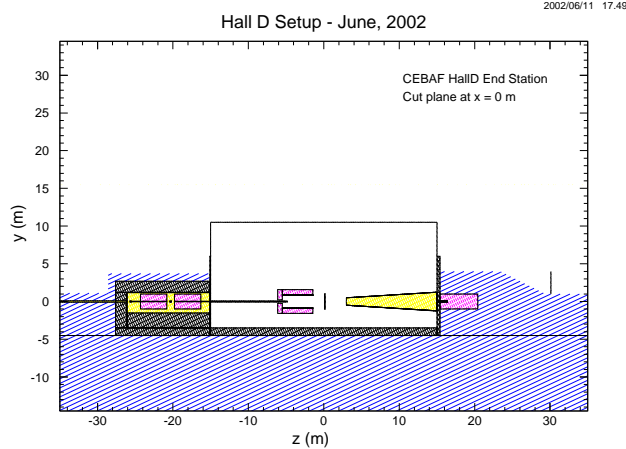


Figure A.2: Side view of the HALL D building and shielding. The upstream enclosure contains the photon collimator. The photon beam dump is downstream (right).

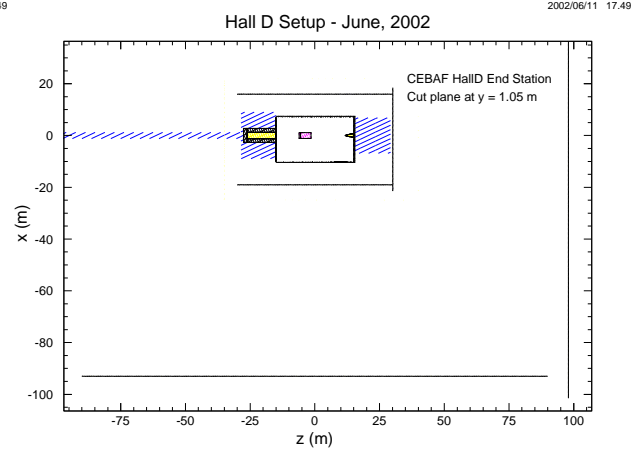


Figure A.3: Top view of shielding modeled in the simulations. Also shown are the scoring planes where radiation doses were recorded.

against data in existing experimental areas. The photon beam on target was generated using a  $1/E$  spectrum for the incoherent flux plus a coherent spectrum representative of a typical crystal radiator. The total power in the beam was 1.5 W, which corresponds to a tagged rate of  $10^8$  photons/s. The upstream collimator enclosure, where 10 W of the beam is deposited, is assumed to have sufficient shielding so that it does not contribute to the resulting dose rates. The model for the building and shielding are shown in Figs. ??-??.

The model for the HALL D building has concrete walls of different thickness from 10 cm upstream to 40 cm in the forward direction. The height of the walls is 5 m above the local grade level. Above the wall, we use a “tin box” construction of thin steel (0.6 mm thick walls; 0.8 mm thick roof). The target is 30 cm of liquid  $H_2$ , positioned inside the iron cylinder representing the coils and yoke, and the layers of lead representing the lead glass calorimeter (barrel portion, and forward portion). The photon beamline downstream of the detector is filled with He. The photon dump is 10 cm diameter and 1 m long hole in the dump iron. The truck ramp provides access to the building through a thin door. During accelerator operation, a fenced area is required 10 m from the truck ramp entrance.

The calculated radiation doses are shown in Fig. ?? for various locations around the building. In all cases the dose rates are dominated by low energy neutrons which are not completely shielded. The estimated average dose rates are 10  $\mu\text{rem/hr}$  in the Counting House, 20  $\mu\text{rem/hr}$  in the parking lot, 5-10  $\mu\text{rem/hr}$  15 m from the building, and 0.5  $\mu\text{rem/hr}$  at the site boundary.

The present solution appears to be acceptable both from the point of view of site boundary accumulated dose, and from the point of view of the dose rates around the building. The only additional safety measures would be the requirement to restrict access to the truck ramp area (if the entrance door is thin), and some restrictions on performing elevation work close to the Hall (roof of the counting house, light poles/fixtures, etc.)

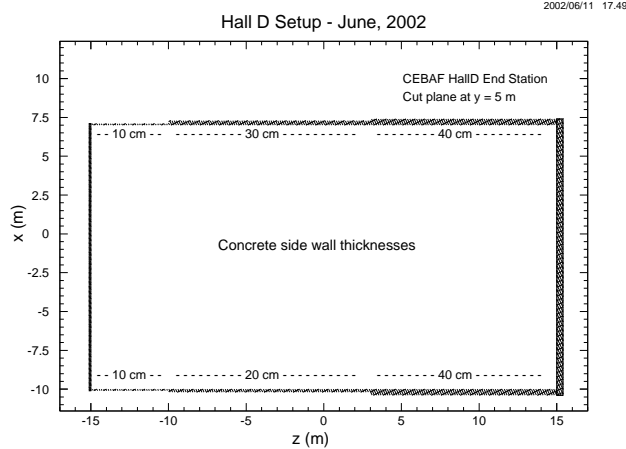


Figure A.4: Top view of the HALL D building showing the wall thickness used in the simulation.

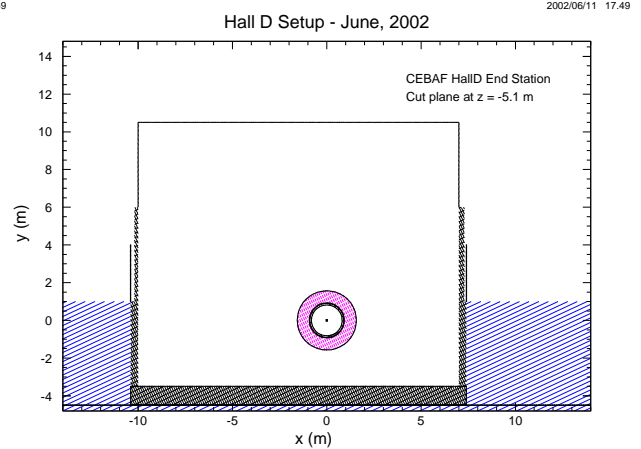


Figure A.5: Cross section of the HALL D building with the magnet.

### A.3.8 Photon beam dump

The photon beam dump is required to absorb up to 1.5 W of photons which survive collimation and are used for experiments in HALL D. The photon beam must be transmitted to the interior of the dump in order to minimize the flux of secondaries scattering back into HALL D. A few meters of steel is adequate to contain the residual muon production, covered by earth to stop neutrons. Most of the muons produced in the collimation enclosure are absorbed before entering HALL D [?, ?].

### A.3.9 Ground water activation

Based on the present design, there are no concerns about surface water, ground water, or soil activation in the vicinity of the end station itself. Any concerns for groundwater and soil activation are limited to the beam transport line up to and including the structures containing the photon tagger assembly and the electron beam dump. Procedures in place for current operation will be used to address these.

## A.4 Geotechnical analysis

Engineering Consulting Services, Ltd. has completed a subsurface exploration and geotechnical analysis to understand the foundation conditions for building construction for the Hall D site on the east end of the accelerator. Details of their findings can be found in their report [?]. We briefly summarize their work and review their conclusions which are of direct interest to the project.

Eleven borings were taken which covered the intended construction site. Each boring obtained nine samples down to a depth of 10 m. The samples were analyzed and classified according to the unified soil classification system. In Figure ?? we have summarized the composition of the soil from the samples. They indicate that the soil above the Yorktown Formation,

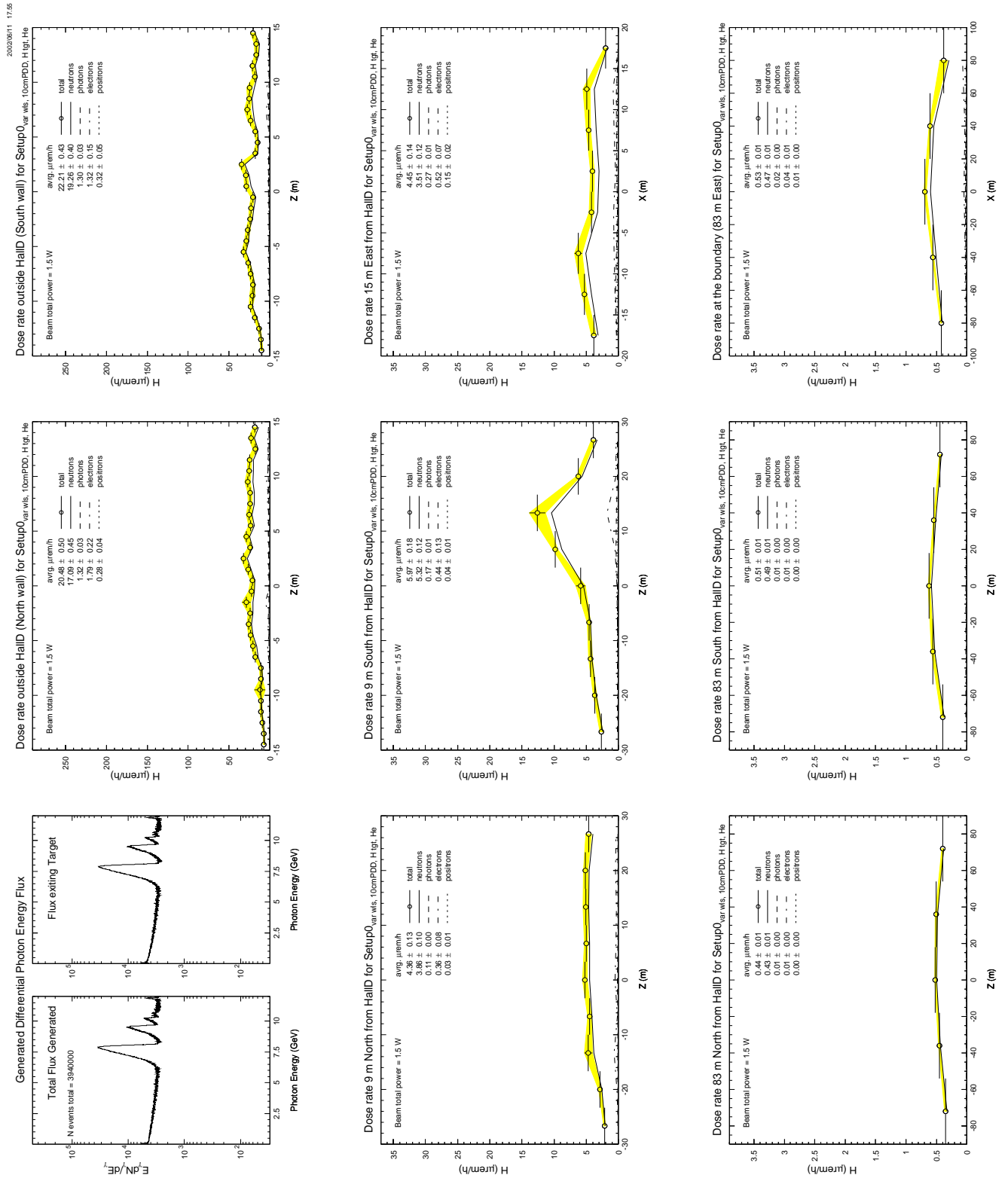


Figure A.6: Dose rates predicted by GEANT simulation code for various locations surrounding HALL D.

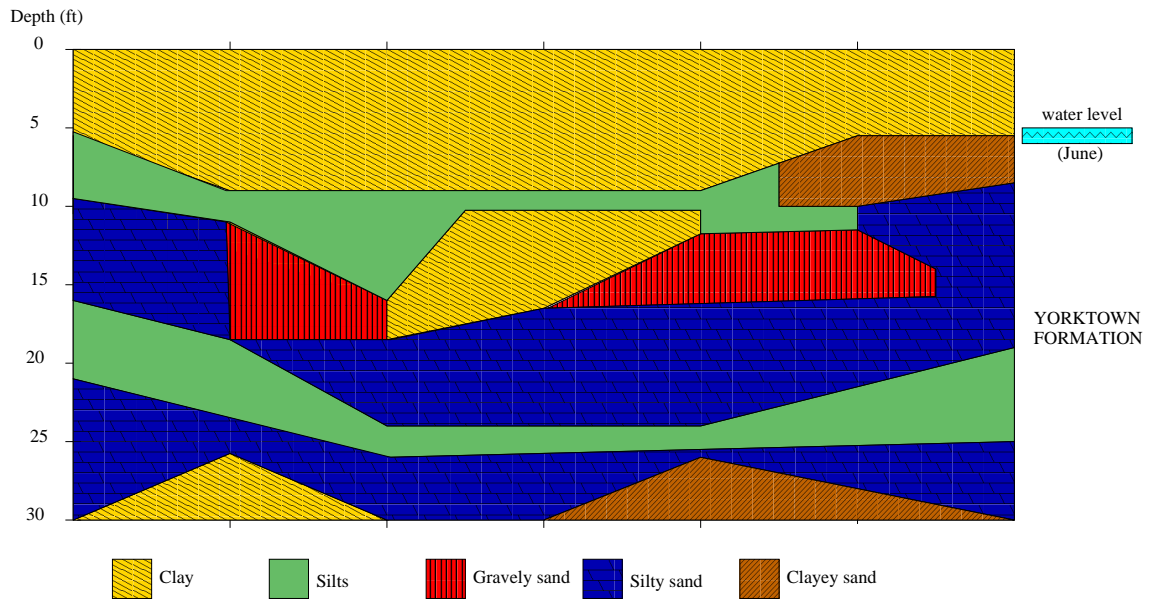


Figure A.7: Typical composition of soil under the HALL D construction site as a function of depth. Note that the horizontal dimension covers the distance from the accelerator to the building. The result of the geotechnical analysis shows that buildings at grade level will require support piles, driven approximately 15-20 *m* into the ground.

starting at depths of 5 to 6 *m* below grade, would not provide stable support for construction. The analysis shows that a mat foundation is an acceptable solution for the current design.

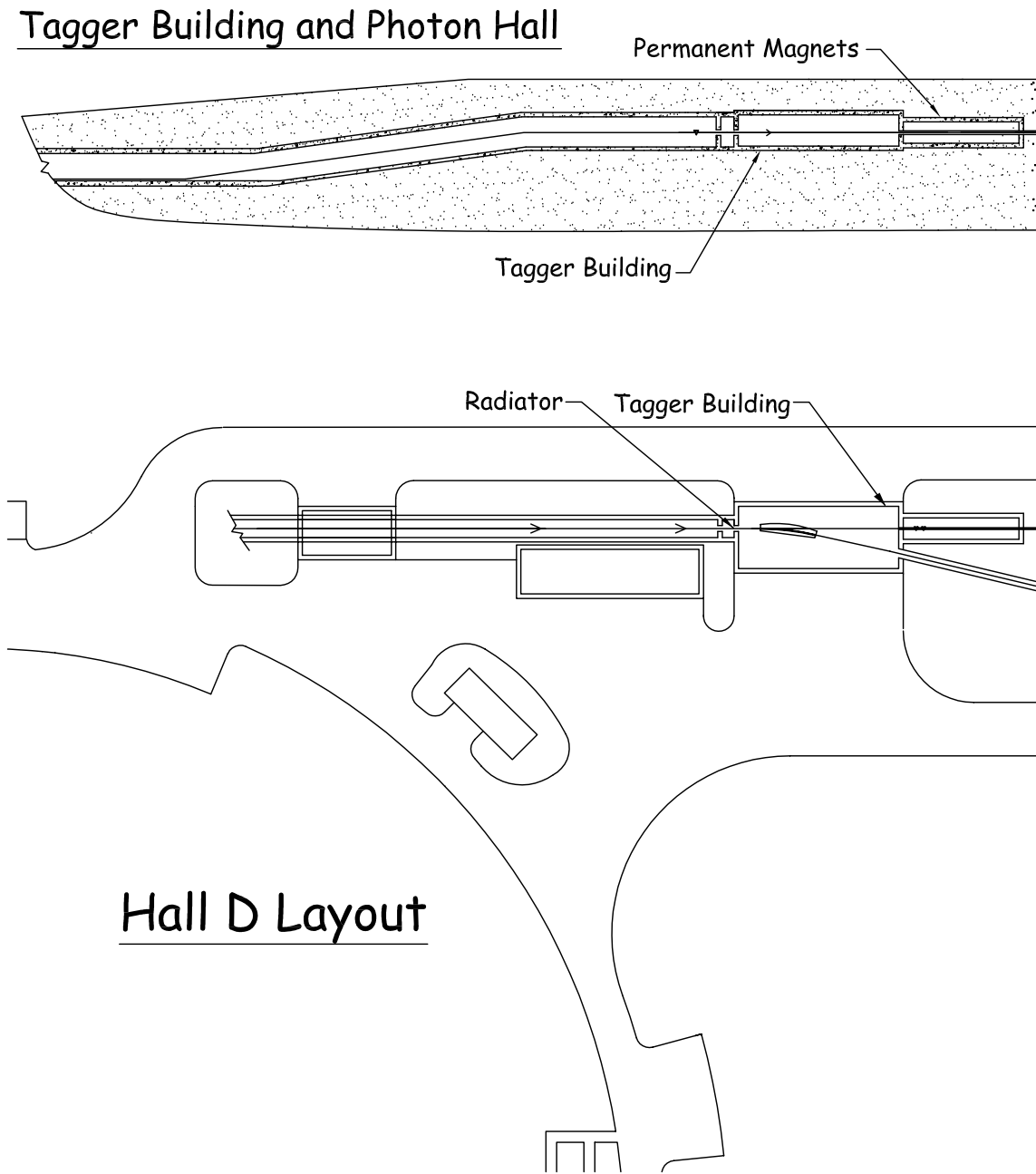


Figure A.8: Tagger building positioning

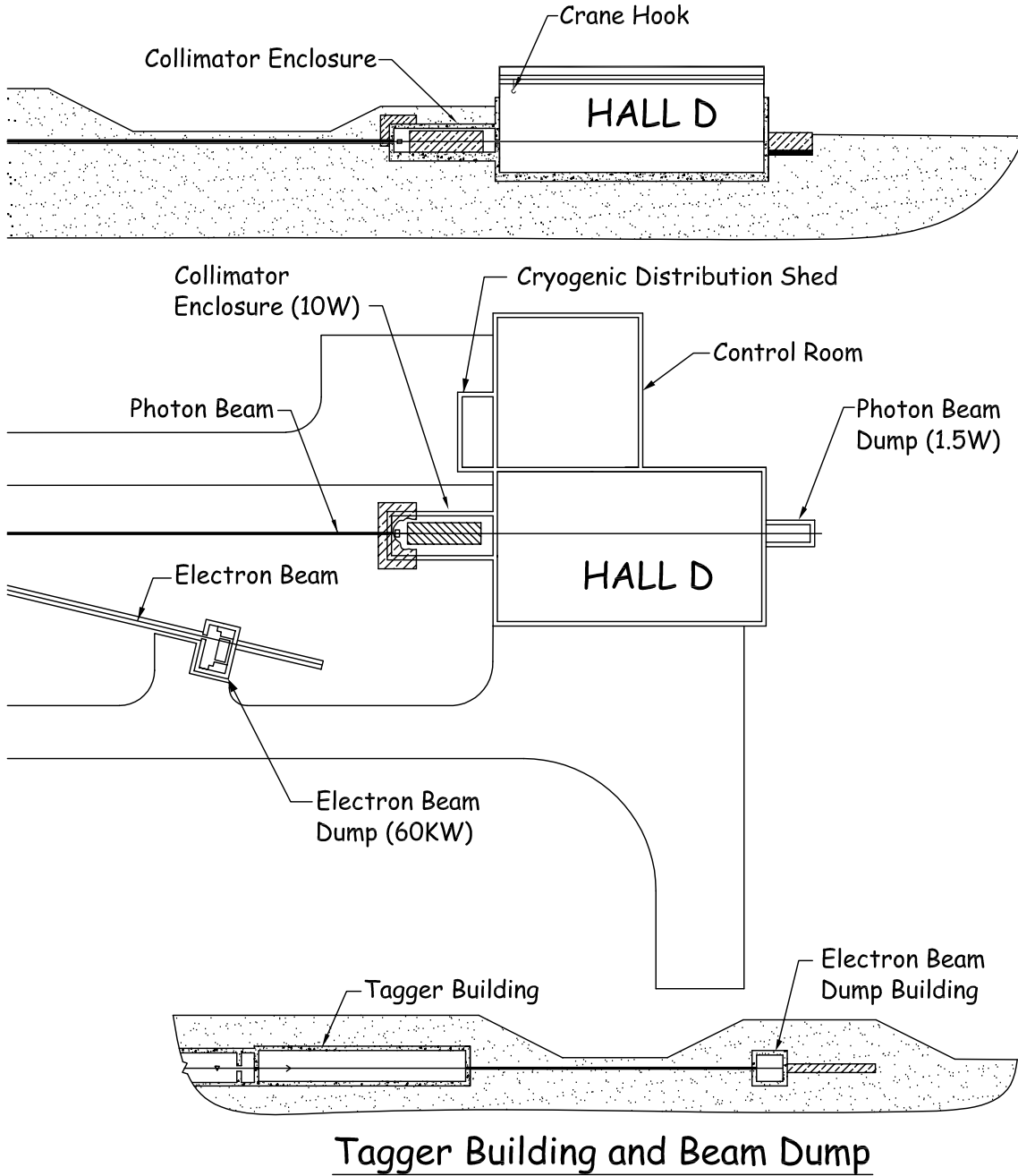


Figure A.9: Hall D building positioning